

Research@ARL

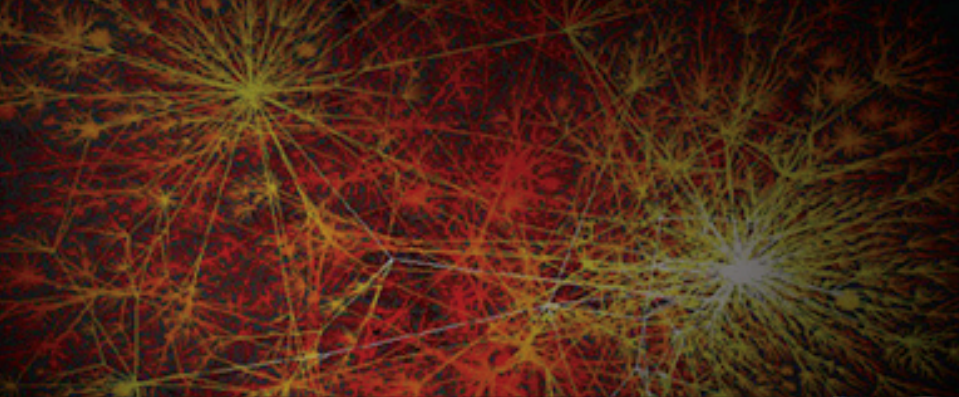
Volume 2, Issue 1, January 2013

Network Sciences

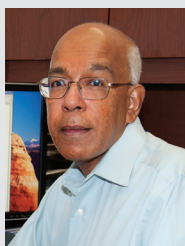


Dr. Ananthram Swami and Dr. Bruce J. West
Editors-in-Chief

U.S. Army Research Laboratory



Editorial Board



Dr. Ananthram Swami
Editor-in-Chief



Dr. Bruce J. West
Editor-in-Chief



Dr. Piotr J. Franaszczuk



Dr. Joseph N. Mait

Advisory Board

Dr. Kwong K. Choi

Dr. Brad E. Forch

Dr. Piotr J. Franaszczuk

Dr. Shashi P. Karna

Dr. Stephen J. Lee

Dr. Tomasz R. Letowski

Dr. Joseph N. Mait

Dr. James W. McCauley

Dr. Nasser M. Nasrabadi

Dr. Peter J. Reynolds

Dr. Paul H. Shen

Dr. Ananthram Swami

Dr. Bruce J. West

Research@**ARL** can be accessed electronically at www.arl.army.mil/ResearchARL

contents

Introduction to ARL

Foreword.....

John Pellegrino, Director (A)

Introduction to ARL Research in Network Sciences.....

Bruce J. West, Ananthram Swami, Joseph N. Mait, and Piotr J. Franaszczuk

Physical Sciences

A New Measure of Network Efficiency.....

Nicholas W. Hollingshad, Malgorzata Turalska, Paolo Allegrini, Bruce J. West, and Paolo Grigolini

Optimal Topology Control and Power Allocation for Minimum Energy Consumption in Consensus Networks.....

Stefania Sardellitti, Sergio Barbarossa, and Ananthram Swami

Efficient Extraction of Drainage Networks from Massive, Radar-Based Elevation Models with Least Cost Path Search

M. Metz, H. Mitasova, and R. S. Harmon

Connectivity of Heterogeneous Wireless Networks

Wei Ren, Qing Zhao, and Ananthram Swami

Life Sciences

Epileptic Seizures from Abnormal Networks: Why Some Seizures Defy Predictability.....

William S. Anderson, Feraz Azhar, Pawel Kudela, Gregory K. Berg, and Piotr J. Franaszczuk

Evolving Communicative Complexity: Insights from Rodents and Beyond.....

Kimberly A. Pollard and Daniel T. Blumstein

Combining the Finite Element Method with Structural Connectome-Based Analysis for Modeling Neurotrauma: Connectome Neurotrauma Mechanics

Reuben H. Kraft, Phillip Justin Mckee, Amy M. Dagro, and Scott T. Grafton

On Allometry Relations.....

Damien West and Bruce J. West

Social Sciences

Distributed Algorithms for Learning and Cognitive Medium Access with Logarithmic Regret.....

Animashree Anandkumar, Nithin Michael, Ao Kevin Tang, and Ananthram Swami

A Survey on Trust Management for Mobile Ad Hoc Networks

Jin-Hee Cho, Ananthram Swami, and Ing-Ray Chen

Temporal Complexity of the Order Parameter at the Phase Transition

Malgorzata Turalska, Bruce J. West, and Paolo Grigolini

Information Sciences

Noncoherent Physical-Layer Network Coding with FSK Modulation: Relay Receiver Design Issues.....

Matthew C. Valenti, Don Torrieri, and Terry Ferrett

Transmission of Information Between Complex Systems: $1/f$ Resonance

Gerardo Aquino, Mauro Bologna, Bruce J. West, and Paolo Grigolini

Robust Control for Mobility and Wireless Communication in Cyber-Physical Systems With Application to Robot Teams

Jonathan Fink, Alejandro Ribeiro, and Vijay Kumar

Biographies of ARL Authors

2

3

4

13

21

39

53

73

87

99

115

173

189

213

221

233

247

263

Introduction to ARL

The Army Research Laboratory of the U.S. Army Research, Development and Engineering Command (RDECOM) is the Army's corporate laboratory. ARL's research continuum focuses on basic and applied research (6.1 and 6.2) and survivability/lethality and human factors analysis (6.6). ARL also applies the extensive research and analysis tools developed in its direct mission program to support ongoing development and acquisition programs in the Army Research, Development and Engineering Centers (RDECs), Program Executive Offices (PEOs)/Program Manager (PM) Offices, and Industry. ARL has consistently provided the enabling technologies in many of the Army's most important weapons systems.

The Soldiers of today and tomorrow depend on us to deliver the scientific discoveries, technological advances, and the analyses that provide Warfighters with the capabilities to execute full-spectrum operations. ARL has Collaborative Technology Alliances in Micro Autonomous Systems and Technology, Robotics, Cognition and Neuroergonomics, and Network Science, an International Technology Alliance, and new Collaborative Research Alliances in Multiscale Multidisciplinary Modeling of Electronic Materials and Materials in Extreme Dynamic Environments. ARL's diverse assortment of unique facilities and dedicated workforce of government and private sector partners make up the largest source of world class integrated research and analysis in the Army.

ARL Mission

The mission of ARL is to "Provide the underpinning science, technology, and analysis that enable full-spectrum operations."

Our Vision

America's Laboratory for the Army: Many Minds, Many Capabilities, Single Focus on the Soldier

ARL's Organization

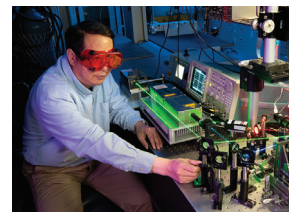
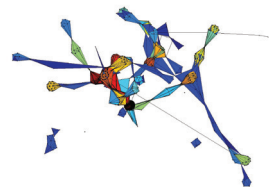
- Army Research Office (ARO) - Initiates the scientific and far reaching technological discoveries in extramural organizations: educational institutions, nonprofit organizations, and private industry.
- Computational and Information Sciences Directorate (CISD) - Scientific research and technology focused on information processing, network and communication sciences, information assurance, battlespace environments, and advanced computing that create, exploit, and harvest innovative technologies to enable knowledge superiority for the Warfighter.
- Human Research and Engineering Directorate (HRED) - Scientific research and technology directed toward optimizing Soldier performance and Soldier-machine interactions to maximize battlefield effectiveness and to ensure that Soldier performance requirements are adequately considered in technology development and system design.
- Sensors and Electron Devices Directorate (SEDD) - Scientific research and technology in electro-optic smart sensors, multifunction radio frequency (RF), autonomous sensing, power and energy, and signature management for reconnaissance, intelligence, surveillance, target acquisition (RISTA), fire control, guidance, fuzing, survivability, mobility, and lethality.
- Survivability/Lethality Analysis Directorate (SLAD) - Integrated survivability and lethality analysis of Army systems and technologies across the full spectrum of battlefield threats and environments as well as analysis tools, techniques, and methodologies.
- Vehicle Technology Directorate (VTD) - Scientific research and technology addressing propulsion, transmission, aeromechanics, structural engineering, and robotics technologies for both air and ground vehicles.
- Weapons and Materials Research Directorate (WMRD) - Scientific research and technology in the areas of weapons, protection, and materials to enhance the lethality and survivability of the Nation's ground forces.

ARL Workforce in 2013

- 1,971 Civilians - 41 Military
- 1,181 Research Performing Workforce
- 578 (49%) hold PhDs
- 13 STs / 26 ARL Fellows

ARL's Primary Sites

- Aberdeen Proving Ground, MD
- Adelphi Laboratory Center, MD
- White Sands Missile Range, NM
- Raleigh-Durham, NC
- Orlando, FL



Visit ARL's web site at www.arl.army.mil

Unique ARL facilities and modeling capabilities provide our scientists and engineers access to world-class research centers.

FOREWORD

Welcome to the second edition of the Research @ARL monograph series. In this edition, we share ARL's leading edge research in the Network Sciences. Today's society is more networked than ever before, and today's Army reflects that reality. However, the tools needed to understand the science of our interconnected global society are not yet fully developed. Many of the networks that touch our everyday lives, both in the Army and outside, are complex networks. They are often governed by local interactions and robust self-organization principles, leading to complex dynamics. And networks do not live in isolation; they are interconnected in surprising ways. A modern Army cannot function—any more than a modern city can—without the latticework of transportation systems, utilities, water and food distribution systems, communication webs, health care delivery organizations, and a myriad of other interconnected, complex networks. These layers of interpenetrating networks paint a picture of today's Army that overarches the traditional physical sciences, social sciences, life sciences, and information sciences. No one discipline or collection of disciplines can fully embrace the spectrum of complex problems that the engineered networking of humanity presents.



ARL's research program in the Network Sciences capitalizes on ARL's expertise in basic and applied research, ranging across a multitude of science areas, while simultaneously drawing upon the talents of others, nationally and internationally, through collaborative alliances with industry, laboratories, and academia. We seek to discover the underlying mathematical principles and universal laws that govern the behavior of co-evolving multi-genre networks. We also seek to understand emergent behavior in such networks, leading to mechanisms for thwarting or accelerating the emergence of interesting behaviors. Our research teams are examining the complex neurological networks within the human brain to determine how individuals make decisions and perform other cognitive tasks under varying levels of stress and uncertainty. The insight gained from this research is being applied to other biological networks to alleviate the injuries and pathologies encountered by the Warfighter. Exploration of cooperative behavior of social networks, such as swarms, is a significant research opportunity to control the mobility of collections of autonomous platforms. In addition to networks in the life and social sciences, ARL teams are examining the connectedness within and between communications and information networks to determine how their complex structures can best facilitate the gathering of intelligence and the formation of collective decisions.

As we investigate the fundamental science addressing these critical applications, we search for laws and principles of Network Science that parallel and compliment those in physics. Tentative principles are presently guiding the development of the mathematical infrastructure necessary for understanding those aspects of complex networks common to multiple phenomena appearing in a variety of scientific disciplines.

ARL's long term commitment to encompass interdisciplinary sciences in such diverse areas as vulnerability assessment, cognitive sciences, human sciences, electronic devices, weapons and materials sciences, information sciences, survivability, and lethality, uniquely positions our teams to investigate and discover previously unrealized commonalities to provide innovative solutions. Our discoveries enhance our country's technological capabilities, our national security, and, ultimately, enable the invincible Soldier of the future.

Dr. John Pellegrino
Director (A), U.S. Army Research Laboratory



Introduction to ARL Research in Network Sciences

B.J. West, A. Swami, J.N. Mait, and P.J. Franaszczuk

1 Army Research Laboratory: Network Science Program

The objective of the Network Science Program of the U.S. Army Research Laboratory (ARL) is to perform foundational research on network science (NS) leading to a fundamental understanding of the interplay within and among the physical, social/cognitive, information, and communication networks. This research is expected to lead to insights on how processes and parameters in one network affect and are affected by those in other networks. The underlying long-term goal is to optimize human performance and to greatly enhance speed and precision for complex networked military operations.

We define Network Science as the study of complex systems whose behavior and responses are determined by exchanges and interactions between subsystems across a possibly dynamic and usually poorly defined set of pathways. The fundamental components of a network are its structure (nodes and links or pathways) and its dynamics, which together specify the network's properties (functions and behaviors).

The Army is embarked upon an information age transformation loosely referred to as Network Centric Warfare (NCW) or Network Centric Operations (NCO). NCW/NCO seeks to dramatically increase mission effectiveness via robust networking for information sharing leading to shared situational awareness, improved collaboration and self-synchronization, and enhanced sustainability and speed of command [1, 2]. Central to this effort is an understanding of the interaction of networks in the physical, informational, cognitive, and social domains; thus, ARL's NS program directly supports NCW/NCO.

Society, as pointed out in the 2005 National Research Council (NRC) report *Network Science* [3], is more interconnected than it has been at any time in world history. A modern city could not function without garbage collection, sewers, electricity, transportation, water, health care, and food and fuel distribution, and would have a much different form without networks of education, banking, telephone service, and the Internet. Some of these activities form local physical or social networks within the city and their forms have been evolving for millennia. Part of that evolution was the development of their interoperability such that these networks are all interconnected and in one way or another they connect to ever-expanding global networks. These interconnections can lead to robustly coevolving networks, but under some conditions, can also lead to cascading failures. This corresponds to the first finding of the NRC report: "Networks enable the necessities and conveniences of modern life." These are the engineered networks of humanity, but there are comparable structures in the biosphere and ecosphere involving plant and animal networks of tremendous variety.

Moreover, our internal world is also an interlacing and interacting collection of networks. The neuronal network carrying the brain's signals to the body's physiological networks is even more complex than the modern city. The bio/eco-networks are certainly as difficult to understand as the physical/social-networks. This led to another finding in the NRC report: "Social and biological networks bear important similarities to engineered networks." Herein we present a number of studies carried out by ARL scientists in collaboration with the broader scientific community to further our understanding of NS. These studies suggest how these similarities might be exploited for the development of NS that is of value to society in general and to the United States Army in particular.

The insights and mathematical characterizations resulting from ARL's NS research will enable us to achieve this underlying goal, by providing the ability to predict and control the individual and composite behavior of the complex interacting physical, communications, information, and social/cognitive networks. Network science is one of ARL's strategic technology investment areas, with a strong program based on the modern research pillars of theory, simulation, emulation, and experimentation. It encompasses a variety of transdisciplinary basic and applied programs across ARL's core competency areas that include close collaborations with academic, military, and industrial research partners throughout the US and internationally. These include ARL's Network Science Collaborative Technology Alliance (CTA), the US-UK Network and Information Sciences International Technology Alliance (ITA), the Micro Autonomous Systems & Technology CTA, the Cognition & Neuroergonomics CTA, and several Multidisciplinary University Research Initiatives (MURIs). The Institute for Collaborative Biotechnology is a University Affiliated Research Center (UARC) that approaches networks from the perspective of biological systems, and ARL's Mobile Network Modeling Institute (MNMI) is an applied research effort that seeks to further the science by enabling full fidelity at-scale modeling and simulation of large scale heterogeneous networks, incorporating live assets in the emulation environment. More information on these programs may be found by navigating ARL's Collaborative Technology and Research Alliances website at <http://www.arl.army.mil/www/default.cfm?page=93>.

The taxonomy of the ARL research efforts in NS can take a number of forms, two of which are given here. To set the stage for the scientific problems, we summarize four grand challenges and identify the Army programs conducting research to address these challenges. A separate and distinct way of organizing the research is via the network category addressed. The individual research papers are identified in this latter grouping according to discipline.

2 Grand Challenges

The ARL research effort in NS seeks to make fundamental advances of and contributions to the science so as to enable the a priori prediction of the behaviors of complex interacting networks in diverse and dynamic environments and an understanding of the design trade-offs and the impacts of various technologies under a wide variety of dynamic and adverse conditions. Moreover, it is intended to quantify the impact of network technologies both technically and operationally to make informed acquisition decisions.

2.1 Underpinning Mathematical Framework: Dynamic Multiple-Scale, Cross-Genre Coupling

Multiple-scale and cross-scale couplings within and across networks are recurrent themes in the study of complex physical, communication, informational, social, and biological networks. Existing formalisms address one, two, or a continuum of scales, but the multi-node problem remains unsolved. Existing mathematical approaches offer insights into the quantitative aspects of complex phenomena with multiple scales (no characteristic scale) in stationary and near equilibrium networks, but what is needed now is a way to describe the dynamics of such complex phenomena/networks when the underlying processes are neither stationary nor near equilibrium [4]. Network characteristics cannot be deduced from the properties of individual components; they emerge during the formation and growth of the network. Consequently a mathematical framework is needed to characterize the interactions between the dynamic network components, the temporal evolution of the network, and its response to external stimuli, including attacks. The framework must take into account heterogeneity, non-stationarity, even non-ergodicity, as well as conflicting constraints and objectives.

One way to characterize the interaction of networks is by understanding how information is propagated within and across complex adaptive networks — how information, in a general sense, flows across networks so as to maximize utility (e.g., as perceived by a decision maker) under constraints, such as timeliness and resource usage. Tools from statistical physics such as continuum percolation theory, stochastic geometry, and modern statistics are used to deal with non-Markovian behaviors, heavy-tailed phenomena, and the mutual interactions between networks. To cope with multiple potentially conflicting constraints and objectives, a generalized control theory of locally reacting multiple agents needs to be developed, perhaps through the mimicking of self-repair and replication identified in biological networks.

2.2 Human Metrics in Complex Networks

A critical element in realizing the vision of Network-Centric Operations (NCO) is that the distributed decision making process must take into account the human dimension in its elements including decision-makers, data and information sources, processed information, communication network elements, etc. The measure or metric of the human dimension must be derived in a distributed fashion; in time-critical and stressful situations; in environments where node capture and subversion are likely; where the underlying communications network is resource-constrained, mobile, and dynamic; and where decision-makers' reliance on and compliance with an information network are subject to numerous internal and external influences. Key barriers include the limited understanding of network-of-networks, composability of heterogeneous networks, and a limited understanding of how the context (e.g., trust and risk) is analytically derived from variously distributed sources of evidence.

A key aspect of a common quantitative framework is an approach for representing uncertainty (probability theory, possibility theory, evidence theory, subjective logic, argumentation theory, or other). Development of metrics is a key issue: metrics that take into account the value of information and human intentions are important in information and C2 networks. Relations between and among these metrics need to be clarified along with the development of a mathematics of network classes. A specific example is the trust metric. The scientific challenge is to understand the different definitions and dimensions of trust, for example, in socio-cognitive and communications networks, and from that understanding develop a composite trust metric. Rather than merely treating the interaction via a simple interface or utility function offered by one network to another, network interactions must be taken into account, as well as the context- and time-varying nature of the trust metric components. Encapsulation of these sub-components as a scalar metric is challenging due to the conflicting nature of the components and the non-convexity of useful metrics. To quantify human performance in networks, measurable features of data from different networks need to be identified to enable the modeling of network complexity and the interactions between different networks.

2.3 Abstracting Common Concepts Across Fields

A set of common concepts for network science that is defined consistently across the various scientific disciplines does not exist. There are discipline-specific nomenclatures that have been developed for specialized needs, but the equivalence of these terminologies for a discipline-independent characterization of networks has not been established. The mathematical formulation of these empirically-based concepts will provide a nascent language for network science.

Mathematical rigor across the component disciplines is promoted by focusing on ubiquitous aspects of the underlying complex networks, such as the appearance of non-stationary, non-ergodic, and non-renewal statistical processes. These properties are manifest through the empirical inverse power-law (IPL) probability density functions (pdf) that appear in physical, social, biological, economic, and physiological networks. Tools from non-equilibrium statistical physics and non-equilibrium information theory are used as well. To understand and facilitate network agility and adaptability, new techniques, methodologies, and analyses from a multi-disciplinary approach have been and will continue to be combined with the application of powerful modeling and simulation to explore the dynamics of networks. High-fidelity simulation, emulation, and experiments for large-scale dynamic networks — based on complexity-performance trades and incorporation of live assets in an emulation environment — will provide us the ability to understand the complicated interactions between large-scale heterogeneous networks.

3 Taxonomy by Discipline

NS is unlike traditional scientific disciplines in that it identifies a particular structure, that of a network, as the basis for the science. Since structural webbing exists within and among all scientific disciplines, the over-arching goal of NS is to develop a body of principles that will enable modeling, design, analysis, prediction, and control of the behavior of the underlying phenomena in the physical (sensors, wireless web), information (communications, knowledge management), social (people, organizations, cultures), and cognitive (perceptions, beliefs, decision-making) sciences, to name only a few. The emphasis is not restricted to the network structure within a given discipline, but is focused on networked phenomena that encompass many disciplines as well as how such complex networks interact with one another. As a nascent science, the underlying principles are still missing, so the grand challenge for this effort is to create and organize the fundamental knowledge upon which to base these principles. Moreover, NS is intended to bridge the knowledge gap between disciplines and breakdown the artificial barriers that have been created between disciplines.

We have partitioned the scientific papers into four sections, each corresponding to a different category of disciplines: the physical sciences, the life sciences, the social sciences and the information sciences. This partitioning is intended to direct the reader to that area of investigation with which s/he is most comfortable. On the other hand, this opening narrative is intended to suggest that NS is more than just a thematic thread that weaves its way through each of the sections; it is intended as an over-arching perspective that encompasses the traditional disciplines. However, in the rush to discuss the tangible aspects of science, the fieldable products of technology, and the immediate needs of the Army, the network view so crucial to the scientific enterprise is often overlooked. It is emphasized here because, like the scientific barrier of complexity, it often represents the problem we would like to solve, but do not know how.

3.1 Physical Sciences

Physics has been the paradigm of science since the time of Newton. Consequently, when investigators wanted to emphasize the use of quantitative methods in their studies, they appended the suffix physics. In the 19th century this strategy resulted in sociology giving rise to sociophysics, psychology spawning psychophysics and biology producing biophysics. Of course, there were also a number of physicists speculating on the use of their techniques to understand non-physical phenomena. As a result, new disciplines evolved at the boundary between previously established disciplines. This way of extending the frontiers of disciplinary science proceeded into the 20th century, producing biochemistry, bioengineering, social engineering, econophysics, and so on. But it was the successes of the mathematical methods of physics that attracted the most attention.

The existence of an empirical law or principle from which the dynamics of a physical system can be determined appears almost mystical when trying to understand cognition or decision making. The 19th century physicists and applied mathematicians were able to take the conservation of energy and from that statement determine the laws of motion for any mechanical system. Such variational calculations in the hands of more practical people subsequently produced control theory and the dynamics of non-mechanical systems consistent with a set of imposed constraints.

Sardellitti and Barbarossa of Sapienza–University of Rome collaborated with Swami of ARL on, “Optimal Topology Control and Power Allocation for Minimum Energy Consumption in Consensus Networks” (page 21), to design a network topology that optimizes the spread of information, exemplified by the computation of globally relevant statistics by exploiting only local

communication among the sensors in a wireless network. As in all design problems, there is a function to be carried out by the network while simultaneously satisfying a given constraint such as maximizing efficiency or minimizing energy consumption. Is the optimal topology sparse or dense? The research of Sardellitti et al. was concerned with minimizing energy use; the paper of Hollingshad et al., discussed later, was concerned with network efficiency, “A New Measure of Network Efficiency” (page 13). Sardellitti et al. developed a method for optimizing the network topology and the power allocation across every link in order to minimize the energy necessary to achieve consensus across the sensor network. Since the topology is the result of optimization, this is a non-deterministic polynomial time (NP) combinatorial problem which the authors circumvent by means of a clever relaxation procedure.

Another approach to handling network complexity is by recognizing that the elements comprising a fighting force are interlinked to such a high degree that changing a single component influences and modifies the response of every other component in the network. Furthermore, each element in the network is itself a network and must be treated as such. This observation does not in itself contribute anything new to the discussion. It has been known since the first recorded wars that small changes in tactics and strategy can lead to overwhelming changes in outcome. This recognition has sometimes led to inaction, because the outcome of any action is unpredictable. What is new about the networking concept is the attempt to formalize the interactions so as to make the response to change predictable. New methods, such as nonlinear dynamics theory and chaos, have enabled us to determine the boundaries of predictability in apparently random dynamic processes, so we can realistically assess what we can and cannot know about a particular network. But it all goes back to the individual Soldier, situational awareness, and leadership involving the synthesis of information in real time.

The research group consisting of Hollingshad, Turalska, and Grigolini at the University of North Texas; Allegrini from the University of Pisa; and West from ARL collaborated on constructing, “A New Measure of Network Efficiency” (page 13). They address the dynamical origin of the scale-free probability distribution function (pdf) and, consequently, the related issue of network topology. Here again, the local interactions are found to determine the global properties of the network, using a nonlinear mathematical model with nearest neighbor interactions on a two-dimensional lattice. The network dynamics undergo a phase transition at a critical value of the control parameter, thereby inducing long-range correlations among the members of the network. The researchers determine that the distribution of links favoring long-range connections increases the efficiency of information transfer, which becomes optimally efficient when the IPL index for the degree pdf is one. They attribute this to the role of network leadership being transient, with the rank differences between the most-linked and least-linked nodes being temporary and over time the highest rank is shared by all members of the network. The full implications of this insight remain to be explored.

A fundamental difficulty with the concept of networking networks, such as nature has done within the human body or as applied to material structures, is related to the multiple scale and multi-physics requirements, as seen, for example, in electronic networks. If all physics were known and we had the necessary mathematical tools, we could model the ultimate performance of any physical network given the atomic composition of the parts. Quantum physics would enable atomic and nano-scale properties to be captured and parameterized yielding the electronic, thermal, and mechanical attributes of materials. From this ability to effectively couple across scales, we could eventually determine the capabilities and performance of multifunctional networks interrelating sensor, information, and communication capabilities. We could do this without fabricating network components, and we could achieve optimization at a level of sophistication that is beyond our wildest dreams using current technology and network development. On the other hand, it seems unreasonable to model every atom and electron in a physical network, yet the atomic level properties affect the composite performance and, therefore, cannot be neglected. At criticality, the smallest fluctuations are often amplified to the macroscopic level and, therefore, contain information on the nature of the large-scale network.

Ren and Zhao of the University of California, Davis have collaborated with Swami of ARL on, “Connectivity of Heterogeneous Wireless Networks” (page 53). This research results in a better understanding of the spatial connectivity of one heterogeneous network (secondary) embedded within another (primary); the heterogeneity is modeled using Poisson statistics for the ad hoc network. The analysis is done using percolation theory, which was initiated in statistical physics and has since developed into its own branch of mathematics. Percolation theory is a natural method for answering the question of whether the secondary network can be connected, i.e., when can a message be transmitted across the entire network without disruption? The researchers establish that when the density of the primary transmitters is beyond a certain level, there are simply not enough spectrum opportunities for any secondary network to be connected. The design parameters are the interference tolerances of the primary and secondary Poisson distributed networks and are used to design the optimal transmission power of the secondary network based on that of the primary. Consequently, the connectivity of large-scale ad hoc heterogeneous wireless networks are expressed in terms of the occurrence of the percolation phenomenon. It turns out that matching the interference ranges of the primary and secondary networks maximizes the tolerance of the secondary network to the primary traffic load. Since the tolerable interference range is an indicator of the receiver’s sophistication, this can be interpreted as an instance of the complexity matching principle discussed in, “Transmission of Information Between Complex Systems: I/f Resonance” (page

233), and “Temporal Complexity of the Order Parameter at the Phase Transition” (page 213).

A systematic procedure based on multiple models at different scales with representations at adjacent scales linked to each other by defined parameterized interfaces that can be calibrated to measurement is one reasonable approach to multi-scale modeling. This is done today through a combination of deterministic and stochastic modeling, where the smaller scales give rise to statistical uncertainty at the larger scales. Thus multi-scale modeling involves multiple organizations and disciplines leading to multiple, seemingly incompatible approaches. One school of thought believes it essential that an object-oriented approach be followed, meaning in this context that there are well defined interfaces to models capturing a particular scale and that the various scales are captured, most likely, by stand-alone programs. This multi-scale modeling is a grand scientific/engineering challenge for Army research.

Metz at the University of Ulm; Mitasova at North Carolina State University; and Harmon at ARL collaborated on, “Efficient Extraction of Drainage Networks from Massive, Radar-Based Elevation Models with Least Cost Path Search” (page 39). They use a least-cost drainage path (LCP) search methodology to significantly improve the accuracy of stream mapping, especially in remote, hard to reach regions and those that can be mapped with massive data sets. The LCP search methods were designed to find the shortest or fastest route from a starting point to a given destination. The success in extracting reliable drainage networks from massive radar-based data sets indicates that nature must optimize a cost function over geophysical time scales in direct analogy to the variation in total energy determining the dynamics of mechanical systems. Here the cost is interpreted in terms of local elevation and the least-cost path is minimal elevation contour.

3.2 Life Sciences

Complex networks in the life sciences generate patterns that have been summarized in a number of empirical relations. In physics we have Ohm’s law, the perfect gas law, and other empirical relations among the variables describing the physical process. These “laws” are, of course, phenomenological rules developed to summarize what has been observed experimentally and that were eventually derived using fundamental theory. In more complex living networks, equally simple rules have been uncovered that typically relate a particular function to the size of an organism, as first observed in biology some two hundred years ago. The first such expression related the mass of an animal’s brain to its total body mass, using mass as a measure of size and giving rise to the nomenclature of allometry relation (AR). Allometry, literally meaning by a different measure, has been defined as the study of body size and its consequences both within a given organism and between species in a given taxon.

The history of ARs is presented by West at Renesselaer Polytechnique Institute and West at ARL, who critiqued the various attempts to construct the theory underlying the scaling observed in ARs in, “On Allometry Relations” (page 115). ARs are critically important because they set the boundary conditions that network models must satisfy in order to be compatible with existing data. For example, the fractal network nutrient transport model used to successfully derive the metabolic AR is one of the network applications reviewed.

Another emerging application of network theory is in analyzing interactions and relationships in groups of animals and/or humans. The network science methodology allows for better understanding of the complexity of interactions and communications between individuals in groups. The review by Pollard, formerly at the University of California, Los Angeles and now with ARL, and Blumstein at ARL, “Evolving Communicative Complexity: Insights from Rodents and Beyond” (page 87), discusses the relationship between social interactions and communication patterns, and how focused studies of communicative complexity can better untangle the underlying evolutionary relationships. The functional relationship between attributes of social complexity and attributes of communicative complexity allow for a better understanding of how socialization and communication evolve.

The importance of interactions in neural networks for understanding of the operation of the brain has been recognized for a long time. However, only recently have advances in theoretical, experimental, and computational approaches to the study of neural networks begun to reveal fundamental principles of brain structure and function. There is emerging consensus among neuroscientists that traditional approaches concentrating on identifying brain structures responsible for specific functions and behavior need to be expanded to include investigations of interactions between these structures. New brain imaging techniques allow for more precise identification of neural tracts connecting different regions of the brain, providing information necessary for creation of the structural connectome network of an individual brain. This allows for analyzing and interpreting characteristic features in different individuals as well as identifying abnormalities caused by neurotrauma. The article by Kraft, McKee, and Dagro at ARL in collaboration with Grafton at the University of California, Santa Barbara, “Combining the Finite Element Method with Structural Connectome-Based Analysis for Modeling Neurotrauma: Connectome Neurotrauma Mechanics” (page 99), presents a novel approach to analysis and interpretation of structural connectome obtained from MRI images by constructing a finite element model (FEM) informed by experimental data at a cellular level. This approach integrates brain injury biomechanics and graph theoretical analysis of neuronal connections to form a computational model capturing spatiotemporal characteristics

of trauma. Time evolving simulations of the trauma investigated in this study show how brain network measures of global and local efficiency are degrading in time after trauma. This approach provides a basis for quantitative analysis tools for interpretation of neuroimaging data. Computational models based on theoretical analysis of neural network connections could help inform subsequent analysis of functional networks.

Neural network models based on neurophysiological properties of neurons provide insight into functional relationships between different brain structures. In recent years, due to increased computational capabilities, it has become possible to model larger networks composed of more realistic neurons. This allows for more realistic simulations of normal and/or pathological brain function, which can be directly compared with experimental or even clinical measurements. The article by Anderson, Azhar, Kudela, and Bergey at Johns Hopkins University in collaboration with Franaszczuk at ARL, “Epileptic Seizures from Abnormal Networks: Why Some Seizures Defy Predictability” (page 73), illustrates how this modeling approach can provide some insights into observed but difficult to interpret phenomena within the human brain. Epileptic seizures are the pathological activity of the brain disrupting the normal activity of an afflicted subject. While a seizure usually lasts only for a relatively short period of time (1-2 minutes), its unpredictability causes significant disruption in the life of the subject and may even cause serious injury due to associated loss of consciousness and body control. There is limited opportunity to record data associated with epileptic seizures. Even during hospitalization, patients may have as few as one or two seizures during an entire week. The computationally realistic modeling allows for investigation of multiple simulated seizures with full control of critical parameters. In Anderson et al., the authors created a computational model of the cortex consisting of more than 60,000 spiking neurons of several types based on histological data. Analysis of simulations of neuronal activity in this model suggest that, in the region of the cortex, with abnormal connectivity analogous to seizure focus in the human brain, it is possible to initiate seizure activity with random fluctuations of input from the surrounding cortical regions. This mechanism helps explain the difficulty in predicting partial seizures in some patients and suggests that intervention not only in the seizure focus area, but also in surrounding areas, may be necessary to prevent seizures from occurring.

The continuing research at ARL is directed toward combining the structural modeling of brain networks, “Combining the Finite Element Method with Structural Connectome-Based Analysis for Modeling Neurotrauma: Connectome Neurotrauma Mechanics” (page 99), with neurophysiological models similar to those presented in “Epileptic Seizures from Abnormal Networks: Why Some Seizures Defy Predictability” (page 73) to create a more complete model of brain neural networks.

The diverse applications of network-based or inspired studies in life sciences presented here show that the network sciences concepts and methodology provide a useful conceptual platform for description and analysis of various phenomena and processes. However, we are in the early stages of applying NS concepts to the various life sciences. Development of more specific mathematical and computational tools is required, but the future applications are limitless.

3.3 Social Sciences

In tactical networks, distributed decision making should take into account trust in the elements: the sources of information, the processors of information, the elements of the communications network (both radio and other) across which the information is transmitted, etc. This trust must often be derived under time-critical conditions, and in a distributed way. It must account for the uncertain provenance of the data, including the fact that information sources and relays in a tactical network are subject to subversion. Trust is a critical element of networked interactions, including interactions between humans and agents, that may be direct or computer-mediated. Trust and reputation are becoming increasingly important due to the explosive growth in electronically mediated social interactions, often with sometimes correspondingly weakened social control. Trust is a multi-faceted concept and depends upon the context, the trustor, the environment, the infrastructure, and the mediating agents or relays. Trust is a critical element of modeling team, group, squad, and company behaviors. It must be taken into account in promoting group cohesiveness and effective problem-solving, and it must be adequately modeled in quantifying the tension and trade-off between individual utility and group welfare. Technology can enhance as well as weaken trust relationships. Currently used models of trust do not adequately capture critical elements of human trust (such as lack of transitivity, symmetry, and reciprocity, which calls for novel mathematical tools). Managing trust in such an environment is challenging. Cho and Swami from ARL collaborated with Chen from Virginia Tech on the paper, “A Survey of Trust Management in Mobile Ad Hoc Networks” (page 189), which addresses some of these challenges. It discusses the concepts and properties of trust pertinent to the constituent elements of a tactical network and proposes composite trust metrics that take into account the interaction between the constituent networks, the resource constraints, and the mission goals. This comprehensive survey discusses the differences between trust and trustworthiness, trust and risk, and trust management schemes.

How can one maximize rewards in an unknown environment? Learning is clearly a crucial element here. There are two important performance criteria to assess the efficacy of learning: consistency and regret bounds. A learning algorithm is consistent if the learned estimates asymptotically converge (in some sense) to the true values. Regret is a measure of the speed of convergence,

the time-averaged loss in performance compared with that obtained by a genie. Anandkumar from the University of California, Irvine, and Michael and Tang from Cornell University collaborated with Swami from ARL on aspects of this problem in the paper, “Distributed Algorithms for Learning and Cognitive Medium Access with Logarithmic Regret” (page 173). The scenario they considered is related to the problem studied in “Connectivity of Heterogeneous Wireless Networks” (page 53). They consider the problem of so-called secondary users learning the unknown rewards (perhaps rates) obtained by accessing a set of channels. They consider a distributed framework where there is no information exchange or prior agreement among the secondary users. This introduces additional challenges: First, one can expect loss of performance due to collisions among users. Second, there is competition since all the secondary users are vying to access channels with the highest rewards. Using the theory of multi-armed bandits, they analyze the trade-off between exploration and exploitation and between cooperation and competition. They propose an order optimal distributed learning and access policy that minimizes the regret. An important notion here is that one must learn from mistakes (collisions and sensing that may be imperfect) and that one can never stop learning (one must continue to explore).

Cooperative interactions can lead to phase transitions and the emergence of spatial and network complexity in many systems. The Ising model has been used to model phase transitions in a variety of phenomena, including ferromagnetism, biological and neurophysiological processes, the flocking of birds, econophysics, etc. But the temporal complexity of such networks had not been explored until recently. Turalska and Grigolini from the University of North Texas collaborated with West of ARL on the paper, “Temporal Complexity of the Order Parameter at the Phase Transition” (page 213), which explores the temporal complexity issue. They study a decision making model in which the time intervals between significant events has a power-law distribution, which they show is equivalent to a two-dimensional Ising model. The underlying process is a renewal process, but it is non-stationary and exhibits long-term correlations. Thus the fundamental property of ergodicity no longer holds, and new mathematical tools are required to analyze these non-Poisson renewal processes. The researchers establish that phase transition leads to temporal complexity as manifested by non-stationary and non-ergodic fluctuations. They argue that this is a basis for complexity matching, a notion elaborated on in, “Transmission of Information Between Complex Systems: 1/f Resonance” (page 233). The pair of papers, “Temporal Complexity of the Order Parameter at the Phase Transition” (page 213) and “Transmission of Information Between Complex Systems: 1/f Resonance” (page 233) indicate that information can be transferred between networks via extremely weak coupling, provided that the complexity of the two networks is matched (in the sense that a form of resonance exists). The concepts of complexity management and complexity matching are likely to find wide applicability in NS.

3.4 Information Sciences

In the social and life sciences, network discovery has led to increased understanding of how the brain works and how information propagates in communities of people. In the information sciences, one wishes to create a physical network that enables communication between entities, either person-to-person, person-to-machine, or machine-to-machine. Design of the physical network must account for the manner and the environment in which the network will be used.

In most non-military situations, the backbone of this network is fixed, for example, through cell towers. Senders and receivers are tethered to the backbone, that is, fixed spatially and hard-wired, or untethered, physically mobile, and wirelessly connected. However, in the environments in which the military operates, designers cannot expect a wireless infrastructure to be available for use. Thus, military units must be capable of establishing and maintaining their own network, which is a challenge during mobile operations. It is even more of a challenge when nodes on the network are small, autonomously mobile platforms operating on city streets and inside buildings, where floor plans and building materials affect the viability of links between nodes.

The use of multiple autonomous platforms is inspired by bionetworks in nature such as insect swarms. Although each single entity in a swarm has limited intelligence, the swarm appears to behave with intent when the entities function in concert. Consider the behavior of social insects, such as bees and ants. Fish and birds are other examples of animals whose collective behavior belies their limited intelligence. Although this analogy is intellectually appealing, differences exist between bionetworks and networks of autonomous mobile platforms that make it difficult to implement. Bionetworks, for example, swarm for survival, either to seek food or provide protection. In our grandest vision, swarms of autonomous platforms will exhibit complex behavior, such as intelligence or sentience through “situational awareness.” Further, communication within animal swarms occurs through proximity, e.g., ants touching antennae or following a chemical trail, line-of-sight vision, or sound. Put simply, biological swarms communicate simple messages primitively to perform primitive behaviors, whereas our vision of autonomous platforms requires complex messaging to achieve complex behaviors.

Given the present state of technology, a better analogy may be a shepherd herding sheep using a sheep dog. That is, a single intelligent entity controls a layered hierarchical network wherein each layer contains more entities of lesser intelligence than the layer above it. Whether a swarm or a pack is the better analogy, in any case, researchers have only scratched the surface

of issues concerned with designing a mobile network created by a collective of autonomous platforms. Controlling the mobility of a pack of autonomous platforms and communicating within it remain unsolved problems.

How platforms move to achieve their mission, for example, generating the floor plan of a building previously unexplored by US units, yet maintain connectivity is the focus of the paper, “Robust Control for Mobility and Wireless Communication in Cyber-Physical Systems with Application to Robot Teams,” by ARL researcher Fink and colleagues Riberio and Kumar at the University of Pennsylvania. The key element of the paper, “Robust Control and Mobility and Wireless Communication in Cyber-Physical Systems With Application to Robot Teams” (page 247), is the authors’ statement that “successful deployment of an autonomous team of robots requires joint cyber-physical controllers that determine (physical) trajectories for the robots while ensuring (cyber) availability of communication resources.” The authors’ approach to solving this problem is to consider communication parameters (bandwidth, attenuation, noise) as virtual obstacles that restrict platform movement. However, in an iterative control cycle, after platforms move, the network readjusts communications parameters to provide reliable communication (e.g., establishes new links, removes old ones, increases transmitted power, or reduces transmission bandwidth).

The basis for control is minimizing a potential function subject to the constraint that data transmission in every established link is above some threshold data rate. The strength of this approach is its global perspective of all links. Previous methods consider mobility from the perspective of local links only. Simulations and experiments with five mobile ground platforms validate the viability of this approach.

Analogies to nature inform the design of these experiments. In addition, they provide a benchmark against which one can measure performance. However, the experiments provide a perspective for reinterpreting and understanding nature. Does the collection of individual movement and communication minimize a global potential? If so, what potential? The total energy expended by the network to achieve goal? How does the mode of communication impact an individual’s movement if the communication is non-line-of-sight versus line-of-sight? The answers to these questions fall back into the realm of network science theory.

Designers of the physical networks that enable the transfer of electronic information need to consider means for simple, rapid, and robust data transfer. In applications where the network is stable and network operators have considerable opportunity to monitor and control the network, for example, commercial networks, message traffic can be handled sequentially. However, in complex, less stable, environments, parallel transmission of messages provides more robust operation. In this case, messages between two channels are transmitted contemporaneously to a relay. The relay combines the messages and retransmits the same composite message to both channels. Since each channel knows the signal they transmitted, it is a simple matter for them to extract the unknown message from the other channel.

However, parallel messaging dictates that messages between channels must arrive within certain time blocks, which requires timing control to minimize transmission delays. As the likelihood of large delays increases, the likelihood of missed messages also increases. Although coherent detection, in which all channels operate on the same time base, minimizes timing delays, it requires precise control of phase. Such control is unlikely in unstable environments. In these situations, designers trade the precision of coherent detection for the simplicity of non-coherent detection, which does not require a frequency or phase base. In their implementation of a non-coherent system, Valenti and Ferrett of West Virginia University and Torrieri of ARL, “Non-coherent Physical-Layer Network Coding with FSK Modulation: Relay Receiver Design Issues” (page 221), use frequency shift keying (FSK) to encode signals. In FSK, the network needs to detect only changes in frequency, not measure absolute frequency, to demodulate signals. Because the encoding does not require a reference frequency, it reduces network requirements on frequency control and on power control.

In this paper, Valenti, Torrieri and Ferrett present the theory, design, and simulated operation of FSK for non-coherent physical-layer network coding. They show that the encoding provides high throughput with low energy efficiency, which is typical of non-coherent systems. To overcome power losses, they employ low rate turbo codes. The authors show that, for the same energy efficiency, their digital network coding (DNC) approach achieves a higher throughput rate in comparison to more traditional link-layer network coding (LNC). In one example, the authors show a one-third rate increase. That is, four messages can be sent using the authors’ approach for every three messages transmitted using LNC.

Aquino of the Imperial College London, Bologna of the Instituto de Alta Investigacion Chile, Grigolini of the University of North Texas, and West of ARL investigated the transport of information between two complex networks to determine the conditions under which the information transport is maximized in, “Transmission of Information Between Complex Systems: I/f Resonance” (page 233). If network theory is ever to become Network Science, there must exist general principles that transcend the level of disciplinary mechanisms and that remain valid across the physical, biological, and social phenomena described above. In this paper, Aquino et al. use arguments from non-equilibrium statistical physics to make the case that if the complexity of a network

can be quantified, then the information transferred is maximized through the matching of the complexity of the interacting networks.

The complexity of networks, from avalanches of neuronal firings within the human brain to the blinking times in colloidal quantum dot fluorescence, is manifest in IPL distributions. The level of complexity of these networks is quantified by the value of the IPL index. Of particular importance is the manner in which information is shuttled back and forth between such networks and whether or not there exists a general principle that guides the flow of information. The mathematician Norbert Wiener speculated that such a principle existed for information-dominated processes. A half century later, Aquino et al. in, "Transmission of Information Between Complex Systems: I/f Resonance" (page 233), proved Wiener's conjecture to be true by establishing the Principle of Complexity Management in which information transport is mitigated by the relative values of the networks' IPL indices. They establish the principle by generalizing the fluctuation-dissipation theorem from non-equilibrium statistical physics to non-ergodic processes. In this way, it is possible for a network with lesser energy, but greater information, to organize a network with greater energy, but lesser information; this is an information-dominated process.

On one hand, a speaker who delivers a lecture standing motionless in front of an audience, talking in a monotone, transfers little or no information. The group very quickly drifts off and stops listening almost independently of the content of the lecture. On the other hand, another speaker with a modulated voice, striding back and forth across the front the room while gesturing dramatically, can hold the audience's attention. The complexity of the presentation matches that of the typical cognitive activity of the brain and information finds its way into the consciousness of the audience member. The success of the second speaker, as well as a myriad of other social and psychological phenomena, are explained by the Principle of Complexity Management and the relative complexity of the two interacting networks.

The following collection of recently published journal articles is a select sample of the broad spectrum of ARL's network science research investigating physical, social/cognitive, information, and communication networks, and their complex interactions. They represent foundational knowledge that will enable optimized human performance and enhanced speed and precision in complex networked environments.

References

- [1] D.S. Alberts and R.E. Hayes, *Power to the Edge: Command and Control in the Information Age*, US DoD CCRP Publishing Services, June 2003.
- [2] *The Networking Information Technology Research and Development (NITRD) Program: 2012 Strategic Plan*; Executive Office of the President, National Science and Technology Council, July 2012.
- [3] *Network Science*, National Research Council of the National Academies, Washington DC, www.nap.edu (2005).
- [4] See, for example: J. G. Andrews, N. Jindal, M. Haenggi, R. Berry, S. Jafar, D. Guo, S. Shakkottai, R. W. Heath, Jr., M. Neely, S. Weber, and A. Yener, "Rethinking Information Theory for Mobile Ad Hoc Networks", *IEEE Communications Magazine*, December 2008

A New Measure of Network Efficiency

Nicholas W. Hollingshad, Malgorzata Turalska,
Paolo Allegrini, Bruce J. West, and Paolo Grigolini

Physica A: Statistical Mechanics and its Applications, 391(4), 1894–1899 (2012)



A new measure of network efficiency

Nicholas W. Hollingshad^{a,*}, Malgorzata Turalaska^a, Paolo Allegrini^b, Bruce J. West^c,
Paolo Grigolini^a

^a Center for Nonlinear Science, University of North Texas, P.O. Box 311427, Denton, TX 76203-1427, USA

^b Istituto di Fisiologia Clinica (IFC-CNR), Via Moruzzi 1, 56124 Pisa, Italy

^c Information Science Directorate, US Army Research Office, Durham, NC 27709, USA

ARTICLE INFO

Article history:

Received 25 July 2011

Received in revised form 3 October 2011

Available online 15 November 2011

Keywords:

Network

ABSTRACT

We address the issue of the dynamical origin of scale-free link distributions. We study a two-dimensional lattice of cooperatively interacting units. Although the units interact only with the four nearest neighbors, a sufficiently large cooperation strength generates dynamically a scale-free network with the power law index ν approaching 1. We explain this result by using a new definition of network efficiency determined by the Euclidean distance between correlated units. According to this definition the link distribution favoring long-range connections makes efficiency increase. We embed an *ad hoc* scale-free network with power index $\nu \geq 1$ into a Euclidean two-dimensional space and show that the network efficiency becomes maximal as ν approaches 1. We therefore conclude that $\nu = 1$ emerging from the cooperative interaction of units may be a consequence of the principle of network maximal efficiency.

© 2011 Elsevier B.V. All rights reserved.

1. Introduction

The work of Albert and Barabási (AB) [1] prompted interest in scale-free networks, namely networks with the inverse power law distribution of links

$$p(k) \propto \frac{1}{k^\nu}, \quad (1)$$

with k denoting the number of links per node. The AB model assumed the preferential attachment of the Yule process and gave rise to the power-law index $\nu = 3$. The ubiquity of these networks has led to the research into the dynamical origin of the scale-free property. Fraiman et al. [2] has recently studied the two-dimensional Ising model at criticality and using a suitable threshold ρ^+ established a link between the nodes with a dynamical correlation exceeding that threshold. The interesting result of that procedure was the emergence of the scale-free distribution density of Eq. (1) with a power index ν that, with the proper choice of average connectivity $\langle k \rangle$, gives values close to $\nu = 2$ [3]. It is remarkable that the same procedure, applied to the brain, yields results very close to those afforded by the Ising model [2].

Like the work of Ref. [2], we begin with a regular two-dimensional network, but then take an entirely different approach. Rather than using the Ising model, we adopt the Decision Making (DM) model of Refs. [4,5] for the creation of the dynamically induced network. The key result is that while we also find the emergence of a scale-free network at criticality, our network has an exponent ν close to 1.

* Corresponding author.

E-mail address: nwh0012@unt.edu (N.W. Hollingshad).

This finding suggests that the cooperative interaction between the units in the network generated from the DM model should make the network very efficient. However, we find herein that the conventional measures of network efficiency [6] are relatively insensitive to $\nu < 2$. The second result of this paper is a new measure of network efficiency, the perception length, that overcomes this limitation, and shows that network efficiency increases as ν approaches 1.

The outline of this paper is as follows. We devote Section 2 to proving the dynamical emergence of the scale-free network with $\nu = 1$. Section 3 shows that ν approaching 1 maximizes the perception length while realizing a statistical condition equivalent to the dynamically generated network. We devote Section 4 to concluding remarks.

2. Dynamically induced scale-free network with $\nu = 1$

The question of whether the network emerging from dynamical correlations is scale-free is not trivial. For this paper, we adopt the Decision Making (DM) model of Refs. [4,5]. Although the DM model yields a phase transition very similar to that of the conventional Ising model [7], the DM model does not have a Hamiltonian foundation. Furthermore, while the Ising model rests on the action of a thermal bath at a finite temperature, and the single spins in isolation and with no thermal driving would be dynamically frozen, the units of the DM model, in isolation, are driven by Poisson dynamics. This difference may lead to a dynamically created scale-free network different from that of Ref. [2].

The DM model considers N discrete variables located at the nodes of a two-dimensional square lattice. Each unit s_i is a stochastic oscillator and can be found in either of two states, “yes” (+1) or “no” (−1). The cooperation among the units is realized by setting the transition rates between two states to the time-dependent form:

$$g_{12}(t) = ge^{K \frac{M_2(t) - M_1(t)}{M}} \quad (2)$$

and

$$g_{21}(t) = ge^{-K \frac{M_2(t) - M_1(t)}{M}} \quad (3)$$

where M denotes the total number of nearest neighbors, which in the case of a two-dimensional lattice results in $M = 4$. $M_1(t)$ and $M_2(t)$ are the nearest neighbors who are making the decision “yes” and “no”, respectively. The single unit in isolation, $K = 0$, fluctuates between “yes” and “no”, with the rate g . When coupling constant $K > 0$, a unit in the state “yes” (“no”) makes a transition to the state “no” (“yes”) faster or slower according to whether $M_2 > M_1$ ($M_1 > M_2$) or $M_2 < M_1$ ($M_1 < M_2$), respectively. The quantity K_c is the critical value of the control parameter K , at which point a phase-transition to a global majority state occurs. It can be shown that for a lattice of infinite size $K_c = 2 \ln(1 + \sqrt{2}) \approx 1.7627$.

All simulations are implemented on a lattice of $N = 100 \times 100$ nodes with periodic boundary conditions. In a single time step, a run over the entire lattice is performed and for every node an appropriate transition rate (g_{12} or g_{21}) is calculated according to which a node is given possibility to change its state. Under those conditions, setting parameter $g = 0.01$, the phase transition to the global majority case occurs at $K_c \approx 1.70$. To study the dynamically induced network topology, we considered the DM model with this critical value of coupling constant. After an initial 10^6 time steps, we record 2000 lattice configurations, obtaining the dynamics of each node $\{s_i(t)\}$. In the next step, we evaluate the linear correlation coefficient between the i -th and the j -th node:

$$r(i, j) = \frac{\langle s_i(t)s_j(t) \rangle - \langle s_i(t) \rangle \langle s_j(t) \rangle}{\sqrt{\langle s_i^2(t) \rangle - \langle s_i(t) \rangle^2} \sqrt{\langle s_j^2(t) \rangle - \langle s_j(t) \rangle^2}}, \quad (4)$$

where $\langle \cdot \cdot \cdot \rangle$ stands for the time average. Nodes i and j of the dynamically induced network are connected by a link when the correlation between nodes i and j of the two-dimensional lattice is greater than a given positive threshold ρ^+ .

We investigated a wide range of positive thresholds $\rho^+ = [0.10 : 0.90]$. As expected, correlation networks constructed with increasing value of the threshold ρ^+ are characterized by a decreasing number of links, which results in significant changes in the corresponding degree distribution. Networks obtained with low values of the threshold ρ^+ result in narrow, peaked degree distributions and relatively high values of the mean degree $\langle k \rangle$. Topologies resulting from very strong correlations, however, are characterized by a distribution of links that has a mean close to the minimum value of $\langle k \rangle = 1$ and drops off very rapidly. Interestingly, in between those conditions there exists a correlation threshold that creates a dynamically induced network with a power-law distribution of degrees that is shown in Fig. 1. The connectivity of a network obtained under this particular condition is inspected and only nodes that are part of a giant component are considered to be a part of new topology. The resulting network consists of 6740 nodes with a mean degree of $\langle k \rangle = 38$. For a correlation threshold $\rho^+ = 0.61$, we find that the distribution of links follows an inverse power law with the scaling parameter $\nu = 1.20 \pm 0.23$ ($R^2 = 0.9556$).

How can the dynamical origin of this extremal condition be explained? From an intuitive point of view there exists a connection between the scale-free distribution of links and Zipf's law [8,9]. In fact, if we rank the nodes moving from the richest to the poorest, according to Zipf [10] we should obtain the relation between the connectivity k and rank r :

$$k(r) = \frac{C}{r^\alpha}, \quad (5)$$

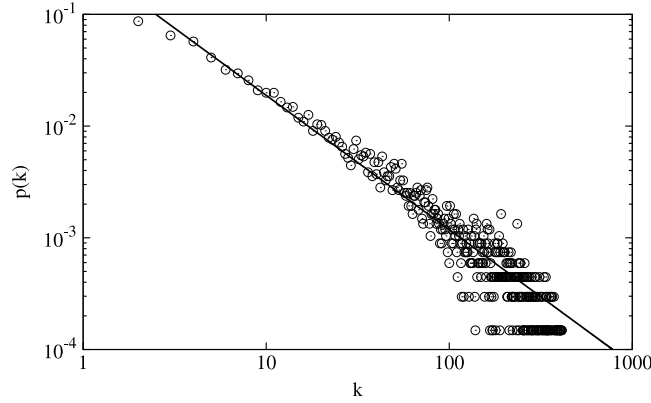


Fig. 1. Degree distribution $p(k)$ for correlation network obtained with a positive threshold $\rho^+ = 0.61$. The line follows estimated power-law relation with the exponent of $\nu = 1.20$.

with the power-law index α being very close to 1. If we select randomly a given rank r with probability $\pi(r)dr$ of being in the interval $[r, r + dr]$, this should be equal to the probability $p(k)dk$, of having k links in the interval $[k, k + dk]$,

$$p(k)dk = \pi(r)dr. \quad (6)$$

Assuming that $\pi(r)$ is constant, we obtain after some algebra

$$p(k) \propto \frac{1}{k^{1+\frac{1}{\alpha}}}, \quad (7)$$

and thus the two power-law indices are related by

$$\nu = 1 + \frac{1}{\alpha}. \quad (8)$$

This leads us to conclude how an efficient complex network is organized if Zipf's law applies. For example, this suggests that the intelligence of human brain should be characterized by $\nu = 2$. The recent research work of Fraiman et al. [2] seems to confirm this prediction. The authors of Ref. [2] studied the two-dimensional Ising model at criticality and using a suitable threshold ρ^+ established a link between the nodes with a dynamical correlation exceeding that threshold. The interesting result of that procedure was the emergence of the scale-free distribution density of Eq. (1) with a power index ν that, with the proper choice of average connectivity $\langle k \rangle$, gives values close to $\nu = 2$ [3]. It is remarkable that the same procedure, applied to the brain, yields results very close to those afforded by the Ising model [2].

It is also interesting to notice that Boettcher and Percus [11] applied the method of extremal optimization to a Ising-like model to evaluate the rank distribution of Eq. (5) and found that when the number of units tend to infinity the rank distribution tends to $\alpha = 1$. This result implies on the basis of the earlier remarks that the cooperation of units in an Ising-like model is expected to confirm Zipf's prediction and consequently $\nu = 2$. For results confirming this prediction, see also Refs. [12,13].

We have found, therefore, that the DM model generates a scale-free network at criticality, but with ν approaching 1 which violates Zipf's condition of $\alpha = 1$. The emergence of $\alpha \gg 1$ corresponds to the number of links k dropping very quickly when we move from $r = 1$ to subsequent ranks.

3. Embedding scale-free networks in a two-dimensional regular lattice

The efficiency of a network has been mainly studied on the basis of topological length L [6]. The topological distance between two nodes is the minimum number of steps needed to move from one node to another. The quantity L is the corresponding mean value of the minimum topological distance between nodes. As a consequence, the emergence of scale-free networks can be explained by making the conjecture that real networks evolve in time so as to realize maximal efficiency. In the case of the scale-free network this efficiency is measured by the minimal value of L .

In 2003, Cohen and Havlin [14] determined that scale-free networks are very efficient. They calculated that networks with N nodes have a topological length L given by

$$L \sim \ln(\ln N), \quad (9)$$

for a power-law index $\nu < 3$, which is smaller than in the AB model.

As a consequence of Eq. (9), the topological length L remains small even if N is very large. This relation between L and N suggests that the complex networks with $\nu < 3$ are very efficient.

The region $\nu < 2$ has not been studied by many authors. As an interesting example of earlier work in this region we refer to the work of Refs. [15,16]. In both cases the authors adopt a kind of generalization of the perspective of Albert and

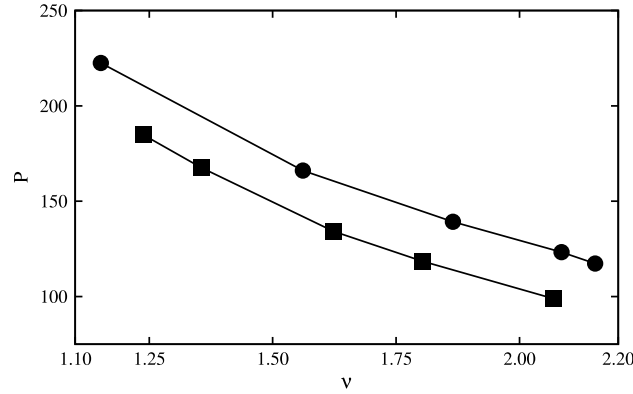


Fig. 2. Perception length P as a function of ν for *ad hoc* scale-free networks. The circles represent networks with constant $\langle k \rangle = 4.95$; the squares represent networks with constant $N = 1313$.

Barabási [1], namely, they grow a network with special prescriptions allowing them to overcome the limiting condition $\nu > 3$ and yielding $\nu < 2$.

More recently there has been some interest in the efficiency of hierarchical networks with $\nu < 2$ [17] and $\nu \sim 1$ [18,19]. These networks are characterized by very small topological lengths. In the case of Ref. [19], for $N \rightarrow \infty$ the authors predict the value $L = 2$. Our numerical calculations show that L is insensitive to ν in the range $1 < \nu < 2$. Thus, there are good reasons to believe that the prediction of Eq. (9) applies with no significant dependence on ν .

There are also good reasons to believe that the dynamic source of scale-free networks has a probabilistic rather than a deterministic origin, as we shall demonstrate. The work of Fraiman et al. [2], although fitting Zipf's condition, allows us to define the concept of perception length, which is then used to shed light onto the condition $\nu = 1$. The nodes of a two-dimensional regular lattice, where each unit interacts with only its four nearest neighbors, correspond to a network whose topological efficiency is very low. However, if we let the units cooperatively interact, and we set a link between two nodes, then when their dynamical correlation is large enough, the resulting dynamical network may have a much lower L . We record the Euclidean distance between each pair of correlated nodes, and we define the network efficiency as the corresponding mean value. More precisely, we define the network efficiency by means of the quantity

$$P = \frac{1}{N} \sum_{i=1}^N \lambda_i, \quad (10)$$

where

$$\lambda_i = \sum_{j=1}^{k_i} d_{ij} \quad (11)$$

and d_{ij} is the Euclidean distance between node i and its nearest neighbor j . We refer to P as the perception length of the system, this being the measure of the network efficiency replacing $1/L$. For numerical analysis, the perception length P is calculated as follows.

1. Create a 2-dimensional square lattice, where a is the length (in units of the lattice) of the side of the square, and it is necessary that $\sqrt{N} < a$.
2. Embed the network on the lattice by randomly assigning the network nodes to lattice points.
3. Using periodic boundary conditions for the lattice, calculate the Euclidean length of each link.
4. These lengths are then used to calculate P in accordance with Eq. (10).

This procedure was then applied to scale-free networks generated according to the method of Catanzaro et al. [20] with $\langle k \rangle = 4.95$ and values of ν ranging from 1 to 2. The nodes were embedded randomly in a square lattice of size just sufficient to contain the network with the largest number of nodes. The perception lengths were calculated, and the results show that over this range the perception length increases as ν approaches 1 (Fig. 2).

We now compare the sensitivity of the conventional network efficiency (defined as the reciprocal of the network length $1/L$) and the perception length P to the variation in ν . These results are shown in Fig. 3. Note that the perception length P and $1/L$ have been normalized to allow the presentation in a convenient scale. These results show that the perception length, as a measure of network efficiency, is more sensitive to changes in ν than the conventional $1/L$.

Applying this approach to the DM network discussed in Section 2 above yields a mean perception length = 1382. To provide a basis for comparison, we calculated the perception length for a comparably sized *ad hoc* scale-free network, also prepared in accordance with the algorithm in Ref. [20]. The results are compared in Table 1, which shows a very good agreement.

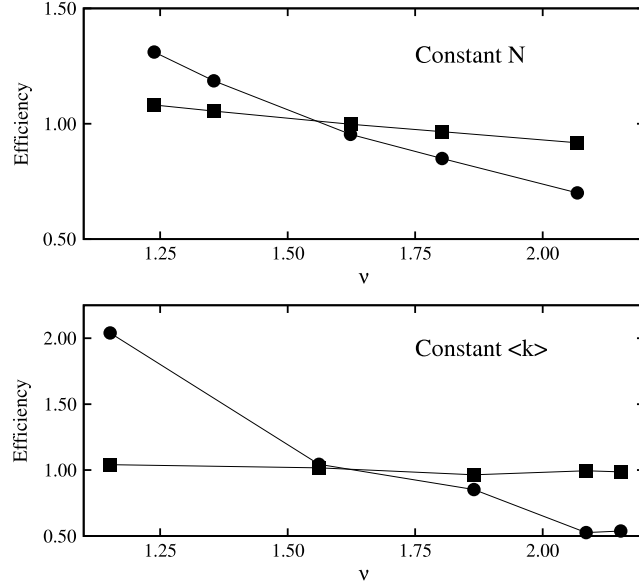


Fig. 3. Network efficiency as a function of ν . In both figures, the circles represent the normalized perception length, and the squares represent the normalized $1/L$. Error bars are not shown; standard deviations for the normalized perception lengths were very small (of the order of 0.005).

Table 1

Comparison of perception lengths for the DM network and a comparable *ad hoc* scale-free network.

	DM network	Ad Hoc network
Degree distribution exponent, ν	1.20	1.19
Number of nodes, N	6740	6744
Number of links, k	128,448	128,413
Perception length, P	1382	1373

4. Concluding remarks

The main result of this paper is the proof that the perception length P defined by Eq. (10) is more sensitive to ν in the range $1 < \nu < 2$, and may therefore be a more useful measure of network efficiency than the topological length L [6]. This new definition is based on the assumption that the scale-free networks, even those derived using deterministic and hierarchical arguments [17–19], are compatible with the dynamical derivation. The apparent conflict between the two kinds of network is explained by noticing that the correlation between different nodes evaluated according to the numerical prescription of Section 2 rests on time windows of finite size and moving these windows to different time regions generate different networks with the same hierarchical topology. An alternative but probably more attractive way to explain this is that the leadership moves in time from some nodes to others. The nodes of the two-dimensional regular lattice that we used for the dynamical derivation of the free-scale distribution of Eq. (1) are totally equivalent, and the rank differences between the richest and the poorest nodes are temporary and in the long time run the same high rank is shared by all the nodes.

There are some questionable aspects of the dynamical derivation of $\nu = 1$, realized in Section 2. First of all this result depends on an arbitrarily selected threshold ρ^+ . In addition, the power index ν derived from the data in Fig. 1 is affected by the large fluctuations of the distribution density $p(k)$ for large values of k , thereby explaining why we derive $\nu = 1$ rather than $\nu = 2$, as in the work of Ref. [3]. However, on one hand, this observation led us to the discovery of the new measure of network efficiency of Eq. (10) and, on the other hand, as already mentioned in Section 1, the DM model is not quite equivalent to the Ising model.

Furthermore, the interesting fact that $\alpha = 1$ (Zipf's law) is related to $\nu = 2$ is not totally convincing. The authors of Ref. [9] established a connection between topological and dynamical properties by running a random walker on a scale-free network with the power index ν . They found that the waiting time distribution density for returns of the walker to a given node are described by an inverse power law with power index $\mu = 3 - \nu$. Using a generalized central limit theorem, they also proved that the same index μ also describes the inverse power law form of the probability density of relative frequencies $p(f) \sim f^{-\mu}$, so that, in analogy with Eq. (8), a rank-frequency law $f \sim r^{-\alpha}$ yields $\mu = 1 + 1/\alpha$, hence $\alpha = 1/(2 - \nu)$, namely $\alpha = 1$ for $\nu = 1$. It is interesting to note that $\nu = 1$ yields $\mu = 2$, and that the value $\mu \approx 2$ emerges from the recent neurophysiological work of Refs. [21,22].

Thus, in addition to the new efficiency measure of Eq. (10), which is the unquestionable result of this paper, we are also led to make the plausible conjecture that the DM model may be an adequate tool to study the emergence of intelligence

in the sense pointed out by Couzin [23] and Cavagna et al. [24]. According to these authors the flocks of birds, as well as the brain [25,26], are systems at criticality, with a correlation length as large as the size of these systems. We are also led to make the conjecture that the dynamical generation of a scale-free network with $\nu = 1$ may be the manifestation of the principle of network maximal efficiency: a network of cooperatively interacting units evolves naturally so as to maximize P , the new measure of network efficiency.

References

- [1] R. Albert, A.-L. Barabási, Statistical mechanics of complex networks, *Rev. Modern Phys.* 74 (2002) 47–97.
- [2] D. Fraiman, P. Balenzuela, J. Foss, D.R. Chialvo, Ising-like dynamics in large-scale functional brain networks, *Phys. Rev. E* 79 (1–10) (2009) 061922.
- [3] E. Tagliazucchi, D.R. Chialvo, The collective brain, in: P. Grigolini, B.J. West (Eds.), *Decision Making: A Psychophysics Application of Network Science*, World Scientific, Singapore, 2011.
- [4] S. Bianco, E. Geneston, P. Grigolini, M. Ignaccolo, Renewal aging as emerging property of phase synchronization, *Physica A* 387 (2008) 1387–1392.
- [5] M. Turala, M. Lukovic, B.J. West, P. Grigolini, Complexity and synchronization, *Phys. Rev. E* 80 (1–12) (2009) 021110.
- [6] S. Boccaletti, V. Latora, Y. Moreno, M. Chavez, D.U. Hwang, Complex networks: structure and dynamics, *Phys. Rep.* 424 (2006) 175–308.
- [7] M. Turala, B.J. West, P. Grigolini, Temporal complexity of the order parameter at the phase transition, *Phys. Rev. E* 83 (1–6) (2011) 061142.
- [8] L.A. Adamic, B.A. Huberman, Zipf's law and the Internet, *Glottometrics* 3 (2002) 143–150.
- [9] P. Allegrini, P. Grigolini, L. Palatella, Intermittency and scale-free networks: a dynamical model for human language complexity, *Chaos Solitons Fractals* 20 (2004) 95–105.
- [10] G.K. Zipf, *Selected Studies of the Principle of Relative Frequency in Language*, Harvard University Press, Cambridge, MA, 1932; *Human Behavior and the Principle of Least Effort*, Addison-Wesley, Cambridge, MA, 1949.
- [11] S. Boettcher, A.G. Percus, Optimization with extremal dynamics, *Phys. Rev. Lett.* 86 (2001) 5211–5214.
- [12] S. Boettcher, Acquiring long-range memory through adaptive avalanches, in: P. Grigolini, B.J. West (Eds.), *Decision Making: A Psychophysics Application of Network Science*, World Scientific, Singapore, 2011.
- [13] It is important to notice that in the work of Ref. [12] the role of Eq. (5) is played by Eq. (4) that refers to the probability that a node of rank r is updated. However, if we divide Eq. (5) by the maximum number of links that a node may have, k is replaced by quantity that can be interpreted as a probability
- [14] R. Cohen, S. Havlin, Scale-free networks are ultrasmall, *Phys. Rev. Lett.* 90 (1–4) (2003) 058701.
- [15] H. Zhou, Scaling exponent and clustering coefficients of a growing random network, *Phys. Rev. E* 66 (1–6) (2002) 016125.
- [16] H. Seyed-allaei, G. Bianconi, M. Marsili, Scale-free networks with an exponent less than two, *Phys. Rev. E* 73 (1–5) (2006) 046113.
- [17] A.-L. Barabási, E. Ravasz, T. Vicsek, Deterministic scale-free networks, *Physica A* 299 (2001) 559–564.
- [18] M. Chen, B. Yu, P. Xu, J. Chen, A new deterministic complex network model with hierarchical structure, *Physica A* 385 (2007) 707–717.
- [19] Y. Gao, J. Sun, A tree-like complex network model, *Physica A* 389 (2010) 171–178.
- [20] M. Catanzaro, M. Boguñá, R. Pastor-Satorras, Generation of uncorrelated random scale-free networks, *Phys. Rev. E* 71 (1–4) (2005) 027103.
- [21] P. Allegrini, D. Menicucci, R. Bedini, L. Fronzoni, A. Gemignani, P. Grigolini, B.J. West, P. Paradisi, Spontaneous brain activity as a source of ideal $1/f$ noise, *Phys. Rev. E* 80 (1–13) (2009) 061914.
- [22] P. Allegrini, D. Menicucci, R. Bedini, A. Gemignani, P. Paradisi, Complex intermittency blurred by noise: theory and application to neural dynamics, *Phys. Rev. E* 82 (1–4) (2010) 015103 (R).
- [23] I. Couzin, Collective minds, *Nature* 445 (2007) 715.
- [24] A. Cavagna, A. Cimarelli, I. Giardinà, G. Parisi, R. Santagati, F. Stefanini, M. Viale, Scale-free correlations in starling flocks, *Proc. Natl. Acad. Sci.* 107 (2010) 11865–11870.
- [25] D.R. Chialvo, Emergent complexity: what uphill analysis or downhill invention cannot do, *New Ideas in Psychology* 26 (2008) 158–173.
- [26] D.R. Chialvo, Complex emergent neural dynamics, *Nature Physics* 6 (2010) 744–750.



Contents lists available at [SciVerse ScienceDirect](#)

Physica A

journal homepage: www.elsevier.com/locate/physa



Erratum

Erratum to “A new measure of network efficiency” [Physica A 391 (4) (2012) 1894–1899]

Nicholas W. Hollingshad*, Malgorzata Turalaska, Paolo Allegrini, Bruce J. West, Paolo Grigolini

Center for Nonlinear Science, University of North Texas, P.O. Box 311427, Denton, TX 76203-1427, USA

Istituto di Fisiologia Clinica (IFC-CNR), Via Moruzzi 1, 56124 Pisa, Italy

Information Science Directorate, US Army Research Office, Durham, NC 27709, USA

ARTICLE INFO

Article history:

Available online 25 July 2012

The publisher regrets to inform you that the below mentioned Acknowledgments were not included for the article “A new measure of network efficiency”

Please find below the Acknowledgments of the above mentioned paper in order to include a funding agency:

“N. W. Hollingshad, M. Turalaska, P. Grigolini warmly thank ARO and Welch for financial support through Grants W911NF1110478 and B-1577, respectively”.

The publisher would like to apologize for any inconvenience caused.

DOI of original article: <http://dx.doi.org/10.1016/j.physa.2011.11.017>.

* Corresponding author at: Center for Nonlinear Science, University of North Texas, P.O. Box 311427, Denton, TX 76203-1427, USA.

E-mail address: nwh0012@unt.edu (N.W. Hollingshad).

0378-4371/\$ – see front matter © 2012 Elsevier B.V. All rights reserved.

doi:10.1016/j.physa.2012.07.035

Optimal Topology Control and Power Allocation for Minimum Energy Consumption in Consensus Networks

Stefania Sardellitti, Sergio Barbarossa, and Ananthram Swami

IEEE Transactions on Signal Processing, 60(1), 383-399 (2012)

Optimal Topology Control and Power Allocation for Minimum Energy Consumption in Consensus Networks

Stefania Sardellitti, Sergio Barbarossa, *Fellow, IEEE*, and Ananthram Swami, *Fellow, IEEE*

Abstract—Consensus algorithms have generated a lot of interest due to their ability to compute globally relevant statistics by only exploiting local communications among sensors. However, when implemented over wireless sensor networks, the inherent iterative nature of consensus algorithms may cause a large energy consumption. Hence, to make consensus algorithms really appealing in sensor networks, it is necessary to minimize the energy necessary to reach a consensus, within a given accuracy. We propose a method to optimize the network topology and the power allocation over each active link in order to minimize the energy consumption. We consider two network models: a deterministic model, where the nodes are located arbitrarily but their positions are known, and a random model, where the network topology is modeled as a random geometric graph (RGG). In the first case, we show how to convert the topology optimization problem, which is inherently combinatorial, into a parametric convex problem, solvable with efficient algorithms. In the second case, we optimize the power transmitted by each node, exploiting the asymptotic distributions of the eigenvalues of the adjacency matrix of an RGG. We further show that the optimal power can be found as the solution of a convex problem. The theoretical findings are corroborated with extensive simulation results.

Index Terms—Consensus algorithms, minimum energy consumption, random graphs, sensor networks, topology control.

I. INTRODUCTION

AVERAGE consensus algorithms have received considerable attention in recent years because of their ability to enable globally optimal decisions using only local exchange of information among nearby nodes [1]–[3]. The price paid for this simplicity and the underlying decentralized philosophy is that consensus algorithms are inherently iterative. As a consequence, the implementation of consensus algorithms over a wireless sensor network (WSN) requires an iterated exchange

of data among the nodes, which might cause an excessive energy consumption. This must be contrasted with a centralized strategy where there is a sink node that, after collecting all the observations from the sensors (perhaps over multiple hops), is virtually able to compute the desired statistic in a single shot. Hence, to make consensus algorithms practically appealing in a sensor network context, it is necessary to minimize the energy consumption necessary to reach consensus. Clearly, the network topology plays a fundamental role in determining the convergence rate [4]. It is well known that, as the network connectivity increases, so does the rate of convergence. However, having a densely connected network requires a high power consumption to guarantee reliable direct links between many nodes. In principle, having a fully connected network is equivalent to having as many sink nodes as sensors, so that the convergence time of fully connected networks is minimum. However, the power consumption necessary to maintain a fully connected network is also maximum. On the other hand, a minimally connected network entails low power consumption to maintain a few links, but, at the same time, it requires a large convergence time. Since what really matters in a WSN is the overall power spent to achieve consensus, this paper addresses the problem of finding the optimal network topology that minimizes this overall power consumption, taking into account convergence time and transmit power necessary to establish reliable links *jointly*. The search for the optimal topology is, *per se*, a combinatorial problem whose solution becomes prohibitive even for small scale networks. Nevertheless, we will present a relaxation technique that converts the problem into a convex problem, with minimum performance loss.

If the links among the nodes are symmetric, or, equivalently, if the graph describing the network topology is undirected, the convergence rate can be lower bounded through the so called *algebraic connectivity*, defined as the second smallest eigenvalue of the graph Laplacian [5]. For this reason, there have been works aimed at maximizing the algebraic connectivity of a given undirected graph by a suitable choice of the weights associated to each edge [6], [7]. Alternatively, in [8] it was shown how some network topologies, such as small world graphs, can greatly increase the convergence rate. In [9], the authors show that nonbipartite Ramanujan graphs constitute a class of topologies maximizing the convergence rate. In [10] it was shown how to add edges from a given set to a graph in order to maximize its algebraic connectivity. Other works, for example [11], proposed strategies to improve the convergence rate of gossip algorithms through geographic routing.

Manuscript received October 25, 2010; revised May 13, 2011; accepted September 21, 2011. Date of publication October 13, 2011; date of current version December 16, 2011. The associate editor coordinating the review of this manuscript and approving it for publication was Dr. Mark Coates. This work was supported in part by the WINSOC project, a Specific Targeted Research Project (Contract Number 0033914) co-funded by the INFOS DG of the European Commission within the RTD activities of the Thematic Priority Information Society Technologies.

S. Sardellitti and S. Barbarossa are with the DIET, Sapienza University of Rome, 00184 Rome, Italy (e-mail: Stefania.Sardellitti@uniroma1.it; sergio@infocom.uniroma1.it).

A. Swami is with the ARL, Adelphi, MD 20783 USA (e-mail: a.swami@ieee.org).

Color versions of one or more of the figures in this paper are available online at <http://ieeexplore.ieee.org>.

Digital Object Identifier 10.1109/TSP.2011.2171683

However, in all these works, the focus is always on convergence time and there is no cost associated with the establishment of the graph topology. Conversely, in our work, since the graph represents a real network, we consider as the optimization metric the power consumption necessary to maintain reliable communication links among the nodes, taking into account the radio propagation model, multiplied by the number of iterations necessary to achieve consensus. From this perspective, enforcing a small world, scale-free, or Ramanujan graph topology may not be the best choice for a wireless network, whose topology should depend on the application at hand as well as on the propagation model.

In the wireless communication network context, there have been works on optimizing the network topology in order to minimize the power consumption necessary to guarantee connectivity, e.g., [12], [13]. These works concentrate on the communication task and do not make any specific reference to the running application. However, it is now well established, in the sensor network context, that, whenever possible, an efficient wireless sensor network design should take into account the specific goal of the sensor network [14]. For this reason, we focus on the achievement of consensus in a WSN. It is well known that one of the most crucial parameters in WSNs is energy consumption, because in many contexts it is hard to recharge the batteries or scavenge energy from the environment. For this reason, in most applications, minimizing energy consumption is more appropriate than minimizing convergence time (although, there are important applications where the latter could be more important). In [15], the minimum energy consumption problem was studied, assuming a common transmit power. As shown in [15], there typically is an optimum power that minimizes the energy necessary to achieve consensus within a prescribed accuracy.

In this work, we generalize the initial idea suggested in [15] and we propose a method for optimizing the network topology and the power allocation across every link in order to minimize the energy necessary to achieve consensus. We consider two classes of networks: a) deterministic topologies, with arbitrary, but known, node locations, and b) random geometries, with unknown node locations, modeled as random variables. In the deterministic case, we optimize both topology and power allocation. Differently from [6], we do not assume any prior topology, as the topology comes out as a result of the optimization. Topology optimization is, in general, a combinatorial problem and hence an NP-hard problem (recall that an undirected graph composed of n nodes may assume $2^{n(n-1)/2}$ topologies). To tackle this issue, we propose a relaxation technique that allows us to formulate topology optimization as a convex parametric problem. Then, we show that the effect of this relaxation on the performance is negligible.

In the random topology case, where the internode distances are unknown, we show how to optimize the single (common) transmit power, modeling the network topology as a random geometric graph, a model suitable for wireless networks. We provide both theoretical and simulation results, exploiting the theory of the eigenvalues of random geometric graphs.

The paper is organized as follows. In Section II, we briefly review the consensus algorithm. In Section III, we introduce our communication model and formulate the optimization problem.

Section IV is devoted to topology optimization for arbitrary networks. In Section V, we start by providing a closed form expression, albeit approximate, for the algebraic connectivity of a random geometric graph. Then we use this expression to proceed with the topology optimization for random geometric graphs. The analytical findings are corroborated with extensive simulation results.

II. BRIEF REVIEW OF CONSENSUS ALGORITHMS

Let us consider a wireless network composed of n sensors. The network topology can be represented as an undirected graph $G = \{V, E\}$ where V denotes the set of n vertices (nodes) v_i and $E \subseteq V \times V$ is the set of bidirectional edges (links) $e_{ij} = e_{ji}$ connecting v_i and v_j . Furthermore, let \mathbf{A} be the $n \times n$ -dimensional symmetric *adjacency* matrix of the graph G , with elements $a_{ij} = 1$ if $e_{ij} \in E$ and $a_{ij} = 0$ otherwise. According to this notation and assuming no self-loops, i.e., $a_{ii} = 0$, $\forall i = 1, \dots, n$, the degree of node v_i is defined as $\deg(v_i) = \sum_{j=1}^n a_{ij} = \sum_{j=1}^n a_{ji}$. The *degree* matrix \mathbf{D} is defined as the diagonal matrix whose diagonal entry is $d_{ii} = \deg(v_i)$. Let \mathcal{N}_i denote the set of neighbors of node i , so that $|\mathcal{N}_i| = \deg(v_i)$ ¹. The *Laplacian* matrix of the graph G is the $n \times n$ symmetric matrix $\mathbf{L} := \mathbf{D} - \mathbf{A}$, whose entries are

$$\ell_{ij} = \ell_{ji} = \begin{cases} \deg(v_i) & \text{if } j = i \\ -a_{ij} & \text{if } j \neq i \end{cases} \quad (1)$$

Given a set of measurements $x_i(0)$, collected by node i , for $i = 1, \dots, n$, the goal of the consensus algorithm is to allow every node to compute a globally optimal function of the measurements, say x^* , through a decentralized mechanism that does not require the presence of a sink node, but builds on the interaction among nearby nodes only. Let us consider, for simplicity, the case where x^* is the average of the measurements. In this case, reaching an average consensus can be seen as the minimization of the disagreement between the states x_i of the interacting nodes. One of the nice properties of the Laplacian is that the disagreement can be expressed as a quadratic form built on the Laplacian [16]

$$\begin{aligned} J(\mathbf{x}) &:= \frac{1}{4} \sum_{i=1}^n \sum_{j \in \mathcal{N}_i} (x_i - x_j)^2 \\ &= \frac{1}{4} \sum_{i=1}^n \sum_{j=1}^n a_{ij} (x_i - x_j)^2 = \frac{1}{2} \mathbf{x}^T \mathbf{L} \mathbf{x}. \end{aligned} \quad (2)$$

An important property of the Laplacian is that it has, by construction, a zero eigenvalue, whose multiplicity is equal to the number of connected components of a graph. Hence, a graph is connected if its zero eigenvalue has multiplicity one [5]. Furthermore, if the graph is connected, the eigenvector associated with the null eigenvalue is the vector $\mathbf{1}$, composed of all ones.

The minimization of the quadratic form in (2) can be achieved using a simple steepest descent technique. In continuous time, the minimum of (2) can be reached through the following updating rule [2]:

$$\dot{\mathbf{x}}(t) = -\mathbf{L} \mathbf{x}(t) \quad (3)$$

¹By $|\cdot|$ we denote the cardinality of the set.

initialized with $\mathbf{x}(0) := \mathbf{x}_0^2$. By construction, the eigenvalues of \mathbf{L} are all nonnegative. Hence, the convergence of (3) is guaranteed. In particular, if the graph is connected, the state vector $\mathbf{x}(t)$ in (3) converges to the projection of the initial state \mathbf{x}_0 onto the nullspace of \mathbf{L} , spanned by the vector $\mathbf{1}$, i.e., [2]

$$\mathbf{x}(t) \xrightarrow[t \rightarrow \infty]{} \frac{1}{n} \mathbf{1} \mathbf{1}^T \mathbf{x}_0. \quad (4)$$

This corresponds to having all the nodes converging to a consensus on the average of the initial observations $x^* = \sum_{i=1}^n x_i(0)/n$. Moreover, the convergence rate is lower bounded by the slowest decaying mode, i.e., by the second smallest eigenvalue of \mathbf{L} , $\lambda_2(\mathbf{L})$, also known as the *algebraic connectivity* of the graph. More specifically, if the graph is connected, the dynamic system (3) converges to consensus exponentially [2], i.e., $\|\mathbf{x}(t) - x^* \mathbf{1}\| \leq \|\mathbf{x}(0) - x^* \mathbf{1}\| O(e^{-rt})$, with $r = \lambda_2(\mathbf{L})$. Defining the disagreement vector as $\Delta \mathbf{x}(t) = \mathbf{x}(t) - x^* \mathbf{1}$, we can write $\|\Delta \mathbf{x}(t)\| \leq \|\Delta \mathbf{x}(0)\| O(e^{-rt})$. As a consequence, the convergence time T_c can be defined (see also [2]) as the time necessary for the slowest mode of the dynamical system (3) to be reduced by a factor $\gamma \ll 1$, i.e., the time for which $\|\Delta \mathbf{x}(T_c)\| \leq \gamma \|\Delta \mathbf{x}(0)\|$. Hence, we can set

$$T_c = -\frac{\log(\gamma)}{\lambda_2(\mathbf{L})}. \quad (5)$$

III. OPTIMIZATION CRITERION

It is well known that one of the most critical issues in WSN is energy consumption. Neglecting for simplicity the power spent for processing operations with respect to the power to be used to enable wireless communications, the overall power spent to reach consensus is the product between the sum of the power P_{tot} necessary to establish the communication links among the nodes and the number of iterations N_{it} necessary to achieve consensus. The exchange of information among the nodes is supposed to take place in the presence of a slotted system, with a medium access control (MAC) mechanism that prevents packet collisions. Denoting by T_s the duration of a time slot unit, the number of iterations is then approximately³ $N_{\text{it}} = T_c/T_s$.

Introducing the power coefficients p_{ij} , $i \neq j$, denoting the power used by node i to transmit to node j with $p_{ij} = p_{ji}$, and the binary coefficients a_{ij} assessing the presence ($a_{ij} = 1$) of a link between nodes i and j or not ($a_{ij} = 0$), the power spent by the whole network in each iteration is then $P_{\text{tot}} = \sum_{i,j} a_{ij} p_{ij}$. Using (5), our goal is to minimize the following performance metric:

$$\mathcal{E} = P_{\text{tot}} N_{\text{it}} = K \frac{\sum_{i=1}^n \sum_{j=1}^n a_{ij} p_{ij}}{\lambda_2(\mathbf{L}(\mathbf{a}))} \quad (6)$$

²The discrete-time counterpart of (3) is [2]

$$\mathbf{x}[k+1] = \mathbf{x}[k] - \tilde{\epsilon} \mathbf{L} \mathbf{x}[k] := \mathbf{W} \mathbf{x}[k]$$

where $\tilde{\epsilon}$ is a parameter chosen so as to ensure that no eigenvalue of \mathbf{W} is greater than one in modulus.

³We neglect rounding errors, which tend to vanish if the duration of the updating time slot is small with respect to the convergence time.

where K incorporates all irrelevant constants. This metric is proportional to the integral of power consumption with respect to time and then it represents an energy consumption. In (6), we have made explicit the dependence of the Laplacian \mathbf{L} on the vector $\mathbf{a} = \mathbf{A}(\cdot)$ containing all binary coefficients a_{ij} , since finding these coefficients is the goal of our optimization. More specifically, our goal is to find the set of active links, i.e., the nonzero coefficients a_{ij} , and the powers p_{ij} that minimize (6), under the constraint of maintaining network connectivity, which entails $\lambda_2(\mathbf{L}(\mathbf{a})) > 0$. The problem can then be formulated as follows:

$$\begin{aligned} \min_{\mathbf{a}, \mathbf{p}} \quad & \frac{\sum_{i=1}^n \sum_{j=1}^n a_{ij} p_{ij}}{\lambda_2(\mathbf{L}(\mathbf{a}))} \\ \text{s.t.} \quad & \epsilon \leq \lambda_2(\mathbf{L}(\mathbf{a})) \quad [\mathbf{P.0}] \\ & a_{ij} \in \{0, 1\} \\ & p_{ij} \geq 0 \quad \forall i, j = 1, \dots, n \end{aligned} \quad (7)$$

where ϵ is an arbitrarily small positive constant used to prevent the algebraic connectivity from going to zero, which would correspond to a disconnected network and \mathbf{p} is the vector with entries p_{ij} .

Since the topology coefficients are binary variables, $[\mathbf{P.0}]$ is a combinatorial problem, with complexity increasing with the size n of the network as $2^{n(n-1)/2}$. Hence, its solution, for medium/large scale networks is prohibitive. Our objective is to modify $[\mathbf{P.0}]$ in order to turn it into a convex problem, with negligible performance losses.

A first simplification comes from observing that the coefficients a_{ij} and p_{ij} are not independent of each other. Their dependence is indeed a consequence of the radio propagation model. In this work, given the complexity of the topology optimization problem, we assume a fairly simple communication model. We state that there is a link between nodes i and j , and then $a_{ij} = 1$, if the signal-to-noise ratio SNR_j at the receiver node j , when node i transmits, exceeds a minimum value s_{\min} , i.e., $\text{SNR}_j > s_{\min}$. If we denote by p_{Rj} the power received by node j when node i transmits, and by σ_n^2 the noise power, assumed for simplicity to be the same at each receiving node, we have $a_{ij} = 1$, if $p_{Rj} > s_{\min} \sigma_n^2 := p_{\min}$, or otherwise $a_{ij} = 0$. Assuming flat fading channel modeling, we use the following propagation model:

$$p_{Rj} = \frac{p_{ij}}{1 + (r_{ij}/r_0)^\eta} \quad (8)$$

where r_{ij} is the distance between nodes i and j , and η is the path loss exponent. The parameter r_0 plays the role of a scaling factor or reference distance, and typically corresponds to the so called Fraunhofer distance, such that, if $r_{ij} \gg r_0$, the receiver is in the transmit antenna far-field, where the received power is inversely proportional to r_{ij}^η ; conversely, if $r_{ij} \ll r_0$, the receiver is in the transmit antenna near-field, where the received power is approximately equal to the transmitted one. The unity term in the denominator of (8) is used to avoid the unrealistic situation in which the received power could be greater than the transmitted one. Given the propagation model (8), the relation

between the power coefficients p_{ij} and the topology coefficients a_{ij} is then

$$a_{ij} = \begin{cases} 1 & \text{if } p_{ij} > p_{\min} \left[1 + \left(\frac{r_{ij}}{r_0} \right)^\eta \right] \\ 0 & \text{otherwise} \end{cases} \quad (9)$$

In the following sections we will show how to relax this relation in order to simplify the solution of the optimal topology control problem. We will consider two scenarios: a) a deterministic topology, with arbitrary node geometry, where the distances between the nodes are known, and b) a random topology, where the positions of the nodes are unknown and modeled as random variables. In case a), since the distances among the nodes are known, we optimize the power allocated to each link. This strategy is also instrumental in determining the topology, which is equivalent to finding the $n(n-1)/2$ entries a_{ij} of the adjacency matrix. Conversely, in the random topology case, since the distances are not known, we assume broadcast communications, and look for the optimization of the coverage radius of each node. The deterministic topology case will be the subject of Section IV, whereas the random case will be studied in Section V.

IV. OPTIMAL TOPOLOGY AND POWER ALLOCATION FOR ARBITRARY NETWORKS

In the case where the distances between the nodes are known, the optimization criterion amounts to solving problem [P.0], which involves a combinatorial strategy that makes the problem numerically very hard to solve, especially for medium/large scale networks. The relation (9) reduces the set of unknowns to the set p_{ij} , but the problem still retains most of its difficulties. To make problem [P.0] to be numerically tractable, we introduce a first relaxation so that, instead of requiring a_{ij} to be binary, we assume a_{ij} to be a real variable belonging to the interval $[0, 1]$. Under this assumption, problem [P.0] is not combinatorial anymore, but it is still a nontrivial nonlinear constrained problem. The first important contribution of this paper is to propose a relaxation technique that transforms the previous problem into a *convex* problem that can be solved with well established and efficient numerical tools. We achieve this goal by first introducing the following relationship between the coefficients a_{ij} and the distances r_{ij} :

$$a_{ij} = \frac{1}{1 + (r_{ij}/r_{c_{ij}})^\alpha} \quad (10)$$

where α is a positive coefficient and $r_{c_{ij}}$ is the coverage radius, which depends on the transmit power. According to (10), a_{ij} is close to one when node j is within the coverage radius of node i , i.e., $r_{ij} \ll r_{c_{ij}}$, whereas a_{ij} is close to zero, when $r_{ij} \gg r_{c_{ij}}$. The switching from zero to one can be made steeper by increasing the value of α .

Given the propagation model (8), the coverage radius $r_{c_{ij}}$ is related to the power p_{ij} and the minimum power required for reliable communication p_{\min} , as follows:

$$r_{c_{ij}} = r_0 \left(\frac{p_{ij}}{p_{\min}} - 1 \right)^{1/\eta} \quad (11)$$

Plugging (11) in (10), the coefficients a_{ij} can be written explicitly in terms of the power coefficients as follows:

$$a_{ij} = a_{ij}(p_{ij}) = \frac{r_0^\alpha (p_{ij} - p_{\min})^{\alpha/\eta}}{r_0^\alpha (p_{ij} - p_{\min})^{\alpha/\eta} + r_{\min}^\alpha p_{\min}^{\alpha/\eta}} \quad (12)$$

This relation can be also inverted to find the coefficients p_{ij} as a function of a_{ij} , as follows:

$$p_{ij} = q(a_{ij}) = p_{\min} + k_1 \left(\frac{a_{ij}}{1 - a_{ij}} \right)^{\eta/\alpha} \quad (13)$$

with $k_1 = p_{\min} \frac{r_{ij}^\eta}{r_0^\eta}$. Expression (12) becomes our relaxed version of (9) and it allows us to reduce the set of variables to the only power vector \mathbf{p} . Consequently, problem [P.0] can be relaxed into the following problem:

$$\begin{aligned} \min_{\mathbf{p}} \quad & \frac{\mathbf{p}^T \mathbf{1}}{\lambda_2(\mathbf{L}(\mathbf{p}))} \\ \text{s.t.} \quad & \epsilon \leq \lambda_2(\mathbf{L}(\mathbf{p})) \quad [\mathbf{P.1}] \\ & p_{\min} \mathbf{1} \leq \mathbf{p} \end{aligned} \quad (14)$$

where, thanks to (12), the Laplacian is now written explicitly in terms of the power coefficients p_{ij} . In principle, the last inequality in (14) makes any link feasible. But this does not imply that the final network will be fully connected, because some coefficients a_{ij} might turn out to be equal zero, implying that the link between node i and j is not active. The first important result, related to the solution of (14), is the following.

Theorem 1: Given the propagation model in (8), using the relations (12) between the topology coefficients a_{ij} and the power terms p_{ij} , problem [P.1] is a convex-concave fractional problem if $\eta \geq \alpha$.

Proof: Let us consider the objective function in [P.1]. The numerator of [P.1] is clearly a convex function of \mathbf{p} . We only have to prove the concavity of the algebraic connectivity $\lambda_2(\mathbf{L}(\mathbf{p}))$ with respect to the transmit powers. As a first step, we prove that $a_{ij}(p_{ij})$ is a concave function of p_{ij} . Then, we use this to show that $\lambda_2(\cdot)$ is a concave function of \mathbf{p} .

(i) $a_{ij}(p_{ij})$ is a concave function of p_{ij} : We compute the second-order derivative of the function in (12) with respect to p_{ij}

$$\frac{d^2 a_{ij}(p_{ij})}{d^2 p_{ij}} = k_3 [(\alpha - \eta)k_4 - k_2(\alpha + \eta)(p_{ij} - p_{\min})^{\alpha/\eta}] \quad (15)$$

where the constants k_2 , k_3 and k_4 are given by

$$\begin{aligned} k_2 &= r_0^\alpha, \quad k_3 = \frac{\alpha k_4 k_2 (p_{ij} - p_{\min})^{\alpha/\eta - 2}}{[k_4 + k_2 (p_{ij} - p_{\min})^{\alpha/\eta}]^3 \eta^2}, \\ k_4 &= r_{\min}^\alpha p_{\min}^{\alpha/\eta}. \end{aligned}$$

Note that $k_2, k_4 > 0$; since $p_{ij} \geq p_{\min} \forall i, j$, we also have $k_3 \geq 0$. From (15), we see that, if $\alpha \leq \eta$, the second-order derivative is always nonpositive and then $a_{ij}(p_{ij})$ is a concave function of p_{ij} .

(ii) $\lambda_2(\cdot)$ is concave in \mathbf{p} : Exploiting the properties of the Laplacian [16], we can write the quadratic form associated to \mathbf{L} as in (2). From (12), we also note that each coefficient a_{ij}

depends only on the corresponding link power p_{ij} , and not on the other link powers. Given any pair of power vectors $\mathbf{p}^{(1)}$ and $\mathbf{p}^{(2)}$, let $\mathbf{p} = \beta\mathbf{p}^{(1)} + (1 - \beta)\mathbf{p}^{(2)}$, with $0 \leq \beta \leq 1$. Hence, we have

$$\begin{aligned} \mathbf{x}^T \mathbf{L}(\mathbf{a}(\mathbf{p})) \mathbf{x} &= \frac{1}{2} \sum_{i=1}^n \sum_{j=1}^n a_{ij}(p_{ij})(x_i - x_j)^2 \\ &= \frac{1}{2} \sum_{i=1}^n \sum_{j=1}^n a_{ij} \left(\beta p_{ij}^{(1)} + (1 - \beta) p_{ij}^{(2)} \right) (x_i - x_j)^2 \\ &\geq \frac{1}{2} \sum_{i=1}^n \sum_{j=1}^n \left[\beta a_{ij} \left(p_{ij}^{(1)} \right) + (1 - \beta) a_{ij} \left(p_{ij}^{(2)} \right) \right] (x_i - x_j)^2 \\ &= \beta \mathbf{x}^T \mathbf{L} \left(\mathbf{a} \left(\mathbf{p}^{(1)} \right) \right) \mathbf{x} + (1 - \beta) \mathbf{x}^T \mathbf{L} \left(\mathbf{a} \left(\mathbf{p}^{(2)} \right) \right) \mathbf{x} \end{aligned} \quad (16)$$

where the inequality follows from the concavity of $a_{ij}(p_{ij})$.

We further recall that the algebraic connectivity $\lambda_2(\mathbf{L})$ is the solution of the following positive semidefinite program (SDP) [5]:

$$\lambda_2(\mathbf{L}) = \min_{\mathbf{x} \perp \mathbf{1}, \|\mathbf{x}\|=1} \mathbf{x}^T \mathbf{L} \mathbf{x}. \quad (17)$$

Hence, using (16), we obtain

$$\begin{aligned} \lambda_2 \left(\mathbf{L} \left(\beta \mathbf{p}^{(1)} + (1 - \beta) \mathbf{p}^{(2)} \right) \right) \\ \geq \lambda_2 \left(\beta \mathbf{L} \left(\mathbf{p}^{(1)} \right) + (1 - \beta) \mathbf{L} \left(\mathbf{p}^{(2)} \right) \right) \\ \geq \beta \lambda_2 \left(\mathbf{L} \left(\mathbf{p}^{(1)} \right) \right) + (1 - \beta) \lambda_2 \left(\mathbf{L} \left(\mathbf{p}^{(2)} \right) \right) \end{aligned}$$

where the last equality follows from a majorization theorem for eigenvalues⁴. Thus, the algebraic connectivity is a concave function of the vector of transmit powers. Hence, (14) is a convex-concave fractional problem since it is the ratio of a convex and a concave function of \mathbf{p} . ■

Since (14) is a convex-concave fractional problem, we can use one of the methods that solve quasi-convex optimization problems, see, e.g., [18], [19]. For example, we can use the nonlinear parametric formulation proposed in [19]. To do so, we introduce the following function:

$$h(\mu) = \min \{ \mathbf{p}^T \mathbf{1} - \mu \lambda_2(\mathbf{L}(\mathbf{p})) : \mathbf{p} \in \Gamma \}$$

where μ is a real positive parameter and $\Gamma = \{ \mathbf{p} : \mathbf{p} \geq \mathbf{1} p_{\min}, \lambda_2(\mathbf{L}(\mathbf{p})) \geq \epsilon \}$. In order to find the solution of this problem we could use the following result, proved in [19] and [20].

Theorem 2: Let $f(x)$ and $g(x)$ be continuous real-valued functions $\forall x \in \Theta$, where Θ is a nonempty compact subset of \mathbb{R}^n and $g(x) > 0 \forall x \in \Theta$. Then

$$\mu^* = \frac{f(x^*)}{g(x^*)} = \min \left\{ \frac{f(x)}{g(x)} : x \in \Theta \right\}$$

⁴Let \mathbf{A} , \mathbf{B} be Hermitian matrices, and let $\mathbf{C} = \mathbf{A} + \mathbf{B}$. Let their eigenvalues be sorted in nondecreasing order. Then the vector of eigenvalues $\lambda(\mathbf{C})$ majorizes the vector $\lambda(\mathbf{A}) + \lambda(\mathbf{B})$. Since $\lambda_1(\mathbf{L}) = 0$ for the graph Laplacian, it follows that $\lambda_2(\mathbf{A} + \mathbf{B}) \geq \lambda_2(\mathbf{A}) + \lambda_2(\mathbf{B})$. See [17, Theorem 4.3.27].

with $x^* \in \Theta$, if, and only if

$$h^* = h(\mu^*, x^*) = \min \{ f(x) - \mu^* g(x) : x \in \Theta \} = 0$$

where $h(\mu^*, x^*)$ means that for $\mu = \mu^*$ the minimum of $\{ f(x) - \mu^* g(x) : x \in \Theta \}$ is taken on at $x = x^*$.

Before applying Theorem 2, it is useful to further convert the convex-concave optimization problem [P.1] into the following parametric problem:

$$\begin{aligned} \min_{\mathbf{p}} \quad & \mathbf{p}^T \mathbf{1} - \mu \lambda_2(\mathbf{L}(\mathbf{p})) \\ \text{s.t.} \quad & \epsilon \leq \lambda_2(\mathbf{L}(\mathbf{p})) \quad [\text{P.2}] \\ & \mathbf{1} p_{\min} \leq \mathbf{p}. \end{aligned} \quad (18)$$

By Theorem 1, $\lambda_2(\mathbf{L}(\mathbf{p}))$ is a concave function of \mathbf{p} . Hence, the objective function in [P.2], as sum of convex functions, is a convex function. The constraint sets are convex. Then, problem [P.2] is a convex parametric problem, whose solution is a function of the parameter μ that controls the tradeoff between the global transmit power and the convergence time. Later on, we will show how to find the optimal μ .

Since problem [P.2] is convex, it can be solved using numerically efficient convex programming tools. However, before applying any convex tool, it is worth noticing that the feasible set in [P.2] is not compact. Hence, even if a solution exists, in principle, it could be unreachable in finite time. To overcome this potential drawback, we propose next an alternative formulation of [P.2]: Instead of looking for the set of power coefficients p_{ij} , and then for the a_{ij} , using (13), we can reformulate [P.2] so as to look directly for the variables a_{ij} . Then the optimization problem in (18) can be rewritten in terms of vector \mathbf{a} , as follows:

$$\begin{aligned} \min_{\mathbf{a}} \quad & \phi(\mathbf{a}) - \mu \lambda_2(\mathbf{L}(\mathbf{a})) \\ \text{s.t.} \quad & \epsilon \leq \lambda_2(\mathbf{L}(\mathbf{a})) \quad [\text{P.3}] \\ & \mathbf{0} \leq \mathbf{a} < \mathbf{1} \end{aligned} \quad (19)$$

where $\phi(\mathbf{a}) = \sum_{i=1}^n \sum_{j=1, j \neq i}^n q(a_{ij})$. We verify next that this problem is still convex. To study the behavior of $\phi(\mathbf{a})$, we compute the second-order derivative of $q(a_{ij})$, obtaining

$$\frac{d^2 q(a_{ij})}{da_{ij}^2} = k_1 \frac{\eta}{\alpha} \left(\frac{a_{ij}}{1 - a_{ij}} \right)^{\eta/\alpha - 2} \frac{1}{(1 - a_{ij})^4} \left(\frac{\eta}{\alpha} - 1 + 2a_{ij} \right).$$

We infer that

$$\frac{d^2 q(a_{ij})}{da_{ij}^2} \geq 0 \Leftrightarrow \eta - \alpha + 2\alpha a_{ij} \geq 0.$$

We note that, if $\eta \geq \alpha$, then $\frac{d^2 q(a_{ij})}{da_{ij}^2} \geq 0$ for $0 \leq a_{ij} < 1$, so that $\phi(\mathbf{a})$, as a sum of convex functions, is convex⁵. Finally, the algebraic connectivity $\lambda_2(\mathbf{L}(\mathbf{a}))$ is a concave function of \mathbf{a} , as can be proved following the same steps as in Theorem

⁵Note that $\phi(\mathbf{a})$ is the sum of functions of the single variables a_{ij} . Hence the convexity of $\phi(\mathbf{a})$ can be studied looking at the convexity of the single functions $q(a_{ij})$.

1. Then, the optimization problem [P.3] is also a convex parametric problem, perfectly equivalent to the original problem in (18), since the change of variables $p_{ij} = q(a_{ij})$ in (13) ensures a one-to-one mapping $q : \mathbb{R} \rightarrow \mathbb{R}$, for $0 \leq a_{ij} < 1$, with image covering the problem domain in (18) (see [21, p. 130]). Hence, assuming $\mathbf{0} \leq \mathbf{a} \leq \mathbf{1} - \epsilon'$, with ϵ' an infinitesimal positive constant so that the feasible set of (19) $\Upsilon = \{\mathbf{a} : \mathbf{0} \leq \mathbf{a} \leq \mathbf{1} - \epsilon', \lambda_2(\mathbf{L}(\mathbf{a})) \geq \epsilon\}$ is a compact convex set in $\mathbb{R}^{n(n-1)/2}$, we ensure that the set of minima of (19) is nonempty and by the convexity of the problem we can deduce that all local minima are also global. Note that since the optimization problem in (19) is convex an optimal solution can be found via efficient numerical tools. Furthermore, using Dinkelbach's algorithm [19], based on Theorem 2, we are also able to find the optimal parameter μ in [P.3]. More specifically, the Dinkelbach's algorithm, applied to our problem, proceeds through the following steps:

1. Set $i = 1$ and let \mathbf{a}_i be a feasible point of Υ , with $\mu_i = \frac{\phi(\mathbf{a}_i)}{\lambda_2(\mathbf{L}(\mathbf{a}_i))}$;
2. Set $\mu = \mu_i$ and find $\mathbf{a}_{i+1} \in \Upsilon$ that solves the minimization problem in [P.3];
3. If $|h(\mu, \mathbf{a}_{i+1})| = |\phi(\mathbf{a}_{i+1}) - \mu \lambda_2(\mathbf{L}(\mathbf{a}_{i+1}))| \leq \epsilon''$, with ϵ'' an arbitrarily small positive constant, stop and take \mathbf{a}_{i+1} as the optimal link coefficient vector; otherwise, set $i = i + 1$, $\mu_i = \frac{\phi(\mathbf{a}_i)}{\lambda_2(\mathbf{L}(\mathbf{a}_i))}$ and go to step 2.

Since the topology coefficients a_{ij} obtained in this way are real variables belonging to the interval $[0, 1]$, to obtain the network topology, it is necessary to quantize them to convert them into binary values, 1 or 0, indicating the presence or absence of a link. This quantization is achieved by comparing each a_{ij} with a threshold a_{th} . Of course, the final topology will depend on the threshold value. Moreover, the thresholding operation will also affect the final result in terms of convergence time and energy consumption. It is then of interest to check how sensitive the final topology, as well as convergence time and energy consumption, are to the choice of a_{th} . In the ensuing section, we present some numerical results to shed light on the resulting topologies and their dependence on the propagation model parameters.

A. Numerical Examples

Since our optimization procedure is based on a relaxation technique, the first important step is to evaluate the impact of the relaxation on the final topology and performance.

Example 1: Comparison Between Exhaustive Search and Relaxed Technique: We compare now the topology obtained as a solution of the relaxed problem [P.3] with the optimal graph obtained by solving directly problem [P.0] using an exhaustive search over all possible topologies. For complexity reasons, of course we can only perform this comparison for small scale networks. We consider networks of $n = 4$ and 6 nodes.

To provide results not conditioned to a specific geographic node deployment, we averaged the results over 100 statistically independent realizations of the nodes locations. In each iteration we compute the minimum energy \mathcal{E}_{op} reached using the optimal exhaustive search over all possible topologies, and the energy \mathcal{E}_r corresponding to the network topology whose coefficients a_{ij} are obtained by solving problem [P.3] and thresholding the

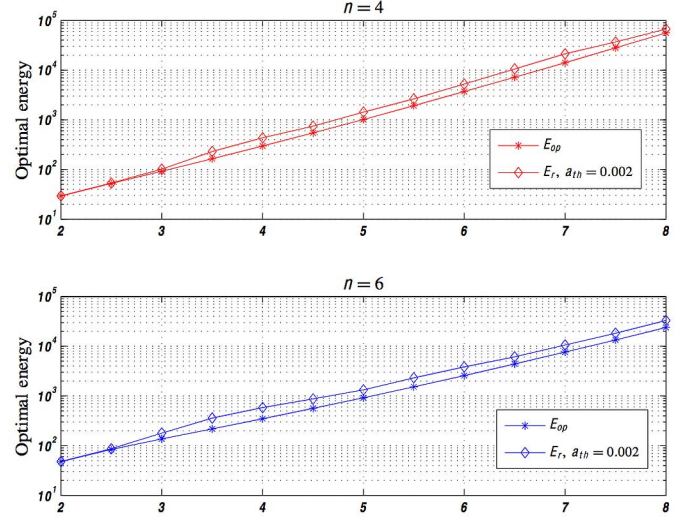


Fig. 1. Optimal average energy obtained with exhaustive search and average energy obtained by solving the relaxed problem [P.3] versus η , for different n values.

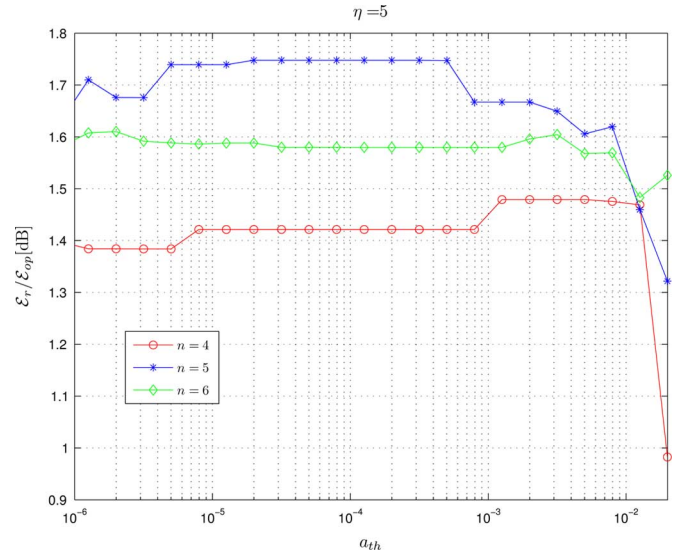


Fig. 2. Ratio between the optimal energy obtained with exhaustive search and the energy obtained by solving the proposed relaxed problem [P.3], versus a_{th} , for different values of n .

result with the threshold $a_{th} = 2 \times 10^{-3}$. In Fig. 1, we report the average energies \mathcal{E}_{op} and \mathcal{E}_r versus η . We can note from Fig. 1 that the loss in terms of optimal energy due to the relaxation of the original problem is negligible (the energy loss is less than 1.7 dB).

Example 2: Impact of Thresholding Operation on Final Topology: Clearly, the selection of the threshold a_{th} plays a role in the identification of the final topology. To evaluate the impact of a_{th} on the final topology, in Fig. 2 we report the ratio $\frac{\mathcal{E}_r}{\mathcal{E}_{op}}$ versus a_{th} for different numbers of nodes n and for $\eta = 5$. The energies are averaged over 100 independent node realizations. We can observe from Fig. 2 that there is a wide range of values of a_{th} such that the energy loss is practically independent of a_{th} . This shows that our proposed procedure is

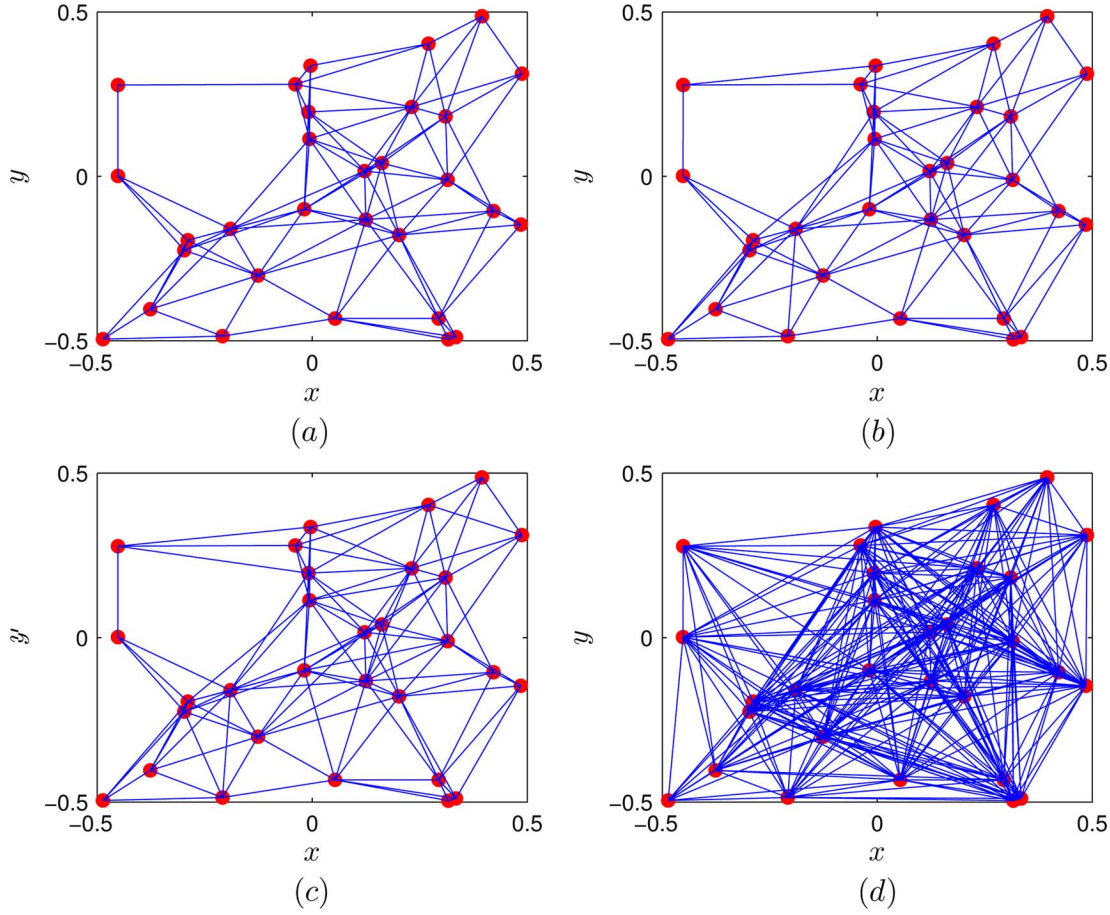


Fig. 3. Optimal topologies, for different threshold values and fixed $\eta(\eta = 6)$: (a) $a_{th} = 0.09$. (b) $a_{th} = 0.05$. (c) $a_{th} = 5 \times 10^{-4}$. (d) $a_{th} = 10^{-7}$.

rather robust with respect to the choice of a_{th} . It is now interesting to check the effect of the threshold a_{th} on the topology, considering larger scale networks (in this case, we can only run our algorithm, as the exhaustive search is not feasible). As an example, in Fig. 3 we show the topologies obtained by solving problem [P.3], for a network composed of $n = 30$ nodes, using different values of a_{th} , for $\eta = 6$. Comparing the four cases reported in Fig. 3, we notice that, only for very low values of the threshold [i.e., case (d)], we appreciate a sensitive change of topology, whereas for a large range of values of a_{th} , the final topology is practically the same. This means that the proposed algorithm, in spite of the relaxation step and the subsequent quantization, yields rather stable solutions.

The previous results pertain to a specific realization of the node locations. To provide results of more general validity, in Fig. 4, we report the average value of: a) fraction of active links $\frac{\sum_{i=1}^n |\mathcal{N}_i|}{n(n-1)}$; b) $\lambda_2(L)$; and c) the average energy \mathcal{E}_r , as a function of the threshold a_{th} . The averages are carried out over 100 independent realizations of the nodes location. From Fig. 4, we observe that there is an interval of values of a_{th} (roughly, between 10^{-5} to 10^{-2}) for which we obtain a strong reduction in the fraction of active links, with respect to the situation where there is no threshold, still achieving nearly the same performance, in terms of algebraic connectivity and energy consumption. This is indeed an important result, as it shows that the relaxed algorithm is weakly sensitive to the choice of a_{th} .

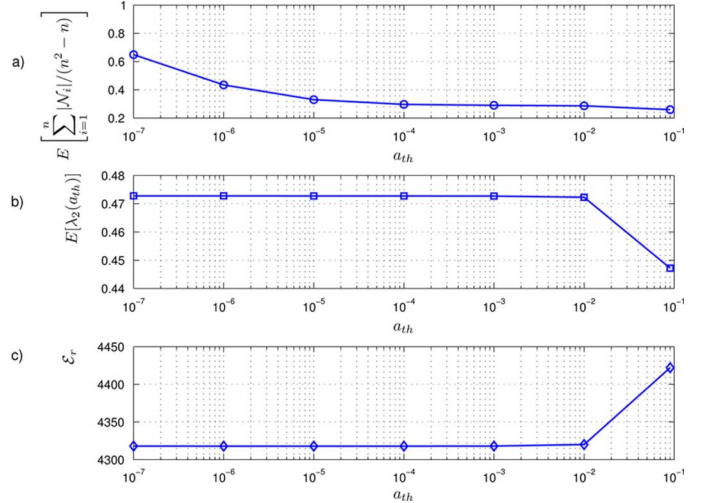


Fig. 4. Average value of (a) fraction of active links. (b) $\lambda_2(L)$. (c) energy versus threshold value for $\eta = 6$.

Example 3: Impact of Propagation Parameters on Final Topology: It is also interesting to look at the change in topology as a function of the radio communication model. To this end, in Fig. 5, we plot the optimal topologies achieved for the same node locations as in Fig. 3, but pertaining to different path loss exponents η , for a given threshold. Interestingly, we

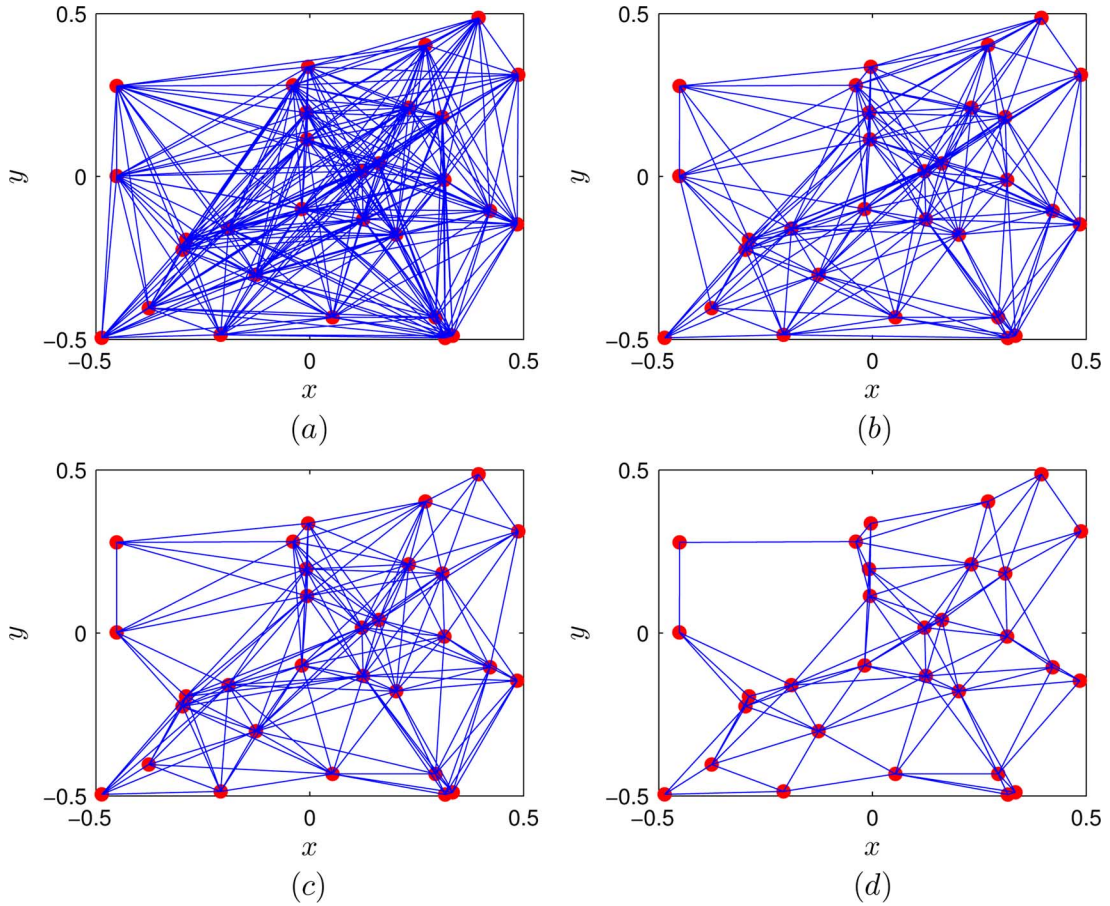


Fig. 5. Optimal topologies, for different path loss exponents η and fixed threshold ($a_{\text{th}} = 0.09$): (a) $\eta = 3$. (b) $\eta = 4$. (c) $\eta = 5$. (d) $\eta = 6$.

notice, as expected, that, as the propagation loss increases (i.e., η increases), the network tends to become more and more sparse.

The results shown in Fig. 5 refer to a single realization of the node positions. To draw conclusions of more general validity, we averaged over 100 statistically independent realizations of the node locations, for networks of 30 nodes. In Fig. 6, we report the same performance metrics as in Fig. 4, but now as a function of the path loss exponent η , setting $a_{\text{th}} = 0.09$. From Fig. 6, we observe that when the attenuation is high (i.e., η is large), reducing the number of links (making the topology sparser) is more important than reducing convergence time. Conversely, when the attenuation is low (i.e., η is small), increasing network connectivity is more important than reducing power consumption. This behavior sounds reasonable and in agreement with intuition.

V. OPTIMAL TOPOLOGY FOR RANDOM GEOMETRIC NETWORKS

In this section, we remove the assumption that the node locations are known a priori and model the network as a random geometric graph (RGG). In such a case, the graph connectivity properties and the convergence time can only be established in a probabilistic sense, asymptotically, as the number of nodes tends to infinity. We refer to [22] for the first basic result about the convergence of consensus algorithms over random graphs and to [23] for a more recent generalization of the convergence

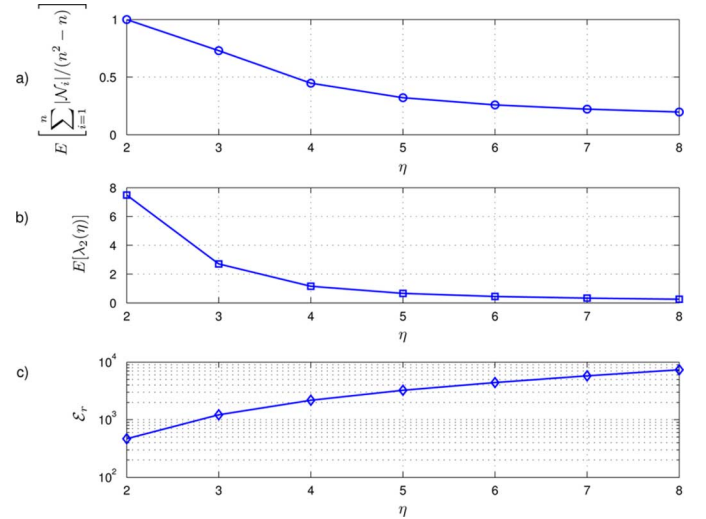


Fig. 6. Average value of (a) fraction of active links. (b) $\lambda_2(\mathbf{L})$. (c) energy versus path loss η for $a_{\text{th}} = 0.09$.

conditions under stochastic disturbances. As shown in [22], the rate of convergence of consensus algorithms in the random graph case is dictated by the expected value $E[e^{-2T_s \lambda_2(\mathbf{L})}]$. In the following, exploiting the concentration properties of the eigenvalues of RGGs [24], [25], we will show how to relate the convergence time to the expected value of $\lambda_2(\mathbf{L})$. This link

will be fundamental to derive the optimal coverage radius, and then transmit power, that minimize the energy consumption necessary to achieve consensus over RGGs. To achieve this goal, it is fundamental to recall and extend some results about the spectrum of RGGs.

A. RGGs

A random graph is obtained by distributing n points randomly over the d -dimensional space \mathbb{R}^d and connecting the nodes according to a given rule. Let $V_n = \{\mathbf{x}_1, \mathbf{x}_2, \dots, \mathbf{x}_n\}$ be a set of d -dimensional vectors \mathbf{x}_i , belonging to a compact set $\Omega = [-1/2, 1/2]^d$ of \mathbb{R}^d , whose entries denote the coordinates of the nodes in \mathbb{R}^d , and let $\|\cdot\|$ be the Euclidean norm on \mathbb{R}^d . The graph topology is captured by the adjacency matrix \mathbf{A} which, in this case, is a random matrix. An important class of random matrices, encompassing the adjacency matrix of our problem, is the so-called Euclidean Random Matrix (ERM) class, introduced in [26]. Given a set of n points located at positions $\mathbf{x}_i, i = 1, \dots, n$, an $n \times n$ adjacency matrix \mathbf{A} is an ERM if its generic (i, j) entry depends only on the difference $\mathbf{x}_i - \mathbf{x}_j$, i.e., $a_{ij} = F(\mathbf{x}_i - \mathbf{x}_j)$, where F is a measurable mapping from \mathbb{R}^d to \mathbb{R} . An important subclass of ERM is given by the adjacency matrices of the so-called RGGs. In such a case, the entries a_{ij} of the adjacency matrix are either zero or one depending only on the distance between nodes i and j , i.e.

$$a_{ij} = \begin{cases} 1 & \text{if } \|\mathbf{x}_i - \mathbf{x}_j\| \leq r \\ 0 & \text{otherwise} \end{cases} \quad (20)$$

where r is the coverage radius. This is a particular case of an ERM, corresponding to having

$$F(\mathbf{x}_i - \mathbf{x}_j) = \begin{cases} 1 & \text{if } \|\mathbf{x}_i - \mathbf{x}_j\| \leq r \\ 0 & \text{otherwise} \end{cases}. \quad (21)$$

We will use the symbol $G(n, r)$ to indicate an RGG composed of n points, with coverage radius r .

The RGG model is the most appropriate to capture the topology of a wireless network, as it basically states that there is a link between two nodes only if they are within the coverage radius of each other⁶.

Next, we recall some of the most important properties of RGG's, in terms of connectivity and spectrum, as they are relevant to our optimization problem.

1) *Connectivity*: Some interesting results on the asymptotic connectivity of random geometric graphs have been derived in a seminal work by Gupta and Kumar [27] who proved that, given a set of n points uniformly distributed within a unit square (i.e., $d = 2$), the graph is connected almost surely if the coverage radius behaves as

$$r_0(n) = \sqrt{\frac{\log(n) + c_n}{\pi n}}$$

with $c_n \rightarrow \infty$, as $n \rightarrow \infty$. Conversely, if $c_n \rightarrow -\infty$, the graph is disconnected almost surely. This means that the expression $\sqrt{\frac{\log(n)}{\pi n}}$ represents a threshold distance. In the following, we

⁶In practice, a wireless channel is also affected by fading, multipath, and shadowing. Hence, the presence of a link between two nodes depends on two sources of randomness: distance and fading. In this work, we concentrate on the single source of randomness, given by the distance between the nodes, but considering both sources of randomness will be an interesting extension of this paper.

will often use the shorthand notation $r^+(n)$ to indicate the law $\sqrt{\frac{\log(n) + c_n}{\pi n}}$, with $c_n \rightarrow \infty$, as $n \rightarrow \infty$. Hence, a coverage radius $r_0(n)$ behaving as $r^+(n)$ represents a law that ensures connectivity with high probability, as $n \rightarrow \infty$. We will use the notation $r_0(n) \sim r^+(n)$ to indicate such a behavior.

In [4], [28], it has been shown that the degree of a RGG $G(n, r)$ of points uniformly distributed over a two-dimensional unit torus⁷ is equal to

$$d(n) = \pi r^2 n \quad (22)$$

with high probability, i.e., with probability $1 - 1/n^2$, if the radius behaves as $r_0(n) \sim r^+(n)$. This implies that an RGG tends to behave, asymptotically, as a regular graph, if the coverage radius is chosen so as to guarantee connectivity with high probability.

We are primarily interested in the second eigenvalue of the Laplacian, $\mathbf{L} = \mathbf{D} - \mathbf{A}$, where \mathbf{D} is the degree matrix and \mathbf{A} is the adjacency matrix [see (1)]. From (22), $\mathbf{D} = \pi r^2 n \mathbf{I}$, so that we only need to investigate the second *largest* eigenvalue of \mathbf{A} . Hence, in the ensuing section, we study the spectrum of \mathbf{A} .

2) *Spectrum of a Random Geometric Graph*: In [24], [25], it is shown that the eigenvalues of the adjacency matrix, or of the transition probability matrix⁸, tend to be concentrated, as the number of nodes tend to infinity. In particular, in [24] it is shown that the eigenvalues of the normalized adjacency matrix $\mathbf{A}_n = \mathbf{A}/n$ of an RGG $G(n, r)$, composed of points uniformly distributed over a unit bidimensional torus, tend to the Fourier series coefficients of the function F defined in (21)

$$\hat{F}(\mathbf{z}) = \int_{\Omega_r} \exp(-2\pi j \mathbf{z}^T \mathbf{x}) d\mathbf{x} \quad (23)$$

almost surely, for all $\mathbf{z} = [z_1, z_2] \in \mathbb{Z}^2$, where $\Omega_r = \{\mathbf{x} = [x_1, x_2]^T \in \mathbb{R}^2 : \|\mathbf{x}\| \leq r\}$. Using polar coordinates, i.e., $x_1 = \rho \sin \theta$ and $x_2 = \rho \cos \theta$, with $0 \leq \rho \leq r$ and $0 \leq \theta \leq 2\pi$, we obtain

$$\hat{F}(\mathbf{z}) = \int_0^r \int_0^{2\pi} \exp(-2\pi j \rho (z_1 \sin \theta + z_2 \cos \theta)) \rho d\rho d\theta.$$

This integral can be computed in closed form. Setting $z_1 = A \sin \phi$ and $z_2 = A \cos \phi$, we have

$$\hat{F}(A, \phi) = \int_0^r \int_{-\phi}^{2\pi - \phi} \exp(-2\pi j \rho A \cos(\xi)) \rho d\rho d\xi$$

with $\xi = \theta - \phi$. Furthermore, using the integral expression for the Bessel function of the first kind of order k , $J_k(x) = \frac{1}{2\pi} \int_{-\pi}^{\pi} \exp(jx \sin(\xi) - jk\xi) d\xi$, we get

$$\hat{F}(A, \phi) = \hat{F}(A) = 2\pi \int_0^r J_0(2\pi \rho A) \rho d\rho.$$

Finally, using the identity $\int_0^u v J_0(v) dv = u J_1(u)$, we can make explicit the dependence of $\hat{F}(A)$ on the index pair $[z_1, z_2]$

$$\hat{F}(z_1, z_2) = \frac{r}{\sqrt{z_1^2 + z_2^2}} J_1\left(2\pi r \sqrt{z_1^2 + z_2^2}\right). \quad (24)$$

⁷A torus geometry is typically used to get rid of border effects.

⁸The transition probability matrix is the adjacency matrix, normalized with respect to the node degree, so that the i th row of the adjacency matrix is divided by the degree of node i .

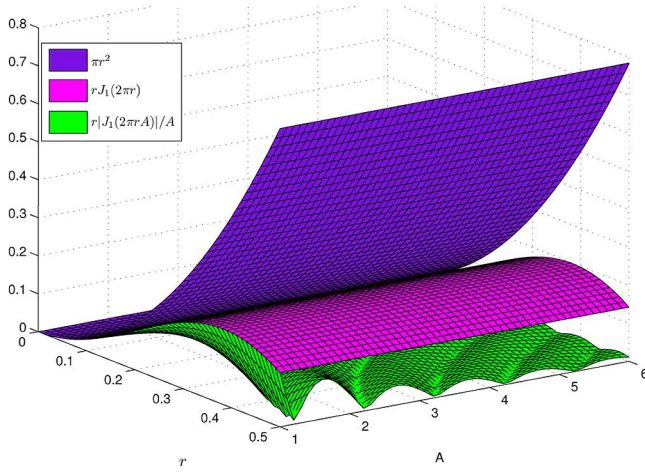


Fig. 7. Verification of the inequalities in (26).

This formula allows us to rank the eigenvalues of $\mathbf{A}_n = \mathbf{A}/n$. In particular, we are interested in the second largest eigenvalue of \mathbf{A}_n . Considering that the minimum coverage radius ensuring connectivity behaves as $r(n) \sim \sqrt{\frac{\log(n)}{n}}$, i.e., it is a vanishing function of n , we can use the Taylor series expansion of $\hat{F}(z_1, z_2)$, for small r . Recalling that, for small x , $J_1(x) = x/2 - x^3/16 + o(x^5)$, we can approximate the eigenvalues as

$$\hat{F}(z_1, z_2) = \pi r^2 - \frac{\pi^3(z_1^2 + z_2^2)r^4}{2} + o(r^6). \quad (25)$$

This expansion shows that, at least for small r , the largest eigenvalue equals πr^2 and occurs at $z_1 = z_2 = 0$, whereas the second largest eigenvalue corresponds to the cases $(z_1 = 1, z_2 = 0)$ and $(z_1 = 0, z_2 = 1)$. More generally, we can check numerically that, for $r \leq 1/2$ and $A \geq 1$, the following inequalities hold true:

$$\pi r^2 \geq r J_1(2\pi r) \geq \frac{r}{A} |J_1(2\pi r A)|. \quad (26)$$

The validity of these inequalities can be verified from Fig. 7, which shows the three terms in (26) as a function of r and A .

In summary, denoting the spectral radius of \mathbf{A}_n as $\zeta_1(\mathbf{A}_n) = \max_{1 \leq i \leq n} \frac{|\lambda_i(n)|}{n}$, where $\{\lambda_i(n)\}_{i=1}^n$ is the set of eigenvalues of \mathbf{A} , it follows that

$$\lim_{n \rightarrow \infty} \zeta_1(\mathbf{A}_n) = \max_{z \in \mathbb{Z}^2} |\hat{F}(z)| = \hat{F}(0, 0) = \pi r^2 \quad (27)$$

while the second largest eigenvalue of \mathbf{A}_n , $\zeta_2(\mathbf{A}_n)$, converges to

$$\lim_{n \rightarrow \infty} \zeta_2(\mathbf{A}_n) = \hat{F}(1, 0) = \hat{F}(0, 1) = r J_1(2\pi r). \quad (28)$$

We are now able to derive the asymptotic expression for the second largest eigenvalue of the normalized Laplacian $\mathbf{L}_n = \mathbf{D}_n - \mathbf{A}_n$, where $\mathbf{D}_n := \mathbf{D}/n$ is the normalized degree matrix. Because of the asymptotic property of the degree of an RGG,

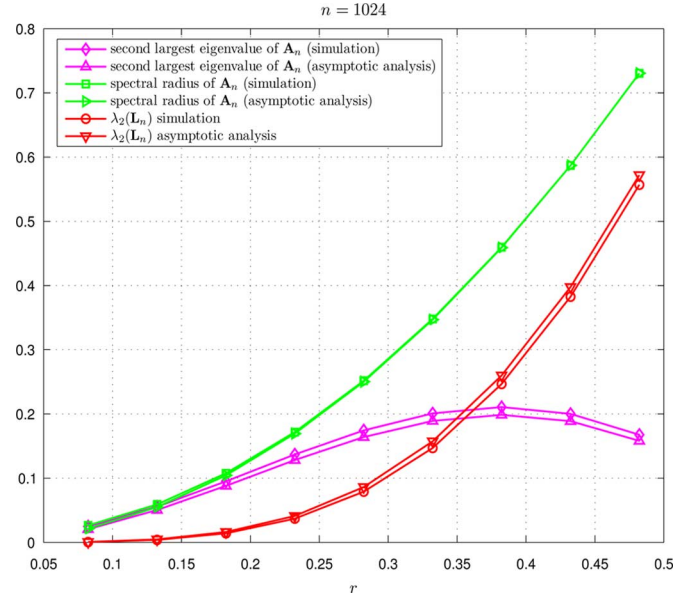


Fig. 8. Asymptotic analysis and simulation results for some eigenvalues of \mathbf{A}_n and for $\lambda_2(\mathbf{L}_n)$ versus the transmission radius.

shown in (22), the second largest eigenvalue of \mathbf{L}_n tends asymptotically to

$$\lambda_2(\mathbf{L}_n) = \pi r^2 - \zeta_2(\mathbf{A}_n). \quad (29)$$

Thus, the algebraic connectivity of the graph can be approximated, asymptotically, as

$$\lambda_2(\mathbf{L}) = \pi n r^2 - n r J_1(2\pi r). \quad (30)$$

Since the previous expressions have been derived in the asymptotic regime, in Fig. 8 we compare the analytic formulas for the first and the second largest eigenvalues of \mathbf{A}_n , as given in (27) and (28), with the numerical results obtained by averaging over 100 independent realizations of RGG's composed of $n = 1024$ nodes. We can notice the good agreement in Fig. 8 between the theoretical expression for the algebraic connectivity $\lambda_2(\mathbf{L}_n)$, given in (29), and the simulation results.

B. Minimization of the Energy Consumption: An Analytic Approach

We can now exploit the previous analytic expressions to study the energy minimization problem for RGG's. In the random topology case, since the distances are unknown, we cannot optimize the power associated with each link. However, we can seek the common transmit power that minimizes energy consumption. Thus, in the random setting we assume a broadcast communication model, where each node broadcasts the value to be shared with its neighbors. In the lack of any information about distances among the nodes, we assume that each node uses the same transmit power. In this case, the network topology can be modeled as a random graph model. It can be shown [22], [23] that the system in (3) converges to consensus almost surely, i.e., $\Pr\{\lim_{t \rightarrow \infty} \mathbf{x}(t) = x^* \mathbf{1}\} = 1$ assuming that each node has a coverage radius so that the network is asymptotically connected

with probability one [14]. Then the rate of convergence of the dynamical system in (3) is given [22], [23] by $E[e^{-2T_s\lambda_2(\mathbf{L})}]$. Note that defining $f(\lambda_2) = e^{-2T_s\lambda_2(\mathbf{L})}$ and using the Taylor series expansion of $f(\lambda_2)^9$ at the point $\lambda_2^0 = E[\lambda_2] = m_{\lambda_2}$, we can write

$$\begin{aligned} f(\lambda_2) &= f(m_{\lambda_2}) + f^{(1)}(m_{\lambda_2})(\lambda_2 - m_{\lambda_2}) \\ &\quad + \frac{f^{(2)}(m_{\lambda_2})}{2}(\lambda_2 - m_{\lambda_2})^2 \\ &\quad + \sum_{k=3}^{\infty} \frac{f^{(k)}(m_{\lambda_2})}{k!}(\lambda_2 - m_{\lambda_2})^k. \end{aligned} \quad (31)$$

Consequently, taking the expected value, we get

$$E[f(\lambda_2)] = f(m_{\lambda_2}) + \frac{f^{(2)}(m_{\lambda_2})}{2}\sigma_{\lambda_2}^2 + \dots \quad (32)$$

denoting with $\sigma_{\lambda_2}^2 = E[(\lambda_2 - m_{\lambda_2})^2]$ the variance of λ_2 . But since all central moments of order greater than one of the eigenvalues tend to zero, because of the concentration property, we can use the approximation

$$E[e^{-2T_s\lambda_2}] \approx e^{-2T_s E[\lambda_2]}. \quad (33)$$

As a consequence, the energy spent to achieve consensus can now be approximated as

$$\mathcal{E} = K \frac{np}{2E[\lambda_2(L(p))]} \quad (34)$$

This is the performance metric we wish to minimize in the random scenario, with respect to the single unknown p .

In particular, using the asymptotic expression (30) for the algebraic connectivity, we can introduce the following metric

$$\mathcal{E}(r) = \frac{np_{\min}[1 + (r/r_0)^\eta]}{n\pi r^2 - rnJ_1(2\pi r)}. \quad (35)$$

We now check, numerically, that the function $\mathcal{E}(r)$ given in (35) is a convex function of r , for $r_0(n) \leq r \leq 0.5$, where $r_0(n) \sim r^+(n)$, to ensure connectivity.

Let us rewrite (35) as

$$\mathcal{E}(r) = \frac{g(r)}{\lambda_2(r)}$$

with $g(r) = np_{\min}[1 + (r/r_0)^\eta]$ and $\lambda_2(r)$ as in (30). The first- and second-order derivatives of $g(r)$ are, respectively

$$\begin{aligned} g'(r) &= \frac{dg(r)}{dr} = np_{\min}\eta \frac{r^{\eta-1}}{r_0^\eta} > 0 \\ g''(r) &= \frac{d^2g(r)}{dr^2} = np_{\min}\eta(\eta-1) \frac{r^{\eta-2}}{r_0^\eta} > 0 \end{aligned}$$

⁹For simplicity we drop in λ_2 the dependence on L .

so that $g(r)$ is a convex increasing positive function of r . Let us now study the behavior of $\lambda_2(r)$. Using

$$\frac{d[r^m J_m(r)]}{dr} = r^m J_{m-1}(r) \quad \text{for } m = 0, 1, 2, \dots$$

we obtain

$$\lambda_2'(r) = \frac{d\lambda_2(r)}{dr} = 2\pi r n [1 - J_0(2\pi r)]$$

with $\lambda_2'(r) > 0$ for $r_0(n) \leq r \leq 0.5$. Moreover, since

$$\frac{dJ_m(r)}{dr} = \frac{m}{r} J_m(r) - J_{m+1}(r) \quad \text{for } m = 0, 1, 2, \dots$$

we have

$$\lambda_2''(r) = \frac{d^2\lambda_2(r)}{dr^2} = 2\pi n [1 - J_0(2\pi r)] + 4\pi^2 r n J_1(2\pi r). \quad (36)$$

Observe that the first term on the right-hand side (RHS) of (36) is always positive. Furthermore, if $r \leq 1/2$, the second term is also positive, since $J_1(2\pi r) > 0$ for $r \leq 1/2$. Hence, $\lambda_2''(r) > 0$ and we can conclude that the algebraic connectivity is an increasing and convex function of r for $r_0(n) \leq r \leq 0.5$, where $r_0(n) \sim r^+(n)$.

We can now compute the first- and second-order derivatives of the energy function with respect to r . We get

$$\mathcal{E}'(r) = \frac{g'(r)}{\lambda_2(r)} - \frac{\lambda_2'(r)g(r)}{\lambda_2^2(r)}$$

and, substituting the corresponding expressions, the extremal points can be obtained by solving the following nonlinear equation:

$$\mathcal{E}'(r) = a_1(r) + a_2(r)J_0(2\pi r) - a_3(r)J_1(2\pi r) = 0$$

with $a_1(r) = \pi[(\eta-2)r^\eta - 2r_0^\eta]$, $a_2(r) = 2\pi(r^\eta + r_0^\eta)$ and $a_3(r) = \eta r^{\eta-1}$. Furthermore, the second derivative of $\mathcal{E}(r)$ is given by the equation shown at the bottom of the page. In Fig. 9, we report $\mathcal{E}''(r)$ as a function of r , for different values of η . From Fig. 9, we can check that the second derivative is always positive in the range of interest. This verifies that $\mathcal{E}(r)$ is indeed a convex function of r defined on the compact convex set $r_0(n) \leq r \leq 0.5$. As a consequence, we can state that there is always at least a radius r that globally minimizes the energy consumption in a RGG.

Numerical examples. In Fig. 10, we compare the value of $\mathcal{E}(r)$ obtained by our theoretical approach and by simulation, for various values of the path loss exponent, $2 \leq \eta \leq 6$. The results are averaged over 100 independent realizations of random geometric graphs composed of $n = 1000$ nodes. For each η , the pair of radius and energy providing minimum energy consumption is indicated by a circle (simulation) or a star (theory). We observe

$$\mathcal{E}''(r) = \frac{(g''(r)\lambda_2(r) - 2\lambda_2'(r)g'(r))\lambda_2(r) + g(r)(2\lambda_2'^2(r) - \lambda_2''(r)\lambda_2(r))}{\lambda_2^3(r)}.$$

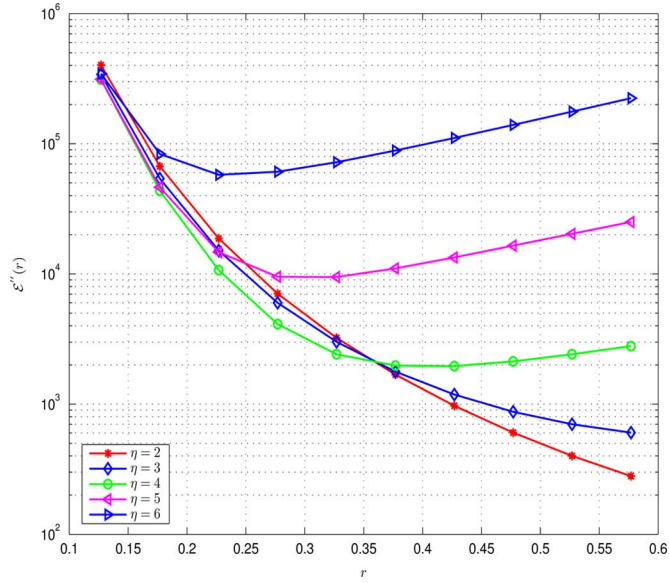


Fig. 9. Second derivative of the energy versus the transmission radius for several values of η .

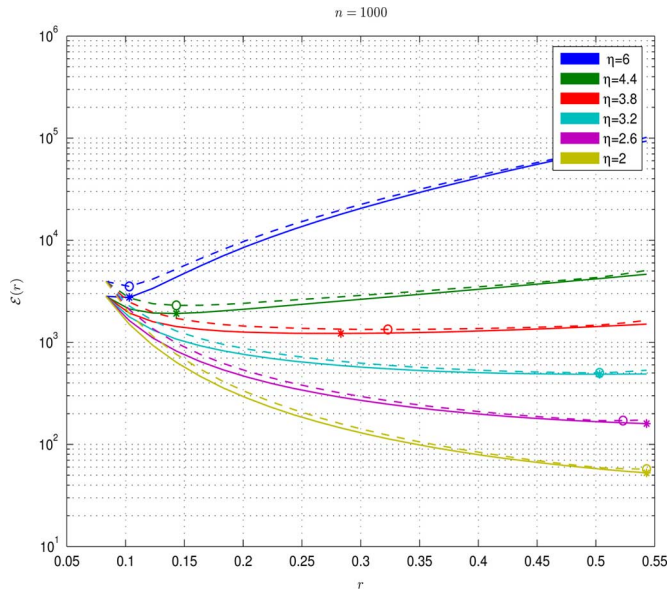


Fig. 10. Global energy consumption versus transmission radius for an RGG; theoretical values (solid) and simulation (dashed).

that the theoretical derivations provide a very good prediction of the performance achieved by simulation. Furthermore, for each η , there is a coverage radius value that minimizes energy consumption.

The optimal values of the coverage radius as a function of η , as predicted by our theoretical derivations or by simulation, are reported in Fig. 11. From this figure, we observe that there is a clear transition from the low power attenuation regime (i.e., $\eta < 3.5$), where the optimal radius tends to make the network fully connected, as opposed to the strong attenuation situation ($\eta > 4.5$), where the network is minimally connected. This means that in the low attenuation case, minimizing convergence time is more important than minimizing power consumption.

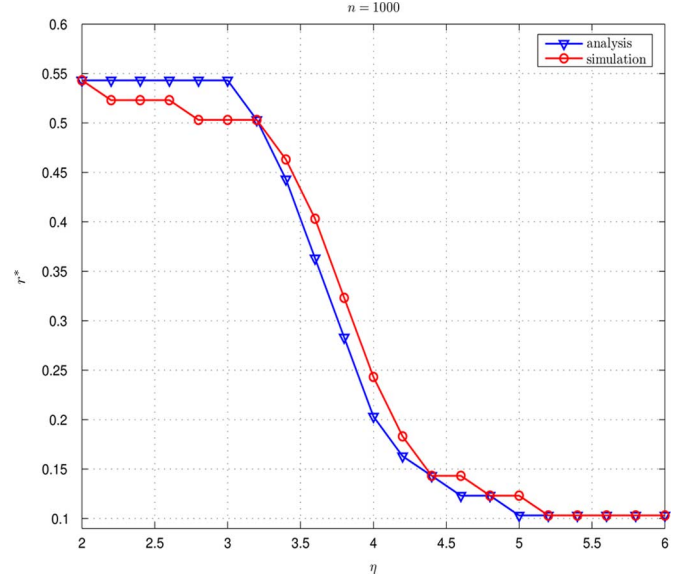


Fig. 11. Optimal transmission radius versus η .

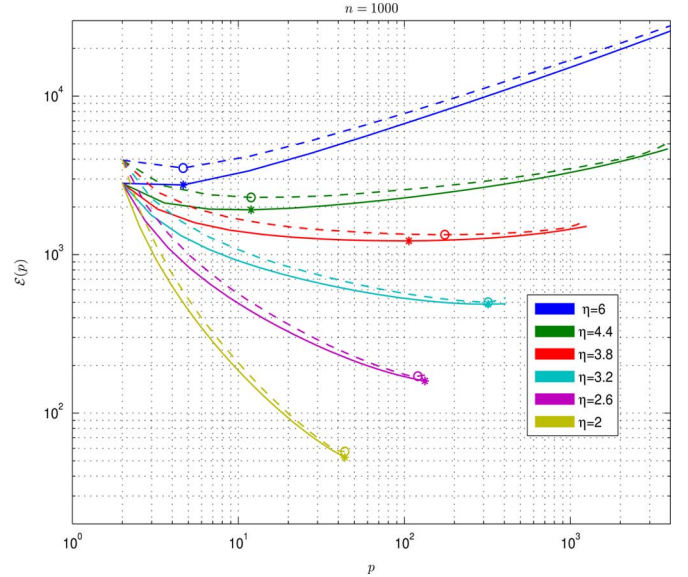
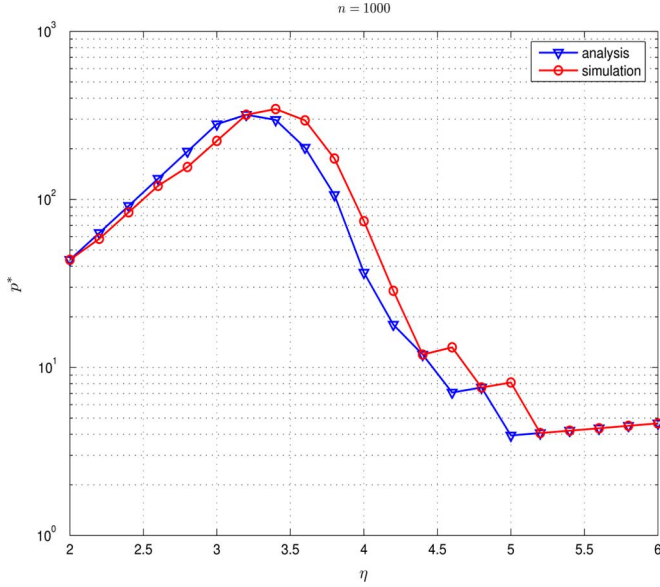


Fig. 12. Global energy consumption versus per node transmit power for an RGG; theoretical values (solid) and simulation (dashed).

Conversely, in the large attenuation case, it is more important to minimize power consumption, by limiting the number of links as much as possible, compatibly with the constraint of ensuring connectivity.

Fig. 12 shows the average energy consumption versus the per node transmit power p , under the same settings of Fig. 10. The circles (simulation) and the stars (theory) represent, again, the values of p that minimize energy consumption, for each η . It can be verified the existence of an optimal transmit power value minimizing the energy consumption.

Finally, Fig. 13 shows the optimal per node power versus η . For low values of η , the transmit power increases with η because it must cope with higher attenuations to guarantee connectivity. Conversely, for large values of η , the optimal power decreases with η because, in such a case, it is more beneficial to limit

Fig. 13. Optimal per node transmit power versus η .

the number of links, until the minimum power guaranteeing the connectivity constraint is reached.

C. Random Topologies versus Uniformly Spaced Grids

Finally, it is interesting to compare the energy consumption achievable with a random geometric graph and a deterministic grid. In the deterministic case, we may also distinguish between a graph with nodes scattered arbitrarily in a given area, but with positions known, and a regular uniform grid, where the points are located over a rectangular grid.

1) *Eigenvalues of a Planar Uniform Grid:* We start by deriving the algebraic connectivity of a square grid whose n nodes are uniformly spaced within a unit square, at a distance $\delta = 1/\sqrt{n} = 1/\sqrt{n_1}$. To avoid undesired border effects, we consider the wrapping of the unit square in order to form a toroidal surface. Each node is assumed to have a link with the neighboring nodes only if they are at a distance less than a coverage radius $r(p)$, that depends on the transmit power p , as with geometric graphs. In Appendix A, we derive a closed form expression for the network degree and for the algebraic connectivity [see, e.g., (45)–(48)].

A numerical check of our derivations is reported in Fig. 14, where we show the numerical value of $\lambda_2(\mathbf{L})$, obtained through the eigendecomposition of \mathbf{L} , and the value given in (48), for different values of η . From Fig. 14, we can see a perfect agreement between our closed form expression and the numerical results. Notice, in particular, the sharp transition behavior: the eigenvalues tend to n or 0 depending on whether the transmit power is above or below a threshold; further, the threshold increases with η .

In Fig. 15, we compare the algebraic connectivity of the rectangular grid, given by (48), with the theoretical value obtained for the random geometric graph, given in (30), assuming the same node density, over the same toroidal surface. As shown in previous works, see, e.g., [4], RGGs tend to behave asymptotically as a regular graph. The result shown in Fig. 15 is a further

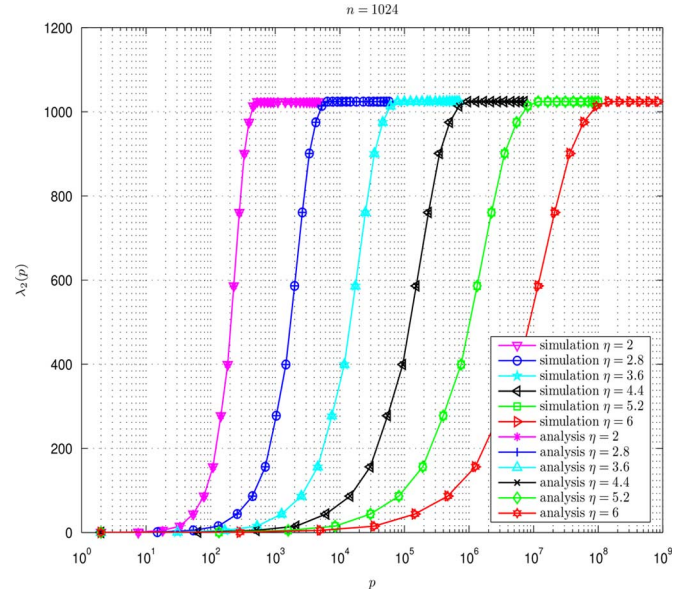


Fig. 14. Network algebraic connectivity versus per node transmit power for several values of the path loss coefficient.

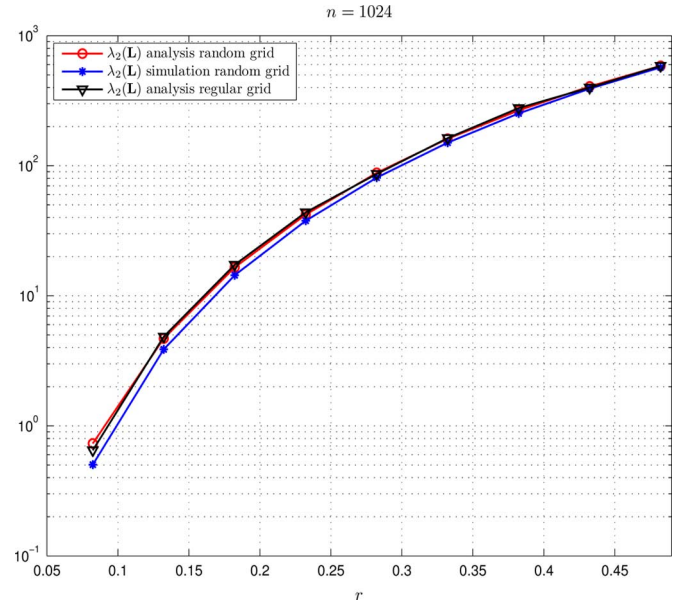


Fig. 15. Algebraic connectivity of random geometric graph and rectangular grid versus transmission radius.

confirmation of this property. In the same figure, we also report simulation results for the algebraic connectivity, obtained by averaging over 100 independent realizations of a RGG. We can check, once again, the good agreement between theory and simulation.

Finally, in Fig. 16 we compare the energy consumption obtained assuming full *a priori* knowledge of the nodes' locations or no knowledge at all. In the first case, the topology and the power allocation over each link are optimized according to the method illustrated in Section IV. The optimal values, for each η , are indicated by colored dots. In the second case, we report (solid line) the energy consumption versus the average power, assuming that all nodes transmit with the same power (since they

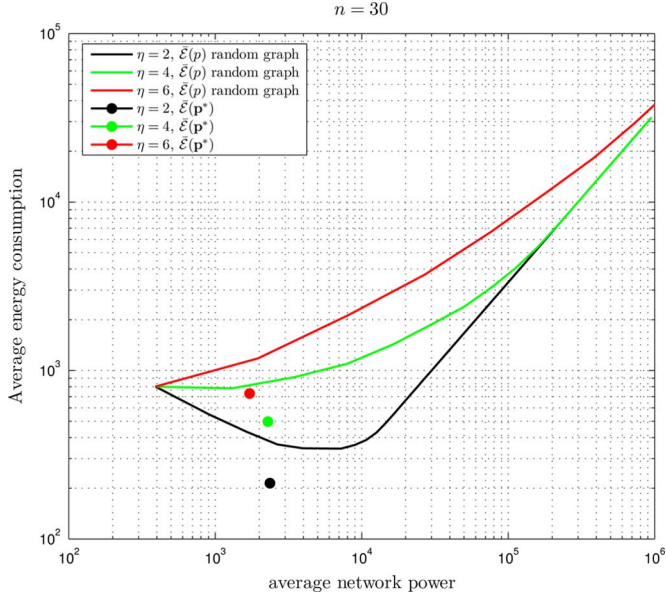


Fig. 16. Average network energy consumption versus average network power.

do not have any prior information about the other nodes positions). To make a fair comparison between the two cases, we consider in both cases the sum of the powers associated with each active link. This means that, in the second case, the energy consumption is measured, for every common transmit power p ,

as $\mathcal{E}(p) = \frac{p \sum_{i=1}^n n_i(p)}{\lambda_2(p)}$, where $n_i(p)$ denotes the number of neighbors of node i . The results shown in Fig. 16 have been obtained by averaging the results obtained in the two settings over the same set of 100 independent random deployments of $n = 30$ nodes, uniformly distributed over the unit square.

From Fig. 16 we can see that, as expected, the method assuming perfect *a priori* knowledge of the node positions (in the figure denoted as $\bar{\mathcal{E}}(p^*)$) is indeed able to achieve better performance than the other method ($\bar{\mathcal{E}}(p)$), as it is able to take advantage of the *a priori* knowledge. The optimal average power is the result of a tradeoff between transmit power and convergence time, and always depends on the path loss exponent.

VI. CONCLUSION

In this paper we have addressed the problem of finding the network topology that minimizes the energy consumption necessary to achieve consensus in a WSN. Assuming a simple flat fading propagation model, we have studied two main network models: 1) arbitrary networks, where the nodes are arbitrarily located, but with known positions, and 2) a random model, where the positions are not known *a priori*, but are modeled as random variables. In the first case, we have shown how to optimize the network topology and the power allocated to each active link in order to minimize the total energy necessary to achieve consensus within a prescribed accuracy. Topology optimization is, in general, a combinatorial problem and hence computationally demanding. To simplify the solution, we introduced a relaxation step that enabled us to reformulate the energy minimization

problem as a convex-concave fractional program. This alternative formulation can be cast as an equivalent parametric convex problem, which enables efficient solutions. The link weights resulting from the solution of the convex problem must then be thresholded to find out the network topology. We have shown through numerical results that the thresholding operation may yield a considerable reduction of the number of active links, yet with very limited effect on performance.

In our deterministic setting, we assumed point-to-point links and we optimized the power over each link. In practice, a consensus algorithm running over a wireless network could benefit from the broadcast channel. Deciding between broadcast or one-to-one links entails a proper choice of the medium access strategy, to establish in which time slot each node has to listen to which broadcaster.

Conversely, in the random network case, lacking any information about the internode distances, we assumed a broadcast communication strategy. In such a case, the network topology is modeled as a random geometric graph. We have derived closed form expressions, albeit valid only asymptotically, for the algebraic connectivity, assuming a common transmit power. Then, building on these expressions, we have shown that the energy consumption is a convex function of the coverage radius. We have also shown that a random geometric graph performs, asymptotically, as a regular graph built over a rectangular grid. This confirms previous results, although now in the context of energy minimization over consensus networks.

Finally, we have compared the performance achievable with arbitrary and random graphs. Clearly, the knowledge of the node locations allows better power allocation, that translates into lower energy consumption to achieve consensus. However, in practice there is a price associated with the knowledge of node location. This knowledge requires the acquisition of the node positions first and then a centralized optimization. Conversely, the random approach can be followed also in a decentralized fashion, with only minimal information about some global parameters like number of nodes and area covered by the network, and it does not need any extra hardware or computation to acquire the nodes' locations.

In this paper, we have assumed a simple flat fading channel model, whose effect is only to introduce attenuation and superimpose noise. The simple model captures the essence of the problem and keeps the overall problem complexity under control. However, looking at potential applications, it would be interesting to generalize the approach to the case where the channel model is more complicated. Furthermore, the network topology has been assumed to be static. However, a dynamic topology, possibly adapted to the consensus state, might provide better performance.

APPENDIX A

In this section, we derive an analytical expression for the eigenvalues of the adjacency matrix \mathbf{A} of a rectangular grid over a unit torus, as a function of the coverage radius $r(p)$. We assume, for simplicity that the number of nodes n is a square number, i.e., $n = n_1^2$, with n_1 integer. We number the rows of

the grid, 1 to n_1 , going from bottom to top. The $n \times n$ matrix \mathbf{A} can be expressed in a cyclic block form, as

$$\mathbf{A} = \begin{bmatrix} \mathbf{A}_0 & \mathbf{A}_1 & \mathbf{A}_2 & \dots & \mathbf{A}_{n_1-2} & \mathbf{A}_{n_1-1} \\ \mathbf{A}_{n_1-1} & \mathbf{A}_0 & \mathbf{A}_1 & \dots & \mathbf{A}_{n_1-3} & \mathbf{A}_{n_1-2} \\ \mathbf{A}_{n_1-2} & \mathbf{A}_{n_1-1} & \mathbf{A}_0 & \dots & \mathbf{A}_{n_1-4} & \mathbf{A}_{n_1-3} \\ \vdots & \vdots & \vdots & \ddots & \vdots & \vdots \\ \mathbf{A}_1 & \mathbf{A}_2 & \mathbf{A}_3 & \dots & \mathbf{A}_{n_1-1} & \mathbf{A}_0 \end{bmatrix}$$

where each block \mathbf{A}_i , for $i = 0, \dots, n_1 - 1$, is an $n_1 \times n_1$ circulant matrix. In particular, the block \mathbf{A}_0 is the adjacency matrix between the nodes lying on the same row of the grid, starting from the leftmost node and proceeding along the row. \mathbf{A}_i represents the adjacency matrix between the nodes of row j and the nodes lying on the $(i+j)$ th row, for $i = 1, \dots, n_1 - j$, and on the $(i+j-n_1)$ th row for $i = n_1 - j + 1, \dots, n_1 - 1$. The toroidal structure, used to avoid border effects, reflects into the cyclic structure of \mathbf{A} , so that we have $\mathbf{A}_{n_1-i} = \mathbf{A}_i$ if

$$\begin{aligned} i &= (n_1 - 1)/2 + 1, \dots, n_1 - 1 \quad \text{and} \quad n_1 \text{ odd} \\ i &= n_1/2 + 1, \dots, n_1 - 1 \quad \text{and} \quad n_1 \text{ even.} \end{aligned}$$

We also note that \mathbf{A} is a block circulant matrix with circulant blocks (BCCB). Since each block \mathbf{A}_i for $i = 0, \dots, n_1 - 1$ is an $n_1 \times n_1$ -dimensional circulant matrix, the eigenvalues of \mathbf{A}_i admit the following decomposition

$$\mathbf{A}_i = \tilde{\mathbf{F}}_{n_1}^H \mathbf{\Lambda}_i \tilde{\mathbf{F}}_{n_1}$$

with

$$\tilde{\mathbf{F}}_{n_1} = \frac{1}{\sqrt{n_1}} \begin{bmatrix} 1 & 1 & \dots & 1 & 1 \\ 1 & \omega & \omega^2 & \dots & \omega^{n_1-1} \\ \vdots & \vdots & \vdots & \ddots & \vdots \\ 1 & \omega^{n_1-1} & \omega^{n_1-2} & \dots & \omega \end{bmatrix}$$

where $\omega = \exp(-j2\pi/n_1)$; $\mathbf{\Lambda}_i$ is a diagonal matrix whose entries are the eigenvalues of \mathbf{A}_i , i.e., the discrete Fourier transform (DFT) of the first row of \mathbf{A}_i . Hence, the matrix \mathbf{A} admits the following diagonalization:

$$\mathbf{A} = (\tilde{\mathbf{F}}_{n_1} \otimes \tilde{\mathbf{F}}_{n_1})^H \mathbf{\Lambda} (\tilde{\mathbf{F}}_{n_1} \otimes \tilde{\mathbf{F}}_{n_1})$$

where \otimes denotes the Kronecker product and

$$\mathbf{\Lambda} = \sum_{k=0}^{n_1-1} \mathbf{\Omega}_{n_1}^k \otimes \mathbf{\Lambda}_k$$

with $\mathbf{\Omega}_{n_1} = \text{diag}[1, \omega, \dots, \omega^{n_1-1}]$. The entries $\lambda_{l,m}(\mathbf{A})$ of the matrix $\mathbf{\Lambda}$ can be also expressed, after a few algebraic manipulations, as

$$\begin{aligned} \lambda_{l,m}(\mathbf{A}) &= \sum_{i=0}^{n_1-1} \sum_{k=0}^{n_1-1} a_k^{(i)}(p) \\ &\quad \times \exp(-j2\pi kl/n_1) \exp(-j2\pi mi/n_1) \quad (37) \end{aligned}$$

for $l, m = 0, \dots, n_1 - 1$ and the coefficient $a_k^{(i)}(p)$ is k th entry of the first row of \mathbf{A}_i for $k, i = 0, \dots, n_1 - 1$. Equivalently, (37) can be seen as the two-dimensional DFT of a matrix $\tilde{\mathbf{A}}$ whose rows $\tilde{\mathbf{A}}(i, :)$ are given by $\tilde{\mathbf{A}}(i, :) = \mathbf{A}_i(1, :)$ for $i = 0, \dots, n_1 - 1$, applying the 1-DFT to the rows and then to the columns of $\tilde{\mathbf{A}}$.

In general, for a regular grid where each node has degree $d(p)$, the algebraic connectivity can be expressed as

$$\begin{aligned} \lambda_2(\mathbf{L}(p)) &= d(r(p)) \\ &\quad - \sum_{i=0}^{n_1-1} \sum_{k=0}^{n_1-1} a_k^{(i)}(p) \exp(-j2\pi k/n_1) \quad (38) \end{aligned}$$

where the coefficients $a_k^{(i)}(p)$ can be expressed as follows. Let $u(x)$ denote the step function, i.e., $u(x) = 1$ for $x > 0$ and zero otherwise. For n_1 odd, we have

$$\begin{aligned} a_0^{(0)}(p) &= 0 \quad \text{and} \\ a_0^{(i)}(p) &= u(r(p) - i\delta) \quad i = 1, \dots, (n_1 - 1)/2, \\ a_k^{(0)}(p) &= u(r(p) - k\delta) \quad \text{and} \\ a_k^{(i)}(p) &= u(r(p) - \sqrt{i^2 + k^2}\delta) \quad i, k = 1, \dots, (n_1 - 1)/2 \end{aligned} \quad (39)$$

$$\begin{aligned} a_k^{(i)}(p) &= a_{n_1-k}^{(i)}(p) \quad k = (n_1 - 1)/2 + 1, \dots, n_1 - 1 \quad \text{and} \\ i &= 0, \dots, (n_1 - 1)/2. \end{aligned} \quad (40)$$

Finally $\mathbf{A}_i = \mathbf{A}_{n_1-i}$ for $i = (n_1 - 1)/2 + 1, \dots, n_1 - 1$. Similarly, in the case of n_1 even, we have

$$\begin{aligned} a_0^{(0)}(p) &= 0 \quad \text{and} \\ a_0^{(i)}(p) &= u(r(p) - i\delta) \quad i = 1, \dots, n_1/2, \\ a_k^{(0)}(p) &= u(r(p) - k\delta) \quad \text{and} \\ a_k^{(i)}(p) &= u(r(p) - \sqrt{i^2 + k^2}\delta) \quad i, k = 1, \dots, n_1/2, \\ a_k^{(i)}(p) &= a_{n_1-k}^{(i)}(p) \quad k = n_1/2 + 1, \dots, n_1 - 1 \quad \text{and} \\ i &= 0, \dots, n_1/2 \end{aligned} \quad (41)$$

with $\mathbf{A}_i = \mathbf{A}_{n_1-i}$ if $i = n_1/2 + 1, \dots, n_1 - 1$.

Finally, we can derive analytical expressions of the network degree and of the algebraic connectivity for n_1 odd as

$$\begin{aligned} d(p) &= \sum_{k=1}^{(n_1-1)/2} 2a_k^{(0)}(p) \\ &\quad + 2 \sum_{i=1}^{(n_1-1)/2} \left(a_0^{(i)}(p) + 2 \sum_{k=1}^{(n_1-1)/2} a_k^{(i)}(p) \right) \end{aligned} \quad (42)$$

and

$$\begin{aligned} \lambda_2(\mathbf{L}(p)) &= \sum_{k=1}^{(n_1-1)/2} 2a_k^{(0)}(p)(1 - \cos(2\pi k/n_1)) \\ &\quad + 4 \sum_{i=1}^{(n_1-1)/2} \sum_{k=1}^{(n_1-1)/2} a_k^{(i)}(p)(1 - \cos(2\pi k/n_1)) \end{aligned} \quad (43)$$

and for n_1 even

$$\begin{aligned}
 d(p) = & \sum_{k=1}^{n_1/2-1} 2 \left(a_k^{(0)}(p) + a_k^{(n_1/2)}(p) \right) \\
 & + \sum_{i=1}^{n_1/2-1} 2 \left(a_{n_1/2}^{(i)}(p) + a_0^{(i)}(p) \right) \\
 & + a_{n_1/2}^{(0)}(p) + a_0^{(n_1/2)}(p) \\
 & + a_{n_1/2}^{(n_1/2)}(p) + 4 \sum_{i=1}^{n_1/2-1} \sum_{k=1}^{n_1/2-1} a_k^{(i)}(p) \quad (47)
 \end{aligned}$$

and

$$\begin{aligned}
 \lambda_2(L(p)) = & 4 \sum_{i=1}^{n_1/2-1} \sum_{k=1}^{n_1/2-1} a_k^{(i)}(p) \\
 & + \sum_{k=1}^{n_1/2-1} 2 \left(a_k^{(0)}(p) + a_k^{(n_1/2)}(p) \right) \\
 & \times (1 - \cos(2\pi k/n_1)) + 4 \sum_{i=1}^{n_1/2-1} a_{n_1/2}^{(i)}(p) \\
 & + 2a_{n_1/2}^{(0)}(p) + 2a_{n_1/2}^{(n_1/2)}(p) \\
 & - 4 \sum_{i=1}^{n_1/2-1} \sum_{k=1}^{n_1/2-1} a_k^{(i)}(p) \cos(2\pi k/n_1). \quad (48)
 \end{aligned}$$

For example, in the case where $r(p) < \sqrt{2}\delta$, i.e., assuming a regular grid of degree $d(p) = 4$, we obtain

$$A_{n_1-1} = A_1 = I \quad \text{and} \quad A_i = O \quad \forall i = 2, \dots, n_1 - 2 \quad (49)$$

while A_0 is a circulant matrix whose first row is the n_1 -dimensional vector $[0100\dots 001]$. Then, the eigenvalues are given by $\lambda_l(A_0) = 2\cos(2\pi l/n_1)$ and applying the formula in (37) the eigenvalues of A are $\lambda_{l,m}(A) = 2\cos(2\pi l/n_1) + 2\cos(2\pi m/n_1)$ for $l, m = 0, \dots, n_1 - 1$. The second largest eigenvalue of A is obtained for $l = 1$ and $m = 0$ and is given by $\lambda_{1,0}(A) = 2\cos(2\pi/n_1) + 2$. Thus the eigenvalues of the Laplacian matrix can be expressed as $\lambda_i(L) = 4 - \lambda_i(A)$ and the algebraic connectivity of the network is given by $\lambda_2(L) = 2 - 2\cos(2\pi/n_1)$.

REFERENCES

- [1] R. O. Saber and R. M. Murray, "Agreement problems in networks with directed graphs and switching topology," in *Proc. 42nd IEEE Conf. on Decision Contr. (CDC 03)*, Maui, HI, Dec. 2003.
- [2] R. Olfati-Saber, J. A. Fax, and R. M. Murray, "Consensus and cooperation in networked multi-agent systems," *Proc. IEEE*, vol. 95, pp. 215–233, Jan. 2007.
- [3] S. Barbarossa and G. Scutari, "Decentralized maximum-likelihood estimation for sensor networks composed of nonlinearly coupled dynamical systems," *IEEE Trans. Signal Process.*, vol. 55, pp. 3456–3470, Jul. 2007.
- [4] S. Boyd, A. Ghosh, B. Prabhakar, and D. Shah, "Randomized gossip algorithms," *IEEE Trans. Inf. Theory*, vol. 52, pp. 2508–2530, Jun. 2006.
- [5] M. Fiedler, "Algebraic connectivity of graphs," *Czechoslovak Math. J.*, vol. 23, pp. 298–305, 1973.
- [6] L. Xiao and S. Boyd, "Fast linear iterations for distributed averaging," *Syst. Contr. Lett.*, vol. 53, pp. 65–78, Sept. 2004.

- [7] S. Boyd, "Convex optimization of graph Laplacian eigenvalues," in *Proc. Int. Congr. Math.*, Madrid, Spain, 2006, pp. 1311–1319.
- [8] R. Olfati-Saber, "Ultrafast consensus in small-world networks," in *Proc. 2005 Amer. Control Conf. (ACC 05)*, Portland, OR, Jun. 2005, pp. 2371–2378.
- [9] S. Kar, S. Aldosari, and J. M. F. Moura, "Topology for distributed inference on graphs," *IEEE Trans. Signal Process.*, vol. 56, pp. 2609–2613, Jun. 2008.
- [10] A. Ghosh and S. Boyd, "Growing well-connected graphs," in *Proc. 45th IEEE Conf. on Decision Control (CDC 06)*, San Diego, CA, Dec. 2006, pp. 6605–6611.
- [11] A. D. G. Dimakis, A. D. Sarwate, and M. J. Wainwright, "Geographic gossip: Efficient averaging for sensor networks," *IEEE Trans. Signal Process.*, vol. 56, pp. 1206–1216, Mar. 2008.
- [12] A. K. Das and M. Mesbahi, "K-node connectivity power efficient topologies in wireless networks: A semidefinite programming approach," in *Proc. IEEE Global Telecomm. Conf. (GLOBECOM)*, St. Louis, MO, Nov.–Dec. 2005, vol. 1, pp. 468–473.
- [13] R. Ramanathan and R. Sasaes-Hain, "Topology control of multihop wireless networks using transmit power adjustment," in *Proc. Ann. Joint Conf. IEEE Comput. Commun. Soc. (INFOCOM)*, Tel Aviv, Israel, Mar. 2000, vol. 2, pp. 404–413.
- [14] A. Giridhar and P. R. Kumar, "Toward a theory of in-network computation in wireless sensor networks," *IEEE Commun. Mag.*, vol. 44, pp. 98–107, Apr. 2006.
- [15] S. Barbarossa, G. Scutari, and A. Swami, "Achieving consensus in self-organizing wireless sensor networks: The impact of network topology on energy consumption," in *Proc. IEEE ICASSP 2007*, Honolulu, HI, Apr. 2007.
- [16] C. Godsil and G. Royle, *Algebraic Graph Theory*. New York: Springer-Verlag, 2001, vol. 207, Graduate Texts in Mathematics.
- [17] R. A. Horn and C. R. Johnson, *Matrix Analysis*. Cambridge, U.K.: Cambridge Univ. Press, 1985.
- [18] A. Joffe, "A parametric study for solving nonlinear fractional problems," *Ann. St. Univ. Ovidius Constanta*, vol. 11, pp. 87–92, 2003.
- [19] W. Dinkelbach, "On nonlinear fractional programming," *Manage. Sci.*, vol. 13, pp. 492–498, Mar. 1967.
- [20] R. Jagannathan, "On some properties of programming problems in parametric form pertaining to fractional programming," *Manage. Sci.*, vol. 12, pp. 609–615, Mar. 1966.
- [21] S. Boyd and L. Vandenberghe, *Convex Optimization*. New York: Cambridge Univ. Press, 2004.
- [22] Y. Hatano and M. Mesbahi, "Agreement over random networks," *IEEE Trans. Autom. Control*, vol. 50, pp. 1867–1872, Nov. 2005.
- [23] T. C. Aysal and K. E. Barner, "Convergence of consensus models with stochastic disturbances," *IEEE Trans. Inf. Theory*, vol. 56, pp. 4101–4113, Aug. 2010.
- [24] C. Bordenave, "Eigenvalues of Euclidean Random Matrices," in *Random Structures & Algorithms*. New York: Wiley, Dec. 2008, vol. 33, pp. 515–532.
- [25] S. Rai, "The spectrum of a random geometric graph is concentrated," *J. Theoret. Probabil.*, vol. 20, pp. 119–132, Jun. 2007.
- [26] M. Mezard, G. Parisi, and A. Zee, "Spectra of euclidean random matrices," *Nucl. Phys. B*, vol. 559, pp. 689–701, Oct. 1999.
- [27] P. Gupta and P. Kumar, "Critical Power for Asymptotic Connectivity in Wireless Networks," in *Stochastic Analysis, Control, Optimization and Applications: A Volume in Honor of W. H. Fleming, W. M. McEneaney, G. Yin, and Q. Zhang (Eds.)*. Boston, MA: Birkhauser, 1998, pp. 547–566.
- [28] S. Boyd, A. Ghosh, B. Prabhakar, and D. Shah, "Mixing times for random walks on geometric graphs," in *Proc. Workshop on Analytic Algorithmics Combinator. (ANALCO'05)*, Vancouver, BC, Canada, Jan. 2005.



Stefania Sardellitti received the Dr. Eng. degree in electronic engineering from the University of Rome "La Sapienza," Italy, in 1998 and the Ph.D. degree in electrical and information engineering from the University of Cassino, Italy, in 2005.

Since 2005, she has been an Appointed Professor of digital communications at the University of Cassino. She is currently a Research Assistant with the DIET Department, Sapienza, University of Rome. She has participated in the European project WINSOC, on wireless sensor networks. Her research

interests are in the area of statistical signal processing, in particular on multiple antenna and multiple access systems. Currently, her primary research activity

is in the field of cognitive radios, femtocell networks, and wireless sensor networks, with emphasis on distributed decision.



Sergio Barbarossa (F'11) received the M.Sc. degree in 1984 and the Ph.D. degree in electrical engineering in 1988, both from the University of Rome "La Sapienza," Rome, Italy, where he is now a full professor.

He has held positions as a Research Engineer at Selenia SpA (1984–1986), at the Environmental Institute of Michigan (1988) and Visiting Professor at the University of Virginia (1995 and 1997), the University of Minnesota (1999), and he has taught short graduated courses at the Polytechnic University of Catalonia (2001 and 2009). He has been principal investigator in several international projects. He has been the scientific lead of the European project WINSOC, on wireless sensor networks. He is currently the scientific lead of the European Project FREEDOM, on femtocell networks and is a principal investigator on the European Project SIMTISYS, on the monitoring of maritime traffic from constellations of satellites. He is also involved in the design of the radar system to be used for the landing module of ExoMars, a spacecraft to be launched by the European Space Agency aimed to land on Mars. He is the author of a research monograph titled "Multiantenna Wireless Communication Systems." His current research interests lie in the areas of cognitive radios, femtocell networks, sensor networks, cooperative communications, spaceborne radars, distributed detection, and estimation.

Dr. Barbarossa has been a member of the IEEE Signal Processing for Communications Technical Committee (1998–2004) and served as an Associate Editor of the IEEE TRANSACTIONS ON SIGNAL PROCESSING (1998–2001 and 2004–2006). He has been a plenary speaker at SAM 2008 and SPAWC 2009. He has co-edited a Special Issue on Optimization of MIMO Transceivers for Realistic Communication Networks: Challenges and Opportunities of the IEEE JOURNAL ON SELECTED AREAS IN COMMUNICATIONS and a Special Issue of the EURASIP *Journal of Applied Signal Processing on MIMO Communications and Signal Processing*. He received the 2000 IEEE Best Paper Award from the IEEE Signal Processing Society and the 2010 EURASIP Technical Achievements Award.



Ananthram Swami (F'08) received the B.Tech. degree from Indian Institute of Technology (IIT), Bombay; the M.S. degree from Rice University, Houston, TX, and the Ph.D. degree from the University of Southern California (USC), Los Angeles, all in electrical engineering.

He has held positions with Unocal Corporation, USC, CS-3, and Malgudi Systems. He was a Statistical Consultant to the California Lottery, developed a Matlab-based toolbox for non-Gaussian signal processing, and has held visiting faculty positions at INP,

Toulouse, France. He is with the U.S. Army Research Laboratory (ARL) where he is the ST for Network Science. His work is in the broad area of network science, with emphasis on wireless communication networks. He was the co-editor of "Wireless Sensor Networks: Signal Processing & Communications Perspectives" (New York: Wiley, 2007).

Dr. Swami is a member of the IEEE SPS Technical Committee on Sensor Array and Multi-channel systems, and serves on the Senior Editorial Board of the IEEE JOURNAL ON SELECTED TOPICS IN SIGNAL PROCESSING. He is an ARL Fellow. He has served as an Associate Editor for the IEEE TRANSACTIONS ON SIGNAL PROCESSING, SIGNAL PROCESSING LETTERS, *Signal Processing Magazine*, the IEEE TRANSACTIONS ON CIRCUITS AND SYSTEMS II, the IEEE TRANSACTIONS ON WIRELESS COMMUNICATIONS, and as Guest Editor for the IEEE JOURNAL ON SELECTED AREAS IN COMMUNICATIONS. He was a tutorial speaker on "Networking Cognitive Radios for Dynamic Spectrum Access" at ICASSP 2008, DySpan 2008, MILCOM 2008, and ICC 2010. He received the Best Conference Paper Award at IEEE Trustcom 2008, and was Co-Organizer and Co-Chair of three IEEE workshops related to signal processing and communications, including IEEE SPAWC'10.

Efficient Extraction of Drainage Networks from Massive, Radar-Based Elevation Models with Least Cost Path Search

M. Metz, H. Mitasova, and R. S. Harmon

Hydrology and Earth System Sciences, 15, 667–678 (2011)

Efficient extraction of drainage networks from massive, radar-based elevation models with least cost path search

M. Metz¹, H. Mitasova², and R. S. Harmon³

¹Institute of Experimental Ecology, University of Ulm, Ulm, Germany

²Department of Marine, Earth and Atmospheric Sciences, North Carolina State University, Raleigh, North Carolina, USA

³Environmental Sciences Division, Army Research Office, US Army Research Laboratory, Durham, North Carolina, USA

Received: 22 April 2010 – Published in Hydrol. Earth Syst. Sci. Discuss.: 27 May 2010

Revised: 1 December 2010 – Accepted: 11 February 2011 – Published: 25 February 2011

Abstract. The availability of both global and regional elevation datasets acquired by modern remote sensing technologies provides an opportunity to significantly improve the accuracy of stream mapping, especially in remote, hard to reach regions. Stream extraction from digital elevation models (DEMs) is based on computation of flow accumulation, a summary parameter that poses performance and accuracy challenges when applied to large, noisy DEMs generated by remote sensing technologies. Robust handling of DEM depressions is essential for reliable extraction of connected drainage networks from this type of data. The least-cost flow routing method implemented in GRASS GIS as the module *r.watershed* was redesigned to significantly improve its speed, functionality, and memory requirements and make it an efficient tool for stream mapping and watershed analysis from large DEMs. To evaluate its handling of large depressions, typical for remote sensing derived DEMs, three different methods were compared: traditional sink filling, impact reduction approach, and least-cost path search. The comparison was performed using the Shuttle Radar Topographic Mission (SRTM) and Interferometric Synthetic Aperture Radar for Elevation (IFSARE) datasets covering central Panama at 90 m and 10 m resolutions, respectively. The accuracy assessment was based on ground control points acquired by GPS and reference points digitized from Landsat imagery along segments of selected Panamanian rivers. The results demonstrate that the new implementation of the least-cost path method is significantly faster than the original version, can cope with massive datasets, and provides the most accurate results in terms of stream locations validated against reference points.

1 Introduction

Shuttle Radar Topographic Mission (SRTM; Farr et al., 2007) and various airborne Interferometric Synthetic Aperture Radar for Elevation (IFSARE) surveys provide a new generation of elevation data in regions that have had only limited, often low resolution coverage. These topographic data sets are increasingly used to improve mapping of geomorphic and hydrologic features, especially in remote, hard to reach areas and at regional to global scales (e.g., Kinner et al., 2005; Lehner and Döll, 2004; World Wildlife Fund, 2009).

In spite of significant advances in the development of flow routing algorithms (e.g. Quinn et al., 1991; Costa-Cabral and Burges, 1994; Holmgren, 1994; Quinn et al., 1995; Tarboton, 1997), accurate extraction of drainage networks from Digital Elevation Models (DEMs) generated by remote sensing technologies such as SRTM or IFSARE remains challenging. To fully understand the problem, it is important to realize that the mapped elevation surfaces include the top of the forest canopy, as well as anthropogenic features, rather than the ground surface required for flow routing. Although homogeneous forest canopy generally follows the shape of the ground surface, gaps in vegetation that can stretch over hundreds of meters create large, often nested, depressions that pose difficulties for flow routing. In addition to these large depressions, the surface over forested areas is noisy, creating numerous small depressions and barriers that further complicate drainage network extraction. Therefore, one of the important questions investigated in this paper was whether such data are suitable for drainage network extraction at all and if yes, how accurate are the extracted drainage networks and which methods provide the most reliable results.

At the same time, the broad availability of elevation data dramatically increased the extent of regions that can be analyzed at relatively high resolutions, given the computational capabilities that can support processing of massive DEMs.



Correspondence to: M. Metz
 (markus.metz@uni-ulm.de)

Therefore, significant effort has been devoted to the development of new flow tracing and watershed analysis algorithms that support efficient processing of large DEMs and address the issue of routing through complex nested depressions (e.g. Rivix Limited Liability Company, 2001; Arge et al., 2003; Danner et al., 2007).

The most widespread method for handling depressions is sink filling, up to the level of the sink spill point, combined with routing through the resulting flat area (Jenson and Domingue, 1988; Fairfield and Leymarie, 1991; Planchon and Darboux, 2001; Wang and Liu, 2006). Improved sink filling methods (e.g. Garbrecht and Martz, 1997; Grimaldi et al., 2007; Santini et al., 2009) first fill sinks, and then introduce a gradient to all flat areas to provide non-zero gradients for flow routing. The method complementary to sink filling is carving or breaching (Rieger, 1998; Martz and Garbrecht, 1998) where a channel is carved out of each sink, breaking through the (artificial) obstacle. Both principles can be combined in an impact reduction approach (IRA; Lindsay and Creed, 2005) that for each sink determines the method that causes the least impact on the source dataset. All these approaches alter the elevation data in order to ensure full drainage, assuming that sinks are artifacts created either by too low (artificial pits) or too high (artificial drainage blocks) elevation values.

An alternative to the modification of elevation data is to determine the least-cost drainage paths (LCP) through unaltered terrain and out of sinks. LCP search methods were generally designed to find the shortest or fastest route from a starting point to a given destination, used for example in car navigation devices or to generate cumulative cost surfaces. A particular LCP search method (A* Search; Hart et al., 1968) was adapted for flow routing and watershed analysis and implemented as the module *r.watershed* (Ehlschlaeger, 1989) in GRASS GIS (Neteler and Mitasova, 2008, see GRASS Development Team 2010 for binaries and source code). When applied to IFSARE derived DEMs, this approach has provided more accurate flow routing through large, nested depressions with fewer artifacts than traditional sink filling (Kinner et al., 2005). However, the module was not designed to handle the massive DEMs that are currently available (Arge et al., 2003). To render the module suitable for analysis of very large datasets at ever higher resolutions, and to reduce the artifacts in flow patterns due to the single flow direction (SFD) algorithm (Quinn et al., 1991; Holmgren, 1994; Tarboton, 1997), redesign of the implementation and addition of more flow routing options was necessary.

In this study, we present substantial improvements to the LCP method implementation and evaluation of its efficiency and accuracy when applied to radar-based DEMs. We compare the performance of the improved module with (1) its original implementation, (2) a module based on a disk input/output (I/O) efficient method (Arge et al., 2003), and (3) the IRA implementation in the Terrain Analysis System (TAS, Lindsay and Creed, 2005). We also analyze the impact

of mapping technology (IFSARE, SRTM), resolution, and DEM resampling on the accuracy of the extracted drainage networks. Although the LCP method has been used since early 90ies, the literature that describes the algorithm, its implementation and properties is very limited (Ehlschlaeger, 1989). This paper aims to fill this gap in literature and to highlight the value of this method and its improvements for analysis of modern DEMs.

2 Methods

2.1 Improved least cost path search algorithm

The LCP algorithm (A* Search, Hart et al., 1968; Ehlschlaeger, 1989) used for flow routing, flow accumulation, and watershed analysis of raster-based DEMs was redesigned to increase the processing speed and decrease memory consumption. The implementation in the GRASS module *r.watershed* (Fig. 1) starts with potential outlet points. Natural ultimate outlets are e.g. river mouths opening into oceans or lakes without outflow. On gridded elevation models, potential outlets are grid cells along the map boundaries or cells with at least one neighbor with unknown elevation, e.g. masked ocean. All potential outlet grid points are inserted into a list sorted by costs. Costs are measured as elevation and order of addition to the sorted list (grid cells added earlier have higher precedence in case of equal elevation). For the actual search, the grid cell with the lowest elevation (smallest cost) is extracted and removed from the sorted list, marked as processed and its neighbors are investigated. This causes the search to proceed along the least steep uphill slope. At each step during the search, only neighboring grid cells that are not yet in the search list and not yet processed are added to the list, and drainage direction for these neighboring grid cells is set towards the current grid cell. If a depression is encountered, the search follows the steepest downhill slope to the bottom of a depression and then proceeds again along the least steep uphill slope. The search proceeds in this manner upstream along the least steep slope and terminates when all grid points have been processed. The LCP search provides two results: (a) flow direction for each cell in a standard D8 manner (O'Callaghan and Mark, 1984), and (b) the order in which cells must be processed for flow accumulation.

The search component of the original implementation was modified by augmenting it with a minimum heap used as priority queue (Atkinson et al., 1986; Metz and Ehlschlaeger, 2010), which led to a substantial speed improvement. In the original implementation, the time needed to keep the sorted list sorted increased exponentially with the number of grid cells, while in the new implementation this time increase is logarithmic. Removal of redundant information in intermediate data as well as reduced memory requirements for both the search and the flow accumulation components

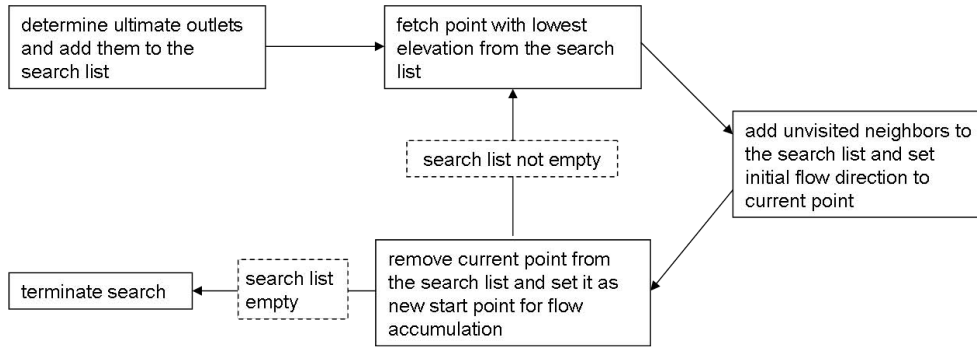


Fig. 1. Flowchart illustrating the least cost path search algorithm.

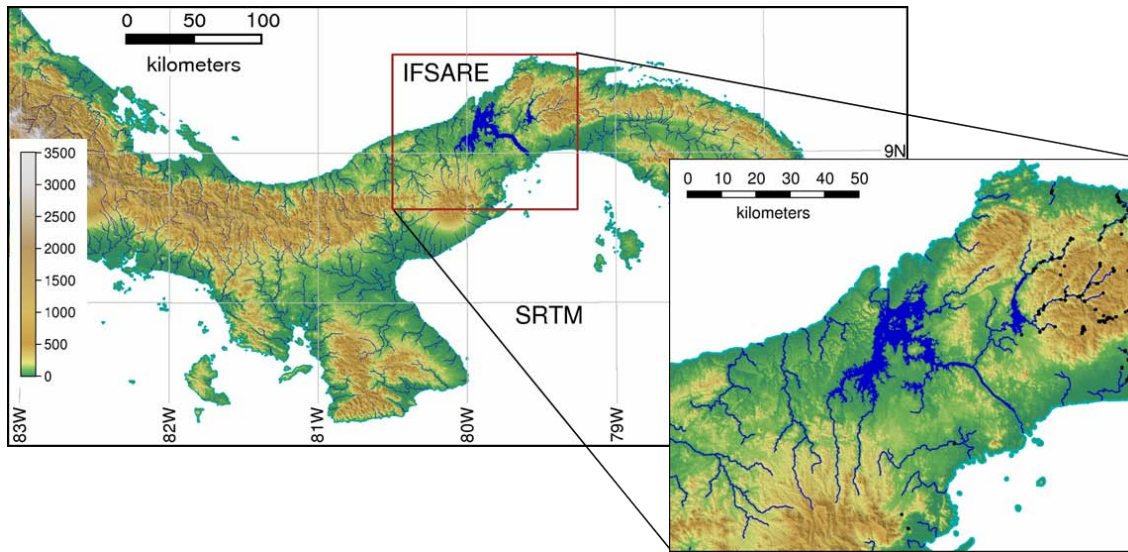


Fig. 2. SRTM and IFSARE coverage of Panama. GPS ground control points are displayed in black.

have further enhanced the module's capacity to process larger DEMs. For massive datasets that can not be processed with the amount of memory available, the module can optionally use external memory with intermediate data stored on disk. These changes, aimed at improving the computational performance, did not affect the quality of the results.

To improve the flow routing accuracy and to reduce artifacts in the flow accumulation pattern, a multiple flow direction (MFD) algorithm, based on Holmgren (1994), was implemented using the order determined by the LCP search with an option to control the strength of flow convergence. For grid-based elevation models, an MFD approach conforms better to theoretical surface flow dispersion than single flow direction in which only one neighboring cell can receive surface flow from the current cell (Freeman, 1991; Quinn et al., 1991; Holmgren, 1994; Tarboton, 1997). Initial D8 flow directions as determined by the LCP search are used to route flow out of depressions when all unprocessed neighboring grid cells have higher elevation than the current grid cell.

2.2 Elevation data

Two different sources of elevation data were used to demonstrate the improvements in the LCP method (Fig. 2). Countrywide elevation coverage of Panama was available as a 3 arc second resolution SRTM DEM (Farr et al., 2007). SRTM version 2.1 provided by the NASA Jet Propulsion Laboratory (<http://www2.jpl.nasa.gov/srtm/>, download at <http://dds.cr.usgs.gov/srtm/>) was selected for this study as the most reliable version in terms of accuracy and minimal artifacts, after evaluating properties of the SRTM products available at the time of writing (v1, v2.1, v3, v4.1). The published absolute vertical error of the version 2.1 SRTM DEM is 6.2 m for South America including Panama (Farr et al., 2007), although several studies report higher accuracies (see e.g. Rodriguez et al., 2006). A recent airborne IFSARE survey has provided new, more detailed information about the topography in central Panama at 10 m resolution, using technology with published vertical accuracy of ~3 m

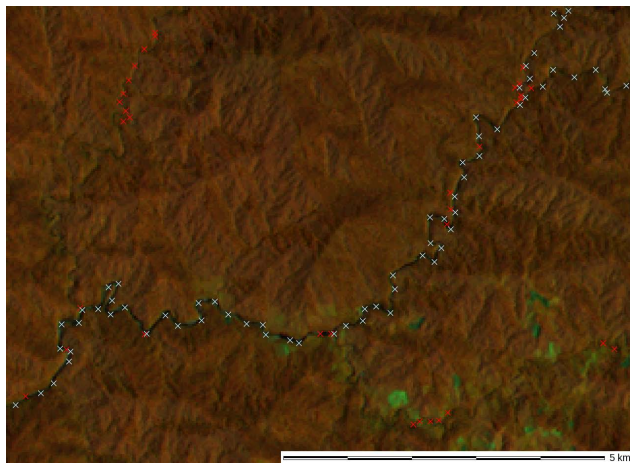


Fig. 3. Shaded relief of a Landsat false color composite (R,G,B = 4,5,3) overlaid with GPS reference points in red and points digitized from Landsat in grey.

(Andersen et al., 2006). IFSARE (InterFerometric Synthetic Aperture Radar - Elevation) is derived in a way very similar to SRTM, with the main difference that IFSARE is airborne and SRTM data was recorded with sensors onboard the Space Shuttle Endeavour. Both IFSARE and SRTM used two antennas to collect radar data; elevation information was derived by analyzing the data recorded by the two antennas (the general concept of the new satellite-borne TanDEM-X mission is similar, collecting radar data with two antennas). Neither of the surveys penetrated the forest canopy to the ground surface and the elevation surface was over large regions defined by a triple canopy tropical forest environment with tree heights of more than 30 m above ground. Given the widespread use of the SRTM data, one of the important questions explored in this paper was whether such data are suitable for stream extraction at all, and if yes, what is the accuracy and which methods provide the most reliable results in this challenging environment.

SRTM v2 tiles covering all of Panama were combined and gaps in the dataset filled using the regularized spline with tension (RST) interpolation method (GRASS module *r.fillnulls*; Mitasova and Mitas, 1993). The seamless SRTM coverage was then reprojected with bicubic interpolation from geographic to the UTM zone 17N coordinate system with 90 m resolution to keep reprojection modifications to a minimum. To evaluate the impact of resampling on stream extraction accuracy (see e.g. Valeriano et al., 2006) and to generate data for additional performance testing, the reprojected 90 m SRTM DEM was reinterpolated to 30 m resolution using the RST method.

The IFSARE data were provided as a 10 m resolution DEM (Kinner et al., 2005) in the UTM zone 17N coordinate system and did not require additional processing. For additional testing purposes, the IFSARE DEM was down-sampled to 30 m resolution using bicubic interpolation in order to have DEMs from two sources (SRTM and IFSARE) with different level of detail, but identical resolution of 30 m.

2.3 Stream location data

Two sets of data points were used to evaluate horizontal accuracy of the drainage network extraction methods: (i) stream segments digitized from Landsat imagery (TM 5, year 2000, scene id LT50120542000087XXX02, provided by the United States Geological Survey – USGS) and (ii) GPS field measurements. Bands 3, 4, and 5 of the Landsat TM scene were used at its native resolution of 30 m. The geographic projection for this study (UTM 17 North) was identical to the projection of this Landsat scene, i.e. the Landsat grid geometry and values were not modified. A Landsat false color composite with Red, Green, and Blue assigned to the channels 4, 5, and 3 respectively, clearly separated vegetation from waterbodies and provided the background for manual digitization of points along the river centerlines. Only streams and rivers with a width less or equal to 4 grid cells (120 m) were digitized in order to exclude lakes, anabranching or braided rivers, and rivers too broad to reliably determine a stream center using Landsat imagery (Fig. 3). The horizontal accuracy of these manually digitized reference points is given by the imagery resolution of 30 m or better, depending on the stream width and the location of the stream centerline in relation to the grid cells.

GPS points were collected in the field using a Corvalis Microtechnology March v3.7 GPS unit with ~2 m positional accuracy. Sites in the Chagres river watershed were measured during the years 2002 to 2007 and sites at lower reaches of most major rivers across Panama were measured during 2005 and 2009 years. GPS points were collected along clearly identifiable perennial rivers at locations where a reliable GPS signal was available. The GPS measurements included a larger proportion of points acquired in mountainous regions along smaller rivers, while most of the points located along larger rivers in low-gradient flood plain and coastal plain landscapes were digitized from Landsat imagery (Fig. 3).

The SRTM water body database was not used for the accuracy evaluation because this cannot be regarded as an independent data source since it was used in the creation of the SRTM DEM v2, and because even the larger rivers visible on Landsat imagery were still too narrow to be captured in the SRTM water body database.

We have also considered and rejected the use of hydrography (blue lines) from topographic maps because of their low reliability and a relatively coarse scale of 1:50 000. Several studies that have compared the blue lines with on-ground

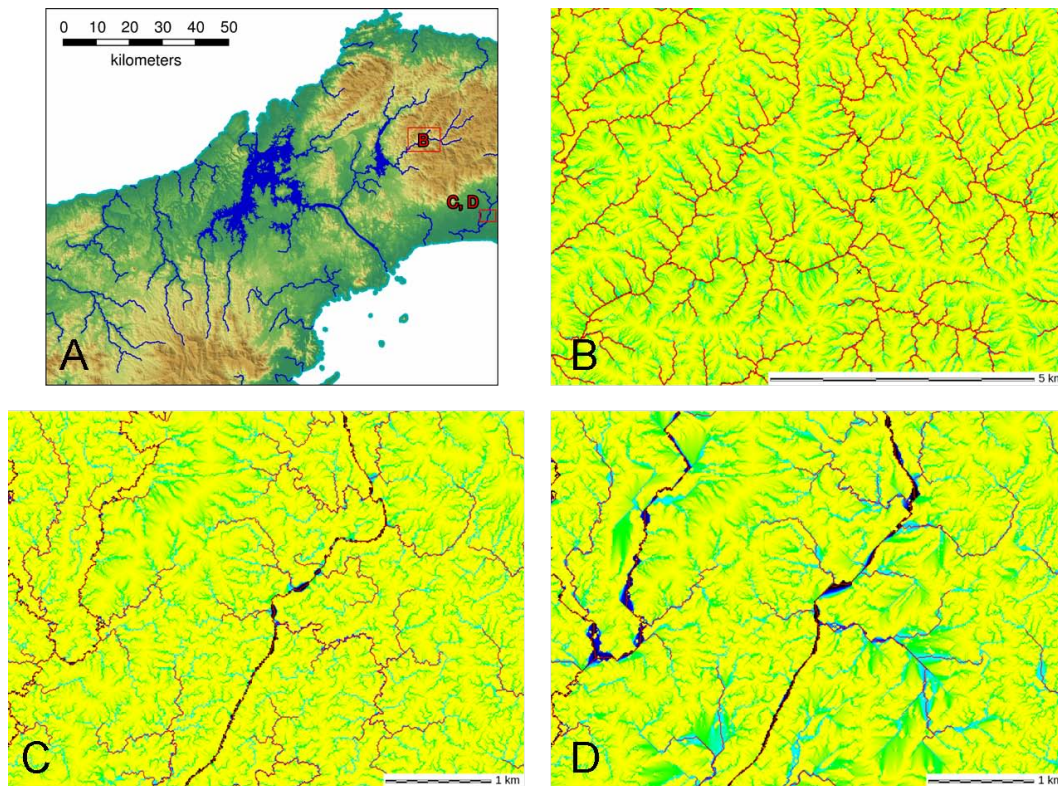


Fig. 4. Extraction of a single main channel: (A) Location of areas shown in images (B), (C), and (D); (B) The starting points of the extracted streams (red lines) were well upstream of the reference points (black crosses). Flow accumulation derived from IFSARE 10 m is used as background. The extracted streams (red lines) are located within broader stream tubes in low-gradient areas close to the coast, for both (C) LCP-derived streams and (D) streams derived with sink filling. IFSARE 10 m was used for both (C) and (D) representing the same area.

surveys of existing streams demonstrated that the blue lines were the least accurate source of stream location information (see e.g. Colson, 2006 and the references therein), often based on old data digitized from aerial photographs with large errors in locations where the streams were not visible, due to the presence of vegetation. In fact, one of the major motivations for deriving the drainage network from the IFSARE data in Panama was the inadequate scale of available blue lines with many larger streams missing and with errors in the mapped streams location. Until recently, the relative inaccessibility of some regions (e.g. the upper Chagres river) and an incessant cloud cover have discouraged mapping in these areas (Kinner et al., 2005).

2.4 Flow accumulation and evaluation of extracted drainage networks

Several tests were performed to evaluate the tested flow routing algorithms. The first test evaluated the processing speed and capability to handle large DEMs when computing flow accumulation maps. In this test, the performance of the new LCP implementation was compared with the old *r.watershed* module (GRASS Development Team, 2008) and with a relatively new, I/O-efficient algorithm, used in the module

r.terraflow (Arge et al., 2003). All computations were done on the same hardware (AMD Athlon X2 3 GHz and 8 GB RAM) but different operating systems (Linux 64 bit for the GRASS modules *r.watershed* and *r.terraflow*, and Windows XP 32 bit for TAS GIS which is a 32 bit application for Microsoft Windows and was not available as 64 bit application at the time of writing).

The second test evaluated the horizontal accuracy of the extracted drainage paths for algorithms with different handling of depressions. Three approaches were tested: (i) sink filling as implemented in *r.terraflow*, (ii) the impact reduction approach (IRA) as implemented in TAS GIS (Lindsay and Creed, 2005), and (iii) the LCP algorithm as implemented in the enhanced version of *r.watershed* in GRASS GIS 6.4. To test the sink filling method, *r.terraflow* was used because of its capability to efficiently process massive DEMs.

The third test evaluated the impact of DEM resolution and level of detail on the horizontal accuracy of the extracted drainage paths for all tested algorithms (*r.watershed*, *r.terraflow*, and TAS).

The tests were performed for the central Panama region using both the IFSARE and SRTM data at the 10 m, 30 m and 90 m resolutions by computing flow accumulation with

MFD dispersal and extracting drainage networks from the computed flow accumulation.

Drainage networks were extracted from all MFD flow accumulation maps using a minimum upstream catchment area of 100 000 m² as a threshold. This threshold was selected for testing purposes and to ensure that all measured or digitized points were located downstream from the extraction starting point and that all points had a drainage path associated with it (Fig. 4b). Accurate identification of the channel head zones was beyond the scope of this paper because it requires more than elevation data as it is often significantly influenced by local geology, groundwater level, and land cover (North Carolina Division of Water Quality NCWQ, 2010). According to the NCWQ (2010) study, “the stream origins usually occur as transition zones in which the location and length of the zone is subject to fluctuations in groundwater levels and precipitation”. The tested 90 m and 30 m resolution SRTM DEMs measured over at least 30 m high canopy of dense tropical forest did not provide sufficient information for accurate identification and mapping of the dynamic channel heads zones. Therefore our focus was on mapping streams and rivers that have sufficiently large contributing areas that the existence of a well defined stream can be expected.

In order to extract a single main channel in broader floodplains where MFD flow accumulation generates several cells wide stream tubes that may include cells above the given threshold, a new stream starting point was defined only if it was not located within such a stream tube (Fig. 4). Downstream channel tracing followed the steepest slope and maximum flow accumulation within the stream tube. To egress from depressions using the LCP method, streams again followed the maximum flow accumulation which was in these cases identical to the drainage direction initially determined during the LCP search. As a result, the drainage paths extracted from MFD flow accumulation were a single grid cell wide and were easily vectorized for further analysis. This approach of extracting single cell wide dendritic and topologically correct drainage networks from flow accumulation obtained with any kind of flow distribution method avoids the problems associated with skeletonizing rasterized MFD channels. The MFD capabilities to map flow dispersal in floodplains can then be preserved and single flow direction (SFD) routing is not necessary for flow accumulation and subsequent channel extraction (although it remains an option).

Assessment of drainage network extraction accuracy was then performed by calculating distances between the drainage paths derived from the IFSARE and SRTM DEMs and the points measured along the streams, consisting of 338 on-ground GPS measurements and 995 points digitized along rivers from the Landsat imagery (Figs. 3, 4).

In order to determine which method or level of detail provided more accurate results, we determined the distance of reference points to the nearest extracted drainage path. The

difference in the distance to reference points between methods or level of detail was then used to assess which method or level of detail provided more accurate results. Distance differences were tested with two-tailed Student's t-tests for statistical significance and $\alpha = 0.05$. If distance differences were significantly different from zero, i.e. one of the tested methods/levels of detail was more accurate than the other, the sign of the difference indicated which method/level of detail was more accurate.

3 Results

3.1 Performance comparison

To demonstrate the improvement in computational performance of the new LCP method implementation, the processing times needed by the old and new version of *r.watershed*, and *r.terraflow* were compared, with the results summarized in Table 1. For flow accumulation computation, the new version was 350 times faster than the old version for the central Panama area represented by a relatively small DEM with 2 million grid cells at 90 m resolution. The improvement was even more dramatic for the countrywide coverage at 90 m resolution with 27 million grid cells: the new version was about 1750 times faster. Although absolute processing times are dependent on the specific hardware used for testing, we expect that relative time differences will be similar on other systems because the software optimizations are hardware-independent. Processing the larger regions used in this study with the old version was impractical because it could easily take days (Arge et al., 2003), whereas the new version required only minutes to execute. The computational time needed by the I/O-efficient *r.terraflow* was significantly lower than that for the old *r.watershed*, but the *r.terraflow* module was not as fast as the new LCP implementation on our test system (Table 1). We have also considered the case when the data do not fit into memory and *r.watershed* uses segmented processing, with intermediate data being stored on disk. This leads to longer processing times than for the all-in-memory mode. Processing times observed on our testing system in the segmented mode were still shorter than for *r.terraflow*, which uses I/O-efficient algorithms specifically designed for large datasets (Arge et al., 2003). The size of intermediate data created by *r.watershed* in the segmented mode was less than 20% of those created by *r.terraflow*. This can be of advantage if intermediate data are just a bit too large to fit into memory. It is important to note that, theoretically, *r.terraflow* with its advanced I/O-efficient algorithms should be faster than *r.watershed* for DEMs much larger than the ones processed here and on systems with less physical memory.

TAS GIS was not included in the performance comparisons, because its memory requirements for processing the 10 m IFSARE DEM and the 30 m SRTM DEM for all of

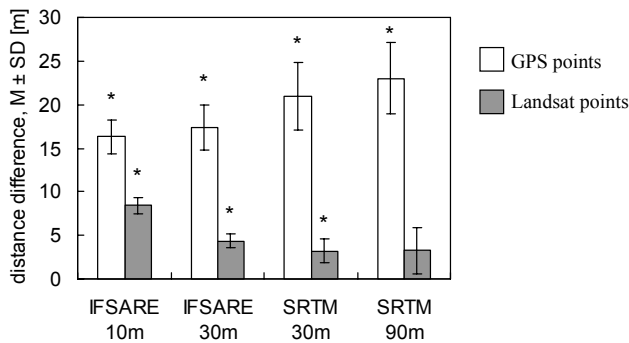
Table 1. Processing time for the different DEMs on a Linux 64 bit system with an AMD Athlon X2 3 GHz CPU and 8 GB RAM.

	SRTM 90 m Central Panama 1.9 million cells	IFSARE 30 m central Panama 17 million cells	SRTM 90 m all of Panama 27 million cells	IFSARE 10 m central Panama 156 million cells	SRTM 30 m all of Panama 241 million cells
old <i>r.watershed</i> , all in memory	23.2min	23 h 10 min	30 h 46 min	> 2 days not measured	> 2 days not measured
new <i>r.watershed</i> , all in memory	0.07 min	0.83 min	1.05 min	9.97 min	12.3 min
new <i>r.watershed</i> , data on disk	0.15 min	1.73 min	2.05 min	30.7 min	32.18 min
<i>r.terraflow</i>	0.45 min	4.4 min	5.05 min	66.95 min	58.7 min

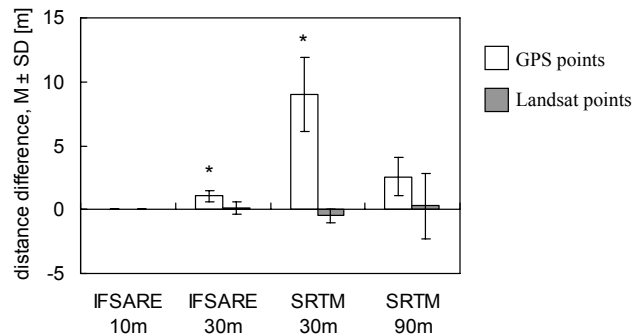
Table 2. Median distances of reference points to nearest extracted stream in meters.

	GPS filling	IRA	LCP	Landsat filling	IRA	LCP
IFSARE 10 m	62.65	N/A*	34.40	43.75	N/A*	39.25
IFSARE 30 m	77.15	71.42	70.71	48.88	48.27	47.75
SRTM 30 m	99.78	92.46	89.13	84.25	82.81	83.72
SRTM 90 m	124.84	119.69	121.00	94.30	94.69	94.92

* Computation cancelled by software with out of memory error.

**Fig. 5.** Mean and standard deviation of the distance differences between sink filling and least-cost path search. A positive distance difference indicates that streams extracted with least-cost path search are closer to reference points than streams extracted with sink filling.

Panama exceeded available system memory. TAS GIS is a 32 bit application for Microsoft Windows and can only utilize as much memory as a 32 bit application can manage, i.e. 3 GB. As opposed to *r.terraflow* and *r.watershed*, TAS GIS keeps all intermediate data in memory, thus limiting the size of the DEMs that can be processed. The test system provided as much memory as TAS GIS could theoretically uti-

**Fig. 6.** Mean and standard deviation of the distance differences between impact reduction approach and least-cost path. A positive distance difference indicates that streams extracted with least-cost path search are closer to reference points than streams extracted with the impact reduction approach.

lize, hence the out-of-memory error was regarded as a limitation of this application and not as a hardware limitation. Therefore, TAS was used only for the sink treatment methods in comparison with the 30 m and 90 m DEM covering the central Panama subregion (Fig. 2) and results of the IRA method were not available for 10 m IFSARE. At the time of writing, IRA was not included in WhiteboxGAT (Lindsay, 2009) that has replaced TAS.

3.2 Comparison between different methods of sink treatment

To evaluate the impact of different approaches in the handling of elevation surface depressions, median distances of reference points to extracted drainage paths for each sink treatment method and each processed DEM were computed and the results are summarized in Table 2. As expected, the location of extracted drainage paths improved with increasing detail available in the DEM. While the drainage paths for

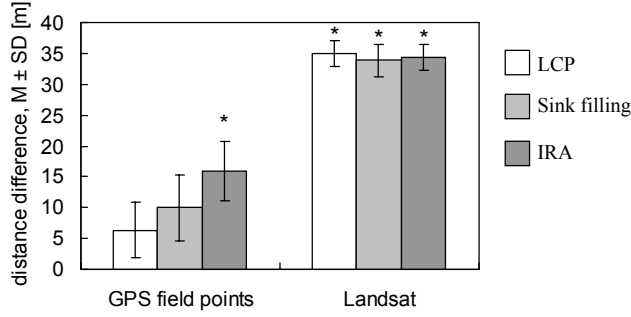


Fig. 7. Mean and standard deviation of the distance differences between the 30 m SRTM DEM and the 30 m IFSARE DEM. A positive distance difference indicates that streams extracted from the 30 m IFSARE DEM are closer to reference points than streams extracted from the 30 m SRTM DEM. LCP: least-cost path search; IRA: impact reduction approach.

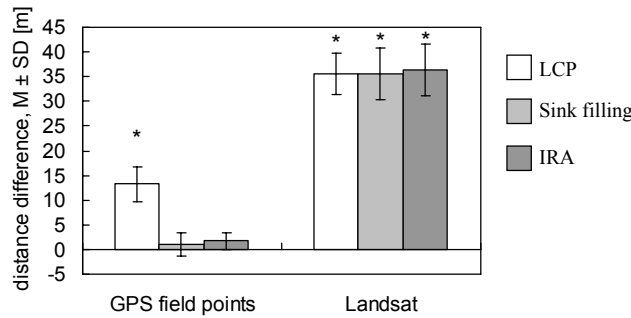


Fig. 8. Mean and standard deviation of the distance differences between the 90 m and the 30 m SRTM DEM. A positive distance difference indicates that streams extracted from the 30 m SRTM DEM are closer to reference points than streams extracted from the 90 m SRTM DEM. LCP: least-cost path search; IRA: impact reduction approach.

the 90 m SRTM DEM were about 100 m away from reference points, the median distances improved down to 34.4 m for the IFSARE 10 m DEM.

Drainage paths extracted from the LCP flow accumulation were closer to the GPS field points (t-tests, all $t_{337} < -5.4$, all $p < 0.0001$) for all DEMs at all tested resolutions (IFSARE 10 m, 30 m, and SRTM 30 m, 90 m) when compared with the sink filling method (Fig. 5 showing bar graphs with mean and standard deviation of the distance differences). The drainage paths extracted from LCP were also closer to the points digitized from Landsat for all DEMs (t-tests, all $t_{994} < -2.3$, all $p < 0.0001$), except for the 90 m SRTM where the distance difference was not significant for (t-test, $t_{994} = -1.213$, $p = 0.23$).

When compared to the IRA method (Fig. 6 showing bar graphs with mean and standard deviation of the distance differences), drainage paths extracted from LCP flow accumulation were closer to the GPS field points for the 30 m IFSARE

(t-test, $t_{337} = -2.361$, $p = 0.018$) and 30 m SRTM (t-test, $t_{337} = -3.088$, $p = 0.002$), but for the 90 m SRTM the difference was not significant (t-test, $t_{337} = -1.745$, $p = 0.08$). For the points digitized from Landsat, drainage paths extracted from LCP accumulation were not closer than IRA drainage paths for any of the tested DEMs (t-tests, all absolute $t_{994} < 1.0$, all $p > 0.3$).

3.3 Comparison between different levels of detail at constant resolution

The 10 m IFSARE and 90 m SRTM were interpolated to the same resolution of 30 m. We investigated how much the different levels of detail at identical resolution influenced the accuracy of extracted drainage paths for all three sink treatment methods (Fig. 7 showing bar graphs with mean and standard deviation of the distance differences). The distance between the reference points and drainage paths extracted from the 30 m IFSARE DEM was subtracted from the distance between the reference points and drainage paths extracted from the 30 m SRTM DEM to measure the difference in accuracy of drainage paths extracted from these two DEMs. For larger rivers in flat areas (Landsat points), the accuracy of drainage path locations was considerably higher for the 30 m IFSARE DEM than for the 30 m SRTM DEM (t-test, all $t_{994} < -13.0$, all $p < 0.001$; on average 35 m closer) for all methods. For smaller rivers not broader than 30 m in mountainous regions (GPS points), only IRA showed a significant improvement in accuracy from the 30 m SRTM DEM to the 30 m IFSARE DEM (t-test, $t_{337} = -3.315$, $p = 0.001$, all other $t_{337} > -1.9$ and < 0 , $p > 0.05$). However, as shown in the previous section for the 30 m IFSARE DEM, IRA drainage path locations in mountainous regions were significantly less accurate than LCP drainage path locations.

3.4 Effects of RST resampling on the accuracy of drainage network extraction

In order to assess the effect of SRTM resampling from 90 m to 30 m resolution by the RST method, the drainage paths extracted from the 90 m SRTM DEM were compared with drainage paths extracted from the resampled 30 m SRTM DEM by calculating the difference in drainage path distances to reference points (Fig. 8 showing bar graphs with mean and standard deviation of the distance differences). Corresponding median distances of reference points to drainage path locations are given in Table 2. The accuracy of drainage path locations was improved by resampling for larger rivers in flat landscape for all sink treatment methods (t-tests, all $t_{994} < -6.5$, all $p < 0.001$), however, for GPS points in mountainous regions only the results obtained by the least-cost path search were improved (t-test, $t_{337} = -3.734$, $p < 0.001$, all other $t_{337} > -1$ and < 0 , $p > 0.3$).

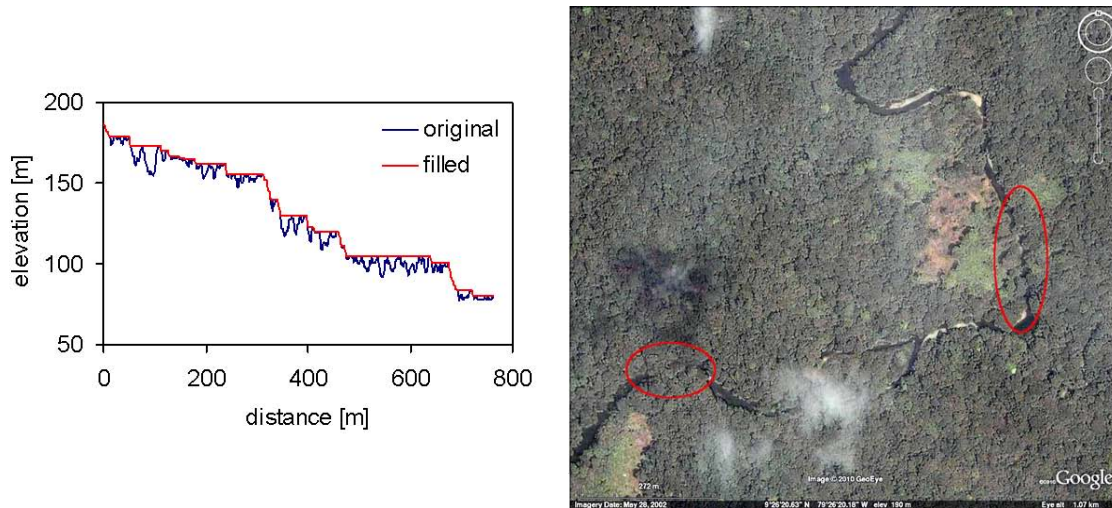


Fig. 9. A typical example for the impact of sink filling along a section of a river course extracted from the 30 m SRTM DEM. Along this section, 92% of all elevation values were modified. Parts of the river course obscured by trees are highlighted in the GoogleEarth screenshot.

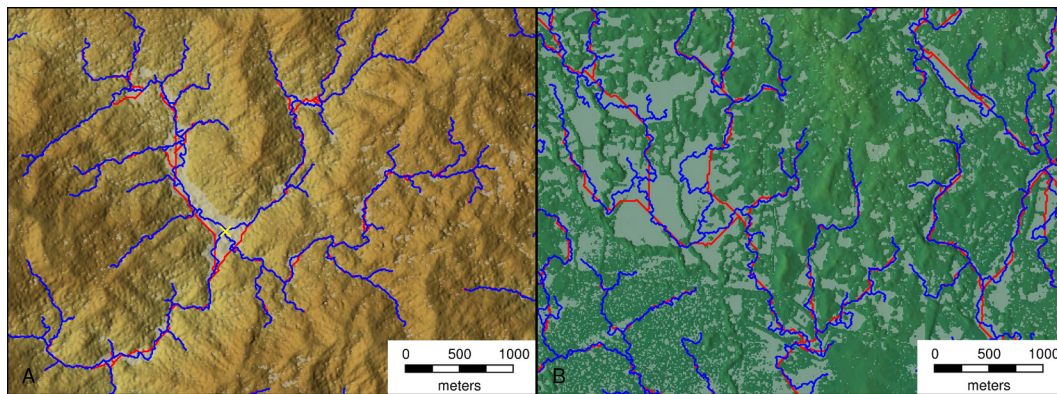


Fig. 10. Typical effects of different sink treatment methods on extracted stream courses in (A) mountainous areas and (B) costal plains. Filled sinks are grayed. Streams extracted from sink-filling in red are overlaid by streams extracted from least-cost path search in blue. Points of confluences (yellow cross) in mountainous areas can be shifted considerably, and in coastal plains, sink filling can lead to long straight lines. A shaded relief of the 10 m IFSARE DEM was used as background.

4 Discussion

Digital Terrain Models, as an approximation of real terrain at a given level of detail, include random noise and errors. For example, an in depth analysis of SRTM accuracy and source of errors is provided by Rodriguez et al. (2006) and Farr et al. (2007). The errors can have significant impact on the results of DEM analysis and their treatment has been the focus of broad research (e.g. Jenson and Domingue, 1988; Lindsay and Creed, 2005; Hutchinson, 2000). Sink (depression) removal was designed to remove small depressions introduced as artifacts of elevation data processing for the first generation of DEMs to facilitate continuous flow routing (Jenson and Domingue, 1988). This procedure, referred to as hydrological conditioning, has become widespread even for next generations of elevation data and is now a pre-processing

step required by a number of applications for hydrological analysis and modeling. In order to alleviate the problem of routing surface flow through the flat areas created by sink filling, efforts have been made to add a gradient to these flat areas (e.g. Martz and Garbrecht, 1998; Wang and Liu, 2006; Grimaldi et al., 2007; Santini et al., 2009). Nevertheless, as modern high resolution data such as LiDAR demonstrate, actual terrain includes many true depressions, especially in riffle-and-pool portions of mountainous rivers, and on flood-plains and coastal plains (Notebaert et al., 2009). Therefore, sink filling is not always an appropriate approach for hydrological conditioning of a DEM because the measured elevation data are replaced with new elevation values based on the rather unrealistic assumption that the terrain has no depressions (Jenson and Domingue, 1988; Tarboton, 1997),

be they artificial or real. Although many hydrologic models require depression-less DEMs, removal of sinks can alter the true hydrological state that includes standing water in depressions. Moreover, in IFSARE and SRTM DEMs that include vegetation cover, many of the observed depressions are caused by gaps in canopy, canopy closing over river courses, or by vegetation partially obstructing narrow and deep valleys. The filling of such features requires altering elevations by several meters and over areas of hundreds of m^2 , leading to large flats and an artificial drainage network geometry that does not represent reality. Figure 9 presents an example of the barriers across the river channel created by overhanging trees and a profile that illustrates the extensive modification in elevation that can result from such filling. Preserving most of the drainage directions of the original DEM is preferable to hydrological conditioning in this case.

Our results suggest that the adverse effects of sink filling become more pronounced for higher resolution DEMs (see Fig. 10 for drainage paths extracted from 10 m IFSARE). By contrast, at lower resolutions such as 90 m, the coarsest resolution tested in this study, there was often no significant difference in drainage path locations between the compared methods, particularly for Landsat reference points. Landsat points were predominantly located in flood plain and coastal plain landscapes where both the horizontal and the vertical resolution of 90 m SRTM were often not sufficient to locate rivers and no method was able to accurately delineate drainage paths in these areas from 90 m SRTM (Hancock et al., 2006; Valeriano et al., 2006).

When comparing SRTM and IFSARE DEMs at the same resolution of 30 m, the drainage networks extracted from the IFSARE DEM were, as expected, more accurate than drainage networks extracted from SRTM DEM, particularly for Landsat points in relatively flat areas. As shown in previous studies (Hancock et al., 2006; Valeriano et al., 2006), the SRTM DEM close to its native resolution of 3 arc sec does not provide sufficient vertical detail to determine river courses in flat areas. The applied RST resampling method significantly improved the accuracy of extracted drainage path locations for SRTM in regions with low topography. Apparently the level of detail has been not just increased but also improved because resampling to a higher horizontal (and for SRTM also higher vertical) resolution seems to be helpful in improving the results of watershed analysis from low-resolution DEMs (see also Valeriano et al., 2006). The global SRTM coverage at 3 arc sec horizontal resolution has been created by averaging the original 1 arc sec coverage (Farr et al., 2007). Depending on the method used, reinterpolating the 3 arc sec version back to 1 arc sec can result in narrowed valleys and ridges and increased channel sinuosity. Interestingly, only the LCP search method benefited from the reinterpolation in mountainous regions and provided here the most accurate drainage path locations for the 30 m SRTM DEM.

It is important to note that the differences in the tested methods were significant due to the particularly challenging

study region. Smaller differences between the methods could be expected in topography with gentle slopes and uniformly low vegetation cover. Although network connectivity, topology and channel morphometry has not been investigated, the visual inspection of the results indicates that there were differences between the results obtained by different methods and resolutions in the coastal plain areas. None of the tested DEMs or methods produced sufficiently reliable results and higher resolution did not always lead to correct topology. These results are similar to those found for LiDAR-based DEMs (Colson, 2006) and require further research.

Although the tests presented here demonstrated the performance of the LCP method for radar-based data, the new, improved version of *r.watershed* has in fact been developed using LiDAR data provided by the USGS in addition to the 1 m LiDAR DEM examples and data provided by Neteler and Mitasova (2008). The presented method processes a DEM without modifying its elevation values and is thus to a degree (quantitatively narrowed by this study) dependent on the reliability of the provided DEM. The LCP search approach, despite its capability to route flow through depressions, will therefore, like other methods, fail to accurately extract drainage networks if the input DEM deviates too far from real topography.

5 Conclusions

We presented a method for fast computation of flow accumulation and drainage network extraction for large DEMs with nested depressions and evaluated it against other commonly used methods for sink treatment. The accuracy assessment using ground control points and Landsat satellite imagery provided insight into the accuracy of drainage network extraction from radar elevation data in a challenging tropical forest environment and coastal plain setting. The results suggest that the conceptually simple sink filling approach is not suitable for the IFSARE and SRTM DEMs in regions with significant vegetation cover whereas both the tested impact reduction approach of Lindsay and Creed (2005) and the LCP search provide more accurate drainage networks.

The performance testing has demonstrated that the new implementation dramatically improves computational efficiency while preserving the high accuracy of the LCP routing capabilities. The increase in computational performance is particularly relevant for the modern mapping technologies that can rapidly produce massive DEMs at high resolutions for large areas and the slow processing and analysis has become bottleneck in their application. Fast processing of massive DEMs opens their application to a new level of detail and spatial extent, for example in rapid response operations or for mapping in remote regions where the streams are covered by dense vegetation and no reliable stream data are available.

Acknowledgements. The support of the US Army Research Office for this research is gratefully acknowledged. We would also like to thank two anonymous reviewers for their valuable comments.

Edited by: R. Purves

References

- Andersen, H. E., Reutebuch, S. E., and McGaughey, R. J.: Accuracy of an IFSAR-derived digital terrain model under a conifer forest canopy, *Can. J. Remote Sens.*, 31, 283–288, 2005.
- Arge, L., Chase, J. S., Halpin, P. N., Toma, L., Vitter, J. S., Urban, D., and Wickremesinghe, R.: Flow computation on massive grid terrains, *GeoInformatica*, 7, 283–313, 2003.
- Atkinson, M. D., Sack, J.-R., Santoro, N., and Strothotte, T.: Min-max heaps and generalized priority queues, *Programming techniques and Data structures*, *Comm. ACM*, 29, 996–1000, 1986.
- Colson, T. P.: Stream network delineation from high-resolution digital elevation models, Ph.D. Dissertation, Department of Forestry & Environmental Resources, North Carolina State University, Raleigh, NC, available at <http://www.lib.ncsu.edu/theses/available/etd-10302006-122024/>, 2006.
- Costa-Cabral, M. C. and Burges, S. J.: Digital elevation model networks (DEMON): A model of flow over hillslopes for computation of contributing and dispersal areas, *Water Resour. Res.*, 30, 1681–1692, 1994.
- Danner, A., Yi, K., Moelhave, T., Agarwal, P. K., Arge, L., and Mitasova, H.: TerraStream: From Elevation Data to Watershed Hierarchies, *Proc. ACM GIS*, 28, doi:10.1145/1341012.1341049, 2007.
- Ehlschlaeger, C.: Using the A* Search Algorithm to Develop Hydrologic Models from Digital Elevation Data, *Proceedings of International Geographic Information Systems (IGIS) Symposium*, Baltimore, MD, USA, 275–281, 1989.
- Fairfield, J. and Leymarie, P.: Drainage networks from grid digital elevation models, *Water Resour. Res.*, 27, 709–717, 1991.
- Farr, T. G., Rosen, A. R., Caro, E., Crippen, R., Duren, R., Hensley, S., Kobrick, M., Paller, M., Rodriguez, E., Roth, L., Seal, D., Shaffer, S., Shimanda, J., Umland, J., Werner, M., Oskin, M., Burbank, D., and Alsdorf, D.: The Shuttle Radar Topography Mission, *Rev. Geophys.*, 45, RG2004, doi:10.1029/2005RG000183, 2007.
- Freeman, T. G.: Calculating catchment area with divergent flow based on a regular grid, *Comput Geosci.*, 17, 413–422, 1991.
- Garbrecht, J. and Martz, L. W.: The assignment of drainage direction over flat surfaces in raster digital elevation models, *J. Hydrol.*, 192, 204–213, 1997.
- GRASS Development Team: Geographic Resources Analysis Support System (GRASS) Software, Version 6.3.0. http://grass.osgeo.org/download/software_old.php#g630, 2008.
- GRASS Development Team: Geographic Resources Analysis Support System (GRASS) Software, Version 6.4.0, Open Source Geospatial Foundation, <http://grass.osgeo.org>, 2010.
- Grimaldi, S., Nardi, F., Di Benedetto, F., Istanbuluoglu, E., and Bras, R. L.: A physically-based method for removing pits in digital elevation models, *Adv. Water Resour.*, 30, 2151–2158, 2007.
- Hancock, G. R., Martinez, C., Evans, K. G., and Moliere, D. R.: A comparison of SRTM and high-resolution digital elevation models and their use in catchment geomorphology and hydrology: Australian examples, *Earth Surf. Proc. Land.*, 31, 1394–1412, 2006.
- Hart, P. E., Nilsson, N. J., and Raphael, B.: A Formal Basis for the Heuristic Determination of Minimum Cost Paths, *IEEE T. Syst. Sci. Cyb.*, 4, 100–107, 1968.
- Holmgren, P.: Multiple flow direction algorithms for runoff modeling in grid based elevation models: An empirical evaluation, *Hydrol. Process.*, 8, 327–334, 1994.
- Jenson, S. K. and Domingue, J. O.: Extracting topographic structure from digital elevation data for geographic information system analysis, *Photogramm. Eng. Rem. S.*, 54(11), 1593–1600, 1988.
- Kinner, D., Mitasova, H., Harmon, R. S., Toma, L., and Stalard, R.: GIS-based Stream Network Analysis for The Chagres River Basin, Republic of Panama. In: Harmon R (ed) *The Rio Chagres: A Multidisciplinary Profile of a Tropical Watershed*, Springer/Kluwer, 83–95, 2005.
- Lehner, B. and Döll, P.: Development and validation of a global database of lakes, reservoirs and wetlands, *J. Hydrol.*, 296, 1–22, 2004.
- Lindsay, J. B.: Whitebox <http://www.uoguelph.ca/~hydrogeo/Whitebox/index.html>, 2009.
- Lindsay, J. B. and Creed, F.: Removal of artefact depressions from digital elevation models: towards a minimum impact approach, *Hydrol. Process.*, 19, 3113–3126, 2005.
- Martz, L. W. and Garbrecht, J.: The treatment of flat areas and depressions in automated drainage analysis of raster digital elevation models, *Hydrol. Process.*, 12, 843–855, 1998.
- Metz, M. and Ehlschlaeger, C.: Watershed analysis program *r.watershed*, source code, https://trac.osgeo.org/grass/browser/grass/branches/releasebranch_6_4/raster/r.watershed, 2010.
- Mitasova, H. and Mitas, L.: Interpolation by Regularized Spline with Tension: I. Theory and Implementation, *Math. Geol.*, 25, 641–655, 1993.
- Neteler, M. and Mitasova, H.: *Open Source GIS: A GRASS GIS Approach*, Third Edition, Springer New York, 406 pp., 2008.
- North Carolina Division of Water Quality (NCWQ): Methodology for Identification of Intermittent and Perennial Streams and Their Origins, Version 4.1.1, <http://portal.ncdenr.org/web/wq/swp/ws/401/waterresources/streamdeterminations>, Effective Date: 1 September 2010.
- Notebaert, B., Verstraeten, G., Govers, G., and Poesen, J.: Qualitative and quantitative applications of LiDAR imagery in fluvial geomorphology, *Earth Surf. Proc. Landforms*, 34, 217–231, 2009.
- O’Callaghan, J. F. and Mark, D. M.: The Extraction of Drainage Networks from Digital Elevation Data, *Computer Vision, Graphics, and Image Processing*, 28, 223–344, 1984.
- Peckham, S. D.: Efficient extraction of river networks and hydrologic measurements from digital elevation data, in Barndorff-Nielsen and others, eds., *Stochastic Methods in Hydrology: Rain, Landforms and Floods*: Singapore, World Scientific, 173–203, 1998.
- Planchon, O. and Darboux, F.: A fast, simple and versatile algorithm to fill the depressions of digital elevation models, *Catena*, 46, 159–176, 2001.
- Quinn, P., Beven, K., Chevallier, P., and Planchon, O.: The prediction of hillslope flow paths for distributed hydrological modelling using digital terrain models, *Hydrol. Process.*, 5, 59–79, 1991.

- Quinn, P. F., Beven, K. J., and Lamb, R.: The $\ln(a/\tan\beta)$ index: How to calculate it and how to use it within the topmodel framework, *Hydrol. Process.*, 9, 161–182, 1995.
- Rieger, W.: A phenomenon-based approach to upslope area and depressions in DEMs, *Hydrol. Process.*, 12, 857–872, 1998.
- Rivix Limited Liability Company: RiverTools™ User's Guide release 2001, Boulder, CO, Research Systems, Inc., 202 pp., 2001.
- Rodriguez, E., Morris, C. S., and Belz, J. E.: A global assessment of the SRTM performance, *Photogramm. Eng. Rem. S.*, 72, 249–260, 2006.
- Santini, M., Grimaldi, S., Rulli, M. C., Petroselli, A., and Nardi, F.: Pre-processing algorithms and landslide modeling on remotely sensed DEMs, *Geomorphology*, 113, 110–125, 2009.
- Tarboton, D. G.: A New Method for the Determination of Flow Directions and Contributing Areas in Grid Digital Elevation Models, *Water Resour. Res.*, 33, 309–319, 1997.
- Valeriano, M. M., Kuplich, T. M., Storino, M., Amaral, B. D., Mendes, J. N., and Lima, D. J.: Modeling small watersheds in Brazilian Amazonia with shuttle radar topographic mission 90m data, *Comput. Geosci.*, 32, 1169–1181, 2006.
- Wang, L. and Liu, H. An efficient method for identifying and filling surface depressions in digital elevation models for hydrologic analysis and modelling, *Int. J. Geogr. Inf. Sci.*, 20, 193–213, 2006.
- World Wildlife Fund, HydroSHEDS, <http://hydrosheds.cr.usgs.gov/index.php>, 2009.

Connectivity of Heterogeneous Wireless Networks

Wei Ren, Qing Zhao, and Ananthram Swami

IEEE Transactions on Information Theory, 57(7), 4315-4332 (2011)

Connectivity of Heterogeneous Wireless Networks

Wei Ren, *Student Member, IEEE*, Qing Zhao, *Senior Member, IEEE*, and Ananthram Swami, *Fellow, IEEE*

Abstract—We address the percolation-based connectivity of large-scale ad hoc heterogeneous wireless networks, where secondary users exploit channels temporarily unused by primary users and the existence of a communication link between two secondary users depends on not only the distance between them but also the transmitting and receiving activities of nearby primary users. We introduce the concept of *connectivity region* defined as the set of density pairs—the density of secondary users and the density of primary transmitters—under which the secondary network is connected. Using theories and techniques from continuum percolation, we analytically characterize the connectivity region of the secondary network and reveal the tradeoff between proximity (the number of neighbors) and the occurrence of spectrum opportunities. Specifically, we establish three basic properties of the connectivity region—contiguity, monotonicity of the boundary and uniqueness of the infinite connected component, where the uniqueness implies the occurrence of a phase transition phenomenon in terms of the almost sure existence of either zero or one infinite connected component; we identify and analyze two critical densities which jointly specify the profile as well as an outer bound on the connectivity region; we study the impacts of secondary users’ transmission power on the connectivity region and the conditional average degree of a secondary user and demonstrate that matching the interference ranges of the primary and the secondary networks maximizes the tolerance of the secondary network to the primary traffic load. Furthermore, we establish a necessary condition and a sufficient condition for connectivity, which lead to an outer bound and an inner bound on the connectivity region.

Index Terms—Cognitive radio, connectivity region, continuum percolation, critical densities, heterogeneous wireless network, phase transition.

I. INTRODUCTION

THE communication infrastructure is becoming increasingly heterogeneous, with a dynamic composition of interdependent, interactive and hierarchical network components with different priorities and service requirements. One example is the cognitive radio technology [1] for opportunistic spectrum access which adopts a hierarchical structure for resource sharing

[2]. Specifically, a secondary network is overlaid with a primary network, where secondary users identify and exploit temporarily and locally unused channels without causing unacceptable interference to primary users [2].

A. Connectivity and Connectivity Region

While the connectivity of homogeneous ad hoc networks consisting of peer users has been well studied (see, for example, [3]–[10]), little is known about the connectivity of heterogeneous networks. The problem is fundamentally different from its counterpart in homogeneous networks. In particular, the connectivity of the low-priority network component depends on the characteristics (traffic pattern/load, topology, interference tolerance, etc.) of the high-priority component, thus creating a much more diverse and complex design space.

Due to the hierarchical structure of spectrum sharing, a communication link exists between two secondary users if the following two conditions hold: (C1) they are within each other’s transmission range; (C2) they see a *spectrum opportunity* determined by the transmitting and receiving activities of nearby primary users (see Section II-B-I). We say that a topological link exists between two secondary users if only condition (C1) holds.

Using theories and techniques from continuum percolation, we analytically characterize the percolation-based connectivity of the secondary network in a large-scale ad hoc heterogeneous network. Specifically, we consider a Poisson distributed secondary network overlaid with a Poisson distributed primary network in an infinite two-dimensional Euclidean space¹. We define *network connectivity* as the existence of an infinite connected component formed by communication links almost surely (a.s.), i.e., the occurrence of percolation. This connectivity characterizes the accessibility of two secondary users at a given instant and is thus also called instantaneous mutual connectivity. Given the transmission power and the interference tolerance of both the primary and the secondary users, the connectivity of the secondary network depends on the density of secondary users [due to (C1)] and the traffic load of primary users [due to (C2)].

We thus introduce the concept of *connectivity region* \mathcal{C} , defined as the set of density pairs $(\lambda_S, \lambda_{PT})$ under which the secondary network is connected, where λ_S denotes the density of the secondary users and λ_{PT} the density of primary transmitters (representing the traffic load of the primary users). As illustrated in Fig. 1, a secondary network with a density pair $(\lambda_S, \lambda_{PT})$ inside the shaded region is connected: the secondary network has

Manuscript received August 10, 2009; revised October 20, 2010; accepted January 23, 2011. Date of current version June 22, 2011. This work was supported in part by the Army Research Office under Grant W911NF-08-1-0467 and by the National Science Foundation under Grant CCF-0830685.

W. Ren and Q. Zhao are with the Department of Electrical and Computer Engineering, University of California, Davis, CA 95616 (e-mail: qzhao@ucdavis.edu; wren@ucdavis.edu).

A. Swami is with the Army Research Laboratory, Adelphi, MD 20783 USA (e-mail: a.swami@ieee.org).

Communicated by S. Ulukus, Associate Editor for Communication Networks.

Color versions of one or more of the figures in this paper are available online at <http://ieeexplore.ieee.org>.

Digital Object Identifier 10.1109/TIT.2011.2145650

¹This infinite network model is equivalent in distribution to the limit of a sequence of finite networks with a fixed density as the area of the network increases to infinity, i.e., the so-called *extended network* [11]. It follows from the arguments similar to the ones used in [12, Chapter 3] for homogeneous ad hoc networks that this infinite ad hoc heterogeneous network model represents the limiting behavior of large-scale networks.

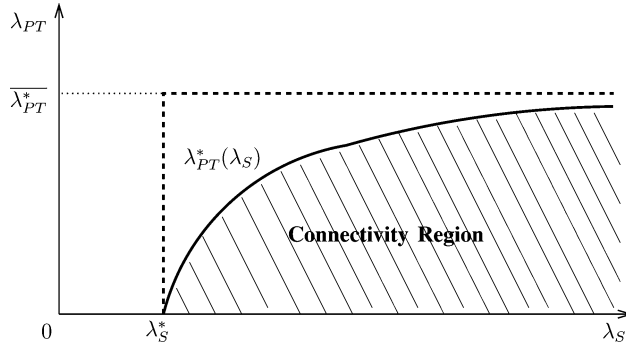


Fig. 1. Connectivity region \mathcal{C} (the upper boundary $\lambda_{PT}^*(\lambda_S)$ is defined as the supremum density of the primary transmitters that ensures connectivity with a *fixed* density of the secondary users; the critical density λ_S^* of the secondary users is defined as the infimum density of the secondary users that ensures connectivity under a *positive* density of the primary transmitters; the critical density λ_{PT}^* of the primary transmitters is the supremum density of the primary transmitters that ensures connectivity with a *finite* density of the secondary users).

a giant connected component which includes infinite number of secondary users. The existence of the giant connected component enables bidirectional communications between distant secondary users via multihop relaying. On the other hand, a secondary network with a density pair $(\lambda_S, \lambda_{PT})$ outside this region is not connected: the network is separated into an infinite number of *finite* connected components. Consequently, any secondary user can only communicate with users within a limited range.

It is shown in [13] and [14] that when the primary network is static, this instantaneous connectivity is equivalent to the connectivity defined in terms of the finiteness of the minimum multihop delay (referred to as fd-connectivity); when the primary traffic has temporal dynamics (no matter how small the range of the dynamics is), this instantaneous connectivity is stronger than the fd-connectivity and the secondary network can be intermittently connected as long as it is topologically connected [13], [14].

The objective of this paper is to establish analytical characterizations of the connectivity region and to study the impact of system design parameters (in particular, the transmission power of the secondary users) on network connectivity. The main results are summarized in the subsequent two subsections.

B. Analytical Characterizations of the Connectivity Region

We first establish three basic properties of the connectivity region: contiguity, monotonicity of the boundary and uniqueness of the infinite connected component. Specifically, based on a coupling argument, we show that the connectivity region is a contiguous area bounded below by the λ_S -axis and bounded above by a monotonically increasing function $\lambda_{PT}^*(\lambda_S)$ (see Fig. 1), where the upper boundary $\lambda_{PT}^*(\lambda_S)$ is defined as

$$\lambda_{PT}^*(\lambda_S) \triangleq \sup\{\lambda_{PT} : \mathcal{G}(\lambda_S, \lambda_{PT}) \text{ is connected}\} \quad (1)$$

with $\mathcal{G}(\lambda_S, \lambda_{PT})$ denoting the secondary network of density λ_S overlaid with a primary network specified by the density λ_{PT} of the primary transmitters. The uniqueness of the infinite connected component is established based on ergodic theory and certain combinatorial results. It shows that once the secondary

network is connected, it contains a unique infinite connected component a.s.

Second, we identify and analyze two critical parameters of the connectivity region: λ_S^* and λ_{PT}^* . They jointly specify the profile as well as an outer bound on the connectivity region. Referred to as the critical density of the secondary users, λ_S^* is the infimum density of the secondary users that ensures connectivity under a positive density of the primary transmitters

$$\lambda_S^* \triangleq \inf\{\lambda_S : \exists \lambda_{PT} > 0 \text{ s.t. } \mathcal{G}(\lambda_S, \lambda_{PT}) \text{ is connected}\}. \quad (2)$$

We show that λ_S^* equals the critical density λ_c of a *homogeneous* ad hoc network (i.e., in the absence of primary users), which has been well studied [15]. This result shows that the “takeoff” point in the connectivity region is completely determined by the effect of proximity—the number of neighbors (nodes within the transmission range of a secondary user).

Referred to as the critical density of the primary transmitters, λ_{PT}^* is the supremum density of the primary transmitters that ensures the connectivity of the secondary network with a finite density of the secondary users:

$$\lambda_{PT}^* \triangleq \sup\{\lambda_{PT} : \exists \lambda_S < \infty \text{ s.t. } \mathcal{G}(\lambda_S, \lambda_{PT}) \text{ is connected}\}. \quad (3)$$

We obtain an upper bound on λ_{PT}^* , which is shown to be achievable in simulations. More importantly, this result shows that when the density of the primary transmitters is higher than the (finite) value given by this upper bound, the secondary network cannot be connected no matter how dense it is. This parameter λ_{PT}^* thus characterizes the impact of opportunity occurrence on the connectivity of the secondary network: when the density of the primary transmitters is beyond a certain level, there are simply not enough spectrum opportunities for any secondary network to be connected.

Since a precise characterization of the upper boundary $\lambda_{PT}^*(\lambda_S)$ of the connectivity region is intractable, we establish a necessary and a sufficient condition for connectivity to provide an outer and an inner bound on the connectivity region. The necessary condition is expressed in the form of the conditional average degree of a secondary user and is derived by the construction of a branching process. The sufficient condition is obtained by the discretization of the continuum percolation model into a dependent site percolation model.

C. Impact of Transmission Power on Connectivity: Proximity Versus Opportunity

The study of the impact of the secondary users’ transmission power p_{tx} on network connectivity reveals an interesting tradeoff between proximity and opportunity in the design of heterogeneous networks. As illustrated in Fig. 2, we show that increasing p_{tx} enlarges the connectivity region \mathcal{C} along the λ_S -axis (i.e., better proximity leads to a smaller “takeoff” point), but at the price of reducing \mathcal{C} along the λ_{PT} -axis. Specifically, with a large p_{tx} , few secondary users experience spectrum opportunities due to their large interference footprint with respect to the primary users. This leads to a poor tolerance to the primary traffic load parameterized by λ_{PT} .

The transmission power p_{tx} of the secondary network should thus be chosen according to the operating point of the hetero-

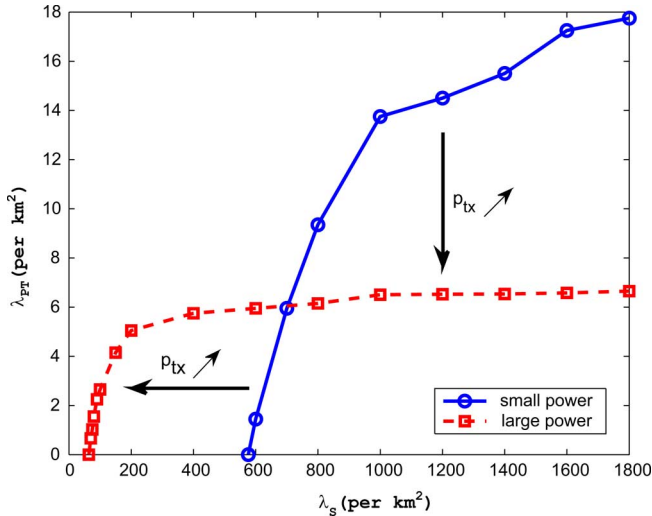


Fig. 2. Simulated connectivity regions for two different transmission powers (p_{tx} denotes the transmission power of the secondary users and the large p_{tx} is 3^α times the small p_{tx} , where α is the path-loss exponent).

geneous network given by the density of the secondary users and the traffic load of the co-existing primary users. Using the tolerance to the primary traffic load as the performance measure, we show that the interference range r_I of the secondary users should be equal to the interference range R_I of the primary users in order to maximize the upper bound on the critical density $\bar{\lambda}_{PT}^*$ of the primary transmitters. Given the interference tolerance of the primary and secondary users, we can then design the optimal transmission power p_{tx} of the secondary users based on that of the primary users.

D. Related Work

To our best knowledge, the connectivity of large-scale ad hoc heterogeneous networks has not been characterized analytically or experimentally in the literature. There are a number of classic results on the connectivity of homogeneous ad hoc networks. For example, it has been shown that to ensure either 1-connectivity (there exists a path between any pair of nodes) [3], [4] or k -connectivity (there exist at least k node-disjoint paths between any pair of nodes) [5], the average number of neighbors of each node must increase with the network size. On the other hand, to maintain a weaker connectivity— p -connectivity (i.e., the probability that any pair of nodes is connected is at least p), the average number of neighbors is only required to be above a certain “magic number” which does not depend on the network size [6].

The theory of continuum percolation has been used by Dousse *et al.* in analyzing the connectivity of a homogeneous ad hoc network under the worst-case mutual interference [7], [8]. In [9], [10], the connectivity and the transmission delay in a homogeneous ad hoc network with static or dynamic on-off links are investigated from a percolation-based perspective.

In [13] and [14], the impact of temporal dynamics of primary traffic on the connectivity and multihop delay of the secondary network is studied. In particular, it is shown that in the presence of primary traffic dynamics, the secondary network is connected

(either instantaneously or intermittently) as long as it is topologically connected. Optimal power control in heterogeneous networks has been studied in [16], which focuses on a single pair of secondary users in a Poisson network of primary users. The impacts of secondary users’ transmission power on the occurrence of spectrum opportunities and the reliability of opportunity detection are analytically characterized.

E. Organization and Notations

The rest of this paper is organized as follows. Section II presents the Poisson model of the heterogeneous network. In particular, the conditions for the existence of a communication link in the secondary network is specified based on a rigorous definition of spectrum opportunity. In Section III, we introduce the concept of connectivity region and establish its three basic properties. The two critical densities are analyzed, followed by a necessary and a sufficient condition for connectivity. In Section IV, we demonstrate the tradeoff between proximity and opportunity by studying the impact of the secondary users’ transmission power on the connectivity region and on the conditional degree of a secondary user. Further, we obtain the optimal transmission power of the secondary users, adopting the secondary network’s tolerance of the primary traffic load as the performance measure. Section V contains detailed proofs of the main results and Section VI concludes the paper.

Throughout the paper, we use capital letters for parameters of the primary users and lowercase letters for those of the secondary users.

II. NETWORK MODEL

We consider a Poisson distributed secondary network overlaid with a Poisson distributed primary network in an infinite two-dimensional Euclidean space. The models of the primary and secondary networks are specified in the following two subsections.

A. The Primary Network

The primary transmitters are distributed according to a two-dimensional Poisson point process with density λ_{PT} . Each primary transmitter’s receiver is uniformly distributed within its transmission range R_p . Here we have assumed that all primary transmitters use the same transmission power and the transmitted signals undergo isotropic path loss. Based on the displacement theorem [17, Chapter 5], it is easy to see that the primary receivers form a two-dimensional Poisson point process with density λ_{PT} . Note that the two Poisson processes formed by the primary transmitters and receivers are correlated.

B. The Secondary Network

The secondary users are distributed according to a two-dimensional Poisson point process with density λ_S , independent of the Poisson processes of the primary transmitters and receivers. The transmission range of the secondary users is denoted by r_p .

Communication Links: In contrast to the case in a homogeneous network, the existence of a communication link between two secondary users depends on not only the distance between them but also the availability of the communication channel

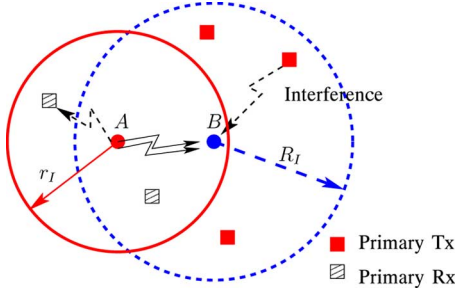


Fig. 3. Definition of spectrum opportunity.

(i.e., the presence of a spectrum opportunity). The latter is determined by the transmitting and receiving activities in the primary network as described below.

As illustrated in Fig. 3, there exists an opportunity from A , the secondary transmitter, to B , the secondary receiver, if the transmission from A does not interfere with nearby *primary receivers* in the solid circle and the reception at B is not affected by nearby *primary transmitters* in the dashed circle [18]. Referred to as the interference range of the secondary users, the radius r_I of the solid circle at A depends on the transmission power of A and the interference tolerance of the primary receivers, whereas the radius R_I of the dashed circle (the interference range of the primary users²) depends on the transmission power of the primary users and the interference tolerance of B .

It is clear from the above discussion that spectrum opportunities depend on both transmitting and receiving activities of the primary users. Furthermore, spectrum opportunities are *asymmetric*. Specifically, a channel that is an opportunity when A is the transmitter and B the receiver may not be an opportunity when B is the transmitter and A the receiver. In other words, there exist unidirectional communication links in the secondary network. Since unidirectional links are difficult to utilize in wireless networks [19], we only consider bidirectional links in the secondary network when we define connectivity. As a consequence, when we determine whether there exists a communication link between two secondary users, we need to check the existence of spectrum opportunities in both directions.

To summarize, under the disk signal propagation and interference model, there is a (bidirectional) link between A and B if and only if (C1) the distance between A and B is at most r_p ; (C2) there exists a bidirectional spectrum opportunity between A and B , i.e., there are no primary transmitters within distance R_I of either A or B and no primary receivers within distance r_I of either A or B .

Connectivity: We interpret the connectivity of the secondary network in the percolation sense: the secondary network is connected if there exists an infinite connected component a.s.

Based on the above conditions (C1, C2) for the existence of a communication link, we can obtain an undirected random graph $\mathcal{G}(\lambda_S, \lambda_{PT})$ corresponding to the secondary network, which is determined by three Poisson point processes: the secondary

²Since the minimum transmission power for successful reception is, in general, higher than the maximum allowable interference power, it follows that the transmission range R_p of primary users is smaller than R_I . Furthermore, under the disk signal propagation and interference model, we have $R_p = \beta R_I$ ($0 < \beta < 1$). A similar relationship holds for r_p and r_I .

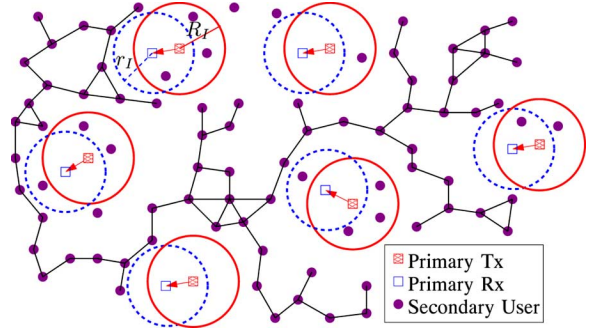


Fig. 4. Realization of the heterogeneous network. The random graph $\mathcal{G}(\lambda_S, \lambda_{PT})$ consists of all the secondary nodes and all the bidirectional links denoted by solid lines. The solid circles with radii R_I denote the interference regions of the primary transmitters within which secondary users cannot successfully receive and the dashed circles with radii r_I denote the required protection regions for the primary receivers within which the secondary users should refrain from transmitting.

users with density λ_S , the primary transmitters with density λ_{PT} and the primary receivers with density λ_{PT} (correlated with the process of the primary transmitters)³. See Fig. 4 for an illustration of $\mathcal{G}(\lambda_S, \lambda_{PT})$.

The question we aim to answer in this paper is: when is the secondary network connected, i.e., when does percolation occur in $\mathcal{G}(\lambda_S, \lambda_{PT})$?

III. ANALYTICAL CHARACTERIZATIONS OF THE CONNECTIVITY REGION

Given the transmission power and the interference tolerance of both the primary and the secondary users (i.e., R_p , R_I , r_p and r_I are fixed), the connectivity of the secondary network is determined by the density λ_S of the secondary users and the density λ_{PT} of the primary transmitters. We thus introduce the concept of connectivity region \mathcal{C} of a secondary network, which is defined as the set of density pairs $(\lambda_S, \lambda_{PT})$ under which the secondary network $\mathcal{G}(\lambda_S, \lambda_{PT})$ is connected (see Fig. 1)

$$\mathcal{C} \triangleq \{(\lambda_S, \lambda_{PT}) : \mathcal{G}(\lambda_S, \lambda_{PT}) \text{ is connected.}\}.$$

A. Basic Properties of the Connectivity Region

We next establish three basic properties of the connectivity region.

Theorem 1: Basic Properties of the Connectivity Region.

T1.1 The connectivity region \mathcal{C} is contiguous, that is, for any two points $(\lambda_{S1}, \lambda_{PT1}), (\lambda_{S2}, \lambda_{PT2}) \in \mathcal{C}$, there exists a continuous path in \mathcal{C} connecting the two points.

T1.2 The lower boundary of the connectivity region \mathcal{C} is the λ_S -axis. Let $\lambda_{PT}^*(\lambda_S)$ denote the upper boundary of the connectivity region \mathcal{C} defined by (1), then we have that $\lambda_{PT}^*(\lambda_S)$ is monotonically increasing with λ_S .

³The two Poisson point processes of the primary transmitters and receivers are essentially a snap shot of the realizations of the primary transmitters and receivers. In different time slots, different sets of primary users become active transmitters/receivers. Thus, even if a secondary user is isolated at one time due to the absence of spectrum opportunities, it may experience an opportunity at a different time and be connected to other secondary users.

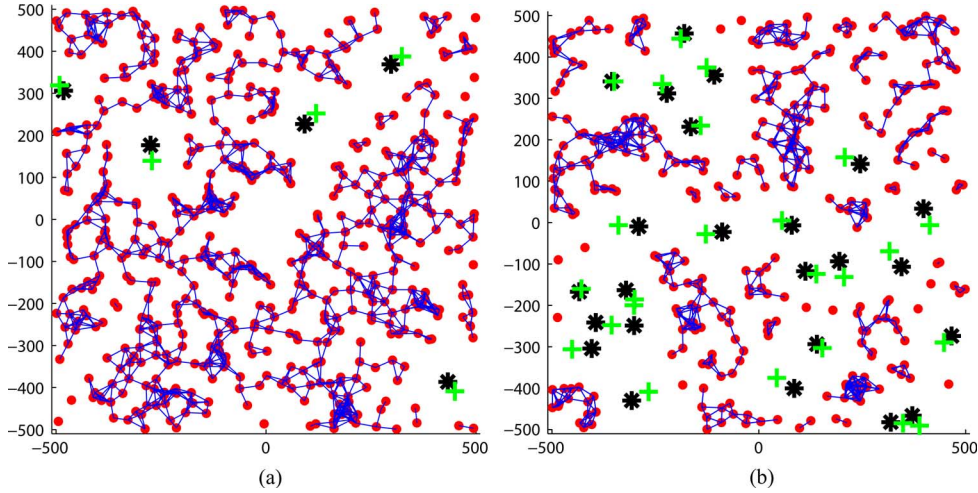


Fig. 5. Two realizations of the Poisson heterogeneous network (black stars denote primary transmitters, green plus signs denote primary receivers, red dots denote secondary users and blue segments denote the bidirectional links between secondary users). We have removed secondary users who do not see opportunities for clarity. The simulation parameters are given by $R_p = 50$ m, $R_I = 80$ m, $\lambda_S = 650$ km $^{-2}$, $r_p = 50$ m, $r_I = 80$ m and the critical density in this case is $\lambda_c(50) \approx 576$ km $^{-2}$ (a) percolation occurs ($\lambda_{PT} = 10$ km $^{-2}$) (b) percolation does not occur ($\lambda_{PT} = 20$ km $^{-2}$).

T1.3 There exists either zero or one infinite connected component in $\mathcal{G}(\lambda_S, \lambda_{PT})$ a.s.

Proof: The proofs of T1.1 and T1.2 are based on the coupling argument, a technique frequently used in continuum percolation [15, Section 2.2]. The proof of T1.3 is based on the ergodicity of the random model driven by the three Poisson point processes of the primary transmitters, the primary receivers and the secondary users. The details of the proofs are given in Section V-B. ■

T1.1 and T1.2 specify the basic structure of the connectivity region, as illustrated in Fig. 1. T1.3 implies the occurrence of a phase transition phenomenon, that is, there exists either a unique infinite connected component a.s. or no infinite connected component a.s. This uniqueness of the infinite connected component excludes the undesirable possibility of having more than one (maybe infinite) infinite connected component in the secondary network. We point out that such a property is not always present in wireless networks. Two examples where more than one infinite connected component exists in a homogeneous ad hoc network can be found in [20].

B. Critical Densities

In this subsection, we study the critical density λ_S^* of the secondary users and the critical density λ_{PT}^* of the primary transmitters defined by (2) and (3), respectively. We have the following theorem.

Theorem 2: Critical Densities.

Given R_p , R_I , r_p and r_I , we have:

T2.1 $\lambda_S^* = \lambda_c(r_p)$, where $\lambda_c(r_p)$ is the critical density for a homogeneous ad hoc network with transmission range r_p (i.e., in the absence of the primary network).

T2.2

$$\lambda_{PT}^* \leq \frac{\lambda_c(1)}{4 \max\{R_I^2, r_I^2\} - r_p^2} \quad (4)$$

where the constant $\lambda_c(1)$ is the critical density for a homogeneous ad hoc network with a unit transmission range.

Proof: The basic idea of the proof of T2.1 is to approximate the secondary network $\mathcal{G}(\lambda_S, \lambda_{PT})$ by a discrete edge-percolation model on the grid. This discretization technique is often used to convert a continuum percolation model to a discrete site/edge percolation model (see, for example, [15, Chapter 3], [8]). The details of the proof are given in Section V-C-I.

The proof of T2.2 is based on the argument that if there is an infinite connected component in the secondary network, then an infinite vacant component must exist in the two Poisson Boolean models driven by the primary transmitters and the primary receivers, respectively. The key point is to carefully choose the radii of the two Poisson Boolean models in order to obtain a valid upper bound on λ_{PT}^* . The details of the proof can be found in Section V-C-II. ■

Fig. 5(a) shows one realization of the heterogeneous network when λ_S is slightly larger than $\lambda_c(r_p)$ and λ_{PT} is small. At least one left-to-right (L-R) crossing and at least one top-to-bottom (T-B) crossing can be found in the square network. It is thus expected that these L-R and T-B crossings in finite square regions can form an infinite connected component in the whole network on \mathbb{R}^2 . If we slightly increase λ_{PT} , then we observe from Fig. 5(b) that the reduction in spectrum opportunities eliminates numerous communication links in the secondary network, creating several disjoint small components.

Fig. 6 shows a simulation example of the connectivity region, where the upper bound on the critical density λ_{PT}^* of the primary transmitters given in T2.2 appears to be achievable.

C. A Necessary Condition for Connectivity

In this subsection, we establish a necessary condition for connectivity which is given in terms of the average conditional degree of a secondary user. This condition agrees with our intuition: the secondary network cannot be connected if the degree of every secondary user is small.

Let $\mathbb{I}(A, d, \text{rx/tx})$ denote the event that there exist primary receivers/transmitters within distance d of a secondary user A . Let $\bar{\mathbb{I}}(A, d, \text{rx/tx})$ denote the complement of $\mathbb{I}(A, d, \text{rx/tx})$. Since a

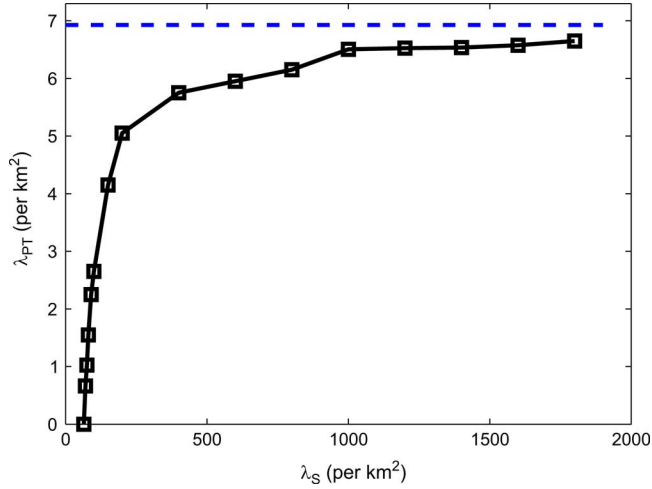


Fig. 6. Simulated connectivity regions when $r_p = 150$ m, $r_I = 240$ m, $R_p = 100$ m and $R_I = 120$ m. The blue dashed line is the upper bound (4) on the critical density $\bar{\lambda}_{PT}^*$ of primary transmitters given in T2.2. The area of the simulated heterogeneous network is $2000 \text{ m} \times 2000 \text{ m}$. For a fixed density λ_S of the secondary users, the upper boundary $\lambda_{PT}^*(\lambda_S)$ is equal to the minimum density of the primary transmitters such that over all the 1000 realizations, the percentage of the ones in which there exists at least one L-R crossing is below 50%. The intuitive reason for choosing the existence of an L-R crossing as the criterion for connectivity is illustrated in Fig. 5 and is discussed in Section V-C.

secondary user is isolated if it does not see a spectrum opportunity, we focus on secondary users who experience spectrum opportunities and define the conditional average degree μ of such a secondary user A as

$$\mu = \mathbb{E}[\deg(A) | \overline{\mathbb{I}(A, r_I, \text{rx})} \cap \overline{\mathbb{I}(A, R_I, \text{tx})}] \quad (5)$$

where $\deg(A)$ denotes the degree of A , r_I the interference range of the secondary users and R_I the interference range of the primary users. Notice that the degree of A is the number of secondary users within the transmission range of A and experiencing bidirectional opportunities with A . We arrive at the following necessary condition for connectivity.

Theorem 3: A necessary condition for the connectivity of $\mathcal{G}(\lambda_S, \lambda_{PT})$ is $\mu > 1$, where μ is the conditional average degree of a secondary user defined in (5).

Proof: The basic idea is to construct a branching process, where the conditional average degree μ is the average number of offspring. This branching process provides an upper bound on the number of secondary users in a connected component. If $\mu \leq 1$, then the branching process is finite a.s. It thus follows that there is no infinite connected component a.s. in $\mathcal{G}(\lambda_S, \lambda_{PT})$. Details can be found in Section V-D. ■

To apply the necessary condition given in Theorem 3, the conditional average degree μ of a secondary user A needs to be evaluated based on the network parameters. Let B be a secondary user randomly and uniformly distributed within transmission range r_p of A . Let $g(\lambda_{PT}, r_p, r_I, R_p, R_I)$ denote the probability of a bidirectional opportunity between A and B conditioned on the event that A sees an opportunity. Based on the statistical equivalence and independence of different points in a Poisson point process, the conditional average degree μ of a secondary user A is given by this conditional probability $g(\cdot)$ of a bidirectional opportunity between A and a randomly chosen

neighbor multiplied by the average number of neighbors of A , i.e.,

$$\mu = (\lambda_S \pi r_p^2) \cdot g(\lambda_{PT}, r_p, r_I, R_p, R_I). \quad (6)$$

The detailed derivation of (6) and an expression for $g(\cdot)$ are given in Appendix A. It is also shown in Appendix A that $g(\cdot)$ is a strictly decreasing function of λ_{PT} . Thus $g^{-1}(\cdot)$, the inverse of $g(\cdot)$ with respect to λ_{PT} , is well-defined.

Combining (6) with Theorem 3, we obtain an outer bound on the connectivity region. Specifically, let $\mu(\lambda_S, \lambda_{PT})$ denote the conditional average degree of a secondary user in $\mathcal{G}(\lambda_S, \lambda_{PT})$. Then those density pairs $(\lambda_S, \lambda_{PT})$ satisfying $\mu(\lambda_S, \lambda_{PT}) \leq 1$ are outside the connectivity region.

Corollary 1: Given R_p, R_I, r_p and r_I , an outer bound on the connectivity region \mathcal{C} is given by

$$\lambda_{PT} = g^{-1}\left(\frac{1}{\lambda_S \pi r_p^2}\right)$$

where $g^{-1}(\cdot)$ is the inverse of the conditional probability $g(\cdot)$ with respect to λ_{PT} .

D. A Sufficient Condition for Connectivity

In this subsection, we establish a sufficient condition for connectivity, which provides an inner bound on the connectivity region and a criterion for checking whether a secondary network is connected.

Our sufficient condition for connectivity is established by using the discretization technique. The continuum percolation model is mapped onto a dependent site-percolation model \mathcal{L} in the following way. As illustrated in Fig. 7, we partition \mathbb{R}^2 into (dashed) squares with side length d_s and locate a site at the center of each square. Sites whose associated dashed squares share at least one common point are considered connected (as illustrated by solid lines in Fig. 7). Thus, each site is connected to eight neighbors⁴ (see the eight neighbors O_1, \dots, O_8 of site O in Fig. 7). Let B_O be the associated dashed square of O , then O is occupied if there exists in B_O at least one secondary user who sees an opportunity.

Since the largest distance between two points in two neighboring dashed squares is $2\sqrt{2}d_s$, it follows that if we set $d_s = \frac{r_p}{2\sqrt{2}}$, then every pair of secondary users in two neighboring dashed squares are within transmission range r_p of each other. Based on the definitions of occupied site in \mathcal{L} and communication link in the secondary network, we conclude that the existence of an infinite occupied component (a connected component consisting of only occupied sites) in \mathcal{L} implies the existence of an infinite connected component in the secondary network.

Due to the fact that spectrum opportunities are spatially dependent, the state of one site is correlated with the states of its adjacent sites. Thus, the above site-percolation model \mathcal{L} is a dependent model. Define the dependence range k as the minimum distance such that the state of any two sites at distance larger than k are independent, where the distance between two sites

⁴For the commonly used square site-percolation model, each site has four neighbors. The site-percolation model constructed here provides a better inner bound.

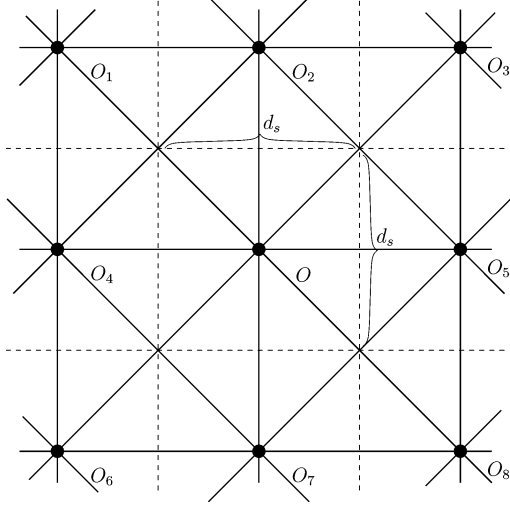


Fig. 7. Illustration of the dependent site-percolation model \mathcal{L} with side length d_s (solid dots denote sites, solid lines denote edges connecting every two sites and dashed lines denote the squared partition).

is the minimum number of neighboring sites that must be traversed from one site to the other. Then the dependence range of \mathcal{L} is given by

$$k = \left\lceil 8 \max \left\{ R_I + \frac{r_p}{4}, r_I + \frac{r_p}{4} \right\} / r_p \right\rceil - 1. \quad (7)$$

Let p_c denote the upper critical probability of \mathcal{L} which is defined as the minimum probability of occupancy p^* such that if the probability of occupancy $p > p^*$, an infinite occupied component containing the origin exists in \mathcal{L} with a positive probability (wpp.). Since the dependence range k of \mathcal{L} is finite, it follows from [12, Theorem 2.3.1] that $p_c < 1$. Now we present a sufficient condition for connectivity in the following theorem.

Theorem 4: Let p_c denote the upper critical probability of the dependent site-percolation model \mathcal{L} specified above. Define

$$I(r, R_p, r_I) = 2 \int_0^r t \frac{S_I(t, R_p, r_I)}{\pi R_p^2} dt \quad (8)$$

where $S_I(t, R_p, r_I)$ is the common area of two circles with radii R_p and r_I and centers t apart. Then the secondary network is connected if the equation shown at the bottom of the page holds.

Proof: The proof is based on the ergodicity of the heterogeneous network model and its relation with the constructed dependent site-percolation model \mathcal{L} . Details can be found in Section V-E. ■

By applying a general upper bound on the upper critical probability p_c for a site-percolation model with finite dependence range [12, Theorem 2.3.1], we arrive at the following corollary.

Corollary 2: A sufficient condition for the connectivity of $\mathcal{G}(\lambda_S, \lambda_{PT})$ is

$$\lambda_{PT} < \frac{1}{\pi [R_I^2 + r_I^2 - I(R_I, R_p, r_I)]} \ln \frac{1 - \exp\left(-\frac{\lambda_S r_p^2}{8}\right)}{1 - \left(\frac{1}{3}\right)^{(2k+1)^2}}$$

where $I(R_I, R_p, r_I)$ is defined in (8) and k is the dependence range of the site-percolation model defined in (7).

IV. IMPACT OF TRANSMISSION POWER: PROXIMITY VERSUS OPPORTUNITY

In this section, we study the impact of the secondary users' transmission power on the connectivity and the conditional average degree of the secondary network. As has been illustrated in Fig. 2, there exists a tradeoff between proximity and opportunity in designing the secondary users' transmission power for connectivity. Specifically, increasing the transmission power of the secondary users leads to a smaller critical density λ_S^* of the secondary users, but at the same time, a lower tolerance to the primary traffic load manifested by a smaller critical density λ_{PT}^* of the primary transmitters.

A. Impact on the Conditional Average Degree

As discussed in Section III-C, the expression for the conditional average degree μ can be decomposed into the product of two terms: $\lambda_S \pi r_p^2$ and $g(\lambda_{PT}, r_p, r_I, R_p, R_I)$. The first term is the average number of neighbors of a secondary user, which increases with the transmission power p_{tx} of the secondary users (i.e., enhanced proximity). The other term $g(\lambda_{PT}, r_p, r_I, R_p, R_I)$ is the conditional probability of a bidirectional opportunity, which decreases with p_{tx} due to reduced spectrum opportunities. This tension between proximity and opportunity is illustrated in Fig. 8, where we observe that the impact of p_{tx} on proximity dominates when p_{tx} is small (μ increases with p_{tx}) while its impact on the occurrence of opportunities dominates when p_{tx} is large (μ decreases with p_{tx}).

Corollary 3: Let p_{tx} be the transmission power of secondary users and μ the conditional average degree defined in (5), then under the disk signal propagation and interference model we have⁵

$$\mu = O\left((p_{tx})^{-2/\alpha}\right) \text{ as } p_{tx} \rightarrow \infty$$

where α is the path-loss exponent.

Proof: We show this corollary by deriving an upper bound on μ . Details can be found in Appendix B. ■

⁵Here we use the Big O notation: $f(x) = O(g(x))$ as $x \rightarrow \infty$ if and only if $\exists M > 0, x_0 > 0$ such that $|f(x)| \leq M|g(x)|$ for all $x > x_0$.

$$\left[1 - \exp\left(-\frac{\lambda_S r_p^2}{8}\right) \right] \exp\left\{-\lambda_{PT} \pi [R_I^2 + r_I^2 - I(R_I, R_p, r_I)]\right\} > p_c.$$

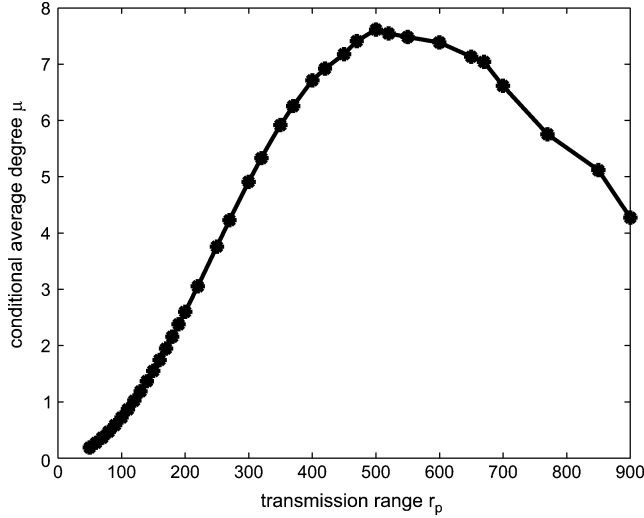


Fig. 8. Conditional average degree μ of secondary users vs transmission range r_p of secondary users. $r_p \propto (p_{tx})^{\frac{1}{\alpha}}$, where p_{tx} is the transmission power of secondary users and α is the path-loss exponent and simulation parameters are given by $\lambda_{PT} = 2.5 \text{ km}^{-2}$, $R_p = 200 \text{ m}$, $R_I = 250 \text{ m}$, $\lambda_S = 25 \text{ km}^{-2}$, $r_I = r_p/0.8$.

For a homogeneous network, the average degree of a user is $\lambda \pi r_p^2$, which increases with p_{tx} at rate $(p_{tx})^{2/\alpha}$. In sharp contrast, this corollary tells us that for a heterogeneous network, when p_{tx} is large enough, the conditional average degree μ of a secondary user actually *decreases* with p_{tx} at least as fast as $(p_{tx})^{-2/\alpha}$.

B. Impact on the Connectivity Region

From the scaling relation of the critical density [15, Proposition 2.11], we know that in a homogeneous two-dimensional network

$$\lambda_c(r_p) = \lambda_c(1) (r_p)^{-2} \propto (p_{tx})^{-\frac{2}{\alpha}}$$

where the constant $\lambda_c(1)$ is the critical density for a homogeneous ad hoc network with a unit transmission range. Thus, if each secondary user adopts a high transmission power, then $\lambda_c(r_p)$ decreases. It follows from T2.1 that the critical density λ_S^* of secondary users required to achieve connectivity decreases due to the enhanced proximity.

On the other hand, from the upper bound on the critical density $\overline{\lambda_{PT}^*}$ of the primary transmitters given in T2.2, we have that

$$\overline{\lambda_{PT}^*} = O\left((p_{tx})^{-2/\alpha}\right) \text{ as } p_{tx} \rightarrow \infty$$

where we have assumed that $r_p = \beta r_I$ for some $\beta \in (0, 1)$ under the disk signal propagation and interference model. Thus, when the transmission power p_{tx} of the secondary network is large enough, the critical density $\overline{\lambda_{PT}^*}$ of the primary transmitters decreases with p_{tx} at least as fast as $(p_{tx})^{-2/\alpha}$ due to reduced spectrum opportunities.

C. Optimal Design of Transmission Power

Due to the tension between proximity and opportunity, there does not exist a transmission power of the secondary users that

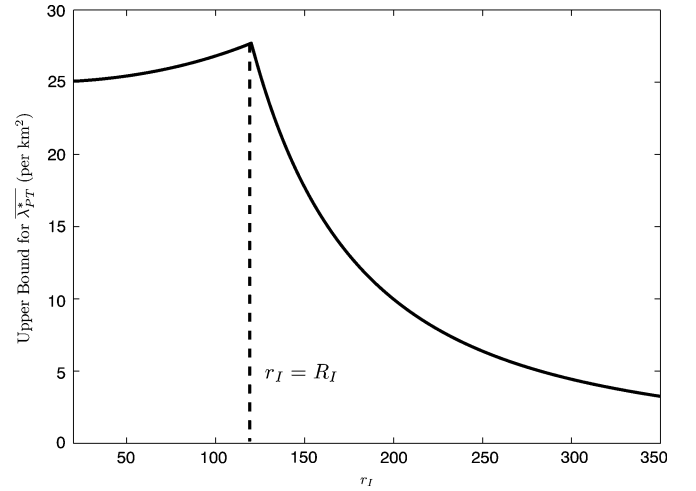


Fig. 9. Example of the upper bound on $\overline{\lambda_{PT}^*}$ as a function of r_I (parameters are given by $R_I = 120 \text{ m}$, $r_p = 0.625 r_I$).

leads to the “largest” connectivity region (largest in the sense that its connectivity region contains all regions achievable with any finite transmission power p_{tx} of the secondary users). Thus, the optimal design of p_{tx} depends on the operating point of the heterogeneous network. For instance, when a sparse secondary network is overlaid with a primary network with low traffic load, a large p_{tx} may be desirable to achieve connectivity. The opposite holds when a dense secondary network is overlaid with a primary network with high traffic load.

Focusing on a secondary network whose density exceeds the critical density of the secondary users, we address the design of its transmission power for the maximum tolerance to the primary traffic. Due to its tractability and achievability, the upper bound on the critical density $\overline{\lambda_{PT}^*}$ of the primary transmitters given in T2.2 is used as the performance measure (see Fig. 6 for a simulation example).

Theorem 5: Let r_I and R_I denote the interference range of the secondary and the primary users. For a fixed R_I , the upper bound on $\overline{\lambda_{PT}^*}$ given in T2.2 is maximized when the primary and secondary networks have matching interference ranges: $r_I = R_I$.

Proof: Since under the disk signal propagation and interference model, $r_p = \beta r_I$ for some $\beta \in (0, 1)$, the upper bound on $\overline{\lambda_{PT}^*}$ can be written as

$$\overline{\lambda_{PT}^*} \leq \begin{cases} \frac{\lambda_c(1)}{4R_I^2 - \beta^2 r_I^2} & \text{for } r_I \leq R_I \\ \frac{\lambda_c(1)}{(4 - \beta^2) r_I^2} & \text{for } r_I > R_I. \end{cases}$$

Then the above theorem can be readily shown by finding the maximal point for the two cases: $r_I \leq R_I$ and $r_I > R_I$. ■

An example of the upper bound on $\overline{\lambda_{PT}^*}$ is plotted as a function of r_I in Fig. 9. Notice that there is a distinct difference in the slope on the two sides of the optimal point. As a consequence, the operating region of $r_I < R_I$ is preferred over that of $r_I > R_I$ when the optimal point $r_I = R_I$ cannot be achieved. We point out that the desired operating region of $r_I < R_I$ is the typical case of a secondary network coexisting with a privileged primary network.

V. PROOFS

In this section, we present proofs of the main results presented in Sections III–IV. We start with a brief overview of several basic results in percolation theory that will be used in the proofs.

A. Percolation Theory: Some Basic Results

Poisson Boolean Model: Poisson Boolean model [15], often referred to as $\mathcal{B}(X, \rho, \lambda)$, is specified by two elements: a Poisson point process X on \mathbb{R}^d with density λ and a radius ρ , a random variable with a given distribution. Under this model, each point in X is the center of a ball in \mathbb{R}^d with a random radius distributed according to the distribution of ρ . Radii associated with different points are independent and they are also independent of points in X . Under a Poisson Boolean model, the whole space is partitioned into two regions: the occupied region, which is the region covered by at least one ball and the vacant region, which is the complement of the occupied region. We define occupied (vacant) components as those connected components in the occupied (vacant) region.

Assume that nodes in a homogeneous ad hoc network form a Poisson point process with density λ and their transmission range is r . It is easy to see that the connectivity of this network can be studied through examination of the occupied connected components in the corresponding Poisson Boolean model $\mathcal{B}(X, r/2, \lambda)$.

Sharp Transition in Two Dimensions: For the Poisson Boolean model in two dimensions, the sharp transition phenomenon is remarkable in the sense that the critical density for the a.s. existence of infinite occupied components is equal to that for the a.s. existence of infinite vacant components. Let $\lambda_c(2\rho)$ denote the critical density for the Poisson Boolean model $\mathcal{B}(X, \rho, \lambda)$, then we have that:

- when $\lambda < \lambda_c(2\rho)$, there is no infinite occupied component a.s. and there is a unique infinite vacant component a.s.;
- when $\lambda > \lambda_c(2\rho)$, there is a unique infinite occupied component a.s. and there is no infinite vacant component a.s.

The exact value of λ_c is not known. For a deterministic radius ρ , simulation results [21] indicate that $\lambda_c(2\rho) \approx 0.36\rho^{-2}$, while rigorous bounds $0.192\rho^{-2} < \lambda_c(2\rho) < 0.843\rho^{-2}$ are provided in [15] and [22].

Crossing Probabilities: A continuous curve in the occupied region is called an occupied path. An occupied path γ is an occupied L-R crossing of the rectangle $\{0 \leq x \leq l_1\} \times \{0 \leq y \leq l_2\}$ if γ intersects both the left and the right boundaries of the rectangle, i.e., $\gamma \cap (\{x = 0\} \times \{0 \leq y \leq l_2\}) \neq \emptyset$, $\gamma \cap (\{x = l_1\} \times \{0 \leq y \leq l_2\}) \neq \emptyset$ and the segment between the two intersecting points is fully contained in the rectangle. Similarly, we define an occupied T-B crossing by requiring that γ intersects with the top and bottom boundaries of the rectangle. Let

$$\begin{aligned} \sigma((l_1, l_2), \lambda, L-R) &= \Pr\{\exists \text{ an occupied L-R crossing of } [0, l_1] \times [0, l_2]\} \\ \sigma((l_1, l_2), \lambda, T-B) &= \Pr\{\exists \text{ an occupied T-B crossing of } [0, l_1] \times [0, l_2]\} \end{aligned}$$

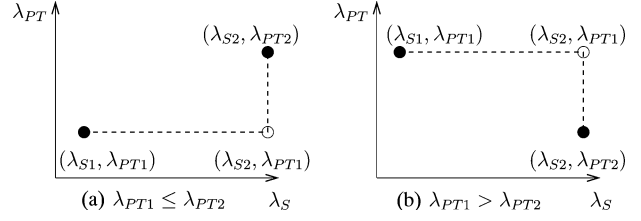


Fig. 10. Continuous path connecting the two points $(\lambda_{S1}, \lambda_{PT1})$ and $(\lambda_{S2}, \lambda_{PT2})$ in the connectivity region \mathcal{C} . (a) $\lambda_{PT1} \leq \lambda_{PT2}$. (b) $\lambda_{PT1} > \lambda_{PT2}$.

denote the two crossing probabilities in the rectangle $[0, l_1] \times [0, l_2]$. Then for a Poisson Boolean model $\mathcal{B}(X, \rho, \lambda)$ in two dimensions with a.s. bounded ρ , we have [15, Corollary 4.1] that for any $k \geq 1$

$$\lim_{n \rightarrow \infty} \sigma((kn, n), \lambda, L-R) = \begin{cases} 1, & \text{if } \lambda > \lambda_c(2\rho) \\ 0, & \text{if } \lambda < \lambda_c(2\rho). \end{cases} \quad (9)$$

Due to the symmetry of the Poisson Boolean model, similar results hold for the T-B crossing probability $\sigma((n, kn), \lambda, T-B)$.

B. Proof of Theorem 1

Proof of T1.1: To prove T1.1, it suffices to show that for any two given points $(\lambda_{S1}, \lambda_{PT1})$ and $(\lambda_{S2}, \lambda_{PT2})$ in \mathcal{C} , we can find a path in \mathcal{C} that connects these two points. In particular, the path we constructed is given by a horizontal segment and a vertical segment as shown in Fig. 10, where we assume, without loss of generality, that $\lambda_{S1} \leq \lambda_{S2}$.

Consider case (a) in Fig. 10 where $\lambda_{PT1} \leq \lambda_{PT2}$. Case (b) can be proven similarly. First, we show every point $(\lambda_S, \lambda_{PT1})$ ($\lambda_{S1} \leq \lambda_S \leq \lambda_{S2}$) on the horizontal segment belongs to \mathcal{C} . Let $\lambda' = \lambda_S - \lambda_{S1}$. A Poisson point process X with density λ_S is statistically equivalent to the superposition of a Poisson point process X_1 with density λ_{S1} and an independent Poisson point process X' with density λ' . It follows that any realization of the heterogeneous network with densities λ_S and λ_{PT1} can be generated by adding more secondary nodes to a realization of the heterogeneous network with densities λ_{S1} and λ_{PT1} . Thus, the existence of an infinite connected component in $\mathcal{G}(\lambda_{S1}, \lambda_{PT1})$ implies the existence of an infinite connected component in $\mathcal{G}(\lambda_S, \lambda_{PT1})$. We thus have that $(\lambda_S, \lambda_{PT1}) \in \mathcal{C}$ for $(\lambda_{S1} \leq \lambda_S \leq \lambda_{S2})$.

Now we know that the two end points $(\lambda_{S2}, \lambda_{PT1})$ and $(\lambda_{S2}, \lambda_{PT2})$ of the vertical segment belong to \mathcal{C} . For a point $(\lambda_{S2}, \lambda_{PT})$ ($\lambda_{PT1} \leq \lambda_{PT} \leq \lambda_{PT2}$) on the vertical segment, let $\lambda' = \lambda_{PT2} - \lambda_{PT}$, then any realization of the heterogeneous network with densities λ_{S2} and λ_{PT} can be obtained by independently removing each primary transmitter-receiver pair with probability λ'/λ_{PT2} from a realization of the heterogeneous network with densities λ_{S2} and λ_{PT2} . It follows from the definition of communication link in the secondary network (see Section II-B-I) that the existence of an infinite connected component in $\mathcal{G}(\lambda_{S2}, \lambda_{PT2})$ implies the existence of an infinite connected component in $\mathcal{G}(\lambda_{S2}, \lambda_{PT})$. Thus, we have $(\lambda_{S2}, \lambda_{PT}) \in \mathcal{C}$ ($\lambda_{PT1} \leq \lambda_{PT} \leq \lambda_{PT2}$).

Proof of Theorem 1.2: Suppose that $(\lambda_S, \lambda_{PT}) \in \mathcal{C}$ ($\lambda_{PT} > 0$), then by using the coupling argument for showing that the vertical segment belongs to \mathcal{C} in the above proof of T1.1, we conclude that $(\lambda_S, 0) \in \mathcal{C}$, i.e., the λ_S -axis is the lower boundary of \mathcal{C} .

Suppose that $\lambda_{S2} > \lambda_{S1} > 0$. In order to prove the monotonicity of $\lambda_{PT}^*(\lambda_S)$ with λ_S it suffices to show that $\forall \lambda_{PT} \geq 0$, if $(\lambda_{S1}, \lambda_{PT}) \in \mathcal{C}$ then $(\lambda_{S2}, \lambda_{PT}) \in \mathcal{C}$. This is a direct consequence of the coupling argument for showing that the horizontal segment belongs to \mathcal{C} in the above proof of T1.1.

Proof of Theorem 1.3: We first establish the ergodicity⁶ of the heterogeneous network model.

Lemma 1: The heterogeneous network model is ergodic.

Proof of Lemma 1: The proof of this lemma is inspired by the proof of the ergodicity of the Poisson Boolean model [15, Proposition 2.8]. The difficulty here is that for the heterogeneous network model, we have two correlated Poisson point processes: the primary transmitters and the primary receivers. The definition of the shift transformation for the primary network model is thus more complicated than the standard Poisson Boolean model with a deterministic radius ρ . To prove Lemma 1, we first show the ergodicity of the primary network model and then we show the mixing property⁷ of the secondary network model. Since the primary network model is independent of the secondary network model, it follows from [24, Theorem 2.6.1] that the heterogeneous network model is ergodic.

Let \mathcal{B}^d denote the Borel σ -algebra in \mathbb{R}^d and N the set of all simple counting measures⁸ on \mathcal{B}^d . Construct a σ -algebra \mathcal{N} for N generated by sets of the form

$$\{n \in N : n(A) = k\}$$

where $A \in \mathcal{B}^d$ and k is an integer. A point process X can now be defined as a measurable mapping from a probability space (Ω, \mathcal{F}, P) into (N, \mathcal{N}) [23, Chapter 7]. The measure μ on \mathcal{N} induced by X is defined as $\mu(G) = P(X^{-1}(G))$, for all $G \in \mathcal{N}$.

In order to define the shift transformation on Ω , it is convenient to identify (Ω, \mathcal{F}) with (N, \mathcal{N}) . Let $\omega(A)$ denote the number of points in $A \in \mathcal{B}^d$, $\forall \omega \in \Omega$ and T_x be the shift according to a vector $x \in \mathbb{R}^d$. Then T_x induces a shift transformation $S_x : \Omega \rightarrow \Omega$ through the following equation for every $A \in \mathcal{B}^d$:

$$(S_x \omega)(A) = \omega(T_x^{-1} A). \quad (10)$$

⁶A measure preserving (m.p.) dynamical system $(\Omega, \mathcal{F}, \mu, T)$ consists of a set Ω , a σ -algebra \mathcal{F} of measurable subsets of Ω , a nonnegative measure μ on (Ω, \mathcal{F}) and an invertible m.p. transformation $T : \Omega \rightarrow \Omega$ such that $\mu(T^{-1}F) = \mu(F)$ for all $F \in \mathcal{F}$. A set $F \in \mathcal{F}$ is said to be T-invariant if $T^{-1}F = F$. The m.p. dynamical system $(\Omega, \mathcal{F}, \mu, T)$ is said to be ergodic if the σ -algebra of T-invariant sets is trivial, i.e., for any invariant set, either it has measure 0 or its complement has measure 0.

⁷An m.p. dynamical system $(\Omega, \mathcal{F}, \mu, T)$ is said to be mixing if for all $E, F \in \mathcal{F}$, $\lim_{n \rightarrow \infty} \mu(T^n E \cap F) = \mu(E)\mu(F)$.

⁸A simple counting measure on \mathcal{B}^d is an integer-valued measure for which the measures of bounded Borel sets are all finite and the measure of a point is at most 1.

Let $(\Omega_{PT}, \mathcal{F}_{PT}, P_{PT})$ be the probability space of the Poisson point process X_{PT} for the primary transmitters with density λ_{PT} . Let Ω_{PR} be the product space $\prod_{n \in \mathbb{N}} \prod_{z \in \mathbb{Z}^2} C_{R_p}$ for the primary receivers, where $C_{R_p} = \{(x, y) : x^2 + y^2 \leq R_p\}$. Then we equip Ω_{PR} with the usual product σ -algebra and product measure P_{PR} with all marginal probability measure being μ_U , where μ_U is a uniform probability measure on C_{R_p} . Finally, we set $\Omega_P = \Omega_{PT} \times \Omega_{PR}$ and equip Ω_P with the product measure $P_P = P_{PT} \times P_{PR}$ and the usual product σ -algebra. It follows that the primary network model is a measurable mapping from Ω_P into $N_{PT} \times \Omega_{PR}$ defined by $(\omega_{PT}, \omega_{PR}) \rightarrow (X_{PT}(\omega_{PT}), \omega_{PR})$, where N_{PT} is specified in the definition of the point process.

The positions of the primary transmitters corresponding to $(\omega_{PT}, \omega_{PR}) \in \Omega_{PT} \times \Omega_{PR}$ are easily known from ω_{PT} . For the primary receivers, the positions are obtained as follows. Consider binary cubes

$$K(n, z) := \prod_{i=1}^2 (z_i 2^{-n}, (z_i + 1) 2^{-n}] \text{ for all } n \in \mathbb{N} \text{ and } z \in \mathbb{Z}^2.$$

For each primary transmitter x_{PT} , there exists a unique smallest integer $n_0 = n_0(x_{PT})$ such that it is contained in a binary cube $K(n_0, z(n_0, x_{PT}))$ which contains no other primary transmitters. The relative position of x_{PT} 's receiver with respect to x_{PT} is then given by $\omega_{PR}(n_0, z(n_0, x_{PT}))$.

Let e_1, e_2 denote the unit vectors in \mathbb{R}^2 , then the translation $T_{e_i} : \mathbb{R}^2 \rightarrow \mathbb{R}^2$ ($i = 1, 2$) defined by $x \rightarrow x + e_i$ induces a shift transformation U_{e_i} on Ω_{PR} through the equation

$$(U_{e_i} \omega_{PR})(n, z) = \omega_{PR}(n, z - 2^n e_i), \text{ for } i = 1, 2.$$

Hence T_{e_i} also induces a shift transformation \tilde{T}_{e_i} on $\Omega_P = \Omega_{PT} \times \Omega_{PR}$ as follows:

$$\tilde{T}_{e_i}(\omega_P) = (S_{e_i} \omega_{PT}, U_{e_i} \omega_{PR}), \text{ for } i = 1, 2$$

where S_{e_i} is defined in (10). By using techniques similar to the proof of Boolean models [15, Proposition 2.8], we have that the m.p. dynamical system $(\Omega_P, \mathcal{F}_P, P_P, \tilde{T}_{e_1})$ is ergodic.

Since the transmission range r_p of secondary users is fixed, the probability space of the secondary network model is the probability space $(\Omega_S, \mathcal{F}_S, P_S)$ for the Poisson point process X_S of secondary users with density λ_S . It follows from the proof of Poisson point processes [15, Proposition 2.6] that the m.p. dynamical system $(\Omega_S, \mathcal{F}_S, P_S, S_{e_1})$ is mixing.

Since the primary network model is independent of the secondary network model, the sample space of the heterogeneous network model Ω can be written as the product of Ω_P and Ω_S , i.e., $\Omega = \Omega_P \times \Omega_S$. We equip Ω with product measure $P = P_P \times P_S$ and the usual product σ -algebra. Similarly, the translation T_{e_i} ($i = 1, 2$) induces a transformation \hat{T}_{e_i} on $\Omega = \Omega_P \times \Omega_S$, which is given by

$$\hat{T}_{e_i}(\omega) = (\tilde{T}_{e_i} \omega_P, S_{e_i} \omega_S).$$

Then it follows from [24, Theorem 2.6.1] that the product m.p. dynamical system $(\Omega, \mathcal{F}, P, \hat{T}_{e_1})$ is ergodic. Since the σ -algebra invariant under the transformation group $\{\hat{T}_z : z \in \mathbb{Z}^2\}$ is a subset of the σ -algebra invariant under the transformation

\hat{T}_{e_1} , we conclude that $\{\hat{T}_z : z \in \mathbb{Z}^2\}$ acts ergodically, i.e., the heterogeneous network model is ergodic. ■

Based on Lemma 1, we have the following lemma.

Lemma 2: The number of infinite connected component in $\mathcal{G}(\lambda_S, \lambda_{PT})$ is a constant a.s. and it can only take value from $\{0, 1, \infty\}$.

Proof of Lemma 2: Let K denote the (random) number of infinite connected components in $\mathcal{G}(\lambda_S, \lambda_{PT})$, then since for all $k \geq 0$, the event $\{K = k\}$ is invariant under the group of shift transformations, it follows from Lemma 1 and the definition of ergodicity that $\Pr\{K = k\} = 0$ or 1. Consequently, we have that K is a.s. constant. Then it suffices to exclude the possibility of $K \geq 2$. This is shown by contradiction, that is, if there exist $K \geq 2$ infinite connected components, then they can be linked together as one connected component wpp. The proof is inspired by the proof of Proposition 3.3 in [15] and a major difference is that here we need to consider the impact of the primary network on the connectivity of the secondary network.

Suppose that there are $K \geq 2$ infinite connected components a.s. If we remove all the secondary nodes centered inside a box $B = [-n, n]^2$, then the resulting secondary network should contain at least K unbounded components a.s. Let, for $A \subseteq \mathbb{R}^2$, $\mathcal{G}[A]$ denote the graph formed by secondary nodes in A . Given a box B and $\epsilon > 0$, consider the event $E(B, \epsilon)$ shown at the bottom of the page.

Partition the box B into squares with side length $a > 0$ and let $\mathcal{S}_a = \{S_1, \dots, S_N\}$ denote the collection of all the squares which are adjacent to the boundary of B . Clearly, for a box B and $\epsilon > 0$, we can find $a = a(B, \epsilon) \in (0, r_p/\sqrt{5})$ and $\eta = \eta(a) > 0$ such that for any point $x \notin B$ with $d(x, B) \leq r_p - \epsilon/2$, there exists a square $S = S(x) \in \mathcal{S}_a$ for which we have $\sup_{y \in S} d(x, y) \leq r_p - \eta$. This means that, if we center in each square of \mathcal{S}_a a secondary node and there are neither primary transmitters nor primary receivers within a bigger box $\bar{B} = [-n - \max\{r_I, R_I\}, n + \max\{r_I, R_I\}]^2$, then every infinite component U in $\mathcal{G}[B^c]$ with $d(U, B) \leq r_p - \epsilon$ is connected to some secondary node in \mathcal{S}_a .

Let $E(a, \eta)$ be the event that each square in \mathcal{S}_a contains at least one secondary node and $E(\bar{B})$ the event that there are neither primary transmitters nor primary receivers within \bar{B} . Since $E(a, \eta)$ depends on the configuration of secondary nodes inside the box B , $E(B, \epsilon)$ depends on the configuration of secondary nodes outside B and the configuration of primary nodes, based on the independence of the primary network and the secondary network, we have

$$\begin{aligned} \Pr(E(B, \epsilon) \cap E(a, \eta) \cap E(\bar{B})) \\ = \Pr(E(B, \epsilon))\Pr(E(a, \eta))\Pr(E(\bar{B})|E(B, \epsilon)). \end{aligned}$$

If $E(B, \epsilon)$, $E(a, \eta)$ and $E(\bar{B})$ all occur wpp., then there is only one infinite connected component⁹ wpp. By using arguments similar to the proof for [15, Proposition 3.3], we have that there exists a large enough box B and $\epsilon > 0$ such that $\Pr(E(B, \epsilon)) > 0$. Obviously, $\Pr(E(a, \eta)) > 0$. Moreover, it is easy to see that $\Pr(E(\bar{B})|E(B, \epsilon)) \geq \Pr(E(\bar{B})) > 0$. ■

Now we have that the number K of infinite connected components is equal to zero, one or infinity a.s. To exclude the possibility of $K = \infty$, we can use the proof of [15, Theorem 3.6] for Poisson Boolean models, which is based on several combinatorial results. The details are omitted.

C. Proof of Theorem 2

Proof of T2.1: To prove T2.1, it suffices to show that:

- (a) for any $\lambda_S \leq \lambda_c(r_p)$, the secondary network is not connected for any $\lambda_{PT} \geq 0$;
- (b) for any $\lambda_S > \lambda_c(r_p)$, there exists a $\lambda_{PT}^*(\lambda_S) > 0$ such that $\forall \lambda_{PT} \leq \lambda_{PT}^*(\lambda_S)$, the secondary network is connected.

From Section IV-A, we know that for a Poisson homogeneous ad hoc network with density λ and transmission range r , the necessary and sufficient condition for connectivity is $\lambda > \lambda_c(r)$. Since the existence of an infinite connected component in the secondary network implies the existence of an infinite connected component in the homogeneous ad hoc network with the same density and the same transmission range, by using a coupling argument, we conclude that when $\lambda_S \leq \lambda_c(r_p)$, there does not exist an infinite connected component a.s. in the secondary network for any $\lambda_{PT} \geq 0$. This proves part (a).

The basic idea of the proof of part (b) is to approximate the secondary network $\mathcal{G}(\lambda_S, \lambda_{PT})$ by a discrete dependent edge-percolation model on the grid. This discrete dependent edge-percolation model \mathcal{L} is constructed in a way such that the existence of an infinite connected component in \mathcal{L} implies the existence of an infinite connected component in $\mathcal{G}(\lambda_S, \lambda_{PT})$.

Construct the square lattice \mathcal{L} on \mathbb{R}^2 with side length d_e . Note that each site in \mathcal{L} is virtual and is not related to any node either in the secondary network or in the primary network. Next we specify the conditions for an edge being open in \mathcal{L} , which is the key to the mapping from $\mathcal{G}(\lambda_S, \lambda_{PT})$ to \mathcal{L} .

For each edge e in \mathcal{L} , let (x_e, y_e) denote the middle point of e . Then we introduce three random fields A_e , B_e and C_e , all associated with the edge e in \mathcal{L} , where $C_e = A_e B_e$ is the indicator of the edge e being open, A_e represents the condition (C1) of the distance between two users for the existence of a communication link in the secondary network and B_e represents the condition (C2) of the spectrum opportunity. Specifically, consider the Poisson Boolean model $\mathcal{B}(X_S, r_p/2, \lambda_S)$ where X_S

⁹Since $a < r_p/\sqrt{5}$, every secondary node in a square of \mathcal{S}_a is connected to those secondary nodes in the neighboring squares.

$$E(B, \epsilon) := \{d(U, B) \leq r_p - \epsilon \text{ for any infinite connected component } U \text{ in } \mathcal{G}[B^c]\}$$

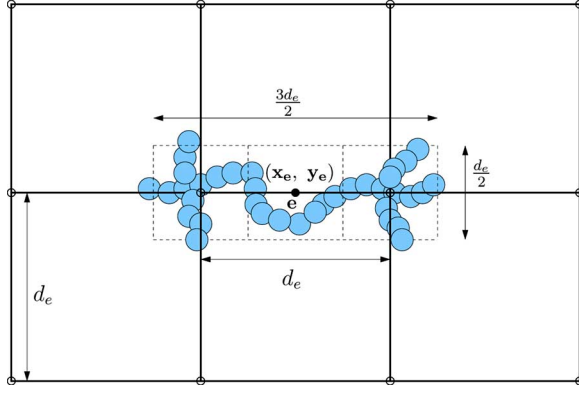


Fig. 11. Realization where $A_e = 1$ for the edge e (hollow points are sites in \mathcal{L} and solid segments are edges in \mathcal{L}).

is the Poisson point process generated by secondary users, then for a horizontal edge e , $A_e = 1$ if the following two events (illustrated in Fig. 11) are true:

- (i) there is an occupied L-R crossing of the rectangle $[x_e - 3d_e/4, x_e + 3d_e/4] \times [y_e - d_e/4, y_e + d_e/4]$ in $\mathcal{B}(X_S, r_p/2, \lambda_S)$;
- (ii) there are two occupied T-B crossings of the square $[x_e - 3d_e/4, x_e - d_e/4] \times [y_e - d_e/4, y_e + d_e/4]$ and the square $[x_e + d_e/4, x_e + 3d_e/4] \times [y_e - d_e/4, y_e + d_e/4]$ in $\mathcal{B}(X_S, r_p/2, \lambda_S)$; and $A_e = 0$ otherwise. For a vertical edge e , the definition of A_e is similar, where the horizontal and vertical coordinates are switched in the above two events.

Next, we define the random field B_e . For an edge e in \mathcal{L} , $B_e = 1$ if $A_e = 1$ and the following two events are true:

- (i) there is no primary transmitter within distance R_I of any secondary node of the three crossings in the definition of A_e ;
- (ii) there is no primary receiver within distance r_I of any secondary node of the three crossings in the definition of A_e ; and $B_e = 0$ otherwise. It follows from the definition of communication link in the secondary network (see Section II-B-I) that if $A_e = 1$ and $B_e = 1$, then the three crossings in $\mathcal{B}(X_S, r_p/2, \lambda_S)$ are also three crossings in $\mathcal{G}(\lambda_S, \lambda_{PT})$.

Let $C_e = A_e B_e$, then we claim that the edge e is open if $C_e = 1$ and e is closed if $C_e = 0$. We observe from Fig. 11 that whether the edge e is open is correlated with the states of the other edges. This model \mathcal{L} thus is a dependent edge-percolation model. Furthermore, as shown in Fig. 12, if there exists an infinite open connected component in \mathcal{L} , then those crossings associated with the edges in the infinite component in \mathcal{L} comprise an infinite connected component in $\mathcal{G}(\lambda_S, \lambda_{PT})$. As a consequence, by considering the uniqueness of the infinite connected component in $\mathcal{G}(\lambda_S, \lambda_{PT})$, we only need to prove the following lemma in order to show T2.1.

Lemma 3: Let $C(O)$ denote the open connected component containing the origin O in \mathcal{L} . Then given $\lambda_S > \lambda_c(r_p)$, $\exists D > 0$, $\lambda_{PT}^* > 0$ such that for $d_e = D$ and any $\lambda_{PT} \leq \lambda_{PT}^*$, we have

$$\Pr\{|C(O)| = \infty\} > 0$$

where $|C(O)|$ is the number of edges in $C(O)$.

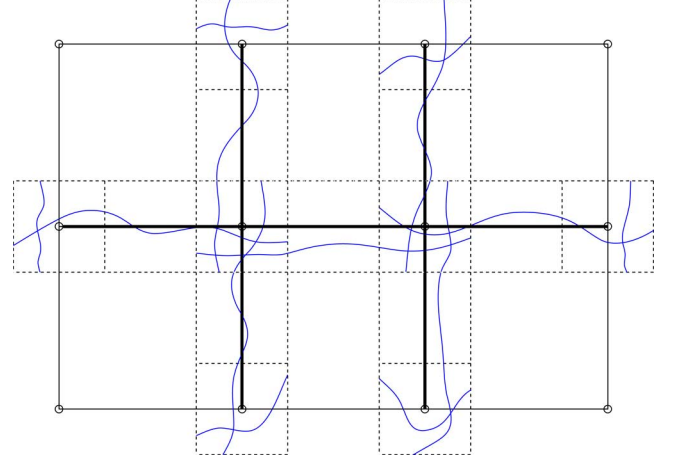


Fig. 12. Percolation in \mathcal{L} (thick segments are open edges in \mathcal{L} and thin segments are closed edges in \mathcal{L} and blue curves are those crossings associated with the open edges).

Proof of Lemma 3: For an arbitrary edge e in \mathcal{L} , let $q = \Pr\{C_e = 0\}$, then we have

$$q = \Pr\{(A_e = 0) \cup (B_e = 0)\} \leq \Pr\{A_e = 0\} + \Pr\{B_e = 0\}.$$

From the result on the crossing probabilities given in (9), we know that when $\lambda_S > \lambda_c(r_p)$,

$$\begin{aligned} \Pr\{A_e = 0\} &= \Pr\{\text{at least one crossing does not exist}\} \\ &\leq \left[1 - \sigma\left(\left(\frac{3d_e}{2}, \frac{d_e}{2}\right), \lambda_S, \text{L-R}\right)\right] \\ &\quad + \left[1 - \sigma\left(\left(\frac{d_e}{2}, \frac{d_e}{2}\right), \lambda_S, \text{T-B}\right)\right] \\ &\quad + \left[1 - \sigma\left(\left(\frac{d_e}{2}, \frac{d_e}{2}\right), \lambda_S, \text{T-B}\right)\right] \\ &\rightarrow 0 \text{ as } d \rightarrow \infty, \text{ i.e., } \lim_{d_e \rightarrow \infty} \Pr\{A_e = 0\} = 0. \end{aligned}$$

Thus, when $\lambda_S > \lambda_c(r_p)$, $\forall \epsilon > 0$, $\exists D > 0$ such that $\Pr\{A_e = 0\} < \frac{\epsilon}{3}$ for $d_e = D$.

Given $A_e = 1$, let S_{R_I} be the area of the region covered by the circles with radii R_I centered at those secondary nodes in the three crossings and S_{r_I} be the area of the region covered by the circles with radii r_I centered at those secondary nodes in the three crossings. Then we have

$$\begin{aligned} \Pr\{B_e = 0 \mid A_e = 1\} &= \Pr\{\exists \text{ some primary transmitter in } S_{R_I}\} \\ &\quad + \Pr\{\exists \text{ some primary receiver in } S_{r_I}\}. \end{aligned}$$

Since $S_{R_I} \leq \left(\frac{3d_e}{2} + 2R_I + r_p\right) \left(\frac{d_e}{2} + 2R_I + r_p\right)$ and $S_{r_I} \leq \left(\frac{3d_e}{2} + 2r_I + r_p\right) \left(\frac{d_e}{2} + 2r_I + r_p\right)$, it follows from the basic property of Poisson point processes that

$$\begin{aligned} \Pr\{B_e = 0 \mid A_e = 1\} &\leq 1 - \exp\left[-\lambda_{PT} \left(\frac{3d_e}{2} + 2R_I + r_p\right) \left(\frac{d_e}{2} + 2R_I + r_p\right)\right] \\ &\quad + 1 - \exp\left[-\lambda_{PT} \left(\frac{3d_e}{2} + 2r_I + r_p\right) \left(\frac{d_e}{2} + 2r_I + r_p\right)\right]. \end{aligned}$$

Obviously, $\lim_{\lambda_{PT} \rightarrow 0} \Pr\{B_e = 0 \mid A_e = 1\} = 0$ for fixed d_e . Thus if we choose $d_e = D$, then $\forall \epsilon > 0, \exists \lambda_{PT}^* > 0$ such that

$$\Pr\{B_e = 0 \mid A_e = 1\} < \frac{\epsilon}{3} \text{ for all } \lambda_{PT} \leq \lambda_{PT}^*.$$

It implies that when $d_e = D$, for all $\lambda_{PT} \leq \lambda_{PT}^*$

$$\begin{aligned} \Pr\{B_e = 0\} &= \Pr\{A_e = 0\} + \Pr\{B_e = 0 \mid A_e = 1\} \Pr\{A_e = 1\} \\ &\leq \Pr\{A_e = 0\} + \Pr\{B_e = 0 \mid A_e = 1\} \\ &< \frac{2\epsilon}{3}. \end{aligned}$$

Thus, for $d_e = D$ and all $\lambda_{PT} \leq \lambda_{PT}^*$, we have

$$q \leq \Pr\{A_e = 0\} + \Pr\{B_e = 0\} < \epsilon. \quad (11)$$

From Fig. 11, we can see that if $d_e \geq \max\{4R_I + 2r_p, 4r_I + 2r_p\}$, then the state of edge e is only correlated with its six adjacent edges and it is independent of other edges. In this case, by using the ‘‘Peierls argument’’ [25, Chapter 1], we can show that if the probability of an edge being closed $q < \left(\frac{11-2\sqrt{10}}{27}\right)^4$, then

$$\Pr\{|C(O)| = \infty\} > 0. \quad (12)$$

The proof of the above statement follows the one of [7, Theorem 3] except that the upper bound on the probability of n edges all being closed is given by the following fact.

Fact 1: [8, Proposition 1]: For any collection $\{e_i\}_{i=1}^n$ of n distinct edges in \mathcal{L} , we have

$$\Pr\{(C_1 = 0) \cap (C_2 = 0) \cap \dots \cap (C_n = 0)\} \leq q^{\frac{n}{4}}$$

where C_i is the indicator of e_i being closed, and q is the probability of an edge being closed.

Thus, by combining (12) with (11), we conclude that given $\lambda_S > \lambda_c(r_p)$, $\exists D > 0, \lambda_{PT}^* > 0$ such that for fixed $d_e = \max\{D, 4R_I + 2r_p, 4r_I + 2r_p\}$ and any $\lambda_{PT} \leq \lambda_{PT}^*$

$$\Pr\{|C(O)| = \infty\} > 0.$$

Notice that λ_{PT}^* depends on D which is chosen according to the crossing probability and is determined by λ_S . As a consequence, λ_{PT}^* is a function of λ_S , i.e., $\lambda_{PT}^* = \lambda_{PT}^*(\lambda_S)$. ■

Proof of T2.2: From the conditions for the existence of a communication link in the secondary network specified in Section II-B-I, we know that for every secondary node in an infinite connected component, there can exist neither any primary transmitter within distance R_I of it nor any primary receiver within distance r_I of it. In other words, every secondary node in an infinite connected component must be located outside all the circles centered at the primary transmitters and the primary receivers with radii R_I and r_I , respectively. Thus, if there is an infinite connected component in the secondary network, then an infinite vacant component must exist in the two Poisson Boolean models $\mathcal{B}(X_{PT}, R_{PT}, \lambda_{PT})$ and $\mathcal{B}(X_{PR}, R_{PR}, \lambda_{PT})$ driven by the primary transmitters and the primary receivers, respectively. Here R_{PT} and R_{PR} are

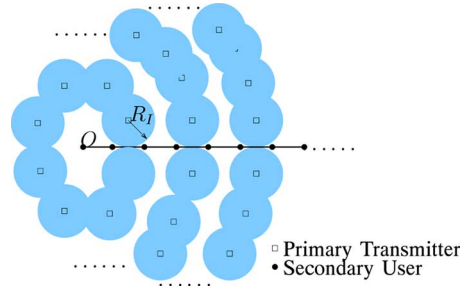


Fig. 13. Counterexample for choosing $R_{PT} = R_I$. All the secondary nodes in the infinite path are located outside those circles centered at the primary transmitters with radii R_I , which form a series of rings surrounding the origin O and there is no infinite vacant component in the Poisson Boolean model $\mathcal{B}(X_{PT}, R_I, \lambda_{PT})$ driven by the primary transmitters.

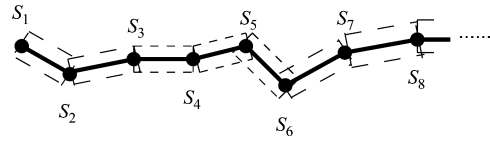


Fig. 14. Infinite path in the secondary network. The dashed segments form an inner bound on the infinite vacant component in the Poisson Boolean model driven by the primary receivers.

some appropriate radii which will be specified later. A natural choice for R_{PT} is R_I , but if we consider the counterexample given in Fig. 13, then we can clearly see that even if there is an infinite path in the secondary network, no infinite vacant component exists in the Poisson Boolean model $\mathcal{B}(X_{PT}, R_I, \lambda_{PT})$ driven by the primary transmitters. Similarly, counterexamples can be easily constructed for choosing $R_{PR} = r_I$.

Suppose there is an infinite connected component in the secondary network. Then we can find a sequence of secondary users $\{S_1, S_2, S_3, \dots\}$ such that they comprise an infinite path starting from S_1 (see Fig. 14).

Assume that S_i and S_{i+1} ($i \geq 1$) are two adjacent secondary nodes in the above infinite path. Notice that the distance $d_{i, i+1}$ between S_i and S_{i+1} satisfies $d_{i, i+1} \leq r_p < r_I$, where the second inequality $r_p < r_I$ follows from the fact that the minimum transmission power for successful reception is in general higher than the maximum allowable interference power.

As we know, all the primary receivers must be outside the two circles with radii r_I centered at S_i and S_{i+1} , respectively, as shown in Fig. 15. Given $\epsilon > 0$, consider the rectangle $[-\frac{d_{i, i+1}}{2}, \frac{d_{i, i+1}}{2}] \times [-\epsilon, \epsilon]$ between S_i and S_{i+1} . By a simple computation in geometry, we have that the minimum distance from all the primary receivers to the rectangle is $\sqrt{r_I^2 - \frac{r_p^2}{4}} - \epsilon$. As illustrated in Fig. 14, it implies that there exists an infinite vacant component in the Poisson Boolean model $\mathcal{B}\left(X_{PR}, \sqrt{r_I^2 - \frac{r_p^2}{4}} - \epsilon, \lambda_{PT}\right)$ driven by the primary receivers¹⁰. By recalling the known results in Section V-A-II, we thus conclude that for all $\epsilon > 0$

$$\lambda_{PT} \leq \left(2\sqrt{r_I^2 - \frac{r_p^2}{4}} - \epsilon\right)^{-2} \lambda_c(1).$$

¹⁰This technique used here can also be applied to the case when $r_p \geq r_I$, where only the minimum distance from all the primary receiver to the bar between S_i and S_{i+1} needs to be recomputed.

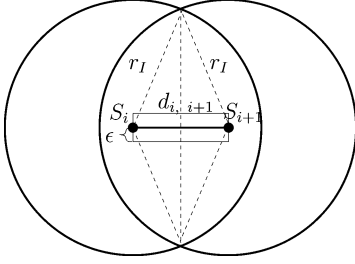


Fig. 15. One edge (S_i, S_{i+1}) in the infinite path.

Let $\epsilon \rightarrow 0$, then it yields

$$\lambda_{PT} \leq \frac{1}{4r_I^2 - r_p^2} \lambda_c(1).$$

The other term $\frac{1}{4R_I^2 - r_p^2} \lambda_c(1)$ in the upper bound is obtained by applying the same argument to the Poisson Boolean model driven by the primary transmitters.

D. Proof of Theorem 3

Consider the connected component C_A containing an arbitrarily chosen secondary user A . Assuming that $|C_A| > 1$, we construct a branching process as follows. Notice that if $|C_A| > 1$, then A must see an opportunity, i.e., $\mathbb{I}(A, r_I, \text{rx}) \cap \mathbb{I}(A, R_I, \text{tx})$ is true. Call A the initial point (or 0-th generation) of the branching process. Then the children of A (i.e., the first generation of the branching process) are secondary users which satisfy the following two conditions:

- i) it is within distance r_p of A , where r_p is the transmission range of secondary users;
- ii) there exist neither any primary receiver within distance r_I of the secondary user nor any primary transmitter within distance R_I of the secondary user.

The n -th ($n \geq 2$) generation of the branching process is obtained similarly and these children are connected to their parents in the $(n-1)$ -th generation of the branching process via bidirectional links. Obviously, all the secondary users in C_A are counted in the constructed branching process model. But some of them may probably be counted more than once, since we do not exclude the previous n generations (including generation 0) when we consider the n -th generation. Thus, this branching process gives us an upper bound on the number of secondary users in C_A . It follows that if the branching process does not grow to infinity wpp., then there does not exist an infinite connected component a.s. in $\mathcal{G}(\lambda_S, \lambda_{PT})$, due to the stationarity of the heterogeneous network model. Since the conditional average degree μ is the average number of offspring for every generation, the necessary condition follows immediately from the classic theorem for branching processes¹¹ [1, Theorem 2.1.1].

¹¹The lower bound on the conditional average degree can be improved by constructing a multi-type branching process. Specifically, when we consider the children of a secondary user, we categorize them into different types based on their distances from the secondary user. A similar construction has been used to obtain the lower bound on the critical density of Poisson Boolean models [1, Sec. 3.9]. This multi-type branching process is, however, difficult to analyze and requires substantial further investigation.

E. Proof of Theorem 4

From the construction of the dependent site-percolation model \mathcal{L} , we know that the existence of an infinite occupied component in \mathcal{L} implies the existence of an infinite connected component in $\mathcal{G}(\lambda_S, \lambda_{PT})$. Then in order to obtain a sufficient condition for the connectivity of the secondary network, it suffices to find a sufficient condition for the existence of an infinite occupied component in \mathcal{L} .

Let p be the probability that one site is occupied. Then based on the definition of the upper critical probability p_c of \mathcal{L} , we have that if $p > p_c$, an infinite occupied component containing the origin exists in \mathcal{L} wpp. It implies that if $p > p_c$, there exists an infinite connected component in the secondary network wpp. Since the event that there exists an infinite connected component in the secondary network is invariant under the group of shift transformations, it follows from the ergodicity of the heterogeneous network model (see Lemma 1) that if $p > p_c$, there exists an infinite connected component in the secondary network a.s.

Let $F_k(B_O)$ denote the event that there exist exactly k secondary users in the associated dashed square B_O of a site O and let $G_i(B_O)$ ($1 \leq i \leq k$) denote the event that the secondary user A_i sees an opportunity. Then based on the definition of occupied site in \mathcal{L} , we obtain a lower bound on p as follows:

$$\begin{aligned} p &= \sum_{k=1}^{\infty} \Pr\{F_k(B_O)\} \Pr\{\cup_{i=1}^k G_i(B_O)\} \\ &\geq \sum_{k=1}^{\infty} \Pr\{F_k(B_O)\} \Pr\{G_1(B_O)\} \\ &= \Pr\{G_1(B_O)\} \sum_{k=1}^{\infty} \Pr\{F_k(B_O)\} \\ &= [1 - \exp(-\lambda_S d_s^2)] \Pr\{\overline{\mathbb{I}(A_1, r_I, \text{rx})} \cap \overline{\mathbb{I}(A_1, R_I, \text{tx})}\} \\ &= \left[1 - \exp\left(-\frac{\lambda_S r_p^2}{8}\right)\right] \exp\{-\lambda_{PT} \pi [R_I^2 + r_I^2 - I(R_I, R_p, r_I)]\}. \end{aligned}$$

In the last step, $\Pr\{\overline{\mathbb{I}(A_1, r_I, \text{rx})} \cap \overline{\mathbb{I}(A_1, R_I, \text{tx})}\}$ has been obtained by setting the distance $d = 0$ in the expression for the probability of an unidirectional opportunity between two secondary users with distance d apart given in [16, Proposition 1].

VI. CONCLUSION AND FUTURE DIRECTIONS

We have studied the connectivity of a large-scale ad hoc heterogeneous wireless network in terms of the occurrence of the percolation phenomenon. We have introduced the concept of connectivity region to specify the dependency of connectivity on the density of the secondary users and the traffic load of the primary users. We have shown several basic properties of the connectivity region: the contiguity of the region, the monotonicity of the boundary and the uniqueness of the infinite connected component. We have analytically characterized the critical density of the secondary users and the critical density of the primary transmitters; they jointly specify the profile of the connectivity region. We have also established a necessary and a sufficient condition for connectivity, which give an outer and an

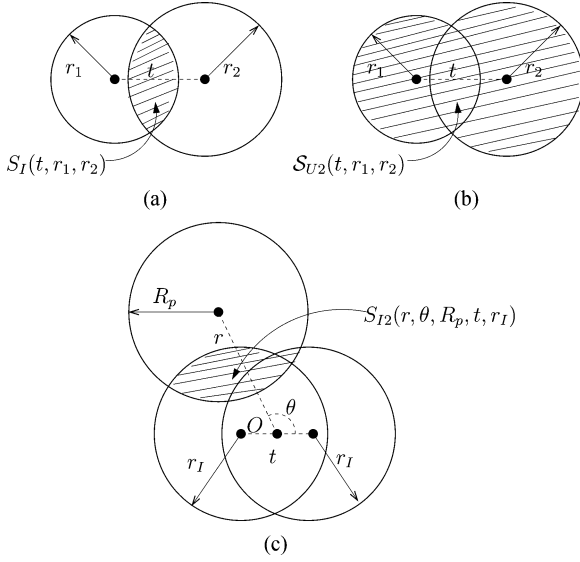


Fig. 16. Illustration of $S_I(t, r_1, r_2)$ (the common area of two circles with radii r_1 and r_2 and centers t apart), $S_{U2}(t, r_1, r_2)$ (the union area of two circles with radii r_1 and r_2 and centers t apart) and $S_{I2}(r, \theta, R_p, t, r_I)$ (the intersection area between one circle with radius R_p and the union of the two identical circles with radii r_I).

inner bound, respectively, on the connectivity region. Furthermore, by examining the impacts of the secondary users' transmission power on the connectivity region and on the conditional average degree of a secondary user, we have demonstrated the tradeoff between proximity and spectrum opportunity. In establishing these results, we have used techniques and theories in continuum percolation, including the coupling argument, ergodic theory, the discretization technique, and an approximation using a branching process.

To highlight the interaction between the primary users and the secondary users in a heterogeneous network, we have ignored the fading effect and the mutual interference between secondary users. If we take into account these factors, then the received signal to interference-plus-noise ratios at two secondary users will replace the distance between them in condition (C1) for the existence of a communication link between them. This will result in a random connection model (RCM) with correlated links, where the correlation between links is due to the mutual interference and condition (C2) on the presence of the bidirectional opportunity. There will be a tradeoff between proximity and mutual interference in addition to the tradeoff between proximity and opportunity and the combination of these two tradeoffs will complicate the characterization of the connectivity of the secondary network. But since the RCM shares several basic properties (e.g., ergodicity and existence of the critical density) with the Boolean model used in this paper, we expect that most of the results established here (e.g., connectivity region, critical densities) can be extended to the RCM.

APPENDIX A

EXPRESSION FOR CONDITIONAL AVERAGE DEGREE

An expression for the conditional average degree μ of a secondary user is presented in the following proposition.

Proposition 1: Let λ_S and λ_{PT} be the density of secondary users and primary transmitters. Let r_I and R_I be the interference range of the secondary and primary users and r_p and R_p the transmission range of the secondary and primary users. Let $g(\lambda_{PT}, r_p, r_I, R_p, R_I)$ denote the probability of a bidirectional opportunity between A and B conditioned on the event that A sees an opportunity. Then the conditional average degree μ of a secondary user is given by

$$\begin{aligned} \mu &= (\lambda_S \pi r_p^2) \cdot g(\lambda_{PT}, r_p, r_I, R_p, R_I) \\ &= \lambda_S \pi r_p^2 \int_0^{r_p} \frac{2t}{r_p^2} \exp \left\{ -\lambda_{PT} \left[\pi(r_I^2 + R_I^2 + I(R_I, R_p, r_I)) \right. \right. \\ &\quad \left. \left. - S_I(t, r_I, r_I) - S_I(t, R_I, R_I) \right. \right. \\ &\quad \left. \left. - \int \int_{S_{U2}(t, R_I, R_I)} \frac{S_{I2}(r, \theta, R_p, t, r_I)}{\pi R_p^2} r dr d\theta \right] \right\} dt \end{aligned} \quad (A1)$$

where

$$I(R_I, R_p, r_I) = 2 \int_0^{R_I} t \frac{S_I(t, R_p, r_I)}{\pi R_p^2} dt$$

$S_I(t, r_1, r_2)$ the common area of two circles with radii r_1 and r_2 and centers t apart [see Fig. 16(a)] and $S_{U2}(t, r_1, r_2)$ is the union of two circles with radii r_1 and r_2 and centers t apart [see Fig. 16(b)]. $S_{I2}(r, \theta, R_p, t, r_I)$ is the intersection area between one circle with radius R_p and the union of the two circles with both radii r_I [see Fig. 16(c)]. For $S_{I2}(r, \theta, R_p, t, r_I)$, the two identical circles are centered t apart and the other circle is centered at (r, θ) , where the middle point of the centers of the two identical circles is chosen to be the origin O .

Expressions for $I(R_I, R_p, r_I)$ and $S_I(t, r_1, r_2)$ can be obtained in explicit form, which can be found in [1, Appendix A]. The expression for $S_{I2}(r, \theta, R_p, t, r_I)$ depends on the expression for the common area of three circles which is tedious and is given in [26]. By applying the basic property of the exponential function to (A1), we can easily show that $g(\cdot)$ is a strictly decreasing function of λ_{PT} .

Proof: Let $F_k(A)$ denote the event that there exist exactly k neighbors of a secondary user A . We thus have the first equation shown at the bottom of the next page.

When $k = 0$, it is obvious that $\deg(A) = 0$. When $k > 0$, let B_i be a neighbor of A and $\mathbf{1}_{B_i}$ an indicator function for B_i such that $\mathbf{1}_{B_i} = 1$ if $\overline{\mathbb{I}(B_i, r_I, \text{rx})} \cap \overline{\mathbb{I}(B_i, R_I, \text{tx})}$ occurs and $\mathbf{1}_{B_i} = 0$ otherwise. Then by considering the statistical independence and equivalence of the k secondary users, we have the second equation shown at the bottom of the next page. It follows that we get (A2), as shown at the bottom of the next page.

According to the definition of spectrum opportunity, $\Pr\{\overline{\mathbb{I}(A, r_I, \text{rx})} \cap \overline{\mathbb{I}(A, R_I, \text{tx})}\}$ can be obtained by setting the distance $d = 0$ in the expression for the probability of a unidirectional opportunity between two secondary users with distance d apart given in Proposition 1 in [16].

$$\begin{aligned} \Pr\{\overline{\mathbb{I}(A, r_I, \text{rx})} \cap \overline{\mathbb{I}(A, R_I, \text{tx})}\} \\ = \exp[-\lambda_{PT} \pi (r_I^2 + R_I^2 - I(R_I, R_p, r_I))] \end{aligned} \quad (A3)$$

Next, we derive the expression for the probability of a bidirectional opportunity, i.e., $\Pr\{\overline{\mathbb{I}(B_1, r_I, \text{rx})} \cap \overline{\mathbb{I}(B_1, R_I, \text{tx})} \cap \overline{\mathbb{I}(A, r_I, \text{rx})} \cap \overline{\mathbb{I}(A, R_I, \text{tx})}\}$, which depends on the location of B_1 only through its distance to A . Since B_1 is uniformly distributed within distance r_p of A , the density function of the distance t between B_1 and A is given by $\frac{2t}{r_p^2}$ for $0 \leq t \leq r_p$. In this case, the probability of a bidirectional opportunity can be written as shown in (A4), also shown at the bottom of the page, where the integrand can be written as shown in (A5), at the bottom of the page.

Next, we compute the two probabilities in (A5) one by one. Since the primary receivers admit a Poisson point process with density λ_{PT} , we have

$$\Pr\{\overline{\mathbb{I}(B_1, r_I, \text{rx})} \cap \overline{\mathbb{I}(A, r_I, \text{rx})} \mid d(B_1, A) = t\} = \exp[-\lambda_{PT}(2\pi r_I^2 - S_I(t, r_I, r_I))] \quad (\text{A6})$$

where $S_I(t, r_I, r_I)$ is the common area of two circles with both radii r_I and centers t apart [see Fig. 16(a)].

$$\begin{aligned} \mu &= \mathbb{E}[\deg(A) \mid \overline{\mathbb{I}(A, r_I, \text{rx})} \cap \overline{\mathbb{I}(A, R_I, \text{tx})}] \\ &= \mathbb{E}_k[\mathbb{E}[\deg(A) \mid \overline{\mathbb{I}(A, r_I, \text{rx})} \cap \overline{\mathbb{I}(A, R_I, \text{tx})} \cap F_k(A)]] \\ &= \sum_{k=0}^{\infty} e^{-\lambda_S \pi r_p^2} \frac{(\lambda_S \pi r_p^2)^k}{k!} \mathbb{E}[\deg(A) \mid \overline{\mathbb{I}(A, r_I, \text{rx})} \cap \overline{\mathbb{I}(A, R_I, \text{tx})} \cap F_k(A)] \end{aligned}$$

$$\begin{aligned} &\mathbb{E}[\deg(A) \mid \overline{\mathbb{I}(A, r_I, \text{rx})} \cap \overline{\mathbb{I}(A, R_I, \text{tx})} \cap F_k(A)] \\ &= \sum_{i=1}^k \mathbb{E}[\mathbf{1}_{Bi} \mid \overline{\mathbb{I}(A, r_I, \text{rx})} \cap \overline{\mathbb{I}(A, R_I, \text{tx})}] \\ &= k \mathbb{E}[\mathbf{1}_{B1} \mid \overline{\mathbb{I}(A, r_I, \text{rx})} \cap \overline{\mathbb{I}(A, R_I, \text{tx})}] \\ &= k \Pr\{\overline{\mathbb{I}(B_1, r_I, \text{rx})} \cap \overline{\mathbb{I}(B_1, R_I, \text{tx})} \mid \overline{\mathbb{I}(A, r_I, \text{rx})} \cap \overline{\mathbb{I}(A, R_I, \text{tx})}\} \\ &= k \frac{\Pr\{\overline{\mathbb{I}(B_1, r_I, \text{rx})} \cap \overline{\mathbb{I}(B_1, R_I, \text{tx})} \cap \overline{\mathbb{I}(A, r_I, \text{rx})} \cap \overline{\mathbb{I}(A, R_I, \text{tx})}\}}{\Pr\{\overline{\mathbb{I}(A, r_I, \text{rx})} \cap \overline{\mathbb{I}(A, R_I, \text{tx})}\}} \end{aligned}$$

$$\mu = \lambda_S \pi r_p^2 \frac{\Pr\{\overline{\mathbb{I}(B_1, r_I, \text{rx})} \cap \overline{\mathbb{I}(B_1, R_I, \text{tx})} \cap \overline{\mathbb{I}(A, r_I, \text{rx})} \cap \overline{\mathbb{I}(A, R_I, \text{tx})}\}}{\Pr\{\overline{\mathbb{I}(A, r_I, \text{rx})} \cap \overline{\mathbb{I}(A, R_I, \text{tx})}\}} \quad (\text{A2})$$

$$\begin{aligned} &\Pr\{\overline{\mathbb{I}(B_1, r_I, \text{rx})} \cap \overline{\mathbb{I}(B_1, R_I, \text{tx})} \cap \overline{\mathbb{I}(A, r_I, \text{rx})} \cap \overline{\mathbb{I}(A, R_I, \text{tx})}\} \\ &= \int_0^{r_p} \frac{2t}{r_p^2} \Pr\{\overline{\mathbb{I}(B_1, r_I, \text{rx})} \cap \overline{\mathbb{I}(B_1, R_I, \text{tx})} \cap \overline{\mathbb{I}(A, r_I, \text{rx})} \cap \overline{\mathbb{I}(A, R_I, \text{tx})} \mid d(B_1, A) = t\} dt \end{aligned} \quad (\text{A4})$$

$$\begin{aligned} &\Pr\{\overline{\mathbb{I}(B_1, r_I, \text{rx})} \cap \overline{\mathbb{I}(B_1, R_I, \text{tx})} \cap \overline{\mathbb{I}(A, r_I, \text{rx})} \cap \overline{\mathbb{I}(A, R_I, \text{tx})} \mid d(B_1, A) = t\} \\ &= \Pr\{\overline{\mathbb{I}(B_1, R_I, \text{tx})} \cap \overline{\mathbb{I}(A, R_I, \text{tx})} \mid \overline{\mathbb{I}(B_1, r_I, \text{rx})} \cap \overline{\mathbb{I}(A, r_I, \text{rx})} \cap d(B_1, A) = t\} \\ &\quad \cdot \Pr\{\overline{\mathbb{I}(B_1, r_I, \text{rx})} \cap \overline{\mathbb{I}(A, r_I, \text{rx})} \mid d(B_1, A) = t\} \end{aligned} \quad (\text{A5})$$

$$\begin{aligned}
& \Pr\{\overline{\mathbb{I}(B_1, R_I, \text{tx})} \cap \overline{\mathbb{I}(A, R_I, \text{tx})} \mid \overline{\mathbb{I}(B_1, r_I, \text{rx})} \cap \overline{\mathbb{I}(A, r_I, \text{rx})} \cap d(B_1, A) = t\} \\
&= \exp \left\{ -\lambda_{PT} \int \int_{S_{U2}(t, R_I, R_I)} \left[1 - \frac{S_{I2}(r, \theta, R_p, t, r_I)}{\pi R_p^2} r dr d\theta \right] \right\} \\
&= \exp \left\{ -\lambda_{PT} \left[2\pi R_I^2 - S_I(t, R_I, R_I) - \int \int_{S_{U2}(t, R_I, R_I)} \frac{S_{I2}(r, \theta, R_p, t, r_I)}{\pi R_p^2} r dr d\theta \right] \right\} \tag{A7}
\end{aligned}$$

$$\mu = \lambda_S \pi r_p^2 \int_0^{r_p} \frac{2t}{r_p^2} \exp \left[-\lambda_{PT} \left(\pi r_I^2 - 2r_I^2 \arccos \left(\frac{t}{2r_I} \right) + t \sqrt{r_I^2 - \frac{t^2}{4}} \right) \right] dt.$$

$$\begin{aligned}
\mu &\leq \lambda_S \pi r_p^2 \int_0^{r_p} \frac{2t}{r_p^2} \exp \left\{ -\lambda_{PT} \left[\pi r_I^2 - 2r_I^2 \left(\frac{\pi}{2} - \frac{t}{2r_I} \right) + t \sqrt{r_I^2 - \frac{t^2}{4}} \right] \right\} dt \\
&\leq \lambda_S \pi r_p^2 \int_0^{r_p} \frac{2t}{r_p^2} \exp(-\lambda_{PT} t r_I) dt \\
&= \lambda_S \pi \left(\frac{2}{\lambda_{PT}^2 r_I^2} - \frac{2}{\lambda_{PT}^2 r_I^2} \exp(-\lambda_{PT} \beta r_I^2) - \frac{2\beta}{\lambda_{PT}} \exp(-\lambda_{PT} \beta r_I^2) \right) \\
&\leq \frac{2\lambda_S \pi}{\lambda_{PT}^2} (r_I)^{-2}
\end{aligned}$$

$$\begin{aligned}
& \Pr\{\overline{\mathbb{I}(B_1, r_I, \text{rx})} \cap \overline{\mathbb{I}(B_1, R_I, \text{tx})} \cap \overline{\mathbb{I}(A, r_I, \text{rx})} \cap \overline{\mathbb{I}(A, R_I, \text{tx})} \mid d(B_1, A) = t\} \\
&= \exp \left\{ -\lambda_{PT} \left[2\pi(r_I^2 + R_I^2) - S_I(t, r_I, r_I) - S_I(t, R_I, R_I) \right. \right. \\
&\quad \left. \left. - \int \int_{S_{U2}(t, R_I, R_I)} \frac{S_{I2}(r, \theta, R_p, t, r_I)}{\pi R_p^2} r dr d\theta \right] \right\} \tag{A8}
\end{aligned}$$

Let X_{PT} denote the Poisson point process formed by primary transmitters. If we remove from X_{PT} primary transmitters whose receivers are within distance r_I of B_1 or A , then it follows from the Coloring Theorem [17, Chapter 5] that all the remaining primary transmitters form another Poisson point process with density $\lambda_{PT} \left[1 - \frac{S_{I2}(r, \theta, R_p, t, r_I)}{\pi R_p^2} \right]$, where $S_{I2}(r, \theta, R_p, t, r_I)$ is the area of the circle with radius R_p and centered at (r, θ) intersecting the two circles both with radii r_I and centers t apart [see Fig. 16(c)]. We thus have (A7), at the top of the page, where $S_{U2}(t, R_I, R_I)$ is the union of two circles with both radii R_I and centers t apart [see Fig. 16(b)].

Substitute (A6), (A7) into (A5), we have (A8), as shown at the top of the page. The expression for the conditional average degree μ thus follows by plugging (A8) into (A4) and then (A3), (A4) into (A2).

APPENDIX B PROOF OF COROLLARY 3

From [1, Appendix A] and Figs. 16(b) and (c), we know that when $r_I \geq R_p + R_I$

$$\begin{aligned}
I(R_I, R_p, r_I) &= R_I^2 \tag{B1} \\
\int \int_{S_{U2}(t, R_I, R_I)} \frac{S_{I2}(r, \theta, R_p, t, r_I)}{\pi R_p^2} r dr d\theta &= S_{U2}(t, R_I, R_I) \\
&= 2\pi R_I^2 - S_I(t, R_I, R_I). \tag{B2}
\end{aligned}$$

Substitute (B1) and (B2) into (A1), we have

$$\mu = \lambda_S \pi r_p^2 \int_0^{r_p} \frac{2t}{r_p^2} \exp[-\lambda_{PT}(\pi r_I^2 - S_I(t, r_I, r_I))] dt. \tag{B3}$$

Plugging the expression for $S_I(t, r_I, r_I)$ [1, Appendix A] into (B3) yields the equation shown at the top of the previous page.

By applying the inequality $\arccos(x) \leq \frac{\pi}{2} - x$ for $0 \leq x \leq 1$, we have the equation at the top of the previous page, where we have assumed that $r_p = \beta r_I$ ($0 < \beta < 1$) under the disk signal propagation and interference model. Since $r_I \propto (p_{tx})^{1/\alpha}$, we arrive at Corollary 3.

ACKNOWLEDGMENT

The authors would like to thank D. Cheowtirakul for his help in generating several simulation results.

REFERENCES

- [1] J. Mitola, III and G. Maguire, Jr, "Cognitive radio: Making software radios more personal," *IEEE Personal Commun.*, vol. 6, pp. 13–18, Aug. 1999.
- [2] Q. Zhao and B. M. Sadler, "A survey of dynamic spectrum access," *IEEE Signal Process. Mag.*, vol. 24, no. 3, pp. 79–89, May 2007.
- [3] P. Gupta and P. R. Kumar, "Critical power for asymptotic connectivity in wireless networks," in *Stochastic Analysis, Control, Optimization and Applications: A Volume in Honor of W. H. Fleming*, W. M. McEneaney, G. Yin, and Q. Zhang, Eds., 1998, pp. 547–566.
- [4] T. K. Philips, S. S. Panwar, and A. N. Tantawi, "Connectivity properties of a packet radio network model," *IEEE Trans. Inf. Theory*, vol. 35, no. 5, pp. 1044–1047, Sep. 1989.
- [5] C. Bettstetter, "On the minimum node degree and connectivity of a wireless multihop network," in *Proc. ACM Int. Symp. Mobile Ad Hoc Networking and Computing (MobiHoc)*, Jun. 9–11, 2002, pp. 80–91.
- [6] J. Ni and S. A. G. Chandler, "Connectivity properties of a random radio network," *IEEE Proc. Commun.*, vol. 141, no. 4, pp. 289–296, Aug. 1994.
- [7] O. Dousse, F. Baccelli, and P. Thiran, "Impact of interference on connectivity in ad hoc networks," *IEEE/ACM Trans. Netw.*, vol. 13, no. 2, pp. 425–436, Apr. 2005.
- [8] O. Dousse, M. Franceschetti, N. Macris, R. Meester, and P. Thiran, "Percolation in the signal to interference ratio graph," *J. Appl. Probabil.*, vol. 43, no. 2, pp. 552–562, 2006.
- [9] Z. N. Kong and E. M. Yeh, "Connectivity and latency in large-scale wireless networks with unreliable links," in *Proc. IEEE Conf. Computer Communications (Infocom)*, Apr. 15–17, 2008.
- [10] Z. N. Kong and E. M. Yeh, "Connectivity, percolation and information dissemination in large-scale wireless networks with dynamic links," in *IEEE Transactions on Information Theory*, Feb. 2009 [Online]. Available: <http://arxiv.org/abs/0902.4449>
- [11] O. Léveque and I. E. Telatar, "Information-theoretic upper bounds on the capacity of large extended ad hoc wireless networks," *IEEE Trans. Inf. Theory*, vol. 51, no. 3, pp. 858–865, Mar. 2005.
- [12] M. Franceschetti and R. Meester, *Random Networks for Communication: From Statistical Physics to Information Systems*. New York: Cambridge University Press, 2007.
- [13] W. Ren, Q. Zhao, and A. Swami, "On the connectivity and multihop delay of ad hoc cognitive radio networks," *IEEE J. Select. Areas Commun. (Special Issue on Cognitive Radio Networking and Communications)*, vol. 29, no. 4, pp. 805–818, Apr. 2011.
- [14] W. Ren, Q. Zhao, and A. Swami, Temporal Traffic Dynamics Improve the Connectivity of Ad Hoc Cognitive Radio Networks Tech. Rep. (TR-10-02) 2010 [Online]. Available: <http://www.ece.ucdavis.edu/~qzhao/TR-10-02.pdf>
- [15] R. Meester and R. Roy, *Continuum Percolation*. New York: Cambridge University Press, 1996.
- [16] W. Ren, Q. Zhao, and A. Swami, "Power control in cognitive radio networks: How to cross a multi-lane highway," *IEEE J. Select. Areas Commun. (Special Issue on Stochastic Geometry and Random Graphs for Wireless Networks)*, vol. 27, no. 7, pp. 1283–1296, Sep. 2009.
- [17] J. F. C. Kingman, *Poisson Processes*. Oxford, U.K.: Clarendon Press, 1993.
- [18] Q. Zhao, "Spectrum opportunity and interference constraint in opportunistic spectrum access," in *Proc. IEEE Int. Conf. Acoustics, Speech and Signal Processing (ICASSP)*, Apr. 15–20, 2007, pp. (III)605–(III)608.
- [19] V. Ramasubramanian, R. Chandra, and D. Mosse, "Providing a bidirectional abstraction for unidirectional adhoc networks," in *Proc. IEEE Conf. Computer Communications (INFOCOM)*, Jun. 23–27, 2002, pp. (III)1258–(III)1267.
- [20] R. Meester and R. Roy, "Uniqueness of unbounded occupied and vacant components in Boolean models," *Annal. Appl. Probabil.*, vol. 4, no. 3, pp. 933–951, 1994.
- [21] J. Quintanilla, S. Torquato, and R. M. Ziff, "Efficient measurement of the percolation threshold for fully penetrable discs," *J. Phys. A*, vol. 33, pp. L399–L407, 2000.
- [22] Z. N. Kong and E. M. Yeh, "Characterization of the critical density for percolation in random geometric graphs," in *Proc. IEEE Int. Symp. Information Theory (ISIT)*, Jun. 24–29, 2007, pp. 151–155.
- [23] D. J. Daley and D. Vere-Jones, *An Introduction to the Theory of Point Processes*. New York: Springer-Verlag, 1988.
- [24] K. Petersen, *Ergodic Theory*. New York: Cambridge University Press, 1989.
- [25] G. R. Grimmett, *Percolation*, 2nd ed. New York: Springer, 1999.
- [26] M. P. Fewell, Area of Common Overlap of Three Circles, Technical Note Oct. 2006 [Online]. Available: <http://handle.dtic.mil/100.2/ADA463920>

Wei Ren (S'07) received the B.Sc. and M.Sc. degrees in electrical engineering from Peking University, Peking, China, in 2003 and 2006, respectively, and the Ph.D. degree in electrical and computer engineering from the University of California (UC), Davis, in 2011.

His current research interests are in cognitive radio systems and wireless networks. He is also interested in algorithmic theory and optimization techniques for communications.

Qing Zhao (S'97–M'02–SM'08) received the Ph.D. degree in electrical engineering in 2001 from Cornell University, Ithaca, NY.

In August 2004, she joined the Department of Electrical and Computer Engineering at the University of California (UC), Davis, where she is currently a Professor. Prior to that, she was a Communications System Engineer with Aware, Inc., Bedford, MA, and a Postdoctoral Research Associate with Cornell University. Her research interests are in the general area of stochastic optimization and decision theory in dynamic systems and communication networks.

Dr. Zhao received the 2010 IEEE Signal Processing Magazine Best Paper Award and the 2000 Young Author Best Paper Award from IEEE Signal Processing Society. She holds the title of UC Davis Chancellor's Fellow and received the 2008 Outstanding Junior Faculty Award from the UC Davis College of Engineering. She is also a coauthor of two papers that received student paper awards at IEEE ICASSP 2006 and IEEE Asilomar Conference 2006. She served as an Associate Editor of the IEEE TRANSACTIONS ON SIGNAL PROCESSING from 2006 to 2009 and is currently an elected member of the IEEE Signal Processing Society SP-COM Technical Committee.

Ananthram Swami (F'08) received the B.Tech. degree from the Indian Institute of Technology (IIT), Bombay, the M.S. degree from Rice University, Houston, TX, and the Ph.D. degree from the University of Southern California (USC), Los Angeles, all in electrical engineering.

He has held positions with Unocal Corporation, USC, CS-3 and Malgudi Systems. He was a Statistical Consultant to the California Lottery, developed HOSAT, a MATLAB-based toolbox for non-Gaussian signal processing and has held visiting faculty positions at INP, Toulouse, France. He is the ST for Network Science at the U.S. Army Research Laboratory. He is co-editor of the book *Wireless Sensor Networks: Signal Processing & Communications Perspectives* (New York: Wiley, 2007).

Dr. Swami is a member of the IEEE Signal Processing Society's Technical Committee on Sensor Array and Multichannel systems and serves on the Senior Editorial Board of the IEEE JOURNAL ON SELECTED TOPICS IN SIGNAL PROCESSING. He was a tutorial speaker on Networking Cognitive Radios for Dynamic Spectrum Access at IEEE ICC 2010, co-chair of IEEE SPAWC'10, and has served on the IEEE SPS BoG.

Epileptic Seizures from Abnormal Networks: Why Some Seizures Defy Predictability

William S. Anderson, Feraz Azhar, Pawel Kudela,
Gregory K. Bergey, and Piotr J. Franaszczuk

Epilepsy Research, 99(3), 202–213 (2012)



Epileptic seizures from abnormal networks: Why some seizures defy predictability

William S. Anderson^{a,*}, Feraz Azhar^{b,1}, Pawel Kudela^{c,2},
Gregory K. Bergey^{c,3}, Piotr J. Franaszczuk^{d,e,4}

^a The Johns Hopkins University School of Medicine, Department of Neurosurgery, Meyer 5-109E, 600 North Wolfe Street, Baltimore, MD 21287, USA

^b The Johns Hopkins University School of Medicine, Department of Neurosurgery, Meyer 5-157, 600 North Wolfe Street, Baltimore, MD 21287, USA

^c The Johns Hopkins University School of Medicine, Department of Neurology, Meyer 2-147, 600 North Wolfe Street, Baltimore, MD 21287, USA

^d The Johns Hopkins University School of Medicine, Department of Neurology, USA

^e U.S. Army Research Laboratory, Human Research and Engineering Directorate, Aberdeen Proving Ground, 2800 Powder Mill Road, Adelphi, MD 20783, USA

Received 15 June 2011; received in revised form 19 October 2011; accepted 18 November 2011

Available online 12 December 2011

KEYWORDS

Computational simulation;
Neural network model;
Seizure prediction;
Seizure generation

Summary Seizure prediction has proven to be difficult in clinically realistic environments. Is it possible that fluctuations in cortical firing could influence the onset of seizures in an ictal zone? To test this, we have now used neural network simulations in a computational model of cortex having a total of 65,536 neurons with intercellular wiring patterned after histological data. A spatially distributed Poisson driven background input representing the activity of neighboring cortex affected 1% of the neurons. Gamma distributions were fit to the interbursting phase intervals, a non-parametric test for randomness was applied, and a dynamical systems analysis was performed to search for period-1 orbits in the intervals. The non-parametric analysis suggests that intervals are being drawn at random from their underlying joint distribution and the dynamical systems analysis is consistent with a nondeterministic dynamical interpretation of the generation of bursting phases. These results imply that in a region of cortex with abnormal

* Corresponding author. Tel.: +1 443 287 4561; fax: +1 443 287 6423.

E-mail addresses: wanders5@jhmi.edu, wanderso68@gmail.com (W.S. Anderson), fazhar1@jhmi.edu (F. Azhar), pkudela@jhmi.edu (P. Kudela), gbergey@jhmi.edu (G.K. Bergey), pfranaszczuk@gmail.com (P.J. Franaszczuk).

¹ Tel.: +1 443 287 4561; fax: +1 443 287 6423.

² Tel.: +1 443 287 8295; fax: +1 410 955 0751.

³ Tel.: +1 410 955 7338; fax: +1 410 502 2507.

⁴ Tel.: +1 410 278 8003; fax: +1 410 278 8828.

connectivity analogous to a seizure focus, it is possible to initiate seizure activity with fluctuations of input from the surrounding cortical regions. These findings suggest one possibility for ictal generation from abnormal focal epileptic networks. This mechanism additionally could help explain the difficulty in predicting partial seizures in some patients.

© 2011 Elsevier B.V. All rights reserved.

Introduction

Epileptic seizures are brief, episodic phenomena. Partial seizures, the most common seizure type, arise from focal brain regions (e.g. temporal, parietal) (Niedermeyer, 2005).

While in some instances there may be an identifiable cause for the seizures (e.g. tumor, cavernoma, hippocampal sclerosis), in other instances no clear pathology is determined. The hallmark of an epileptic seizure is the involvement of local or regional neural networks; repetitive firing of a single neuron does not produce symptoms without this network involvement. What causes the interictal to ictal transition? A typical partial seizure lasts less than 2 min plus any postictal state (Afra et al., 2008). Therefore, even if a patient has very frequent seizures, the majority of time is spent in the interictal state. While some seizures can be provoked or are more likely to occur under certain situations (e.g. sleep deprivation, photic stimulation), the majority of seizures appear to occur spontaneously without known association with definable influences.

There has been considerable interest in seizure prediction in recent years. Obviously if seizures could be reliably predicted, then the option for targeted therapy exists (e.g. stimulation), or at least the patient could remove themselves from potentially dangerous situations. The underlying hypothesis for seizure prediction is that there are changes in cerebral dynamics that may precede the clinical seizure by minutes to hours (reviewed in Sackellares, 2008). These changes may be local (i.e. near the seizure focus) or remote. These changes are not apparent with visual analysis of the EEG, even with intracranial recording arrays. Some groups have identified high frequency activity that may signal the onset of neocortical partial seizures, but this is an example of improved seizure detection, not prediction (Worrell et al., 2004, 2008; Bragin et al., 2010). Reliable seizure prediction has been challenging and even the most enthusiastic proponents of the prediction hypothesis acknowledge the difficulties with current algorithms (Lehnertz et al., 2007; Mormann et al., 2007; Andrzejak et al., 2009).

Seizure prediction may be difficult due to rapid bistable state changes at the time of ictal onset in the neocortex (Suffczynski et al., 2006; Lopes da Silva et al., 2003).

The mechanisms underlying a bistable state change may be quite different between primary generalized (e.g. absence) and partial epileptic seizures. A bistable state change may be more applicable to these primary generalized seizures which have abrupt bilateral cerebral onset. In this paper, a different possible mechanism is presented under which seizure prediction would be difficult in some patients with focal seizure onset.

Knowing, as we do, that partial seizures are a reflection of transient abnormal regional network activity, it is reasonable to postulate that these seizures in at least some (perhaps many) patients result from abnormal neural

networks (e.g. the epileptogenic zone) (Jacobs et al., 2000). We describe here a model of the epileptogenic zone where the epileptic focus is represented by an abnormal neural network that has very slightly altered connectivity so that, while seizures only occur infrequently, they can be triggered by normal background activity originating from outside the epileptogenic zone. This background activity could be influenced by various physiologic factors (e.g. sleep), but nevertheless this background activity would not result in seizure activity in the non-epileptic brain. This does not discount the possibility that some changes in neural network synchrony may occur in the "normal" brain since the cumulative lifetime incidence of unprovoked seizures approaches 4% (Hauser et al., 1993). Often these seizures are provoked (e.g. medications and alcohol) and less than half of these patients have recurrent seizures. The lifetime cumulative risk of developing epilepsy only ranges from 1.4% to 3.3% (Krumholz et al., 2007; Berg and Shinnar, 1991). In this model, however, where normal background activity, occasionally or rarely produces a seizure in abnormal regional networks, seizure prediction would be difficult since detectable preictal changes would not be present; the first changes would in fact be seizure initiation.

Epileptic networks in neocortex or the hippocampus show anatomical changes compared to normal tissue (Jacobs et al., 2000; Sallin et al., 1995). These changes can progress with time (Sallin et al., 1995; Arellano et al., 2004). This could result in neuronal networks more amenable to seizure generation (electrical or clinical) over large regional areas. There is a complex interrelationship, much of it not well understood, between neurons which are dysfunctional and the neural networks which can promote seizures (Leussis and Heinrichs, 2007; Kumar et al., 2007; Swann et al., 2007). Even in the non-epileptic brain, excitatory connections predominate with 80–90% of synapses being excitatory (Braitenberg and Schüz, 1998).

With neuronal network simulations it is possible to control, study, and quickly change the various influences on network behavior. Recently, we presented the results of computational simulation studies examining the role of external field stimulation on ongoing bursting activity in a neural network (Anderson et al., 2007, 2009). The cortical model used in these studies consists of discrete single compartment Hodgkin–Huxley type cells which are spatially arranged in a realistic fashion having both a layered and columnar structure. Since neural network behavior reflects the aggregate output of the component neurons, single compartment neurons allow greater computational efficiency and the ability to model larger networks in studies of network behavior. Arrangements of connected simulated neurons in this manner can demonstrate spontaneous bursting phases and have spatial characteristics similar to seizures recorded from humans (Anderson et al., 2007, 2009; Kudela et al., 1997, 2003a,b, 2005; Franaszczuk et al.,

2003). We now present the results of a similar neuronal network model with random surrounding background inputs. The goal of this study was to investigate the statistical structure of the resulting bursting network activity to seek the presence or absence of predictable patterns in the behavior.

Materials and methods

Computational model format

The individual neurons in this neocortical model were represented by single compartment neurons bearing synaptic connections from the rest of the network, and embedded with a fixed set of ionic conductances. The membrane potential varies as:

$$C_m \frac{dV}{dt} = I_{\text{syn}} - I_{\text{Na}} - I_{\text{Ca}} - I_K - I_{K(\text{Ca})} - I_A - I_L.$$

The individual currents include the input synaptic current I_{syn} , inward sodium and calcium currents I_{Na} and I_{Ca} , outward potassium currents including a delayed rectifier current I_K , a calcium dependent potassium current $I_{K(\text{Ca})}$, a transient potassium current I_A , and a leakage current I_L (Av-Ron, 1994). The minicolumns used in the simulation consist of 16 cells with intrinsic intracolumnar wiring, adapted from the neocortical work of Douglas and Martin (2004), as described more fully in previous studies (Anderson et al., 2007, 2009). This is both for its ease of implementation computationally and for its experimental support in somatosensory and visual cortex (Douglas and Martin, 2004). The geometry imposed on a computational model becomes relevant when studying any spatially dependent effects on the resultant spreading activity. The minicolumns in this simulation have a 25 μm center-to-center spacing in a square lattice repeating structure. The total number of cells examined was 65,536, representing a simulated cortical surface area of 1.6 mm \times 1.6 mm. Fig. 1 demonstrates a schematic of the intracolumnar excitatory cell connections and the organization of the minicolumns in planar space as well as snapshots of the resultant activity in the layer II/III pyramidal cell component during model bursting activity. The model connectivity and synaptic currents are described further in the [Supplementary material](#).

The base connection pattern studied in this report is representative of one that can produce robust bursting as previously studied (Anderson et al., 2007). The numbers of extra-columnar connections formed by each cell class are presented in [Supplementary Table 1](#). There are seven cell classes modeled: four classes of excitatory cells including layer II/III pyramidal cells, layer IV stellate cells, layer V pyramidal cells, and layer VI pyramidal cells, and three classes of interneurons including basket cells, double bouquet cells, and chandelier cells. Most of the model changes described in the described studies involve alterations in connection numbers between layer II/III pyramidal cells, one of the known robust horizontal connections systems in the cortex supporting epileptic propagation (Telfeian and Connors, 1998). The base connection for this system, $N_{2/3:2/3} = 178$, is defined as the number of layer II/III pyramidal cells a given layer II/III pyramidal cell contacts in its axonal distribution.

The model in general illustrates consistent bursting behavior, with epochs of spontaneous bursting onset and cessation given a random background input of Poisson based charge injection to 1% of the cells in the model. This is an effort to treat the underlying cortical activity as input from neighboring cortex, with the model itself treated as the epileptic focus given its ability to produce network bursting epochs. The synaptic input used for the background was not periodic in nature. Average rates for these Poisson distributions are described in "Activity changes with mean background frequency" section and Fig. 2. The synaptic activations used for the

background inputs were the same used in the cell to cell connections, and followed the same rise and decay times appropriate for postsynaptic potentials.

The pseudo-random number generator used for the application of the noise pulses was a linear congruential generator implemented with the C-function *drand48*, with an intrinsic period of 281×10^{12} . For a 30s simulation and 10^{-5} s time-step, this function was called 1.966×10^9 times for 1% of the cells undergoing background input. The period length for the pseudo-random generator is 143,000 times larger than this number.

Statistics and analysis

The interbursting phase intervals in the model were fit with a gamma distribution (Suffczynski et al., 2005, 2006). The functional form of this distribution $f(\dots)$ is given by

$$f(\Delta\tau) = (\beta^\alpha \Gamma(\alpha))^{-1} \Delta\tau^{\alpha-1} \exp\left(\frac{-\Delta\tau}{\beta}\right),$$

where $\Delta\tau$ is the interbursting phase interval, α is the shape parameter, β is the scale parameter, and $\Gamma(\dots)$ represents the gamma function. Parameters were estimated using the MATLAB function *gamfit* which returns maximum likelihood estimates and 95% confidence intervals for the shape and scale parameters. A non-parametric test of randomness was used to attempt to establish whether intervals were being drawn at random from their underlying joint distribution. This was based on the circular definition of the lag-1 serial correlation coefficient (Wald and Wolfowitz, 1943). *p*-Values were computed under the assumption of asymptotic normality of the test statistic.

A method for the detection of unstable periodic orbits (of period-1) in successive interbursting phase intervals was applied (So et al., 1996, 1997). A period-1 orbit is a fixed point of the nonlinear map expressing the evolution of the state of a system, iterated a single time (Guckenheimer and Holmes, 1983). Intervals were embedded in a two dimensional state space and 10^4 sets of transformed intervals were obtained after randomization. Dimensional reduction was instituted using circles of radius 9.4ms centered along the diagonal of the state space (Le Van Quyen et al., 1997). One hundred surrogates were produced to test the significance of peaks which appeared along this diagonal. The surrogates were generated using the amplitude adjusted Fourier transform algorithm (Theiler et al., 1992). This shuffles the original sequence of interbursting phase intervals, maintaining the original amplitude distribution of the data while approximately matching its Fourier power spectrum.

Results

A total of 1600s of discontinuous 20- and 30-s data segments were obtained, holding the base connectivity of the layer II/III pyramidal cells to layer II/III pyramidal cells at $N_{2/3:2/3} = 178$. Only the random number seed supplied to the background input generator was varied for each of these runs. Additionally, five continuous segments of data were obtained with the base connectivity set at $N_{2/3:2/3} = 172$ of lengths 320s, 250s and $N_{2/3:2/3} = 178$ of lengths 195s, 140s, and 208s. These data were used for the dynamical systems analysis presented below. In addition to these data, sixteen 20-s runs were obtained with the model while varying the mean background input frequency at the base level of connectivity. Five 20-s runs were obtained at the base connectivity while varying the temporal pattern of the background input, and ten 20-s runs were obtained with a fixed

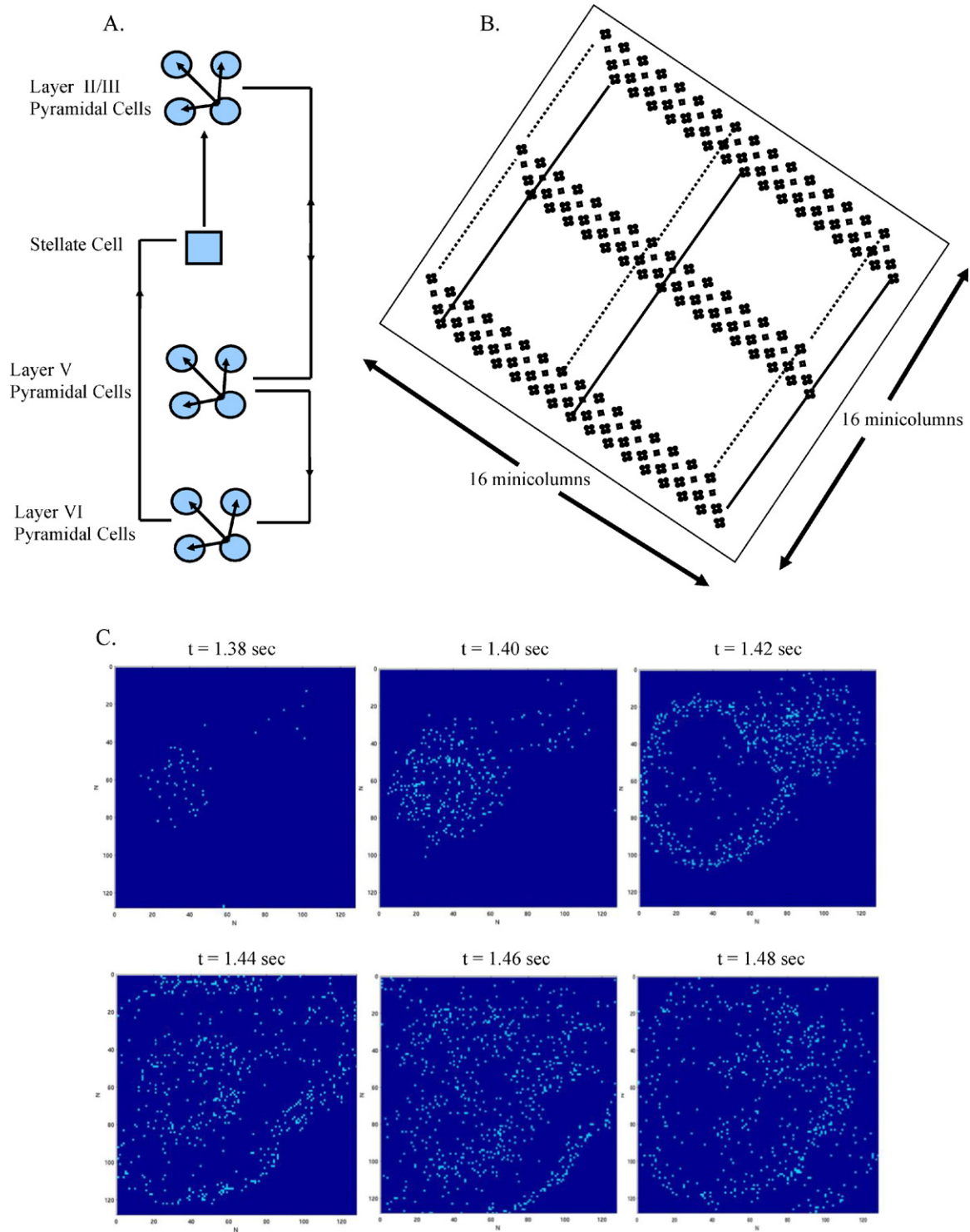


Figure 1 (A) Representative connectivity of the excitatory cellular component in a given modeled minicolumn, wiring after (Douglas and Martin, 2004). (B) Three dimensional arrangement of the 16×16 array of minicolumns in space. (C) Representative snapshots of evolving activity over 0.02s in the layer II/III pyramidal cell component. Each pixel represents one cell, color coded proportionally to the number of action potentials fired in bins of 1/100 of a second.

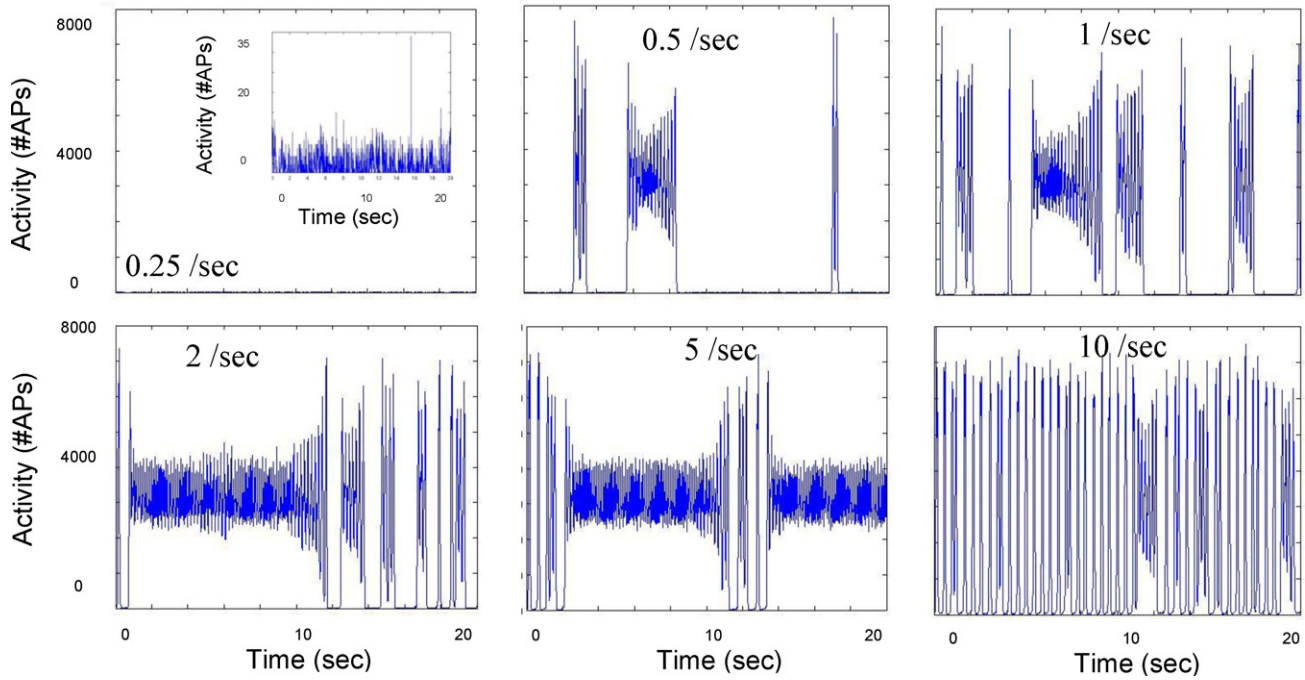


Figure 2 Network activity produced by sequential increases in the mean frequency of the applied background activity (background synaptic input provided to a fixed 1% set of the modeled cells, summed layer II/III pyramidal cell action potentials in 10 ms bins). The model exhibits a transition from episodic bursting to a very regular bursting behavior driven by the background input.

sequence of background input while varying the overall layer II/III to layer II/III connectivity ($N_{2/3:2/3}$).

Activity changes with mean background frequency

These experiments were performed with the base connectivity of the layer II/III pyramidal cell system set at the base value of $N_{2/3:2/3} = 178$. If the mean frequency of the applied background synaptic input is varied from 0.25/s up to 10/s, several patterns of activity become apparent (Fig. 2). At 0.25/s, only the low level set of activity produced with action potential production by the background input is observed, at the cells where the input takes place. This plot essentially demonstrates the Poisson-based random network activity between the bursting phases. At 0.5/s, sporadic bursting activity transmitted to the network as a whole can be observed, with long quiescent epochs. As the applied mean background frequency is further increased, longer and longer periods of constant bursting activity can be observed up to 5/s. After this, a second activity transition is observed, in which the activity changes from continuous bursting into short periods of very large amplitude bursting (in terms of numbers of active neurons) punctuated by brief periods of quiescence. At 10/s it appears to dominate the activity. This implies a saturation mechanism in this class of connected network, which comes into play after a critical percentage of cells are excited per time step. This saturation behavior is again an intrinsic property of the fixed network being probed. Additionally, these studies imply that seizure onset can be driven by neighboring cortical activity, albeit regular patterns that might not be typical of random background input activity utilized here.

Network activity altered with input pattern changes

Within the context of this model, it is possible to change the random pattern of connectivity between represented cells, and still keep the total number of connections between the various cell classes constant. By varying the random number seed supplied to the generator distributing the connections, different patterns of activity can be demonstrated, even with the same application of underlying cortical activity applied to the same cells. Examples of the changes in activity are presented in Fig. 3A. The pattern produced ranges from almost constant bursting throughout the 20s examined, to brief periods of on and off bursting. Similarly, the connectional pattern can be held constant along with the cells in which the background activity is applied, while varying the random number seed responsible for producing the order in which background pulses are injected into the cells. This produces similar alterations in network activity demonstrated in Fig. 3B, and can include several time scales of bursting epochs. These studies imply a rich dynamics of stochastic behavior in randomly connected neural networks receiving temporally uncorrelated background input, and again point toward difficulties in predicting when the bursting phases might begin.

Network activity is very sensitive to numbers of excitatory connections

Finally, changing the numbers of connections in this network model can produce substantial alterations in network behavior. Fig. 4 presents a sequence of plots of the layer

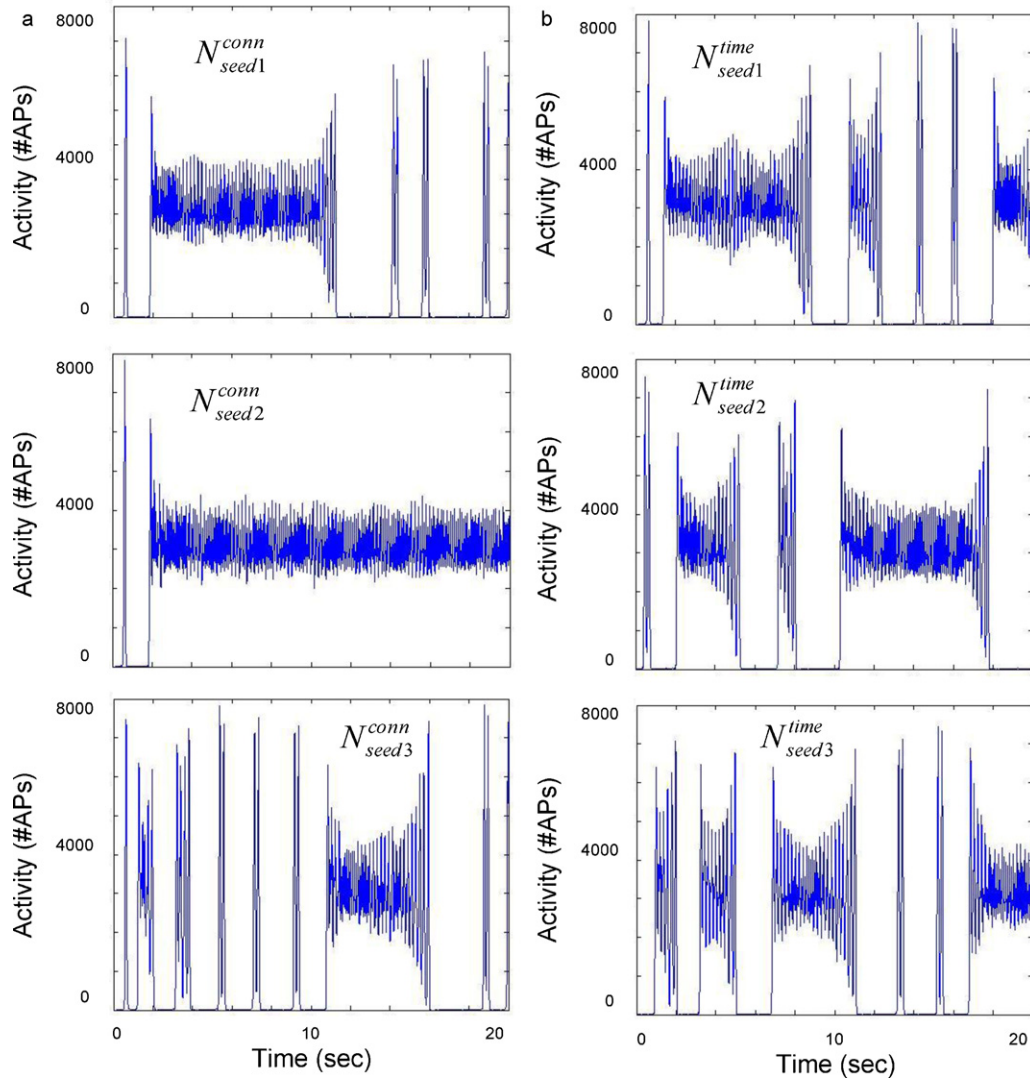


Figure 3 (A) Network activity induced by varying the random connectivity pattern between cell classes (different connectivity seeds, N_{seed}^{conn} , for the random number generator). Numbers of action potentials in layer II/III pyramidal cell component, 10 ms time bins. (B) Network activity induced by varying the random time sequence of background synaptic input, N_{seed}^{time} . In these experiments, all cellular connections remain fixed, and the identity of the cells undergoing background synaptic input remain fixed.

II/III pyramidal cell activity (time-binned action potential numbers) for various degrees of extracolumnar connectivity between the layer II/III pyramidal cells. The base activity explored in this manuscript is shown in the plot with total number of connections held at $N_{2/3:2/3} = 178$ (between extra-minicolumnar layer II/III pyramidal cells). A rapid reduction in network bursting is shown for a connection number reduced below this, and almost continuous activity is shown for connection numbers above this. Fig. 3A and B data were obtained with the connectivity set at $N_{2/3:2/3} = 178$. Only the random pattern of connectivity is varied in Fig. 3A and the time sequence of background input in Fig. 3B. These studies were performed in the context of a constant average level of surrounding background input, and imply the importance of internal connectivity in the development of uncontrolled bursting of the network.

Statistical analysis of interburst phase intervals

The statistical properties of the interburst phase intervals for five continuous runs of the model at connectivities of $N_{2/3:2/3} = 178$ and 172 were analyzed. This was motivated from a dynamical systems perspective, where periodicity in sequential intervals was sought for. Fig. 5A displays a histogram approximation to the probability density function for interbursting phase intervals for Continuous Run 1, which consisted of 163 intervals collected from a 320 s run of the simulation. Fig. 5D displays the same histogram approximation for Continuous Run 4, with a total of 58 intervals collected from a 140 s run of the simulation. Gamma distributions were used to fit these densities (Fig. 5A and D (blue traces)) (see “Materials and methods” section; Suffczynski et al., 2005, 2006). In the case of Continuous Run 1

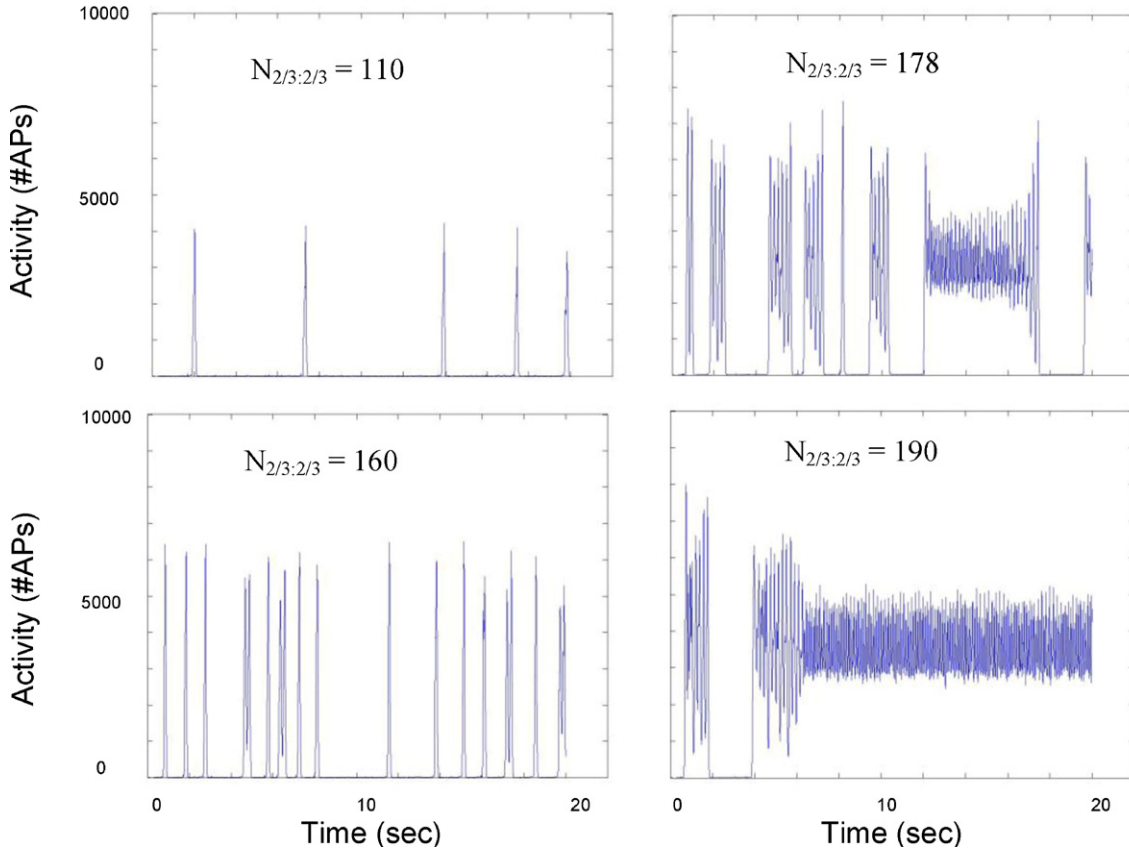


Figure 4 Changing the absolute connectivity in the layer II/III pyramidal cell component (number of layer II/III pyramidal cells contacted by a given layer II/III pyramidal cell, $N_{2/3:2/3}$) in the model produces alterations in the network bursting behavior. At very low absolute connectivity ($N_{2/3:2/3} = 110$) network bursting is brief and isolated, while at higher levels of absolute connectivity periods of constant bursting can be observed.

(Fig. 5A) we found $\alpha = 6.09$ (4.61–8.04) for the shape parameter of the distribution, and $\beta = 0.26$ (0.20–0.35) for the scale parameter (95% confidence intervals in parentheses). For Continuous Run 4 (Fig. 5D), the corresponding values were $\alpha = 7.14$ (5.00–10.19), and $\beta = 0.23$ (0.16–0.33) (similar results were obtained for 3 further continuous runs and one discontinuous run – results not shown). In accord with the interpretation of Suffczynski et al. (2005, 2006), the fact that the shape parameter α was larger than one in all runs, suggests the potential presence of periodicity in the generation of bursting epochs. To probe this link further, additional statistical tests were performed as described below.

To ascertain how intervals were being drawn from their underlying joint distribution, we applied a non-parametric test of randomness to the interbursting phase intervals (Wald and Wolfowitz, 1943). In the case of Continuous Run 1, we found that one cannot reject the null hypothesis of randomness at the 5% significance level (p -value 0.93). For Continuous Run 4, we found the same conclusion at the 5% significance level (p -value 0.29). This conclusion was also borne out for the remaining three continuous runs.

A method for the detection of unstable periodic orbits (of period-1) was then applied to test for the presence of deterministic dynamics in the generation of interbursting phase intervals (So et al., 1996, 1997). This method institutes a transformation of the sequence of intervals such

that the transformed sequence is clustered around locations of potential periodic orbits. One can compare the peaks of these clusters to those generated by surrogate data (Theiler et al., 1992), to compute the statistical significance of the peaks, and thereby ascertain the potential existence of periodic orbits in the data. Fig. 5C and F shows the peaks of the clusters were not significantly greater than those generated by surrogate data (see caption), and so no period-1 orbits were detected for either run (nor for the remaining three continuous runs), at the limit of detection in the current data set.

Discussion

Our results demonstrate that while holding the mean properties of the network stable (mean connectivity numbers, mean background excitation rates), very rich and strikingly different dynamics are produced by changing the model details. Epileptogenic behavior can be created in these networks, as described above, by changes in the random pattern of connectivity, while holding fixed the intrinsic active or passive membrane properties in the constituent neurons. Such changes in connectivity could be analogous to changes in underlying connectivity that might occur following cerebral insults, or repetitive seizures. Similar modeling

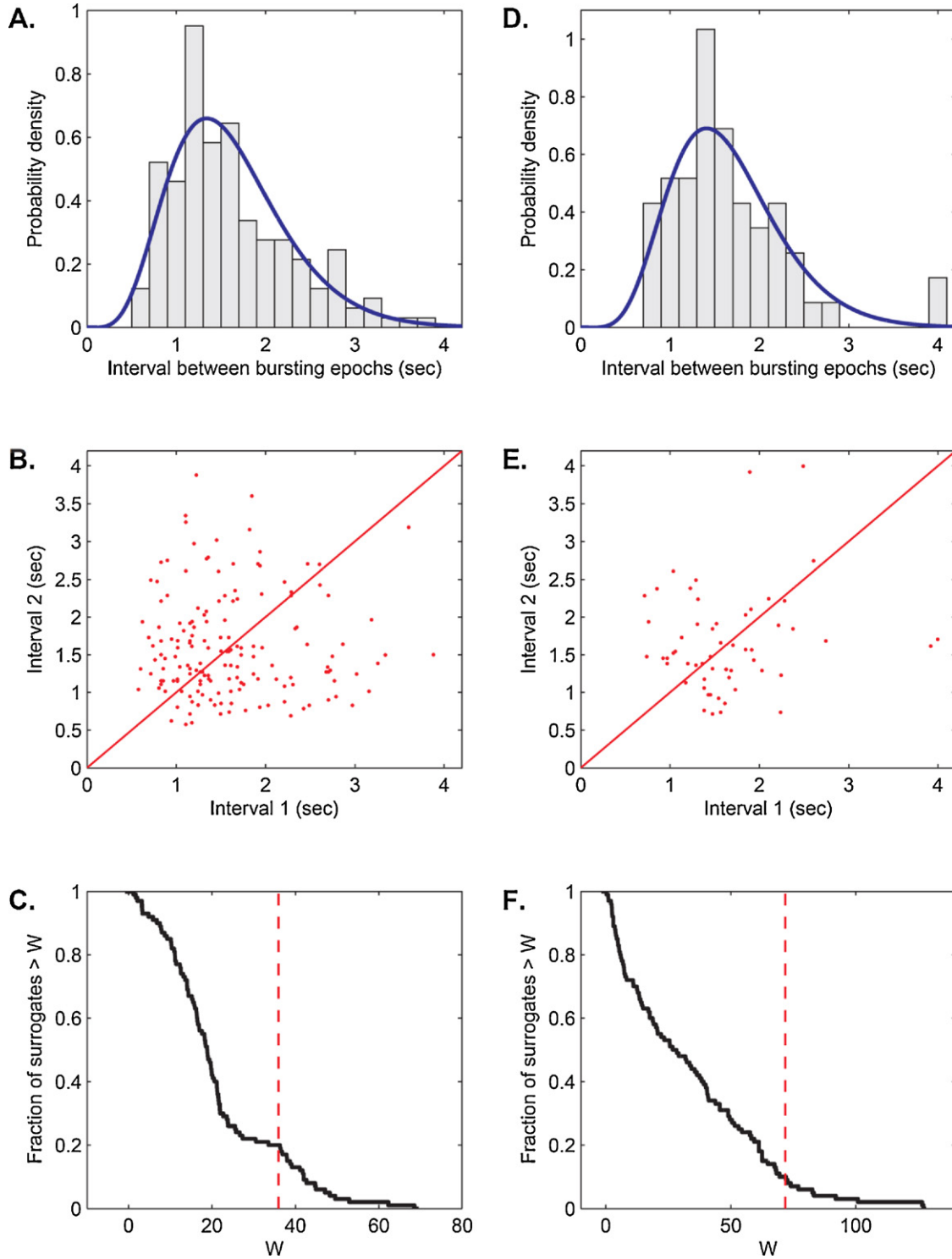


Figure 5 Statistical analysis of the interbursting phase intervals. (A and D) Interval histograms are fit with gamma distributions revealing shape parameters $\alpha > 1$ in the case of Continuous Run 1 (A) and Continuous Run 4 (D). (B and E) Two dimensional delay embedding of sequential intervals (Spearman correlation coefficients are not significantly different from zero) for Continuous Runs 1 and 4, respectively. (C and F) Testing the significance of potential period-1 orbits detected through a dynamical analysis of the sequence of points displayed in (B) and (E), respectively. The y-axis represents the fraction of surrogate (shuffled, see "Materials and methods" section) sequences with a maximal deviation from the mean surrogate result of greater than W (So et al., 1996, 1997) (10^4 random matrices and 10^2 surrogates were used). The horizontal dotted (red) line displays the maximal deviation for the simulation data. Since there exists a significant fraction of surrogates with deviation greater than that for the simulation data (for both C – 20% and F – 10%), neither plot displays convincing evidence of the existence of a period-1 orbit. (For interpretation of the references to color in this figure legend, the reader is referred to the web version of this article.)

work has been performed on changes in connectivity with resultant epileptic effects in hippocampus (Morgan and Soltesz, 2008; Dyhrfeld-Johnsen et al., 2007). In our results, local increases or decreases in connectivity in the model may alter the network in a similar manner (a tempting comparison which must be tempered by our lack of understanding of the functional significance of new or absent connections, see Sallin et al., 1995; Dinocourt et al., 2003; Marco et al., 1997; Dudek and Sutula, 2007; Maglósky, 2010). In the model above, the external background activity can be held constant or changed in a variety of time-frequency manipulations. Various simulations can be created where seizures occur rarely or very frequently.

Similarly, human epileptic seizures are episodic, transient events. Whether epileptic seizures are random events is not clear, but times of ictal onset can behave as a random process (Suffczynski et al., 2006). In some patients there are no identifiable contributing factors, in other patients such conditions such as sleep deprivation may increase the chance of seizure occurrence and in still other patients seizures can be provoked by specific stimuli (e.g. hyperventilation, intermittent photic stimulation; Lu et al., 2008; Vinogradova et al., 2009; Kaplan et al., 2009). In these examples there may be resulting alterations of background activity within and outside the epileptogenic zone (not evident from the EEG) that make it more likely that a seizure may arise from the existing focal epileptogenic network. While these influences might create a state where seizures are more likely to occur, this facilitatory state should be distinguished from the presence (or absence) of a preictal state in unprovoked seizures.

Random behavior of network

One interesting aspect of this model is its ability to demonstrate both spontaneous periods of bursting activity as well as self-termination of the bursting. As illustrated in Figs. 2–5, these periods of bursting can be quite variable in their length. Throughout the bursting and quiescent phases, the distributed background activity is constantly active, affecting approximately 1% of the total cells. We believe this model may represent the type of network behavior described by Lopes da Silva et al. (2003), in which epileptic activity within the network cannot be predicted from the interictal state. The non-parametric and nonlinear dynamical analyses described in the “Results” section support this, however inference from this is somewhat limited given the finite size of the data set, the small region of modeled area, and the gamma distribution fits described earlier.

This obviously may not be true of all types of clinical and model epileptiform behavior. For example Osorio et al. (2009, 2010) show that pharmacoresistant seizures tend to cluster, and may have an inherent self-triggering capacity. This might make a prediction algorithm possible to implement in a useful fashion. Others (Suffczynski et al., 2005, 2006), however demonstrate that seizure onset can be described in both experimental and model data as a random walk process, with possibly a deterministic mechanism ascribed to seizure termination. The random onset nature would (in a bistable network with Poisson transitions) be difficult to predict.

In the case of our model the underlying fluctuations leading to seizure onset are the random background activity we have imposed on the network. The properties of the network connectivity then support the bursting frequency observed (Anderson et al., 2007). These types of grossly synchronized bursting states in the context of a neural network have been studied extensively by Kowalski et al. (1992). They are truly pathological in the sense that they would block or confound any information flow through this network. It is also a network-generated state, and can be stopped by eliminating synaptic transmission (Kowalski et al., 1992; Keefer et al., 2001; Rhoades and Gross, 1994).

Many limiting cases of the gamma distribution have physical interpretations that might make it easier to understand spiking data from cortex when used for fitting (Papoulis, 1984; Suffczynski et al., 2005). When the shape parameter, α , in the gamma distribution is an integer, the distribution is known as an Erlang distribution and represents the probability distribution of the waiting time until the α th event from a sampled Poisson process with characteristic time β . This might be comparable to the distribution of the number of spiking or underlying synaptic events required to trigger the network bursting behavior. One could envision trying to extract the integer value of α from either computational or experimental data. Similarly, the Maxwell–Boltzmann distribution can be related to the gamma distribution under certain restrictions on the gamma scale and shape parameters, implying the possibility of extracting almost thermal-like or statistical mechanical interpretations of the network activity (Hegyi, 1996).

Limitations of the model

Our plots demonstrate gross summed numbers of time-binned action potentials in the model for given neuron classes. The interictal activity is a random Poisson input to 1% of the cells in the model and is demonstrated in the plots, particularly in Fig. 2, Panel 1, inset. We chose to impose this random interictal behavior on the model to demonstrate that these fluctuations can produce very coherent synchronous oscillations in an unpredictable fashion. However, the surrounding input might not have to be completely random to bring about the same effect. Epilepsies involving specific stimuli might require a coherent surrounding input to give rise to the seizure (Lu et al., 2008; Vinogradova et al., 2009; Kaplan et al., 2009). A more realistic technique would be to treat the interictal background as a log-normal process which does have some support in the literature (see Farkhoori et al., 2009; Waters and Helmchen, 2006). Newer recording methods from invasively monitored epilepsy patients might help determine what patterns of background activity are causative (Truccolo et al., 2011; van Gompel et al., 2008). Our intent was to represent the resting interictal cellular activity as fundamentally sparse with a random component. This was most easily implemented as a low frequency Poisson process.

It is possible to view the single synaptic input (driven by the background source) as representing several weaker but synchronized inputs. This represents a limitation to this modeling approach, a limitation that in large degree could be corrected with more elaborate multicompartment and

synaptic representations of the cells to make the multiple weaker inputs more independent. Additionally in this limited data set, we are unable to say much about time epochs larger than several hundreds of seconds (our largest continuous simulation being 320s). This is clearly a limitation in this technique and future computational work, including efforts in our laboratory will explore longer time intervals of ictal and interictal behavior, and possibly push the detection limit for predictable activity lower (or detect it more accurately). Models such as this particular rigid crystalline arrangement of neurons with many fixed cellular properties in some sense have less inherent “randomness” than real neocortex. This work was primarily meant to spark interest in a possible mechanism for the difficulties inherent in seizure prediction, but by no means should it be interpreted too literally.

Implications for seizure prediction

The purpose of the model presented here is not to judge the effectiveness of seizure prediction, but rather to present a plausible, alternative hypothesis for partial seizure occurrence that could explain situations where seizure prediction may not be possible. Indeed, it is conceptually attractive to consider that, just as partial seizures may result from various pathologies and mechanisms, that some partial seizures may not be reliably predicted. It is beyond the scope of this discussion to address the various methods being used in attempts to predict epileptic seizures. It is always important to differentiate true seizure prediction from improved seizure detection. Other commentaries and reviews address these methods and include discussions of the challenges and frustrations to date in routine seizure prediction even with intracranial electrodes (Estellar et al., 2001; Litt and Echauz, 2002; Sackellares et al., 2006; Haas et al., 2007; Osorio et al., 2001).

This study focused on the interval to the time of the next “seizure” or busting phase in the model. Our interest was in the occurrences of the transitions from the quiescent or background state into the pathologic state, since that is what most seizure prediction algorithms are optimized for. There is fairly strong evidence, certainly in the case of complex partial seizures in temporal lobe epilepsy, that the length of clinical seizures can be fairly uniform in a given patient (see for instance Afra et al., 2008). The time interval durations of the seizures themselves may also prove to have to predictive guidance as well and should be explored in the future in modeling efforts. This may be more useful in the case of neocortical epilepsy with its rapid spread and possible involvement of larger regions of tissue.

Additionally, this model can incorporate incremental changes in connectivity in the epileptogenic zone, changes that could be a model for progressive epileptogenesis (e.g. sprouting). This type of model also provides data that is comparable to clinical data from epilepsy patients. The simulated network activity is taken from a small region of modeled cortex comparable in size to the surface area under a typical subdural grid electrode, and makes comparisons between modeling efforts and clinical data easy to perform (Anderson et al., 2007, 2009; Kudela et al., 1997, 2003a,b; Franaszczuk et al., 2005). Indeed the major advantage of

neural network modeling is the ability to simultaneously monitor activity in all of the network neurons under given experimental conditions, something not possible with biological systems, even with sophisticated recording arrays.

Conflict of interest

None of the authors has any conflict of interest to disclose.

Acknowledgements

WSA is supported by NIH-NINDS K08 (K08NS066099-01A1).

The model described in this manuscript has been posted to the Yale SenseLab ModelDB database of computational neuroscience models, web address: <http://senselab.med.yale.edu/modeldb/default.asp>.

Appendix A. Supplementary data

Supplementary data associated with this article can be found, in the online version, at doi:10.1016/j.eplepsyres.2011.11.006.

References

- Afra, P., Jouny, C.C., Bergey, G.K., 2008. Duration of complex partial seizures: an intracranial EEG study. *Epilepsia* 49 (4), 677–684.
- Anderson, W.S., Kudela, P., Cho, R.J., Bergey, G.K., Franaszczuk, P., 2007. Studies of stimulus parameters for seizure disruption using neural network simulations. *Biol. Cybern.* 97, 173–194.
- Anderson, W.S., Weinberg, S., Kudela, P., Bergey, G.K., Franaszczuk, P., 2009. Phase dependent stimulation effects on bursting activity in a neural network cortical simulation. *Epilepsy Res.* 84, 42–55.
- Andrzejak, R.G., Chicharro, D., Elger, C.E., Mormann, F., 2009. Seizure prediction: any better than chance? *Clin. Neurophysiol.* 120 (8), 1465–1478.
- Arellano, J.I., Muñoz, A., Ballesteros-Yáñez, I., Sola, R.G., DeFelipe, J., 2004. Histopathology and reorganization of chandelier cells in the human epileptic sclerotic hippocampus. *Brain* 127, 45–64.
- Av-Ron, E., 1994. The role of a transient potassium current in a bursting neuron model. *J. Math. Biol.* 33, 71–87.
- Berg, A.T., Shinnar, S., 1991. The risk of seizure recurrence following a first unprovoked seizure: a quantitative review. *Neurology* 41, 965–972.
- Bragin, A., Engel, J., Staba, R.J., 2010. High-frequency oscillations in epileptic brain. *Curr. Opin. Neurol.* 23 (2), 151–156.
- Braitenberg, V., Schüz, A., 1998. *Cortex: Statistics and Geometry of Neuronal Connectivity*, 2nd edition. Springer, Berlin.
- Dinocourt, C., Petanjek, Z., Freund, T.F., Ben-Ari, Y., Esclapez, M., 2003. Loss of interneurons innervating pyramidal cell dendrites and axon initial segments in the CA1 region of the hippocampus following pilocarpine-induced seizures. *J. Comp. Neurol.* 459, 407–425.
- Douglas, R.J., Martin, K.A.C., 2004. Neuronal circuits of the neocortex. *Annu. Rev. Neurosci.* 27, 419–451.
- Dudek, F.E., Sutula, T.P., 2007. Epileptogenesis in the dentate gyrus: a critical perspective. *Prog. Brain Res.* 163, 755–753.
- Dyhrfjeld-Johnsen, J., Santhakumar, V., Morgan, R.J., Huerta, R., Tsimring, L., Soltesz, I., 2007. Topological determinants of epileptogenesis in large-scale structural and functional models

- of the dentate gyrus derived from experimental data. *J. Neurophysiol.* 97 (2), 1566–1587.
- Estellar, R., Echaz, J., Tchong, T., Litt, B., Pless, B., 2001. Line length: an efficient feature of seizure onset detection. In: *Proc 23rd Annu Int Conf IEEE Eng Med Biol Soc, Istanbul*, pp. 1707–1710.
- Farkhooi, F., Strube-Bloss, M.F., Nawrot, M.P., 2009. Serial correlation in neural spike trains, experimental evidence, stochastic modeling, and single neuron variability. *Phys. Rev. E: Stat. Nonlin. Soft Matter Phys.* 79, 021905.
- Franaszczuk, P.J., Kudela, P., Bergey, G.K., 2003. External excitatory stimuli can terminate bursting in neural network models. *Epilepsy Res.* 53, 65–80.
- Guckenheimer, J., Holmes, P., 1983. *Nonlinear Oscillations, Dynamical Systems, and Bifurcations of Vector Fields*. Springer-Verlag, New York.
- Haas, S.M., Frei, M.G., Osorio, I., 2007. Strategies for adapting automated seizure detection algorithms. *Med. Eng. Phys.* 29 (8), 895–909.
- Hauser, W.A., Annegers, J.F., Kurland, L.T., 1993. Incidence of epilepsy and unprovoked seizures in Rochester, Minnesota: 1935–1984. *Epilepsia* 34, 453–468.
- Hegy, S., 1996. Multiplicity distributions in strong interactions: a generalized negative binomial model. *Phys. Lett. B* 387, 642–650.
- Jacobs, K.M., Graber, K.D., Kharazia, V.N., Parada, I., Prince, D.A., 2000. Postlesional epilepsy: the ultimate brain plasticity. *Epilepsia* 41 (Suppl. 6), S153–S161.
- Kaplan, Y., Kurt, S.G., Karaer, H., Sarikaya, B., Bebek, N., 2009. Intra-familial incidence and characteristics of hot water epilepsy. *Can. J. Neurol. Sci.* 36 (5), 575–581.
- Keefer, E.W., Gramowski, A., Gross, G.W., 2001. NMDA receptor-dependent periodic oscillations in cultured spinal cord networks. *J. Neurophysiol.* 86, 3030–3042.
- Kowalski, J.M., Albert, G.L., Rhoades, B.K., Gross, G.W., 1992. Neuronal networks with spontaneous, correlated bursting activity: theory and simulations. *Neural Netw.* 5, 805–822.
- Krumholz, A., Wiebe, S., Gronseth, G., Shinnar, S., Levisohn, P., Ting, T., Hopp, J., Shafer, P., Morris, H., Seiden, L., Barkley, G., French, J., 2007. Practice parameter: evaluating an apparent unprovoked first seizure in adults (an evidence-based review). Report of the quality standards subcommittee of the American Academy of Neurology and the American Epilepsy Society. *Neurology* 69, 1996–2007.
- Kudela, P., Franaszczuk, P.J., Bergey, G.K., 1997. A simple computer model of excitable synaptically connected neurons. *Biol. Cybern.* 77, 71–77.
- Kudela, P., Franaszczuk, P.J., Bergey, G.K., 2003a. Changing excitation and inhibition in simulated neural networks: effects on induced bursting behavior. *Biol. Cybern.* 88, 276–285.
- Kudela, P., Franaszczuk, P., Bergey, G.K., 2003b. Reduction of intracellular calcium removal rate can explain changes in seizure dynamics: studies in neuronal network models. *Epilepsy Res.* 57, 95–109.
- Kudela, P., Franaszczuk, P.J., Bergey, G.K., 2005. Synaptic and cellular influences on the composite EEG signal during seizures. In: *Proc 2nd Inter IEEE EMBS Conf Neural Eng. IEEE, Arlington, VA*, pp. 245–247.
- Kumar, S.S., Jin, X., Buckmaster, P.S., Huguenard, J.R., 2007. Recurrent circuits in layer II of medial entorhinal cortex in a model of temporal lobe epilepsy. *J. Neurosci.* 27, 1239–1246.
- Lehnertz, K., Mormann, F., Osterhage, H., Müller, A., Prusseit, J., Chernihovskyi, A., Staniek, M., Krug, D., Bialonski, S., Elger, C.E., 2007. State-of-the-art of seizure prediction. *J. Clin. Neurophysiol.* 24 (2), 147–153.
- Leussis, M.P., Heinrichs, S.C., 2007. Temporal ontogeny of circuit activation prior to the onset of seizure susceptibility in EL/Suz mice. *Neuroscience* 145, 33–41.
- Le Van Quyen, M., Martinerie, J., Adam, C., Varela, F.J., 1997. Unstable periodic orbits in human epileptic activity. *Phys. Rev. E* 56 (3), 3401–3411.
- Litt, B., Echaz, J., 2002. Prediction of epileptic seizures. *Lancet Neurol.* 1, 22–30.
- Lopes da Silva, F., Blanes, W., Kalitzin, S.N., Parra, J., Suffczynski, P., Velis, D.N., 2003. Epilepsies as dynamical diseases of brain systems: basic models of the transition between normal and epileptic activity. *Epilepsia* 44 (Suppl. 12), 72–83.
- Lu, Y., Waltz, S., Stenzel, K., Muhle, H., Stephani, U., 2008. Photosensitivity in epileptic syndromes of childhood and adolescence. *Epileptic Disord.* 10 (2), 144–145.
- Maglócsky, Z., 2010. Sprouting in human temporal lobe epilepsy: excitatory pathways and axons of interneurons. *Epilepsy Res.* 89, 52–59.
- Marco, P., Sola, R.G., Ramón y Cajal, S., DeFelipe, J., 1997. Loss of inhibitory synapses on the soma and axon initial segment of pyramidal cells in human epileptic peritumoural neocortex: implications for epilepsy. *Brain Res. Bull.* 44, 47–66.
- Morgan, R.J., Soltesz, I., 2008. Nonrandom connectivity of the epileptic dentate gyrus predicts a major role for neuronal hubs in seizures. *Proc. Natl. Acad. Sci. U.S.A.* 105 (16), 6179–6184.
- Mormann, F., Andrzejak, R.G., Elger, C.E., Lehnertz, K., 2007. Seizure prediction: the long and winding road. *Brain* 130, 314–333.
- Niedermeyer, E., 2005. Epileptic seizure disorders. In: *Niedermeyer, E., Lopes da Silva, F. (Eds.), Electroencephalography*, 5th edition. Lippincott Williams & Wilkins, Philadelphia, pp. 505–619.
- Osorio, I., Frei, M.G., Manly, B.F.J., Sunderam, S., Bhavaraju, N.C., Wilkinson, S.B., 2001. An introduction to contingent (closed-loop) brain electrical stimulation for seizure blockage, ultra-short-term clinical trials, and to multidimensional statistical analysis of therapeutic efficacy. *J. Clin. Neurophysiol.* 18 (6), 533–544.
- Osorio, I., Frei, M.G., Sornette, D., Milton, J., 2009. Pharmacoresistant seizures: self-triggering capacity, scale-free properties and predictability? *Eur. J. Neurosci.* 30, 1554–1558.
- Osorio, I., Frei, M.G., Sornette, D., Milton, J., Lai, Y.-C., 2010. Epileptic seizures: quakes of the brain? *Phys. Rev. E* 82, 021919.
- Papoulis, A., 1984. *Probability, Random Variables, and Stochastic Processes*, 2nd edition. McGraw-Hill, New York.
- Rhoades, B.K., Gross, G.W., 1994. Potassium and calcium channel dependence of bursting in cultured neuronal networks. *Brain Res.* 643, 310–318.
- Sackellares, J.C., Shiao, D.S., Principe, J.C., Yang, M.C., Dance, L.K., Suharitdamrong, W., Chaovaitwongse, W., Pardalos, P.M., Iasemidis, L.D., 2006. Predictability analysis for an automated seizure prediction algorithm. *J. Clin. Neurophysiol.* 23, 509–520.
- Sackellares, J.C., 2008. Seizure prediction. *Epilepsy Curr.* 8 (3), 55–59.
- Sallin, P., Tseng, G.-F., Hoffman, S., Parada, I., Prince, D.A., 1995. Axonal sprouting in layer V pyramidal neurons of chronically injured cerebral cortex. *J. Neurosci.* 15 (12), 8234–8245.
- So, P., Ott, E., Schiff, S.J., Kaplan, D.T., Sauer, T., Grebogi, C., 1996. Detecting unstable periodic orbits in chaotic experimental data. *Phys. Rev. Lett.* 76 (25), 4705–4708.
- So, P., Ott, E., Sauer, T., Gluckman, B.J., Grebogi, C., Schiff, S.J., 1997. Extracting unstable periodic orbits from chaotic time series data. *Phys. Rev. E* 55 (5), 5398–5417.
- Suffczynski, P., Lopes da Silva, F., Parra, J., Velis, D., Kalitzin, S., 2005. Epileptic transitions: model predictions and experimental validation. *J. Clin. Neurophysiol.* 22 (5), 288–299.
- Suffczynski, P., Lopes da Silva, F.H., Parra, J., Velis, D.N., Bouwman, B.M., van Rijn, C.M., van Hese, P., Boon, P., Khosravani, H., Derchansky, M., Carlen, P., Kalitzin, S., 2006. Dynamics of epileptic phenomena determined from statistics of ictal transitions. *IEEE Trans. Biomed. Eng.* 53 (3), 524–532.

- Swann, J.W., Le, J.T., Lee, C.L., 2007. Recurrent seizures and the molecular maturation of hippocampal and neocortical glutamatergic synapses. *Dev. Neurosci.* 29, 168–178.
- Telfeian, A.E., Connors, B.W., 1998. Layer-specific pathways for the horizontal propagation of epileptiform discharges in neocortex. *Epilepsia* 39, 700–708.
- Theiler, J., Eubank, S., Longtin, A., Galdrikian, B., Farmer, J.D., 1992. Testing for nonlinearity in time series: the method of surrogate data. *Physica D* 58, 77–94.
- Truccolo, W., Donoghue, J., Hochberg, L., Eskandar, E., Madsen, J.R., Anderson, W.S., Halgren, E., Cash, S.S., 2011. Single neuron dynamics during human focal seizures. *Nat. Neurosci.* 14 (5), 635–641.
- van Gompel, J.J., Stead, S.M., Giannini, C., Meyer, F.B., Marsh, W.R., Fountain, T., So, E., Cohen-Gadol, A., Lee, K.H., Worrell, G.A., 2008. Phase I trial: safety and feasibility of intracranial electroencephalography using hybrid subdural electrodes containing macro- and microelectrode arrays. *Neurosurg. Focus* 25 (3), E23.
- Vinogradova, L.V., Kuznetsova, G.D., Coenen, A.M., 2009. Unilateral cortical spreading depression induced by sound in rats. *Brain Res.* 1286, 201–207.
- Wald, A., Wolfowitz, J., 1943. An exact test for randomness in the non-parametric case based on serial correlation. *Ann. Math. Stat.* 14 (4), 378–388.
- Waters, J., Helmchen, F., 2006. Background synaptic activity is sparse in neocortex. *J. Neurosci.* 26 (32), 8267–8277.
- Worrell, G.A., Gardner, A.B., Stead, S.M., Hu, S., Goerss, S., Cascino, G.J., Meyer, F.B., Marsh, R., Litt, B., 2008. High-frequency oscillations in human temporal lobe: simultaneous microwire and clinical macroelectrode recordings. *Brain* 131 (Pt 4), 928–937.
- Worrell, G.A., Parish, L., Cranstoun, S.D., Jonas, R., Baltuch, G., Litt, B., 2004. High-frequency oscillations and seizure generation in neocortical epilepsy. *Brain* 127 (Pt 7), 1496–1506.

Evolving Communicative Complexity: Insights From Rodents and Beyond

Kimberly A. Pollard and Daniel T. Blumstein

Philosophical Transactions of the Royal Society B, 367, 1869-1878 (2012)

Evolving communicative complexity: insights from rodents and beyond

Kimberly A. Pollard and Daniel T. Blumstein

Phil. Trans. R. Soc. B 2012 **367**, 1869–1878
doi: 10.1098/rstb.2011.0221

References

[This article cites 74 articles, 15 of which can be accessed free](#)

<http://rstb.royalsocietypublishing.org/content/367/1597/1869.full.html#ref-list-1>

Subject collections

Articles on similar topics can be found in the following collections

[behaviour](#) (391 articles)

[evolution](#) (533 articles)

Email alerting service

Receive free email alerts when new articles cite this article - sign up in the box at the top right-hand corner of the article or click [here](#)

Evolving communicative complexity: insights from rodents and beyond

Kimberly A. Pollard^{1,2,*} and Daniel T. Blumstein¹

¹*Department of Ecology and Evolutionary Biology, University of California, Los Angeles, CA 90095, USA*

²*Human Research and Engineering Directorate, Perceptual Sciences Branch, US Army Research Laboratory, Aberdeen Proving Ground, MD 21005, USA*

Social living goes hand in hand with communication, but the details of this relationship are rarely simple. Complex communication may be described by attributes as diverse as a species' entire repertoire, signallers' individualistic signatures, or complex acoustic phenomena within single calls. Similarly, attributes of social complexity are diverse and may include group size, social role diversity, or networks of interactions and relationships. How these different attributes of social and communicative complexity co-evolve is an active question in behavioural ecology. Sciurid rodents (ground squirrels, prairie dogs and marmots) provide an excellent model system for studying these questions. Sciurid studies have found that demographic role complexity predicts alarm call repertoire size, while social group size predicts alarm call individuality. Along with other taxa, sciurids reveal an important insight: different attributes of sociality are linked to different attributes of communication. By breaking social and communicative complexity down to different attributes, focused studies can better untangle the underlying evolutionary relationships and move us closer to a comprehensive theory of how sociality and communication evolve.

Keywords: sociality; individuality; repertoire size; alarm call; information theory; vocal complexity

1. WHAT IS COMPLEXITY?

While most of us have an intuitive idea of what constitutes complexity, complexity is difficult to define [1]. A system is typically considered more complex if it contains more parts, more variability or types of parts, more connections or types of connections between parts or more layers of embedded meaning. The information [2] required to describe a system can be thought of as a measure of the system's complexity ('Kolmogorov complexity', after [3]). To illustrate, Dawkins [4, p. 265] provides a simple thought experiment: when comparing two items or systems, imagine writing a book to describe each one. The longer book will describe the more complex system. Information-based definitions of complexity are most useful because they allow complexity to be quantified and compared with a single metric [5].

Social complexity can be defined in numerous ways (e.g. the number of individuals [6–8], the number of demographic or social roles [9,10], the strength of social bonds [11–13], the complexity of group sub-structure and relationships [14–18] and combinations of these [19,20]). Each of these definitions can be considered an attribute of sociality. What these definitions have in common is they quantify social complexity via the number or variability of the social system's parts, connections or layers of categorization (table 1).

One integral attribute of social complexity is perhaps the most straightforward: social group size. The number of individual animals present in a social group influences that group's resource needs [21], disease ecology [22] and predation risk [23]. Furthermore, social group size defines boundaries for other attributes of social complexity, such as mating systems or social networks [24]. Group size also directly affects the communicative landscape, since more individuals may be communicated with, followed, discriminated or ignored [5,25–27]. Social group size is often straightforward to quantify. If a social group's boundaries are well defined, then a simple head count is all that is needed. For all these reasons, it is not surprising that social group size is one of the most commonly studied attributes of social complexity and has been used in a variety of taxa [7,28–38].

Another critical attribute of social complexity is the number or variability of social roles in a social group. A role can be thought of as a socially expected behavioural pattern. For instance, social roles may be based on whether an individual is a dominant or subordinate, a producer or scrounger, or a breeder or non-breeder. Blumstein & Armitage [39] quantified social roles by focusing on demographic (age/sex) roles in social groups, which can be quantified using information theory. The key assumption was that groups with more overlapping generations, and those with more age-sex classes present, were more socially complex in their demographic roles.

Complexity in communication can be defined analogously to complexity in sociality, i.e. via the number or

* Author for correspondence (kpollard@ucla.edu).

One contribution of 13 to a Theme Issue 'The social network and communicative complexity in animals'.

Table 1. A selection of attributes of social systems and communication systems that can vary in complexity. The categories suggested here are neither mutually exclusive nor exhaustive, and no causal relationships are implied.

	number of system parts	types of system parts	connections between parts	layers of structure, categorization or meaning	openness and variability
social complexity	group size social group size colony, aggregation, or community size foraging group size	roles social demographic reproductive	social bonds may be quantified with social network statistics and may be agonistic or affiliative matriline structures social hierarchies territorial neighbour networks	group substructure matrilines coalitions group superstructure fission – fusion group aggregations post-dispersal ties	fluidity or variability of social attributes group membership social hierarchies reproductive roles
communicative complexity	repertoire size (within a signal type) entire repertoire repertoire within an age class, sex or situational context	repertoire size (across signal types)	syntax connections between signals	referential and functionally referential communication communication of signal urgency or signaller's affective state embedded signature information signaller's age, sex, condition or individual identity	learning and modification of signals openness of signal repertoires and syntax

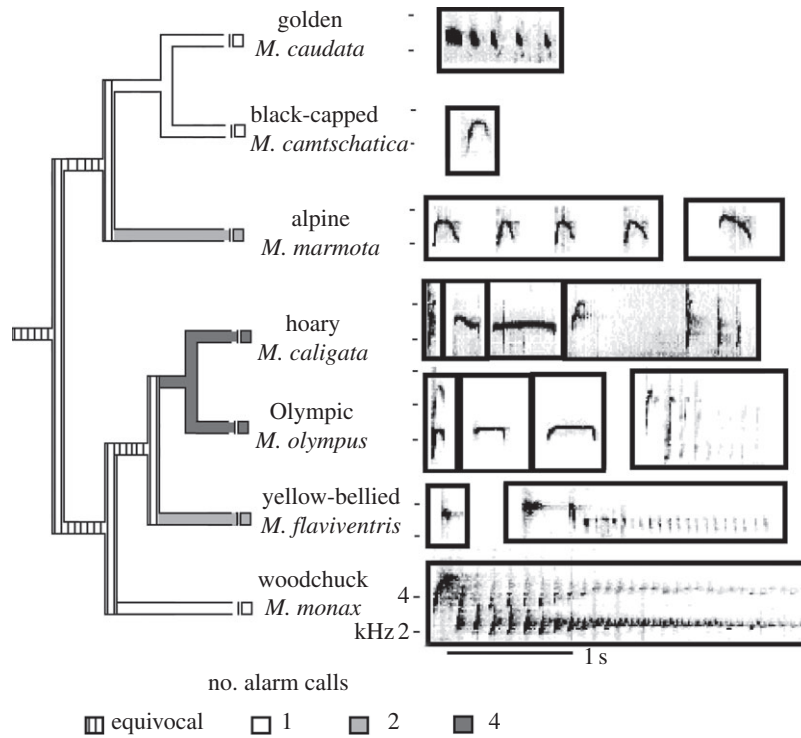


Figure 1. Alarm call repertoires of seven species of marmots (*Marmota* spp.). Sciurid rodents differ in the acoustic structure of their alarm calls and in the size of their alarm call repertoires.

variability of the signal's or system's parts, connections, or layers of meaning (table 1). For acoustic communication, attributes of communicative complexity can include a species' repertoire size (number of call types [32,39]) or the syntactical complexity or uncertainty [40,41] of sequences of calls. Signals may also be complex in their association with external referents, such as functionally referential alarm calls that communicate predator type or response strategy, in addition to alarm [42–45]. Communication of urgency or affective state is another form of complexity, providing additional information about the situation [46–48]. For example, many species of marmots alter the rate of their alarm calls with the urgency of the situation or the degree of risk [49]. The presence of embedded signature information (such as age, sex or individual caller identity [50–54]) also adds complexity to communicative signals.

As social complexity, however quantified, increases, more complex communication might be needed to manage this social complexity [55–59]. Attributes of social complexity may thus generate a need for animals to exhibit different types of communicative complexity.

2. SCIURIDS AS A MODEL SYSTEM

Sciurid rodents (Rodentia: Sciuridae), particularly ground-dwelling social species (tribe Marmotini, including ground squirrels *Spermophilus* spp. and related genera, prairie dogs *Cynomys* spp., and marmots *Marmota* spp.), present an excellent model comparative system for studying the relationship between social and communicative complexity, for several reasons.

First, ground-dwelling sciurids constitute a speciose clade that exhibits a wide range of social structures. On one end of the spectrum, some species are nearly solitary or live in simple family groups (e.g.

woodchucks, *Marmota monax*, live in groups of a mother plus her young of the year). Within the same clade, more complicated group structures are seen, such as those in Eurasian marmots (e.g. *M. caudata*, *M. marmota* [60]) in which young delay dispersal for one, two or more years, adult males participate in group life, and females may aggregate in harems or matriline. Social group size also varies considerably across ground-dwelling sciurids, as does group cohesion. In addition, sciurids also vary in their tiers or levels of social complexity [61,62], with some species exhibiting complex relationships between segregated social groups (e.g. some prairie dogs). Importantly, variation in social group size is not strictly tied to variation in other attributes of social structure [9], allowing these different attributes to be teased apart in comparative study.

Secondly, ground-dwelling sciurids offer a communication system amenable to comparative study. Ground-dwelling sciurids produce vocal alarm calls in response to predatory stimuli [63]. These calls are typically loud and perceptually salient, and they can be elicited and recorded by researchers. Within the sciurid alarm call system, an array of communicative complexity is exhibited. Species vary in the acoustic structure of their calls [39,54,64], the size of their alarm call repertoires [39,49] (figure 1), the response urgency or distance to predator encoded in their calls [65–67], syntactic or ordering differences in calls [64], and the degree to which age and sex and individual identity are encoded [54,68]. As with social complexity, we can view these as attributes of communicative complexity and they can be independently studied in comparative analyses.

Thirdly, published phylogenies [69–71] aid phylogenetically controlled evolutionary analyses in this taxon.

To date, two phylogenetically controlled studies have examined the correlated evolution of social complexity and communicative complexity in ground-dwelling sciurid rodents [39,54]. Importantly, comparative studies in sciurids permit us to decouple drivers of complexity, and, as discussed below, have revealed that social complexity, broadly defined, does not simply select for more complex communication. Rather, different attributes of sociality seemingly select for specific attributes of communicative complexity.

3. DEMOGRAPHIC COMPLEXITY DRIVES REPERTOIRE SIZE EVOLUTION

Blumstein & Armitage [39] used 22 species of ground-dwelling sciurids to test for a relationship between one attribute of social complexity (demographic role complexity) and one attribute of communicative complexity (alarm call repertoire size). They defined a social complexity index via information theory, using data on dispersal patterns, the age/sex composition of groups and variability in these traits [39]. The resulting numbers, expressed in bits, quantify the amount of information needed to describe the demographic role complexity in different species.

For species with multiple alarm call types, different call types may be used to communicate about different types of predators [42,43,45], to communicate different degrees of risk or response urgency [46,48], or to communicate both predator type and urgency [44,72]. Species living in more complex social groups, such as groups with more social demographic roles, may have greater need to signal alarm in a more complex manner and thus may use larger alarm call repertoires. Across ground-dwelling sciurids, alarm call repertoire size varies from one to five (see examples in figure 1). Blumstein & Armitage [39] used a combination of field recordings and literature review to establish the alarm call repertoire size for 22 species of sciurid and regressed this against the social complexity index. Demographic role complexity significantly explained variation in alarm call repertoire size, both in analyses of raw data and independent contrasts (figure 2).

More up-to-date phylogenies have since been published, so we re-ran the independent contrasts analysis using more recent phylogeny taken from Herron *et al.* [70] and Steppan *et al.* [71]. The relationship between social demographic complexity and alarm call repertoire size remained significant ($r^2 = 0.228$, $y = 1.049x$, $p = 0.025$, $n = 21$ independent contrasts). An increase in social demographic roles appears to drive the ability to communicate via a larger, more complex repertoire of alarm calls. The functional explanation underlying this correlation is unknown. Future study of alarm call type use in different contexts or between different caller–receiver dyads may be necessary to untangle how more demographically complex species may benefit from a more diverse alarm call repertoire.

4. SOCIAL GROUP SIZE DRIVES THE EVOLUTION OF INDIVIDUAL SIGNATURES

Pollard & Blumstein [54] compared sciurid vocal signature individuality (individual distinctiveness) against

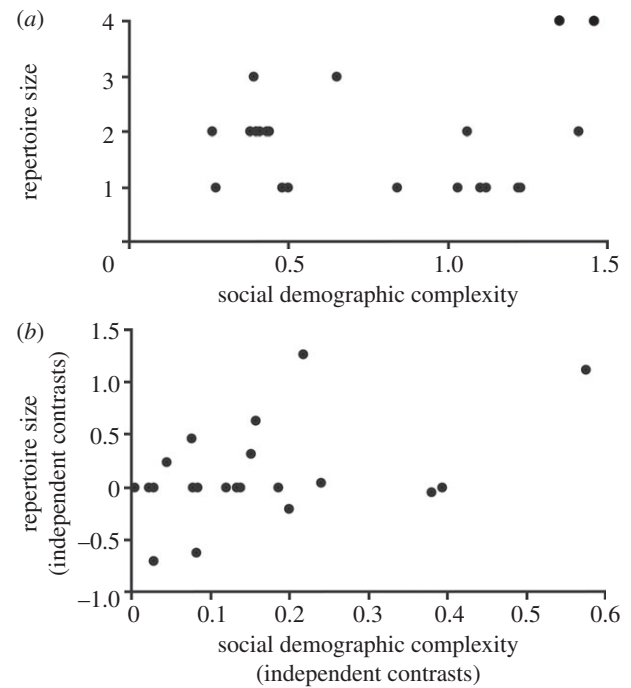


Figure 2. Relationship between social demographic complexity and alarm call repertoire size across 22 species of sciurid rodents, in raw (a) and independent contrasts (b) data. Social complexity (variability in demographic roles) correlates with alarm call repertoire size. (a) Adapted from Blumstein & Armitage [39], with permission from Chicago Journals.

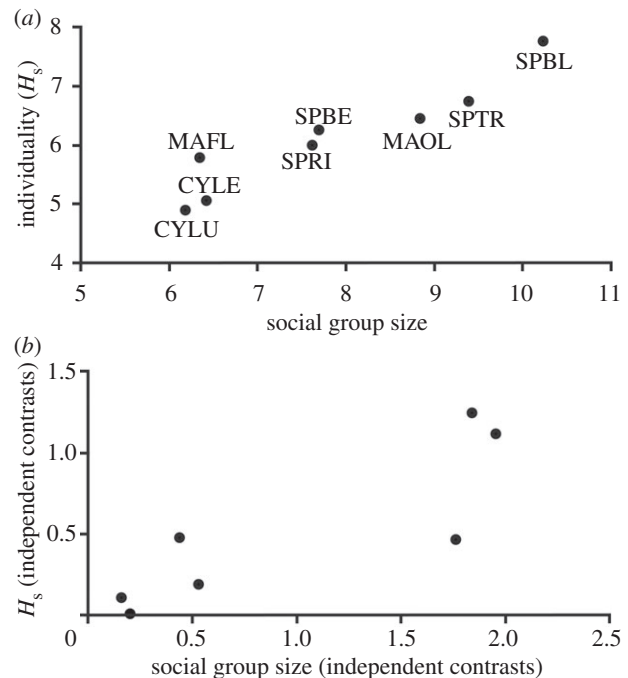


Figure 3. Relationship between social group size and alarm call individuality across eight species of sciurid rodents. In raw (a) and independent contrasts (b) data, social group size correlates with vocal individuality (H_s) in sciurid alarm calls ($r^2 > 0.88$, $p < 0.001$ in both cases). Species in (a) are *Cynomys leucurus* (CYLU), *C. ludovicianus* (CYLE), *Marmota flaviventris* (MAFL), *M. olympus* (MAOL), *Spermophilus beecheyi* (SPBE), *S. beldingi* (SPBL), *S. richardsonii* (SPRI) and *S. tridecemlineatus* (SPTR). Figure adapted from Pollard & Blumstein [54], with permission from Elsevier.

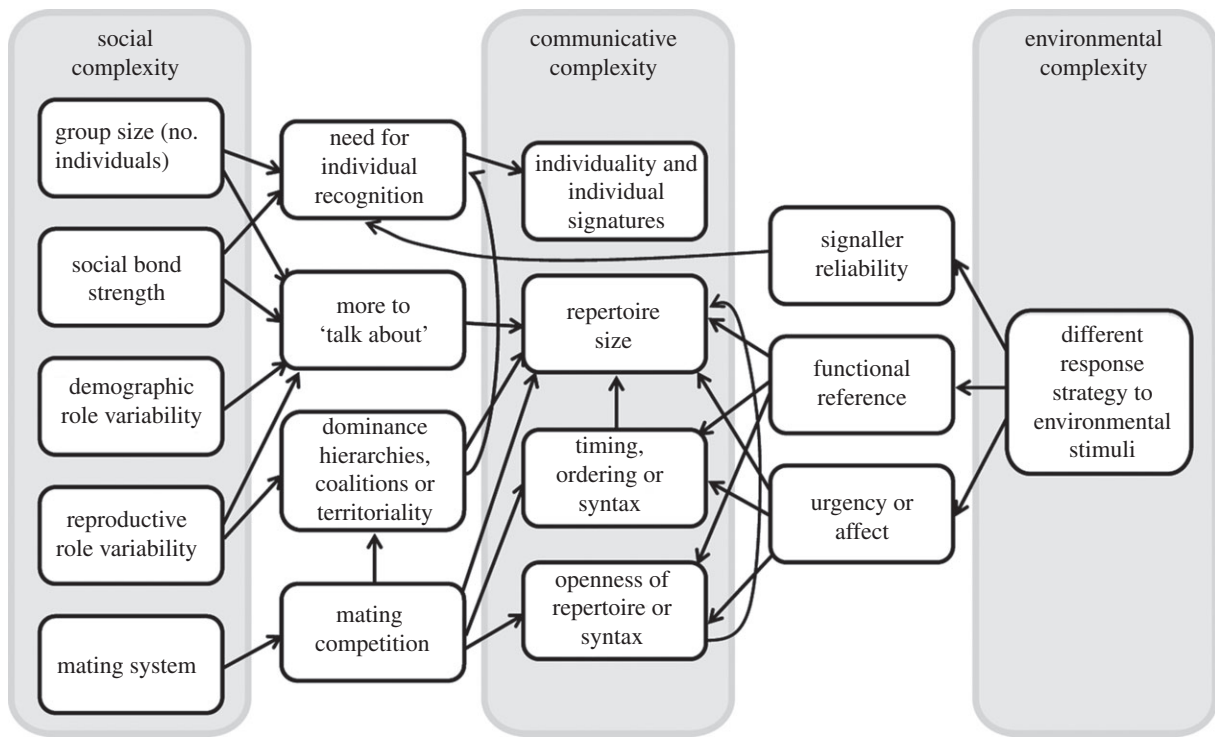


Figure 4. Possible functional relationships between attributes of social complexity and attributes of communicative complexity. For specific examples of relationships that are supported in the literature, see table 2.

social group size, Blumstein & Armitage's [39] demographic complexity index, and two other indices of social structure complexity [61,62]. Group size was not correlated with these other complexity indices [54]. Because studies quantifying vocal individuality are not common, this analysis required novel data, and eight species of ground-dwelling sciurid were thus captured, individually marked and recorded on multiple occasions. Individuality was calculated from acoustic traits using an information-theory metric developed by Beecher [5,73] and used in previous studies [25,27,52,74]. The individuality information statistic quantifies, in bits, the amount of individually specific information content present in a species' vocalizations. This statistic was used as the quantitative metric of one attribute of communicative complexity.

Individual signatures in alarm calls are important for animals such as sciurids [75–77]. Individuals vary in their alarm signal reliability, and listeners benefit when they recognize the individual identity of an alarm caller, as this allows them to better calibrate their behavioural response [76–80]. Ground-dwelling sciurids live in groups of closely related kin, such that the signaller and receiver are often close relatives. This may allow callers to benefit via kin selection by aiding related receivers in individual discrimination and reliability assessment [54,77], although they may also benefit via reciprocal altruism [81].

Individuality is expected to evolve with group size [5,25–27,52,54,73]. As social group size increases, the number of individuals that must be discriminated increases accordingly, making individual recognition tasks more difficult. Increased individuality would be necessary to permit successful discrimination of all the individuals in the group. Since other attributes of

sociality affect communicative complexity [39,82], these other attributes may also influence individuality.

Pollard & Blumstein [54] gathered typical social group size data from the literature and regressed this against the individuality metric. Group size explained considerable variation in vocal individuality, both in the raw data and in an analysis using independent contrasts (figure 3). As predicted, social group size appears to drive the evolution of individual signature information.

Interestingly, it is group size, not other social complexity attributes, that seems responsible for the evolution of individually specific vocalizations. Signature information was also regressed against three other measures of social structure complexity, including Blumstein & Armitage's [39] demographic complexity index, Michener's [62] social grade, and Armitage's [61] sociality index. 'Social grade' and 'sociality index' are somewhat subjective numerical assignments intended to quantify the complexity of each species' social structure and mating system. Individuality was not significantly related to any of these three other social complexity attributes, even after controlling for variation in group size.

5. ATTRIBUTES OF SOCIALITY, ATTRIBUTES OF COMMUNICATION

Results from sciurid studies highlight an important caveat about the evolution of social and communicative complexity. Both sociality and communication have multiple attributes (table 1), and these attributes affect one another in complex ways (figure 4). The main insight from our integrative overview is that different attributes of social complexity are likely to drive different attributes of communicative complexity. Thus, it is

Table 2. Comparative relationships among attributes of social and communicative complexity. Studies indicate that different attributes of social complexity affect different attributes of communicative complexity.

attribute of social complexity	attribute of communicative complexity	taxon	no. species in study	signal type	phylogenetic control	citation	details
social group size	potential for repertoire size	anthropoid primates	12	facial expressions (visual)	generalized least-squares	[35]	social group size predicts facio-muscular ability to produce varied facial expressions
social group size	repertoire size	primates	42	vocalizations (auditory)	independent contrasts	[32]	social group size predicts repertoire size for adult vocalizations
social group size	signal variability	whales	34	vocalizations (auditory)	independent contrasts	[83]	social group size predicts the amount of tonal modulation in cetacean whistles
social group size	potential to perceive diverse repertoire individuality	strepsirrhine primates	11	acoustic signals (auditory)	none	[84,85]	foraging group size predicts auditory sensitivity and high frequency hearing
social group size	individuality	sciurid rodents	8	vocal alarm calls (auditory)	independent contrasts	[54]	social group size predicts individual distinctiveness in vocal alarm calls
colony size	individuality	<i>Hirundo</i> swallows	2	vocal contact calls (auditory)	comparison within genus	[25]	nesting colony size predicts individual distinctiveness in chick begging calls
colony size	individuality	<i>Larus</i> gulls	2	vocal contact calls (auditory)	comparison within genus	[26]	mobile crèche size predicts individual distinctiveness in adult 'long calls'
colony size	individuality	microchiropteran bats	8	vocal contact calls (auditory)	none	[27]	roosting colony size predicts individual distinctiveness in infant isolation calls
diversity/variability of demographic roles	repertoire size	sciurid rodents	22	vocal alarm calls (auditory)	independent contrasts	[39]	diversity/flexibility in demographic roles within social groups predicts repertoire size for vocal alarm calls
diversity/variability of reproductive roles	individuality	<i>Polistes</i> wasps	25	facial coloration patterns (visual)	concentrated changes	[82]	flexibility in nest-founding strategies predicts variability (individual distinctiveness) in visual facial markings
social structure complexity	repertoire size	<i>Eulemur</i> lemurs	8	glandular chemical secretions (olfactory)	none	[86]	social structure predicts diversity of odour chemicals in female perianal secretions
social structure complexity	repertoire size	<i>Papio</i> and <i>Theropithecus</i> monkeys	2	acoustic signals (auditory)	none	[87]	social structure predicts vocal repertoire size
mating system complexity	repertoire size	phocid seals	12	underwater vocalizations (auditory)	none	[88]	mating system predicts repertoire size for male underwater vocalizations
mating system complexity	repertoire size	lizards	41	bodily ornamentation (visual)	model fitting	[89]	mating system predicts the number of bodily ornaments and colour dichromatism
social bonding	repertoire size	primates	20	vocalizations (auditory)	independent contrasts	[32]	time spent in social grooming predicts repertoire size for adult vocalizations
social bonding	potential for repertoire size	catarrhine primates	10	facial expressions (visual)	generalized least-squares	[90]	time spent in social grooming predicts facial nucleus volume in the brain

important to think clearly about the nature of the relationship because different attributes work different ways (see also [1]). Studies from other taxa also support taking a nuanced look at the correlated evolution of social and communicative complexity (table 2). For example, the complexity of reproductive roles was found to influence individuality in wasp facial markings [82], while nesting or roosting colony size was found to influence individuality in avian and chiropteran contact calls [25–27]. In phocid seals, underwater repertoire size increased with mating system complexity [88]. In primates, social group size and time spent in social grooming influenced vocalization repertoire size [32], while group size influenced ability to produce varied facial expressions [35]. Furthermore, social complexity may influence not just the complexity of communicative signals themselves but also the perceptual capacity to receive such signals, e.g. social group size predicts auditory sensitivity in lemurs [84]. Social and communicative complexity can also covary within species or on short time scales; for example, chickadees placed in larger groups displayed more variability in their call types and combinations [40]. In all these cases, a different attribute of social complexity is associated with a different attribute of communicative complexity.

As a general rule, we would predict that the types of communicative complexity that are most relevant to a specific aspect of sociality would be evolving with those aspects of sociality. For example, if individual recognition is important, and if all members of a group must be recognized, we would predict a specific type of communicative complexity (individualistic signatures) to evolve with a particular attribute of social complexity (group size). This has been found in birds, bats and sciurids [25–27,54]. If calls are used to attract or impress mates, we would predict specific attributes of communicative complexity (such as syntactical complexity or repertoire size) to evolve with a specific attribute of social complexity (mating system). Indeed, male repertoire size seems to have evolved with mating system in phocid seals [88]. However, these relationships are not always obvious, and attributes of sociality may influence communication in diverse and complicated ways (figure 4). Future studies in more taxa will be necessary to comprehensively identify the many ways in which distinct attributes of social and communicative complexity are evolutionarily or functionally linked. With the discovery that social network statistics can be used by behavioural biologists [18,91,92], there are many precisely defined attributes of sociality that could be studied. From a comparative perspective, available data are often a limiting factor, but over time, there will be more data from different species available with which to study the evolution of social and communicative attributes [93]. As these databases are developed, sciurid rodents can continue to play a valuable role in this pursuit, because these species vary in several attributes of social and communicative complexity, and systematic study can help identify which of these attributes covary. These attributes can be further examined with respect to different environmental conditions in sciurids' diverse habitats, and/or mapped onto available phylogenies to estimate when and how complexity evolved.

6. CONCLUSIONS

The relationship between social complexity and communicative complexity is multi-faceted. Different attributes of sociality may drive the evolution of different attributes of communication. For example, in sciurid rodents, social demographic complexity explains the evolution of alarm call repertoire size, while social group size explains the evolution of alarm call vocal individuality. Sciurids are one of many excellent model systems in which to explore the evolution of social and communicative complexity, and future work in sciurid and non-sciurid taxa will help build a comparative database in which these questions can be thoroughly examined. The ever-growing comparative database will ultimately help us develop a comprehensive understanding of how social complexity and communicative complexity evolve.

We thank Todd Freeberg, Indrikis Krams and Cecilia Kullberg for organizing the ABS/IEC 2011 symposium on social complexity and communicative complexity and two anonymous reviewers for comments on a previous version of this manuscript. We thank our field collaborators and colleagues—Ken Armitage, Abigail Benson, Dean Biggins, Suzanne Cox-Griffin, David Eads, Chris Evans, Greg Grether, Jim Hare, John Hoogland, Marta Manser, Jill Mateo, Peter Nonacs, Don Owings, Dan Salkeld and Joan Silk—for access to animals and insightful comments over the years. For funding, we thank the American Philosophical Society, American Society of Mammalogists, Animal Behavior Society, Explorers Club, Mildred Mathias/UC Reserves, National Geographic Society, National Institute of Health, National Science Foundation, Rocky Mountain Biological Laboratory, Sigma Xi, UCLA, UC Davis and the University of Kansas. We also thank the many wonderful lab and field assistants who have helped both of us study the evolution of complex sociality and communication.

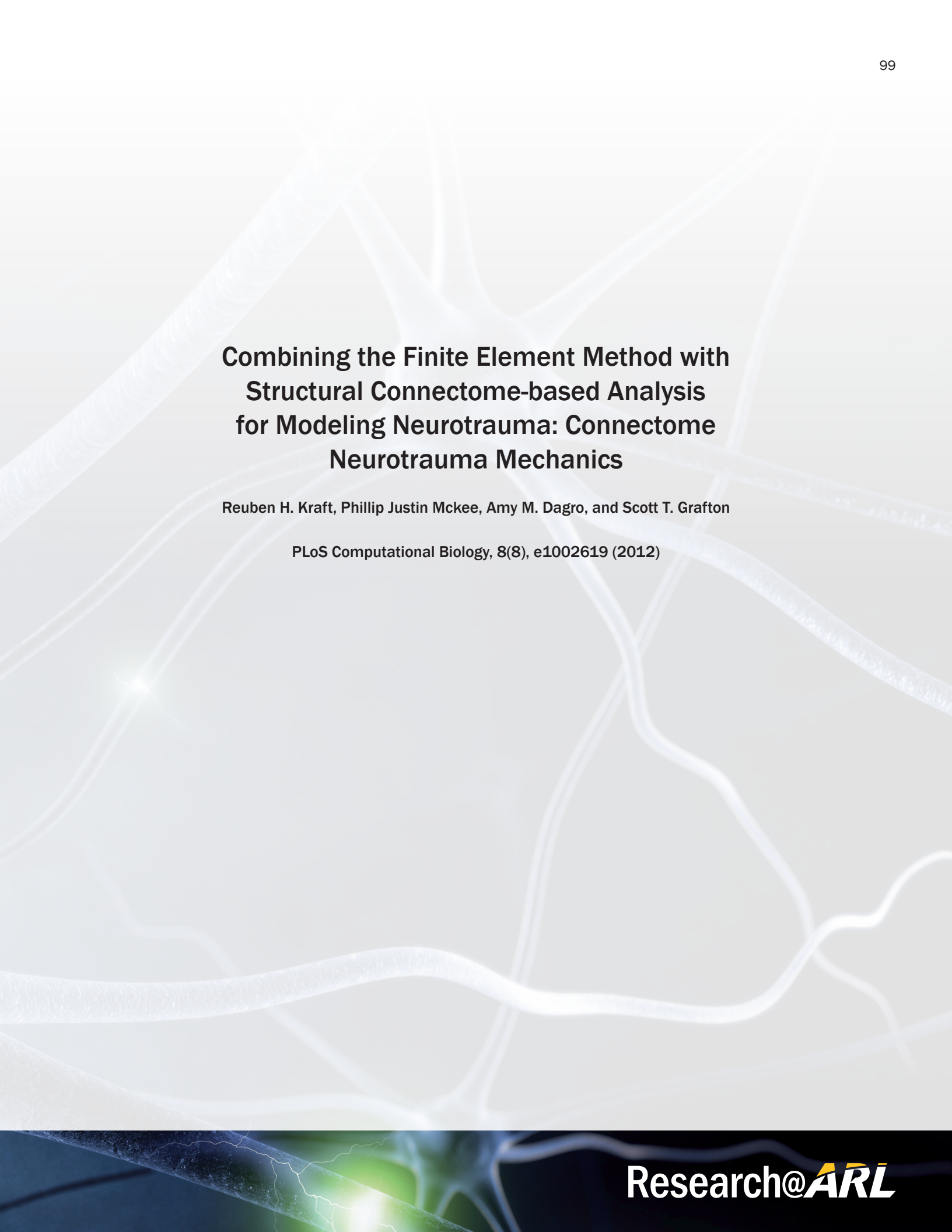
REFERENCES

- Edmonds, B. 1999 What is complexity?—The philosophy of complexity *per se* with application to some examples in evolution. In *The evolution of complexity* (eds F. Heylighen, J. Bollen & A. Riegler), pp. 1–18. Dordrecht, The Netherlands: Kluwer Academic.
- Shannon, C. E. & Weaver, W. 1949 *The mathematical theory of communication*. Urbana, IL: University of Illinois Press.
- Kolmogorov, A. 1965 Three approaches to the quantitative definition of information. *Probl. Info. Transm.* **1**, 1–7.
- Dawkins, R. 1992 Progress. In *Keywords in evolutionary biology* (eds E. F. Keller & E. A. Lloyd), pp. 263–272. Cambridge, MA: Harvard University Press.
- Beecher, M. D. 1989 Signalling systems for individual recognition: an information theory approach. *Anim. Behav.* **38**, 248–261. (doi:10.1016/S0003-3472(89)80087-9)
- Bekoff, M., Diamond, J. & Mitton, J. B. 1981 Life-history patterns and sociality in canids: body size, reproduction, and behavior. *Oecologia* **50**, 386–390. (doi:10.1007/BF00344981)
- Dunbar, R. I. M. 1992 Neocortex size as a constraint on group size in primates. *J. Hum. Evol.* **20**, 469–493. (doi:10.1016/0047-2484(92)90081-J)
- Deaner, R. O., Nunn, C. L. & van Schaik, C. P. 2000 Comparative tests of primate cognition: different scaling methods produce different results. *Brain Behav. Evol.* **55**, 44–52. (doi:10.1159/000006641)

- 9 Blumstein, D. T. & Armitage, K. B. 1998 Life history consequences of social complexity: a comparative study of ground-dwelling sciurids. *Behav. Ecol.* **9**, 8–19. (doi:10.1093/beheco/9.1.8)
- 10 Shultz, S. & Dunbar, R. I. M. 2006 Both social and ecological factors predict ungulate brain size. *Proc. R. Soc. B* **273**, 207–215. (doi:10.1098/rspb.2005.3283)
- 11 Stanford, C. B. 1998 Predation and male bonds in primate societies. *Behaviour* **135**, 513–533. (doi:10.1163/156853998793066212)
- 12 Henzi, S. P., Lycett, J. E., Weingrill, A. & Piper, S. E. 2000 Social bonds and the coherence of mountain baboon troops. *Behaviour* **137**, 663–680. (doi:10.1163/156853900502277)
- 13 Silk, J. B., Alberts, S. C. & Altmann, J. 2003 Social bonds of female baboons enhance infant survival. *Science* **302**, 1231–1234. (doi:10.1126/science.1088580)
- 14 Hinde, R. A. 1975 Interactions, relationships and social structure in non-human primates. In *Proc. Symp. of the Fifth Congress of the Int. Primatological Society, Nagoya, Japan, August 1974* (eds S. Kondo, M. Kawai, A. Ehara & S. Kawamura), pp. 13–24. Tokyo, Japan: Japan Science Press.
- 15 Foley, R. A. & Lee, P. C. 1989 Finite social space, evolutionary pathways, and reconstructing hominid behavior. *Science* **243**, 901–906. (doi:10.1126/science.2493158)
- 16 Colmenares, F. 1992 Clans and harems in a colony of hamadryas and hybrid baboons: male kinship, familiarity and the formation of brother-teams. *Behaviour* **121**, 61–94. (doi:10.1163/156853992X00444)
- 17 Barrett, L. & Henzi, S. P. 2002 Constraints on relationship formation among female primates. *Behaviour* **139**, 263–289. (doi:10.1163/156853902760102672)
- 18 Wey, T., Blumstein, D. T., Shen, W. & Jordán, F. 2008 Social network analysis of animal behaviour: a promising tool for the study of sociality. *Anim. Behav.* **75**, 333–334. (doi:10.1016/j.anbehav.2007.06.020)
- 19 Crook, J. H. & Gartlan, J. S. 1966 Evolution of primate societies. *Nature* **210**, 1200–1203. (doi:10.1038/2101200a0)
- 20 Eisenberg, J. F., Rudran, R. & Muckenhi, N. A. 1972 Relation between ecology and social structure in primates. *Science* **176**, 863. (doi:10.1126/science.176.4037.863)
- 21 Krause, J. & Ruxton, G. D. 2002 *Living in groups*. Oxford, UK: Oxford University Press.
- 22 Altizer, S. *et al.* 2003 Social organization and parasite risk in mammals: integrating theory and empirical studies. *Annu. Rev. Ecol. Evol. Sci.* **34**, 517–547. (doi:10.1146/annurev.ecolsys.34.030102.151725)
- 23 Caro, T. 2005 *Antipredator defenses in birds and mammals*. Chicago, IL: University of Chicago Press.
- 24 Janson, C. H. 1992 Evolutionary ecology of primate social structure. In *Evolutionary ecology and human behavior* (eds E. A. Smith & B. Winterhalder), pp. 95–130. New York, NY: Walter de Gruyter.
- 25 Medvin, M. B., Stoddard, P. K. & Beecher, M. D. 1993 Signals for parent-offspring recognition: a comparative analysis of the begging calls of cliff swallows and barn swallows. *Anim. Behav.* **45**, 841–850. (doi:10.1006/anbe.1993.1105)
- 26 Mathevon, N., Charrier, I. & Jouventin, P. 2003 Potential for individual recognition in acoustic signals: a comparative study of two gulls with different nesting patterns. *C. R. Biol.* **326**, 329–337. (doi:10.1016/S1631-0691(03)00072-6)
- 27 Wilkinson, G. S. 2003 Social and vocal complexity in bats. In *Animal social complexity: intelligence, culture, and individualized societies* (eds F. B. M. de Waal & P. L. Tyack), pp. 322–341. Cambridge, MA: Harvard University Press.
- 28 Wittenberger, J. F. 1980 Group size and polygamy in social mammals. *Am. Nat.* **115**, 197–222. (doi:10.1086/283555)
- 29 Wrangham, R. W., Gittleman, J. L. & Chapman, C. A. 1993 Constraints on group size in primates and carnivores: population density and day-range as assays of exploitation competition. *Behav. Ecol. Sociobiol.* **32**, 199–209.
- 30 Chapman, C. A. & Chapman, L. J. 2000 Determinants of group size in primates: the importance of travel costs. In *On the move: how and why animals travel in groups* (eds S. Boinski & P. A. Garber), pp. 24–42. Chicago, IL: University of Chicago Press.
- 31 Beauchamp, G. & Fernández-Juricic, E. 2004 Is there a relationship between forebrain size and group size in birds? *Evol. Ecol. Res.* **6**, 833–842.
- 32 McComb, K. & Semple, S. 2005 Coevolution of vocal communication and sociality in primates. *Biol. Lett.* **1**, 381–385. (doi:10.1098/rsbl.2005.0366)
- 33 Korstjens, A. H., Verhoeckx, I. L. & Dunbar, R. I. M. 2006 Time as a constraint on group size in spider monkeys. *Behav. Ecol. Sociobiol.* **60**, 683–694. (doi:10.1007/s00265-006-0212-2)
- 34 Pollard, K. A. & Blumstein, D. T. 2008 Time allocation and the evolution of group size. *Anim. Behav.* **76**, 1683–1699. (doi:10.1016/j.anbehav.2008.08.006)
- 35 Dobson, S. D. 2009 Socioecological correlates of facial mobility in nonhuman anthropoids. *Am. J. Phys. Anthropol.* **139**, 413–420. (doi:10.1002/ajpa.21007)
- 36 Kamilar, J. M., Bribiescas, R. G. & Bradley, B. J. 2010 Is group size related to longevity in mammals? *Biol. Lett.* **6**, 736–739. (doi:10.1098/rsbl.2010.0348)
- 37 Turnbull, C. *et al.* 2011 Antimicrobial strength increases with group size: implications for social evolution. *Biol. Lett.* **7**, 249–252. (doi:10.1098/rsbl.2010.0719)
- 38 Wong, M. Y. L. 2011 Group size in animal societies: the potential role of social and ecological limitations in the group-living fish, *Paragobiodon xanthosomus*. *Ethology* **117**, 638–644. (doi:10.1111/j.1439-0310.2011.01913.x)
- 39 Blumstein, D. T. & Armitage, K. B. 1997 Does sociality drive the evolution of communicative complexity? A comparative test with ground-dwelling sciurid alarm calls. *Am. Nat.* **150**, 179–200. (doi:10.1086/286062)
- 40 Freeberg, T. M. 2006 Social complexity can drive vocal complexity. *Psychol. Sci.* **17**, 557–561. (doi:10.1111/j.1467-9280.2006.01743.x)
- 41 Clay, Z. & Zuberbühler, K. 2011 Bonobos extract meaning from call sequences. *PLoS ONE* **6**, e18786. (doi:10.1371/journal.pone.0018786)
- 42 Seyfarth, R. M., Cheney, D. L. & Marler, P. 1980 Monkey responses to 3 different alarm calls: evidence of predator classification and semantic communication. *Science* **210**, 801–803. (doi:10.1126/science.7433999)
- 43 Evans, C. S., Evans, L. & Marler, P. 1993 On the meaning of alarm calls: functional reference in an avian vocal system. *Anim. Behav.* **46**, 23–38. (doi:10.1006/anbe.1993.1158)
- 44 Manser, M. B. 2001 The acoustic structure of suricates' alarm calls varies with predator type and the level of response urgency. *Proc. R. Soc. Lond. B* **268**, 2315–2324. (doi:10.1098/rspb.2001.1773)
- 45 Slobodchikoff, C. N., Paseka, A. & Verdolin, J. L. 2009 Prairie dog alarm calls encode labels about predator colors. *Anim. Cogn.* **12**, 435–439. (doi:10.1007/s10071-008-0203-y)
- 46 Hollen, L. I. & Manser, M. B. 2007 Motivation before meaning: motivational information encoded in meerkat alarm calls develops earlier than referential information. *Am. Nat.* **169**, 758–767. (doi:10.1086/516719)
- 47 Blumstein, D. T. & Récapet, C. 2009 The sound of arousal: the addition of novel non-linearities increases

- responsiveness in marmot alarm calls. *Ethology* **115**, 1074–1081. (doi:10.1111/j.1439-0310.2009.01691.x)
- 48 Fallow, P. M. & Magrath, R. D. 2010 Eavesdropping on other species: mutual interspecific understanding of urgency information in avian alarm calls. *Anim. Behav.* **79**, 411–417. (doi:10.1016/j.anbehav.2009.11.018)
 - 49 Blumstein, D. T. 2007 The evolution, function, and meaning of marmot alarm communication. *Adv. Stud. Behav.* **37**, 371–401. (doi:10.1016/S0065-3454(07)37008-3)
 - 50 Reby, D., Joachim, J., Lauga, J., Lek, S. & Aulagnier, S. 1998 Individuality in the groans of fallow deer (*Dama dama*) bucks. *J. Zool.* **245**, 79–84. (doi:10.1111/j.1469-7998.1998.tb00074.x)
 - 51 Aubin, T. & Jouventin, P. 2002 How to vocally identify kin in a crowd: the penguin model. *Adv. Stud. Behav.* **31**, 243–277. (doi:10.1016/S0065-3454(02)80010-9)
 - 52 Blumstein, D. T. & Munos, O. 2005 Individual, age and sex-specific information is contained in yellow-bellied marmot alarm calls. *Anim. Behav.* **69**, 353–361. (doi:10.1016/j.anbehav.2004.10.001)
 - 53 Yorzinski, J. L., Vehrencamp, S. L., Clark, A. B. & McGowan, K. J. 2006 The inflected alarm call of the American crow: differences in acoustic structure among individuals and sexes. *Condor* **108**, 518–529. (doi:10.1650/0010-5422(2006)108[518:TIACOT]2.0.CO;2)
 - 54 Pollard, K. A. & Blumstein, D. T. 2011 Social group size predicts the evolution of individuality. *Curr. Biol.* **21**, 413–417. (doi:10.1016/j.cub.2011.01.051)
 - 55 Marler, P. 1977 The evolution of communication. In *How animals communicate* (ed T. A. Sebeok). Bloomington, IN: Indiana University Press.
 - 56 Waser, P. M. 1982 The evolution of male loud calls among mangabeys and baboons. In *Primate communication* (eds C. T. Snowdon, C. H. Brown & M. R. Petersen), pp. 117–143. Cambridge, UK: Cambridge University Press.
 - 57 Marler, P. & Mitani, J. C. 1988 Vocal communication in primates and birds: parallels and contrasts. In *Primate vocal communication* (eds D. Todt, P. Goedeckinck & D. Symmes), pp. 3–14. Berlin, Germany: Springer.
 - 58 Philips, M. & Austad, S. N. 1990 Animal communication and social evolution. In *Interpretation and explanation in the study of animal behavior* (eds M. Bekoff & D. Jamieson), pp. 254–268. Boulder, CO: Westview.
 - 59 Hauser, M. D. 1996 *The evolution of communication*. Cambridge, MA: MIT Press.
 - 60 Blumstein, D. T. & Armitage, K. B. 1999 Cooperative breeding in marmots. *Oikos* **84**, 369–382. (doi:10.2307/3546418)
 - 61 Armitage, K. B. 1981 Sociality as a life-history tactic of ground squirrels. *Oecologia* **48**, 36–49. (doi:10.1007/BF00346986)
 - 62 Michener, G. R. 1983 Kin identification, matriarchies, and the evolution of sociality in ground-dwelling sciurids. In *Advances in the study of mammalian behavior* (eds J. F. Eisenberg & D. G. Kleiman), pp. 528–572. Stillwater, OK: American Society of Mammalogists.
 - 63 Blumstein, D. T. 2007 The evolution of alarm communication in rodents: structure, function, and the puzzle of apparently altruistic calling in rodents. In *Rodent Societies* (eds J. O. Wolff & P. W. Sherman), pp. 317–327. Chicago, IL: University of Chicago Press.
 - 64 Blumstein, D. T. 1999 Alarm calling in three species of marmots. *Behaviour* **136**, 731–757. (doi:10.1163/156853999501540)
 - 65 Robinson, S. R. 1981 Alarm communication in Belding's ground squirrels. *Z. Tierpsychol.* **56**, 150–168. (doi:10.1111/j.1439-0310.1981.tb01293.x)
 - 66 Burke da Silva, K., Kramer, D. L. & Weary, D. M. 1994 Context-specific alarm calls of the eastern chipmunk, *Tamias striatus*. *Can. J. Zool.* **72**, 1087–1092. (doi:10.1139/z94-146)
 - 67 Blumstein, D. T. 1995 Golden marmot alarm calls. I. The production of situationally specific vocalizations. *Ethology* **100**, 113–125.
 - 68 Matrosova, V. A., Blumstein, D. T., Volodin, I. A. & Volodina, E. V. 2011 The potential to encode sex, age, and individual identity in the alarm calls of three species of Marmotinae. *Naturwissenschaften* **98**, 181–192. (doi:10.1007/s00114-010-0757-9)
 - 69 Harrison, R. G., Bogdanowicz, S. M., Hoffmann, R. S., Yensen, E. & Sherman, P. W. 2003 Phylogeny and evolutionary history of the ground squirrels (Rodentia: Marmotinae). *J. Mamm. Evol.* **10**, 249–276. (doi:10.1023/B:JOMM.0000015105.96065.f0)
 - 70 Herron, M. D., Castoe, T. A. & Parkinson, C. L. 2004 Sciurid phylogeny and the paraphyly of Holarctic ground squirrels (*Spermophilus*). *Mol. Phylogenet. Evol.* **31**, 1015–1030. (doi:10.1016/j.ympev.2003.09.015)
 - 71 Steppan, S. J., Kenagy, G. J., Zawadzki, C., Robles, R. & Lyapunova, E. A. 2011 Molecular data resolve placement of the Olympic marmot and estimate dates of trans-Beringian interchange. *J. Mammal.* **92**, 1028–1037. (doi:10.1644/10-MAMM-A-272.1)
 - 72 Manser, M. B., Seyfarth, R. M. & Cheney, D. L. 2002 Suricate alarm calls signal predator class and urgency. *Trends Cogn. Sci.* **6**, 55–57. (doi:10.1016/S1364-6613(00)01840-4)
 - 73 Beecher, M. D. 1982 Signature systems and kin recognition. *Am. Zool.* **22**, 477–490.
 - 74 Pollard, K. A., Blumstein, D. T. & Griffin, S. C. 2010 Pre-screening acoustic and other natural signatures for use in noninvasive individual identification. *J. Appl. Ecol.* **47**, 1103–1109. (doi:10.1111/j.1365-2664.2010.01851.x)
 - 75 Hare, J. F. 1998 Juvenile Richardson's ground squirrels, *Spermophilus richardsonii*, discriminate among individual alarm callers. *Anim. Behav.* **55**, 451–460. (doi:10.1006/anbe.1997.0613)
 - 76 Blumstein, D. T., Verneyre, L. & Daniel, J. C. 2004 Reliability and the adaptive utility of discrimination among alarm callers. *Proc. R. Soc. Lond. B* **271**, 1851–1857. (doi:10.1098/rspb.2004.2808)
 - 77 Pollard, K. A. 2011 Making the most of alarm signals: the adaptive value of individual discrimination in an alarm context. *Behav. Ecol.* **22**, 93–100. (doi:10.1093/beheco/arq179)
 - 78 Cheney, D. L. & Seyfarth, R. M. 1988 Assessment of meaning and the detection of unreliable signals by vervet monkeys. *Anim. Behav.* **36**, 477–486. (doi:10.1016/S0003-3472(88)80018-6)
 - 79 Gouzoules, H., Gouzoules, S. & Miller, K. 1996 Skeptical responding in rhesus monkeys (*Macaca mulatta*). *Int. J. Primatol.* **17**, 549–568. (doi:10.1007/BF02735191)
 - 80 Hare, J. F. & Atkins, B. A. 2001 The squirrel that cried wolf: reliability detection by juvenile Richardson's ground squirrels (*Spermophilus richardsonii*). *Behav. Ecol. Sociobiol.* **51**, 108–112. (doi:10.1007/s002650100414)
 - 81 Krams, I., Krama, T. & Igaune, K. 2006 Alarm calls of wintering great tits *Parus major*: warning of mate, reciprocal altruism or a message to the predator? *J. Avian Biol.* **37**, 131–136. (doi:10.1111/j.0908-8857.2006.03632.x)
 - 82 Tibbetts, E. A. 2004 Complex social behaviour can select for variability in visual features: a case study in *Polistes* wasps. *Proc. R. Soc. Lond. B* **271**, 1955–1960. (doi:10.1098/rspb.2004.2784)
 - 83 May-Collado, L. J., Agnarsson, I. & Wartzok, D. 2007 Phylogenetic review of tonal sound production in

- whales in relation to sociality. *BMC Evol. Biol.* **7**, 1–20. (doi:10.1186/1471-2148-7-1)
- 84 Ramsier, M. A., Cunningham, A. J., Finneran, J. J. & Dominy, N. J. 2010 Social drive and the coevolution of auditory sensitivity with group size in strepsirrhine primates. *Am. J. Phys. Anthropol.* **141**(Suppl. 50), 194.
 - 85 Ramsier, M. A., Cunningham, A. J., Finneran, J. J. & Dominy, N. J. 2012 Social drive and the evolution of primate hearing. *Phil. Trans. R. Soc. B* **367**, 1860–1868. (doi:10.1098/rstb.2011.0219)
 - 86 delBarco-Trillo, J., Sacha, C., Dubay, G. & Drea, C. 2012 *Eulemur*, me lemur: the evolution of scent-signal complexity in a primate clade. *Phil. Trans. R. Soc. B* **367**, 1909–1922. (doi:10.1098/rstb.2011.0225)
 - 87 Gustison, M., le Roux, A. & Bergman, T. 2012 Derived vocalizations of geladas (*Theropithecus gelada*) and the evolution of vocal complexity in primates. *Phil. Trans. R. Soc. B* **367**, 1847–1859. (doi:10.1098/rstb.2011.0218)
 - 88 Stirling, I. & Thomas, J. A. 2003 Relationships between underwater vocalizations and mating systems in phocid seals. *Aquat. Mamm.* **29**, 227–246. (doi:10.1578/016754203101024176)
 - 89 Ord, T. & Garcia-Porta, J. 2012 Is sociality required for the evolution of communicative complexity? Evidence weighted against alternative hypotheses in diverse taxonomic groups. *Phil. Trans. R. Soc. B* **367**, 1811–1828. (doi:10.1098/rstb.2011.0215)
 - 90 Dobson, S. D. 2012 Face to face with the social brain. *Phil. Trans. R. Soc. B* **367**, 1901–1908. (doi:10.1098/rstb.2011.0224)
 - 91 Croft, D. P., James, R. & Krause, J. 2008 *Exploring animal social networks*. Princeton, NJ: Princeton University Press.
 - 92 Wey, T. W. & Blumstein, D. T. In press. Social attributes and associated performance measures in marmots: bigger male bullies and weakly affiliating females have higher annual reproductive success. *Behav. Ecol. Sociobiol.*
 - 93 Kasper, C. & Voelkl, B. 2009 A social network analysis of primate groups. *Primates* **50**, 343–356. (doi:10.1007/s10329-009-0153-2)



Combining the Finite Element Method with Structural Connectome-based Analysis for Modeling Neurotrauma: Connectome Neurotrauma Mechanics

Reuben H. Kraft, Phillip Justin Mckee, Amy M. Dagro, and Scott T. Grafton

PLoS Computational Biology, 8(8), e1002619 (2012)

Combining the Finite Element Method with Structural Connectome-based Analysis for Modeling Neurotrauma: Connectome Neurotrauma Mechanics

Reuben H. Kraft^{1*}, Phillip Justin Mckee², Amy M. Dagro¹, Scott T. Grafton³

1 Soldier Protection Sciences Branch, Protection Division, U.S. Army Research Laboratory, Aberdeen Proving Ground, Maryland, United States of America, **2** Dynamic Science, Inc., Aberdeen Proving Ground, Maryland, United States of America, **3** Department of Psychology, University of California, Santa Barbara, Santa Barbara, California, United States of America

Abstract

This article presents the integration of brain injury biomechanics and graph theoretical analysis of neuronal connections, or connectomics, to form a neurocomputational model that captures spatiotemporal characteristics of trauma. We relate localized mechanical brain damage predicted from biofidelic finite element simulations of the human head subjected to impact with degradation in the structural connectome for a single individual. The finite element model incorporates various length scales into the full head simulations by including anisotropic constitutive laws informed by diffusion tensor imaging. Coupling between the finite element analysis and network-based tools is established through experimentally-based cellular injury thresholds for white matter regions. Once edges are degraded, graph theoretical measures are computed on the “damaged” network. For a frontal impact, the simulations predict that the temporal and occipital regions undergo the most axonal strain and strain rate at short times (less than 24 hrs), which leads to cellular death initiation, which results in damage that shows dependence on angle of impact and underlying microstructure of brain tissue. The monotonic cellular death relationships predict a spatiotemporal change of structural damage. Interestingly, at 96 hrs post-impact, computations predict no network nodes were completely disconnected from the network, despite significant damage to network edges. At early times ($t < 24$ hrs) network measures of global and local efficiency were degraded little; however, as time increased to 96 hrs the network properties were significantly reduced. In the future, this computational framework could help inform functional networks from physics-based structural brain biomechanics to obtain not only a biomechanics-based understanding of injury, but also neurophysiological insight.

Citation: Kraft RH, Mckee PJ, Dagro AM, Grafton ST (2012) Combining the Finite Element Method with Structural Connectome-based Analysis for Modeling Neurotrauma: Connectome Neurotrauma Mechanics. *PLoS Comput Biol* 8(8): e1002619. doi:10.1371/journal.pcbi.1002619

Editor: Olaf Sporns, Indiana University, United States of America

Received: March 22, 2012; **Accepted:** June 6, 2012; **Published:** August 16, 2012

This is an open-access article, free of all copyright, and may be freely reproduced, distributed, transmitted, modified, built upon, or otherwise used by anyone for any lawful purpose. The work is made available under the Creative Commons CC0 public domain dedication.

Funding: This work was funded by the U.S. Department of Defense, Department of the Army. The funders had no role in study design, data collection and analysis, decision to publish, or preparation of the manuscript.

Competing Interests: The authors have declared that no competing interests exist.

* E-mail: reuben.kraft@gmail.com

Introduction

The finite element method is often used to study neurotrauma [1–9] and continues to emerge as a useful tool in the field of neuroscience [10–13]. Models continue to advance in biofidelity by incorporating an increased level of anatomic detail [4,13,14], improved representation of the material behavior at various loading rates [15–20], and advanced measures and predictions of injury [8,21,22]. Finite element models are commonly used to understand the biomechanics of brain and skull deformation when the head is subjected to insult, leading to improved insight into mechanisms of acute injury. For example, modeling axonal injury mechanisms within white matter of the brain has been the focus of some recent efforts and provides a means to relate an insult to a cellular injury mechanism [8]. By using diffusion tensor imaging (DTI) fiber tractography, the structural orientation of neuronal axonal bundles can be incorporated into the finite element model and can be used to compute the axonal strain during brain white matter deformation [8,23]. Then, by using an axonal injury threshold, the occurrence of diffuse axonal injury (DAI) is

predicted [8]. Wright and Ramesh [8] show that the degree of injury predicted is highly dependent on the incorporation of the axonal orientation information and the inclusion of material anisotropy into the constitutive model for white matter. By modeling the underlying mechanism of DAI, an enhanced understanding of the neurotrauma is attained through a spatio-temporal description of tissue deformation. In general, finite element simulations may help to elucidate the injury mechanisms of neurotrauma.

As finite element models advance, experimentally based models of neurotrauma also continue to become more sophisticated, ranging from the macroscopic [24,25] to the cellular level [26–29]. Various biomechanical and physiological injury thresholds for neurotrauma have been proposed in the past, including intracranial pressure [21] and strain [8,30,31]. While these thresholds offer an immediate prediction of injury, they lack a long-term description of functional degradation. A time-evolving injury model is attractive since the biological response occurs on a slower time scale than an injurious stimulus as a consequence of mechanotransduction cascades [27]. There have been significant

Author Summary

According to the Centers for Disease Control and Prevention in the United States, approximately 1.7 million people, on average, sustain a traumatic brain injury annually. During the last few decades, brain neurotrauma biomechanics has been an active area of research involving medical clinicians and a broad range of scientists and engineers. In addition, advances and fast growth of human connectomics continues to reveal new insights into the damaged brain. With recent advances in computational methods and high performance computing, we see the need and the exciting possibility to merge brain neurotrauma biomechanics and human connectomics science to form a new area of investigation - connectome neurotrauma mechanics. For neurotrauma, the idea is simple - inform human structural connectome analysis using physics-based predictions of biomechanical brain injury. If successful, this technique may be further used to inform human functional connectome analysis, thus providing a new tool to help understand the pathophysiology of mild traumatic brain injury.

efforts to develop empirically based time-evolving cellular injury thresholds, which many times use in vitro cellular and tissue culture models. Morrison III et al. [27] suggest that for brain biomechanics, neuronal culture models that accurately mimic specific brain features can be used to explore tissue properties and tolerances or thresholds to mechanical loading. Cell death has been primarily used as a definition of injury within the neuronal culture model community and has been applied to determine tissue-level tolerance criteria using local values of axonal strain, strain rate, and time from “insult” [32,33]. Furthermore, as Morrison III et al. [27] point out, empirical functions for cellular death based on culture models could be incorporated into finite element analyses, thereby enabling biological predictions to supplement mechanical predictions of local tissue stress and strain. In the study presented here, this concept is further explored and used as a bridge to a network-based analysis of the brain.

As physics-based models become more capable of predicting tissue-level injury mechanisms from improved computational and experimental resources for biomechanics, there remains a need to understand how structural damage in a given location of the brain evolves, and how it may influence functional or cognitive performance over time. Such a goal is complex and difficult. For example, as Kaiser et al. point out [34], in some instances the brain can be robust to physical damage, and in other instances physical damage can cause severe functional deficits. Nevertheless, Kaiser et al. [34] pursue the important and unanswered question: Are the severity and nature of the effects of localized damage predictable? To help explore the answer to this question, tools are being developed for the quantitative analysis of brain network organization, based largely on graph theory [35,36]. Typically, network nodes represent brain regions, often obtained from high resolution magnetic resonance imaging (MRI). The network links or edges between brain regions represent interregional pathways that convey neuronal signals and are commonly obtained from non-invasive DTI or diffusion spectrum imaging (DSI) [37,38]. The connection matrix of the network of the human brain forms the so-called “human connectome” [35,36,39,40]. Recently, Jirsa et al. [41] used connectomics to establish a framework for a “virtual brain”, in which network modeling is used to understand the intact and damaged brain. Similar to previous work, hypothetical or random deletion of nodes or edges were used to

degrade the structural connectome [42]. More recently, structural and diffusion images from 14 healthy subjects were used to create spatially unbiased white matter connectivity importance maps that quantify the amount of disruption to the overall brain network that would be incurred if that region were compromised [43]. In this study, we attempt to extend the capabilities of neurocomputational models by providing a physics-based approach for predicting degraded regions of interest. Physics-based injury predictions may help inform structural connectome analysis.

In this study, neurotrauma is investigated by using finite element simulations of a single individual subjected to a simulated head impact. Tissue damage is computed using empirically based damage models that provide a link from macroscopic biomechanical deformation to mesoscopic damage. Axonal bundle tracts are explicitly modeled using a multiscale description of white matter tracts obtained from diffusion tensor imaging. Then, using the physics-based injury predictions for white matter tissue from finite element simulations, the structural brain connectivity or connectome is degraded, and various network measures are computed. This is an important contribution because finite element simulation predictions of tissue damage provide physics-based reasoning for removing nodes or degrading edges to create the “damaged” brain connection matrix. In turn, this approach may provide further insight into mild traumatic brain injury by shedding light on the relationship between mechanical stimulus to the brain and neurobiological processes that result. Furthermore, if successful, the computational framework presented herein could supplement ongoing efforts to evaluate the use of non-invasive medical imaging tools, such as diffusion tensor and spectrum imaging, to detect white matter disruption for neurotrauma diagnostics [44,45] by providing a time-evolving history of tissue injury.

Methods

A suite of medical imaging and software tools are used to obtain an individual-specific finite element model and structural connectome-based analysis. The overarching process is schematically shown in Figure 1 and is outlined below.

Individual Specific Models

T1 and diffusion tensor magnetic resonance images are taken from a single individual (the corresponding data can be found in [37]). The T1 image (Figure 1a) is segmented into different head materials (Figure 1b) using the software Amira [46] and the Connectome Mapper Toolkit [47]. The segmented geometry is then used to create a biofidelic three-dimensional finite element volume mesh (Figure 1c). In order to create a corresponding structural connectome or network, the T1 image is parcellated into 83 regions of interest (ROI) representing the location of anatomical regions of the brain based on the Desikan-Killiany atlas extended to include subcortical regions [48]. Since diffusion tensor images (Figure 1e) are used to generate axonal bundle fiber tractography based on the direction of peak water diffusion in each voxel [49], the DTI fiber tractography (Figure 1f) represents the approximate location of neuronal axonal bundles [50]. Fibers are filtered for connectome creation to include only fibers that begin and end within ROI. The structural connectome is assembled using the Connectome Mapper Toolkit [47] and is composed of nodes representing ROI generated at the centroid, connected by edges that represent structural pathways for which the DTI tractography traverses. Following the segmentation enabled by the Desikan-Killiany brain atlas, there are 83 network nodes and 1029 network edges. Furthermore, DTI fiber tractography is

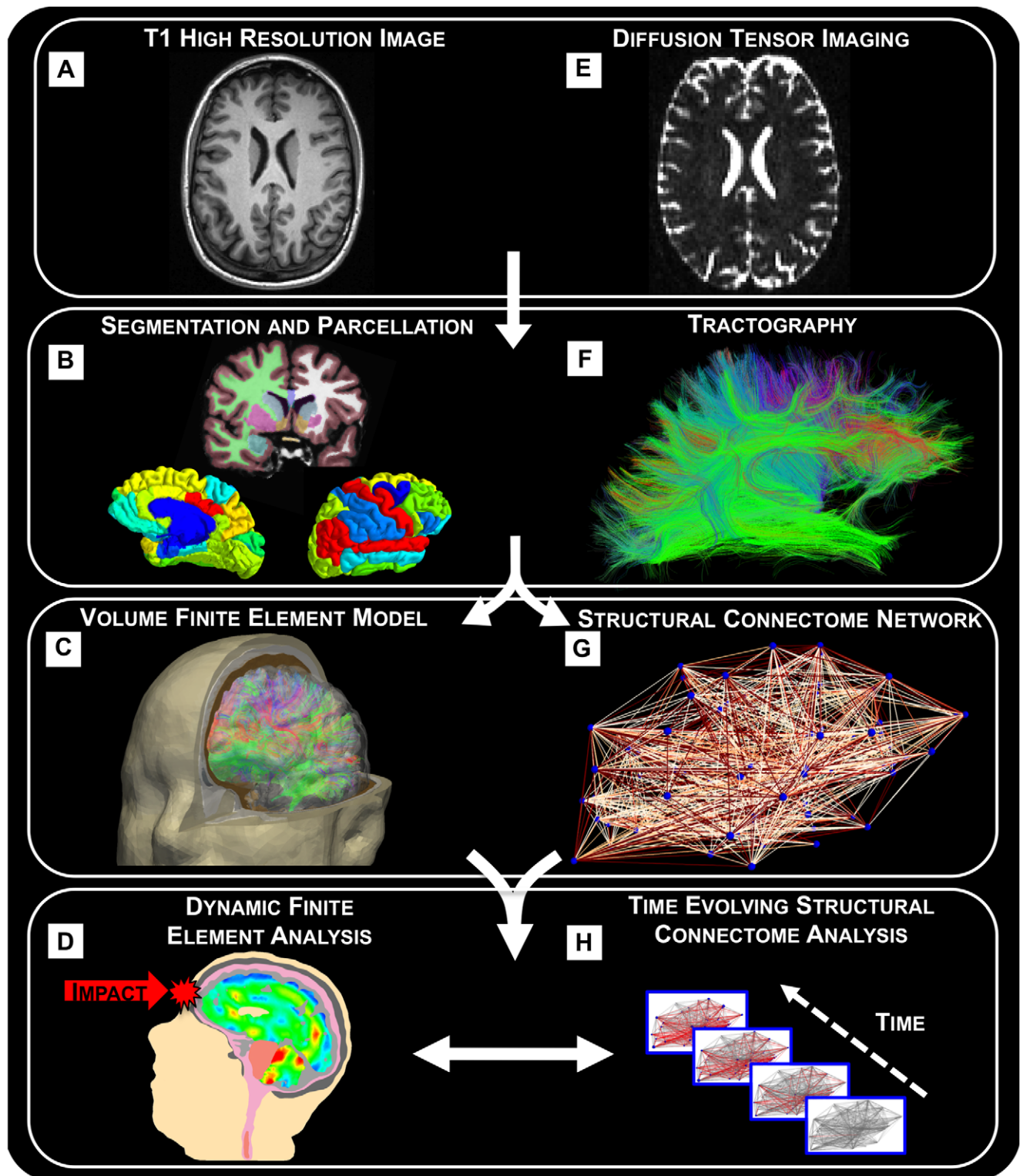


Figure 1. A flowchart of the process for creating the finite element model and connectome from T1 and diffusion MRI. (a) The T1 image is (b) segmented into different head materials. The segmented geometry is then used to create (c) a biofidelic three-dimensional finite element volume mesh. The mesh is required for (d) an explicit dynamic finite element simulation that captures the biomechanical response from frontal impact. (e) Diffusion tensor images are used to generate (f) axonal bundle fiber tractography which is used to inform finite element transversely isotropic constitutive descriptions of white matter tissue behavior (c). Tractography is also used to create (g) a network model of the brain that can be (h) degraded over time.

doi:10.1371/journal.pcbi.1002619.g001

incorporated into the finite element model by using a transverse isotropic material model specifically developed for representing white matter tissue [23,51] where each finite element within white matter regions is assigned an orientation based on the superposition of fiber tractography [52]. Details of the numerical implementation are published elsewhere [52], but it is important to point out that various different cases needed to be considered while assigning one orientation per finite element. For example, in the case of multiple fibers that overlap the spatial bounds of a single element, the multiple fiber orientations were averaged.

Damage and Injury Thresholds for Coupling FEM Results to the Connectome Analysis

Herein, finite element simulations of the human head are designed to mimic experimental conditions for cadaveric impact tests, which are conducted to understand the dynamics of a frontal impact and the associated compression-tension damage [53]. In this study, the explicit dynamic finite element method [54] is used to capture the transient response of head impact. Supplementary information about the finite element method is included in the supporting information, Text S1. In addition to a volume mesh for the head, the finite element model also requires material constitutive descriptions and properties for all its components: skull, cortex, brain stem, cerebrospinal fluid, and soft tissue, which represents a homogenized mixture of muscle and skin. A detailed list of the material constitutive laws used to relate tissue strain to stress is included in the supporting information, Text S2. Once again, we point out that diffusion tensor imaging is used to inform the constitutive model for white matter tissue, which has been applied in the past for studying non-human primates [31] and human injury [8,22,55]. The entire finite element model consisted of 1,394,945 tetrahedral elements and 237,115 finite element nodes. For boundary conditions, the bottom of the neck is fixed, and a force was applied to a circular area on the forehead (about 3 mm^2) in the anteroposterior direction. The input force-time curve was a sinusoidal shape with a peak force of 7,000 N at 2.75 ms. The finite element simulation computes the time-evolving mechanical strain and stress in the direction of axonal fiber bundles. The strain in the direction of axonal bundles is referred to as the axonal strain.

One limitation of the current finite element model is the exclusion of viscoelasticity in the constitutive description of brain matter. The authors acknowledge that to accurately model the progression of damage, the constitutive model should be extended to account for the time-dependent behavior of brain tissue. The exclusion may have an effect on the outcome of our results, leading to larger shear stresses, but smaller shear strains, thus, less predicted damage. For example, Chafi et al. [56] shows that viscoelasticity plays a major role in the dynamic response of the brain under blast loading. Future efforts are focused on improving the mechanical description of brain tissue.

In order to model damage using a physics-based approach, either an explicit failure mechanism should be modeled or an empirically based failure threshold is required. For this study, measures of axonal strain and strain rate computed for white matter regions are used as input for empirically based injury threshold predictions that are obtained from cellular culture experiments. Specifically, experimental results for cellular death are described using a mathematical function for tolerance criteria that relates strain to resultant cell death evaluated for up to four days post-injury [27,32,33]. Experimental data exists for the CA1 and CA3 regions of the hippocampus, dentate gyrus, and cortex for the rat. Experiments suggest that some regions of the rat brain are sensitive to loading rate, while other brain regions are not.

That is, Elkin et al. [33] found that cortical cell death was dependent on applied strain rate, whereas hippocampal cell death was not. The relations used in the present model, obtained from Morrison III et al. [27], are:

$$D_{CA1/CA3} = 0.0389 \left[\varepsilon^{0.3663} \right] \left[t^{2.015} \right] \quad (1)$$

$$D_{DG} = 0.0323 \left[\varepsilon^{0.3721} \right] \left[t^{1.8209} \right] \quad (2)$$

$$D_{Cortex} = 0.094 \left[\varepsilon^{1.5293} \right] \left[t^{0.8337} \right] \left[\dot{\varepsilon}^{0.1175} \right] \quad (3)$$

where t is time from insult, ε is the local strain, and $\dot{\varepsilon}$ is the local strain rate [27]. Similar to Morrison III et al. [27], the units of time are days, strain is dimensionless and strain rate is inverse seconds. The damage parameter, D , is defined as the percent area of cell death. Using Equations 1–3, the axonal strain and strain rate from the finite element simulations, as well as time, are used to calculate percent cell death for a tissue region. Due to insufficient resolution of the MRI data used in this study, segmentation of the hippocampus into CA1, CA2 and dentate gyrus regions was not possible, thus the more conservative equation for D_{DG} was used to compute cell death for the entire hippocampus. Equations 1–3 are monotonic functions that only increase with time, thus cellular repair mechanisms and regeneration are not currently captured. Potential issues with monotonic cellular death predictions, as well as using rat brain injury thresholds instead of human cellular injury thresholds, will be discussed later. Since the explicit dynamic finite element method is used, the transient wave propagation for solid mechanics is resolved; however, this is computationally costly and limits the total time of biomechanical prediction. The explicit dynamic simulation runs to 15 ms, thus the “long-term” structural mechanics of brain swelling, relaxation, etc., are not captured in the current model, although could be adapted in the future by using quasi-static, implicit finite element solvers.

The reader should understand that we use the local tissue strain and strain rates predicted from finite element simulations of short duration, about 15 ms, as input to experimentally based cellular death models that were developed over a 96 hour period. This assumes that the tissue damage due to large deformations occurs immediately and initiates an injury process that grows with time. This assumption is based on the observation that cell death was not immediate in response to deformation, but instead, increased over 4 days after injury [27].

It should be noted that the cellular death estimates that Morrison III et al. [27] developed were not based on axonal strain but instead on nominal strain applied to the back of the substrate on which the neuronal cells were attached. Thus, Equations 1–3 may not accurately describe the actual relationship between axonal strain and injury. Furthermore, the neuronal cell bodies in the experiments were not aligned in a specific orientation, so the response is not strictly representative of axonal strain injury. There are research efforts examining stretching of individual axons but have not proposed empirical relationships for cellular death in terms of applied strain, rate of loading and time from insult [57,58]. Experimental measurements of the cellular response of white matter, especially axonal bundles, would be interesting to explore and could provide a more accurate representation of cell damage in the future.

Furthermore, the experiments performed by Morrison III et al. [27] used the rat hippocampus, which is mostly comprised of gray

matter. Thus, it should be noted that the empirical data described in Equations 1–3 was not intended to describe white matter injury response so there may be limitations in applying Equations 1–3 to predict cellular white matter injury. Cellular injury threshold data for isolated white matter is currently limited; however there have been some efforts to characterize mechanical damage to axons [57–59]. We hope a computational framework described here will help to motivate efforts to obtain different white matter and gray matter empirical functions, which could then be used for each of region of the brain separately. As mentioned before, the application of this approach raises the possible need for understanding properties of white matter fiber bundles.

In order to map the finite element results to network-based analysis tools, output data from each finite element that represents white matter is mapped to a corresponding voxel in the MRI data that is used to create the DTI tractography. This mapping is referred to as the element-to-voxel map. Multiple finite elements within a single voxel are averaged. The element-to-voxel map enables voxels to be assigned additional data, including axonal strain and strain rate from the finite element simulation. Alstott et al. [42] chose to generate brain lesions by altering the structural connectivity matrix of the brain by deleting nodes using various methods. In the present work, instead of deleting nodes, we degrade the edges of the network based on the computed cellular death at the voxel level.

To understand how the structural network is degraded, consider the schematic shown in Figure 2. Edges in the network are constructed from voxels that connect two different ROIs. The edge strength is relative to the number of tracts between two ROI. Cellular death for each voxel is computed using Equations 1–3 and may grow to reach the chosen critical value of cellular death, D_c (discussed shortly). Voxels with a predicted cellular death greater than D_c are shown in red in Figure 2. For this study, if a tract traverses a voxel that is greater than the threshold, the entire tract is considered damaged, thus the edge strength is decreased. This procedure is similar to that used by Kuceyeski et al. [43] who simulated lesions at each voxel and removed tracts passing through the lesion in order to create a damaged network to enable analysis of changes in network measures and the evaluation of the importance of each voxel. Similar to Honey et al. [60], the connection strengths were resampled to a Gaussian distribution with a mean of 0.5 and a standard deviation of 0.1. As Alstott et al. point out [42], this transformation does not alter the rank-ordering of strong to weak pathways, but simply compresses the scale of connection strengths. There are other possible ways to degrade the structural network that will be discussed later.

Since Equations 1–3 predict some degree of cell death for non-zero values of axonal strain, strain rate, and time, the additional critical value of cell death, D_c , was required as a rule in order to degrade a voxel. The critical cellular death of $D_c = 3\%$ was chosen

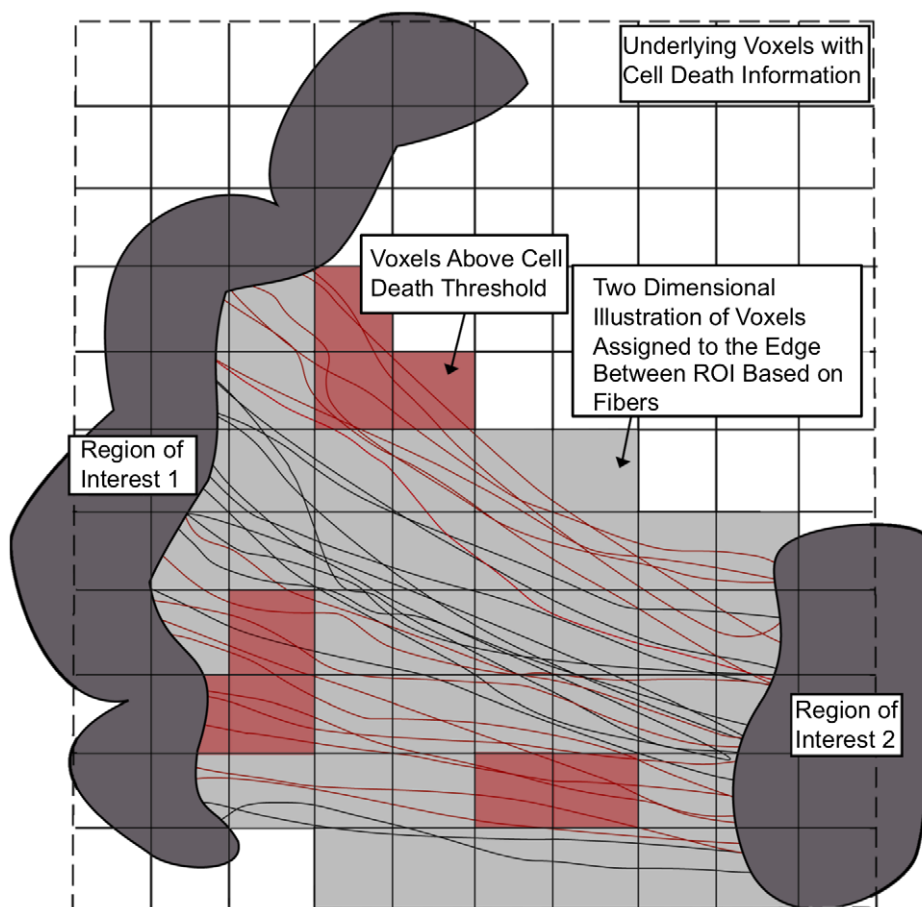


Figure 2. Schematic showing how structural network edges are degraded over time. Red voxels indicate that the chosen critical cellular death threshold, D_c , is reached. For this study, DTI tracts that traverse a damaged voxel are removed, thus degrading the connection strength of the network edge.

doi:10.1371/journal.pcbi.1002619.g002

because it predicted similar levels of damage as compared to other proposed thresholds, including 18% axonal strain, which was used previously as a threshold that indicated degradation in electrophysiological function [30]. During the calculation of cellular death, positive values of strain and strain rate were used (negative strain was not used to calculate cellular death). The choice of injury threshold, as well as the micromechanics of axonal fiber bundles, is an active area of research that would assist making the current methodology more accurate in the future. During the 15 ms dynamic simulation, strain and strain rate data for each voxel is output at 0.1 ms increments. Cell death is calculated at each voxel for each of these increments. Then, the maximum cell death value calculated in each voxel is used to predict cell death up to 96 hrs. It is important to note that cell death calculations are the result of the combination of variables at each increment rather than considering each variable independently.

Results

Finite Element Analysis of Head Impact

The deformed configurations of the head, along with contours and response curves for various locations within the brain (frontal, parietal, occipital, temporal, corpus callosum and cerebellum) are shown in Figures 3a–f. Output variables including pressure, axonal strain, and effective strain rate, useful for understanding the anisotropic biomechanical response for white matter, are shown. Confidence in the finite element model is established by comparing output from the computations to pre-existing experimental data on cadaveric head impact [53]. The values of axonal strain and strain rate were taken from specific locations in each of the six regions plotted in Figure 3. Four out of six of the locations represented the locations of the pressure transducers for the experiments of Nahum et al. [53]. Locations within the cerebellum and corpus callosum were also added for the strain and strain rate analysis. A variation of results will exist in each region, and taking an average of values in a anatomical region could help resolve this problem, but including simulation data points that are located farther from the experimental sampling points could also make the results less accurate. The head impact simulation took about 30 hours on 32 processors in order to reach 15 ms.

As seen in Figure 3b, the intracranial pressure quickly increases to positive values in the frontal and parietal regions, while quickly increasing to negative pressures in the occipital and posterior fossa regions. The anteroposterior pressure gradient (seen in Figure 3a) is commonly observed in experimental and computational studies - giving rise to the so-called coup and contrecoup loading scenario, for which there are an associated number of proposed injury mechanisms. Short duration intracranial pressure gradients with high positive pressures are observed at the coup region, with negative pressures at the contrecoup region. The maximum positive pressure of approximately 160 kPa is reached in about 2.5 ms in the frontal lobe, closest to the impact, while the maximum negative pressure of approximately -80 kPa is reached in about 2.0 ms in the posterior fossa region. The computed pressure response is directly compared to Nahum et al.'s [53] experimental results in Figure 3b and show similar trends. In addition, validation of the strain response against cadaveric experiments of Hardy et al. [61] is also described in the Supplemental Text S3.

Axonal strain at the various brain regions responds slower than the pressure response. The axonal strain begins to substantially grow at 1 ms and shows a gradual rate of change of strain, with a maximum of 33% at 12 ms over the duration of the simulation within the temporal region. Unlike the pressure, an obvious

transcranial gradient is not apparent for the axonal strain. While the frontal region had the highest predicted pressure, the temporal and occipital brain locations have the largest values of axonal strain in the regions specifically examined. Later, in the structural network analysis, these areas are associated with the largest amount of cellular death. Interestingly, if a threshold of injury of 18% axonal strain is chosen [8,30], our results show the onset of injury occurs at approximately 9.1 ms within the temporal lobe, despite the intracranial pressure reaching approximately 100 kPa in 2 ms. The time scales at which the pressure and strain grow will be discussed later in the context of injury cascades.

The effective strain rate, also commonly referred to as rate of loading or loading rate, has a maximum value of approximately 85 s^{-1} in the temporal lobe. From the contours shown in Figure 3e there appears to be a strain rate focusing, with lower strain rates closer to the skull and higher values more central to the brain. Shear strain focusing has been reported earlier [3,62] and is attributed to the partial conversion of energy of the axial impact into a shear mechanical stress wave as a result of the material response of the brain, cerebrospinal fluid, and skull [62]. The maximum strain rate is observed before maximum axonal strain because the axonal strain accounts for magnitudes of deformation, while the strain rate relates to the rate of change of strain.

FEM Informed Structural Connectome Analysis

The axonal strain and strain rate output from the finite element simulations are used to compute the amount of cellular death, according to Equations 1–3. Figure 4 shows the evolution of damaged tractography up to 96 hrs post-impact, using a critical cellular death of $D_c = 3\%$ as a threshold for injury and the corresponding evolution of the degraded structural network for sagittal and transverse views. The edges in the network, which are fully damaged, are shown in red for visualization. In reality, each edge is weighted and has degraded values before it is fully damaged. The network nodes are scaled by the percentage of connections that were removed, so that larger nodes have lost more connections compared to original values ($1 - [\text{Degree}_{\text{new}} / \text{Degree}_{\text{original}}]$). The sagittal and transverse views are shown to provide insight about where the damage is predicted and how it progresses through time. At 24 hrs, the top four regions affected include the cuneus (medial surface of left cerebral hemisphere in the occipital lobe), fusiform gyrus (temporal lobe), lingual gyrus (occipital lobe), and pericalcarine. Together, damage in these brain regions have 559 tractography fibers removed from network edges. Note that the total number of fiber tracts prior to impact was 497,442, so this damage corresponds to a 0.011% degradation of tractography. The percentage of fully degraded edges for 24, 48, 72, and 96 hrs are listed in Table 1. Using an 18% strain criterion, 17.3% of the edges were fully degraded.

Figure 4b shows that structural damage occurs first in left cuneus and the right superiotemporal regions, resulting in one fully damaged edge at 24 hrs. The edge between the two regions had only three tract fibers with less than one voxel or 2 mm between them. The edge also had a high mean fiber length of 131.7 mm (the original total mean fiber length was 81.7 mm). This suggests that network edges associated with few tract fibers and long fiber length are more susceptible to damage. Asymmetry of the predicted damage occurs due to the asymmetry of the underlying anatomy associated with the finite element mesh, as well as potential asymmetry of the fiber tractography, which has been studied in recent work [63]. At 48 hrs, predicted damage seems to show a high density of damaged fibers in the anteroposterior direction in both hemispheres of the brain. Lateral tractography damage is also predicted within the corpus collusum. As time

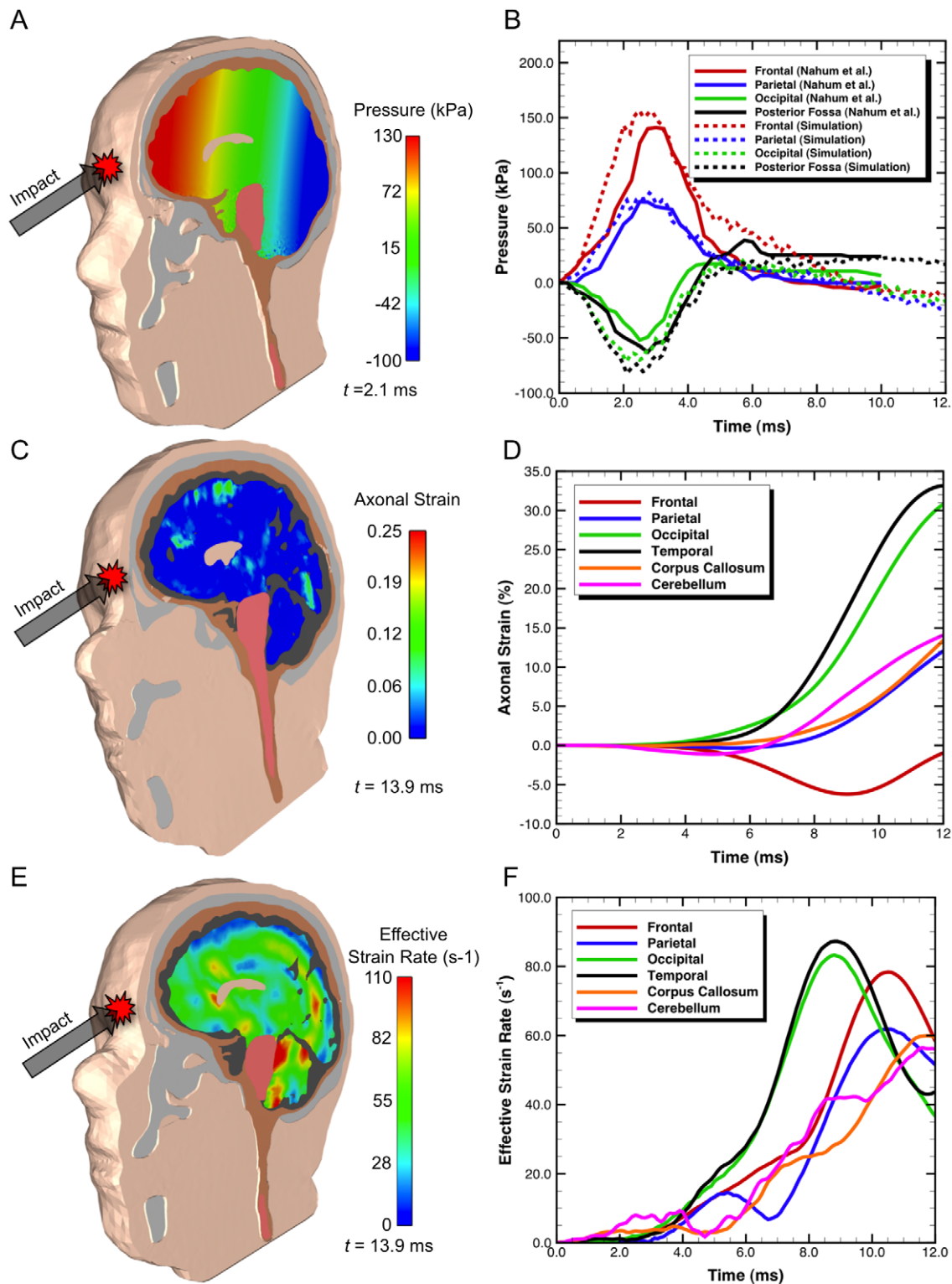


Figure 3. Orthographic view of the local three-dimensional response measured at various locations in the brain for (a–b) pressure, (c–d) axonal strain and (e–f) strain rate predicted using a finite element simulation for impact to the head. Prediction of the intracranial pressure response is compared to cadaveric experiments [53] and is shown in (b).
doi:10.1371/journal.pcbi.1002619.g003

progresses, fully damaged rostrocaudal tracts are predicted and continue to increase.

Structural changes to the tractography and resulting network arise because of the underlying voxel condition. That is, if a tract

goes through a voxel that has reached the critical cellular death value, D_c , the tract is removed. Therefore, it is useful to examine how the inherent voxel properties influence results. Figure 5a shows the distribution of voxels above the predicted critical cellular

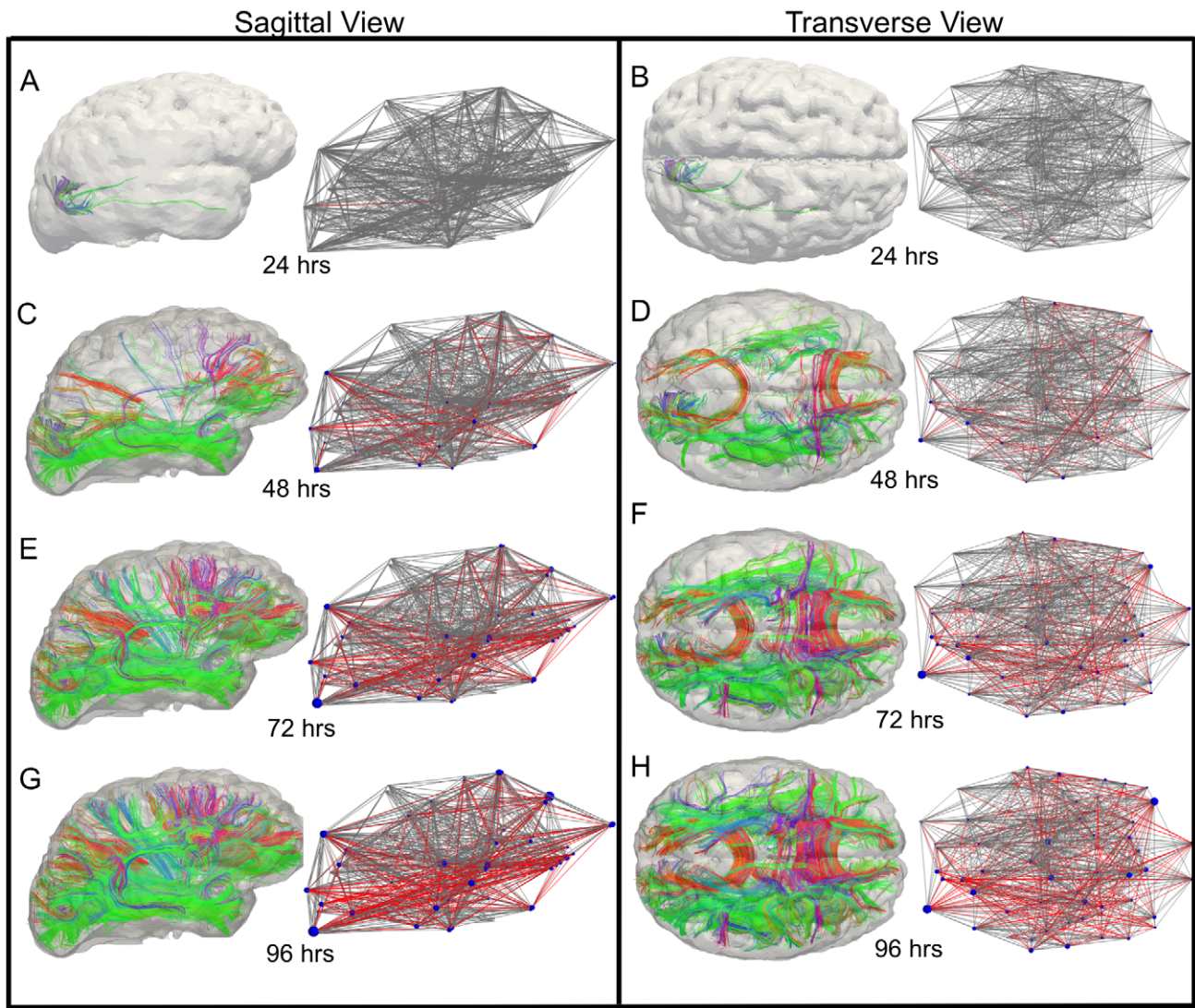


Figure 4. Evolution of damaged tracts and the corresponding structural networks. Using empirically-based cellular death predictions obtained from in vitro models of neural tissues, local strain and strain rate values computed from finite element simulations are used to specify injury. A computed cellular death of 3% was used as a critical value for defining white matter disruption. Damage is shown in red and the node size represents the percent change of degree. The predicted evolution of damage is shown for the sagittal and corresponding transverse views for 24 (a and b), 48 (c and d), 72 (e and f), and 96 hours (g and h).
doi:10.1371/journal.pcbi.1002619.g004

death of 3% as a function of angle between the axonal fiber bundle direction and the direction of the head impact (i.e., frontal impact on the anteroposterior axis). If the tract fiber direction within a

Table 1. The percentage of fully degraded edges and percentage of voxels above the 3% threshold for 24, 48, 72, and 96 hrs post-injury.

Post-Injury (hrs)	% Fully Damaged	% Voxels Above
	Edges	3% Threshold
24	0.097	0.008
48	7.19	1.1
72	14.1	2.7
96	19.7	4.2

doi:10.1371/journal.pcbi.1002619.t001

voxel is parallel with the impact direction, the angle is zero. This shows the distribution of damage as a function of angle with respect to the impact direction. Because of the high degree of mechanical rotation observed through the shear focusing in the temporal and occipital brain regions, tract fibers with large angles with respect to the impact direction are damaged initially. This is seen in Figure 5a at 24 hrs (see red bars in plot) and in Figure 4a–b.

This data can be further analyzed by normalizing the number of damaged voxels for a given orientation by the *total* number of undamaged voxels with a given orientation from the impact direction. This measure is referred to as the angle-normalized number of damaged voxels. The distribution of angle-normalized number of voxels is shown in Figure 5b, and is important because it takes into account the original distribution of the number of tract fibers eligible to be damaged with respect to the impact direction. For example, Figure 5a shows 18 voxels above the 3% cell death threshold at 48 hrs; thus, one might assume that axonal bundles oriented 0–10° from the impact direction have little importance.

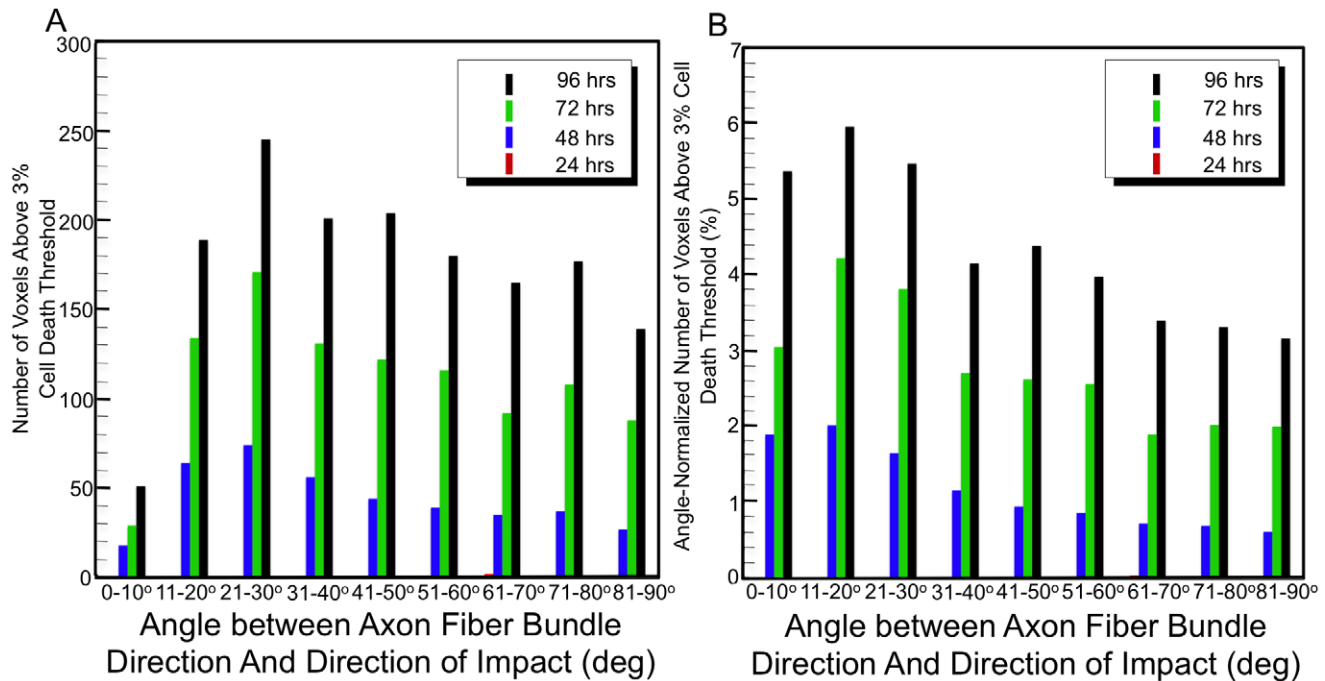


Figure 5. Distribution of (a) the number of voxels with predicted cellular death above 3% for each day as a function of angle between axonal fiber bundle direction and direction of impact to the head, and (b) the number of voxels with predicted cellular death above 3% for each day as a function of angle between axonal fiber bundle direction and direction of impact to the head normalized by the initial distribution of fiber angle with respect to the loading condition.

doi:10.1371/journal.pcbi.1002619.g005

However, when the original number of voxels available to be damaged is taken into consideration (Figure 5b), 11–20° angles have the highest percentage of damage at 48 hrs. In other words, depending on the underlying white matter microstructure, i.e., the axonal bundle orientation, with respect to the direction of impact, the node, and edge degradation in the structural network may be affected differently. This is directly related to the structural mechanics (as opposed to structural connectomics) of the underlying constitutive or material law used within the finite element simulation.

However, because a monotonic function is used to describe the empirical cellular death prediction, this trend becomes more dilute as time progresses (but should not be extrapolated past 96 hrs since Equations 1–3 are not validated beyond that time). From Figure 4g–h, at 96 hours the predicted damaged axonal pathways can be seen in many directions and across all white matter brain regions indicating diffuse structural degradation. To summarize, at 24 hrs fibers in the areas of large rotational tissue strain are susceptible, while at greater times, neuronal tracts that align with the direction of impact seem more susceptible to damage (using the assumed threshold of cellular death). In the future, additional empirical cellular death predictions that are non-monotonic (if valid), or cellular regeneration and repair models, would be useful to explore.

Figure 6a–e shows the evolution of the structural connectivity strength matrices predicted as a result of head impact simulations. The original structural connectivity strength is defined as a Gaussian distribution, created by using a mean of 0.5 and standard deviation of 0.14 distributed over the total number of edges in the network. Each figure represents a snapshot in time starting with $t=0$ and ending at 96 hours. Within the 96 hr period (for which the monotonic cellular death criteria are validated), as long as regions have non-zero strain and strain rate computed

from the finite element simulation, edges in the network become degraded. This decline in network strength is evident in Figure 6e. Since a 3% critical cellular death value is only one possible injury criteria that could be chosen, an additional criterion was examined. Results using two different damage thresholds are shown in Figure 6e and f. Figure 6e is the connection matrix using the 3% threshold at 96 hrs, while Figure 6f is connection matrix using the 18% axonal strain threshold at $t=15$ ms, as used in previous work [8,31]. Connection strengths show qualitatively similar trends in magnitude and location of edge degradation. While the two criteria offer a similar prediction of network damage, the cellular death Equations 1–3 are, perhaps, more useful because effects of strain, strain rate, and time have been decomposed into separate multiplicative terms that allow a compartmentalized study of extrinsic biomechanical conditions.

In general, a network's global efficiency represents how well-connected the network is compared to a perfectly connected network [64] and captures the network's capacity for communication along short paths [65]. Herein, values are reported as normalized global efficiency, which is the global efficiency of the network divided by the efficiency of an ideal network. Ideal network efficiency is calculated as a network where all nodes are connected at the minimum cost. The cost for each edge is defined as unity minus Gaussian strength. While strength offers a measure of the capacity to send information, the cost indicates the resistance to sending information - connections with high strength are low in cost. Local efficiency is a network measure that Latora [65] suggests helps to reveal the fault tolerance of the network system and shows how efficient communication between first node neighbors is. For this study, local efficiency is calculated for the same set of nodes used to make the local network of the undamaged network, even if a node loses its edge to the primary node. This method is used to provide a more direct comparison of

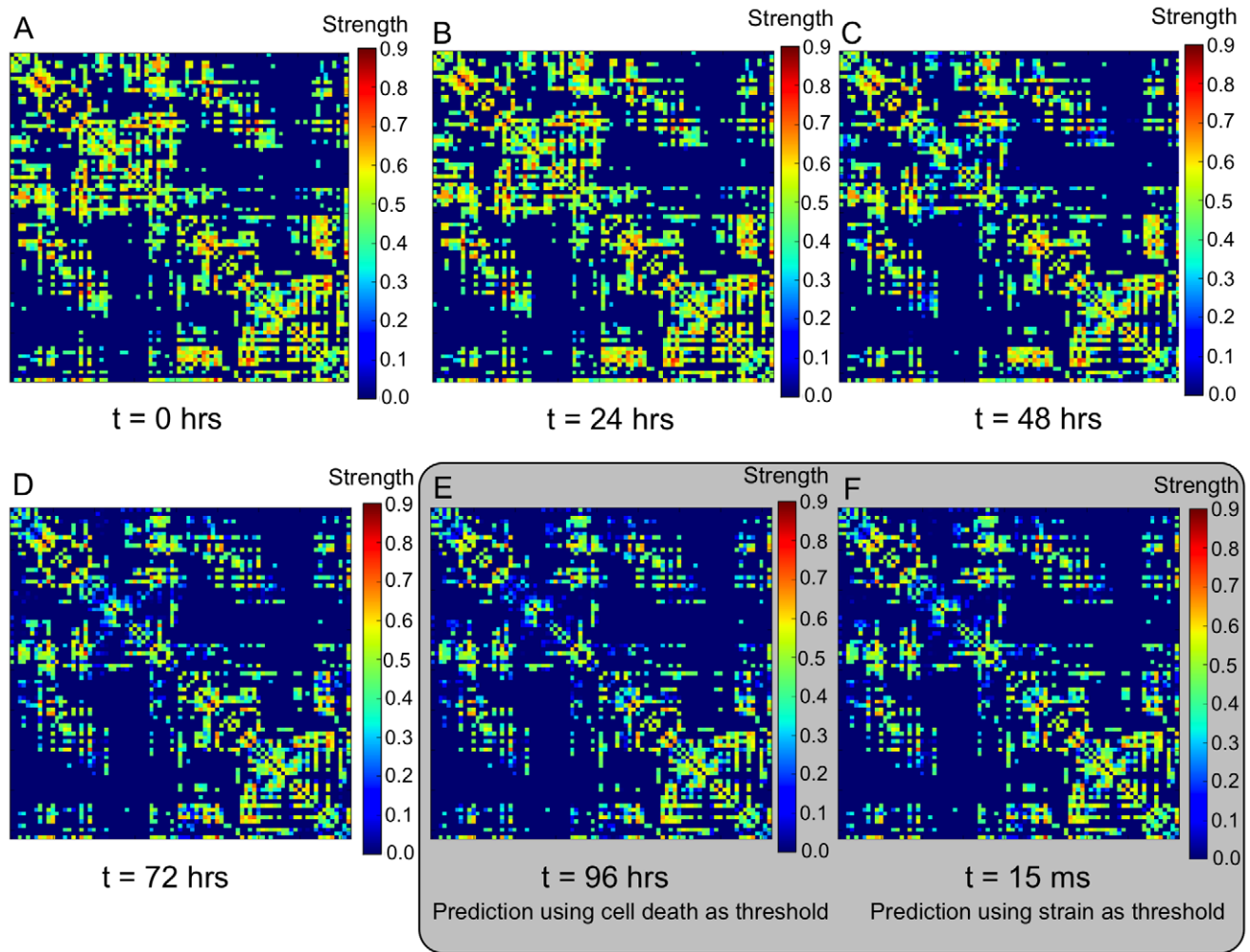


Figure 6. Connection strength matrices showing degradation over time, t . Connection strengths were resampled to a Gaussian distribution with a mean of 0.5 and a standard deviation of 0.1. Because of the monotonic cellular death criterion, as long as regions have non-zero axonal strain and strain rate from the finite element simulation, edges in the network eventually become degraded. The connection strength matrices at $t = 0$ hrs is shown in (a). The evolution of connection strength matrices for 0 (a), 24 (b), 48 (c), 72 (d), and 96 hours (e) are shown, as well as (f) the connection strength matrix for the case when a 18% strain threshold is used.

doi:10.1371/journal.pcbi.1002619.g006

the network after damage by accounting for edges that were removed. As a result, edges can no longer be part of a short path between nodes and cannot contribute to the efficiency, while also taking into account all nodes that should be a part of the local network without damage.

The normalized global and mean local efficiencies as a function of time are shown in Figure 7. The normalized global efficiency is approximately 0.14 at $t = 0$ hrs and is about the same at 24 hrs, indicating the network remains capable to send information. However, at 48 hrs an 8.8% reduction in normalized global efficiency is predicted and continues to reduce with time. A similar trend is observed in the mean local efficiency. At 96 hrs the normalized global efficiency was reduced 24%, while the mean local efficiency was reduced 27%. By 96 hrs, all but sixteen nodes had greater than 20% reduction of local efficiency. Also, note that there were no nodes completely disconnected from the network, although there were edges completely removed. The total number of edges at $t = 0$ hrs was 1029; at $t = 96$ hrs, 203 edges were removed using the cellular death threshold. Using an injury threshold of 18% strain, 161 edges were removed.

Watts and Strogatz [66] define the small-world network based on the clustering coefficient of the network and the characteristic path length of the network. The clustering coefficient, C , is the fraction of triangles around a node and is weighted by the geometric mean of weights associated with edges of a triangle [64]. It measures how well the first neighbors of a node are connected to each other. The characteristic path length, L , is the average shortest path between all nodes of the network. To qualify as small-world, the networks clustering coefficient should be greater than that of an equivalent random network, whereas the characteristic path length should be approximately equal [66]. The small-world coefficient is defined as $(C/C_{\text{rand}})/(L/L_{\text{rand}})$ [64]. This value was found to be 1.87, 1.87, 2.03, 2.31, and 2.64 for $t = 0, 24, 48, 72$, and 96 hrs, respectively. When using axonal strain as the threshold variable, a value of 2.38 was computed. The increase seen in the small-world coefficient is due to the more rapid decrease in clustering coefficient of the random network compared to the damaged network that it is based on. In addition, the increase seen in the small-world coefficient also shows the ability of the network to maintain its modular structure more effectively than the random network that it was compared to.

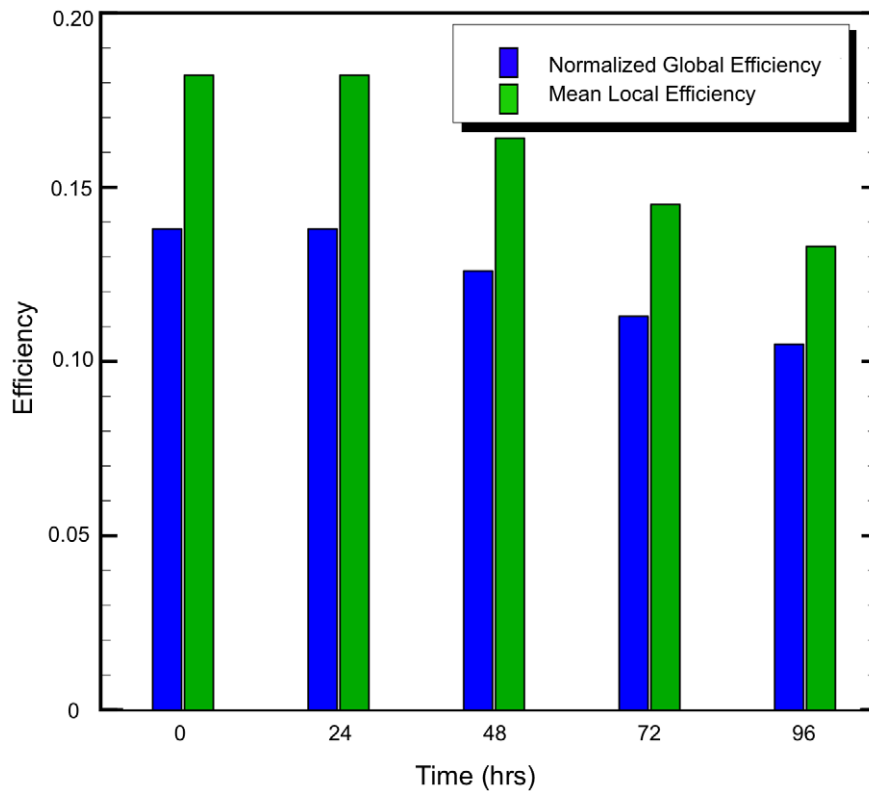


Figure 7. Global and local efficiency in terms of time from impact.
doi:10.1371/journal.pcbi.1002619.g007

The percent reduction of local efficiencies and the associated betweenness for the top 10 regions affected by impact at 96 hrs are listed in Table 2. Betweenness is defined as the number of times a node is part of a shortest path between nodes, and is one indication of a node's network centrality that help to describe the "importance" of a node [64,65]. Hubs within the connectome are identified using betweenness centrality. The maximum betweenness of the original network at $t=0$ is 226, while the minimum value is zero. Recall from Figures 4a–b and 5a, white matter disruption is observed in the left cuneus and the right supariotemporal regions, which has a betweenness centrality of 41 and 17, respectively. The moderate to low betweenness of the regions first affected at 24 hrs helps to explain why the normalized global efficiency was not significantly reduced during this time and shows the importance of a robust brain network. At 96 hrs, the right hemisphere lateral orbitofrontal region shows the largest degradation in local efficiency of approximately 45.4%; however, that region also has a zero betweenness centrality. On the other hand, the right hemisphere medial orbitofrontal region has a betweenness of 110 and shows a 37.4% reduction of local efficiency, indicating it may have a more significant effect to the brain network. At 96 hrs, there are 10 network nodes with betweenness greater than 100 that have at least a 20% reduction of local efficiency. Local efficiency and betweenness for all ROIs are included in Supplemental Figures S2 and S3, respectively.

The results reported thus far are based on a critical cell death value of $D_c=3\%$, as well as a critical strain threshold of 18%. However, it is also useful to evaluate the sensitivity of the results to the choice of D_c . An analysis of network properties was performed for multiple critical cell death values, in the range from $D_c=2-10\%$, and are shown in Figure 8a–b. Figure 8a shows the percent reduction in total edge strength as a function of the

critical cell death threshold choice. Figure 8b shows the percent reduction in global efficiency as a function of the critical cell death threshold choice. Results show that the choice of the critical threshold significantly affects both network measures that were examined. For example, for a change of D_c between 3% or 4%, the reduction in global efficiency is 23.9% and 16.4%, respectively. In other words, from only a 1% change in the choice of D_c results in a 7.5% change in global efficiency reduction. Therefore,

Table 2. Structural measures of simulated lesions for the top ten regions ranked according to percent reduction in local efficiency.

Brain Region	% Reduction	
	Local Eff. at 96 hrs	Betweenness at 0 hrs
Lateral Orbitofrontal (RH)	45.4	0
Parahippocampal (RH)	44.2	0
Parsorbitalis (RH)	44.1	0
Transverse Temporal (RH)	42.0	0
Pericalcarine (RH)	39.4	1
Parstriangularis (RH)	39.3	2
Temporal Pole (RH)	39.1	3
Rostral Anterior Cingulate (RH)	38.4	0
Frontal Pole (RH)	38.1	12
Superior Temporal (RH)	37.9	21

RH and LH refer to right and left hemispheres, respectively.
doi:10.1371/journal.pcbi.1002619.t002

the choice of D_c will be important in obtaining accurate results and highlights the need for future experimentation to characterize cellular injury criteria for all areas of the brain in order to improve the accuracy of this modeling approach.

Discussion

For the first time, a physics-based model has been linked to a network-based analysis that establishes a coupled computational method to study the effects of localized structural damage or lesions. In the presented work, lesions are simulated by using a state-of-the-art finite element model of the human head, developed for a single individual directly from MRI, impacted on the forehead region. The local finite element variables are coupled to a network-based analysis through an empirically based cellular injury model. The new approach attempts to capture the spatiotemporal structural characteristics of brain trauma. Foundations of this idea stem from previous studies that attempted to establish relationships of lesion sites and the resulting functional impact [42,67].

The first part of our study involved developing a new three-dimensional human head finite element model for simulating the biomechanical response from frontal impact and comparing it to experimental data obtained from cadavers. The finite element model is unique in that it uses diffusion tensor imaging tractography to inform structural mechanics constitutive laws of the underlying white matter anisotropy in an effort to help elucidate the injury mechanisms of impact neurotrauma. Simulations of frontal impact capture the coup and contrecoup loading profiles, including short duration intracranial pressure gradients with high positive pressures at the coup region, and negative pressures at the contrecoup region (Figure 3a–b). The computed pressure compares well to past experimental results [53]. While the frontal region had the highest predicted pressure, the temporal and occipital brain locations had the largest values of axonal strain in the regions specifically examined and responded slower than the pressure response. Because of varied mechanical tissue properties

and constraints with the head, translational cranial motion causes relative brain movements that happens after peak pressure, and leads to large brain deformations and significant localized regions of axonal strain (Figure 3e–f).

Empirically based cellular death thresholds were used to predict the time-evolving damage in various brain regions based on finite element-based predictions of local axonal strain and strain rate. The biomechanical simulations predict that the temporal and occipital regions undergo the most axonal strain and strain rate at short times (less than 24 hrs), which leads to cellular death initiation that produces damage which shows dependence on angle of impact and underlying microstructure of brain tissue. The cellular death model that was used in this study is based on experimental observations that cell death was not immediate in response to deformation, but instead increased over four days after insult. Tissue damage becomes more dilute as time progresses (Figure 4g–h). At 96 hours, the predicted damaged axonal pathways can be seen in many directions and across all white matter brain regions, indicating diffuse structural degradation.

Interestingly, when using injury criteria proposed in the past, including thresholds of axonal strain [8,30] or intracranial pressure [21], the finite element simulations predict injury within 10 ms of frontal impact. However, when using a cellular death criteria, damage takes longer to develop but offers a similar result to the resulting network strength (Figure 6). Thus, while the model may be limited in the most accurate description of cellular injury, it does seem to capture the underlying pathology of diffuse brain injury, i.e., widespread damage to axons in the brain, to some degree. While the two criteria offer similar prediction of network damage, cellular death, is perhaps, more useful because effects of strain, strain rate, and time have been decomposed into separate multiplicative terms that allow a compartmentalized study of extrinsic biomechanical conditions. On the other hand, as Morrison et al. [27] point out, purely mechanical definitions of injury thresholds may be too insensitive to identify the onset of injury for the brain, since biological tissues are alive and perform some form of active, physiological functions. For brain tissue,

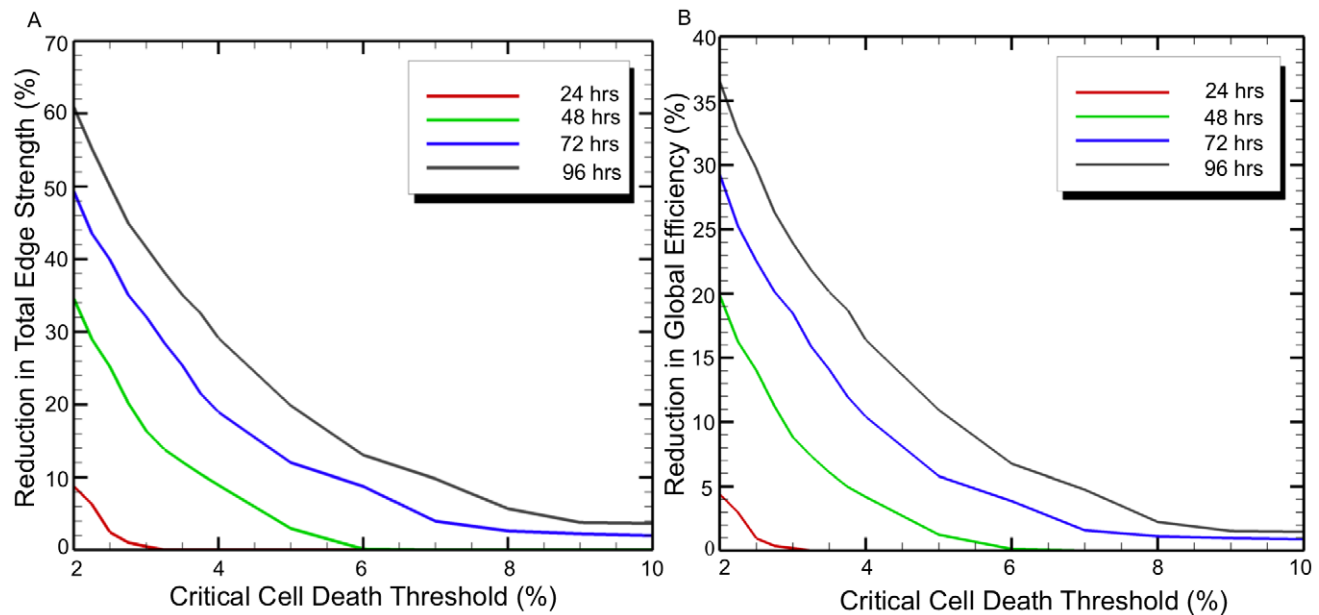


Figure 8. Changes in (a) total edge strength and (b) global efficiency with change in critical cell death threshold for 24, 48, 72, and 96 hours.

doi:10.1371/journal.pcbi.1002619.g008

failure can be defined in various ways and may occur far below mechanical failure limits. Therefore, additional tolerance criterion that capture degradation of the electrophysiological function may be also required for brain tissue, since injury mechanisms that may alter neuronal function without requiring cell death are observed and may become activated more quickly than cell death [68].

This work has attempted to establish a physics-based methodology to inform structural connectome analysis. In the current model, network edges are degraded by weight rather than simply deleting nodes, in an attempt to include the effects of damage on white matter “fibers of passage” that Alstott et al. [42] refer to. It is assumed that tracks representing bundles of axons are able to be disconnected when passing through regions of high cell death, simulating reduction in the strength of a structural connection, and are related to a decrease in localized white matter integrity. All network damage was linked directly to predicted tissue deformation and predicted cellular death. Interestingly, at 96 hrs post-impact, the methods used here did not lead to any node completely disconnected from the network (although there were edges completely disconnected). At early times ($t < 24$ hrs) network measures of global and local efficiency were degraded little, however, as time increased to 96 hrs the network properties were significantly reduced (Figures 6 and 7). Alstott et al. [42] found that random removal of nodes did not affect network integrity until almost all of the nodes were deleted. Thus, this method may capture some structural network features of very mild neurotrauma at early times, but would benefit from a functional network analysis to explore the potential outcomes. As the network was damaged in certain areas, edges were lost or degraded, raising the cost to send information between nodes and producing different short paths between nodes. As a result, the brain network was not able to maintain efficiency by using alternate paths or finding strong hub connections past 24 hrs post-impact, thus demonstrating a potential limitation of the brain to retain network robustness in extreme conditions that cause neurotrauma.

While global efficiency is able to demonstrate widespread effects of damage, local efficiency provided a measure to investigate localized damage within the network related to areas of concentrated axonal strain and strain rate in particular areas of the brain. There was a much larger reduction in local efficiency at areas of high cell damage compared to reduction in the normalized global efficiency, indicating that the brain as a whole is resistant to some degree of localized damage. Brain regions that experienced the largest cellular death showed a larger reduction in local efficiency compared to the global efficiency of the network (Table 2). However, the low betweenness of many of these ROI suggest that they were not as necessary for communication outside their local area. This suggests that the modular nature of the network, including its small world properties, helped to prevent loss of efficiency on the global scale from damage at the local scale. This is interesting because the network considered here is a rigid, static, anatomic network in which there is no adaptability built into the model. However, it seems that damaged structural network hubs retain the ability for long distance communications. In addition, the increase predicted in the small-world coefficient also shows that modularity was not as affected by the damaged static network, as compared to a random network.

Limitations and Future Work

There are exciting possibilities for future work, as well as limitations to the current modeling approach. The current model did not attempt to model the coupled effects to the functional network; instead, we provided an example for a single individual in order to establish a methodology to link physics-based predictions

of tissue damage with structural network analysis for frontal impact neurotrauma. It is important to note that the empirical relationships may only be accurate for the rat (not the human), and most likely, there are many more regions that need to be characterized. Our results and conclusions may be altered according to these injury thresholds. Although human injury thresholds are currently limited, as additional brain region injury thresholds are experimentally characterized and improved they can be included in the future. Due to the computational cost of the finite element simulations, the brain was only segmented into 83 different regions. In the future, increased segmentation of regions of interest and improved biofidelity of the finite element model would increase the resolution of the analysis. While this study does not address the resulting functional outcome from structural degradation, coupled structure-function relationships as a result of neurotrauma would be interesting to explore. For example, a coupled analysis may enable functional stimulus that may prohibit or enhance further cell death. For the prediction of tissue damage, additional physics, such as electrochemical reactions, may be useful by incorporating diffusional properties. In addition, increased resolution of the biomechanical response may also be improved by further developing white matter material response descriptions that use multiple fiber tract orientations within a single element, thereby enabling the capability to use diffusion spectrum imaging. There is also an opportunity to use this framework to explore additional injury mechanisms or thresholds from empirical or experimental data, such as intracranial pressure. Note that the current methodology degrades network edges, instead of nodes. In the future, it may be useful to investigate methods for degrading nodes in addition to edges because the all of the nodes represent cortical gray matter, and the gray matter does experience significant strains. This would require a choice of strain measurement other than axonal strain since the gray matter is treated as isotropic. With this type of criteria, it may be possible to degrade a node based on a ratio of damaged voxels within a region of interest compared to the voxel volume of the region as a whole.

Further work should also work to validate this approach in humans. There are at least two distinct areas associated with connectome damage that should be explored in order to validate the approach described herein. The first deals with how well the location of damage within the network description is captured using physics-based predictions. The second validation strategy should address the nature in which edges and nodes in the network are degraded. There are various approaches that may be useful for addressing both areas. For example, in order to validate how well the location of damage is captured, further understanding about how cellular level changes effect fractional anisotropy, that results in altered fiber tractography would be useful to develop. Some of this information may be obtained from various ongoing studies that are examining the ability of DTI to diagnose mTBI, which could also be extended to create degraded structural connectomes. One way to do this may be to use DTI studies pre- and post-injury from typical loading conditions that cause rotation-induced diffuse axonal injury. By providing similar loading profiles within the simulation and comparing computed DTI tractography damage with the clinical data set, maybe results can be compared. Perhaps this may be accomplished using sports-related impact injury, such as American football, where many helmets have sensors built-in to record impact loads.

In conclusion, this work has explored “connectome neurotrauma mechanics” by using physics-based finite element simulations to help elucidate injury mechanisms associated with neurotrauma by using various cellular injury thresholds to define

tissue damage, and established a coupled computational framework to inform structural connectome analysis.

Supporting Information

Figure S1 The magnitude of peak relative displacement between skull and brain for validation of finite element model. (EPS)

Figure S2 Percent reduction in local efficiency at 96 hrs for all brain regions. (TIF)

Figure S3 Percent reduction in betweenness at 96 hrs for all brain regions. (TIF)

References

- Horgan TJ, Gilchrist MD (2003) The creation of three-dimensional finite element models for simulating head impact biomechanics. *Int J Crashworthiness* 8: 353–366.
- Takhounts EG, Eppinger RH, Campbell JQ, Tannous RE, Power ED, et al. (2003) On the development of the simon finite element head model. *Stapp Car Crash J* 47: 107–33.
- Sayed TE, Mota A, Fraternali F, Ortiz M (2008) Biomechanics of traumatic brain injury. *Comput Methods Appl Mech Eng* 197: 4692–4701.
- Ho J, Kleiven S (2009) Can sulci protect the brain from traumatic injury? *J Biomech* 42: 2074–2080.
- Moss WC, King MJ, Blackman EG (2009) Skull ejection from blast waves: A mechanism for brain injury with implications for helmet design. *Phys Rev Lett* 103: 108702.
- Moore DF, Jérusalem A, Nyein M, Noels L, Jaffee MS, et al. (2009) Computational biology -modeling of primary blast effects on the central nervous system. *NeuroImage* 47, Supplement 2: T10–T20.
- Nyein MK, Jason AM, Yu L, Pita CM, Joannopoulos JD, et al. (2010) In silico investigation of intracranial blast mitigation with relevance to military traumatic brain injury. *Proc Natl Acad Sci U S A* 107: 20703–20708.
- Wright RM, Ramesh KT (2011) An axonal strain injury criterion for traumatic brain injury. *Biomech Model Mechanobiol* 11: 245–60.
- Yang KH, Mao H, Wagner C, Zhu F, Chou CC, et al. (2011) Modeling of the brain for injury prevention. In: Bilston LE, editor. *Neural Tissue Biomechanics. Studies in Mechanobiology, Tissue Engineering and Biomaterials*. Springer Berlin Heidelberg, pp. 69–120.
- Woo EJ, Hua P, Webster JG, Tompkins WJ (1994) Finite-element method in electrical impedance tomography. *Med Biol Eng Comput* 32: 530–536.
- Zhang Y, Ding L, Van Dongen W, Hecox K, Frim DM, et al. (2006) A cortical potential imaging study from simultaneous extra- and intracranial electrical recordings by means of the finite element method. *NeuroImage* 31: 1513–1524.
- Rullmann M, Anwender A, Dannhauer M, Warfield SK, Duffy FH, et al. (2009) EEG source analysis of epileptiform activity using a 1 mm anisotropic hexahedra finite element head model. *NeuroImage* 44: 399–410.
- Lee WH, Kim TS (2012) Methods for high-resolution anisotropic finite element modeling of the human head: Automatic MR white matter anisotropy-adaptive mesh generation. *Med Eng Phys* 34: 85–98.
- Acar ZA, Makeig S (2010) Neuroelectromagnetic forward head modeling toolbox. *J Neurosci Methods* 190: 258–270.
- Saraf H, Ramesh KT, Lennon AM, Merkle AC, Roberts JC (2007) Mechanical properties of soft human tissues under dynamic loading. *J Biomech* 40: 1960–1967.
- Pervin F, Chen WW (2009) Dynamic mechanical response of bovine gray matter and white matter brain tissues under compression. *J Biomech* 42: 731–735.
- Shafieian M, Bao J, Darvish K (2011) Mechanical properties of brain tissue in strain rates of blast injury. In: *Bioengineering Conference (NEBEC), 2011 IEEE 37th Annual Northeast*; 1–3 April 2011; Philadelphia, Pennsylvania, United States.
- Trexler MM, Lennon AM, Wickwire AC, Harrigan TP, Luong QT, et al. (2011) Verification and implementation of a modified split hopkinson pressure bar technique for characterizing biological tissue and soft biosimulant materials under dynamic shear loading. *J Mech Behav Biomed Mater* 4: 1920–1928.
- Bernick KB, Prevost TP, Suresh S, Socrate S (2011) Biomechanics of single cortical neurons. *Acta Biomater* 7: 1210–1219.
- Sanborn B, Nie X, Chen W, Weerasooriya T (2012) Inertia effects on characterization of dynamic response of brain tissue. *J Biomech* 45: 434–439.
- Zhang L, Yang KH, King AI (2004) A proposed injury threshold for mild traumatic brain injury. *J Biomech Eng* 126: 226–236.
- Ning X, Zhu Q, Lanir Y, Margulies SS (2006) A transversely isotropic viscoelastic constitutive equation for brainstem undergoing finite deformation. *J Biomech Eng* 128: 925–930.
- Arbogast KB, Margulies SS (1999) A fiber-reinforced composite model of the viscoelastic behaviour of the brainstem in shear. *J Biomech* 32: 865–870.
- Rafaels K, Bass CR, Salzar RS, Panzer MB, Woods W, et al. (2011) Survival risk assessment for primary blast exposures to the head. *J Neurotrauma* 28: 2319–28.
- Säljö A, Mayorga M, Bolouri H, Svensson B, Hamberger A (2011) Mechanisms and pathophysiology of the low-level blast brain injury in animal models. *NeuroImage* 54, Supplement 1: S83–S88.
- Cullen DK, Vernekar VN, Laplaca MC (2011) Trauma-induced plasmalemma disruptions in three-dimensional neural cultures are dependent on strain modality and rate. *J Neurotrauma* 28: 2219–33.
- Morrison III B, Cullen DK, LaPlaca M (2011) In vitro models for biomechanical studies of neural tissues. In: Bilston LE, editor. *Neural Tissue Biomechanics. Studies in Mechanobiology, Tissue Engineering and Biomaterials*. Springer Berlin Heidelberg, pp. 247–285.
- Cernak I, Merkle AC, Koliatsos VE, Bilik JM, Luong QT, et al. (2011) The pathobiology of blast injuries and blast-induced neurotrauma as identified using a new experimental model of injury in mice. *Neurobiol Dis* 41: 538–551.
- Effen GB, Hue CD, Vogel III EW, Panzer MB, Meaney DF, et al. (2012) A multiscale approach to blast neurotrauma modeling: part ii: Methodology for inducing blast injury to in vitro models. *Front Neurol* 3: 23.
- Bain AC, Meaney DF (2000) Tissue-level thresholds for axonal damage in an experimental model of central nervous system white matter injury. *J Biomech Eng* 122: 615–622.
- Mendis K (1992) Finite element modeling of the brain to establish diffuse axonal injury criteria. Ph.D. thesis, Ohio State University.
- Cater HL, Sundstrom LE, Morrison III B (2006) Temporal development of hippocampal cell death is dependent on tissue strain but not strain rate. *J Biomech* 39: 2810–2818.
- Elkin BS, Morrison III B (2007) Region-specific tolerance criteria for the living brain. *Stapp Car Crash J* 51: 127–138.
- Kaiser M, Martin R, Andras P, Young MP (2007) Simulation of robustness against lesions of cortical networks. *Eur J Neurosci* 25: 3185–3192.
- Bullmore E, Sporns O (2009) Complex brain networks: graph theoretical analysis of structural and functional systems. *Nat Rev Neurosci* 10: 186–198.
- Honey CJ, Thivierge JP, Sporns O (2010) Can structure predict function in the human brain? *NeuroImage* 52: 766–776.
- Bassett DS, Brown JA, Deshpande V, Carlson JM, Grafton ST (2011) Conserved and variable architecture of human white matter connectivity. *NeuroImage* 54: 1262–1279.
- Jarbo K, Verstynen T, Schneider W (2012) In vivo quantification of global connectivity in the human corpus callosum. *NeuroImage* 59: 1988–1996.
- Sporns O, Tononi G, Kötter R (2005) The human connectome: A structural description of the human brain. *PLoS Comput Biol* 1: e42.
- Reijneveld JC, Ponten SC, Berendse HW, Stam CJ (2007) The application of graph theoretical analysis to complex networks in the brain. *Clin Neurophysiol* 118: 2317–31.
- Jirsa V, Sporns O, Breakspear M, Deco G, McIntosh AR (2010) Towards the virtual brain: Network modeling of the intact and the damaged brain. *Arch Ital Biol* 148: 189–205.
- Alstott J, Breakspear M, Hagmann P, Cammoun L, Sporns O (2009) Modeling the impact of lesions in the human brain. *PLoS Comput Biol* 5: 12.
- Kucyeski A, Maruta J, Niogi SN, Ghajar J, Raj A (2011) The generation and validation of white matter connectivity importance maps. *NeuroImage* 58: 109–121.
- Mac Donald CL, Dikranian K, Song SK, Bayly PV, Holtzman DM, et al. (2007) Detection of traumatic axonal injury with diffusion tensor imaging in a mouse model of traumatic brain injury. *Exp Neurol* 205: 116–131.
- Mac Donald CL, Johnson AM, Cooper D, Nelson EC, Werner NJ, et al. (2011) Detection of blast-related traumatic brain injury in U.S. military personnel. *N Engl J Med* 364: 2091–2100.
- Visage Imaging GmbH. Available: www.amira.com.

Text S1 A concise description of the finite element method. (PDF)

Text S2 Material constitutive laws and associated parameters used for the head finite element model. (PDF)

Text S3 Additional finite element validation. (PDF)

Author Contributions

Conceived and designed the experiments: RHK PJM AMD STG. Performed the experiments: RHK PJM AMD STG. Analyzed the data: RHK PJM AMD STG. Contributed reagents/materials/analysis tools: RHK PJM AMD STG. Wrote the paper: RHK PJM AMD STG.

47. The Connectome Mapping Toolkit. Available: www.cmtk.org.
48. Desikan RS, Sgonne F, Fischl B, Quinn BT, Dickerson BC, et al. (2006) An automated labelling system for subdividing the human cerebral cortex on MRI scans into gyral based regions of interest. *NeuroImage* 31: 968–980.
49. Hagmann P, Jonasson L, Maeder P, Thiran JP, Wedeen VJ, et al. (October 2006) Understanding diffusion MR imaging techniques: From scalar diffusion-weighted imaging to diffusion tensor imaging and beyond. *Radiographics* 26: S205–S223.
50. Dauguet J, Peled S, Berezovskii V, Delzescaux T, Warfield SK, et al. (2007) Comparison of fiber tracts derived from in-vivo dti tractography with 3d histological neural tract tracer reconstruction on a macaque brain. *NeuroImage* 37: 530–538.
51. Margulies SS, Prange MT (2002) Regional, directional, and age-dependent properties of the brain undergoing large deformation. *J Biomech Eng* 124: 244–252.
52. Kraft RH, Dagro AM (2011) Design and implementation of a numerical technique to inform anisotropic hyperelastic finite element models using diffusion-weighted imaging. Technical Report ARL-TR-5796, U. S. Army Research Laboratory.
53. Nahum AM, Smith R, Ward CC (1977) Intracranial pressure dynamics during head impact. Proceedings of the 21st STAPP Car Crash Conference.
54. Belytschko T, Liu WK, Moran B (2000) *Nonlinear Finite Elements for Continua and Structures*. New York: John Wiley & Sons, LTD.
55. Colgan NC, Gilchrist MD, Curran KM (2010) Applying dti white matter orientations to finite element head models to examine diffuse tbi under high rotational accelerations. *Prog Biophys Mol Biol* 103: 304–309.
56. Chafi MS, Ganpule S, Gu L, Chandra N (2011) Dynamic Response of Brain Subjected to Blast Loadings: Influence of Frequency Ranges. *Int J Appl Mech* 3: 803.
57. Tang-Schomer MD, Patel AR, Baas PW, Smith DH (2010) Mechanical breaking of microtubules in axons during dynamic stretch injury underlies delayed elasticity, microtubule disassembly, and axon degeneration. *FASEB J* 24: 1401–1410.
58. Hosmane S, Fournier A, Wright R, Rajbhandari L, Siddique R, et al. (2011) Valve-based microfluidic compression platform: single axon injury and regrowth. *Lab Chip* 11: 3888–3895.
59. Effgen GB, Hue CD, Vogel III E, Panzer MB, Meaney DF, et al. (2012) A multiscale approach to blast neurotrauma modeling: part II: Methodology for inducing blast injury to in vitro models. *Front Neurol* 3: 1–10.
60. Honey CJ, Sporns O, Cammoun L, Gigandet X, Thiran JP, et al. (2009) Predicting human resting-state functional connectivity from structural connectivity. *Proc Natl Acad Sci U S A* 106: 2035–2040.
61. Hardy WN, Foster CD, Mason MJ, Yang KH, King AI, et al. (2001) Investigation of head injury mechanisms using neutral density technology and high-speed biplanar x-ray. *Stapp Car Crash J* 45: 337–368.
62. Chen Y, Ostojic-Starzewski M (2010) MRI-based finite element modeling of head trauma: spherically focusing shear waves. *Acta Mech* 213: 155–167.
63. Iturria-Medina Y, Pérez Fernández A, Morris DM, Canales-Rodríguez EJ, Haroon HA, et al. (2011) Brain hemispheric structural efficiency and interconnectivity rightward asymmetry in human and nonhuman primates. *Cereb Cortex* 21: 56–67.
64. Rubinov M, Sporns O (2010) Complex network measures of brain connectivity: Uses and interpretations. *NeuroImage* 52: 1059–1069.
65. Latora V, Marchiori M (2001) Efficient behavior of small-world networks. *Phys Rev Lett* 87: 198701.
66. Watts DJ, Strogatz SH (1998) Collective dynamics of small-world networks. *Nature* 393: 440–442.
67. Honey CJ, Sporns O (2008) Dynamical consequences of lesions in cortical networks. *Hum Brain Mapp* 29: 802–809.
68. Yu Z, Morrison III B (2010) Experimental mild traumatic brain injury induces functional alteration of the developing hippocampus. *J Neurophysiol* 103: 499–510.

On Allometry Relations

Damien West and Bruce J. West

International Journal of Modern Physics B, 26(18), 1230010-1-57 (2012)

International Journal of Modern Physics B
 Vol. 26, No. 18 (2012) 1230010 (57 pages)
 © World Scientific Publishing Company
 DOI: 10.1142/S0217979212300101

 **World Scientific**
 www.worldscientific.com

ON ALLOMETRY RELATIONS

DAMIEN WEST* and BRUCE J. WEST†

**Physics Department, Rensselaer Polytechnic Institute, Troy, New York*

*†Information Sciences Directorate, US Army Research Office,
 Research Triangle Park, NC 27709, USA*

Received 8 June 2012

Published 6 July 2012

There are a substantial number of empirical relations that began with the identification of a pattern in data; were shown to have a terse power-law description; were interpreted using existing theory; reached the level of “law” and given a name; only to be subsequently fade away when it proved impossible to connect the “law” with a larger body of theory and/or data. Various forms of allometry relations (ARs) have followed this path. The ARs in biology are nearly two hundred years old and those in ecology, geophysics, physiology and other areas of investigation are not that much younger. In general if X is a measure of the size of a complex host network and Y is a property of a complex subnetwork embedded within the host network a theoretical AR exists between the two when $Y = aX^b$. We emphasize that the reductionistic models of AR interpret X and Y as dynamic variables, albeit the ARs themselves are explicitly time independent even though in some cases the parameter values change over time. On the other hand, the phenomenological models of AR are based on the statistical analysis of data and interpret X and Y as averages to yield the empirical AR: $\langle Y \rangle = a\langle X \rangle^b$. Modern explanations of AR begin with the application of fractal geometry and fractal statistics to scaling phenomena. The detailed application of fractal geometry to the explanation of theoretical ARs in living networks is slightly more than a decade old and although well received it has not been universally accepted. An alternate perspective is given by the empirical AR that is derived using linear regression analysis of fluctuating data sets. We emphasize that the theoretical and empirical ARs are not the same and review theories “explaining” AR from both the reductionist and statistical fractal perspectives. The probability calculus is used to systematically incorporate both views into a single modeling strategy. We conclude that the empirical AR is entailed by the scaling behavior of the probability density, which is derived using the probability calculus.

Keywords: Allometry; fractals; physiology; scaling; statistical analysis; ontogenetic growth.

1. Introduction

At the turn of the nineteenth century the German polymath Gauss⁶⁴ and the American mathematician Adrian¹ introduced into science the law of frequency of errors, the French physicist Laplace¹¹⁶ proved the central limit theorem and the French zoologist Cuvier³⁴ determined that the brain mass of a mammal increases more slowly than does its total body mass (TBM). Cuvier's observations initiated the field of Allometry that relates the size of an organ to that of the host organism with mass serving as a measure of size. The roads of statistical analysis and observation (experiment) converge in the twenty-first century to explain the origin of allometry relations (ARs).

Allometry, literally meaning by a different measure, has acquired a mathematical description through its relations along with a number of theoretical interpretations to account for its mathematical form. However no one theory has been universally accepted as successfully explaining ARs in their many guises so the corresponding origins remain controversial. Consequently, in reviewing the properties of allometry data along with their various theoretical explanations we herein provide a glimpse as to those origins.

We use the generic term network in our narration in order to slip smoothly from ARs in physical networks with identical particles and van de Waal's forces, to biological networks with structured elements and chemical interactions, to geophysical networks with complex tributaries and branching architectures. This nomenclature also enables us to transition from arcane historical theory to a modern perspectives of complex networks. The mathematics of renormalization group (RG) theory,^{103,259} fractional differential equations,^{126,144} fractional stochastic differential equations²³⁶ and transitioning from dynamic variables to phase space variables to express the probability calculus in terms of fractional diffusion equations^{108,207,236} are herein found to provide insight into different aspects of the origins of ARs.

Allometry has been defined as the study of body size and its consequences^{79,176} both within a given organism and between species in a given taxon. Gayon⁶⁵ reviewed the history of the concept of allometry, defined as the study of body size and its consequences^{79,176} within a given organism and between species in a given taxon, and distinguished between four different forms: (1) ontogenetic allometry, which refers to relative growth in individuals; (2) phylogenetic allometry, which refers to constant differential growth ratios in lineages; (3) intraspecies allometry, which refers to adult individuals within a species; (4) interspecies allometry, which refers to the same kind of phenomenon among related species. The theoretical entailment of static from dynamic allometry models has not been systematically studied, although there has been some recent effort in that direction.^{67,243} Herein we review the use of phenomenological dynamic equations from physical biology to relate the dynamic allometry of the first two categories to their static counterparts in the last two.

Galileo⁶² recognized that in order for an organism or physical structure to retain a constant function as size increases requires its shape (architecture) and/or the

materials with which it is constructed to change. This simple physical picture has biological and social analogs in which the size of a network has unavoidable consequences.^{164,213} We focus on ARs for physiologic phenomena, but we do indicate where insight might also be gained from other disciplines as well.

1.1. What is the equation?

Sir Julian Huxley⁹⁸; grandson of the Huxley of Darwin evolution fame, brother of the novelist Aldous (*Brave New World*) and half-brother of the biophysicist Andrew (the Hodgkin–Huxley equations)²⁰⁹; proposed that two parts of the same organism have proportional rates of growth. In this way if Y is a living subnetwork observable with growth rate ϑ and X is a measure of the size of a living host network with growth rate γ then the fractional increase in the two is denoted according to Huxley by:

$$dX/\gamma X = dY/\vartheta Y. \quad (1)$$

This equation can be directly integrated to obtain:

$$Y = aX^b, \quad (2)$$

the time-independent AR where a and $b (= \gamma/\vartheta)$ are empirically determined. The theoretical AR given by Eq. (2) considered by Huxley is the basis of subsequent theoretical discussions in such excellent books as Schmidt–Nielson¹⁹⁵ and Calder.³¹

The intraspecies AR relates a property of an organism within a species to its TBM. The interspecies AR relates a property across species such as the basal metabolic rate (BMR) to TBM.^{31,195} These two allometry groups are distinctly different and the models developed to determine the theoretical forms of the allometry coefficient a and exponent b in the two cases are quite varied, as shown subsequently.

Equation (2) looks very much like the scaling relations that have become so popular in the study of complex networks over the last decade.^{3,30,153,221,239} Historically the nonlinear nature of Eq. (2) has precluded the direct fitting of the equation to data. A logarithmic transformation is traditionally made and a linear regression to the data on the equation

$$\ln Y = \ln a + b \ln X \quad (3)$$

is used to estimate the parameters a and b . In Sec. 2 we review a myriad of phenomena from a number of disciplines in which ARs have been brought to light. In Sec. 3 we discuss the fitting of ARs to data.

All complex dynamical networks manifest fluctuations, either due to intrinsic nonlinear dynamics producing chaos^{124,155} or due to coupling of the network to an infinite dimensional, albeit unknown environment,¹¹⁸ or both. The modeling strategies adopted to explain ARs have traditionally taken one of two roads: the statistical approach in which residual analysis is used to understand statistical patterns and

to identify the causes of variation in the AR;^{31,195} or the reductionist approach to identify mechanisms that explain specific values of the allometry parameters.^{10,247} We find that neither approach separately provides a complete explanation of the variety of phenomena described by ARs. The influence of the environment, whether inducing fluctuations in a reductionist model, or producing a systematic change in a statistical model, has been taken into account in multiple studies.^{71,73,141} In Sec. 5 we take the road of the probability calculus that systematically incorporates both reductionistic and statistical mechanism into the phenomenological explanation of ARs. This calculus enables modelers to associate characteristics of the measured probability density function (*pdf*) with specific deterministic mechanisms and with structural properties of the coupling between variables and fluctuations.^{118,175}

1.2. Is there universality?

In physics the notion of universality occurs in the context of critical phenomena, where in the vicinity of a phase transition a network ceases to have a characteristic scale and can be characterized by a set of critical exponents. The principle of universality claims that networks that undergo a phase transition can be grouped into one of a small number of universality classes. Gisiger⁶⁸ discusses universality in the context of invariance in biology; specifically addressing the role of $1/f$ noise. In the context of AR universality might imply that the allometry exponent plays the role of a critical exponent. The empirical evidence suggests that this interpretation of the allometry exponent is not appropriate. A somewhat less stringent definition of universality may be defensible; one in which the details of the interactions are washed out but the form of the AR persists with the allometry exponent in a restricted interval.

In biology the ARs associate functional variables with measures of body size, such as the TBM $X = M$ raised to a noninteger power M^b . The average BMR is one such functional variable $Y = B$ that can be expressed in terms of TBM. The most prevalent theories of metabolic allometry argue for either $b = 2/3$, based on body cooling, or $b = 3/4$, based on energy efficiency. Selected data sets have been used by various investigators to support either of these two values. However, there is also strong evidence that there is no universal value of b that is satisfied by all metabolic data. In fact, Bokma²¹ presents a large amount of fish data to demonstrate that no single universal value of the allometry exponent b exists. This argument is supported by Glazier⁷² who observes that the isometric ($b = 1$) metabolic scaling of pelagic animals is an evolutionarily malleable trait that responds to environmental changes.

On the other hand, West and Brown²⁵² argue that living networks do have universal scaling laws. Their arguments rest on patterns observed in biological and botanical data and the quantitative theory of the fractal structure, organization and dynamics of the branching networks in living systems. The theory developed by West *et al.*,²⁴⁷ which we review in Sec. 4, has as one of its tenets the existence of hierarchical fractal-like branching networks for the delivery of nutrients resulting in

D. West & B. J. West

$b = 3/4$. They attribute this origin of metabolic AR to evolution's solution to the grand challenge of how highly complex, self-sustaining, reproducing, living networks service enormous numbers of localized microscopic units in an efficient and "democratic" way. Their conclusion, like that of the earlier analysis others,^{230,231} was that fractal networks have an evolutionary advantage over those that scale classically,²¹³ independently of what the networks distribute from macroscopic reservoirs to microscopic sites.

Scaling is a ubiquitous property of large complex networks indicating that the observables simultaneously fluctuate over many time and/or space scales. In the physical sciences such phenomena have historically been categorized as $1/f$ noise²²⁵ or $1/f$ variability.²³⁹ Mandelbrot¹³¹ was probably the first to recognize the wide-ranging significance of this $1/f$ variability with his introduction of fractals into the scientist's lexicon. The existence of ARs has been closely tied to fractal geometry by some investigators²⁴⁷ and in Sec. 5 we show that the origin of AR may reside in fractal statistics, the scaling of *pdfs*, and not in fractal geometry.

1.3. *Some comments on fractals*

Mandelbrot^{131,132} identified ARs masquerading under a variety of empirical "laws" and argued that they were a consequence of complex phenomena not having characteristic scales. Subsequent interpretations of ARs often involve fractals and so we recall some fundamental properties of fractals that are subsequently useful. To begin let us give a qualitative definition of a fractal:¹³³ "A fractal is a shape made of parts similar to the whole in some way."

The fractal concept arises in three distinct, but related guises; geometry, statistics and dynamics. Geometric fractals deal with the self-similarity of complex geometric forms. A fractal object examined with ever increasing magnification reveals ever greater levels of detail; detail that is self-similar in character. The basic mathematical properties of geometric fractals and their myriad of applications can be found in a number of excellent books^{17,55,57,131,133,143,238} and is not repeated here. We merely record and interpret those properties that may be needed for the analyses of ARs. The number of self-similar objects N required to cover an object of dimension D is given by $N = r^{-D}$, where r is the size of the "ruler". In this way the fractal dimension of the object being covered can be mathematically defined as:

$$D = -\ln N / \ln r \quad (4)$$

in the limit of vanishing r . As the ruler size goes to zero the number of rulers necessary to cover the object diverges to infinity in such a way that D remains finite for self-similar objects and this dimension is not necessarily integer valued.

An observable $Z(t)$ is scaling if for a positive constant c it satisfies the homogeneity relation

$$Z(ct) = c^H Z(t). \quad (5)$$

Modifying the units of the independent variable therefore only changes the overall observable by a multiplicative factor; this is self-affinity. Barenblatt¹³ remarked that such scaling laws are not merely special cases of more general relations; they never appear by accident and they always reveal self-similarity. Note that scaling alone is not sufficient to prove that a function is fractal, but if a function is fractal it does scale.

In the sequel we relax the distinction between self-affine and self-similar, since self-similarity has been extended to encompass both meanings in the physics literature. Meakin¹⁴³ asserts that in homogeneous scaling relations it is the coefficient that embodies the “real physics” behind power-law relations. He further observed that the allometry exponents are universal in many homogeneous scaling phenomena and the allometry coefficients provide the only means to control physical properties and behavior.

Scale invariance or scaling requires that a function $\Phi(X_1, \dots, X_N)$ be such that scaling each of the N variables by an appropriate choice of exponents $(\alpha_1, \dots, \alpha_N)$ always recovers the same function $\Phi(X_1, \dots, X_N)$ up to an overall constant:

$$\Phi(X_1, \dots, X_N) = \gamma^\beta \Phi(\gamma^{\alpha_1} X_1, \dots, \gamma^{\alpha_N} X_N). \quad (6)$$

We observe that Eq. (2) is possibly the simplest of such scaling relations between two variables such that they satisfy the RG relation

$$X(\gamma Y) = \gamma^b X(Y).$$

The lowest-order solution to this equation is, of course, given by Eq. (2) and we provide the general solution subsequently. Changes in the host network X (size) control (regulate) changes in the subnetwork Y (property) in living networks and in some physical networks through the homogeneous scaling relation.

Inhomogeneity in space and intermittency in time are the hallmarks of fractal statistics and it is the statistical rather than the geometrical sameness that is evident at increasing levels of magnification. In geometrical fractals the observable scales from one level to the next. In statistical fractals where the phase space variables (z, t) replaces the dynamic variable $Z(t)$ it is the *pdf* $P(z, t)$ that satisfies a scaling relation:

$$P(\alpha z, \beta t) = \beta^{-\mu} P(z, t); \quad \mu = \ln \alpha / \ln \beta, \quad (7)$$

where $\mu = 2H$ and the homogeneity relation is interpreted in the sense of the *pdf* in Eq. (7). Time series with such statistical properties are found in multiple disciplines including finance,¹³⁴ economics,¹³⁵ neuroscience,^{4,226} geophysics,²¹⁵ physiology²⁴⁰ and general complex networks.²⁴⁴ A complete discussion of statistical data with such scaling behavior is given by Beran²⁰ in terms of the long-term memory captured by the scaling exponent. One example of a scaling *pdf* is given by:

$$P(z, t) = \frac{1}{t^\mu} F_z \left(\frac{z}{t^\mu} \right) \quad (8)$$

and in a standard diffusion process $Z(t)$ is the displacement of the diffusing particle from its initial position at time t , $\mu = 1/2$ and the functional form of $F_z(\cdot)$ is a Gauss distribution. However, for general complex phenomena there is a broad class of distributions for which the functional form of $F_z(\cdot)$ is not Gaussian and the scaling index $\mu \neq 1/2$, see Sec. 5 for additional discussion.

Dynamic fractals do not directly enter our discussion of ARs. However for completeness we mention that in a dynamic fractal the geometry of the manifold on which the dynamics of a network unfolds is fractal, so that the associated chaotic time series is also fractal.¹⁵⁵

2. Empirical Allometry

In this section we review areas of investigation where size has been observed to control the properties of a phenomenon. In so doing we catalog a number of phenomenological relations that are not often discussed from the same perspective. There is a nontrivial number of empirical relations that began as the identification of a pattern in data; were shown to have a terse power-law description; were interpreted using existing theory; reached the level of “law” and given a name, not always after the discoverer; only to subsequently fade away when it proved impossible to connect the “law” with a larger body of theory and/or data. An example drawn from the *Notebooks* of Leonardo da Vinci¹⁷⁷ relates the diameter of a parent limb d_0 to two daughter limbs d_1 and d_2 :

$$d_0^\alpha = d_1^\alpha + d_2^\alpha. \quad (9)$$

The da Vinci scaling relation supplies the phenomenological mechanism necessary for AR to emerge in a number of disciplines, as we subsequently discuss.

Nearly five hundred years after de Vinci recorded his observations Murray¹⁵⁰ used energy minimization to derive the same equation with the theoretical value $\alpha = 3$, which is known in the literature as Murray’s Law or the Murray–Hess Law. In the simplest case $d_1 = d_2$ the da Vinci scaling relation reduces to scaling between sequential generations of a bifurcating branching network having daughter branches of equal radii:

$$d_{k+1} = 2^{-1/\alpha} d_k \quad (10)$$

resulting in an exponential reduction in branch diameter from generation to generation.

2.1. Living networks

Living networks have static intraspecies ARs that link two distinct but interacting parts of the same organism in terms of mass, with mass serving as a measure of size. Smith²⁰² maintained that concentrating on a power function as the method for evaluating the biological consequences of size has masked the complexity of the

allometry problem. We agree with this observation, but perhaps in ways that Smith would not have anticipated, as will become evident.

2.1.1. Biology

Cuvier³⁴ was the first to recognize that brain mass increases more slowly than TBM as we proceed from small to large species within a taxon. This empirical observation was subsequently made between many other biological observables and was first expressed mathematically as an allometric relation by Snell²⁰⁴:

$$\text{brainweight} = a(\text{bodyweight})^b, \quad (11)$$

where on log-log graph paper a is the intercept with the vertical axis and b is the slope of the line segment. Mammalian neocortical quantities Y have subsequently been empirically determined to change as a function of neocortical grey matter volume X as an AR. The neocortical allometry exponent was first measured by Tower²¹⁴ for neuron density to be approximately $-1/3$. The total surface area of the mammalian brain was found to have an allometry exponent of approximately $8/9$.^{94,100,167} Changizi³³ points out that the neocortex undergoes a complex transformation covering the five orders of magnitude from mouse to whale depicted in Fig. 1 but the ARs persist; those mentioned here along with many others.

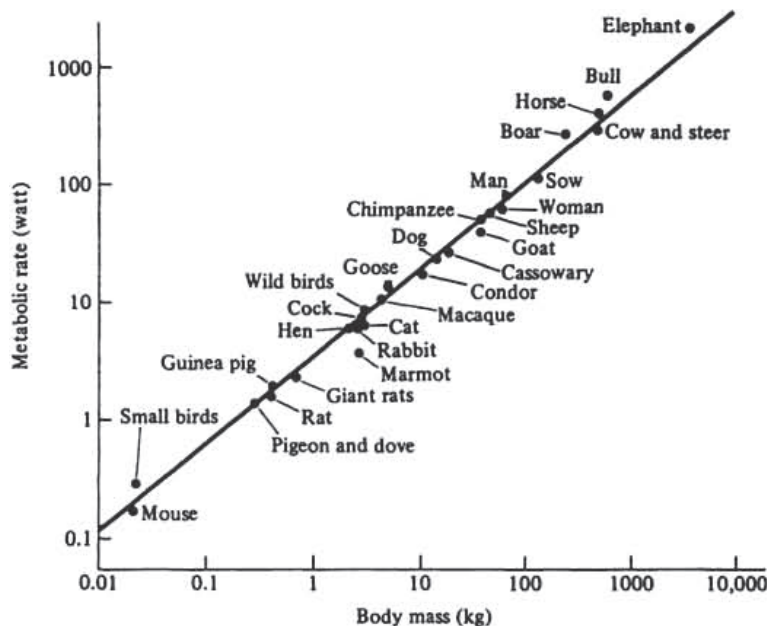


Fig. 1. Mouse to elephant curve. BMR of mammals and birds are plotted versus TBM on log-log graph paper. The solid line segment is the best linear regression of Eq. (2) to the data with a slope very close to $3/4$. [reproduced from Schmidt-Nielsen¹⁹⁵ with permission].

D. West & B. J. West

Another quantity of interest is the time; not the chronological time measured by a clock but the intrinsic time of a biological process first called biological time by Hill.⁹³ Hill reasoned that since so many properties of an organism change with size that time itself may scale with TBM. Lindstedt and Calder¹¹⁹ develop this concept further and determine experimentally that biological time, such as species longevity, satisfies an AR with Y being the biological time. Lindstedt *et al.*¹²¹ clarify that biological time τ is an internal mass-dependent time scale

$$\tau = aM^b \quad (12)$$

to which the duration of biological events are entrained. They present a partial list of such events that includes breath time, time between heart beats, blood circulation time and time to reach sexual maturity. In all these examples and many others the allometry exponent clusters around the theoretical value $b = 1/4$. Note that the total energy of an organism seen as a bioreactor is proportional to volume (M) and the biological time is proportional to $M^{1/4}$, so the metabolic rate (energy/time) would scale as $M^{3/4}$.

2.1.2. Botany

Niklas¹⁵⁴ shows in Fig. 2 an impressive statistical trend spanning twenty orders of magnitude in the mass of aquatic and terrestrial nonvascular and vascular plant species. The annual growth in plant body biomass G_T (net annual gain in dry mass per individual) and M_T (total dry mass per individual) are related by the

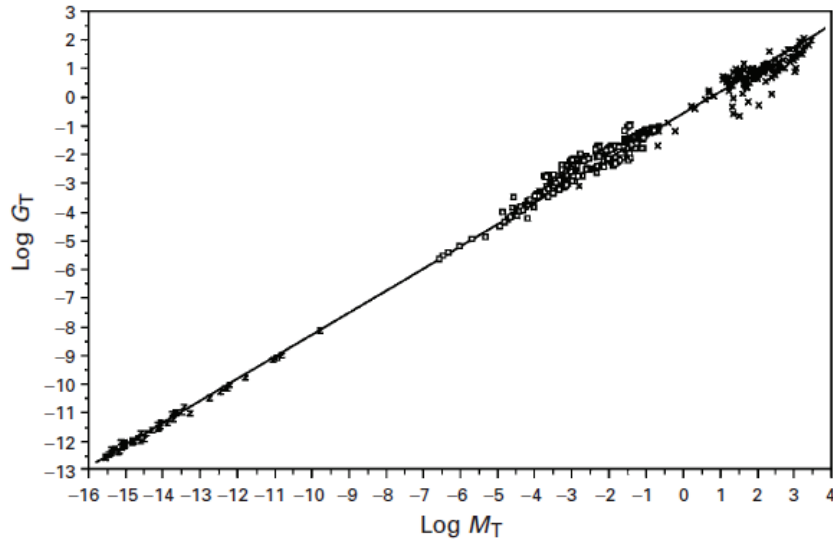


Fig. 2. Log-log bivariate plot of total annual growth rate in dry body mass per individual G_T versus TBM. Line segment denotes reduced major axis regression curves for the entire data set. [adapted from Niklas¹⁵⁴ with permission].

empirical AR:

$$G_T \propto M_T^{3/4}. \quad (13)$$

Figure 2 shows linear regression on logarithmically transformed data

$$\log G_T = \log a + 0.75 \log M_T \quad (14)$$

and the parameter a is the intercept with the vertical axis. In the data analyses recorded herein the terms weight, mass and volume are used almost interchangeably as measures of size. The allometry exponent is $3/4$ for the data in Fig. 2 but empirically differs from this value when the data sets are graphed individually. The allometry coefficients of the separate data sets may vary as a function of habitat as well. The agreement between the biomass data and the AR with exponent $3/4$ is very suggestive but it must be viewed critically because of methodological limitations.

Reich *et al.*¹⁷⁴ analyzed data for approximately 500 observations of 43 perennial plant species of coupled measurements of whole-plant dry mass and G_T from four separate studies. Collectively, the observations span five of the approximately 12 orders of magnitude of size in vascular plants.⁵³ The result of each experiment yielded an isometric scaling of $b \approx 1$ and not $b = 3/4$ as did the scaling of G_T to TBM for whole plants. Consequently, even when data look as appealing as they do in Fig. 2 things are not always what they seem.

2.1.3. Clearance curves

Another allometry phenomenon is the dependence of drug-dosing range on TBM and is referred to as clearance.⁹⁷ Zenobiotic clearance is the rate at which any foreign compound not produced by an organism's metabolism is passed from the organism. The application of allometry ideas to pharmacokinetics and to determining human parameters from those in animals is fairly recent.^{22,127,191} The early studies did not address questions of variability in the allometry parameters and were primarily concerned with whether the allometry exponent more closely tracked the value $2/3$ or $3/4$ by doing linear regression on log-transformed data.¹²²

Hu and Hayton⁹⁷ addressed the possible impact of statistical variability in the AR parameters on the predicted pharmacokinetic parameter values. They found considerable uncertainty in the value of the allometry exponent, which they fit to a Gaussian distribution with mean value 0.74. Even though they could not determine whether the variability in the allometry exponent was due to experimental error or to biological mechanisms they did find that there was no systematic deviation from the AR. However it appears that whether $b = 3/4$ or $2/3$ depends on which of the major elimination pathways is used, metabolism for the $3/4$ value and renal excretion for the $2/3$ value.

D. West & B. J. West

2.1.4. *Physiology*

The most studied of the interspecific ARs does not concern relative growth but is that associating the average BMR measured in watts to average TBM measured in kilograms of multiple species such that:

$$B = aM^b. \quad (15)$$

The metabolic rate refers to the total utilization of chemical energy for the generation of heat by the body of an animal and is often measured by the oxygen intake during respiration.

The earliest physiologic model for the value of the allometry exponent in the intraspecies AR was given by Sarrus and Rameaux.¹⁸⁸ Schmidt-Nielsen¹⁹⁵ records that this team of a mathematician and a physician reasoned that the heat generated by a warm blooded animal is proportional to the volume and the heat loss is proportional to the animal's free surface. Experiments on dogs by Rubner¹⁸³ supported their argument and lead to the wide acceptance of the "surface law" in which $b = 2/3$. In Fig. 1 the "mouse-to-elephant" curve depicts the BMR for mammals and birds plotted versus TBM on log-log graph paper spanning six orders of magnitude. The solid line segment is the fit of the AR to the data and yields the empirical value $b \approx 3/4$.

As Niklas¹⁵⁴ noted the expectation was that the metabolic rate would be proportional to the $2/3$ power of the TBM as prescribed by the surface law. Surprisingly, this turned out not to be the case. The research of Kleiber¹⁰⁹ and Brody²⁴ revealed that the slope was closer to $3/4$ than to $2/3$. Subsequent observational studies have reinforced the allometric pattern observed in the data predicted by Eq. (15) including some relating the $3/4$ -rule to plants, see, for example, Hemmingsen.⁸⁶ Consequently the phenomenological value of the allometry exponent b remains controversial.^{47,71,91}

Controversy also persists regarding the theoretical explanation as to why the allometry exponent b should have a specific value. The simple geometrical argument of Sarrus and Rameaux suggests $b = 2/3$ as reviewed in a number of excellent sources.^{31,47,91} On the other hand, the quarter-power AR is explained by West, Brown and Enquist (WBE) using geometric scaling arguments from fractal physics to establish the value $b = 3/4$ and other quarter-power scaling laws in physiology, see Sec. 4.

Heusner⁹¹ adopted geometric scaling arguments to obtain $b = 2/3$ in the AR between BMR and TBM. He argued that the various other values experimentally observed for the power-law index by investigators are a consequence of differing values of the allometric coefficient a . He reasoned that two or more data sets with $b = 2/3$ but with different values of a graph as parallel line segments on log-log graph paper, but when the two or more data sets are grouped together and analyzed as a single data set the aggregate is fit by a single line segment with net slope $b > 2/3$. The same argument can be found in a number of other references.^{176,195} But unlike those earlier references Heusner⁹¹ concluded that it is the allometry

coefficient that remains the central mystery of allometry and not the allometry exponent. We investigate the implications of Heusner's conjecture in Sec. 3 where we numerically explore the implications of treating the allometry coefficient as a random variable.

It is useful to list the various forms of physiological allometry given by Lindstedt and Schaeffer¹²²: pulmonary and cardiac allometry with $b = -1/4$; renal allometry with $b = -0.85$; liver allometry with $b = -0.85$; pulmonary blood volume with $b = 1.0$; cardiac output with $b = 3/4$ and pulmonary transit times with $b = 1/4$.

2.1.5. Information transfer

There are literally dozens of physiologic ARs for physiologic time τ , relative to clock time t , that increases with increasing body size $\tau = aM^{b120}$ and describes chemical processes such as the turnover time for glucose with $b = 1/4$ ⁹ to the life span of various animals in captivity with $b = 0.20$.¹⁸⁵ Schmidt-Nielsen¹⁹⁵ explains how a variety of physiologic time scales such as the length of a heart beat and respiration all scale with body size and from that deduce a number of interesting relations. It is only recently however that Hempleman *et al.*⁸⁸ hypothesized a mechanism to explain how information about the size of an organism is communicated to the organs within the organism. Their hypothesis involved matching the neural spike code to body size to convey this information.

Hempleman *et al.*⁸⁸ suggest that mass-dependent scaling of neural coding may be necessary for preserving information transmission with decreasing body size. They point out that action potential spike trains are the mechanisms for long distance information transmission in the nervous system. They go on to say that neural information may be "rate coded" with average spike rate over a time period encoding stimulus intensity or "time coded" with the occurrence of a single spike encoding the occurrence of a rapid stimulus transition. The hypothesis is that some phasic physiological traits are sufficiently slow in large animals to be neural rate coded, but are rapid enough in small animals to require neural time coding. These trait include such activities as breathing rates that scale with $b = -1/4$.

They tested for this allometry scaling of neural coding by measuring action potential spike trains from sensory neurons that detect lung CO₂ oscillations linked to breathing rate in birds ranging in body mass from 0.045 to 5.23 kg. While it is well known that spike rate codes occur in the sensing of low frequency signals and spike timing codes occur in the sensing of high frequency signals, their experiment was the first designed to test the transition between these two coding schemes in a single sensory network due to variation in body mass. The results of their experiments on breathing rate was an allometry exponent in the interval $-0.26 \leq b \leq -0.23$ and although taken on a small number of birds their results do suggest a preservation of information transmission rates for high frequency signals in intrapulmonary chemoreceptors and perhaps other sensory neurons as well. The implications of these experiments strongly suggest the need to continue such investigations.

On the more theoretical side Moses *et al.*¹⁴⁹ apply the scaling ideas of metabolic allometry developed by West *et al.*²⁴⁷ to information networks consisting of microprocessors to form a network. Moses *et al.*¹⁴⁹ use a fractal argument to construct a two-dimensional hierarchal self-similar branching network, an H-tree that Mandelbrot¹³¹ originally used in his discussion of the space filling behavior of the human lung. They show that this branching network of microprocessors have a striking similarity to such networks in organisms even though the latter has evolved by natural selection and the former are designed by engineers.

Along this same line E. F. Rent, while an IBM employee in the 1960s, wrote a number of internal memos (unpublished) relating the number of pins at the boundaries of an integrated circuit (X) to the number of internal components (Y), such as logic gates, to obtain an AR with $b < 1.0$. This rule has historically been used by engineers to estimate power dissipation in interconnections and for the placement of components in very large scale integrated (VLSI) circuit design. More recently Rent's Rule has been used to model information processing networks in the human brain¹⁶ where the mass of grey and white matter are shown to satisfy an AR as first noted by Schlenska.¹⁹⁴ Beiu and Ibrahim¹⁸ suggested that the allometry exponent for grey and white matter between species is identical to the Rent exponent within a species and this was supported using MRI data by Bassett *et al.*¹⁶

2.2. Physical networks

Some of the oldest ARs involve physical networks, or more specifically geophysical networks. The skeptic need only return to da Vinci's scaling relation. In his notebooks da Vinci explains the meaning of this equation not only in the context of relating tree trunks to subsequent branches, but to the branchings of rivers as well. Long before the conservation of energy and the continuity of fluid flow were known to scientists, the enigmatic Italian painter, sculptor, military engineer and anatomist understood the basics of hydrologic networks.

2.2.1. Geology and geomorphology

Horton's law of river numbers is another empirical regularity observed in the topology of river networks.⁹⁵ As observed by Scheidegger¹⁹² the number of river segments in successive order form a geometrical sequence such that, the

$$\text{number of rivers with } k \text{ tributaries} \propto R_b^{1-k}. \quad (16)$$

The bifurcation parameter R_b is the constant ratio between successive numbers of river networks, known as Horton's law of stream numbers $n_k/n_{k+1} = R_b$ and has the empirical value between 4.1 and 4.7 in natural river networks,^{159,160} in contrast to the random model that predicts a value of four. Note that the system of counting begins at the smallest tributary that are the most numerous $R_b > 1$ and these feed into larger tributaries that are fewer in number.

Dodds and Rothman⁴⁶ point out that universality arises when the qualitative character of a network is sufficient to quantify its essential features, such as the exponents that characterize scaling laws. They go on to say that scaling and universality have found application in the geometry of river networks and the statistical structure of topography within geomorphology. They maintain that the source of scaling in river networks and whether or not such scaling belongs to a single universality class is not yet known. They do provide a critical analysis of Hack's law, see also, Rodriguez-Iturbe and Rinaldo.¹⁸²

2.2.2. Hydrology

Hack's law is a hydrologic AR having to do with the drainage basins of rivers. Hack⁸³ developed an empirical relation between mainstream length of a river network and the drainage basin area at the closure of the river. Hack's law is given by,

$$\text{mainstreamlength} \propto (\text{area})^h, \quad (17)$$

where h is the Hack exponent with the typical empirical value $h \approx 0.57$. Hack asserted that river networks are not self-similar.

Mandelbrot¹³¹ relates Hack's exponent to the fractal dimension of the river network and debates the interpretation of the equation. Feder⁵⁷ observed that defining a fractal dimension for river networks was obscure and required further study. A modern version of this discussion in terms of hydrologic allometry is given by Rinaldo *et al.*¹⁸¹ who point out that optimal channel networks yield $h = 0.57 \pm 0.02$ suggesting that *feasible optimality*¹⁷⁸ implies Hack's law. Another viable model is given by Sagar and Tein¹⁸⁶ that is geomorphology realistic giving rise to general ARs in terms of river basin areas, as well as parallel and perpendicular channel lengths.

Maritan *et al.*¹³⁶ consider an analogy with the metabolic AR using $M \propto B^\alpha$, that is, $\alpha = 1/b$ so that $\alpha = 1 + h$ with the limiting values $\alpha = 3/2$ and $h = 1/2$ in the case of geometric self-similarity. Geometric self-similarity is the preservation of the river's shape as the basin increases in area. The observed values lie in the range $1.5 \leq \alpha \leq 1.6$ and the scatter of individual curves (analog of intraspecies data) is remarkably small. These values suggest that the branching nature of rivers is fractal, that is, $\alpha > 3/2$ in most cases. The ensemble average of Hack's exponents from different basins extend over 11 orders of magnitude and is indistinguishable from $h = 1/2$.¹⁴⁶ Maritan *et al.*¹³⁶ conclude that like the interspecies metabolic rate, the slope of the intraspecies h 's are washed out in the ensemble average, resulting in the value $h = 1/2$.

2.3. Natural History

Natural History embraces the study, description and classification of the growth and development of natural phenomena. The focus of investigation includes such

important contemporary areas as ecology and paleontology, parts of which rely heavily on AR and scaling.

2.3.1. Ecology

Ecology is the scientific study of the distribution, abundance and relations of organisms and their interactions with the environment. Such living networks include both plant and animal populations and communities along with the network of relations among organisms of different scales of organization. Of concern to us here are the species traits determined by body size and how these in turn affect food web stability. Woodward *et al.*²⁶¹ along with many others point out that the largest metazoans, for example, whales (10^8 grams) and giant sequoias, weigh over 21 orders of magnitude more than the smallest microbes (10^{-13} grams).^{102,234} They go on to stress the considerable variation in body mass among members of the same food web.

We do not address the traditional linking of species through such mechanisms as the prey–predator relation within food webs⁷⁶ but instead we focus on body size. The significance of body size has been systematically studied in ecology.^{27,35,102} Identifying X with species abundance and Y with TBM in Eq. (2) there is, in fact, an AR between the species at the base of a food web and the largest predator at the top.³⁵ We note that species-area power functions have a vital history in ecology^{166,258} even though the domain of sizes over which the power law appears valid is controversial.^{25,256}

Woodward *et al.*²⁶¹ emphasize that AR has been used to explain the observed relations between body size and each of: home range size, nutrient cycling rates, numerical abundance and biomass production. They speculate that body size may capture a suite of covarying species traits into a single dimension, without the necessity of having to observe the traits directly.

Brown *et al.*²⁶ discuss the universality of the documented ARs in plants, animals and microbes; to terrestrial, marine and freshwater habitats; and to human-dominated as well as “natural” ecosystems. They emphasize that the observed self-similarity is a consequence of a few basic physical, biological and mathematical principles; one of the most fundamental being the extreme variability of the data. The variety of distributions of allometry coefficients and exponents are discussed both phenomenologically and theoretically in subsequent sections.

Farr’s law²⁹ is an example of the change in ARs in the transition from organismic to environmental allometry. Farr collected data on the number of patients committed because of their mental condition and their mortality from a variety of asylums in 1830s England.⁵⁶ From these humble beginnings he was able to summarize the “evil effect of crowding” into a relation between mortality rate R and population density ρ ⁹⁶:

$$R = a\rho^b. \quad (18)$$

Here we see that the size measure used in the metabolic AR, the mass, is replaced with a measure of community structure, the population density. The ARs that capture life histories in ecology and sociology are often expressed in terms of numbers of animals and areas in addition to body mass. Calder³¹ points out that size and time seem to be the principle characteristics of life history and ecology.

The factors necessary for the formation of social groups with a restricted geographic area are not understood, but certain ARs help clarify them. The population density ρ of herbivorous mammals has been determined to be related to their mass M by³⁹ $\rho^{-1} = cM^{0.75}$ where the animals freely roam on a “home range” of given area: $A_{\text{hr}} = c'M^{1.02}$. A similar relation exists for carnivores.¹⁴⁵ Consequently, as explained by Calder,³¹ herbivorous mammals above a certain size range over an area greater than their per capita share of the local habitat. The degree of overlap was empirically determined to be⁴⁰ $A_{\text{hr}}\rho = c''M^{0.34}$, where the empirical exponent 0.34 ± 0.11 is statistically indistinguishable from that obtained by combining the separate exponents for the population density and area, that being, $1.02 - 0.75 = 0.27$. Calder conjectures that the greater the product $A_{\text{hr}}\rho$ the greater the intensity of competition and the greater the desirability of social networks that contribute to mutual tolerance within these groups. Makarieva *et al.*¹²⁹ argue that animal home range represents a biological footprint of the undisturbed state of an econetwork, however the population density adapts to disturbances in the econetwork. Consequently, the deviation of the home range-population product from isometry reflects the degree of econetwork disturbance.

The AR between maximum abundance and body size for terrestrial plants $N \propto M^{-b}$ was extended by Belgrano *et al.*¹⁹ to the maximum population densities of marine phytoplankton with $b = 3/4$. They draw the implication that maximum plant abundance is constrained by rates of energy supply in both terrestrial and marine networks as dictated by a common AR. Earlier investigators found $b > 3/4$.^{37,49}

2.3.2. Zoology and acoustics

Mice squeak, birds chirp and elephants trumpet due to scaling. Fitch⁵⁹ discusses the relationship between an organism’s body size and acoustic characterization of its vocalization under the rubric of acoustic allometry. Data indicate an AR between palate length (the skeletal proxy for vocal tract length) and body mass for a variety of mammalian species. He shows that the interspecies allometry exponent attains the geometric value of three in the regression of skull length and body mass, whereas the intraspecies allometry exponent varies a great deal. The significant variability in the intraspecies allometry exponent suggest taxon-specific factors influencing the AR.^{137,199}

Fitch⁵⁹ gives the parsimonious interpretation that the variability in the intraspecies allometry exponent could be the result of each species adopting allometric scaling during growth as postulated by Huxley, with a different proportionality

factor for each species. On the other hand, the interspecies allometry exponent could result from the common geometric constraints across species due to the wide range of body sizes. He concludes that the AR between vocal tract dimensions and body size could provide accurate information about a vocalizer's size in many mammals.

2.3.3. Paleontology

Pilbeam and Gould¹⁶⁴ provide reasons as to why body size has played such a significant role in biological macroevolution. The first is the statistical generalization known as Cope's Law or Rule, which states that population lineages increase in body size over evolutionary time scales,³⁶ that is, the body size of a species is an indication of how long it has survived on geological time scales. A second reason is the one mentioned earlier, Galileo's observation that large organisms must change shape in order to function in the same way as do their smaller prototypes.

One quantitative measure of evolution is the development of the brain in mammals at various stages of evolution. Jerison⁹⁹ showed that the brain-body relation given by Eq. (2) is satisfied by mammals with an exponent that is statistically indistinguishable from 2/3. He suggested that a may be an appropriate measure of brain evolution in mammals as a class, following the proposal of Dubois⁴⁸ that a quantitative measure of cephalization in contemporary mammals be based on the ratio; $a = \text{brain weight}/(\text{body weight})^b$. These hypotheses were directly tested by Jerison⁹⁹ using endocranial volumes and body volumes for fossil mammals at early and intermediate evolutionary stages. The data did in fact support the hypothesis.

White and Gould²⁵³ emphasize in their review of the meaning of the allometry coefficient a that it had generated a large and inconclusive literature. Reiss¹⁷⁶ notes that if brain mass is regressed on TBM across individuals in a species the slopes are shallower than of regressions calculated across mean values for different species within a single family (genus). This argument had also been presented by Gould⁸⁰ who emphasized the importance of the allometry coefficient in the geometric similarity of allometric growth. This interpretation of the allometry coefficient was at odds with the belief of the majority of the scientific community at the time that the allometry coefficient was independent of body size. This latter view is also contradicted by the data analysis in Sec. 3.

Allometry has been used by Alberch *et al.*² as the first step in creating a unifying theory in developmental biology and evolutionary ecology in their study of morphological evolution. They demonstrate how their proposed formalism relate changes in size and shape during ontogeny and phylogeny.

3. Data Statistics

In this section the phenomenology of analyzing AR measurement using statistics is discussed; collecting data, identifying patterns (laws) in the data and developing

methods of statistical analysis. Warton *et al.*²²⁰ point out that fitting a line to a bivariate data set is not a simple task and the AR literature is filled with debate over the proper methodology. Sir Julian readily adopted the statistical approach of linear regression to Eq. (3) on multiple data sets to determine the allometry coefficient a and exponent b . The sophisticated statistical techniques such as principle component analysis were not available to Sir Julian and although they can be found in the modern AR literature least-square regression still appears to be the method of choice.^{73,189}

Measures of complex phenomena always contain uncertainty and the data sets invariably fluctuate from measurement to measurement. Thus, $X(t)$ and $Y(t)$ are stochastic variables, and by implication $X(Y)$ is a random function of its argument as well. Consequently the deterministic algebraic equations relating network size and network function never unambiguously represent what is actually being measured. Subsequently, we examine the corresponding mathematical modeling, shifting the focus from the dynamic stochastic variable to the associated dynamic *pdf*.

We examine the phenomenology of the random data from measurements of various properties of allometry networks that determine empirical ARs. In particular we focus on how allometry coefficients and exponents are interpreted given that the data on which they are based fluctuate to such a large extent. Part of the reason for taking this approach is that a significant number of scientists adopt the viewpoint that fluctuations reflect lack of control and/or ignorance about what is being measured. Here we adopt the more sympathetic view that networks are generically random because they are dynamic and complex in which case statistics provide information about the fundamental nature of that complexity.

3.1. Fluctuations

All complex dynamic networks are stochastic, either due to intrinsic nonlinear dynamics producing chaos,^{123,124,155} or due to coupling of the network to an infinite dimensional albeit unknown environment,¹¹⁸ or both; completely aside from measurement errors. Consequently, it is necessary to understand how statistical uncertainty may be included in modeling allometry data. Kaitaniemi¹⁰⁴ pointed out that the potential information content of the allometry coefficient has been largely neglected, an observation also made by Glazier⁷³ among others. Kaitaniemi examined the different ways this parameter may vary for different sources of random fluctuations. Here we follow a similar strategy, but we use actual data rather than computer generated random fluctuations.

The normal or Gauss *pdf* suggests that the statistical variations between the variables in the AR Eq. (2) may be additive leading some scientists^{70,130,203} to propose the form:

$$Y = \bar{a}X^{\bar{b}} + \eta, \quad (19)$$

D. West & B. J. West

where η depicts the random fluctuations and the overbars denote the fitted values of the parameters. Packard and Boardman¹⁵⁷ also investigate the regression of data to a three-parameter power law that does not pass through the origin

$$Y = Y_0 + \bar{a}X^{\bar{b}} + \eta. \quad (20)$$

In the near isometry case where $\bar{b} \approx 1$ linear regression analysis is appropriate and additive fluctuations provide a satisfactory representation of the statistical variability. On the other hand when the allometry exponent is substantially different from unity the determination of the nature of the fluctuations requires preliminary statistical analysis, see, for example, Packard.¹⁵⁶

Packard and Boardman¹⁵⁷ emphasize that the additive form of fluctuations in ARs is quite different from the situation involving the logarithmically transformed data. For the transformed data introducing additive random fluctuations yields:

$$\log Y = \log \bar{a} + \bar{b} \log X + \eta, \quad (21)$$

and the empirical constants \bar{a} and \bar{b} are fit to the transformed data. In terms of the original AR we obtain:

$$Y = \bar{a}e^{\eta}X^{\bar{b}} \quad (22)$$

with the fluctuations being exponentially amplified through e^{η} . It is evident that when the fluctuations are considered to be focused in the allometry coefficient, as they are here, they are multiplicative. The multiplicative character of the fluctuations implies that the influence of the random variations is amplified far beyond their additive cousins.

They emphasize that the focus of the research on log-transformed data is to characterize patterns of variation in morphology, physiology and ecology in organisms spanning a broad range in body size in an attempt to identify underlying principles in the design of biological networks, see, for example, Brown *et al.*²⁷ and references therein. They go on to assert that many of the patterns identified by this research are inaccurate and misleading and these mischaracterizations likely contribute to the ongoing debate about ways in which animals are constructed.

We saw that fluctuations in the log-transformed data may be equivalent to multiplicative fluctuations in the original data. So the important question is whether it is necessary to perform the logarithmic transformation at all. Packard and Boardman¹⁵⁷ point out that the original motivation for the log-transform was to linearize the equations thought to represent the data and therefore facilitate the implementation of graphical and statistical analysis.^{162,203} However, they go on to show the biasing problems associated with log-transforms using computer generated data sets and caution that with the present day computer software for fitting nonlinear equations linearization is no longer a sufficient rationale for log-transforms. So are there other reasons to transform the data?

Kerkhoff and Enquist¹⁰⁶ strongly disagree with the conclusions of Packard (2008) that standard methods for fitting allometry models produce “biased and

misleading” results. They point out that most biological phenomena are inherently multiplicative^{63,66} and it is the proportional rather than absolute variation that matters. The multiplicative influence of noise seen in the log-transformed data is often misinterpreted as bias.^{203,263} Kerkhoff and Enquist¹⁰⁶ maintain that the multiplicative error model is an appropriate feature, rather than a defect, of standard allometry analysis. Recent research suggests that geometric error resulting from multiplicative fluctuations should be the default standard for parameter estimation in biology^{66,81} and not additive error.

3.2. Phenomenological distributions

We now consider the statistics of the fluctuations in the AR using data from the literature. The data relating the average energy expended by a given species in watts to the average TBM of that species in kilograms for 391 species of mammal is plotted in Fig. 3 and also in Heusner⁹¹ as well as in Dodds *et al.*⁴⁷ A fit of Eq. (3) to these data that minimizes the mean-square error is a straight line on double logarithmic graph paper and was found to have slope $\bar{b} = 0.71 \pm 0.008$ so that empirically $2/3 < \bar{b} < 3/4$ and the allometry coefficient $\bar{a} = 0.02$. As West and West²⁴⁵ reviewed Heusner⁹⁰ had somewhat earlier questioned Kleiber’s value of $3/4$ and concluded from data analysis that this value of $3/4$ was a statistical artifact. Feldman and McMahon⁵⁸ agreed with Heusner’s conclusions, but suggested that there was no compelling reason for the intraspecies and interspecies allometric exponents to be the same, with the intraspecies exponent being $2/3$ based on geometric similarity and the interspecies exponent being $3/4$ based on McMahon’s elastic similarity.

There is a great deal of variability around the line segment that gives the AR model in Fig. 3. West and West²⁴⁵ interpret these fluctuations as random variations

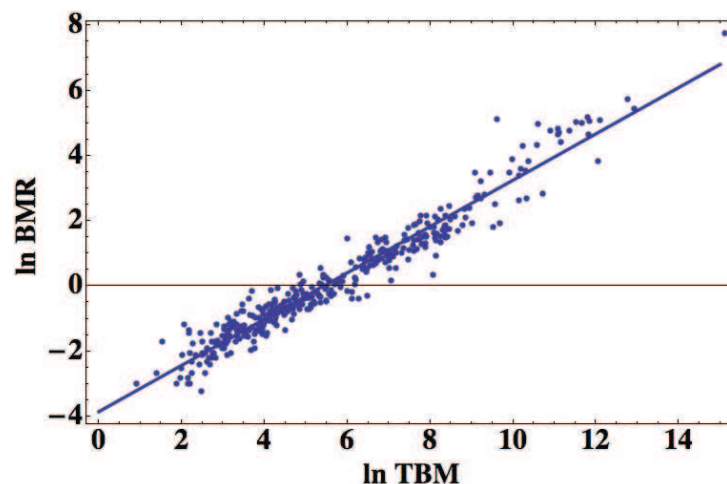


Fig. 3. The linear regression to Eq. (3) for Heusner’s data⁹¹ is indicated by the line segment. The slope of the dashed line segment is 0.71 ± 0.008 .

in either the allometry coefficient or the allometry exponent. If the fluctuations are assumed to be contained in the allometry coefficient we can define

$$\frac{a}{\bar{a}} = e^\eta = \frac{B}{\bar{a}M^{\bar{b}}} \quad (23)$$

so that each data point in the (X, Y) -plane yields a single value of the allometry coefficient. In a complex network a linear response such as suggested by Fig. 3 does not necessarily occur since there can be independent fluctuations in both X and Y resulting in what Warton *et al.*²²⁰ call equation error; also known as natural variability, natural variation and intrinsic scatter. In the present case the AR is not predictive, but instead summaries vast amounts of data.²⁵⁵ This natural variability is manifest in fluctuations in the allometry parameters (a, b) .

West and West²⁴² calculate the statistical distribution for the random allometry coefficient determined from Eq. (23) under the assumption that \bar{b} is fixed. The variability in the allometry coefficient determined by the data is partitioned into 20 equal sized bins in the logarithm of the allometry coefficient. A histogram is then constructed by counting the number of data points within each of the bins as indicated by the dots in Fig. 4. The solid line segment in this figure is the best fit to these 20 numbers with minimum mean-square error. The functional form for the histogram is indicated by the curve in Fig. 4^{241,242} and the quality of the fit to the diversity data is determined by the correlation coefficient $r^2 = 0.98$. The normalized histogram $G(\ln a')$ on the interval $(0, \infty)$ using the transformation

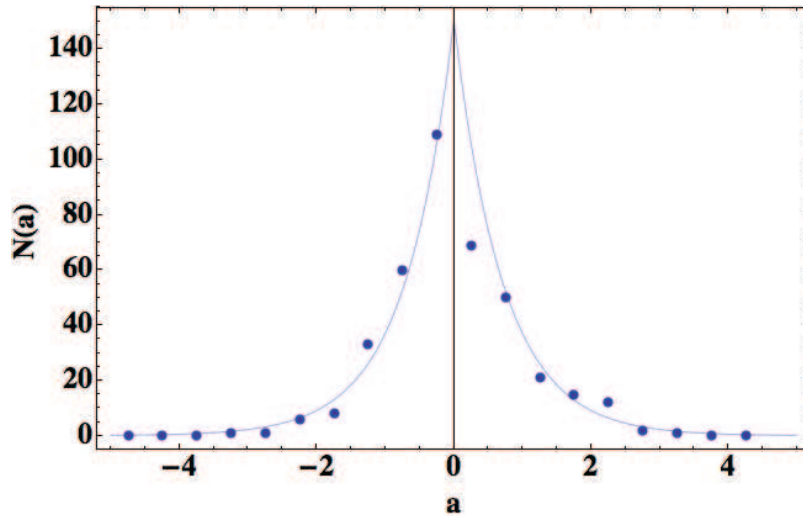


Fig. 4. The histogram of the deviations from the prediction of the AR using the data depicted in Fig. 3 partitioned into 20 equal sized bins in the logarithm of the normalized variable $a' = a/\bar{a}$. Here $\bar{a} = 0.02$ and $\bar{b} = 0.71$. The solid line segment is the best fit of Eq. (24) to the 20 histogram numbers, which yields the power-law index $\alpha = 2.79$ and the quality of the fit is measured by the correlation coefficient $r^2 = 0.98$. (Reproduced from West and West²⁴² with permission).

$G(\ln a')d\ln a' = P(a')da'$ gives the empirical *pdf*:

$$P(a') = \frac{\alpha}{2} \begin{cases} \frac{1}{a'^{1-\alpha}}; & a' \leq 1 \\ \frac{1}{a'^{1+\alpha}}; & a' \geq 1 \end{cases} \quad (24)$$

and $\alpha = 3.28$ yielding a standard deviation 0.017 in essentially exact agreement with the empirical data. Note that this coefficient differs from the best fit value given in the caption of Fig. 4 but this results in only a 1% change in the value of r^2 .

The same inverse power-law form is obtained with $\alpha = 3.89$ and $r = 0.96$ using the avian BMR data of McNab¹⁴² for 533 species of bird. The distribution of the deviations from the AR for both the avian and mammalian data sets fall off as inverse power laws on either side of $a = \bar{a}$. Equation (24) quantifies the qualitative argument used earlier to associate power-law *pdf*'s with multiplicative fluctuations, see also Sec. 5.

Alternatively the fluctuations can be assumed to be contained within the allometry exponent as:

$$\eta = \frac{\log(B/\bar{a})}{\log M} - \bar{b}. \quad (25)$$

If we assume $\bar{b} = 0.71$ and $a = \bar{a}$ then Eq. (25) provides us with the statistical fluctuations in the allometry exponent are used to construct a histogram exactly as we did previously. The solid line segment in Fig. 5 is the best fit to the 20 numbers of the histogram with minimum mean-square error. The functional form for the histogram of deviations from the allometry exponent \bar{b} is determined by the curve in Fig. 5 and the quality of the fit to the histogram is determined by the correlation coefficient $r^2 = 0.97$. The histogram is fit by the Laplace *pdf*

$$\Psi(b) = \frac{\beta}{2} \exp[-\beta|b - \bar{b}|], \quad (26)$$

with the empirical value $\beta = 12.85$.

3.2.1. Co-variation of allometry coefficient and exponent

We have obtained two separate distributions for two different parametric representations of the same data. As pointed out by Glaizer⁷³ species within a taxon represent a cloud of different metabolic rates and not the linear metabolic level determined by linear regression. His cloud is incorporated into the present context by abandoning the assumption that the allometry coefficient and exponent are independent and requiring that the probability of a given fluctuation is the same regardless of the representation so that $\mathcal{P}(a)da = \Psi(b)db$. In order to calculate a nonzero Jacobian of the transformation between the two allometry parameters requires that they be functionally related. West and West²⁴³ assume $b = \bar{b} - c \ln a$, so that by inserting the

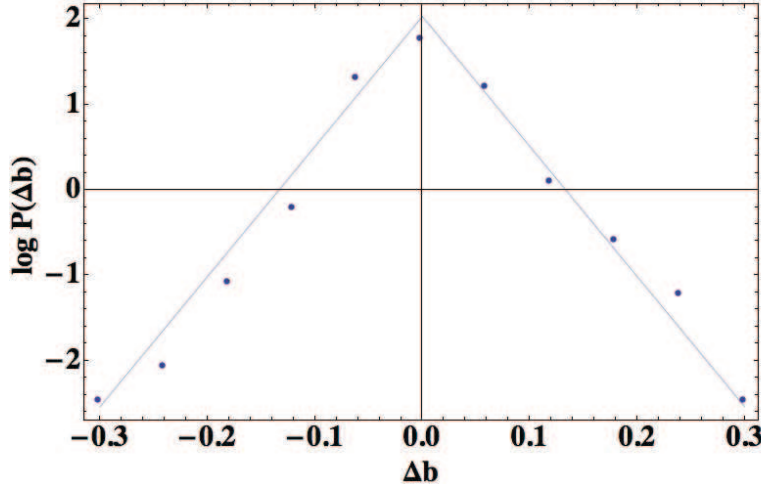


Fig. 5. The histogram of the deviations from the prediction of the AR using the allometry exponent fluctuation data partitioned into 20 equal sized bins. The solid line segment is the best fit of Eq. (26) with $\Delta b \equiv b - \bar{b}$, to the 20 histogram numbers, and the quality of the fit is measured by the correlation coefficient $r^2 = 0.97$. (Reproduced from West and West²⁴² with permission).

allometry exponent *pdf* Eq. (26) into that for equal probabilities and simplifying yields:

$$\mathcal{P}(a) = \frac{\beta c}{2} \begin{cases} a^{\beta c - 1} & \text{for } a \leq \bar{a} \\ \frac{1}{a^{\beta c + 1}} & \text{for } a \geq \bar{a} \end{cases} \quad (27)$$

and comparing Eq. (27) with Eq. (24) they identify $\alpha = \beta c$ and obtain the empirical *pdf* for the allometry coefficient $P(a')da' = \mathcal{P}(a)da$. Using the fitted values $\alpha = 2.79$ and $\beta = 12.85$ yields $c = 0.217$ and consequently the empirical transformation can be written as:

$$b = 0.71 - 0.50 \log_{10} a. \quad (28)$$

Note that this functional dependency of the allometry exponent on the allometry coefficient is consistent with the empirical co-variation relation obtained by Glazier⁷³ who used linear regression on large amounts of parametric data. West and West²⁴³ emphasize that this co-variation of the allometry parameters implies that there is no universal value for the allometry exponent.

3.2.2. Other scaling distributions

The tent shaped distribution in Fig. 5 also arises using a different approach to quantifying the variability of BMR. Labra *et al.*¹¹⁵ investigate BMR fluctuations by considering O₂ volume time series and examining the scaling of the high frequency fluctuations across species. They determined empirically that the standard

deviation in the BMR is proportional to the average BMR by the scaling law:

$$SD_{\text{BMR}} \propto B^\lambda$$

and $\lambda = -0.352 \pm 0.072$. This relation is known as the power curve in the ecology literature⁸⁵ and was discovered by Taylor²¹⁰ in his determination of the number of new species that can be found in a given plot of ground. It was expanded to the determination of scaling in time series by Taylor and Woivold²¹¹ and applied in physiology as Taylor's law in West.²³⁸

On the other hand Labra *et al.*¹¹⁵ determined the standard deviation of BMR to be proportional to a power of the TBM:

$$SD_{\text{BMR}} \propto M^\gamma$$

and $\gamma = -0.241 \pm 0.103$. Consequently, combining the two empirical expressions for the variance we obtain:

$$B \propto M^{\gamma/\lambda} \quad (29)$$

with $\gamma/\lambda = 0.69$ a value consistent with the many fits made to the allometry data. They determine that all the species they studied show the same invariant distribution of BMR fluctuations, regardless of the difference in their phylogeny, physiology and body size. The distribution has the form Eq. (26) with the independent variable given by the fluctuation in the BMR ΔB and $\beta = \sqrt{2}/SD_{\text{BMR}}$; in terms of the scaling variable $B_{\text{sc}} \equiv \sqrt{2}\Delta B/SD_{\text{BMR}}$ curves for 12 different species collapse onto a single universal curve.

3.2.3. Paleobiology and scaling

Phenomena with intermittent properties described by inverse power-law statistics are apparently ubiquitous²³³ and paleobiology is no exception. Bak and Boettcher⁸ interpreted Charles Lyell's¹²⁵ uniformitarianism as meaning that all geologic activity should be explainable in terms of readily available processes working at all times and all places with the same intensity. They go on to argue that the existence of earthquakes, volcanic eruptions, floods and tsunamis all indicate that the physical world is not in equilibrium. Moreover the intermittent nature of the paleontological record indicates that macroevolution is also out of equilibrium and consequently the inverse power-law statistics are possibly suitable for their description.

Eldredge and Gould⁵² argued that punctuated change dominates the history of life and that relatively rapid episodes of speciation constitute biological macroevolution. The intermittency of speciation in time has been explained by one group as *punctuated equilibria*⁵¹ and has been indirectly related to fractal statistics by identifying it as a self-organized critical phenomenon.⁸ In the self-organized criticality model of speciation Bak and Boettcher⁸ associate an avalanche of activity with exceeding a threshold and the distribution of returns to the threshold with a "devil's staircase" having a distribution of steps of stasis of lengths given by the

D. West & B. J. West

inverse power-law *pdf*, that is, $T^{-\gamma}$ with $\gamma = 1.75$. Moreover, as explained by Sneppen *et al.*,²⁰⁶ the number of genera N , with a lifetime T can be fitted very well to a power law $T^{-\beta}$ with $\beta \approx 2$.¹⁷³ More recently Rikvold and Zia¹⁷⁹ put forward an explanation of punctuated equilibrium based on $1/f$ noise in macroevolutionary dynamics that also yields an inverse power-law *pdf* for the life time of ecological communities with $\beta = 2$.

Solé *et al.*²⁰⁸ analyzed the statistics of the extinction fossil record (time series) and determined that the power spectrum has the form:

$$S(f) \propto 1/f^\mu,$$

with $0 < \mu < 2$. They find $0.80 \leq \mu \leq 0.90$ and argue that these values support the self-organized criticality interpretation of extinction. On the other hand, Plotnick and Sepkowski¹⁶⁵ also find a $1/f$ power spectrum with a power-law index for extinction consistent with Solé *et al.*²⁰⁸ and indices for species generation of approximately half that for extinction. However the latter authors conclude that their results are incompatible with self-organized criticality and instead are compatible with multifractal self-similarity in both the extinction and generation records.

4. Models of Allometry

Two distinct methods dominate the many derivations of AR. One method is based on the first-principles reductionistic approach starting from an assumed form for the underlying mechanisms and from that deducing the necessity of Eq. (2). The other method is phenomenological involving statistical analysis and identifying patterns in the data analysis and from these patterns deducing the necessity of the empirical AR. A number of the statistical methods were reviewed in the previous section. The ARs stand out as empirical relations that have withstood the test of time, whereas the same cannot be said for the models developed to explain how they come about. In this section we examine attempts to formulate general principles from which the underlying mechanisms, whether reductionist or statistical, producing the ARs can be identified.

The search for an *unifying principle* parallels such historical activities as the determination of “least action” in analytic mechanics or optimization in control theory. More recently investigators have rediscovered Newton’s “principle of similitude” introduced in the *Principia* (II, Proposition 32). Scaling and the principle of similitude have been present in the study of complex physical phenomena since physics became a science. In modern times it is RG theory that provides a formalism for determining how force is transferred across multiple scale.^{103,111,259} Part of the reason for exploring this approach is that fractal geometry and fractal statistics are able to capture some of the regularity observed in vast amounts of data in the life and social sciences in addition to the physical sciences. The implementation of fractal geometry and RG theory to study the architecture of physiological forms,^{17,228,247} interacting networks of chemical reactions^{45,78,169} and

the topology of ecological webs²⁷ over the past quarter century has lead to some remarkable insights. In particular the descriptive success of investigations using fractals^{15,131,135,143} suggests that branching networks with fractal architectures have an evolutionary advantage^{230,231,235} as do fractal stochastic processes.²³⁶

4.1. Optimization principles

Optimization provides one of the best recipes for determining network dynamics consistent with a given set of constraints. It is through the specification of the constraints that insight into a phenomenon is introduced. The biological sciences employ ideas such as energy minimization; the minimal use of materials along with the maximization of efficiency. So whether the extremum is a minimum or maximum depends on one's purpose and the quantity being varied.

4.1.1. Energy minimization

Scaling relations in living networks result from the balancing of various constraints. One such biological balancing is that of energy utilization against the energy cost of carrying out a biological function. A technique that has been used both implicitly and explicitly in the derivation of ARs is supplying nutrients to various parts of an organism through the venous and capillary networks as well as through the respiratory network. Murray¹⁵⁰ considered a fluid with viscosity ν and laminar flow Q within a tube of length l and radius r . The flow had to overcome the vascular resistance that generates a pressure difference along the length of the tube given by Poiseuille's law $\Delta p = 8\nu Q l / \pi r^4$.

A constraint on the flow is the cost of transporting fluid of cylindrical volume $V = \pi l r^2$ along the tube so that introducing c as the cost factor the total work to be done per unit time is given by:

$$E = Q\Delta p + cV = \frac{8\nu Q^2 l}{\pi r^4} + c\pi l r^2. \quad (30)$$

Consequently, minimizing this expression with respect to the radius yields the optimal flow: $Q = Cr^3$ with the constant $C = \sqrt{c\pi^2/16\nu}$. The cubic dependence of the flow rate on radius is known as Murray's law²²³ and is indicative of the maximum efficiency of the flow.

Murray¹⁵¹ subsequently extended his result to bifurcating networks such as occurs in bronchial airways. The flow from a parent vessel of radius r_0 branches into two daughter vessels r_1 and r_2 such that the flow divides:

$$Q_0 = Q_1 + Q_2.$$

Therefore inserting Murray's law into this expression yields da Vinci's equation with $\alpha = 3$ and in the case of equal radii in the daughter branches $r_1 = r_2$ we obtain the scaling relation $r_1 = 2^{-1/3}r_0$. Thus, the maximally efficient bifurcating network in terms of energy transport cost has radii decreasing as the cube root of two. As

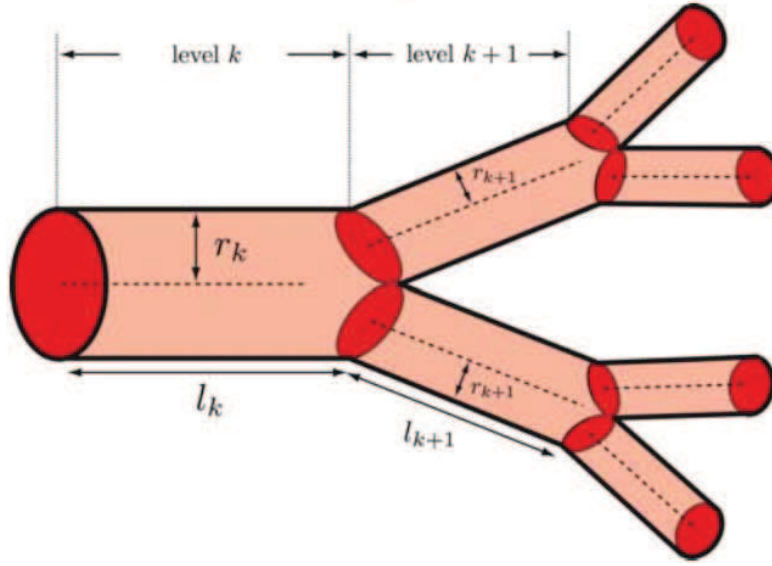


Fig. 6. Sketch of a branching structure such as a blood vessel or bronchial airway with the parameters used in a bifurcating network model.

pointed out by Weibel²²³ this last result is also known as Murray's law. However this law was actually first formulated by Hess⁸⁹ for blood vessels and subsequently is more properly called the Hess–Murray law.

4.1.2. Optimal design

Rashevsky¹⁷² introduced the *principle of optimal design* in which the material used and the energy expended to achieve a prescribed function is minimal. He applied the principle to the basic problem of how the arterial network could branch in space in order to supply blood to every element of tissue. To address this problem he used the model of a bifurcating branching network supplying blood to a restricted volume and reducing the total resistance to the flow of blood. His purpose was to determine the condition imposed by the requirement that the total resistance is minimum.

Here we assume the branching network is composed of N generations from the point of entry (0) to the terminal branches (N). A typical tube at some intermediate generation k has length l_k , radius r_k and pressure drop across the length of the branch Δp_k as sketched in Fig. 6. The volume flow rate Q_k is expressed in terms of the flow velocity averaged over the cross sectional area u_k : $Q_k = \pi r_k^2 u_k$. Each tube branches into n smaller tubes with the branching of the vessel occurring over some distance that is substantially smaller than the lengths of the tubes of either generation. Consequently, the total number of branches generated up to generation k is $N_k = n^k$. The pressure difference at generation k between the ends of a tube

is given by a suitably indexed version of Poiseuille's law and the total resistance to the flow is given by the ratio of the pressure to flow rate

$$\Omega_k = \frac{\Delta p_k}{Q_k} = \frac{8\nu l_k}{\pi r_k^4}. \quad (31)$$

The total resistance for a network branch with m identical tubes in parallel is $1/m$ the resistance of each individual tube. Thus, in this oversimplified case we can write the total network resistance as:

$$\Omega_T = \frac{8\nu l_1}{\pi r_0^4} + \frac{8\nu}{\pi} \sum_{j=1}^N \frac{1}{N_j} \frac{l_k}{r_j^4}. \quad (32)$$

In order to minimize the resistance for a given mass Rachevsky first expressed the initial radius r_0 in terms of the total mass of the network. The optimum radii for the different branches of the bifurcation network having the total mass M are then determined such that the total resistance is a minimum $\partial\Omega_T/\partial r_j = 0$ yielding the equality $r_k = N_k^{-1/3} r_0$. The ratio of the radii between successive generations is $r_{k+1}/r_k = (N_k/N_{k+1})^{1/3}$ so that inserting the number of branches at the k th generation $N_k = n^k$ yields:

$$r_{k+1}/r_k = n^{-1/3}, \quad (33)$$

yielding an exponential reduction in the branch radii across generations. Note the formal similarity of this ratio to Horton's law in which the ratio of numbers of river branches is independent of generation number.

Rashevsky considered the bifurcating case $n = 2$ where the ratio of radii reduces to $r_{k+1}/r_k = 2^{-1/3} = 0.794$. This is the classic "cube law" branching of Thompson²¹³ in which he used the "principle of similitude". The value $2^{-1/3}$ was obtained by Weibel and Gomez²²² for the reduction in the diameter of bronchial airways for the first ten generations of the bronchial tree. However they noted a sharp deviation away from this constant fractional reduction after the tenth generation. The value $2^{-1/3}$ was also obtained by Wilson²⁶⁰ who explained the proposed exponential decrease in the average radius of a bronchial tube with generation number by showing that this is the functional form for which a gas of given composition can be provided to the alveoli with minimum metabolism or entropy production in the respiratory musculature. He proposed minimum entropy production⁶⁹ as the design principle for biological networks to carry out a given function.

The deviation from classical (exponential) scaling above generation ten shown in Fig. 7 was eventually explained using an alternative model of the bronchial airways in terms of fractal statistics²²⁸ as we subsequently discuss.

4.2. Metabolic allometry

Barenblatt and Monin¹⁴ proposed that metabolic scaling might be a consequence of the fractal nature of biology, but they did not provide a mechanistic model for its

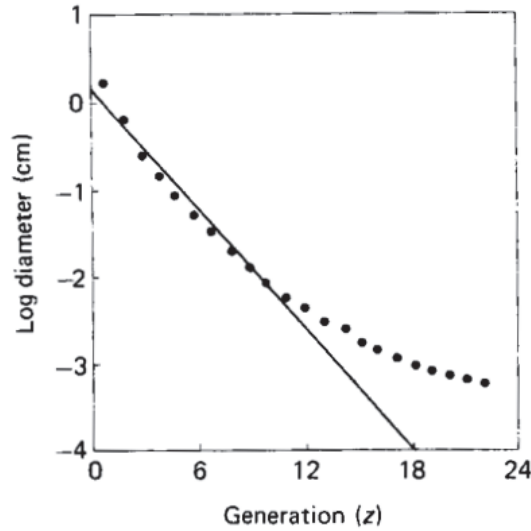


Fig. 7. As the bronchial tree branches out, its tubes on average decrease in size. A theory consistent with the Principle of Similitude²¹³ predicts that their diameters should decrease by about the same ratio from one generation to the next; exponential decline. This semilog graph shows measurements from Weibel and Gomez²²² for 23 generations of bronchial tubes in the human lung. The prediction is a straight line that fits the anatomic data (dots) until about the tenth generation, after which they deviate systematically from an exponential decline. [adapted from West and Goldberger.²²⁹]

description. This shortcoming has been overcome by a number of investigators who have devised numerous fractal models to describe AR in a variety of contexts.^{228,247}

4.2.1. Elastic similarity model

The first model to analytically predict the allometry exponent $3/4$ was constructed by McMahon.^{139,140} His argument rests on the observation that the weight of a column increases more rapidly with size than does its strength. Moreover as discussed by Schmidt-Nielsen¹⁹⁵ if the column is tall and slender it can fail due to elastic buckling in which small lateral displacements exceed the elastic restoring forces. For a sufficiently slender column with Young's elastic modulus E and density ρ the critical length of a column of diameter d is:

$$l_{cr} = k(E/\rho)^{1/3}d^{2/3} \quad (34)$$

and k is a constant. The elastic criteria of McMahon is therefore given by $l^3 \propto d^2$. The weight of the column is given by the product of the density, length and cross-sectional area,

$$Mg = \rho d^{2/3} \pi d^2 / 4,$$

where the length has been replaced using the elastic criteria yielding $d \propto M^{3/8}$.

The implications for allometry of the scaling between cylinder diameter and mass was discussed by Calder³¹ using the symmorphosis hypothesis of Taylor and Weibel:²¹² "... is regulated to satisfy but not exceed the requirements of the functional system".²³⁷ First off we recognize that locomotion requires the contraction of muscles. During contraction, muscles exert a force that increases with the cross-sectional area of the muscle. The power output of the muscle is the work done per unit time and may be equated with the metabolic rate, the product of the force generated by the muscle and the velocity u of the shortening of the muscle $B \propto d^2 u$. The velocity of the shortening of the muscle appears to be a size-independent constant from species to species⁹² so that using these two equations for the diameter yields:

$$B \propto M^{3/4}.$$

Consequently, the allometry exponent $3/4$ in McMahon's elastic similarity model is required to maintain the flow of energy to the working muscles and is consistent with the principle of symmorphosis.

Versions of the above argument given by both Calder³¹ and Schmidt-Nielsen¹⁹⁵ seem to explain the value of the allometry exponent for warm blooded animals. Dodds *et al.*⁴⁷ critique McMahon's model by noting that there is no compelling reason why the power output of muscles should be the dominant factor in the scaling of BMR. Moreover, Savage *et al.*¹⁸⁹ point out that while the elastic similarity model might apply to the bones of mammals or the trunks of trees that have adapted to gravitational forces, it is doubtful that it is applicable to aquatic or unicellular organisms that also display an allometry exponent of $3/4$.⁸⁷

4.2.2. WBE model

West, Brown and Enquist²⁴⁷ (WBE) published a quantitative model of metabolic AR that has had significant impact on how a significant fraction of today's biology/ecology community understands metabolic ARs. WBE model nutrient distribution within a hierarchal network in which vessels become narrower, shorter and more numerous between successive levels proceeding from the initial to the terminal level reminiscent of representations of river branchings. The scaling in the transport network is a consequence of the constraints imposed by three assumptions: (1) The entire volume of the organism is crammed with a space-filling branching network. (2) The tube properties at the terminus of the network are size-invariant. (3) The energy required to distribute resources using this network is minimal, that is, the hydrodynamic resistance of the network is minimized. We note their claim that this model is the origin of universal scaling laws in biology^{248,249} with $b = 3/4$. However we recall at the start that the existence of an empirical exponent $b = 3/4$ for metabolic AR has been questioned by numerous investigators^{47,91,113,114,128} and we address these concerns and others in due course.

D. West & B. J. West

WBE introduce two parameters to characterize the network branching process, $\beta_k = r_{k+1}/r_k$ the ratio of successive branch radii, as was done in the energy minimization arguments¹⁷² and the other is $\gamma_k = l_{k+1}/l_k$, the ratio of successive branch lengths. They conclude that the total number of terminal branches scales with TBM as $N_T = (M/M_0)^b$. The total number of branches at level k is $N_k = n^k$. Consequently at the network terminus the self-similarity of the network yields $N_T = n^N$ and consequently the total number of branches is:

$$N = b \ln(M/M_0) / \ln n. \quad (35)$$

Rashevsky's energy minimization argument indicates that the transport of nutrients in complex networks is maximally efficient when β_k is independent of k . This is the "fractal" scaling assumption made by WBE.

The estimates of the ratio parameters required two separate assumptions. To estimate the ratio of lengths WBE assume that the volume of a tube at generation k can be replaced by a spherical volume of diameter l_k and in this way implement the space-filling assumption. The conservation of volume between generations therefore leads to the space filling condition:

$$(l_{k+1}/l_k)^3 \approx N_k/N_{k+1} = n^{-1}$$

and consequently to the k -independent parameter

$$\gamma = \gamma_k = n^{-1/3}.$$

They maintain that this level-independent scaling of the lengths is a generic property of all the space-filling networks they consider. This condition for an n -branching network with a reduction in size of $n^{-1/3}$ between successive generations yields using the definition for the fractal dimension $D = \log n / \log n^{1/3} = 3$.

A separate and distinct assumption is made to estimate β using the classic rigid-pipe model to equate the cross-sectional areas between successive generations: $\pi r_j^2 = n \pi r_{j+1}^2$, so that we have

$$\beta = \beta_k = n^{-1/2}.$$

Note that this scaling of β differs from the ratio parameter obtained using energy minimization. Inserting these values of the scaling parameters into the expression for b yields the sought after exponent $b = 3/4$. This value of the exponent in turn determines a number of other quarter-power scaling laws.

WBE point out that this is strictly a geometrical argument applying only to those networks that exhibit area-preserving branching. Moreover the fluid velocity is constant throughout the network and it is independent of size. They go on to say that these features are a natural consequence of the idealized vessel-bundle structure of plant vascular networks in which area-preserving arises automatically because each branch is assumed to be a bundle of n^{N-k} elementary vessels of the same radius. They recognized that this is not the situation with vascular blood flow where the beating of the heart produces a pulsating flow that generates a very

different kind of scaling. Area-preserving is also not true in the mammalian lung where there is a distribution of radii at each level of branching.

A physical property that the area preserving condition violates is that blood slows down in going from the aorta to the capillary bed. Here WBE return to the principle of energy minimization and as stated by West²⁴⁸ assert that to sustain a given metabolic rate in an organism of fixed mass, with a given volume of blood, the cardiac output is minimized subject to a space-filling geometry. This variation is essentially equivalent to minimizing the total impedance since the flow rate is constant and again yields the Hess–Murray law $\beta = n^{-1/3}$ corresponding to area-increasing branching.^{6,190} This change in scaling from the area-preserving $n^{-1/2}$ to the area-increasing $n^{-1/3}$ solves the problem of slowing down blood flow to accommodate diffusion at the capillary level. Moreover, the variation also leads to an allometry exponent $b = 1$. Such an isometric scaling ($b = 1$) suggests that plants and animals follow different allometry scaling relations as was found.^{174,201}

A detailed treatment of pulsate flow is not straightforward and will not be presented here, but see Savage *et al.*¹⁹⁰; Silva *et al.*²⁰¹ and Apol *et al.*⁶ for details and commentary in the context of the WBE model. We do note that for blood flow the walls of the tubes are elastic and consequently the impedance is complex, as is the dispersion relation that determines the velocity of the wave and its frequency. Consequently pulsate flow is attenuated^{32,60} and WBE argue that the impedance changes its r -dependence from r^{-4} for large tubes to r^{-2} for small tubes. The variation therefore changes from area-preserving flow $\beta = n^{-1/2}$ for large vessels to dissipative flow $\beta = n^{-1/3}$ for small vessels where blood flow is forced to slow. Thus β_k is k -dependent in the WBE model for pulsate flow and at an intermediate value of k the scaling changes and this changeover value is species dependent. These results are contradicted in the more extensive analysis of pulsate flow by Apol *et al.*,⁶ who conclude that Kleiber’s law remains theoretically unexplained.

Kozłowski and Konarzewski¹¹³ critique the apparent limitations of the WBE model assumptions. The size-invariance assumption has been interpreted by them to mean that $N_T \propto M$, that is, the terminal number of vessels scales isometrically with size and consequently causes the number of levels to be a function of body size since more levels are required to fill a larger volume with the same density of final vessels. However Brown *et al.*²⁸ assert that $N_T V_T \propto M$ so that

$$N_T \propto M^{3/4} \quad (36)$$

to which Kozłowski and Konarzewski¹¹⁴ respond that such mass dependence is an arbitrary assumption and is not proven, see also Dawson.⁴³ Etienne *et al.*⁵⁴ reconstruct the WBE model without making the self-similarity assumption and in so doing satisfy the concerns of Kozłowski and Konarzewski.^{113,114} The arguments remain unresolved and Cyr and Walker³⁸ refer to the assumption embodied in Eq. (36) as the illusion of mechanistic understanding and maintain that after a century of work the jury is still out on the magnitude of the allometry exponents. Riisgård¹⁸⁰ argues that respiration and growth are integrated through the energetic

costs of growth and that this explains why the b value is not a “natural constant” and that a “3/4 power scaling law cannot be deduced from the interplay between pure physical and geometric constraints of the transport of oxygen.

A quite different critique comes from Savage *et al.*¹⁹⁰ who emphasize that the WBE model is only valid in the limit $N \rightarrow \infty$, that is, for infinite network size (body mass) and that the actual allometry exponent predicted depends on the sizes of the organisms considered. They calculate that the AR between BMR and TBM have corrections for finite N given by:

$$M = a_1 B + a_2 B^{4/3} \quad (37)$$

from which it is clear that $b = 3/4$ only occurs when $a_2 B^{1/3} \gg a_1$. This inequality is not satisfied for bodies of finite size. In their original publication WBE acknowledged the potential importance of such finite-size effects, especially for small animals, but the magnitude of the effect remained unspecified. Using explicit expressions for the coefficients in the WBE model Savage *et al.*¹⁹⁰ show that when accounting for these corrections over a size range spanning the eight orders of magnitude observed in mammals a scaling exponent of $b = 0.81$ is obtained. Moreover in addition to this strong deviation from the desired value of $3/4$ there is a curvilinear relation between the TBM and the BMR in the WBE model given by:

$$\ln M = \ln a_2 + \frac{4}{3} \ln B + \ln \left(1 + \frac{a_1}{a_2} B^{-1/3} \right),$$

whose curvature is opposite to that observed in the data. Consequently they conclude that the WBE model needs to be amended and/or the data analysis needs reassessment to resolve this discrepancy. A start in this direction has been made by Kolokotronis *et al.*¹¹⁰ Agutter and Tuszynski⁵ also review the evidence that the fractal network theory for the two-variable AR is invalid.

Another variation on this theme was made by Price *et al.*¹⁶⁸ who relax the fractal scaling assumptions of WBE and show that allometry exponents are highly constrained and covary according to specific quantitative functions. Their results emphasize the importance of network geometry in determining the allometry exponents and supports the hypothesis that natural selection minimizes hydrodynamic resistance. Moreover they extended McMahon’s elastic similarity model and apply it to plant scaling exponents showing its consistency with their modification of WBE.

Prior to WBE there was no unified theoretical explanation of quarter-power scaling. Banavar *et al.*¹² show that the $3/4$ exponent emerges naturally as an upper bound for the scaling of metabolic rate in the radial explosion network and in the hierarchical branching networks models and they point out that quarter-power scaling can arise even when the underlying network is not fractal.

Finally, Weibel²²⁴ presents a simple and compelling argument on the limitations of the WBE model in terms of transitioning from BMR to the maximal metabolic rate (MMR) induced by exercise. The AR for MMR has an exponent $b = 0.86$

rather than $3/4$, so that a different approach to determining the exponent is needed. Painter¹⁵⁸ demonstrates that the empirical allometry exponent for MMR can be obtained in the manner pioneered by WBE by using the Hess–Murray law for the scaling of branch sizes between levels.

Weibel²²⁴ argues that a single cause for the power function arising from a fractal network is not as reasonable as a model involving multiple causes, see also Agutter and Tuszynski.⁵ Darveau *et al.*⁴¹ propose such a model recognizing that the metabolic rate is a complex property resulting from a combination of functions. West *et al.*²⁵¹ and Banavar *et al.*¹¹ demonstrate that the mathematics in the distributed control model of Darveau *et al.*⁴¹ is fundamentally flawed. In their reply Darveau *et al.*⁴² do not contest the mathematical criticism and instead point out consistency of the multiple-cause model of metabolic scaling with what is known from biochemical²⁰⁵ and physiological¹⁰¹ analysis of metabolic control. The notion of distributed control remains an attractive alternative to the single cause models of metabolic AR. A mathematically rigorous development of AR with fractal responses from multiple causes was recently given by Vlad *et al.*²¹⁸ in a general context. This latter approach may answer the formal questions posed by many of these critics.

4.3. Why fractal transport?

Why are fractals important in the design of allometry networks? Barenblatt and Monin¹⁴ suggested that metabolic scaling might be a consequence of the fractal nature of biology and WBE determined that fractal geometry maximizes the efficiency of nutrient transport in biological networks. Weibel²²³ maintains that the fractal design principle can be observed in all manner of physiologic networks quantifying the observations and speculations of Mandelbrot,^{131,132} as does West.²³⁸

West²³⁰ conjectured that fractals are more adaptive to internal changes and to changes in the environment than are classical processes and structures. Consider a network property characterized by classical scaling at the level k such as the length or diameter of a branch $F_k \propto e^{-\lambda k}$ compared with a fractal scaling characterization of the same property $F_k \propto k^{-\lambda}$. What is significant in these two functional forms for the present argument is the dependence on the parameter λ . The exponential has emerged from a large number of optimization arguments and the inverse power-law results from RG scaling arguments.

Assume the parameter λ is the sum of a constant part λ_0 and a random part ξ . The random part can arise from unpredictable changes in the environment during morphogenesis, non-systematic errors in the code generating the physiologic structure or any of a number of other causes of irregularity. Thus, regardless of whether the errors are induced internally or externally, the average is taken over an ensemble of zero-centered Gaussian fluctuations ξ with variance $\sigma^2/2$. Note that the choice of Gauss statistics has no special significance here except to provide closed form expressions for the averages to facilitate discussion. The relative error generated by

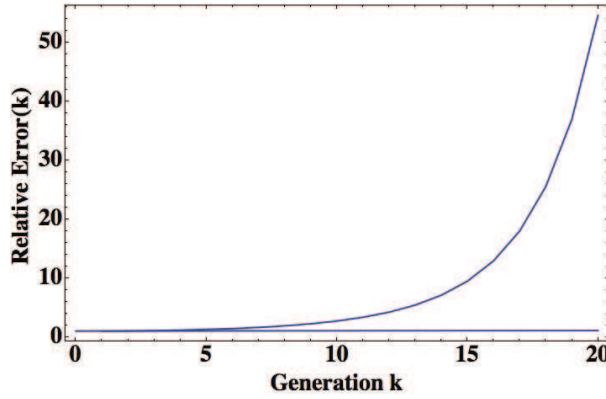


Fig. 8. The error between the model prediction and the prediction averaged over a noisy parameter is shown for the classical model (upper curve) and the fractal model (lower curve).

the fluctuations is given by the ratio of the average value to the function in the absence of fluctuations, yielding the relative error for classical scaling $\varepsilon_k = \exp[\sigma^2 k^2]$ and for fractal scaling $\varepsilon_k = \exp[\sigma^2 (\ln k)^2]$.

The two error functions are graphed in Fig. 8 for fluctuations with a variance $\sigma^2 = 0.01$. At $k = 15$ the error in classical scaling is 9.5. This enormous relative error means that the perturbed average property at generation 15 differs by nearly an order of magnitude from what it would be in an unperturbed network. A biological network with this sensitivity to error would not survive for very long in the wild. For example, the diameter of a bronchial airway in the human lung could not survive this level of sensitivity. However, the property of the fractal network only changes by 10% at the distal point $k = 20$. The implication is that the fractal network is relatively unresponsive to fluctuations.

A fractal network is consequently very tolerant of variability. This error tolerance can be traced back to the broadband nature of the distribution in scale sizes of a fractal object. This distribution ascribes many scales to each generation in the network. The scales introduced by the errors are therefore already present in a fractal object. Thus, the fractal network is *preadapted* to variation and is therefore insensitive to change.^{230,231} These conclusions do not vary with modification in the assumed statistics of the errors. Therefore let us review how fractal statistics have been employed in the understanding of some nonmetabolic physiologic ARs.

4.3.1. WBG bronchial tree

The energy minimization argument applied to a branching network resulted in Horton's law. However, the theoretical arguments justifying this empirical law and others like it assume that the network is geometrically self-similar. Real networks, such as the bronchial tree in the mammalian lung, do not have such deterministic regularity. At any generation of the bronchial airway there is a distribution of

lengths and diameters, with a reduction in the average length and average diameter between successive generations. Consequently, the simple characteristic scale governing the decrease in bronchial dimensions across generations given by the Hess–Murray law must be reexamined. West, Barghava and Goldberger²²⁸ (WBG) assumed the mammalian lung to be a fractal structure having a distribution of scales contributing to the variability in tube size at each generation. This model yields an average bronchial diameter that decreases with generation number, not as an exponential as suggested by Weibel and Gomez,²²² but as an inverse power law.^{229,232,233}

WBG assume that the variability in the diameters of the bronchial tubes at generation k is given by $d(\gamma k)$, where γ is a random variable that determines the size of the diameter. In the energy minimization argument we determined that $\gamma = \ln 2/3$ and the classical reduction in diameter with generation number was exponential $d(\gamma k) = d_0 e^{-\gamma k}$ as shown in Fig. 7. However with real data this is the reduction in the average diameter just as it was for other allometry networks so that the random variation in diameter at generation k is smoothed over to determine the average. Formally the behavior of the average diameter as a function of generation number is given by:

$$\overline{d(k)} = \int d(\gamma k) p(\gamma) d\gamma, \quad (38)$$

with $p(\gamma)$ the *pdf* in scale size. Rather than prescribe a particular functional form to this *pdf* in the formal definition WBG use a RG argument originally developed in an economic context by Montroll and Shlesinger.¹⁴⁸ Assuming the original distribution of scales has an average value $\bar{\gamma}$ the RG argument constructs a new distribution with an infinite number of new scales each a factor of β larger than the preceding scale and each occurring with a relative frequency ζ less often. The distribution resulting from the RG relation gives rise to an empirical average denoted by brackets in terms of the formal average Eq. (38) as follows^{234,235}:

$$\langle d(k) \rangle = \zeta \langle d(\beta k) \rangle + (1 - \zeta) \overline{d(k)}. \quad (39)$$

The dominant behavior for the solution to the RG relation Eq. (39) is determined by the singular part of the solution to the equation, which for simplicity WBG write with a subscript $\langle d(k) \rangle_s = \zeta \langle d(\beta k) \rangle_s$. Shlesinger and West²⁰⁰ note that the solution to this scaling equation that provides the best fit to the data can be written as the real part of:

$$\langle d(k) \rangle_s = \sum_{n=-\infty}^{\infty} \frac{\mathcal{A}_n}{k^{\mu_n}}; \quad \mu_n = b + i2\pi n / \ln \beta; \quad (40)$$

μ_n is the complex fractal dimension of order n for the branching process, with the exponent $b = -\ln \zeta / \ln \beta > 0$ and the \mathcal{A}_n are fit by experimental data. Of course there is in addition to Eq. (40) an analytic part to the solution that WBG calculated but which becomes negligible with increasing k .

D. West & B. J. West

Thus, the average diameter is an inverse power law in the generation number modulated by a slowly oscillating function just as observed in the data depicted in Fig. 9. This fractal model of the bronchial airway provides an excellent fit to the average bronchial tube diameter data in four distinct species: dogs, rats, hamsters

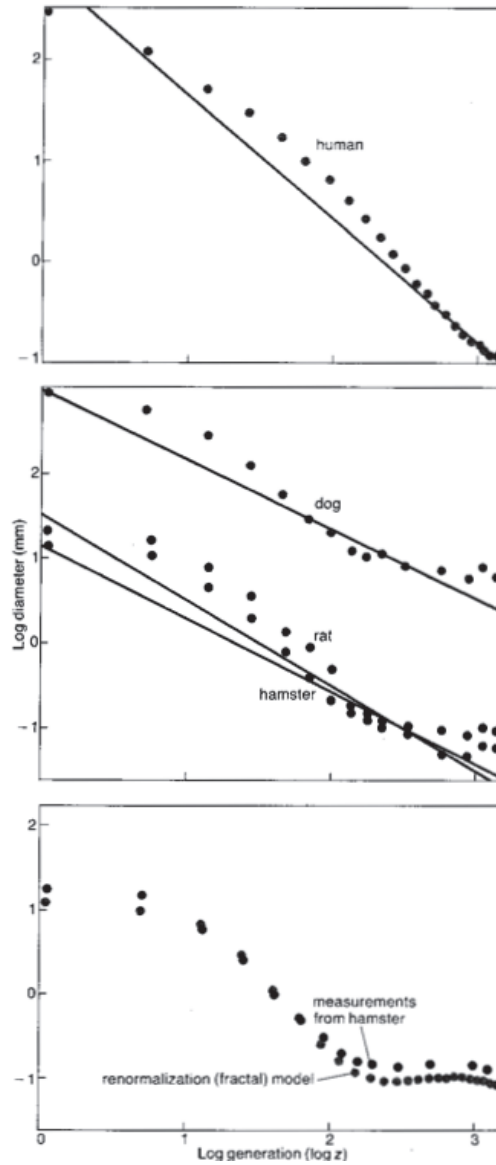


Fig. 9. Top: Replotted data from Fig. 7 on log-log scales for humans. Center: The harmonic variation in measurements for dogs, rats and hamsters taken by Raabe *et al.* (1976). Bottom: The average diameters for the bronchial tubes of a hamster and RG (fractal) model prediction using Eq. (40). [Adapted from West and Goldberger²²⁸].

and humans.¹⁵² The quality of the fit is shown for hamsters in Fig. 9, which restricts the summation index in Eq. (40) to $n = 0, 1, -1$ and $\mathcal{A}_1 = \mathcal{A}_{-1}$ yields a single oscillation of the modulation function fit to the data.

The form of Eq. (40) strongly suggests that the RG relation for the average diameter captures a fundamental property of the structure of the lung that is distinct from classical scaling. There is an AR at each level of the bronchial tree with the average diameter decreasing as k^{-b} with the level being a measure of size. Moreover the data show the same type of scaling for bronchial tube lengths and consequently volume.

4.3.2. Distribution of bronchial diameters

Kitaoka and Suki¹⁰⁷ use a related but distinct analysis of the lung data depicted in Fig. 9 in which they investigate the statistical variability of the bronchial airway diameters. Their analysis was based on the assumed relation between the airflow rate and the airway diameter d :

$$Q = Cd^\alpha,$$

a relation discussed in terms of energy optimization by Murry¹⁵⁰ yielding $\alpha = 3$. The relation was also considered in a bronchial airway context by a number of other investigators.^{82,105,163} The data of Raabe *et al.*¹⁷¹ reveals that the flow rate is a random variable and that the cumulative probability for the flow rate to exceed Q is given by:

$$\Pr(\geq Q) \propto 1/Q$$

with an inverse power-law index of -1 to three significant figures. Note that from the additive form of the flow rate between successive generations and the da Vinci relation between parent and daughter branches that the *pdf* for the diameter of the bronchial airway is determined to be:

$$p(d) = Cd^{-(\alpha+1)}, \quad C = \frac{\alpha(d_0 d_T)^\alpha}{d_0^\alpha - d_T^\alpha} \quad (41)$$

with d_0 the diameter of the thorax and d_T the diameter of the smallest bronchial airway. Here again the empirical distribution for the observable, the bronchial tube diameter rather than the allometry coefficient, is an inverse power-law (Pareto) *pdf*.

Note that in the previous subsection the average diameter was expressed as an inverse power law in the generation number. The distribution in the size of the bronchial airway Eq. (41) does not directly depend on generation number and is an inverse power law in diameter size, that is, in millimeters as depicted in Fig. 10. The data used to construct Fig. 9 was also used to determine the cumulative distribution of airway diameters and yields the inverse power-law distribution with $\alpha = 3.1$ with correlation coefficient of $r^2 = 0.988$. Note that this value of the exponent is slightly different from the optimum as we discuss in the next section. It is also noteworthy that the oscillations around the inverse power law given by the straight line are the

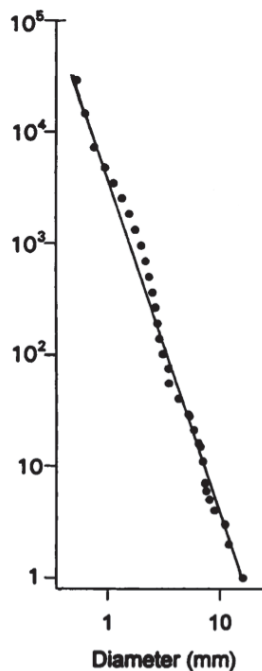


Fig. 10. Cumulative distribution of diameters on log-log plot. The regression model over the full range of diameters yields $\alpha = 3.1$ with $r^2 = 0.988$. [Reproduced from Kitaoka and Suki¹⁰⁷ with permission].

same periodic variation explained using WBG theory except that the oscillations are now a function of distance rather than generation number.

4.3.3. *The optimum can be dangerous*

A question of interest is whether optimal design criteria are ever realized in nature and whether they are even desirable. The WBE model suggests that the allometry exponent value of $3/4$ is proof of the optimality of fractal design of networks for nutrient transport. However the controversy over the empirical value of the allometry exponent calls this implication into question. The present discussion regarding the mammalian lung and whether the bronchial tree is optimal has been investigated by Mauroy *et al.*¹³⁸ They maintain that the bronchial tree of most mammalian lungs is a good example of an efficient distribution network with an approximate fractal structure.^{152,228} They state that physical optimization is critical in that small variations in the geometry can induce large variations in the net air flux and consequently optimality cannot be a sufficient criterion for physiologic design of the bronchial tree. The slight deviations observed in the parameters presumed to be optimized are a manifestation of a safety factor being incorporated into the design and into the capacity for regulating airway caliber.

In the present context the size ratio h of successive airway segments are homothetic with $h = 2^{-1/3} \approx 0.79$ as discussed earlier. Homothetic scaling means that the lengths and diameters have the same ratios between successive generations. Using the resistance minimization argument for the bronchial network Mauroy *et al.*¹³⁸ show that the “best” bronchial tree is fractal with constant reduction factor given by the Hess–Murray law. Do the data support this optimal value and if not what does that imply about the efficiency of bronchial airways?

The fractal dimension for a bronchial airway is $D = -\ln 2 / \ln h$ so that the Hess–Murray law implies $D = 3$ whereas $h > 0.79$ implies $D > 3$. In the human lung it is found that the homothety ratio is $h \approx 0.85$ ²²⁴ and the bronchial network is therefore not optimized: its volume is too large and its overall resistance is too small. Mauroy *et al.*¹³⁸ emphasize that this deviation from optimal is, in fact, a safety margin for breathing with respect to possible bronchial constrictions.

Sapoval¹⁸⁷ has argued that without regulation of the airway caliber¹⁷⁰ there would be a multifractal spatial distribution of air within the lungs, resulting in strongly nonuniform ventilation with some regions of the lung being poorly fed with fresh air. Expanding on this theme using inhomogeneity of the homothety ratio Mauroy *et al.*¹³⁸ show how the optimal network is dangerously sensitive to physiological variability and consequently design of the bronchial tree must incorporate more than just physical optimality. This argument has clear implications for other allometric networks.

5. Probability Calculus and ARs

A fractal processes is one that is rich in scales with no one scale being dominant. Thus, information in fractal phenomena is coupled across multiple scales manifesting long-time memory, as for example, observed in the architecture of the mammalian lung,^{152,223,228} manifest in the long-range correlations in human gait^{84,235} and measured in the human cardiovascular network,¹⁶¹ all of which are discussed in West.²³⁸ These phenomenological characterizations of fractal time series relate back to the observation made earlier that if $X(t)$ and $Y(t)$ are stochastic time series then $Y(X)$ must be a random function of its random argument as well. Consequently the general approach to determining the relation between such variables is through their *pdf*'s.

In this section we examine *pdf*'s that can produce the interspecies metabolic ARs as a relation between moments. To do this requires a brief review of some methods from nonequilibrium statistical physics^{118,175} and their extension to fractional equations of motions.^{108,236}

5.1. Stochastic differential and Fokker–Planck equations

There are two major techniques available in statistical physics for the modeling of stochastic phenomena. The first technique uses the dynamic equations constructed by Langevin¹¹⁷ who introduced uncertainty through a random force in the equations

D. West & B. J. West

of motion. The second technique is based on the phase space evolution of the *pdf* using the Fokker–Planck equation (FPE). The conditions under which these two methods are equivalent have been shown in a number of places, see, for example, Lindenberg and West.¹¹⁸

5.1.1. Additive fluctuations

Consider the dynamics of a simple exponential relaxation process $Z(t)$ that is disrupted by a random force $\xi(t)$:

$$\frac{dZ(t)}{dt} = -\lambda Z(t) + \xi(t). \quad (42)$$

We assume the statistics of the random force are normal with a delta correlated correlation of strength D

$$\langle \xi(t)\xi(t') \rangle = 2D\delta(t-t'). \quad (43)$$

An alternative description of the dynamics is given by the evolution of the probability density in phase space where $P(z, t)dz$ is the probability that the dynamic variable $Z(t)$ has a value in the interval $(z, z + dz)$ at time t given a value $q(t)$ at the origin $z = 0$. The phase space dynamics are formally expressed by the equation:

$$G\left(\frac{\partial}{\partial t}, \frac{\partial}{\partial z}\right) P(z, t) = q(t)\delta(z). \quad (44)$$

The analytic function $G(\cdot, \cdot)$ of the indicated operators along with the inhomogeneous term $q(t)$ determine the dynamics of the process modeled by the *pdf*.

A phase space equation for a classical diffusion process with linear dissipation equivalent to Eq. (42) is determined by:

$$G\left(\frac{\partial}{\partial t}, \frac{\partial}{\partial z}\right) = \frac{\partial}{\partial t} - \frac{\partial}{\partial z} \left[\lambda z + D \frac{\partial}{\partial z} \right] \quad \text{and} \quad q(t) = 1. \quad (45)$$

The corresponding FPE is given by²¹⁷:

$$\frac{\partial P(z, t|z_0, t_0)}{\partial t} = \frac{\partial}{\partial z} \left[\lambda z + D \frac{\partial}{\partial z} \right] P(z, t|z_0, t_0), \quad (46)$$

where $P(z, t|z_0, t_0)dz$ is the probability that the dynamic variable lies in the phase space interval $(z + dz, z)$ at time t conditional on $Z(0) = z_0$ at time $t = t_0$. The solution to Eq. (46) for $t_0 = 0$ is given by:

$$P(z, t|z_0) = \frac{1}{\sqrt{4\pi\sigma^2(t)}} \exp \left[-\frac{(z - \langle z; t \rangle)^2}{2\sigma^2(t)} \right] \quad (47)$$

with average value $\langle z; t \rangle = z_0 e^{-\lambda t}$ and variance $\sigma^2(t) = D/\lambda(1 - e^{-\lambda t})$. In the absence of dissipation the average value is constant and the variance grows linearly in time. However for finite dissipation the average decays exponentially in time and the variance approaches a constant value given by the ratio of the diffusion coefficient and the dissipation rate. If Z is the velocity of a Brownian particle the

variance would be proportional to the temperature of the surrounding fluid resulting in the Einstein relation $D/\lambda = k_B T$, see, for example, Fürth.⁶¹

Multiplicative fluctuations can be addressed by examining the FPE associated with a linear stochastic dissipation parameter.^{118,193} Consider the nonlinear rate equation with multiplicative fluctuations

$$\frac{dX}{dt} = -\lambda X \ln X + \xi(t)X \quad (48)$$

for which the logarithmic transformation $Z = \ln X$ yields the rate equation with additive fluctuations $\xi(t)$ given by Eq. (42). The FPE for the transformed equation is Eq. (46) with the solution Eq. (47). In terms of the original variable the *pdf* is a log-normal distribution, for more details see Goel *et al.*⁷⁶

5.1.2. Stochastic ontogenetic growth model

A more interesting rate equation was first considered by von Bertalanffy²¹⁹ who postulated a simple nonlinear rate equation to describe the growth of TBM m of the form

$$\frac{dm}{dt} = A_\eta m^\eta - C_\beta m^\beta \quad (49)$$

at time t where η and β are unspecified exponents, and A_η and C_β are positives constants. The solution to this equation was studied by von Bertalanffy²¹⁹ with $\eta = 2/3$ and $\beta = 1$. More recently West *et al.*²⁵⁰ constructed Eq. (49), called an ontogenetic growth model (OGM), from a conservation of energy argument and obtained a universal curve from the solution and fit it to data by using $\eta = 3/4$ and $\beta = 1$. In the OGM the parameters are given by $C_\beta = B_m/E_m$ with B_m the metabolic rate required to maintain an existing unit of biomass; E_m the metabolic energy required to create a unit biomass and $A_\eta = a/E_m$. Banavar *et al.*¹⁰ obtained an equivalent universal curve and fit the same data for both $\eta = 2/3, 3/4$ and $\beta = 1$. The OGM equation has the scaling form:

$$\frac{dm}{dt} = m^\eta f(m/M_0), \quad (50)$$

where M_0 is chosen to be the maximum TBM that solves the stationary equation $dm/dt = 0$. The data from 13 organisms graphed as $r = (m/M_0)^{1-\eta}$ versus $\tau = -\ln(1-r)$ collapse onto a single universal curve²⁵⁰ that is fit equally well with $\eta = 2/3$ or $\eta = 3/4$.¹⁰

West and West²⁴⁶ generalized the OGM to incorporate the disordering influence of entropy by including the statistical fluctuations of the measured mass. The dynamics of such a stochastic process eventually erases the influence of the initial state and this gradual loss of information is a manifestation of increasing entropy. They refer to this as the stochastic ontogenetic growth model (SOGM). Consider a phenomenological Langevin equation with multiplicative fluctuations for the TBM where to avoid confusion we use the dummy variable $Z = m$, which is actually the

D. West & B. J. West

TBM for species i and individual j and individual j given by M_{ij} . Thus, we replace Eq. (49) for $\eta = b$ and $\beta = 1$ for the SOGM stochastic differential equation:

$$\frac{dZ}{dt} = A_b Z^b - C_0 Z + Z\xi(t), \quad (51)$$

with $\xi(t)$ given by a delta correlated random process of strength D with normal statistics and correlations given by Eq. (43). Rather than assuming the rate of creating a unit biomass is a single number C_1 they assume it has a stochastic component: $C_1 \rightarrow C_0 + \xi(t)$, with average value C_0 .

An equivalent description of the SOGM is given by the corresponding dynamics of the *pdf* in phase space. The FPE corresponding to Eq. (51) is^{118,193}:

$$\frac{\partial P(z, t)}{\partial t} = \frac{\partial}{\partial z} \left[-(A_b z^b - C_0 z) + D z \frac{\partial}{\partial z} z \right] P(z, t). \quad (52)$$

The general solution to Eq. (52) remains a mystery, but the steady-state solution ($t \rightarrow \infty$) denoted by the *ss* subscript obtained by setting the probability flux to zero is given by:

$$P_{ss}(z) = \frac{\beta \gamma^{\frac{\mu-1}{\beta}}}{\Gamma\left(\frac{\mu-1}{\beta}\right)} \frac{\exp[-\gamma z^{-\beta}]}{z^\mu}; \quad (53)$$

normalized on the interval $(0, \infty)$ with the parameter values $\gamma = A_b/\beta D$, $\mu = 1 + (C_0/D)$ and $\beta = 1 - b$. Note that the steady-state solution to the SOGM FPE replaces the deterministic steady-state solution obtained from the OGM.^{10,250}

West and West²⁴⁶ fit the parameters in Eq. (53) to a data set of mammalian species tabulated by Heusner⁹¹ and this fit is depicted in Fig. 11. They constructed a histogram by partitioning the mass axis into intervals of 20 g and counting the number of species within each interval. The vertical axis is the relative number of species as a function of TBM. The allometry exponent is fixed at $b = 3/4$ so that $\beta = 1/4$ and the remaining parameters are determined to have the best values of $\gamma = 13.4$ and $\mu = 2.04$ with a quality of fit measured by the correlation coefficient $r^2 = 0.96$.

Figure 11 shows the fit to the low-mass species out to 500 g. The remaining fit out to three million grams is not shown but is in fact the more interesting part of the distribution. To capture this information on a single graph we²⁴⁶ construct a second histogram, this one for the asymptotic region from approximately one thousand to three million grams. Figure 12 depicts the fit to the logarithmic histogram data points indicated by the dots starting at a TBM of 1.1 kg. An inverse power-law distribution would be a straight line with a negative slope on this log-log graph. Inserting the parameter values $\mu = 1.67$ and $\gamma = 8.96$ into the steady-state TBM *pdf* given by Eq. (53) yields the solid curve in Fig. 12 which fits the data extremely well. The curve is quite clearly an inverse power law in the interspecies TBM. This coarse-grained description of the interspecies TBM statistics indicates great

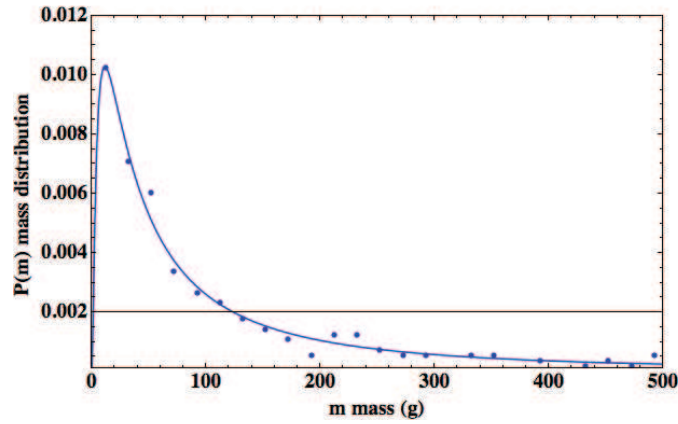


Fig. 11. The histogram constructed from the average TBM data for 391 mammalian species⁹¹ is given by the dots. The mass data has been divided into intervals of 20 g each and the number of species within each such interval counted. The horizontal axis is the relative frequency in each interval and the solid line segment is the least squares fit of Eq. (53) to the data points. The quality of fit is $r^2 = 0.96$.²⁴⁶

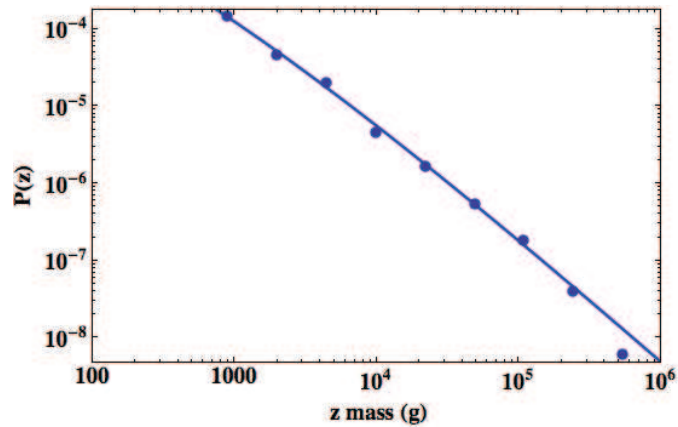


Fig. 12. The average TBM data for 391 mammalian species⁹¹ are used to construct a histogram. The mass interval is divided into 20 equally spaced intervals on a logarithm scale and the number of species within each interval counted. The least-square fit to the nine data points is then made using logrimically transformed distribution, see Ref. 246 for details. The quality of the fit is $r^2 = 0.998$.

variability particularly since $\mu < 2$ indicating that the variance of the interspecies TBM diverges.

5.1.3. Interspecies AR derivation

We^{241,243} explicitly constructed a statistical theory of the fluctuations in the measured species metabolic rate B_i and TBM M_i to calculate the interspecies metabolic

D. West & B. J. West

AR. The strategy was to related the average BMR to the average TBM through the AR. This approach can be followed here from the long-time or steady-state average SOGM TBM using the steady-state *pdf*:

$$\langle z \rangle = \int_0^\infty z P_{ss}(z) dz = \frac{\beta \gamma^{\frac{\mu-1}{\beta}}}{\Gamma\left(\frac{\mu-1}{\beta}\right)} \int_0^\infty z^{1-\mu} \exp[-\gamma z^{-\beta}] dz$$

and replacing z with the TBM for species i reduces the average to:

$$\langle M_i \rangle = \gamma^{1/\beta} \frac{\Gamma\left(\frac{\mu-1}{\beta} - \frac{1}{\beta}\right)}{\Gamma\left(\frac{\mu-1}{\beta}\right)} \approx \left[\gamma \frac{\beta}{\mu-1} \right]^{1/\beta}. \quad (54)$$

Here we interpret the ensemble average in terms of an average over an ensemble of individual members of species i . In this equation we have approximated the ratio of gamma functions by an asymptotic value and substituting the parameter values into the right-hand side of Eq. (54) yields:

$$\langle M_i \rangle \approx \left(\frac{A_b}{C_0} \right)^{1/\beta} = \left(\frac{a}{B_m} \right)^{1/\beta}. \quad (55)$$

The equality in Eq. (55) is obtained by substituting the values of the parameters from OGM and using $b = 3/4$ and $\beta = 1/4$ to yield

$$B_m \approx a \langle M_i \rangle^{-1/4}. \quad (56)$$

Thus, the average metabolic rate necessary to maintain a unit biomass is dependent on the inverse quarter power of the average TBM of the species. This is the same expression obtained by Moses *et al.*¹⁴⁹ if we identify their adult TBM with the average TBM obtained from the steady-state *pdf* of the SOGM.

Note that the average TBM for species i replaces M_0 obtained from the $dm/dt = 0$ solution to Eq. (50). On the other hand the average BMR can be determined from the b th moment of the TBM

$$\begin{aligned} \langle B_i \rangle &= a \langle M_i^b \rangle = a \int_0^\infty z^b P_{ss}(z) dz \\ &= a \gamma^{-1+1/\beta} \frac{\Gamma\left(\frac{\mu-1}{\beta} + 1 - \frac{1}{\beta}\right)}{\Gamma\left(\frac{\mu-1}{\beta}\right)} \approx a \left[\gamma \frac{\beta}{\mu-1} \right]^{1/\beta-1}. \end{aligned} \quad (57)$$

Comparing this last equation with Eq. (54) allows us to write:

$$\langle B_i \rangle \approx a \langle M_i \rangle^{1-\beta} = a \langle M_i \rangle^b, \quad (58)$$

which is the interspecies metabolic AR. We emphasize²⁴⁶ that the interspecies AR is a pheomenological equation that without the SOGM does not have a formal theoretical basis.

The SOGM constitutes the first theoretical construction of an interspecies metabolic AR starting from a fundamental dynamic equation and relating the proper averages. It is true that we used a nonlinear multiplicative Langevin equation, but the original dynamics stem from the conservation of energy argument²⁵⁰ and the fluctuations are a consequence of the dynamics being degraded by entropy.²⁴³ This suggests a possible untraveled path for future research in this area.

5.2. Scaling solution for AR

A phase space equation for anomalous diffusion containing the influence of long-term memory on the dynamics of the *pdf* was first discussed by West and Seshadri²²⁷ in term of the fractional calculus. The resulting fractional diffusion equation^{108,236} (FDE) has subsequently found a variety of uses in the physical sciences. The *pdf* that solves a class of FDEs satisfies the scaling equation

$$P(z, t) = \frac{1}{t^{\mu_z}} F_z \left(\frac{z}{t^{\mu_z}} \right). \quad (59)$$

Note that this scaling of the *pdf* is also a realization of the RG relation for the random variable $Z(bt) = b^\mu Z(t)$.

The function $F_z(\cdot)$ in Eq. (59) is left unspecified but it is analytic in the similarity variable z/t^μ . As mentioned in the introduction a standard diffusion process $Z(t)$ is the displacement of the diffusing particle from its initial position at time t , and for vanishing small dissipation the scaling parameter is $\mu_z = 1/2$ and the functional form of $F_z(\cdot)$ is a normal distribution. However, for general complex phenomenon there is a broad class of distributions for which the functional form of $F_z(\cdot)$ is not Gaussian and the scaling index $\mu_z \neq 1/2$. For example, the α -stable Lévy process^{147,184,198,264} scales in this way and the Lévy index is in the range $0 < \alpha \leq 2$, with the equality holding for the Gauss distribution and the scaling index is related to the Lévy index by $\mu_z = 1/\alpha$, see West, Geneston and Grigolini²³⁹ and Uchaikin²¹⁶ for very different discussions of this scaling.

The Gibbs entropy (Shannon information),^{23,197} can be defined using the *pdf* for the variable $Z(t)$ Eq. (59) to obtain:

$$S_z(t) = - \int P(z, t) \ln P(z, t) dz = S_z^0 + \mu_z \ln t, \quad (60)$$

so the entropy deviation from the reference state $S_z^0 \equiv - \int F_z(q) \ln F_z(q) dq$ integrated with respect to the scaled variable $q = z/t^{\mu_x}$, increases logarithmically in the independent variable t .

Huxley⁹⁸ assumed the differential growth equations in an organism to have the same form with proportional growth rates. West and West^{241,243} adapted this assumption and presumed the two parts of an organism share the same class of probability densities that describe their interacting observables. Here t is clock time, the independent variable, and the network measures are the dependent variables,

D. West & B. J. West

the average of a generic scaling observable using the *pdf* given by Eq. (59) yields:

$$\langle Z(t) \rangle = \int z P(z, t) dz = t^{\mu_z} \int q F_z(q) dq = t^{\mu_z} \bar{Z}. \quad (61)$$

Note that $\bar{Z} = \int q F_z(q) dq$ is a finite, time-independent constant. Comparing Eqs. (61) and (60) enables us to write for the change in entropy relative to a reference state:

$$\Delta S_z = \ln[\langle Z(t) \rangle / \bar{Z}] \quad (62)$$

so that the change in the average value of an observable is determined by the change in entropy

$$\langle Z(t) \rangle = \bar{Z} e^{\Delta S_z(t)}. \quad (63)$$

Consequently Z may be identified with either of the network variables to obtain the relation between entropies from Eq. (60)

$$\Delta S_x / \mu_x = \Delta S_y / \mu_y$$

and using Eq. (63) we can write:

$$\langle Y_i \rangle = \bar{Y} e^{\Delta S_y} = \bar{Y} e^{\frac{\mu_y}{\mu_x} \Delta S_x} = a \langle X_i \rangle^b \quad (64)$$

with the allometry coefficient given by $a = \bar{Y} / \bar{X}^b$ and the allometry exponent by $b = \mu_y / \mu_x$. We have again introduced the index for the single species i to emphasize that this is the interspecies AR. This derivation of the empirical interspecies AR is solely a consequence of the scaling properties of the *pdf*'s.

The rate of entropy generation is determined by the time derivative of Eq. (63) for X and Y and substituting from the entropy balance equation yields:

$$\frac{1}{\mu_x \langle X_i \rangle} \frac{d \langle X_i \rangle}{dt} = \frac{1}{\mu_y \langle Y_i \rangle} \frac{d \langle Y_i \rangle}{dt}. \quad (65)$$

Equation (65) shows the correspondence of the probabilistic approach to AR with that of Huxley, with the dynamic variables of individual species members replaced by averages over an ensemble of individuals. In the present case the allometry exponent is now the ratio of the power-law indices in the *pdf*'s, which from Eq. (65) can also be interpreted as the ratio of growth rates. Moreover, the allometry coefficient is determined by the scaling functions in the *pdf*'s. It is the average response or adaptation of the subnetwork to the average behavior of the host network that is captured by the interspecies AR through the balance of the entropy generated. Moreover it is the scaling in the *pdf* and not necessarily geometric scaling of fractal networks that is the origin of the physiologic AR. Underlying this derivation is the assumption made earlier that this is an information-dominated network and is consequently driven by information (entropy) gradients and not the energy gradient necessary in the fractal geometry derivation of nutrient transport.

6. Conclusion

The statistical analysis of the metabolic data presented herein show that empirical ARs exist across multiple species and consequently the form of ARs are not solely dependent on species specific mechanisms. Moreover we have shown there is no universal value for the allometry exponent for three reasons. First there is the variability in the values of the allometry exponent obtained from data analysis in Sec. 3. We could rehash the arguments here, but an objective observer would have to conclude that although there are indications that a particular value might be strongly indicated in a specific context, the evidence for universality is not compelling. Even in the case of metabolic ARs one could reasonably make a case of $b = 2/3$ for small animals, $b = 3/4$ for large animal and $b = 1$ for plants, but no one value of b that spans the total range of animal and plant sizes. Second, the only theories that predict a universal value of the allometry exponent do so to explain the intraspecies AR and not the interspecies AR. There is no first principles theory that derives the empirical AR between the averaged observables. The phenomenological theory presented in Section 4 successfully derives the interspecies AR and treats the allometry coefficient and allometry exponent as empirical parameters determined by the parameters in the *pdf*'s. Third and last the allometry exponent and coefficient are determined to co-vary using theory²⁴³ and statistical data analysis.⁷²

However let us not be too critical of phenomenological theories. Recall that thermodynamics is a phenomenological theory that has enjoyed remarkable success in explaining a plethora of complex physical phenomena. Even so the physics community has not yet been able to derive thermodynamics from the more reductionist (fundamental) statistical mechanics, so that a mechanistic understanding of thermodynamics remains controversial. By the same token the phenomenological theory of AR presented herein takes the discussion of AR out of the domain of the reductionist approaches previously used to derive the intraspecies ARs and refocuses it on the statistical properties of the empirical interspecies ARs. These analyses indicate a new avenue for the study of physiologic ARs, one that systematically includes both deterministic and statistical aspects using the probability calculus. This new perspective indicates that the origins of physiologic AR reside in the scaling properties of the *pdf*'s for nested complex networks.

In simple physical phenomena the dynamics of a network coupled to the environment is described by a Langevin equation, which is a stochastic differential equation. This mechanical description of the dynamics is equivalent to the phase space dynamics of the *pdf* such as given by the FPE. As the network becomes more complex its past history becomes more and more influential until finally the FPE must be replaced with a FDE and the dynamics are the domain of the fractional calculus. As we saw in Sec. 5 the general solution to a class of FDE's is a scaling *pdf* implying that ARs can result from scaling in the statistical dynamics of the phenomenon. The influence of the history of the growth of an organism on the growth

of an organ leads to intraspecies AR; the history of the size of an organism on the metabolic rate of the organism across species leads to interspecies AR.

The arguments in Sec. 5 imply that empirical ARs are a consequence of information transfer between complex information-dominated networks. Of course we have not rigorously proven that the entropy decrease (information increase) in the host network and the increase in entropy (information decrease) in the subnetwork have the relations assumed, this remains to be done. However the empirical relations are consistent with the Principle of Complexity Management in which the transfer of information between two complex information-dominated networks has been shown^{7,239} to proceed from the network with the greater information content to the network with the lesser.

The phenomenological theory of empirical AR presented herein incorporates both stochastic and reductionistic mechanisms. From this approach we conclude that the empirical AR for the BMR, the life time of an organism and the myriad of other complex phenomena are not completely explained by reductionistic mechanisms. In particular the allometry parameters are determined not to be universal. This was supported by the demonstration that the allometry exponent and coefficient co-vary. On the other hand, the laws from the theory of probability can have universal forms without having universal parameters, for example the Law of Frequency of Errors and the Law of Large Numbers. The empirical AR is in part a consequence of the generic statistical behavior of complex networks that depend on the infinitely divisible nature of the *pdf*.^{74,75} The phenomenological theory of AR presented herein is the application of the probability calculus to the understanding of the origins of the empirical relations between averages of different parts of a complex network. Consequently empirical AR is a manifestation of a law whose origin can be traced back to the probability calculus and the balancing of deterministic and stochastic mechanisms.

References

1. R. Adrian, *Analyst Math. Museum* **1**, 93 (1809).
2. P. Alberch *et al.*, *Paleobiology* **5**, 296 (1979).
3. R. Albert and A.-L. Barabasi, *Rev. Mod. Phys.* **74**, 48 (2002).
4. P. Allegrini *et al.*, *Front. Physiol.* **1**, 28 (2010) doi:10.3389/fphys.2010.00128.
5. P. S. Agutter and J. A. Tuszynski, *J. Exp. Biol.* **214**, 1055 (2011).
6. M. E. F. Apol, R. S. Etienne and H. Olf, *Funct. Ecol.* **22**, 1070 (2008).
7. G. Aquino *et al.*, *Phys. Rev. Lett.* **105**, 069901 (2010).
8. P. Bak and S. Boettcher, *Physica D* **107**, 143 (1997).
9. F. J. Ballard, R. W. Hanson and D. S. Kronfeld, *Fed. Proc.* **28**, 218 (1969).
10. J. R. Banavar *et al.*, *Nature* **420**, 626 (2002).
11. J. R. Banavar *et al.*, *Nature* **421**, 713 (2003).
12. J. R. Banavar *et al.*, *Phys. Rev. Lett.* **98**, 068104 (2007).
13. G. I. Barenblatt, *Scaling Phenomena in Fluid Mechanics* (Cambridge University Press, Cambridge, 1994).
14. G. I. Barenblatt and A. S. Monin, *Proc. Nat. Acad. Sci. USA* **99**, 10506 (1983).
15. M. Barnsley, *Fractals Everywhere* (Academic Press, Boston, 1988).

16. D. S. Bassett *et al.*, *PLoS Comp. Biol.* **6**, 1 (2010).
17. J. B. Bassingthwaite, L. S. Liebovitch and B. J. West, *Fractal Physiology* (Oxford University Press, New York, 1994).
18. V. Beiu and W. Ibrahim, *Proc. IEEE ISCAS* 640 (2008).
19. A. Belgrano *et al.*, *Ecol. Lett.* **5**, 611 (2002).
20. J. Beran, *Statistics of Long-Memory Processes, Monographs on Statistics and Applied Probability*, Vol. 61 (Chapman & Hall, New York, 1994).
21. F. Bokma, *Funct. Ecol.* **18**, 184 (2004).
22. H. Boxenbaum, *J. Pharmacokin. Biopharm.* **10**, 201 (1982).
23. L. Brillouin, *Science and Information Theory* (Academic Press, New York, 1962).
24. S. Brody, *Bioenergetics and Growth* (Reinhold, New York, 1945).
25. J. H. Brown, *Macroecology* (University of Chicago Press, Chicago, IL, 1995).
26. J. H. Brown *et al.*, *Phil. Trans. R. Soc. Lond. B* **357**, 619 (2002).
27. J. H. Brown *et al.*, *Ecology* **85**, 1771 (2004).
28. J. H. Brown, G. B. West and B. J. Enquist, *Funct. Ecol.* **19**, 735 (2005).
29. J. Brownlee, *J. Roy. Soc. Stat. Soc.* **83**, 280 (1920).
30. M. Buchanan, *Nexus* (W. W. Norton, New York, 2002).
31. W. W. Calder III, *Size, Function and Life History* (Harvard University Press, Cambridge, MA, 1984).
32. C. G. Caro *et al.*, *The Mechanics of Circulation* (Oxford University Press, Oxford, 1978).
33. M. A. Changizi, *Biol. Cybern.* **84**, 207 (2001).
34. G. Cuvier, *Recherches sur les ossements fossils* (Paris, 1812).
35. J. E. Cohen, T. Jonsson and S. R. Carpenter, *Proc. Nat. Acad. Sci. USA* **100**, 1781 (2003).
36. E. D. Cope, *The Primary Factors of Organic Evolution* (Open Court Publishing Company, 1896).
37. H. Cyr, Individual energy use and the allometry of population density, in *Scaling in Biology*, eds. J. H. Brown and G. B. West (Oxford University Press, New York, 2000), pp. 267–295.
38. H. Cyr and S. C. Walker, *Ecology* **85**, 1802 (2004).
39. J. Damuth, *Nature* **290**, 699 (1981a).
40. J. Damuth, *Biol. J. Linn. Soc.* **15**, 185 (1981b).
41. C. A. Darveau *et al.*, *Nature* **417**, 166 (2002).
42. C. A. Darveau *et al.*, *Nature* **421**, 714 (2003).
43. T. H. Dawson, *Science* **281**, 751a (1998).
44. L. Demetrius, S. Legendre and P. Harrenões, *Bull. Math. Biol.* **71**, 800 (2009).
45. T. G. Dewey, *Fractals in Molecular Biophysics* (Oxford University Press, Oxford, 1997).
46. P. S. Dodds and D. H. Rothman, *Ann. Rev. Earth Planet Sci.* **28**, 1 (2000).
47. P. S. Dodds, D. H. Rothman and J. S. Weitz, *J. Theor. Biol.* **209**, 9 (2001).
48. E. Dubois, *Bull. Soc. Anthropol. (Paris)* **8**, 337 (1897).
49. C. M. Duarte, S. Agustin and R. H. Peters, *Oecologia* **74**, 272 (1987).
50. A. Einstein, *Ann. Phys.* **22**, 180 (1907).
51. N. Eldredge, *Time Frames* (Princeton University Press, Princeton, NH 1985).
52. N. Eldredge and S. J. Gould, Punctuated equilibria: an alternative to phyletic gradualism, in *Models in Paleobiology*, ed. T. J. M. Schopf (Freeman, Cooper and Co., San Francisco, CA, 1972), pp. 82–115.
53. B. J. Enquist, *Tree Phys.* **22**, 1045 (2002).
54. R. S. Etienne, M. E. Apol and H. Olff, *Funct. Ecol.* **20**, 394 (2006).

55. K. Falconer, *Fractal Geometry* (John Wiley, New York, 1990).
56. W. Farr, *J. Stat. (Lond)* **9**, 17 (1841).
57. J. Feder, *Fractals* (Plenum, New York, 1988).
58. H. A. Feldman and T. A. McMahon, *Resp. Physiol.* **52**, 149 (1983).
59. W. T. Fitch, *Zoology* **103**, 40 (2000).
60. Y. C. Fung, *Biodynamics* (Springer-Verlag, New York, 1984).
61. R. Fürth, *Investigations on the Theory of the Brownian Movement* by Albert Einstein, Ph.D., (1926), translated by A. D. Cowper (Dover, New York, 1956).
62. G. Galileo, This is in the Dialogue of the Second Day in *the Discorsi of 1638*, the work Galileo wrote while under house arrest by the Inquisition. It was translated as *Dialogues Concerning Two New Sciences* by H. Crew and A. De Salvor in 1914 and reprinted by Dover, New York (1952).
63. F. Galton, *Proc. R. Soc. London* **29**, 365 (1879).
64. F. Gauss, *Theoria motus corporum coelestium*, (Hamburg, Dover, 1809); Eng. Trans., *Theory of Motion of Heavenly Bodies Moving about the Sun in Conic Sections*, New York, 1963).
65. J. Gayon, *Am. Zool.* **40**, 748 (2000).
66. P. D. Gingerich, *J. Theor. Biol.* **204**, 201 (2000).
67. L. R. Ginzburg, O. Burger and J. Damuth, *Biol. Lett.* **6**, 850 (2010).
68. T. Gisiger, *Biol. Rev.* **76**, 161 (2001).
69. P. Glansdorf and I. Prigogine, *Thermodynamic Theory of Structure, Stability and Function* (Wiley, New York, 1971).
70. N. R. Glass, *J. Fish Res. Board Can.* **26**, 2643 (1969).
71. D. S. Glazier, *Biol. Rev.* **80**, 611 (2005).
72. D. S. Glazier, *BioScience* **56**, 325 (2006).
73. D. S. Glazier, *Biol. Rev.* **85**, 111 (2010).
74. B. V. Gnedenko and A. N. Kolmogorov, *Limit Distributions for Sums of Independent Random Variables*, translated from Russian by K. L. Chung (Addison-Wesley, Reading, MA, 1954).
75. B. V. Gnedenko, *The Theory of Probability*, translated by B. D. Seckler (Chelsea Pub., New York, 1962).
76. N. S. Goel, S. C. Maitra and E. W. Montroll, *Rev. Mod. Phys.* **43**, 231 (1971).
77. A. L. Goldberger *et al.*, *Biophys. J.* **48**, 525 (1985).
78. A. Goldbeter, *Biochemical Oscillations and Cellular Rhythms* (Cambridge University Press, New York, 1996).
79. S. J. Gould, *Biol. Rev. Cam. Philos. Soc.* **41**, 587 (1966).
80. S. J. Gould, *Am. Natur.* **105**, 113 (1971).
81. J. H. Graham *et al.*, *Biol. J. Linn. Soc.* **80**, 57 (2003).
82. R. A. Groat, *Federation Proc.* **7**, 45 (1948).
83. J. T. Hack, *US Geol. Surv. Prof. Pap.* **294-B**, 52 (1957).
84. J. M. Hausdorff *et al.*, *J. Appl. Physiol.* **80**, 1448 (1996).
85. L. C. Hayek and M. A. Buzas, *Surveying Natural Populations* (Columbia University Press, New York, 1997).
86. A. M. Hemmingsen, *Rep. Steno. Mem. Hosp. (Copenhagen)* **4**, 1 (1950).
87. A. M. Hemmingsen, *Rep. Steno. Memor. Hosp. Nork. Insul.* **9**, 1 (1960).
88. S. C. Hempleman *et al.*, *J. Exp. Biol.* **208**, 3065 (2005).
89. W. R. Hess, *Archiv Anat. Physiol.* **1** (1914).
90. A. A. Heusner, *Resp. Physiol.* **48**, 1 (1982).
91. A. A. Heusner, *J. Exp. Biol.* **160**, 25 (1991).
92. A. V. Hill, *Proc. Roy. Soc. London Ser. B* **126**, 136 (1938).

93. A. V. Hill, *Sci. Prog.* **38**, 209 (1950).
94. M. A. Hofman, *Brain Behav. Evol.* **27**, 28 (1985).
95. R. E. Horton, *Geol. Soc. Amer. Bull.* **56**, 275 (1945).
96. N. A. Humphreys (ed.), *Vital Statistics: A Memorial Volume of Selections from the Reports and Writings of William Farr* (The Sanitary Institute of Great Britain, London, 1885).
97. T.-M. Hu and W. L. Hayton, *AAAPS Pharm. Sci.* **3**, 1 (2001).
98. J. S. Huxley, *Problems of Relative Growth* (Dial Press, New York, 1931).
99. H. J. Jerison, *Science* **133**, 1012 (1961).
100. H. J. Jerison, Allometry, brain size, cortical surface, and convolutedness, in *Primate Brain Evolution*, (eds.) E. Armstrong and O. Falk (Plenum, New York, 1982), pp. 77–84.
101. J. H. Jones, *Comp. Biochem. Physiol. B* **120**, 125 (1998).
102. T. Jonsson, J. E. Cohen and S. R. Carpenter, *Adv. Ecol. Res.* **36**, 1 (2005).
103. L. P. Kadanoff *et al.*, *Rev. Mod. Phys.* **39**, 395 (1967).
104. P. Kaitaniemi, *PLoS ONE* **3**(4), e1932 (2008).
105. A. Kamiya, T. Togawa and A. Yamamoto, *Bull. Math. Biol.* **36**, 311 (1974).
106. A. J. Kerkhoff and B. J. Enquist, *J. Theor. Biol.* **257**, 519 (2009).
107. H. Kitaoka and B. Suki, *J. Appl. Physiol.* **82**, 968 (1997).
108. J. Klafter and R. Metzler, *Phys. Rept.* **339**, 1 (2000).
109. M. Kleiber, *Hilgardia* **6**, 315 (1932).
110. T. Kolokotronis *et al.*, *Nature* **464**, 753 (2010).
111. P. Kopletz, L. Bartosch and L. Schütz, in *Introduction to Functional Renormalization Group*, Lectures in Physics, Vol. 798 (Springer, Berlin, 2010).
112. J. Kozłowski and J. Weiner, *Am. Natur.* **149**, 352 (1997).
113. J. Kozłowski and M. Konarzewski, *Funct. Ecol.* **18**, 283 (2004).
114. J. Kozłowski and M. Konarzewski, *Funct. Ecol.* **19**, 739 (2005).
115. F. A. Labra, P. A. Marquet and F. Bozinovic, *PNAS* **104**, 10900 (2007).
116. P. S. Laplace, *Analytic Theory of Probabilities* (Paris, 1810).
117. P. Langevin, *Comptes Rendus Acad. Sci.* **146**, 530 (1908).
118. K. Lindenberg and B. J. West, *The Nonequilibrium Statistical Mechanics of Open and Closed Systems* (pnVCH, New York, 1990).
119. S. L. Lindstedt and W. A. Calder III, *The Condor* **78**, 91 (1976).
120. S. L. Lindstedt and W. A. Calder III, *Quart. Rev. Biol.* **36**, 1 (1981).
121. S. L. Lindstedt, B. J. Miller and S. W. Buskirk, *Ecology* **67**, 413 (1986).
122. S. L. Lindstedt and P. J. Schaeffer, *Lab. Anim.* **36**, 1 (2002).
123. E. N. Lorenz, *J. Atmos. Sci.* **20**, 130 (1963).
124. E. N. Lorenz, *The Essence of Chaos* (University of Washington Press, Seattle, 1993).
125. C. Lyell, *Principles of Geology* (James Kay Jun & Brother, Philadelphia, 1837).
126. R. L. Magin, *Fractional Calculus in Bioengineering* (Begell House, CN, 2006).
127. I. Mahmood, *Life Sci.* **63**, 2365 (1998).
128. A. M. Makarieva, *J. Theor. Biol.* **237**, 291 (2005a).
129. A. M. Makarieva, V. G. Gorshkov and B.-L. Li, *Ecol. Comp.* **2**, 259 (2005b).
130. R. D. Manaster and S. Manaster, *J. Morphol.* **147**, 299 (1975).
131. B. B. Mandelbrot, *Fractals, Form and Chance* (W.H. Freeman San Francisco, CA, 1977).
132. B. B. Mandelbrot, *The Fractal Geometry of Nature* (W.H. Freeman, San Francisco, CA, 1982).
133. B. B. Mandelbrot, Self-affine fractal sets, in *Fractals in Physics*, eds. L. Pietronero and E. Tosatti (North-Holland, Amsterdam, 1986), pp. 3–28.

134. B. B. Mandelbrot, *Fractals and Scaling in Finance* (Springer, New York, 1997).
135. R. N. Mantegna and H. E. Stanley, *Econophysics* (Cambridge University Press, New York, 2000).
136. A. Maritan *et al.*, *Geophys. Res. Lett.* **29**, 1508 (2001).
137. R. D. Martin and P. H. Harvey, Brain size allometry: Ontogeny and phylogeny, in *Size & Scaling in Primate Biology*, ed. W. L. Jungers (Plenum Press, New York, 1985).
138. B. Mauroy *et al.*, *Nature* **427**, 633 (2004).
139. T. A. McMahon, *Science* **179**, 1201 (1973).
140. T. A. McMahon, *Amer. Nat.* **109**, 547 (1975).
141. B. K. McNab, *The Physiological Ecology of Vertebrates: A View from Energetics* (Comstock Publ. Ass., 2002).
142. B. K. McNab, *Comp. Biochem. Physiol.* **152**, 22 (2009).
143. P. Meakin, *Fractals, Scaling and Growth Far from Equilibrium* (Cambridge University Press, Cambridge, 1998).
144. K. S. Miller and B. Ross, *An Introduction to the Fractional Calculus and Fractional Differential Equations* (John Wiley & Sons, New York, 1993).
145. C. O. Mohr, *Am. Midl. Nat.* **24**, 581 (1940).
146. D. R. Montgomery and W. E. Dierich, *Science* **255**, 826 (1992).
147. E. W. Montroll and B. J. West, On an enriched collection of stochastic processes, in *Fluctuation Phenomena*, eds. E. W. Montroll and J. L. Lebowitz, Studies in Statistical Mechanics, Vol. VII (North-Holland, Amsterdam, 1979).
148. E. W. Montroll and M. F. Shlesinger, *J. Stat. Phys.* **32**, 209 (1983).
149. M. E. Moses *et al.*, *J. R. Soc. Interface* **5**, 1469 (2008).
150. C. D. Murray, *Proc. Nat. Acad. Sci. USA* **12**, 207 (1926a).
151. C. D. Murray, *J. Gen. Physiol.* **9**, 835 (1926b).
152. T. R. Nelson, B. J. West and A. L. Goldberger, *Experientia* **46**, 251 (1990).
153. M. E. J. Newman, *SIAM Rev.* **45**, 167 (2003).
154. K. J. Niklas, *Biol. Rev.* **79**, 871 (2004).
155. E. Ott, *Chaos in Dynamical Systems* (Cambridge University Press, New York, 1993).
156. G. C. Packard, *J. Theor. Biol.* **257**, 515 (2008).
157. G. C. Packard and T. J. Boardman, *Physiol. Biochem. Zool.* **81**, 496 (2008).
158. P. R. Painter, *Theor. Biol. Med. Model.* **2**, 31 (2005).
159. S. Peckham, *Water Resources Res.* **31**, 1023 (1995).
160. S. D. Peckham and V. K. Gupta, *Water Resources Res.* **35**, 2763 (1999).
161. C.-K. Peng *et al.*, *Phys. Rev. Lett.* **70**, 1343 (1993).
162. R. H. Peters, *The Ecological Implications of Body Size* (Cambridge University Press, Cambridge, 1983).
163. C. G. Phillips, S. R. Kaye and R. C. Schroter, *Respir. Physiol.* **98**, 193-217 (1994).
164. D. Pilbeam and S. J. Gould, *Science* **186**, 892 (1974).
165. R. E. Plotnick and J. J. Sepkoski, *Paleobiol.* **27**, 126 (2001).
166. F. W. Preston, *Ecology* **43**, 185 (1962).
167. J. W. Prothero, *J. Brain Res.* **38**, 513 (1997).
168. C. A. Price, B. J. Enquist and V. M. Savage, *PNAS* **104**, 13204 (2007).
169. I. Prigogine and I. Stengers, *Order Out of Chaos: Man's New Dialogue With Nature* (Bantam Books, Toronto, 1984).
170. C. L. Que *et al.*, *J. Appl. Physiol.* **91**, 1131 (2001).
171. O. G. Raabe *et al.*, *Tracheobronchial Geometry: Human, Dog, Rat, Hamster* (Lovelace Foundation for Medical Education and Research, Albuquerque, 1976).

172. N. Rashevsky, *Mathematical Biophysics Physico-Mathematical Foundations of Biology*, Vol. 2, 3rd edn. (Dover Publications, New York, 1960).
173. D. M. Raup and J. J. Skepinski Jr., *Science* **215**, 1501 (1982).
174. P. B. Reich *et al.*, *Nature* **439**, 457 (2006).
175. L. E. Reichl, *A Modern Course in Statistical Physics* (John Wiley & Sons, New York, 1998).
176. M. J. Reiss, *The Allometry of Growth and Reproduction* (Cambridge University Press, Cambridge, 1989).
177. J. P. Richter (ed.) *The Notebooks of Leonardo da Vinci*, Vol. 1 (Dover, New York, 1970); unabridged edition of the work first published in London in 1883.
178. R. Rigon, I. Rodriguez-Iturbe and A. Rinaldo, *Water Resources Res.* **32**, 3367 (1998).
179. P. A. Rikvold and R. K. P. Zia, *Phys. Rev. E* **68**, 031913 (2003).
180. H. U. Riisgård, *Ecol. Lett.* **1**, 71 (1998).
181. A. Rinaldo, J. R. Banavar and A. Maritan, *Water Resources Res.* **42**, 1 (2006).
182. I. Rodriguez-Iturbe and A. Rinaldo, *Fractal River Basins, Chance and Self-organization* (Cambridge University Press, Cambridge, UK, 1997).
183. M. Rubner, *Z. Biol.* **19**, 353 (1883).
184. G. Samorodnitsky and M. S. Taqqu, *Stable Non-Gaussian Random Processes* (Chapman & Hall, New York, 1994).
185. G. A. Sacher, Relation of lifespan to brain weight and body weight in mammals, in *Ciba Foundation Colloquium on Aging*, Vol. 1, ed. G. E. W. Wolstenholme (1959).
186. B. S. Sagar and T. L. Tien, *Geophys. Res. Lett.* **31**(1-4), L06501 (2004).
187. B. Sapoval, *Universalités et Fractales* (Flammarion, Paris, 1997).
188. S. et Rameaux, *Bull. Acad. R. Med. (Paris)* **3**, 1094 (1838–39).
189. V. M. Savage *et al.*, *Funct. Ecol.* **18**, 257 (2004).
190. V. M. Savage, E. J. Deeds and W. Fontana, *PLoS Comput. Biol.* **4**(9), e1000171 (2008).
191. Y. Sawada *et al.*, *J. Pharmacokin Biopharm.* **12**, 241 (1984).
192. A. E. Scheidegger, *Bull. Int. Assoc. Sci. Hyd.* **XV**, 1 (1970).
193. A. Schenzle and H. Brand, *Phys. Rev. E* **20**, 1628 (1979).
194. G. Schlenska, *J. Hirnforsch* **15**, 401 (1974).
195. K. Schmidt-Nielsen, *Scaling, Why is Animal Size so Important?* (Cambridge University Press, Cambridge, 1984).
196. K. Schmidt-Nielsen, *Animal Physiology* (Cambridge University Press, Cambridge, 1997).
197. E. Schrödinger, *What is Life?*, Based on lectures delivered under the auspices of the Dublin Institute for Advanced Studies at Trinity College, Dublin, in February 1943.
198. V. Seshadri and B. J. West, *Proc. Nat. Acad. Sci. USA* **79**, 4501 (1982).
199. B. Shea, *Am. J. Phys. Anthropol.* **56**, 179 (1981).
200. M. F. Shlesinger and B. J. West, *Phys. Rev. Lett.* **67**, 2106 (1991).
201. J. K. L. da Silva, G. J. M. Garcia and L. A. Barbosa, *Phys. Life Rev.* **3**, 229 (2006).
202. R. J. Smith, *J. Theor. Biol.* **87**, 97 (1980).
203. R. J. Smith, *Am. J. Phys. Anthropol.* **90**, 215–228 (1993).
204. O. Snell, *Arch. Psychiatr.* **23**, 436 (1892).
205. K. Snell (ed.), *Understanding the Control of Metabolism* (Portland, London, 1997).
206. K. Sneppe *et al.*, *Proc. Nat. Acad. Sci. USA* **92**, 5209 (1995).
207. I. M. Sokolov, J. Klafter and A. Blumen, *Phys. Today Nov.* 48 (2002).
208. R. V. Solé *et al.*, *Nature* **388**, 764 (1997).
209. C. F. Stevens, *J. Biol.* **8**, 14 (2009).
210. L. R. Taylor, *Nature* **189**, 732 (1961).

D. West & B. J. West

211. C. R. Taylor and I. P. Woiod, *J. Animal Ecol.* **49**, 209 (1980).
212. C. R. Taylor and E. R. Weibel, *Respir. Physiol.* **44**, 1 (1981).
213. D. W. Thompson, *On Growth and Form*, 2nd. edn. (Cambridge University Press, Cambridge, 1963).
214. D. B. Tower, *J. Comp. Neurol.* **101**, 9 (1954).
215. D. L. Turcotte, *Fractals and Chaos in Geology and Geophysics* (Cambridge University Press, Cambridge, 1992).
216. V. V. Uchaikin, *Int. J. Theor. Phys.* **39**, 3805 (2000).
217. G. W. Uhlenbeck and L. S. Ornstein, *Phys. Rev.* **36**, 823 (1930).
218. M. O. Vlad *et al.*, *PNAS* **104**, 4798 (2007).
219. L. Von Bertalanffy, *Q. Rev. Biol.* **32**, 217 (1957).
220. D. I. Warton, *Biol. Rev.* **85**, 259 (2006).
221. D. J. Watts, *Small Worlds* (Princeton University Press, Princeton, NJ, 1999).
222. E. R. Weibel and D. M. Gomez, *Science* **137**, 577 (1962).
223. E. R. Weibel, *Symmorphosis: On Form and Function in Shaping Life* (Harvard University Press, Cambridge, 2000).
224. E. R. Weibel, *Nature* **417**, 131 (2002).
225. M. B. Weissman, *Rev. Mod. Phys.* **60**, 537 (1988).
226. G. Werner, *Front. Physiol.* **1**, 15 (2010) doi:10.3389/fphys.2010.00015.
227. B. J. West and V. Seshadri, *Physica A* **113**, 293 (1982).
228. B. J. West, V. Barghava and A. L. Goldberger, *J. Appl. Physiol.* **60**, 1089 (1986).
229. B. J. West and A. L. Goldberger, *Am. Sci.* **75**, 354 (1987).
230. B. J. West, in *Fractal Physiology and Chaos in Medicine*, Studies of Nonlinear Phenomena in Life Science Vol. 1 (World Scientific, Singapore, 1990a).
231. B. J. West, *Ann. Biomed. Eng.* **18**, 135 (1990b).
232. B. J. West, *Int. J. Mod. Phys. B* **4**, 1629 (1990c).
233. B. J. West and M. Shlesinger, *Am. Sci.* **78**, 40 (1990d).
234. B. J. West, in *The Lure of Modern Science: Fractal Thinking*, Studies of Nonlinear Phenomena in Life Science, Vol. 3 (World Scientific, Singapore, 1999a).
235. B. J. West, *Physiology, Promiscuity and Prophecy at the Millennium: A Tale of Tails*, Studies of Nonlinear Phenomena in Life Science, Vol. 7 (World Scientific, Singapore, 1999b).
236. B. J. West, M. Bologna and P. Grigolini, *Physics of Fractal Operators* (Springer, Berlin, 2003).
237. B. J. West and L. A. Griffin, *Biodynamics: Why the Wirewalker Doesn't Fall* (John Wiley & Sons, Hoboken, 2004).
238. B. J. West, in *Where Medicine Went Wrong*, Studies of Nonlinear Phenomena in Life Science, Vol. 11 (World Scientific, Singapore, 2006).
239. B. J. West, *Phys. Rept.* **468**, 1 (2008).
240. B. J. West, *Front. Physiol.* **1**, 12 (2010) doi:10.3389/fphys.2010.00012.
241. B. J. West and D. West, Origin of allometry hypothesis, in *Fractional Dynamics*, eds. J. Klafter, S. C. Lin and R. Metzler (World Scientific, Singapore, 2012).
242. D. West and B. J. West, *Physica A* **390**, 1733 (2011).
243. D. West and B. J. West, *Europhys. Lett.* **94**, 38005 (2011).
244. B. J. West and P. Grigolini, *Complex Webs: Anticipating the Improbable* (Cambridge University Press, Cambridge, 2011).
245. B. J. West and D. West, *Fractional Calculus Appl. Anal.* **15**, 127 (2012).
246. B. J. West and D. West, *Europhys. Lett.* **97**, 48002 (2012).
247. G. B. West, J. H. Brown and B. J. Enquist, *Science* **276**, 122 (1997).
248. G. B. West, *Physica A* **263**, 104 (1999).

249. G. B. West *et al.*, The origin of universal scaling laws in biology, in *Scaling in Biology*, eds. J. H. Brown and G. B. West (Oxford University Press, Oxford, 2000), pp. 87–112.
250. G. B. West, J. H. Brown and B. J. Enquist, *Nature* **413**, 628 (2001).
251. G. B. West *et al.*, *Nature* **421**, 712 (2003).
252. G. B. West and J. H. Brown, *Phys. Today*, 36 (2004).
253. J. F. White and S. J. Gould, *Am. Natur.* **99**, 5 (1965).
254. C. R. White and R. S. Seymour, *J. Exp. Biol.* **208**, 1611 (2005).
255. C. R. White, P. Cassey and T. M. Blackburn, *Ecology* **88**, 315 (2007).
256. C. B. Williams, *Patterns in the Balance of Nature and Related Problems in Quantitative Ecology* (Academic Press, New York, 1964).
257. R. J. Williams and N. D. Martinez, *Eur. Phys. J. B* **38**, 297 (2004).
258. J. C. Willis, *Age and Area* (Cambridge University Press, Cambridge, 1922).
259. K. G. Wilson, *Rev. Mod. Phys.* **47**, 773 (1975).
260. T. A. Wilson, *Nature* 668 (1967).
261. G. Woodward *et al.*, *TRENDS Ecol. Evol.* **20**, 402 (2005).
262. P. Yodzis and S. Innes, *Am. Nat.* **139**, 1151 (1992).
263. J. H. Zar, *BioScience* **18**, 1118 (1968).
264. V. M. Zolotarev, *One-dimensional Stable Distributions, Translation of Mathematical Monographs*, Vol. 65 (American Mathematical Society, Providence, 1986).

Distributed Algorithms for Learning and Cognitive Medium Access with Logarithmic Regret

Animashree Anandkumar, Nithin Michael, Ao Kevin Tang, and Ananthram Swami

IEEE Journal on Selected Areas in Communications, 29(4), 731-745 (2011)

Distributed Algorithms for Learning and Cognitive Medium Access with Logarithmic Regret

Animashree Anandkumar, *Member, IEEE*, Nithin Michael, *Student Member, IEEE*,
Ao Kevin Tang, *Member, IEEE*, and Ananthram Swami, *Fellow, IEEE*

Abstract—The problem of distributed learning and channel access is considered in a cognitive network with multiple secondary users. The availability statistics of the channels are initially unknown to the secondary users and are estimated using sensing decisions. There is no explicit information exchange or prior agreement among the secondary users and sensing and access decisions are undertaken by them in a completely distributed manner. We propose policies for distributed learning and access which achieve order-optimal cognitive system throughput (number of successful secondary transmissions) under self play, i.e., when implemented at all the secondary users. Equivalently, our policies minimize the sum *regret* in distributed learning and access, which is the loss in secondary throughput due to learning and distributed access. For the scenario when the number of secondary users is known to the policy, we prove that the total regret is logarithmic in the number of transmission slots. This policy achieves order-optimal regret based on a logarithmic lower bound for regret under any uniformly-good learning and access policy. We then consider the case when the number of secondary users is fixed but unknown, and is estimated at each user through feedback. We propose a policy whose sum regret grows only slightly faster than logarithmic in the number of transmission slots.

Index Terms—Cognitive medium access control, multi-armed bandits, distributed algorithms, logarithmic regret.

I. INTRODUCTION

THERE has been extensive research on cognitive radio network in the past decade to resolve many challenges not encountered previously in traditional communication networks (see e.g., [2]). One of the main challenges is to achieve coexistence of heterogeneous users accessing the same part of the spectrum. In a hierarchical cognitive network, there are two classes of transmitting users, viz., the primary users who have priority in accessing the spectrum and the secondary users who opportunistically transmit when the primary user is idle. The secondary users are *cognitive* and can sense the spectrum to detect the presence of a primary transmission. However, due

to resource and hardware constraints, they can sense only a part of the spectrum at any given time.

We consider a slotted cognitive system where each secondary user can sense and access only one orthogonal channel in each transmission slot (see Fig. 1). Under sensing constraints, it is thus beneficial for the secondary users to select channels with higher mean availability, i.e., channels which are less likely to be occupied by the primary users. However, in practice, the channel availability statistics are unknown to the secondary users at the start of the transmissions.

Since the secondary users are required to sense the medium before transmission, can these sensing decisions be used to *learn* the channel availability statistics? If so, using these estimated channel availabilities, can we design channel access rules which maximize the transmission throughput? Designing provably efficient algorithms to accomplish the above goals forms the focus of our paper. Such algorithms need to be efficient, both in terms of learning and channel access.

For any learning algorithm, there are two important performance criteria: *consistency* and *regret bounds* [3]. A learning algorithm is said to be consistent if the learnt estimates converge to the true values as the number of samples goes to infinity. The regret¹ of a learning algorithm is a measure of the speed of convergence, and is thus meaningful only for consistent algorithms. In our context, the users need to learn the channel availability statistics consistently in a distributed manner. The regret in this case is defined as the loss in secondary throughput due to learning when compared to the ideal scenario where the channel statistics are known perfectly (see (2)). It is thus desirable to design distributed learning algorithms with small regret.

Additionally, we consider a distributed framework where there is no information exchange or prior agreement among the secondary users. This introduces additional challenges: it results in loss of throughput due to collisions among the secondary users, and there is now competition among the secondary users since they all tend to access channels with higher availabilities. It is imperative that the channel access policies overcome the above challenges. Hence, a distributed learning and access policy experiences regret both due to learning the unknown channel availabilities as well as due to collisions under distributed access.

¹Note that the sum regret is a finer measure of performance of a distributed algorithm than the time-averaged total throughput of the users since any sub-linear regret (with respect to time) implies optimal average throughput. On the other hand, regret is equivalent to total throughput and hence, optimal regret is equivalent to achieving optimal total throughput.

Manuscript received 1 December 2009; revised 4 June 2010. During the stint of this work, the first author was supported by MURI through AFOSR Grant FA9550-06-1-0324. The second and the third authors are supported in part through NSF grant CCF-0835706. Parts of this paper were presented at [1].

A. Anandkumar is with the Center for Pervasive Communications and Computing at the Department of Electrical Engineering and Computer Science, University of California, Irvine, CA, 92697, USA (e-mail: a.anandkumar@uci.edu).

N. Michael and A. K. Tang are with the School of Electrical and Computer Engineering, Cornell University, Ithaca, NY 14853, USA (e-mail: nm373@atang@ece.cornell.edu).

A. Swami is with the Army Research Laboratory, Adelphi, MD 20783, USA (e-mail: a.swami@ieee.org).

Digital Object Identifier 10.1109/JSAC.2011.110406.

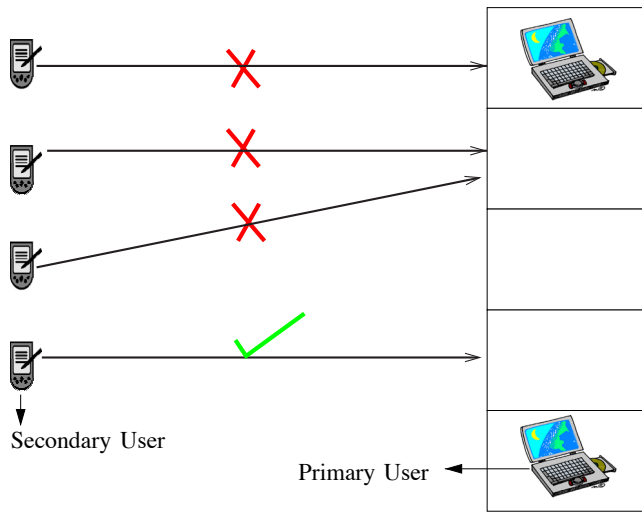


Fig. 1. Cognitive radio network with $U = 4$ secondary users and $C = 5$ channels. A secondary user is not allowed to transmit if the accessed channel is occupied by a primary user. If more than one secondary user transmits in the same free channel, then all the transmissions are unsuccessful.

A. Our Contributions

The main contributions of this paper are two fold. First, we propose two distributed learning and access policies under multiple secondary users in a cognitive network. Second, we provide performance guarantees for these policies in terms of regret. Overall, we prove that one of our proposed algorithms achieves order-optimal regret and the other achieves nearly order-optimal regret, where the order is with respect to the number of transmission slots.

The first policy we propose assumes that the total number of secondary users in the system is known while our second policy removes this requirement. We provide bounds on the total regret experienced by the secondary users under self play, i.e., when implemented at all the secondary users. For the first policy, we prove that the regret is logarithmic, i.e., $O(\log n)$ where n is the number of transmission slots. For the second policy, the regret grows slightly faster than logarithmic, i.e., $O(f(n) \log n)$, where we can choose any function $f(n)$ satisfying $f(n) \rightarrow \infty$, as $n \rightarrow \infty$. Hence, we provide performance guarantees for the proposed distributed learning and access policies.

A lower bound on regret under any *uniformly-good* distributed learning policy has been derived in [4], which is also logarithmic in the number of transmission slots (See (6) for definition of uniformly-good policies). Thus, our first policy (which requires knowledge of the number of secondary users) achieves order-optimal regret. The effects of the number of secondary users and the number of channels on regret are also explicitly characterized and verified via simulations.

The *exploration-exploitation* tradeoff for learning, combined with the *cooperation-competition* tradeoffs among multiple users for distributed medium access have not been sufficiently examined in the literature (see Section I-B for a discussion). Our analysis in this paper provides important engineering insights towards dealing with learning, competition, and cooperation in practical cognitive systems.

Remark on Model Assumptions: We note some of the limitations of our approach. We prove order-optimal regret for our proposed algorithms under an i.i.d. primary transmission model², where the probability of a channel being occupied by any primary user in any slot is assumed to be i.i.d. This is indeed idealistic and in practice, a Markovian model may be more appropriate [5], [6]. The i.i.d. model leads to simple learning schemes for channel availabilities but is not crucial towards deriving regret bounds for our proposed schemes. Extensions of the classical multi-armed bandit problem to a Markovian model are considered in [7]. In principle, our results on achieving order-optimal regret for distributed learning and access can be similarly extended to a Markovian channel model but this entails more complex estimators and rules for evaluating the exploration-exploitation tradeoffs of different channels and is a topic of interest for future investigation.

B. Related Work

Several results on the multi-armed bandit problem will be used and generalized to study our problem. Detailed discussion on multi-armed bandits can be found in [8]–[11]. Cognitive medium access is a topic of extensive research; see [12] for an overview. The connection between cognitive medium access and the multi-armed bandit problem is explored in [13], where a restless bandit formulation is employed. Under this formulation, indexability is established, Whittle's index for channel selection is obtained in closed-form, and the equivalence between the myopic policy and the Whittle's index is established. However, this work assumes known channel availability statistics and does not consider competing secondary users. The work in [14] considers allocation of two users to two channels under a Markovian channel model using a partially observable Markov decision process (POMDP) framework. The use of collision feedback information for learning, and spatial heterogeneity in spectrum opportunities were investigated. However, the difference from our work is that [14] assumes that the availability statistics (transition probabilities) of the channels are known to the secondary users while we consider learning of unknown channel statistics. The works in [15], [16] consider centralized access schemes in contrast to distributed access here, the work in [17] considers access through information exchange and studies the optimal choice of the amount of information to be exchanged given the cost of negotiation. The work in [18] considers access under Q -learning for two users and two channels where users can sense both the channels simultaneously. The work in [19] discusses a game-theoretic approach to cognitive medium access. In [20], learning in congestion games through multiplicative updates is considered and convergence to weakly-stable equilibria (which reduces to the pure Nash equilibrium for almost all games) is proven. However, the work assumes fixed costs (or equivalently rewards) in contrast to random rewards here, and that the players can fully observe the actions of other players.

²By i.i.d. primary transmission model, we do not mean the presence of a single primary user, but rather, this model is used to capture the overall statistical behavior of all the primary users in the system.

Recently, the work in [21] considers combinatorial bandits, where a more general model of different (unknown) channel availabilities is assumed for different secondary users, and a matching algorithm is proposed for jointly allocating users to channels. The algorithm is guaranteed to have logarithmic regret with respect to the number of transmission slots and polynomial storage requirements. A decentralized implementation of the proposed algorithm is proposed but it still requires information exchange and coordination among the users. In contrast, we propose algorithms which removes this requirement albeit in a more restrictive setting of identical channel availabilities for all users.

Recently, Liu and Zhao [4] proposed a family of distributed learning and access policies known as time-division fair share (TDFS), and proved logarithmic regret for these policies. They established a lower bound on the growth rate of system regret for a general class of uniformly-good decentralized policies. The TDFS policies in [4] can incorporate any order-optimal single-player policy while our work here is based on the single-user policy proposed in [11]. Another difference is that in [4], the users orthogonalize via settling at different offsets in their time-sharing schedule, while in our work here, users orthogonalize into different channels. Moreover, the TDFS policies ensure that each player achieves the same time-average reward while our policies here achieve probabilistic fairness, in the sense that the policies do not discriminate between different users. In [22], the TDFS policies are extended to incorporate imperfect sensing.

In our prior work [1], we first formulated the problem of decentralized learning and access for multiple secondary users. We considered two scenarios: one where there is initial common information among the secondary users in the form of pre-allocated ranks, and the other where no such information is available. In this paper, we analyze the distributed policy in detail and prove that it has logarithmic regret. In addition, we also consider the case when the number of secondary users is unknown, and provide bounds on regret in this scenario.

Organization: Section II deals with the system model, Section III deals with the special case of single secondary user and of multiple users with centralized access which can be directly solved using the classical results on multi-armed bandits. In Section IV, we propose distributed learning and access policy with provably logarithmic regret when the number of secondary users is known. Section V considers the scenario when the number of secondary users is unknown. Section VI provides a lower bound for distributed learning. Section VII includes some simulation results for the proposed schemes and Section VIII concludes the paper. Most of the proofs are found in the Appendix.

Since Section III mostly deals with a recap of the classical results on multi-armed bandits, those familiar with the literature (e.g., [8]–[11]) may skip this section without loss of continuity.

II. SYSTEM MODEL & FORMULATION

Notation: For any two functions $f(n), g(n)$, $f(n) = O(g(n))$ if there exists a constant c such that $f(n) \leq cg(n)$ for all $n \geq n_0$ for a fixed $n_0 \in \mathbb{N}$. Similarly, $f(n) = \Omega(g(n))$ if there exists a constant c' such that $f(n) \geq c'g(n)$ for all

$n \geq n_0$ for a fixed $n_0 \in \mathbb{N}$, and $f(n) = \Theta(g(n))$ if $f(n) = \Omega(g(n))$ and $f(n) = O(g(n))$. Also, $f(n) = o(g(n))$ when $f(n)/g(n) \rightarrow 0$ and $f(n) = \omega(g(n))$ when $f(n)/g(n) \rightarrow \infty$ as $n \rightarrow \infty$.

For a vector μ , let $|\mu|$ denote its cardinality, and let $\mu = [\mu_1, \mu_2, \dots, \mu_{|\mu|}]^T$. We refer to the U highest entries in a vector μ as the U -best channels and the rest as the U -worst channels, where $1 \leq U \leq |\mu|$. Let $\sigma(a; \mu)$ denote the index of the a^{th} highest entry in μ . Alternatively, we abbreviate $a^* := \sigma(a; \mu)$ for ease of notation. Let $B(\mu)$ denote the Bernoulli distribution with mean μ . With abuse of notation, let $D(\mu_1, \mu_2) := D(B(\mu_1); B(\mu_2))$ be the Kullback-Leibler distance between the Bernoulli distributions $B(\mu_1)$ and $B(\mu_2)$ [23] and let $\Delta(1, 2) := \mu_1 - \mu_2$.

A. Sensing & Channel Models

Let $U \geq 1$ be the number of secondary users³ and $C \geq U$ be the number⁴ of orthogonal channels available for slotted transmissions with a fixed slot width. In each channel i and slot k , the primary user transmits i.i.d. with probability $1 - \mu_i > 0$. In other words, let $W_i(k)$ denote the indicator variable if the channel is free

$$W_i(k) = \begin{cases} 0, & \text{channel } i \text{ occupied in slot } k \\ 1, & \text{o.w.,} \end{cases}$$

and we assume that $W_i(k) \stackrel{i.i.d.}{\sim} B(\mu_i)$.

The mean availability vector μ consists of mean availabilities μ_i of all channels, i.e., is $\mu := [\mu_1, \dots, \mu_C]$, where all $\mu_i \in (0, 1)$ and are distinct. μ is initially unknown to all the secondary users and is learnt *independently* over time using the past sensing decisions without any information exchange among the users. We assume that channel sensing is perfect at all the users.

Let $T_{i,j}(k)$ denote the number of slots where channel i is sensed in k slots by user j (not necessarily being the sole user to sense that channel). Note that $\sum_{i=1}^C T_{i,j}(k) = k$ for all users j , since each user senses exactly one channel in every time slot. The sensing variables are obtained as follows: at the beginning of the k^{th} slot, each secondary user $j \in U$ selects exactly one channel $i \in C$ for sensing, and hence, obtains the value of $W_i(k)$, indicating if the channel is free. User j then records all the sensing decisions of each channel i in a vector $\mathbf{X}_{i,j}^k := [X_{i,j}(1), \dots, X_{i,j}(T_{i,j}(k))]^T$. Hence, $\cup_{i=1}^C \mathbf{X}_{i,j}^k$ is the collection of sensed decisions for user j in k slots for all the C channels.

We assume the collision model under which if two or more users transmit in the same channel then none of the transmissions go through. At the end of each slot k , each user j receives acknowledgement $Z_j(k)$ on whether its transmission in the k^{th} slot was received. Hence, in general, any policy employed by user j in the $(k+1)^{\text{th}}$ slot, denoted by $\rho(\cup_{i=1}^C \mathbf{X}_{i,j}^k, \mathbf{Z}_j^k)$, is based on all the previous sensing and feedback results.

³A user refers to a secondary user unless otherwise mentioned.

⁴When $U \geq C$, learning availability statistics is less crucial, since all channels need to be accessed to avoid collisions. In this case, design of medium access is more crucial.

Algorithm 1 Single User Policy $\rho^1(\mathbf{g}(n))$ in [10].

Input: $\{\bar{X}_i(n)\}_{i=1,\dots,C}$: Sample-mean availabilities after n rounds, $g(i; n)$: statistic based on $\bar{X}_{i,j}(n)$,
 $\sigma(a; \mathbf{g}(n))$: index of a^{th} highest entry in $\mathbf{g}(n)$.
Init: Sense in each channel once, $n \leftarrow C$, $\text{Curr_Sel} \leftarrow C$.
Loop: $n \leftarrow n + 1$
 $\text{Curr_Sel} \leftarrow$ channel corresponding to highest entry in $\mathbf{g}(n)$ for sensing. If free, transmit.

B. Regret of a Policy

Under the above model, we are interested in designing policies ρ which maximize the expected number of successful transmissions of the secondary users subject to the non-interference constraint for the primary users. Let $S(n; \mu, U, \rho)$ be the expected total number of successful transmissions after n slots under U number of secondary users and policy ρ .

In the ideal scenario where the availability statistics μ are known a priori and a central agent orthogonally allocates the secondary users to the U -best channels, the expected number of successful transmissions after n slots is given by

$$S^*(n; \mu, U) := n \sum_{j=1}^U \mu(j^*), \quad (1)$$

where j^* is the j^{th} -highest entry in μ .

It is clear that $S^*(n; \mu, U) > S(n; \mu, U, \rho)$ for any policy ρ and any finite $n \in \mathbb{N}$. We are interested in minimizing the *regret* in learning and access, given by

$$R(n; \mu, U, \rho) := S^*(n; \mu, U) - S(n; \mu, U, \rho) > 0. \quad (2)$$

We are interested in minimizing regret under any given $\mu \in (0, 1)^C$ with distinct elements.

By incorporating the collision channel model assumption with no avoidance mechanisms⁵, the expected throughput under the policy ρ is given by

$$S(n; \mu, U, \rho) = \sum_{i=1}^C \sum_{j=1}^U \mu(i) \mathbb{E}[V_{i,j}(n)],$$

where $V_{i,j}(n)$ is the number of times in n slots where user j is the sole user to sense channel i . Hence, the regret in (2) simplifies as

$$R(n; \rho) = \sum_{k=1}^U n \mu(k^*) - \sum_{i=1}^C \sum_{j=1}^U \mu(i) \mathbb{E}[V_{i,j}(n)]. \quad (3)$$

III. SPECIAL CASES FROM KNOWN RESULTS

We recap the bounds for the regret under the special cases of a single secondary user ($U = 1$) and multiple users with centralized learning and access by appealing to the classical results on the multi-armed bandit process [8]–[10].

A. Single Secondary User ($U = 1$)

When there is only one secondary user, the problem of finding policies with minimum regret reduces to that of a

⁵If the users employ CSMA-CA to avoid collisions then the regret is reduced. The bounds derived in this paper are applicable for this case as well.

multi-armed bandit process. Lai and Robbins [8] first analyzed schemes for multi-armed bandits with asymptotic logarithmic regret based on the upper confidence bounds on the unknown channel availabilities. Since then, simpler schemes have been proposed in [10], [11] which compute a statistic or an index for each arm (channel), henceforth referred to as the *g-statistic*, based only on its sample mean and the number of slots where the particular arm is sensed. The arm with the highest index is selected in each slot in these works. We summarize the policy in Algorithm 1 and denote it $\rho^1(\mathbf{g}(n))$, where $\mathbf{g}(n)$ is the vector of scores assigned to the channels after n transmission slots.

The sample-mean based policy in [11, Thm. 1] proposes an index for each channel i and user j at time n is given by

$$g_j^{\text{MEAN}}(i; n) := \bar{X}_{i,j}(T_{i,j}(n)) + \sqrt{\frac{2 \log n}{T_{i,j}(n)}}, \quad (4)$$

where $T_{i,j}(n)$ is the number of slots where user j selects channel i for sensing,

$$\bar{X}_{i,j}(T_{i,j}(n)) := \sum_{k=1}^{T_{i,j}(n)} \frac{X_{i,j}(k)}{T_{i,j}(n)}$$

is the sample-mean availability of channel i , as sensed by user j .

The statistic in (4) captures the *exploration-exploitation* tradeoff between sensing the channel with the best predicted availability to maximize immediate throughput and sensing different channels to obtain improved estimates of their availabilities. The sample-mean term in (4) corresponds to exploitation while the other term involving $T_{i,j}(n)$ corresponds to exploration since it penalizes channels which are not sensed often. The normalization of the exploration term with $\log n$ in (4) implies that the term is significant when $T_{i,j}(n)$ is much smaller than $\log n$. On the other hand, if all the channels are sensed $\Theta(\log n)$ number of times, the exploration terms become unimportant in the *g*-statistics of the channels and the exploitation term dominates, thereby, favoring sensing of the channel with the highest sample mean.

The regret based on the above statistic in (4) is logarithmic for any finite number of slots n but does not have the optimal scaling constant. The sample-mean based statistic in [10, Example 5.7] leads to the optimal scaling constant for regret and is given by

$$g_j^{\text{OPT}}(i; n) := \bar{X}_{i,j}(T_{i,j}(n)) + \min \left[\sqrt{\frac{\log n}{2T_{i,j}(n)}}, 1 \right]. \quad (5)$$

In this paper, we design policies based on the g^{MEAN} statistic since it is simpler to analyze than the g^{OPT} statistic. This is because g^{MEAN} is a continuous function in $T_{i,j}(n)$ while g^{OPT} has a threshold on $T_{i,j}(n)$.

We now recap the results which show logarithmic regret in learning the best channel. In this context, we define *uniformly good* policies ρ [8] as those with regret

$$R(n; \mu, U, \rho) = o(n^\alpha), \quad \forall \alpha > 0, \mu \in (0, 1)^C. \quad (6)$$

Theorem 1 (Logarithmic Regret for $U = 1$ [10], [11]):

For any uniformly good policy ρ satisfying (6), the expected time spent in any suboptimal channel $i \neq 1^*$ satisfies

$$\lim_{n \rightarrow \infty} \mathbb{P} \left[T_{i,1}(n) \geq \frac{(1-\epsilon) \log n}{D(\mu_i, \mu_{1^*})}; \boldsymbol{\mu} \right] = 1, \quad (7)$$

where 1^* is the channel with the best availability. Hence, the regret satisfies

$$\liminf_{n \rightarrow \infty} \frac{R(n; \boldsymbol{\mu}, 1, \rho)}{\log n} \geq \sum_{i \in 1\text{-worst}} \frac{\Delta(1^*, i)}{D(\mu_i, \mu_{1^*})}. \quad (8)$$

The regret under the g^{OPT} statistic in (5) achieves the above bound.

$$\lim_{n \rightarrow \infty} \frac{R(n; \boldsymbol{\mu}, 1, \rho^1(\mathbf{g}_j^{\text{OPT}}))}{\log n} = \sum_{i \in 1\text{-worst}} \frac{\Delta(1^*, i)}{D(\mu_i, \mu_{1^*})}. \quad (9)$$

The regret under g^{MEAN} statistic in (34) satisfies

$$R(n; \boldsymbol{\mu}, 1, \rho^1(\mathbf{g}_j^{\text{MEAN}})) \leq \sum_{i \neq 1^*} \Delta(1^*, i) \left[\frac{8 \log n}{\Delta(j^*, i)^2} + 1 + \frac{\pi^2}{3} \right].$$

B. Centralized Learning & Access for Multiple Users

We now consider multiple secondary users under centralized access policies where there is joint learning and access by a central agent on behalf of all the U users. Here, to minimize the sum regret, the centralized policy allocates the U users to orthogonal channels to avoid collisions. Let $\rho^{\text{CENT}}(\mathcal{X}^k)$, with $\mathcal{X}^k := \cup_{j=1}^U \cup_{i=1}^C \mathbf{X}_{i,j}^k$, denote a centralized policy based on the sensing variables of all the users. The policy under centralized learning is a simple generalization of the single-user policy and is given in Algorithm 2. We now recap the results of [9].

Theorem 2 (Regret Under Centralized Policy ρ^{CENT} [9]):

For any uniformly good centralized policy ρ^{CENT} satisfying (6), the expected times spent in a U -worst channel i satisfies

$$\lim_{n \rightarrow \infty} \mathbb{P} \left[\sum_{j=1}^U T_{i,j}(n) \geq \frac{(1-\epsilon) \log n}{D(\mu_i, \mu_{U^*})}; \boldsymbol{\mu} \right] = 1, \quad (10)$$

where U^* is the channel with the U^{th} best availability. Hence, the regret satisfies

$$\liminf_{n \rightarrow \infty} \frac{R(n; \boldsymbol{\mu}, 1, \rho^{\text{CENT}})}{\log n} \geq \sum_{i \in U\text{-worst}} \frac{\Delta(U^*, i)}{D(\mu_i, \mu_{U^*})}. \quad (11)$$

The scheme in Algorithm 2 based on g^{OPT} achieves the above bound.

$$\lim_{n \rightarrow \infty} \frac{R(n; \boldsymbol{\mu}, 1, \rho^{\text{CENT}}(\mathbf{g}^{\text{OPT}}))}{\log n} = \sum_{i \in U\text{-worst}} \frac{\Delta(U^*, i)}{D(\mu_i, \mu_{U^*})}. \quad (12)$$

The scheme in Algorithm 2 based on the g^{MEAN} satisfies for any $n > 0$,

$$\begin{aligned} & R(n; \boldsymbol{\mu}, U, \rho^{\text{CENT}}(\mathbf{g}^{\text{MEAN}})) \\ & \leq \sum_{m=1}^U \sum_{i \in U\text{-worst}} \sum_{k=1}^U \frac{\Delta(m^*, i)}{U} \left[\frac{8 \log n}{\Delta(m^*, i)^2} + 1 + \frac{\pi^2}{3} \right]. \end{aligned} \quad (13)$$

Proof: See Appendix A. \square

Algorithm 2 Centralized Learning Policy ρ^{CENT} in [9].

Input: $\mathcal{X}^n := \cup_{j=1}^U \cup_{i=1}^C \mathbf{X}_{i,j}^n$: Channel availability after n slots, $\mathbf{g}(n)$: statistic based on \mathcal{X}^n ,

$\sigma(a; \mathbf{g}(n))$: index of a^{th} highest entry in $\mathbf{g}(n)$.

Init: Sense in each channel once, $n \leftarrow C$

Loop: $n \leftarrow n + 1$

$\text{Curr_Sel} \leftarrow$ channels with U -best entries in $\mathbf{g}(n)$. If free, transmit.

Notice that for both the single user case $U = 1$ (Theorem 1) and the centralized multi-user case (Theorem 2), the number of time slots spent in the U -worst channels is $\Theta(\log n)$ and hence, the regret is also $\Theta(\log n)$.

IV. MAIN RESULTS

Armed with the classical results on multi-armed bandits, we now design distributed learning and allocation policies.

A. Preliminaries: Bounds on Regret

We first provide simple bounds on the regret in (3) for any distributed learning and access policy ρ .

Proposition 1 (Lower and Upper Bounds on Regret): The regret under any distributed policy ρ satisfies

$$R(n; \rho) \geq \sum_{j=1}^U \sum_{i \in U\text{-worst}} \Delta(U^*, i) \mathbb{E}[T_{i,j}(n)], \quad (14)$$

$$R(n; \rho) \leq \mu(1^*) \left[\sum_{j=1}^U \sum_{i \in U\text{-worst}} \mathbb{E}[T_{i,j}(n)] + \mathbb{E}[M(n)] \right], \quad (15)$$

where $T_{i,j}(n)$ is the number of slots where user j selects channel i for sensing, $M(n)$ is the number of collisions faced by the users in the U -best channels in n slots, $\Delta(i, j) = \mu(i) - \mu(j)$ and $\mu(1^*)$ is the highest mean availability.

Proof: See Appendix B. \square

In the subsequent sections, we propose distributed learning and access policies and provide regret guarantees for the policies using the upper bound in (15). The lower bound in (14) can be used to derive lower bound on regret for any uniformly-good policy.

The first term in (15) represents the lost transmission opportunities due to selection of U -worst channels (with lower mean availabilities), while the second term represents the performance loss due to collisions among the users in the U -best channels. The first term in (15) decouples among the different users and can be analyzed solely through the marginal distributions of the g -statistics at the users. This in turn, can be analyzed by manipulating the classical results on multi-armed bandits [10], [11]. On the other hand, the second term in (15), involving collisions in the U -best channels, requires the joint distribution of the g -statistics at different users which are correlated variables. This is intractable to analyze directly and we develop techniques to bound this term.

Algorithm 3 Policy $\rho^{\text{RAND}}(U, C, \mathbf{g}_j(n))$ for each user j under U users, C channels and statistic $\mathbf{g}_j(n)$.

Input: $\{\bar{X}_{i,j}(n)\}_{i=1,\dots,C}$: Sample-mean availabilities at user j after n rounds, $g_j(i; n)$: statistic based on $\bar{X}_{i,j}(n)$, $\sigma(a; \mathbf{g}_j(n))$: index of a^{th} highest entry in $\mathbf{g}_j(n)$.
 $\zeta_j(i; n)$: indicator of collision at n^{th} slot at channel i
Init: Sense in each channel once, $n \leftarrow C$, $\text{Curr_Rank} \leftarrow 1$, $\zeta_j(i; m) \leftarrow 0$
Loop: $n \leftarrow n + 1$
if $\zeta_j(\text{Curr_Sel}; n - 1) = 1$ **then**
Draw a new $\text{Curr_Rank} \sim \text{Unif}(U)$
end if
Select channel for sensing. If free, transmit.
 $\text{Curr_Sel} \leftarrow \sigma(\text{Curr_Rank}; \mathbf{g}_j(n))$.
If collision $\zeta_j(\text{Curr_Sel}; n) \leftarrow 1$, **Else** 0.

B. ρ^{RAND} : Distributed Learning and Access

We present the ρ^{RAND} policy in Algorithm 3. Before describing this policy, we make some simple observations. If each user implemented the single-user policy in Algorithm 1, then it would result in collisions, since all the users target the best channel. When there are multiple users and there is no direct communication among them, the users need to randomize channel access in order to avoid collisions. At the same time, accessing the U -worst channels needs to be avoided since they contribute to regret. Hence, users can avoid collisions by randomizing access over the U -best channels, based on their estimates of the channel ranks. However, if the users randomize in every slot, there is a finite probability of collisions in every slot and this results in a linear growth of regret with the number of time slots. Hence, the users need to converge to a collision-free configuration to ensure that the regret is logarithmic.

In Algorithm 3, there is adaptive randomization based on feedback regarding the previous transmission. Each user randomizes *only* if there is a collision in the previous slot; otherwise, the previously generated random rank for the user is retained. The estimation for the channel ranks is through the g -statistic, along the lines of the single-user case.

C. Regret Bounds under ρ^{RAND}

It is easy to see that the ρ^{RAND} policy ensures that the users are allocated orthogonally to the U -best channels as the number of transmission slots goes to infinity. The regret bounds on ρ^{RAND} are however not immediately clear and we provide guarantees below.

We first provide a logarithmic upper bound⁶ on the number of slots spent by each user in any U -worst channel. Hence, the first term in the bound on regret in (15) is also logarithmic.

Lemma 1 (Time Spent in U -worst Channels): Under the ρ^{RAND} scheme in Algorithm 3, the total time spent by any user

⁶Note that the bound on $\mathbb{E}[T_{i,j}(n)]$ in (16) holds for user j even if the other users are using a policy other than ρ^{RAND} . But on the other hand, to analyze the number of collisions $\mathbb{E}[M(n)]$ in (19), we need every user to implement ρ^{RAND} .

$j = 1, \dots, U$, in any $i \in U$ -worst channel is given by

$$\mathbb{E}[T_{i,j}(n)] \leq \sum_{k=1}^U \left[\frac{8 \log n}{\Delta(i, k^*)^2} + 1 + \frac{\pi^2}{3} \right]. \quad (16)$$

Proof: The proof is similar along the lines of Theorem 2, given in Appendix A. The only difference is that here, we need to consider the probability of transmission of each user in each U -worst channel while in Appendix A, the probability of transmission by all users is considered. \square

We now focus on analyzing the number of collisions $M(n)$ in the U -best channels. We first give a result on the expected number of collisions in the ideal scenario where each user has perfect knowledge of the channel availability statistics μ . In this case, the users attempt to reach an orthogonal (collision-free) configuration by uniformly randomizing over the U -best channels.

The stochastic process in this case is a finite-state Markov chain. A state in this Markov chain corresponds to a configuration of U number of (identical) users in U number of channels. The number of states in the Markov chain is the number of *compositions* of U , given by $\binom{2U-1}{U}$ [24, Thm. 5.1]. The orthogonal configuration corresponds to the absorbing state. There are two other classes of states in the Markov chain. One class consists of states in which each channel either has more than one user or no user at all. The second class consists of the remaining states where some channels may have just one user. For the first class, the transition probability to any state of the Markov chain (including self transition and absorption probabilities) is uniform. For a state in the second class, where certain channels have exactly one user, there are only transitions to states which have identical configuration of the single users and the transition probabilities are uniform. Let $\Upsilon(U, U)$ denote the maximum time to absorption in the above Markov chain starting from any initial distribution. We have the following result

Lemma 2 (No. of Collisions Under Perfect Knowledge):

The expected number of collisions under ρ^{RAND} scheme in Algorithm 3, assuming that each user has perfect knowledge of the mean channel availabilities μ , is given by

$$\begin{aligned} \mathbb{E}[M(n); \rho^{\text{RAND}}(U, C, \mu)] &\leq U \mathbb{E}[\Upsilon(U, U)] \\ &\leq U \left[\binom{2U-1}{U} - 1 \right]. \end{aligned} \quad (17)$$

Proof: See Appendix C. \square

The above result states that there is at most a finite number of expected collisions, bounded by $U \mathbb{E}[\Upsilon(U, U)]$ under perfect knowledge of μ . In contrast, recall from the previous section, that there are no collisions under perfect knowledge of μ in the presence of pre-allocated ranks. Hence, $U \mathbb{E}[\Upsilon(U, U)]$ represents a bound on the additional regret due to the lack of direct communication among the users to negotiate their ranks.

We use the result of Lemma 2 for analyzing the number of collisions under distributed learning of the unknown availabilities μ as follows: if we show that the users are able to learn the correct order of the different channels with only logarithmic regret then only an additional finite expected

number of collisions occur before reaching an orthogonal configuration.

Define $T'(n; \rho^{\text{RAND}})$ as the number of slots where any one of the top U -estimated ranks of the channels at some user is wrong under the ρ^{RAND} policy. Below we prove that its expected value is logarithmic in the number of transmissions.

Lemma 3 (Wrong Order of g -statistics): Under the ρ^{RAND} scheme in Algorithm 3,

$$\mathbb{E}[T'(n; \rho^{\text{RAND}})] \leq U \sum_{a=1}^U \sum_{b=a+1}^C \left[\frac{8 \log n}{\Delta(a^*, b^*)^2} + 1 + \frac{\pi^2}{3} \right]. \quad (18)$$

Proof: See Appendix D. \square

We now provide an upper bound on the number of collisions $M(n)$ in the U -best channels by incorporating the above result on $\mathbb{E}[T'(n)]$, the result on the average number of slots $\mathbb{E}[T_{i,j}]$ spent in the $i \in U$ -worst channels in Lemma 1 and the average number of collisions $U\mathbb{E}[\Upsilon(U, U)]$ under perfect knowledge of μ in Lemma 2.

Theorem 3 (Logarithmic Number of Collisions Under ρ^{RAND}): The expected number of collisions in the U -best channels under $\rho^{\text{RAND}}(U, C, \mathbf{g}^{\text{MEAN}})$ scheme satisfies

$$\mathbb{E}[M(n)] \leq U(\mathbb{E}[\Upsilon(U, U)] + 1) \mathbb{E}[T'_j(n)]. \quad (19)$$

Hence, from (16), (18) and (17), $M(n) = O(\log n)$.

Proof: See Appendix E. \square

Hence, there are only a logarithmic number of expected collisions before the users settle in the orthogonal channels. Combining this result with Lemma 1 that the number of slots spent in the U -worst channels is also logarithmic, we immediately have one of the main results of this paper that the sum regret under distributed learning and access is logarithmic.

Theorem 4 (Logarithmic Regret Under ρ^{RAND}): The policy $\rho^{\text{RAND}}(U, C, \mathbf{g}^{\text{MEAN}})$ in Algorithm 3 has $\Theta(\log n)$ regret.

Proof: Substituting (19) and (16) in (15). \square

Hence, we prove that distributed learning and channel access among multiple secondary users is possible with logarithmic regret without any explicit communication among the users. This implies that the number of lost opportunities for successful transmissions at all secondary users is only logarithmic in the number of transmissions, which is negligible when there are a large number of transmissions.

We have so far focused on designing schemes that maximize system or social throughput. We now briefly discuss the fairness for an individual user under ρ^{RAND} . Since ρ^{RAND} does not distinguish any of the users, in the sense that each user has equal probability of “settling” down in one of the U -best channels while experiencing only logarithmic regret in doing so. Simulations in Section VII (in Fig. 4) demonstrate this phenomenon.

We also note that the bound on regret under ρ^{RAND} grows rapidly with the number of users U , due to the bound in (17). This is due to uniform channel access by the users without any coordination or information exchange. It is of interest to explore better distributed access schemes, which when combined with learning algorithms yield low regret in the number of users.

Algorithm 4 Policy $\rho^{\text{EST}}(n, C, \mathbf{g}_j(m), \xi)$ for each user j under n transmission slots (horizon length), C channels, statistic $\mathbf{g}_j(m)$ and threshold function ξ .

- 1) **Input:** $\{\bar{X}_{i,j}(n)\}_{i=1,\dots,C}$: Sample-mean availabilities at user j , $g_j(i; n)$: statistic based on $\bar{X}_{i,j}(n)$, $\sigma(a; \mathbf{g}_j(n))$: index of a^{th} highest entry in $\mathbf{g}_j(n)$. $\zeta_j(i; n)$: indicator of collision at n^{th} slot at channel i \hat{U} : current estimate of the number of users. n : horizon (total number of slots for transmission) $\xi(n; k)$: threshold functions for $k = 1, \dots, C$.
 - 2) Init: Sense each channel once, $m \leftarrow C$, $\text{Curr_Sel} \leftarrow C$, $\text{Curr_Rank} \leftarrow 1$, $\hat{U} \leftarrow 1$, $\zeta_j(i; m) \leftarrow 0$ for all $i = 1, \dots, C$
 - 3) Loop 4 to 6: $m \leftarrow m + 1$, stop when $m = n$ or $\hat{U} = C$.
 - 4) **If** $\zeta_j(\text{Curr_Sel}; m - 1) = 1$ **then**
Draw a new $\text{Curr_Rank} \sim \text{Unif}(\hat{U})$. **end if**
Select channel for sensing. If free, transmit.
 $\text{Curr_Sel} \leftarrow \sigma(\text{Curr_Rank}; \mathbf{g}_j(m))$
 - 5) $\zeta_j(\text{Curr_Sel}; m) \leftarrow 1$ if collision, 0 o.w.
 - 6) **If** $\sum_{a=1}^m \sum_{k=1}^{\hat{U}} \zeta_j(\sigma(k; \mathbf{g}_j(m)); a) > \xi(n; \hat{U})$ **then**
 $\hat{U} \leftarrow \hat{U} + 1$, $\zeta_j(i; a) \leftarrow 0$, $i = 1, \dots, C$, $a = 1, \dots, m$.
end if
-

V. DISTRIBUTED LEARNING AND ACCESS UNDER UNKNOWN NUMBER OF USERS

We have so far assumed that the number of secondary users is known, and is required for the implementation of the ρ^{RAND} policy. In practice, this entails initial announcement from each of the secondary users to indicate their presence in the cognitive network. However, in a truly distributed setting without any information exchange among the users, such an announcement may not be possible.

In this section, we consider the scenario, where the number of users U is unknown (but fixed throughout the duration of transmissions and $U \leq C$, the number of channels). In this case, the policy needs to estimate the number of secondary users in the system, in addition to learning the channel availability statistics and designing channel access rules based on collision feedback. Note that if the policy assumed the worst-case scenario that $U = C$, then the regret grows linearly since there is a positive probability that the U -worst channels are selected for sensing in any time slot.

A. Description of ρ^{EST} Policy

We now propose a policy ρ^{EST} in Algorithm 4. This policy incorporates two broad aspects in each transmission slot, viz., execution of the ρ^{RAND} policy in Algorithm 3, based on the current estimate of the number of users \hat{U} , and updating of the estimate \hat{U} based on the number of collisions experienced by the user.

The updating is based on the idea that if there is underestimation of U at all the users ($\hat{U}_j < U$ at all the users j), collisions necessarily build up and the collision count serves as a criterion for incrementing \hat{U} . This is because after a long learning period, the users learn the true ranks of the channels, and target the same set of channels. However, when there is

under-estimation, the number of users exceeds the number of channels targeted by the users. Hence, collisions among the users accumulate, and can be used as a test for incrementing \hat{U} .

Denote the collision count used by the ρ^{EST} policy as

$$\Phi_{k,j}(m) := \sum_{a=1}^m \sum_{b=1}^k \zeta_j(\sigma(b; \mathbf{g}_j(m)); a). \quad (20)$$

which is the total number of collisions experienced by user j so far (till the m^{th} transmission slot) in the top \hat{U}_j -channels, where the ranks of the channels are estimated using the g -statistics. The collision count is tested against a threshold $\xi(n; \hat{U}_j)$, which is a function of the horizon length⁷ and current estimate \hat{U}_j . When the threshold is exceeded, \hat{U}_j is incremented, and the collision samples collected so far are discarded (by setting them to zero) (line 6 in Algorithm 4). The choice of the threshold for incrementing \hat{U}_j is critical; if it is too small it can result in over-estimation of the number of users. On the other hand, if it is too large, it can result in slow learning and large regret. Threshold selection is studied in detail in the subsequent section.

B. Regret Bounds under ρ^{EST}

We analyze regret bounds under the ρ^{EST} policy, where the regret is defined in (3). Let the maximum threshold function for the number of consecutive collisions under the ρ^{EST} policy be denoted by

$$\xi^*(n; U) := \max_{k=1, \dots, U} \xi(n; k). \quad (21)$$

We prove that the ρ^{EST} policy has $O(\xi^*(n; U))$ regret when $\xi^*(n; U) = \omega(\log n)$, and where n is the number of transmission slots.

The proof for the regret bound under the ρ^{EST} policy consists of two main parts: we prove bounds on regret conditioned on the event that none of the users over-estimate U . Second, we show that the probability of over-estimation at any of the users goes to zero asymptotically in the horizon length. Taken together, we obtain the regret bound for the ρ^{EST} policy.

Note that in order to have small regret, it is crucial that none of the users over-estimate U . This is because when there is over-estimation, there is a finite probability of selecting the U -worst channels even upon learning the true ranks of the channels. Note that regret is incurred whenever a U -worst channel is selected since under perfect knowledge this channel would not be selected. Hence, under over-estimation, the regret grows linearly in the number of transmissions.

In a nutshell, under the ρ^{EST} policy, the decision to increment the estimate \hat{U} reduces to a hypothesis-testing problem with hypotheses \mathcal{H}_0 : number of users is less than or equal to the current estimate and \mathcal{H}_1 : number of users is greater than the current estimate. In order to have a sub-linear regret, the false-alarm probability (deciding \mathcal{H}_1 under \mathcal{H}_0) needs to decay asymptotically. This is ensured by selecting appropriate

thresholds $\xi(n)$ to test against the collision counts obtained through feedback.

Conditional Regret: We now give the result for the first part. Define the “good event” $\mathcal{C}(n; U)$ that none of the users over-estimates U under ρ^{EST} as

$$\mathcal{C}(n; U) := \left\{ \bigcap_{j=1}^U \hat{U}_j^{\text{EST}}(n) \leq U \right\}. \quad (22)$$

The regret conditioned on $\mathcal{C}(n; U)$, denoted by $R(n; \mu, U, \rho^{\text{EST}}) | \mathcal{C}(n; U)$, is given by

$$n \sum_{k=1}^U \mu(k^*) - \sum_{i=1}^C \sum_{j=1}^U \mu(i) \mathbb{E}[V_{i,j}(n) | \mathcal{C}(n; U)],$$

where $V_{i,j}(n)$ is the number of times that user j is the sole user of channel i . Similarly, we have conditional expectations of $\mathbb{E}[T_{i,j}(n) | \mathcal{C}(n; U)]$ and of the number of collisions in U -best channels, given by $\mathbb{E}[M(n) | \mathcal{C}(n; U)]$. We now show that the regret conditioned on $\mathcal{C}(n; U)$ is $O(\max(\xi^*(n; U), \log n))$.

Lemma 4: (Conditional Regret): When all the U secondary users implement the ρ^{EST} policy, we have for all $i \in U$ -worst channel and each user $j = 1, \dots, U$,

$$\mathbb{E}[T_{i,j}(n) | \mathcal{C}(n)] \leq \sum_{k=1}^U \left[\frac{8 \log n}{\Delta(i, k^*)^2} + 1 + \frac{\pi^2}{3} \right]. \quad (23)$$

The conditional expectation on number of collisions $M(n)$ in the U -best channel satisfies

$$\mathbb{E}[M(n) | \mathcal{C}(n; U)] \leq U \sum_{k=1}^U \xi(n; k) \leq U^2 \xi^*(n; U). \quad (24)$$

From (15), we have $R(n) | \mathcal{C}(n; U)$ is $O(\max(\xi^*(n; U), \log n))$ for any $n \in \mathbb{N}$.

Proof: See Appendix F. \square

Probability of Over-estimation: We now prove that none of the users over-estimates⁸ U under the ρ^{EST} policy, i.e., the probability of the event $\mathcal{C}(n; U)$ in (22) approaches one as $n \rightarrow \infty$, when the thresholds $\xi(n; \hat{U})$ for testing against the collision count are chosen appropriately (see line 6 in Algorithm 4). Trivially, we can set $\xi(n; 1) = 1$ since a single collision is enough to indicate that there is more than one user. For any other $k > 1$, we choose function ξ satisfying

$$\xi(n; k) = \omega(\log n), \quad \forall k > 1. \quad (25)$$

We prove that the above condition ensures that over-estimation does not occur.

Recall that $T'(n; \rho^{\text{EST}})$ is the number of slots where any one of the top U -estimated ranks of the channels at some user is wrong under the ρ^{EST} policy. We show that $\mathbb{E}[T'(n)]$ is $O(\log n)$.

Lemma 5 (Time spent with wrong estimates): The expected number of slots where any of the top U -estimated

⁷In this section, we assume that the users are aware of the horizon length n for transmission. Note that this is not a limitation and can be extended to case of unknown horizon length as follows: implement the algorithm by fixing horizon lengths to $n_0, 2n_0, 4n_0 \dots$ for a fixed $n_0 \in \mathbb{N}$ and discarding estimates from previous stages.

⁸Note that the ρ^{EST} policy automatically ensures that all the users do not under-estimate U , since it increments \hat{U} based on collision estimate. This implies that the probability of the event that all the users under-estimate U goes to zero asymptotically.

ranks of the channels at any user is wrong under the ρ^{EST} policy satisfies

$$\mathbb{E}[T'(n)] \leq U \sum_{a=1}^U \sum_{b=a+1}^C \left[\frac{8 \log n}{\Delta(a^*, b^*)^2} + 1 + \frac{\pi^2}{3} \right]. \quad (26)$$

Proof: The proof is on the lines of Lemma 3 \square

Recall the definition of $\Upsilon(U, U)$ in the previous section, as the maximum time to absorption starting from any initial distribution of the finite-state Markov chain, where the states correspond to different user configurations and the absorbing state corresponds to the collision-free configuration. We now generalize the definition to $\Upsilon(U, k)$, as the time to absorption in a new Markov chain, where the state space is the set of configurations of U users in k channels, and the transition probabilities are defined on similar lines. Note that $\Upsilon(U, k)$ is almost-surely finite when $k \geq U$ and ∞ otherwise (since there is no absorbing state in the latter case).

We now bound the maximum value of the collision count $\Phi_{k,j}(m)$ under the ρ^{EST} policy in (20) using $T'(m)$, the total time spent with wrong channel estimates, and $\Upsilon(U, k)$, the time to absorption in the Markov chain. Let \leq^{st} denote the stochastic order for two random variables [25].

Proposition 2: The maximum collision count in (20) over all users under the ρ^{EST} policy satisfies

$$\max_{j=1, \dots, U} \Phi_{k,j}(m) \leq^{st} (T'(m) + 1) \Upsilon(U, k), \quad \forall m \in \mathbb{N}. \quad (27)$$

Proof: The proof is on the lines of Theorem 3. See Appendix G. \square

We now prove that the probability of over-estimation goes to zero asymptotically.

Lemma 6 (No Over-estimation Under ρ^{EST}): For threshold function ξ satisfying (25), the event $\mathcal{C}(n; U)$ in (22) satisfies

$$\lim_{n \rightarrow \infty} \mathbb{P}[\mathcal{C}(n; U)] = 1, \quad (28)$$

and hence, none of the users over-estimates U under the ρ^{EST} policy.

Proof: See Appendix H. \square

We now give the main result of this section that ρ^{EST} has slightly more than logarithmic regret asymptotically and this depends on the threshold function $\xi^*(n; U)$ in (21).

Theorem 5 (Asymptotic Regret Under ρ^{EST}): With threshold function ξ satisfying conditions in (25), the policy $\rho^{\text{EST}}(n, C, \mathbf{g}_j(m), \xi)$ in Algorithm 4 satisfies

$$\limsup_{n \rightarrow \infty} \frac{R(n; \boldsymbol{\mu}, U, \rho^{\text{EST}})}{\xi^*(n; U)} < \infty. \quad (29)$$

Proof: From Lemma 4 and Lemma 6. \square

Hence, the regret under the proposed ρ^{EST} policy is $O(\xi^*(n; U))$ under fully decentralized setting without the knowledge of number of users when $\xi^*(n; U) = \omega(\log n)$. Hence, $O(f(n) \log n)$ regret is achievable for all functions $f(n) \rightarrow \infty$ as $n \rightarrow \infty$. The question of whether logarithmic regret is possible under unknown number of users is of interest.

Note the difference between the ρ^{EST} policy in Algorithm 4 under unknown number of users with the ρ^{RAND} policy with known number of users in Algorithm 3. The regret under ρ^{EST}

is $O(f(n) \log n)$ for any function $f(n) = \omega(1)$, while it is $O(\log n)$ under the ρ^{RAND} policy. Hence, we are able to quantify the degradation of performance when the number of users is unknown.

VI. LOWER BOUND & EFFECT OF NUMBER OF USERS

A. Lower Bound For Distributed Learning & access

We have so far designed distributed learning and access policies with provable bounds on regret. We now discuss the relative performance of these policies, compared to the optimal learning and access policies. This is accomplished by noting a lower bound on regret for any *uniformly-good* policy, first derived in [4] for a general class of uniformly-good time-division policies. We restate the result below.

Theorem 6 (Lower Bound [4]): For any uniformly good distributed learning and access policy ρ , the sum regret in (2) satisfies

$$\liminf_{n \rightarrow \infty} \frac{R(n; \boldsymbol{\mu}, U, \rho)}{\log n} \geq \sum_{i \in U\text{-worst}} \sum_{j=1}^U \frac{\Delta(U^*, i)}{D(\mu_i, \mu_{j^*})}. \quad (30)$$

The lower bound derived in [9] for centralized learning and access holds for distributed learning and access considered here. But a better lower bound is obtained above by considering the distributed nature of learning. The lower bound for distributed policies is worse than the bound for the centralized policies in (11). This is because each user independently learns the channel availabilities $\boldsymbol{\mu}$ in a distributed policy, whereas sensing decisions from all the users are used for learning in a centralized policy.

Our distributed learning and access policy ρ^{RAND} matches the lower bound on regret in (15) in the order $(\log n)$ but the scaling factors are different. It is not clear if the regret lower bound in (30) can be achieved by any policy under no explicit information exchange and is a topic for future investigation.

B. Behavior with Number of Users

We have so far analyzed the sum regret under our policies under a fixed number of users U . We now analyze the behavior of regret growth as U increases while keeping the number of channels $C > U$ fixed.

Theorem 7 (Varying Number of Users): When the number of channels C is fixed and the number of users $U < C$ is varied, the sum regret under centralized learning and access ρ^{CENT} in (12) decreases as U increases while the upper bounds on the sum regret under ρ^{RAND} in (15) monotonically increases with U .

Proof: The proof involves analysis of (12) and (15). To prove that the sum regret under centralized learning and access in (12) decreases with the number of users U , it suffices to show that for $i \in U\text{-worst}$ channel,

$$\frac{\Delta(U^*, i)}{D(\mu_i, \mu_{U^*})}$$

decreases as U increases. Note that $\mu(U^*)$ and $D(\mu_i, \mu_{U^*})$ decrease as U increases. Hence, it suffices to show that

$$\frac{\mu(U^*)}{D(\mu_i, \mu_{U^*})}$$

decreases with U . This is true since its derivative with respect to U is negative.

For the upper bound on regret under ρ^{RAND} in (15), when U is increased, the number of U -worst channels decreases and hence, the first term in (15) decreases. However, the second term consisting of collisions $M(n)$ increases to a far greater extent. \square

Note that the above results are for the upper bound on regret under the ρ^{RAND} policy and not the regret itself. Simulations in Section VII reveal that the actual regret also increases with U . Under the centralized scheme ρ^{CENT} , as U increases, the number of U -worst channels decreases. Hence, the regret decreases, since there are less number of possibilities of making bad decisions. However, for distributed schemes although this effect exists, it is far outweighed by the increase in regret due to the increase in collisions among the U users.

In contrast, the distributed lower bound in (30) displays anomalous behavior with U since it fails to account for collisions among the users. Here, as U increases there are two competing effects: a decrease in regret due to decrease in the number of U -worst channels and an increase in regret due to increase in the number of users visiting these U -worst channels.

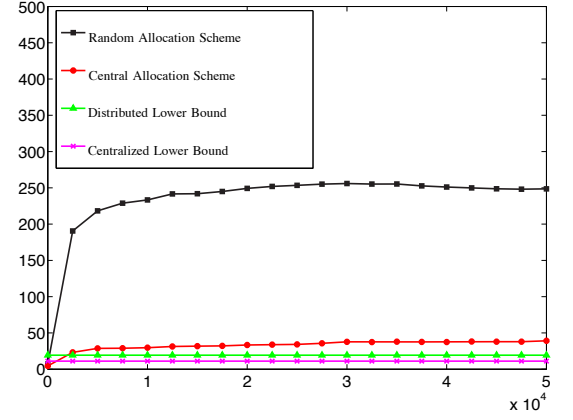
VII. NUMERICAL RESULTS

We present simulations for the algorithms developed in the paper, varying the number of users and channels to verify the performance of the algorithms detailed earlier. We consider $C=9$ channels (or a subset of them when the number of channels is varying) with probabilities of availability characterized by Bernoulli distributions with evenly spaced parameters ranging from 0.1 to 0.9.

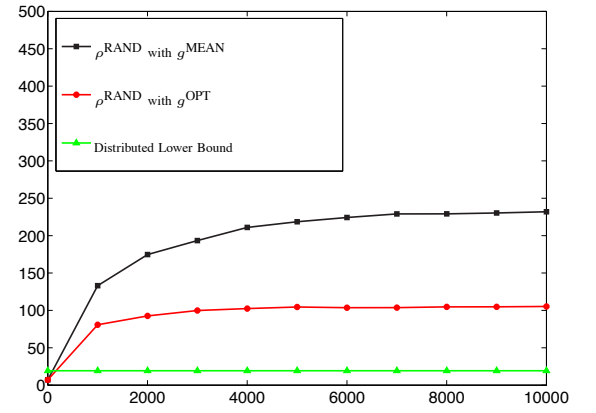
Comparison of Different Schemes: Fig. 2a compares the regret under the centralized and random allocation schemes in a scenario with $U = 4$ cognitive users vying for access to the $C = 9$ channels. The theoretical lower bound for the regret in the centralized case from Theorem 2 and the distributed case from Theorem 6 are also plotted. The upper bounds on the random allocation scheme from Theorem 4 is not plotted here, since the bounds are loose especially as the number of users U increases. Finding tight upper bounds is a subject of future study.

As expected, centralized allocation has the least regret. Another important observation is the gap between the lower bounds on the regret and the actual regret in both the distributed and the centralized cases. In the centralized scenario, this is simply due to using the g^{MEAN} statistic in (34) instead of the optimal g^{OPT} statistic in (5). However, in the distributed case, there is an additional gap since we do not account for collisions among the users. Hence, the schemes under consideration are $O(\log n)$ and achieve order optimality although they are not optimal in the scaling constant.

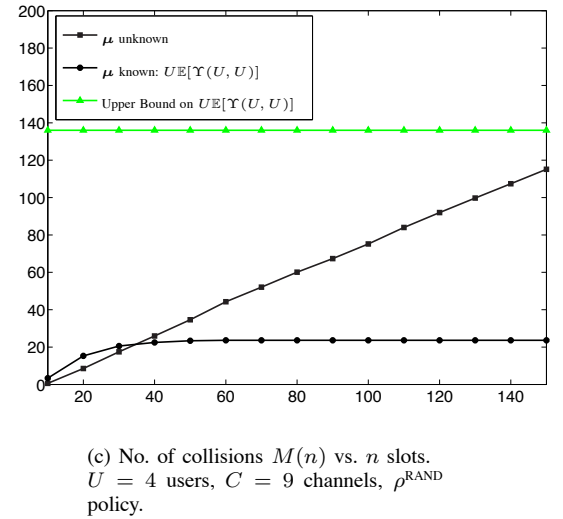
Performance with Varying U and C : Fig. 3a explores the impact of increasing the number of secondary users U on the regret experienced by the different policies with the number of channels C fixed. With increasing U , the regret decreases for the centralized schemes and increases for the distributed schemes, as predicted in Theorem 7. The monotonic increase



(a) Normalized regret $\frac{R(n)}{\log n}$ vs. n slots.
 $U = 4$ users, $C = 9$ channels.



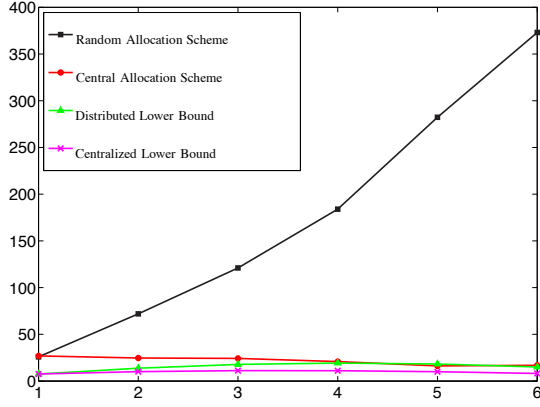
(b) Normalized regret $\frac{R(n)}{\log n}$ vs. n slots.
 $U = 4$ users, $C = 9$ channels.



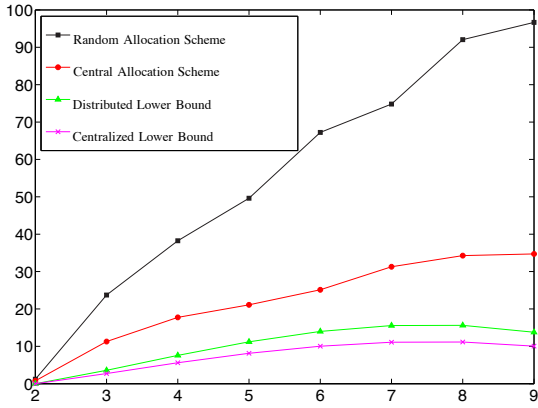
(c) No. of collisions $M(n)$ vs. n slots.
 $U = 4$ users, $C = 9$ channels, ρ^{RAND} policy.

Fig. 2. Simulation Results. Probability of Availability $\mu = [0.1, 0.2, \dots, 0.9]$.

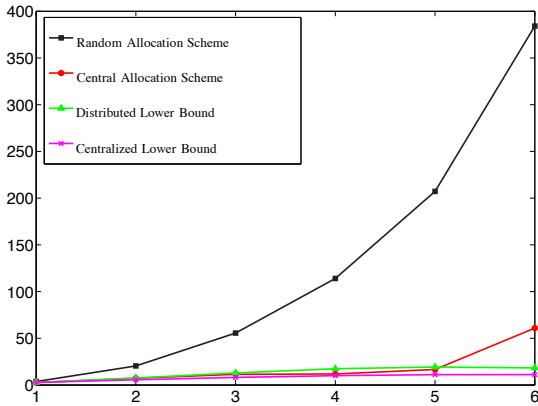
of regret under random allocation ρ^{RAND} is a result of the increase in the collisions as U increases. On the other hand, the monotonic decreasing behavior in the centralized case is because as the number of users increases, the number of U -



(a) Normalized regret $\frac{R(n)}{\log n}$ vs. U users.
 $C = 9$ channels, $n = 2500$ slots.



(b) Normalized regret $\frac{R(n)}{\log n}$ vs. C channels.
 $U = 2$ users, $n = 2500$ slots.



(c) Normalized regret $\frac{R(n)}{\log n}$ vs. U users.
 User-channel ratio $U/C = 0.5$, $n = 2500$ slots.

Fig. 3. Simulation Results. Probability of Availability $\mu = [0.1, 0.2, \dots, 0.9]$.

worst channels decreases resulting in lower regret. Also, the lower bound for the distributed case in (30) initially increases and then decreases with U . This is because as U increases there are two competing effects: decrease in regret due to

decrease in number of U -worst channels and increase in regret due to increase in number of users visiting these U -worst channels.

Fig. 3b evaluates the performance of the different algorithms as the number of channels C is varied while fixing the number of users U . The probability of availability of each additional channel is set higher than those already present. Here, the regret monotonically increases with C in all cases. When the number of channels increases along with the quality of the channels, the regret increases as a result of an increase in the number of U -worst channels as well as the increasing gap in quality between the U -best and U -worst channels.

Also, the situation where the ratio U/C is fixed to be 0.5 and both the number of users and channels along with their quality increase is considered in Fig. 3c and we find that the regret grows in this case as well. Once again, this is in agreement with theory since the number of U -worst channels increases as U and C increase while keeping U/C fixed.

Collisions and Learning: Fig. 2c verifies the logarithmic nature of the number of collisions under the random allocation scheme ρ^{RAND} . Additionally, we also plot the number of collisions under ρ^{RAND} in the ideal scenario when the channel availability statistics μ are known to see the effect of learning on the number of collisions. The low value of the number of collisions obtained under known channel parameters in the simulations is in agreement with theoretical predictions, analyzed as $UE[\Upsilon(U, U)]$ in Lemma 2. As the number of slots n increases, the gap between the number of collisions under the known and unknown parameters increases since the former converges to a finite constant while the latter grows as $O(\log n)$. The logarithmic behavior of the cumulative number of collisions can be inferred from Fig. 2a. However, the curve in Fig. 2c for the unknown parameter case appears linear in n due to the small value of n .

Difference between g^{OPT} and g^{MEAN} : Since the statistic g^{MEAN} used in the schemes in this paper differs from the optimal statistic g^{OPT} in (5), a simulation is done to compare the performance of the schemes under both the statistics. As expected, in Fig. 2b, the optimal scheme has better performance. However, the use of g^{MEAN} enables us to provide finite-time bounds, as described earlier.

Fairness: One of the important features of ρ^{RAND} is that it does not favor any one user over another. Each user has an equal chance of settling down in any one of the U -best channels. Fig. 4 evaluates the fairness characteristics of ρ^{RAND} . The simulation assumes $U = 4$ cognitive users vying for access to $C = 9$ channels. The graph depicts which user asymptotically gets the best channel over 1000 runs of the random allocation scheme. As can be seen, each user has approximately the same frequency of being allotted the best channel indicating that the random allocation scheme is indeed fair.

VIII. CONCLUSION

In this paper, we proposed novel policies for distributed learning of channel availability statistics and channel access of multiple secondary users in a cognitive network. The first

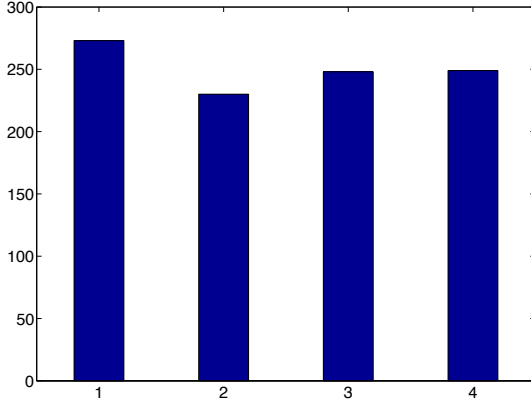


Fig. 4. Simulation Results. Probability of Availability $\mu = [0.1, 0.2, \dots, 0.9]$. No. of slots where user has best channel vs. user. $U = 4$, $C = 9$, $n = 2500$ slots, 1000 runs, ρ^{RAND} .

policy assumed that the number of secondary users in the network is known, while the second policy removed this requirement. We provide provable guarantees for our policies in terms of sum regret. By noting the lower bound on regret for any uniformly-good learning and access policy, we find that our first policy achieves order-optimal regret while our second policy is also nearly order optimal. Our analysis in this paper provides insights on incorporating learning and distributed medium access control in a practical cognitive network.

The results of this paper open up an interesting array of problems for future investigation. Simulations suggest that our lower and upper bounds are not tight in terms of the scaling constant and that better bounds are needed. Our assumptions of an i.i.d. model for primary user transmissions and perfect sensing at the secondary users need to be relaxed. Our policy allows for an unknown but fixed number of secondary users, and it is of interest to incorporate users dynamically entering and leaving the system. Moreover, our model ignores dynamic traffic at the secondary nodes and extension to a queueing-theoretic formulation is desirable. We consider the worst-case scenario that there is no information exchange among the secondary users. Extension to the case with limited information exchange is of interest. The proposed schemes are designed to be simple and tractable for mathematical analysis. It is desirable to obtain more robust schemes with additional design considerations for real-world deployment.

Acknowledgement

The authors thank the guest editors and anonymous reviewers for valuable comments that vastly improved this paper, and for pointing out an error in Proposition 1. The authors thank Keqin Liu and Prof. Qing Zhao for extensive discussions, feedback on the proofs in an earlier version of the manuscript, and for sharing their simulation code. The authors also thank Prof. Lang Tong and Prof. Robert Kleinberg at Cornell, Prof. Bhaskar Krishnamachari at USC and Prof. John Tsitsiklis and Dr. Ishai Menache at MIT for helpful comments.

APPENDIX

A. Proof of Theorem 2

The result in (13) involves extending the results of [11, Thm. 1]. Define $T_i(n) := \sum_{j=1}^U T_{i,j}(n)$ as the number of times a channel i is sensed in n rounds for all users. We will show that

$$\mathbb{E}[T_i(n)] \leq \sum_{k \in U\text{-best}} \left[\frac{8 \log n}{\Delta(k^*, i)^2} + 1 + \frac{\pi^2}{3} \right], \quad \forall i \in U\text{-worst}. \quad (31)$$

We have

$$\begin{aligned} \mathbb{P}[\text{Tx. in } i \text{ in } n^{\text{th}} \text{ slot}] &= \mathbb{P}[g(U^*; n) \leq g(i; n)], \\ &= \mathbb{P}[\mathcal{A}(i; n) \cap (g(U^*; n) \leq g(i; n))] \\ &\quad + \mathbb{P}[\mathcal{A}^c(i; n) \cap (g(U^*; n) \leq g(i; n))], \end{aligned}$$

where

$$\mathcal{A}(i; n) := \bigcup_{k \in U\text{-best}} (g(k; n) \leq g(i; n))$$

is the event that at least one of the U -best channels has g -statistic less than i . Hence, from union bound we have

$$\mathbb{P}[\mathcal{A}(i; n)] \leq \sum_{k \in U\text{-best}} \mathbb{P}[g(k; n) \leq g(i; n)].$$

We have for $C > U$,

$$\mathbb{P}[\mathcal{A}^c(i; n) \cap (g(U^*; n) \leq g(i; n))] = 0,$$

Hence,

$$\mathbb{P}[\text{Tx. in } i \text{ in } n^{\text{th}} \text{ round}] \leq \sum_{k \in U\text{-best}} \mathbb{P}[g(k; n) \leq g(i; n)].$$

On the lines of [11, Thm. 1], we have $\forall k, i$: k is U -best, i is U -worst

$$\sum_{l=1}^n \mathbb{I}[g(k; l) \leq g(i; l)] \leq \frac{8 \log n}{\Delta(k^*, i)^2} + 1 + \frac{\pi^2}{3}.$$

Hence, we have (31). For the bound on regret, we can break R in (2) into two terms

$$\begin{aligned} R(n; \mu, U, \rho^{\text{CENT}}) &= \sum_{i \in U\text{-worst}} \left[\frac{1}{U} \sum_{l=1}^U \Delta(l^*, i) \right] \mathbb{E}[T_i(n)] \\ &\quad + \sum_{i \in U\text{-best}} \left[\frac{1}{U} \sum_{l=1}^U \Delta(l^*, i) \right] \mathbb{E}[T_i(n)]. \end{aligned}$$

For the second term, we have

$$\begin{aligned} &\sum_{i \in U\text{-best}} \left[\frac{1}{U} \sum_{l=1}^U \Delta(l^*, i) \right] \mathbb{E}[T_i(n)] \\ &\leq \mathbb{E}[T^*(n)] \sum_{i \in U\text{-best}} \left[\frac{1}{U} \sum_{l=1}^U \Delta(l^*, i) \right] = 0, \end{aligned}$$

where $T^*(n) := \max_{i \in U\text{-best}} T_i(n)$. Hence, we have the bound. \square

B. Proof of Proposition 1

For convenience, let $T_i(n) := \sum_{j=1}^U T_{i,j}(n)$, $V_i(n) := \sum_{j=1}^U V_{i,j}(n)$. Note that $\sum_{i=1}^C T_i(n) = nU$, since each user selects one channel for sensing in each slot and there are U users. From (3),

$$\begin{aligned} R(n) &= n \sum_{i=1}^U \mu(i^*) - \sum_{i=1}^C \mu(i) \mathbb{E}[V_i(n)], \\ &\leq \sum_{i \in U\text{-best}} \mu(i)(n - \mathbb{E}[V_i(n)]) \\ &\leq \mu(1^*)(nU - \sum_{i \in U\text{-best}} \mathbb{E}[V_i(n)]) \end{aligned} \quad (32)$$

$$= \mu(1^*)(\mathbb{E}[M(n)] + \sum_{i \in U\text{-worst}} \mathbb{E}[T_i(n)]), \quad (33)$$

where Eqn.(32) uses the fact that $V_i(n) \leq n$ since total number of sole occupancies in n slots of channel i is at most n , and Eqn.(33) uses the fact that $M(n) = \sum_{i \in U\text{-best}} (T_i(n) - V_i(n))$.

For the lower bound, since each user selects one channel for sensing in each slot, $\sum_{i=1}^C \sum_{j=1}^U T_{i,j}(n) = nU$. Now $T_{i,j}(n) \geq V_{i,j}(n)$.

$$\begin{aligned} R(n; \mu, U, \rho) &\geq \frac{1}{U} \left[\sum_{k=1}^U \sum_{j=1}^U \sum_{i=1}^C \Delta(U^*, i) \mathbb{E}[T_{i,j}(n)] \right], \\ &\geq \sum_{j=1}^U \sum_{i \in U\text{-worst}} \Delta(U^*, i) \mathbb{E}[T_{i,j}(n)]. \end{aligned}$$

□

C. Proof of Lemma 2

Although, we could directly compute the time to absorption of the Markov chain, we give a simple bound $\mathbb{E}[\Upsilon(U, U)]$ by considering an i.i.d process over the same state space. We term this process as a genie-aided modification of random allocation scheme, since this can be realized as follows: in each slot, a genie checks if any collision occurred, in which case, a new random variable is drawn from $\text{Unif}(U)$ by all users. This is in contrast to the original random allocation scheme where a new random variable is drawn only when the particular user experiences a collision. Note that for $U = 2$ users, the two scenarios coincide.

For the genie-aided scheme, the expected number of slots to hit orthogonality is just the mean of the geometric distribution

$$\sum_{k=1}^{\infty} k(1-p)^k p = \frac{1-p}{p} < \infty, \quad (34)$$

where p is the probability of having an orthogonal configuration in a slot. This is in fact the reciprocal of the number of compositions of U [24, Thm. 5.1], given by

$$p = \binom{2U-1}{U}^{-1}. \quad (35)$$

The above expression is nothing but the reciprocal of number of ways U identical balls (users) can be placed in U different bins (channels): there are $2U - 1$ possible positions to form U partitions of the balls.

Now for the random allocation scheme without the genie, any user not experiencing collision does *not* draw a new variable from $\text{Unif}(U)$. Hence, the number of possible configurations in any slot is lower than under genie-aided scheme. Since there is only one configuration satisfying orthogonality⁹, the probability of orthogonality increases in the absence of the genie and is at least (35). Hence, the number of slots to reach orthogonality without the genie is at most (34). Since in any slot, at most U collisions occur, (17) holds. □

D. Proof of Lemma 3

Let $c_{n,m} := \sqrt{\frac{2 \log n}{m}}$.

Case 1: Consider $U = C = 2$ first. Let

$$\mathcal{A}(t, l) := \{g_j^{\text{MEAN}}(1^*; t-1) \leq g_j^{\text{MEAN}}(2^*; t-1), T'_j(t-1) \geq l\}.$$

On lines of [11, Thm. 1],

$$\begin{aligned} T'(n) &\leq l + \sum_{t=2}^n I[\mathcal{A}(t, l)], \\ &\leq l + \sum_{t=1}^{\infty} \sum_{m+h=l}^t I(\bar{X}_{1^*,j}(h) + c_{t,h} \leq \bar{X}_{2^*,j}(m) + c_{t,m}). \end{aligned}$$

The above event is implied by

$$\bar{X}_{1^*,j}(h) + c_{t,h} \leq \bar{X}_{2^*,j}(h) + c_{t,h+m}$$

since $c_{t,m} > c_{t,h+m}$.

The above event implies at least one of the following events and hence, we can use the union bound.

$$\begin{aligned} \bar{X}_{1^*,j}(h) &\leq \mu_{1^*} - c_{t,h}, \\ \bar{X}_{2^*,j}(m) &\geq \mu_{2^*} + c_{t,h+m}, \\ \mu_{1^*} &< \mu_{2^*} + 2c_{t,h+m}. \end{aligned}$$

From the Chernoff-Hoeffding bound,

$$\begin{aligned} \mathbb{P}[\bar{X}_{1^*,j}(t) \leq \mu_{1^*} - c_{t,h}] &\leq t^{-4}, \\ \mathbb{P}[\bar{X}_{2^*,j}(t) \geq \mu_{2^*} + c_{t,h+m}] &\leq t^{-4}, \end{aligned}$$

and the event that $\mu_{1^*} < \mu_{2^*} + 2c_{t,h+m}$ implies that

$$h + m < \left\lceil \frac{8 \log t}{\Delta_{1^*,2^*}^2} \right\rceil.$$

Since

$$\sum_{t=1}^{\infty} \sum_{m=1}^t \sum_{h=1}^t 2t^{-4} = \frac{\pi^2}{3},$$

$$\mathbb{E}[T'(n; U = C = 2)] \leq \frac{8 \log n}{\Delta_{1^*,2^*}^2} + 1 + \frac{\pi^2}{3}.$$

Case 2: For $\min(U, C) > 2$, we have

$$T'(n) \leq U \sum_{a=1}^U \sum_{b=a+1}^C \sum_{m=1}^n I(g_j^{\text{MEAN}}(a^*; m) < g_j^{\text{MEAN}}(b^*; m)),$$

where a^* and b^* represent channels with a^{th} and b^{th} highest availabilities. On lines of the result for $U = C = 2$, we can show that

$$\sum_{m=1}^n \mathbb{E} I[g_j^{\text{MEAN}}(a^*; m) < g_j^{\text{MEAN}}(b^*; m)] \leq \frac{8 \log n}{\Delta_{a^*,b^*}^2} + 1 + \frac{\pi^2}{3}.$$

Hence, (18) holds. □

⁹since all users are identical for this analysis.

E. Proof of Theorem 3

Define the good event as all users having correct top U -order of the g -statistics, given by

$$\mathcal{G}(n) := \bigcap_{j=1}^U \{\text{Top-}U \text{ entries of } \mathbf{g}_j(n) \text{ are same as in } \boldsymbol{\mu}\}.$$

The number of slots under the bad event is

$$\sum_{m=1}^n I[\mathcal{G}^c(m)] = T'(n),$$

by definition of $T'(n)$. In each slot, either a good or a bad event occurs. Let γ be the total number of collisions in U -best channels between two bad events, i.e., under a run of good events. In this case, all the users have the correct top U -ranks of channels and hence,

$$\mathbb{E}[\gamma | \mathcal{G}(n)] \leq U \mathbb{E}[\Upsilon(U, U)] < \infty,$$

where $\mathbb{E}[\Upsilon(U, U)]$ is given by (17). Hence, each transition from the bad to the good state results in at most $U \mathbb{E}[\Upsilon(U, U)]$ expected number of collisions in the U -best channels. The expected number of collisions under the bad event is at most $U \mathbb{E}[T'(n)]$. Hence, (19) holds. \square

F. Proof of Lemma 4

Under $\mathcal{C}(n; U)$, a U -worst channel is sensed only if it is mistaken to be a U -best channel. Hence, on lines of Lemma 1,

$$\mathbb{E}[T_{i,j}(n) | \mathcal{C}(n; U)] = O(\log n), \quad \forall i \in U\text{-worst}, j = 1, \dots, U.$$

For the number of collisions $M(n)$ in the U -best channels, there can be at most $U \sum_{k=1}^a \xi(n; k)$ collisions in the U -best channels where $a := \max_{j=1, \dots, U} \hat{U}_j$ is the maximum estimate of number of users. Conditioned on $\mathcal{C}(n; U)$, $a \leq U$, and hence, we have (24). \square

G. Proof of Proposition 2

Define the good event as all users having correct top U -order, given by

$$\mathcal{G}(n) := \bigcap_{j=1}^U \{\text{Top-}U \text{ entries of } \mathbf{g}_j(n) \text{ are same as in } \boldsymbol{\mu}\}.$$

The number of slots under the bad event is

$$\sum_{m=1}^n I[\mathcal{G}^c(m)] = T'(n),$$

by definition of $T'(n)$. In each slot, either a good or a bad event occurs. Let γ be the total number of collisions in k -best channels between two bad events, i.e., under a run of good events. In this case, all the users have the correct top U -ranks of channels and hence,

$$\gamma | \mathcal{G}(n) \stackrel{st}{\leq} U \Upsilon(U, k),$$

The number of collisions under the bad event is at most $T'(n)$. Hence, (27) holds. \square

H. Proof of Lemma 6

We are interested in

$$\begin{aligned} \mathbb{P}[\mathcal{C}^c(n); U] &= \mathbb{P}[\bigcup_{j=1}^U \hat{U}_j^{\text{EST}}(n) > U], \\ &= \mathbb{P}[\bigcup_{m=1}^n \bigcup_{j=1}^U \{\Phi_{U,j}(m) > \xi(n; U)\}], \\ &= \mathbb{P}[\max_{j=1, \dots, U} \Phi_{U,j}(n) > \xi(n; U)], \end{aligned}$$

where Φ is given by (20). For $U = 1$, we have $\mathbb{P}[\mathcal{C}^c(n); U] = 0$ since no collisions occur.

Using (27) in Proposition 2,

$$\begin{aligned} &\mathbb{P}[\max_{j=1}^k \Phi_{k,j}(n) > \xi(n; k)] \\ &\leq \mathbb{P}[k \Upsilon(U, k)(T'(n) + 1) > \xi(n; k)] \\ &\leq \mathbb{P}[k(T'(n) + 1) > \frac{\xi(n; k)}{\alpha_n}] + \mathbb{P}[\Upsilon(U, k) > \alpha_n] \\ &\leq \frac{k \alpha_n (\mathbb{E}[T'(n)] + 1)}{\xi(n; k)} + \mathbb{P}[\Upsilon(U, k) > \alpha_n], \end{aligned} \quad (36)$$

using Markov inequality. By choosing $\alpha_n = \omega(1)$, the second term in (36), viz., $\mathbb{P}[\Upsilon(U, k) > \alpha_n] \rightarrow 0$ as $n \rightarrow \infty$, for $k \geq U$. For the first term, from (26) in Lemma 5, $\mathbb{E}[T'(n)] = O(\log n)$. Hence, by choosing $\alpha_n = o(\xi^*(n; k)/\log n)$, the first term decays to zero. Since $\xi^*(n; U) = \omega(\log n)$, we can choose α_n satisfying both the conditions. By letting $k = U$ in (36), we have $\mathbb{P}[\mathcal{C}^c(n); U] \rightarrow 0$ as $n \rightarrow \infty$, and (28) holds. \square

REFERENCES

- [1] A. Anandkumar, N. Michael, and A. Tang, "Opportunistic Spectrum Access with Multiple Users: Learning under Competition," in *Proc. IEEE INFOCOM*, San Deigo, USA, March 2010.
- [2] Q. Zhao and B. Sadler, "A Survey of Dynamic Spectrum Access," *IEEE Signal Proc. Mag.*, vol. 24, no. 3, pp. 79–89, 2007.
- [3] L. Kaelbling, M. Littman, and A. Moore, "Reinforcement learning: A Survey," *J. Artificial Intelligence research*, vol. 4, no. 237–285, pp. 102–138, 1996.
- [4] K. Liu and Q. Zhao, "Decentralized Multi-Armed Bandit with Multiple Distributed Players," *submitted to IEEE Trans. Signal Process.*, Oct. 2009.
- [5] A. Konrad, B. Zhao, A. Joseph, and R. Ludwig, "A Markov-based channel model algorithm for wireless networks," *Wireless Networks*, vol. 9, no. 3, pp. 189–199, 2003.
- [6] S. Geirhofer, L. Tong, and B. Sadler, "Cognitive Medium Access: Constraining Interference Based on Experimental Models," *IEEE J. Sel. Areas Commun.*, vol. 26, no. 1, p. 95, 2008.
- [7] V. Anantharam, P. Varaiya, and J. Walrand, "Asymptotically Efficient Allocation Rules for the Multiarmed Bandit Problem with Multiple Plays-Part II: Markovian Rewards," *IEEE Tran. Autom. Control*, vol. 32, no. 11, pp. 977–982, 1987.
- [8] T. Lai and H. Robbins, "Asymptotically efficient adaptive allocation rules," *Advances in Applied Mathematics*, vol. 6, no. 1, pp. 4–22, 1985.
- [9] V. Anantharam, P. Varaiya, and J. Walrand, "Asymptotically Efficient Allocation Rules for the Multiarmed Bandit Problem with Multiple Plays-Part I: IID rewards," *IEEE Tran. Autom. Control*, vol. 32, no. 11, pp. 968–976, 1987.
- [10] R. Agrawal, "Sample Mean Based Index Policies with $O(\log n)$ Regret for the Multi-Armed Bandit Problem," *Advances in Applied Probability*, vol. 27, no. 4, pp. 1054–1078, 1995.
- [11] P. Auer, N. Cesa-Bianchi, and P. Fischer, "Finite-time Analysis of the Multiarmed Bandit Problem," *Machine Learning*, vol. 47, no. 2, pp. 235–256, 2002.
- [12] Q. Zhao, Y. Chen, and A. Swami, "Cognitive MAC Protocols for Dynamic Spectrum Access," in *Cognitive Wireless Communication Networks*. Springer, 2007, pp. 271–301.
- [13] K. Liu and Q. Zhao, "A restless bandit formulation of opportunistic access: Indexability and index policy," *Submitted IEEE Trans. Inf. Theory*, available on Arxiv, 2008.

- [14] H. Liu, B. Krishnamachari, and Q. Zhao, "Cooperation and Learning in multiuser opportunistic spectrum access," in *IEEE Intl. Conf. on Comm. (ICC)*, Beijing, China, May 2008.
- [15] F. Fu and M. van der Schaar, "Learning to compete for resources in wireless stochastic games," *IEEE Trans. Veh. Technol.*, vol. 58, no. 4, pp. 1904–1919, May 2009.
- [16] H. Gang, Z. Qian, and X. Ming, "Contention-Aware Spectrum Sensing and Access Algorithm of Cognitive Network," in *Intl. Conf. on Cognitive Radio Oriented Wireless Networks and Comm.*, Singapore, May 2008.
- [17] H. Liu, L. Huang, B. Krishnamachari, and Q. Zhao, "A Negotiation Game for Multichannel Access in Cognitive Radio Networks," in *Proc. Intl. Conf. on Wireless Internet*, Las Vegas, NV, Nov. 2008.
- [18] H. Li, "Multi-agent Q-Learning of Channel Selection in Multi-user Cognitive Radio Systems: A Two by Two Case," in *IEEE Conf. on System, Man and Cybernetics*, Istanbul, Turkey, 2009.
- [19] M. Maskery, V. Krishnamurthy, and Q. Zhao, "Game Theoretic Learning and Pricing for Dynamic Spectrum Access in Cognitive Radio," in *Cognitive Wireless Comm. Networks*. Springer, 2007.
- [20] R. Kleinberg, G. Piliouras, and E. Tardos, "Multiplicative Updates Outperform Generic No-regret Learning in Congestion Games," in *Proc. ACM Symp. on theory of computing (STOC)*, Bethesda, MD, May-June 2009.
- [21] Y. Gai, B. Krishnamachari, and R. Jain, "Learning Multiuser Channel Allocations in Cognitive Radio Networks: A Combinatorial Multi-Armed Bandit Formulation," in *IEEE Symp. on Dynamic Spectrum Access Networks (DySPAN)*, Singapore, April 2010.
- [22] K. Liu, Q. Zhao, and B. Krishnamachari, "Distributed learning under imperfect sensing in cognitive radio networks," in *Submitted to Proc. IEEE Asilomar Conf. on Signals, Sys., and Comp.*, Monterey, CA, Oct. 2010.
- [23] T. Cover and J. Thomas, *Elements of Information Theory*. John Wiley & Sons, Inc., 1991.
- [24] M. Bona, *A Walk Through Combinatorics: An Introduction to Enumeration and Graph Theory*. World Scientific Pub. Co. Inc., 2006.
- [25] M. Shaked and J. Shanthikumar, *Stochastic Orders*. Springer, 2007.



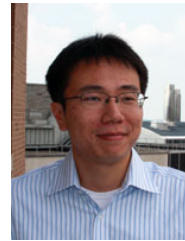
Animashree Anandkumar (S' 02, M' 09) received her B.Tech in Electrical Engineering from the Indian Institute of Technology Madras in 2004 and her Ph.D. in Electrical and Computer Engineering with a minor in Applied Math from Cornell University in 2009. She was a post-doctoral researcher at the Stochastic Systems Group at Massachusetts Institute of Technology between 2009 and 2010. She is currently an assistant professor at the Electrical Engineering and Computer Science Department at University of California, Irvine. She is also a member

of the center for pervasive communications and computing at UCI.

She is the recipient of the 2008 IEEE Signal Processing Society (SPS) Young Author award for her paper co-authored with Lang Tong which appeared in the IEEE Transactions on Signal Processing. She is the recipient of the Fran Allen IBM Ph.D fellowship 2008-09, presented in conjunction with the IBM Ph.D. Fellowship Award. She received the Best Thesis Award 2009 by the ACM Sigmetrics society. Her research interests are in the area of statistical-signal processing, information theory and networking with a focus on distributed inference and learning of graphical models. She serves on the Technical Program Committee of IEEE INFOCOM 2011, ACM MOBIHOC 2011, IEEE ICC 2010, MILCOM 2010 and IEEE PIMRC 2010. She has served as a reviewer for IEEE Transactions on Signal Processing, IEEE Journal on Selected Areas in Communications, IEEE Transactions on Information Theory, IEEE Transactions on Wireless Communications and IEEE Signal Processing Letters.



Nithin Michael (S '06) received the B.S. degree summa cum laude from Drexel University, Philadelphia, PA, in 2008 in electrical engineering. He is currently pursuing the M.S./Ph.D. joint degree program in electrical engineering at Cornell University. Mr. Michael was the recipient of first Honors in ECE and the Highest Academic Achievement Award at Drexel University in 2008. At Cornell University, he has been awarded the Jacobs Fellowship in 2008 and 2010.



Tang was the recipient of the 2006 George B. Dantzig Best Dissertation Award, the 2007 Charles Wilts best dissertation Prize, and a 2009 IBM Faculty Award.

Ao Tang (S' 01 M' 07) received the B.E. in Electronics Engineering from Tsinghua University, Beijing, China, and the Ph.D. in Electrical Engineering with a minor in applied and computational mathematics from the California Institute of Technology, Pasadena, CA, in 1999 and 2006, respectively.

He is an Assistant Professor in the School of Electrical and Computer Engineering at Cornell University, where his current research is on control and optimization of networks including communication networks, power networks and on-chip networks. Dr.

Ananthram Swami (F'08) received the B.Tech. degree from the Indian Institute of Technology (IIT), Bombay; the M.S. degree from Rice University, Houston, TX, and the Ph.D. degree from the University of Southern California (USC), Los Angeles, all in electrical engineering.

He has held positions with Unocal Corporation, USC, CS-3 and Malgudi Systems. He was a Statistical Consultant to the California Lottery, developed HOSAT, a MATLAB-based toolbox for non-Gaussian signal processing, and has held visiting faculty positions at INP, Toulouse, France. He is the ST for Network Science at the U.S. Army Research Laboratory. His work is in the broad areas of signal processing, wireless communications, sensor and mobile ad hoc networks. He is the co-editor of the book *Wireless Sensor Networks: Signal Processing & Communications Perspectives* (New York: Wiley, 2007).

Dr. Swami is a member of the IEEE Signal Processing Society's (SPS) Technical Committee on Sensor Array and Multichannel systems and serves on the Senior Editorial Board of the IEEE Journal on Selected Topics in Signal Processing. He was a tutorial speaker on Networking Cognitive Radios for Dynamic Spectrum Access at IEEE ICC 2010 and co-chair of IEEE SPAWC 2010.

A Survey on Trust Management for Mobile Ad Hoc Networks

Jin-Hee Cho, Ananthram Swami, and Ing-Ray Chen

IEEE Communications Surveys & Tutorials, 13(4), 562-583 (2011)

A Survey on Trust Management for Mobile Ad Hoc Networks

Jin-Hee Cho, *Member, IEEE*, Ananthram Swami, *Fellow, IEEE*, and Ing-Ray Chen, *Member, IEEE*

Abstract—Managing trust in a distributed Mobile Ad Hoc Network (MANET) is challenging when collaboration or cooperation is critical to achieving mission and system goals such as reliability, availability, scalability, and reconfigurability. In defining and managing trust in a military MANET, we must consider the interactions between the composite cognitive, social, information and communication networks, and take into account the severe resource constraints (e.g., computing power, energy, bandwidth, time), and dynamics (e.g., topology changes, node mobility, node failure, propagation channel conditions). We seek to combine the notions of “social trust” derived from social networks with “quality-of-service (QoS) trust” derived from information and communication networks to obtain a composite trust metric. We discuss the concepts and properties of trust and derive some unique characteristics of trust in MANETs, drawing upon social notions of trust. We provide a survey of trust management schemes developed for MANETs and discuss generally accepted classifications, potential attacks, performance metrics, and trust metrics in MANETs. Finally, we discuss future research areas on trust management in MANETs based on the concept of social and cognitive networks.

Index Terms—Trust management, mobile ad hoc networks, social networks, cognitive networks, trust, trust metrics.

I. INTRODUCTION

IN AN INCREASINGLY networked world, increased connectivity could lead to improved information sharing, facilitate collaboration, and enable distributed decision making, which is the underlying concept in Network Centric Operations. In mobile ad hoc networks (MANETs), the distributed decision making should take into account trust in the elements: the sources of information, the processors of information, the elements of the communications network across which the information is transmitted, etc. This trust must often be derived under time-critical conditions, and in a distributed way.

A. Design Challenges in MANET Protocols

A mobile ad hoc network [1] consists of wireless mobile nodes forming a temporary network without the help of centralized infrastructure, and where nodes communicate through multi-hops.

Security protocol designers for MANETs face technical challenges due to severe resource constraints in bandwidth,

memory size, battery life, computational power, and unique wireless characteristics such as openness to eavesdropping, lack of specific ingress and exit points, high security threats, vulnerability, unreliable communication, and rapid changes in topologies or memberships because of user mobility or node failure [1][2][3]. In addition, compared with designing security protocols for civilian MANETs, designing security protocols for military MANETs requires additional caution, since battlefield communication networks must cope with hostile environments, node heterogeneity, often stringent performance constraints, node subversion, high tempo operations leading to rapid changes in network topology and service requirements, and dynamically formed communities of interest wherein participants may not have predefined trust relationships [4]. To cope with these dynamics, networks must be able to reconfigure seamlessly, via low-complexity distributed network management schemes [3]. Security in a tactical network includes notions of communication security which can be easily quantified as opposed to the perception of security which is hard to quantify.

B. Motivation for Trust Management in MANETs

The concept of “Trust” originally derives from social sciences and is defined as the degree of subjective belief about the behaviors of a particular entity [5]. Blaze *et al.* [6] first introduced the term “Trust Management” and identified it as a separate component of security services in networks and clarified that “Trust management provides a unified approach for specifying and interpreting security policies, credentials, and relationships.”

Trust management in MANETs is needed when participating nodes, without any previous interactions, desire to establish a network with an acceptable level of trust relationships among themselves. Examples would be in building initial trust bootstrapping [7], coalition operations without predefined trust, and authentication of certificates generated by another party when links are down or ensuring safety before entering a new zone [8]. In addition, trust management has diverse applicability in many decision making situations including intrusion detection, authentication, access control, key management, isolating misbehaving nodes for effective routing, and other purposes.

Trust management, including trust establishment, trust update, and trust revocation, in MANETs is also much more challenging than in traditional centralized environments. For example, collecting trust information or evidence to evaluate trustworthiness is difficult due to changes in topology induced by node mobility or node failure. Further, resource constraints often confine the trust evaluation process only

Manuscript received 29 September 2009; revised 1 March 2010, 28 June 2010, and 7 July 2010.

Jin-Hee Cho and Ananthram Swami are with the Computational and Information Sciences Directorate, U.S. Army Research Laboratory, 2800 Powder Mill Rd., Adelphi, Maryland 20783, USA (e-mail: {jinhee.cho, ananthram.swami}@us.army.mil).

Ing-Ray Chen is with the Department of Computer Science, Virginia Polytechnic Institute and State University, 7054 Haycock Road, Falls Church, VA 22043, USA (e-mail: irchen@vt.edu).

Digital Object Identifier 10.1109/SURV.2011.092110.00088

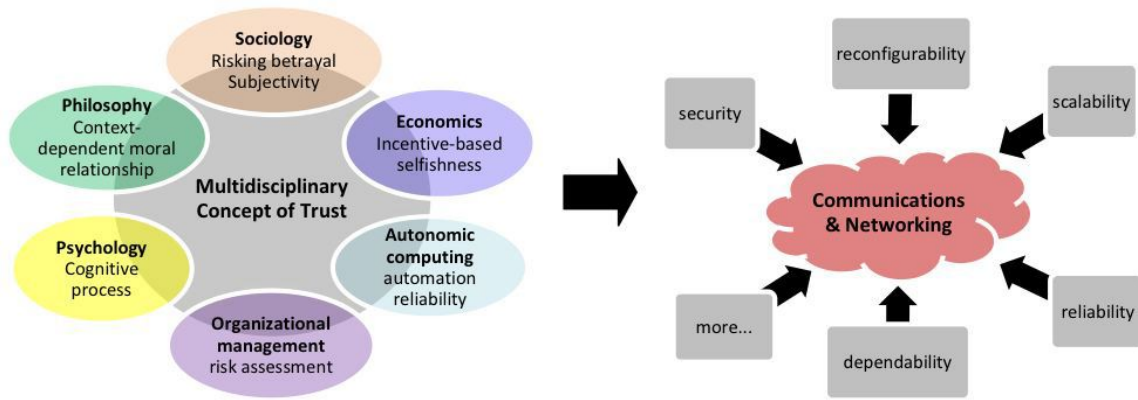


Fig. 1. The multidisciplinary concept of trust and its application in communications and networking.

to local information. The dynamic nature and characteristics of MANETs result in uncertainty and incompleteness of the trust evidence, which is continuously changing over time [8] [9]. Despite a couple of surveys of trust management [10] [11] [12], a comprehensive survey of trust management in MANETs does not exist and is the main aim of this paper. A short version of this paper was presented at ICCRTS 2009 [13]. The contributions of this paper are: (1) to give a clear definition of trust in the communication and networking field, drawing upon definitions from different disciplines; (2) to extensively survey the existing trust management schemes developed for MANETs and investigate their general trends; and (3) to discuss future research areas based on the concept of social and cognitive networks.

The rest of this paper is organized as follows. In Section 2, we discuss the concept of *trust* in diverse disciplines, give a clear distinction between trust and trustworthiness, and discuss the relationship between trust and risk. We also introduce the main properties of trust in MANETs. Section 3 surveys generally accepted classifications of trust management, attacks considered in existing trust management schemes for MANETs, and metrics used to measure the performance of existing MANET trust management schemes. Section 4 surveys trust management schemes that have been developed for specific purposes, including secure routing, authentication, intrusion detection, access control, key management, and trust evidence distribution and evaluation. In Section 5, we discuss design concepts that designers of MANET trust management systems should keep in mind and suggest trust metrics based on the concepts of social trust and quality-of-service (QoS) trust. Section 6 concludes this paper.

II. CONCEPTS AND PROPERTIES OF TRUST

In this section, we review how trust is defined in different disciplines and how these trust concepts can be applied in modeling trust in MANETs. Further, we examine the relationship between trust and risk, and how trust should be defined in order to realistically reflect the unique characteristics of MANETs.

A. Multidisciplinary Concept of Trust

According to *Merriam Webster's Dictionary* [14], trust is defined as "assured reliance on the character, ability, strength,

or truth of someone or something." Despite the subjective nature of trust, the concept of trust has been very attractive to network security protocol designers because of its diverse applicability as a decision making mechanism. We examine the literature to study how trust is defined in various disciplines including sociology, economics, philosophy, psychology, organizational management, and autonomic computing in industrial and system engineering. Finally, we also examine how trust can be defined in communications and networking with the help of definitions in other fields.

Trust in sociology: Gambetta's notion of trust [15] is popularly called *sociological trust* and is defined as an assessor's a priori subjective probability that a person (or agent, or group) will perform specific actions that affect the assessor. That is, Gambetta [15] describes the nature of trust as subjectivity, an indicator for future actions, and dynamicity based on continuous interactions between two entities. Luhmann [16] also emphasized the importance of trust in society as a mechanism for building cooperation among people to extend human interactions for future collaboration. Adams *et al.* [17] rephrased Gambetta's trust concept in applying the sociological concept of trust in computer science; they represented trust as a continuous variable, quantifying trust in the light of context or acceptance of risk. They further stressed that risking betrayal is an important aspect in building trust. To be useful, network trust models must capture this subjective aspect of social trust.

Trust in economics: Economists distinguish between the personal, informal trust that comes from being friendly with your neighbors and the impersonal, institutionalized trust that lets you give your credit card number out over the Internet [18]. Both notions of trust are important in military MANETs. In economics, trust is represented as an expectation that applies to situations in which trustors take risky actions under uncertainty or information incompleteness [19]. However, as illustrated in the *Prisoner's Dilemma (PD) game* [20], trust in economics is based on the assumption that humans are rational and strict utility maximizers of their own interest or incentives. In this sense, when we apply a human trust model to a network trust model, the assumption of selfish nodes seems reasonable. But altruistic behaviors can emerge from mechanisms that may be initially purely selfish [21], and thus making an argument for redemption mechanisms. Economic models are used in

conjunction with trust-based encryption primitives in [22] to develop a trust management paradigm for securing information flows across organizations.

Trust in philosophy: According to the *Stanford Encyclopedia of Philosophy* [23], trust is important but dangerous. Since trust allows us to form relationships with others and to rely on others for love, advice, help, etc., trust is regarded as a very important factor in our life that compels others to give us such things with no outside force such as the law. On the other hand, since trust requires taking a risk that the trustee may not behave as the trustor expects, trust is dangerous implying the possible betrayal of trust. In his comments on Lagerspetz's book titled *Trust: The Tacit Demand*, Lahno [24] describes the author's view on trust as a moral relationship in human society. Langerspetz believes that investigations of trust reveal that "human individuals, their beliefs, desires and actions are only intelligible against the background of existing social practices and social ties" [24]. This implies that depending on the nature of personal relationships between a trustor and a trustee (i.e., moral relationship between them), trustful actions or betrayal can occur.

Trust in psychology: According to the *Wikipedia* definition of trust in psychology [25], trust starts from the birth of the child. As the child grows older, trust also grows stronger. However, the root of trust derives from the relationship between mother (or caregiver) of the child since the strength of the family relies on trust, if the child is raised in a family which is very accepting and loving, the child also returns those feelings to others by trusting them. But if trust is lost, it is hard to regain it. In this sense, trust in psychology emphasizes the cognitive process that human beings learn trust from their experiences. Deutsch [26] defines trust as the confidence that one will find what is desired from another rather than what is feared. An individual may be said to have trust in the occurrence of an event if he expects its occurrence and his expectation leads to the behavior which he perceives to have greater negative consequences if the expectation is not confirmed than positive consequences if it is confirmed. In addition, Hardin [27] and Rotter [28] observed in their experiments that past experience may strikingly affect later capacity for trust. For example, bad experience with people will lower the trust level, leading to fewer trusted relationships with people, and thus fewer opportunities for mutual gain. Further, they recognized that the gains obtained by having high trust relationships exceed the loss by having low trust relationships. For instance, high trustors are less likely to lie or cheat or steal. Also they are less likely to be unhappy, conflicted, or unstable, and sought by more friends. Even though high trustors are deceived more often in novel situations, low trustors are also fooled equally by distrusting trustworthy people, thereby losing the advantages that high trustors may have [28].

Trust in organizational management: In this field, the concept of trust is also defined as the extent to which one party is willing to count on someone or something with a feeling of relative security in spite of possible negative consequences, emphasizing the possibility of facing risk [29]. Schoorman *et al.* [30] defined trust as the willingness to take a risk or willingness to be vulnerable in the relationship in terms of

ability, integrity, and benevolence. They also explained that trust is not necessarily mutual and is not reciprocal. Trust concepts in organizational management can give us insights on how to measure trust by investigating methods to measure ability, integrity, and benevolence of each networked node, as well as on assessing risk. They can also give us insights on defining group trust (i.e., between a person and a group or between groups) which is important for dynamic communities of interest.

Trust in autonomic computing: As technology becomes more complex, fully understanding automation becomes infeasible, if not impossible, and trust in automation becomes critical, particularly when unexpected situations arise and system responses cannot be predicted. Researchers studying autonomic computing in industrial systems engineering have sought to develop models of trust to understand how trust in automation develops and how it may be misplaced. Lee and See [31] define trust as the attitude that an agent will help accomplish an individual's goals in a situation with uncertainty and vulnerability. In this sense, an agent can be automation or another person that actively interacts with the environment on behalf of the person. Parasuraman [32] links the level of trust with automation reliability stating that "Trust often determines automation usage. Operators may not use a reliable automated system if they believe it to be untrustworthy." The notion of automation reliability as a trust metric is one that is applicable in MANETs, where the user's trust in reliability on technology is an important aspect.

Trust in communications and networking: The concept of trust also has been attractive to communication and network protocol designers where trust relationships among participating nodes are critical in building cooperative and collaborative environments to optimize system objectives in terms of scalability, reconfigurability, and reliability (i.e., survivability), dependability, or security. According to Eschenauer *et al.* [9], trust is defined as "a set of relations among entities that participate in a protocol. These relations are based on the evidence generated by the previous interactions of entities within a protocol. In general, if the interactions have been faithful to the protocol, then trust will accumulate between these entities." Capra [34] proposes to use a human trust model based on human interactions in a trust model for fully distributed network environments such as MANETs. Capra defines trust as the degree of a belief about the behavior of other entities (or agents). Li and Singhal [35] define trust as the belief that an entity is capable of performing reliably, dependably, and securely in a particular case; hence, different levels of trust exist in different contexts. For example, Alice may trust her physician to give her advice on her health concerns but may not trust her physician's advice on fixing her car. Aivaloglou *et al.* [36] describe trust as the quantified belief of a trustor regarding competence, honesty, security, and dependability of a trustee in a specific context.

Recently, researchers have recognized the importance of social networks in building trust relationships among entities. Golbeck [37][38][39] introduces the concept of social trust by suggesting the use of social networks as a bridge to build trust relationships among entities. Golbeck proposes the application of a trust concept derived from a sociological

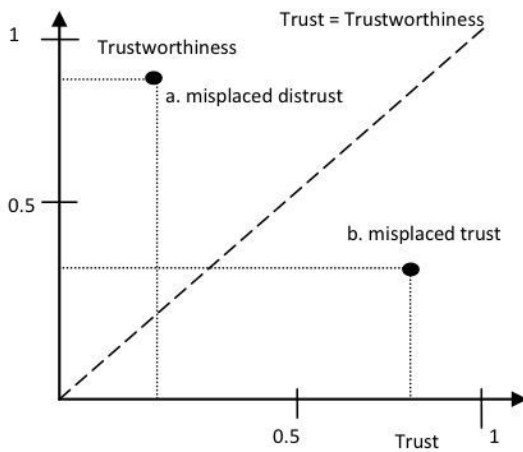


Fig. 2. Trust level [42].

viewpoint to computer science, and describes trust as a well-defined descriptor of security and encryption as a metric to reflect security goals. Wong and Sycara [40] introduce security mechanisms to establish trust in multi-agent systems. They are concerned with both authenticating agents as well as ensuring that agents do not misbehave. Trustworthiness emerges from the security features in their system.

From the definitions of trust derived from various fields as reviewed above, we can construct a trust metric having the following characteristics: (1) trust should be established based on potential risks; (2) trust should be context-dependent; (3) trust should be based on each party's own interest (e.g., selfishness); (4) trust is learned (i.e., a cognitive process); and (5) trust may represent system reliability.

B. Trust, Trustworthiness, and Risk

In the literature, the terms trust and trustworthiness seem to be used interchangeably without clear distinction. Josang *et al.* [41] clarified the difference between trust and trustworthiness based on definitions provided by Gambetta [15]. *Level of trust* is defined as the belief probability varying from 0 (complete distrust) to 1 (complete trust) [41]. In this sense, trustworthiness is a measure of the actual probability that the trustees will behave as expected. Solhaug *et al.* [42] define *trustworthiness* as the objective probability that the trustee performs a particular action on which the interests of the trustor depend.

Figure 2 [42] explains how trust (i.e., subjective probability of trust level) and trustworthiness (i.e., objective probability of trust level) can differ and how the difference affects the level of risk the trustor needs to take. The diagonal dashed line is assumed to be marks of well-founded trust in which trust is equivalent to trustworthiness.

Depending on the extent to which the trustor is ignorant about the difference between the believed (i.e., trust) and the actual (i.e., trustworthiness) probability, there is a miscalculation of the involved risk. That is, the subjective aspect of trust results in incorrect risk estimation and improper risk management accordingly. Figure 2 shows the cases in which the probability is miscalculated. In the area below the diagonal line, there is *misplaced trust* to various degrees that the perceived trust is higher than the actual trustworthiness. Even

though risk is an intrinsic characteristic of trust even in well-founded trust, misplaced trust increases risk and thus enhances the chance of deceit as well, as shown in the example marked with *b* in Figure 2. On the other hand, when the perceived trust is lower than the actual trustworthiness as shown in the example marked with *a*, the trustee is distrusted more than warranted. In this case, the trustor may lose potentially good opportunities to cooperate with partners with high trustworthiness.

From the above discussions, we can conclude that careful risk estimation is closely linked with building accurate trust relations among participating entities in networks. However, Josang *et al.* [41] argue that objective trust may not be applicable to decision making in real situations. They define two interesting types of trust: 1) a context independent *reliability trust* which measures the perceived reliability by another party regardless of the situations which the trustor might face by recognizing possible risk; 2) *decision trust* as "the extent to which a given party is willing to depend on something or somebody in a given situation with a feeling of relative security even though negative consequences are possible." Decision trust deals with components such as utility and risk attitude. As an example, one may not trust an old rope for climbing down from the 3rd floor of a building during a fire exercise (i.e., reliability trust) while trusting the rope in a real fire (i.e., decision trust).

The relationship between trust and risk has been investigated in [41][42]. Figure 3 shows an example of three different risk values: low, medium, and high. The value of risk is low for all trust values when the stake is close to zero. Similarly, if the stake is too high, risk is regarded as high regardless of the estimated trust value. Risk is generally low when the trust value is high. However, the risk value should be determined based on the value at stake (e.g., risk probability) since as shown in Figure 3, high risk exists even for the case of trust value = 1. Also important are the aspects (or probability) of opportunity and prospect (or the positive consequence of an opportunity) [41][42]. To buy rubber is to do risky business, but it also gives the opportunity of selling refined products with net profit. The purchaser of rubber should estimate her/his acceptable risk level in terms of the calculated prospects. Josang *et al.* [41] and Solhaug *et al.* [42] conclude that trust is generally neither proportional nor inversely proportional to risk.

Some researchers have commented that trust and uncertainty are intimately linked - trust is a mechanism to cope with uncertainty. The level of uncertainty in the information used as trust evidence will also considerably influence the accuracy of trust evaluation [43].

C. Trust Properties in MANETs

Due to the unique characteristics of MANET environments and the inherent unreliability of the wireless channel, the concept of trust in MANETs should be carefully defined. The main properties of trust in MANET environments can be summarized as follows (see Figure 4):

First, trust is *dynamic*, not static. Trust establishment in MANETs should be based on temporally and spatially local

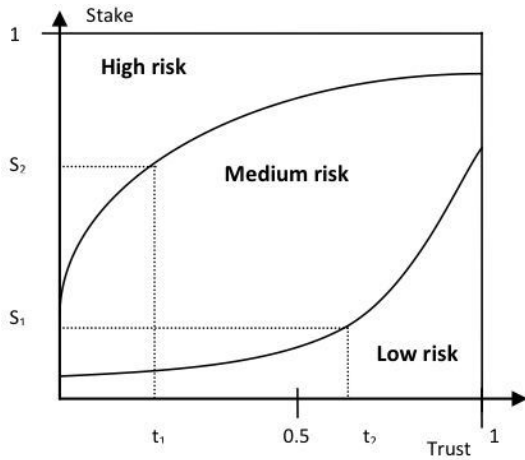


Fig. 3. Risk and trust [41].

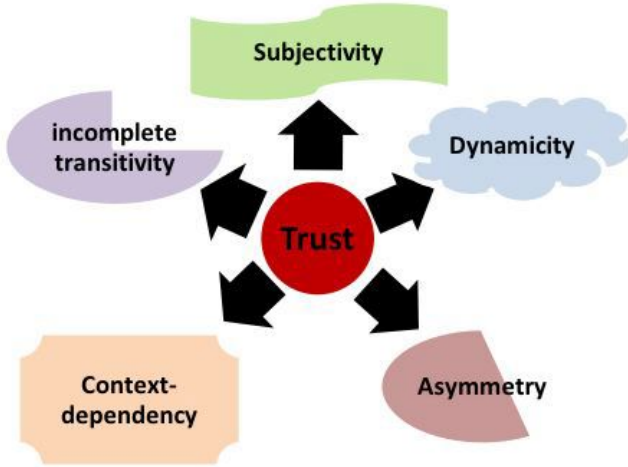


Fig. 4. Trust properties in MANETs.

information: due to node mobility or failure, information is typically incomplete and can change rapidly [8][32]. Adams *et al.* [44] point out that in order to capture the dynamics of trust, trust should be expressed as a continuous variable, rather than as a binary or even discrete-valued entity. A continuous valued variable can represent uncertainty better than a binary variable.

Second, trust is *subjective* [45]. In MANET environments, a trustor node may determine a different level of trust against the same trustee node due to different experiences with the node derived from a dynamically changing network topology.

Third, trust is *not necessarily transitive* [46]. For example, if A trusts B, and B trusts C, it does not guarantee A trusts C. In order to use the transitivity of trust between two entities to a third party, a trustor should maintain two types of trust: trust in a trustee and trust in the trustee's recommendation of the third party. For example, Alice may trust Bob about movies, but not trust him at all to recommend other people whose opinion about movies is worth considering or not trust other people that Bob recommended as much as she trusts Bob.

Fourth, trust is *asymmetric*, not necessarily reciprocal [44]. In heterogeneous MANETs, nodes with higher capability (e.g., more energy or computational power) may not trust nodes

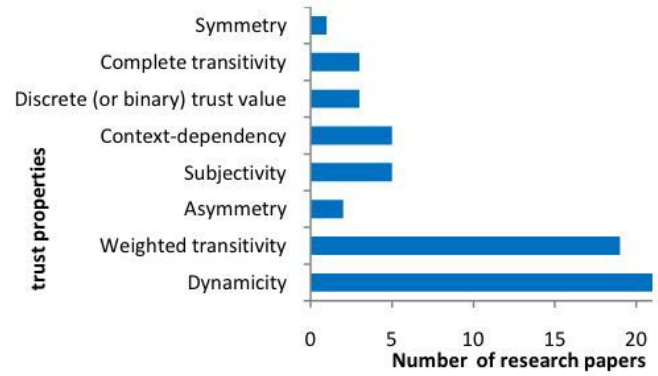


Fig. 5. Trust properties in trust management schemes in MANETs.

with lower capability at the same level that nodes with lower capability trust nodes with higher capability. As a typical example in organizational management, a supervisor tends to trust an employee less than the employee trusts the supervisor.

Fifth, trust is *context-dependent* [33]. For example, A may trust B as a wine expert but not as a car fixer. Similarly in MANETs depending on the given task, different types of trust (e.g., trust in computational power or trust in unselfishness, trust in forwarding versus trust in reporting) are required.

Figure 5 shows how several trust properties are considered in the literature. Dynamicity and weighted transitivity are most often considered. However, we notice that some existing work does not even consider trust properly; some represent trust as a discrete variable, while others assume that trust is symmetric or completely transitive. As such they do not capture characteristics of trust in a MANET. Further, we could not find any prior work that comprehensively considers all five properties of trust shown in Figure 5. Note that Figure 5 is based on 36 papers and each work may consider multiple trust properties.

In order to properly take into account these unique characteristics of trust in MANETs as described above, any trust-based framework for MANETs should consider the following as well:

First, a decision procedure to determine the trust of an entity should be *fully distributed* based on cooperative evaluation with uncertain and incomplete evidence, since one cannot rely on a trusted third party such as a trusted centralized certificate authority to take care of trust management as in wired networks [8][9][34].

Second, trust should be determined in a *highly customizable way* (e.g., flexible to membership changes and to deployment scenarios) without causing disruption to the device computation and communication resources while capturing the various and complicated natural components of an individual's trust into a network model [34][47].

Third, a trust decision framework should not assume that all nodes are cooperative [34]. In resource-restricted environments, *selfishness* is likely to be prevalent over cooperation, for example, in order to save battery life or computational power. Thomas *et al.* [48] discuss the tradeoff between selfishness and altruism of participating nodes in MANETs in terms of prolonging system lifetime (e.g., with system lifetime defined

as the time to a node's death due to energy exhaustion) versus reducing selfish behaviors to enhance system throughput.

Finally, trust should be established in a *self-organized reconfigurable* way in order not to be disrupted by the dynamics of MANET environments [8][48]. In addition to the characteristics mentioned above, trust-based frameworks for MANETs should consider the tradeoff issues between security and performance including reliability, fault tolerance, scalability, and energy consumption where resources are restricted but security vulnerability is relatively high.

III. CLASSIFICATIONS, POTENTIAL ATTACKS, AND METRICS FOR MANET TRUST MANAGEMENT

This section discusses classifications, attacks and performance metrics for MANET trust management. Before reviewing the literature, we would like to clarify some terminologies that have been used interchangeably but sometimes confusingly in the context of trust management.

In general, the term *trust management* is interchangeably used with the term *reputation management* [35]. However, there is a slight difference between trust and reputation. According to Liu *et al.* [49], trust is active while reputation is passive. That is, *trust* is a node's belief in the trust qualities of a peer, thus being extended from a node to its peer. *Reputation* is the perception that peers form about a node. Further, Ruhomaa *et al.* [10] distinguish trust from reputation, noting that trust puts an emphasis on risk and incentives while reputation focuses on a perception that a party creates through past actions about its intentions in the context of the norms effective within a community. Also, recommendation is frequently used as a way to measure trust or reputation. *Recommendation* is simply an attempt at communicating a party's reputation from one community context to another [45][10].

A working definition of trust for Internet applications, and a survey of trust management schemes for such applications may be found in [12].

In most of the literature, reputation management is regarded as part of trust management. Further, the terms *trust management* and *trust establishment* are also interchangeably used. To clarify these two terms, according to Aivaloglou *et al.* [36], trust establishment is a process to deal with the representation, evaluation, maintenance, and distribution of trust among nodes.

Trust management deals with problems such as the formulation of evaluation rules and policies, representation of trust evidence, and evaluation and management of trust relationships among nodes. As Figure 6 explains, trust establishment is one of several trust management tasks.

A. Classifications

According to Solhaug *et al.* [42], trust management is a special case of risk management with a particular emphasis on authentication of entities under uncertainty and decision making on cooperation with unknown entities. However, the application of trust management has been extended from authentication to various aspects of communications and networking, including secure routing for isolating malicious

or selfish nodes, intrusion detection, key management, access control, and other decision making mechanisms. Trust management includes trust establishment (i.e., collection of appropriate trust evidence, trust generation, trust distribution, trust discovery, and evaluation of trust evidence), trust update, and trust revocation [50] [42]. This section surveys popularly used classifications of trust management (or establishment).

Li *et al.* [51] and Li *et al.* [52] classify trust management as *reputation-based framework* and *trust establishment framework*. A reputation-based framework uses direct observations and second-hand information distributed among nodes in a network to evaluate a node. A trust establishment framework evaluates neighboring nodes based on direct observations while trust relations between two nodes without prior direct interactions are built through a combination of opinions from intermediate nodes.

Yonfang [53] suggests two different approaches to evaluate trust: *policy-based trust management* and *reputation-based trust management*. Policy-based trust management is based on strong and objective security schemes such as logical rules and verifiable properties encoded in signed credentials for access control of users to resources. In addition, the access decision is usually on the basis of mechanisms having a well-defined trust management language that has strong verification and proof support. Such a policy-based trust management approach usually makes a binary decision according to which the requester is trusted or not, and accordingly the access request is allowed or not. Due to the binary nature of trust evaluation, policy-based trust management has less flexibility. Furthermore, the availability of (or access to) trusted certificate authorities (CA) cannot always be guaranteed, particularly for distributed systems such as MANETs. On the other hand, reputation-based trust management utilizes numerical and computational mechanisms to evaluate trust. Typically, in such a system, trust is calculated by collecting, aggregating, and disseminating reputation among the entities.

According to Li and Singhal [35], trust management can be classified as *evidence-based trust management* and *monitoring-based trust management*. Evidence-based trust management considers anything that proves trust relationships among nodes: these could include public key, address, identity, or any evidence that any node can generate for itself or other nodes through a challenge and response process. Monitoring-based trust management rates the trust level of each participating node based on direct information (e.g., observing the benign or malicious behaviors of neighboring nodes, such as packet dropping, and packet flooding leading to excessive resource consumption in the network, or denial of service attacks) as well as indirect information (e.g., reputation ratings, such as recommendations forwarded from other nodes).

Aivaloglou *et al.* [36] classify two types of trust establishment frameworks for MANETs: *certificate-based framework* versus *behavior-based framework*. In the former, mechanisms are defined for pre-deployment knowledge of trust relationships within the network, using certificates which are distributed, maintained and managed, either independently or cooperatively by the nodes. Trust decisions can be made based on a valid certificate that proves trustworthiness of the target node by a certificate authority or by other nodes that the issuer

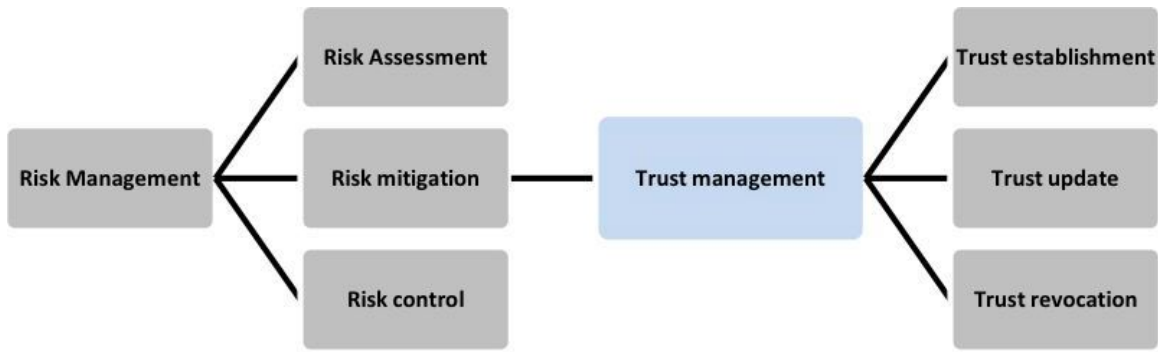


Fig. 6. Definition of trust management.

trusts. In behavior-based framework, each node continuously monitors behaviors of its neighboring nodes in order to evaluate trust. The behavior-based framework is a reactive approach, operating under the assumption that the identities of nodes in the network are ensured by preloaded authentication mechanisms. For example, if a node uses network resources in an unauthorized way, it will be regarded as a selfish or malicious node, and will finally be isolated from other nodes.

Aivaloglou *et al.* [36] also classify trust establishment schemes in terms of the type of architectures used: *hierarchical framework* versus *distributed framework*. In the former, a hierarchy exists among the nodes based on their capabilities or levels of trust. In this framework, centralized certificate authorities or trusted third parties are usually provided for on-line or off-line evidence. Such a centralized infrastructure does not exist in a distributed framework; hence, each node has some, possibly equal, responsibility for acquiring, maintaining, and distributing trust evidence.

Even though reputation management is part of trust management, many researchers further classify reputation management schemes. Adams *et al.* [44] propose three types of reputation systems: positive reputation, negative reputation, and a combination of the two. Positive reputation systems only consider observations or feedback of the positive behaviors of a node. Negative reputation systems only record complaints or observations of the negative behaviors of a node. Peers are assumed to be trusted and so feedback on behaviors is used to negatively reflect a node's reputation. To complement the drawbacks of these mechanisms, hybrid reputation systems have been proposed [53]. For more information on reputation management, the readers may refer to [11].

B. Potential Attacks

It is important to ensure that a trust management system itself should not be easily subverted, attacked or compromised. In this section, we discuss various common attacks and describe features important from the viewpoint of trust management. A survey of threat models and specific attacks on ad hoc routing protocols are described by Argyroudis *et al.* [54] and Djenouri *et al.* [55].

Liu *et al.* [49] describe the characteristics of attacks in MANETs by both the nature of attacks and the type of attackers. One classification of attacks is *passive attack* versus *active attack*. A passive attack occurs when an unauthorized

party gains access to an asset but does not modify its content. Passive attacks include eavesdropping and traffic analysis (e.g., traffic flow analysis). *Eavesdropping* indicates that the attacker monitors transmissions of message content. *Traffic analysis* refers to analyzing patterns of data transmission. An active attack occurs when an unauthorized party modifies a message, data stream, or file. Active attacks usually take the form of one of the following four types or combinations: masquerading (i.e., impersonation attack), replay (i.e., retransmitting messages), message modification, and denial-of-service (DoS) (leading to excessive resource consumption in the network).

Yet another way to characterize attacks is based on the legitimacy of an entity in a network: *insider attack* versus *outsider attack* [56]. If an entity is authorized to access system resources but employs them in a malicious way (e.g., in a way not approved by the authorizer), it is classified as an insider attack. More specifically, inside attackers exploit bugs in privileged system programs or poorly configured privileges, and then they may install backdoors or Trojan horses or other such mechanisms to facilitate subsequent acquisition of privileged access. On the other hand, an outsider attack is initiated by an unauthorized or illegitimate user. They usually acquire access to an authorized account and try to perpetrate insider attacks. Both attackers may spoof network protocols to effectively acquire access to an authorized account.

Many trust management schemes are devised to detect misbehaving nodes, both selfish nodes as well as malicious nodes. Specific attack examples are described as follows (the list is representative, not exhaustive):

- **Routing loop attacks:** A malicious node may modify routing packets in such a way that packets traverse a cycle and so do not reach the intended destination [56].
- **Wormhole attacks:** A group of cooperating malicious nodes can pretend to connect two distant points in the network with a low-latency communication link called a wormhole link, causing disruptions in normal traffic load and flow [57][58][59].
- **Blackhole attacks:** A malicious node, the so called black hole node, may always respond positively to route requests even when it does not have proper routing information. The black hole can drop all packets forwarded to it [60].
- **Grayhole attacks:** A malicious node may selectively drop packets [61], as a special case of a black hole attack. For

example, the malicious node may forward routing packets but not data packets. Similarly, a *sinkhole attacker* attracts nodes to route through it and then selectively routes packets [49].

- **DoS attacks:** A malicious node may block the normal use or management of communications facilities, for example, by causing excessive resource consumption [62].
- **False information or false recommendation:** A malicious node may collude and provide false recommendations/information to isolate good nodes while keeping malicious nodes connected. In the *stacking attack*, a malicious node keeps complaining about a peer node and creates the peer's negative reputation [44][63].
- **Incomplete information:** A malicious node may not cooperate in providing proper or complete information. Usually compromised nodes collude to perform this attack. However, node mobility or link failure, prevalent in MANETs, may also result in the same phenomenon [8][34].
- **Packet modification/insertion:** A malicious node may modify packets or insert malicious packets such as packets with incorrect routing information [64].
- **Newcomer attacks:** A malicious node may discard its bad reputation or distrust by registering as a new user. The malicious node simply leaves the system and joins again for trust revocation, flushing out its previous bad history and starting to accumulate new trust [65].
- **Sybil attacks:** A malicious node can use multiple network identities which can affect topology maintenance and fault tolerant schemes such as multi-path routing [61][49][46].
- **Blackmailing:** A malicious node can blackmail another node by disseminating false information that another node is malicious or misbehaving. This can generate significant amount of traffic and ultimately disrupt the functionality of the entire network [49]. This attack can be seen as false accusation plus DoS attacks in the sense that false information is disseminated leading to a significant amount of resource consumption.
- **Replay attacks:** A malicious node may replay earlier transmitted packets. If the packets include data, this should not cause trouble, and the receiving node just discards erroneous packets. However, if the adversary replays route requests, routing table information would become erroneous, and old locations and routing information might make nodes unreachable [56].
- **Selective misbehaving attacks:** A malicious node behaves badly but selectively to other nodes [66].
- **On-off attacks:** A malicious node may alternatively behave well and badly to stay undetected while disrupting services [66].
- **Conflicting behavior attacks:** A malicious node may behave differently to nodes in different groups to make the opinions from the different good groups conflicting, and ultimately lead to non-trusted relationships [52].

Figure 7 shows various attacks considered in a survey of 43 papers. Note that the "general selfish" category means no specific information is given in the work except that it

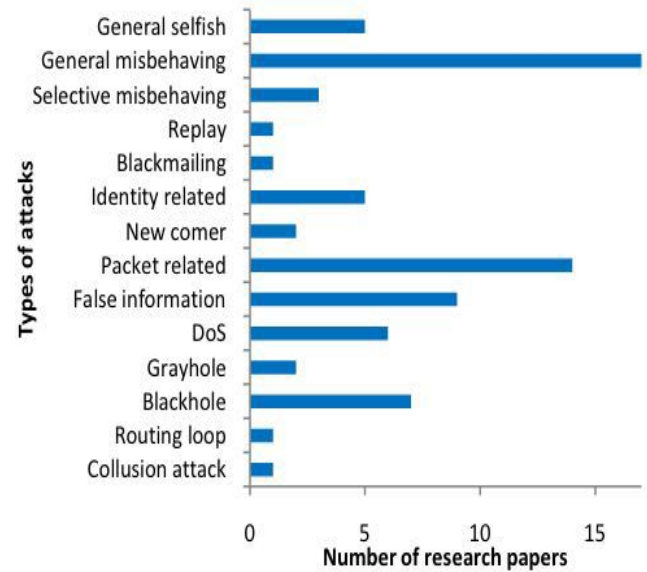


Fig. 7. Attacks considered in existing trust management systems in MANETs.

deals with selfish nodes. Also papers in the "general misbehaving" category deal with a broad range of misbehaving nodes, including malicious and selfish nodes, but do not provide detailed information. "Packet related" attacks include packet dropping, packet modification, packet insertion, and selective packet forwarding. "Identity related" attacks include impersonation, masquerading, and Sybil attacks. Except for the "general selfish" and "general misbehaving" categories, we notice that "false information" (e.g., including false recommendation or reputation) and "packet related" attacks are dominantly considered in the literature on trust management schemes for MANETs. Figure 7 illustrates that most of the attacks considered in the literature on trust management are general attacks often targeted at other aspects of MANETs. Hence, the trust evaluation engine should be robust and degrade gracefully if some information or evidence does not provide a certain level of trust based on partial or potentially corrupted information.

C. Metrics for MANET Trust Management

Although many trust management schemes have been proposed to evaluate trust values, no work clearly addresses what should be *measured* to evaluate network trust. Liu *et al.* [49] defined trust in their model as reliability, timeliness, and integrity of message delivery to the intended next-hop. Also most trust-based protocols for secure routing calculated trust values based on the characteristics of nodes behaving properly at the network layer. Trust measurement can be application-dependent and will be different based on the design goals of proposed schemes.

Based on 31 papers, Figure 8 shows various performance metrics that have been used to evaluate trust management schemes for MANETs. Note that a single work may use multiple performance metrics. Figure 8 shows standard system performance metrics typically used to evaluate trust management systems; these metrics include overhead (e.g., control

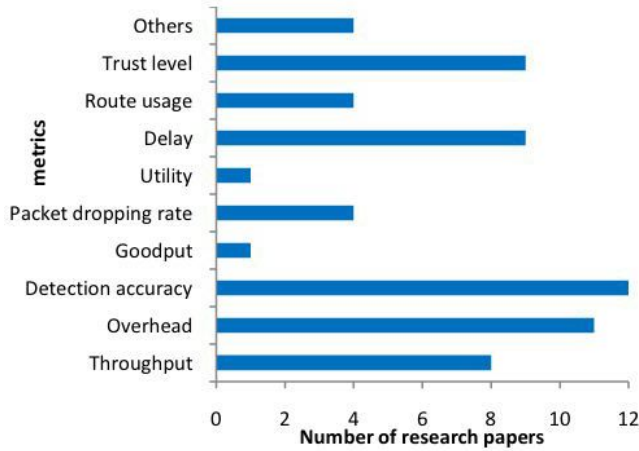


Fig. 8. Metrics considered by MANET trust management systems.

packet overheads), throughput, goodput, packet dropping rate, and delay. "Route usage" refers to the number of routes selected particularly when the purpose is for secure routing. "Trust level" is a recently used system metric. Example metrics using the trust level include confidence level of the trust value, trustworthiness, opinion values about other nodes, and trust level per session. "Others" indicates metrics that consider system tolerance based on incorrect reputation threshold, availability, convergence time to reach steady state in trustworthiness of all participating nodes, and percentage of malicious nodes.

IV. MANET TRUST MANAGEMENT SCHEMES

This section summarizes trust management schemes that have been developed for MANETs.

We describe trust management schemes based on specific design purposes such as secure routing, authentication, intrusion detection, access control (authorization), and key management. Further, we also describe existing general frameworks for trust (or reputation) evidence distribution and evaluation. Figure 9 summarizes 45 trust management schemes proposed for MANETs during 2000-2009 based on their design purposes. Note that under each research category, we will survey existing works in chronological order.

A. Secure Routing

Most reputation-based trust management schemes are devised for collaborative secure routing by detecting misbehaving nodes, both selfish and malicious ones. Marti *et al.* [67] proposed a reputation-based trust management scheme that consists of a *watchdog* that monitors node behaviors and a *pathrater* that collects reputation and takes response actions (e.g., isolating misbehaving nodes as a result of misbehavior detection). This work is an initiative to dynamically incorporate direct observations into trust values for secure routing. It extends DSR (Dynamic Source Routing) but trust evaluation is based only on direct observations.

Buchegger *et al.* [68] initiated a new design to develop a routing protocol by introducing a "trust manager" in their scheme. They determined trust levels based on self-monitored

information while employing reputation collected from both direct and indirect observations and experiences. They did not show any experimental results, but pose several interesting questions such as what is a sustainable relationship between the total number of nodes in the network, the maximum number of malicious nodes the system can tolerate, and the minimum number of friends per node needed to achieve high tolerance, and a prescribed level of trust. Buchegger *et al.* [69] also developed a reputation-based trust management scheme called CONFIDANT (Cooperation Of Nodes-Fairness In Dynamic Ad-hoc NeTworks) based on both direct and indirect observations to detect misbehaving nodes. The unique feature in this work is an incentive mechanism for altruistic nodes to be paid as a result of cooperation.

Paul and Westhoff [70] proposed a context-aware mechanism for detecting selfish nodes by extending DSR with a context-aware inference scheme to punish the accused and the malicious accuser. However, the use of digital signatures to disseminate information about the accused and the malicious accuser may not be viable in a resource-constrained MANET environment.

Michiardi *et al.* [71] proposed CORE (COLlaborative REputation) that has a monitoring mechanism complemented by a reputation functionality that differentiates between direct reputation, indirect reputation, and functional reputation (task-specific behavior). The proposed protocol is developed to make decisions about cooperation or gradual isolation of a node. A unique characteristic of this mechanism is that it exchanges only positive reputation information. However, this may limit its reliance on positive reports without the facility to submit negative feedback.

He *et al.* [72] proposed a reputation-based trust management scheme using an incentive mechanism, called SORI (Secure and Objective Reputation-based Incentive). This scheme encourages packet forwarding and discourages selfish behaviors based on quantified objective measures and reputation propagation by a one-way hash chain based authentication. The performance of this scheme in the presence of malicious nodes, as may be expected in a hostile environment, has not been investigated.

Nekkanti and Lee [73] extended AODV (Ad hoc On-demand Distance Vector) using trust factor and security level at each node. Their approach deals differently with each route request based on the node's trust factor and security level. In a typical scheme, routing information for every request would be encrypted leading to large overheads; they propose to use different levels of encryption based on the trust factor of a node, thus reducing overhead. This approach adjusts the security level based on the recognized hostility level and hence can conserve resources; however, the approach does not treat evaluation of trust itself. Li *et al.* [74] also extended AODV and adopted a trust model to guard against malicious behaviors of nodes at the network layer. They represented trust as *opinion* stemming from *subjective logic*. The opinion reflects the characteristics of trust in MANETs, particularly dynamicity. The key feature is to consider system performance aspects by dealing with each query based on its level of trust. Depending on the level of trust of nodes involved in the query, there is no need for a node to request and

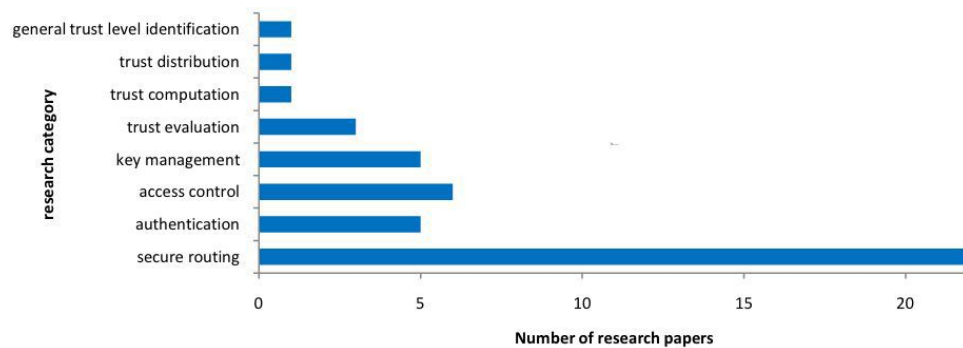


Fig. 9. Metrics considered by MANET trust management systems.

verify certificates all the time, thereby leading to significant reduction of computation and communication overhead. This work advances trust management by considering a generic trust management framework for MANETs.

Pisinou *et al.* [75] devised a secure AODV-based routing protocol for multi-hop ad hoc networks for discovering a secure end-to-end route free of any compromised nodes. Their trust-based routing protocol calculates trust values based only on direct observations, assuming that trust is transitive. As a continuation of [68], Buchegger *et al.* [76] also proposed a fully distributed reputation system in order to cope with false information propagation. The proposed design maintains a reputation and trust rating system about individual nodes by designing a modified Bayesian approach. Recognizing the dynamic nature of trust and reputation, the authors introduced reevaluation and reputation fading as well as redemption mechanisms. Nevertheless, no other characteristics of trust are addressed except for dynamicity.

Ghosh *et al.* [77] enhanced trust management by considering the confidence level of trust. Their use of the confidence level as a weight on the computed trust value and the method for calculating trust in a fully distributed way provide a general framework that can be applied to non-trust-aware routing protocols. In [77], SORI [72] is extended to alleviate the problem of selfish nodes, by considering the number of forwarding packets to evaluate the confidence level.

Wang *et al.* [78] proposed a mechanism to distinguish selfish peers from cooperative ones based solely on local observations of AODV routing protocol behaviors. They use a finite state machine model of locally observed AODV actions to construct a statistical description of each peer's behavior. In order to distinguish between selfish and cooperative peers, a series of well-known statistical tests are applied to features obtained from the observed AODV actions. An interesting extension of this work would be to consider various patterns of node mobility which can give additional insights.

Zouridaki *et al.* [79] proposed a trust establishment mechanism for MANETs called *Herms* to improve the reliability of packet forwarding over multi-hop routes in the presence of potentially malicious nodes. Essentially, direct observations are used to evaluate opinions about others. Also, confidence level is used as a weight to evaluate trust of other nodes based on a Bayesian approach. They also introduced a windowing scheme to systematically expire old data to maintain accuracy

of the opinion metric in the face of dynamics. However, this scheme is vulnerable to attacks that can exploit the windowing scheme to disseminate false information to accuse good nodes and to keep bad nodes in the system (such as badmouthing attacks).

As an extension, Zouridaki *et al.* [80] employed both first-hand trust information based on direct observations and second-hand trust information forwarded from neighboring nodes about non-neighboring nodes. This trust establishment scheme can cope with more attacks, including propagation of false recommendations or information, identifying bad nodes among neighboring nodes, colluding attacks, replay attacks, and duplicate attacks. It is noteworthy that they used only security related metrics to evaluate their scheme, such as trustworthiness and the percentage of nodes recognized as bad.

Pirzada *et al.* [81] proposed and examined the efficacy of trust-based reactive routing protocols in the presence of attacks. This work only considers first hand information to evaluate other nodes' trust values. Thus, trust evaluation is restricted to direct neighboring nodes.

Sun *et al.* [46] proposed trust modeling and evaluation methods for secure ad hoc routing and malicious node detection. The unique part of their design is to consider trust as a measure of uncertainty that can be calculated using *entropy*. In their definition, trust is a continuous variable, and does not need to be transitive, thus capturing some of the characteristics of trust in MANETs. However, this work considers packet dropping as the only component of direct observations to evaluate trust.

Abusalah *et al.* [82] proposed a trust-aware routing protocol (TARP) and developed a trust metric based on six trust components including software configuration, hardware configuration, battery power, credit history, exposure and organizational hierarchy. However, no consideration was given to trust decay over time and space to reflect uncertainty due to dynamics and incomplete information in MANET environments.

Sen *et al.* [83] proposed a trust-based mechanism to detect malicious packet dropping nodes based on reputation of neighboring nodes, and take into account the decay of trust over time. This work assumes that a pair of public/private keys can be preloaded to prevent identity-related attacks. However, this may not be scalable for a large network.

Soltanali *et al.* [84] proposed a distributed mechanism to deal with selfish nodes as well as to encourage cooperation in

MANETs based on the combination of reputation-based and currency-based incentive mechanism mitigating their defects and improving their advantages. Compared to existing works, this work considers more aspects of trust such as dynamicity, weighted transitivity, and subjectivity. However, it used only packet forwarding behaviors to evaluate a node's trust and standard performance metrics to evaluate the proposed trust scheme.

Balakrishnan *et al.* [85] developed a trust model to strengthen the security of MANETs and to deal with the issues associated with recommendations. Their model utilizes only trusted routes for communication, and isolates malicious nodes based on the evidence obtained from direct interactions and recommendations. Their protocol is described as robust to the recommender's bias, honest-elicitation, and free-riding. This work uniquely considered a context-dependency characteristic of trust in extending DSR.

Li *et al.* [52] stated that using only a reputation-based trust framework gives only an incomplete partial solution for trust management. They proposed an objective trust management framework (OTMF) for MANETs based on both direct and indirect information for reputation management and showed the effectiveness of OTMF. This work used the term "objective" trust to refer to trust evaluated based on second-hand information. However, this work did not consider node collusion in obtaining second-hand information, which may lead to incorrect recommendations.

Mundinger and Boudec [86] were the first to analyze the robustness of a reputation system based on a deviation test. Using a mean-field approach in their stochastic model, they showed that liars have no impact unless the number of liars exceeds a certain threshold (a phase transition). They provided precise formulas for the critical values and guidelines for an optimal choice of parameters. This work is unique in that it evaluates a system's tolerance to untrusted nodes; however, the reputation evaluation is based only on the "fake" information.

Moe *et al.* [87] proposed a trust-based routing protocol as an extension of DSR based on an incentive mechanism that enforces cooperation among nodes and reduces the benefits that selfish nodes can enjoy (e.g., saving resources by selectively dropping packets). This work is unique in that they used a hidden Markov model (HMM) to quantitatively measure the trustworthiness of nodes. In this work, selfish nodes are benign and selectively drop packets. Performance characteristics of the protocol when malicious nodes perform active attacks such as packet modifications, identity attacks, etc., need to be investigated further.

In quorum or threshold schemes, a node must successfully interact with at least k of n distributed trusted authority (TA) nodes. Finding k such nodes can be resource intensive. Reidt *et al.* [88] prioritize the TA nodes and find a route to connect to k desirable TA nodes so as to minimize a performance metric such as overhead, taking into account reliability and energy consumption of individual nodes. Significant savings over a standard system were shown. An interesting aspect, not considered yet, would be to incorporate trustworthiness into the TA selection and routing scheme.

Ayachi *et al.* [89] formalized implicit trust relations in AODV and demonstrated that a node can utilize these trust

relations to isolate malicious nodes for secure routing. Nodes overhear neighbors' transmissions from which they can build a neighbor routing table and check for deviation from normal behaviors for AODV. This scheme can detect malicious behaviors such as message replication, message forgery and some instances of message modification. However, it is not amenable to incorporation of other trust metric components, such as intimacy and competence but monitored behaviors could feed into a trust evaluation scheme.

Adnane *et al.* [90] proposed trust-based countermeasures to isolate malicious nodes extending OLSR (Optimized Link State Routing). Their protocol provides secure routing paths by identifying malicious nodes. The focus of the protocol is to prevent usurpation of node identities. Performance analysis under other types of attacks remains to be investigated.

Although many researchers have developed secure routing protocols using trust, most of the approaches have focused on monitoring routing behaviors and the evaluation of trust has been in the context of communication networks. Further steps should be taken to refine issues such as (1) how to quantify trust in a MANET node; (2) how to employ (a continuous-valued) trust in a routing decision; and (3) how to develop a composite trust metric incorporating task performance goals, taking into account the social aspects of a MANET node.

B. Authentication

There have been efforts to establish trust relationships to ensure authentication in MANETs. Weimerskirch *et al.* [91] developed a trust model based on human behavior, noting that society can be properly considered as an ad hoc network. They used recommendations from a distributed trust model to construct trust relationships and extended it by a request for recommendations. Based on models derived from observations of human society, recommendations are used to calculate trust, with weights based on the distance of relationships. Their definition does not assume symmetry or complete transitivity, thus capturing essential features of trust in MANETs. The assumption of low-value transactions does not require any evidence-based mechanism to ensure trust such as authentications using public/private keys. Consequently, it is not applicable to systems where hostility may be high, or where consequences of misplaced trust can be severe.

Verma *et al.* [92] presented an overview of a trust negotiation scheme using DSR and ZRP (Zone Routing Protocol). Their scheme consists of two components. The peer-to-peer component deals with secure communications with neighbors in a lightweight manner. The heavyweight remote component performs trust negotiation and establishes secure end-to-end communication. The main goal of this work is to add robustness in the process of trust negotiation, rather than trust evaluation.

Pirzada and McDonald [93] proposed a trust-based communication model that, based on a notion of a *belief*, provides a dynamic measure of reliability and trustworthiness in MANETs. The merit of this work is to incorporate utility as general trust and time as situational trust into the overall trust metric to evaluate an agent in the network. However, the situational trust considered is limited to monitoring dynamics of packet forwarding behaviors.

Davis [47] proposed a reliable and structured hierarchical model for trust management in MANETs that is robust to malicious accusation exploits. The scheme deals with explicit revocation of certificates in a distributed way, eliminating the case in which revoked certificates can be accepted as valid. This work assumes that the initial certificates and public keys of all nodes are distributed by a centralized trust authority to each node before the network is deployed which may not be scalable in a large scale MANET. The paper does not discuss the issue of false positives which can lead to continual eviction of nodes, and eventually loss of network connectivity. To counteract this, dynamic reissue of certificates may be needed which may incur extra overhead.

Ngai and Lyu [94] proposed a secure public key authentication service based on their trust model to prevent propagation of false public keys in the presence of malicious nodes. Trust is evaluated based on direct monitoring as well as recommendation. However, this work does not consider group membership changes, the distance from the evaluator, and their effect on the performance of their trust management scheme.

In summary, there has been quite a bit of work on using trust for authentication. However, as in the case of trust-based secure routing, the models and protocols used are based solely on monitoring packet forwarding behaviors.

C. Intrusion Detection

Trust can be used as a basis for developing an intrusion detection system (IDS). Also, IDS itself can help nodes measure trust of other nodes when they cooperate with each other to detect malicious nodes. Albers *et al.* [95] proposed a general architecture for an intrusion detection system (IDS) called a Local IDS (LIDS) such that intrusion detection can be performed locally among trustworthy participating nodes. Here, trust is used to detect intrusions in the system. In Ahmed *et al.* [96], IDS provides audit and monitoring capabilities that offer local security to a node and helps perceive the specific trust levels of other nodes. Hence, evaluating trust and identifying intrusions may not be totally separated processes.

D. Access Control

Trust also can be applied in determining whether or not to grant access to certain resources or rights. Gray *et al.* [97] integrated trust-based admission control with standard role-based access control. By doing this, an access control decision is effectively made without being affected by incomplete information collected in MANETs. A simple distributed blackjack card game application is described, in which the trust-based admission control system is used to assign roles to users based on their trust-based admission rights. It is not clear how the approach can be extended to a general framework applicable to MANETs.

Luo *et al.* [98] presented a ubiquitous and robust access control solution (URSA) for MANETs based on a localized group trust model so that only well behaving nodes will have access rights to network resources. Their localized group trust model for MANETs is based on threshold cryptography: a node is globally trusted only if it is individually trusted by any k trusted nodes where k is a system-wide trust threshold.

This work assumes that the node density is large enough so that any node can find k trusted nodes, perhaps by moving to another location. Interesting extensions of the work include consideration of mobility models other than random waypoint, and trust evaluation under high node mobility situations.

Adams and Davis [17] presented a decentralized access control system implementing sociological trust constructs in a quantitative system to evaluate the relationships between entities. A distributed, node-centric approach to reputation management considers a node's behavior feedback and gives a reputation index that nodes can use to determine the trustworthiness of their peers before establishing trust relationships. This work further assessed risk using a Bayesian approach to evaluate trust. Interestingly, this work used reputation as a weight to evaluate direct observations, which is a different approach from most existing works. Extensions of the scheme to handle network dynamics would be useful.

Yunfang [53] proposed an integrated mechanism of policy proof and reputation evolution into trust management for decision-making on access control with the goal of providing firm/objective security as well as social/subjective security. However, this work is based on the assumption that trust is completely transitive, and it is not clear how a more realistic transitivity model can be incorporated into the trust management system.

E. Key Management

Virendra *et al.* [99] proposed a trust-based security architecture for key management in MANETs. This architecture aims to establish keys between nodes based on their trust relationships, and to build secure distributed control using trust as a metric. In their self-organizing trust-based architecture, nodes are organized into trust-based clusters called Physical-Logical Trust Domains (PLTDs), a group of trusted nodes sharing a group key. Nodes can belong to multiple PLTDs. The unique part of this work is that it considers the trust level of each node in a physical as well as a logical sense, e.g., it considers both one-hop nodes as well as previously trusted nodes that are not currently one-hop neighboring nodes. The significant merit of this work is in formalizing a trust metric reflecting trust decay over time and updating trust as dynamics of the network change. However, establishing pair-wise keys based on pair-wise trust may not be feasible in terms of scalability and in the presence of high network dynamics in a large MANET.

Hadjichristofi *et al.* [63] presented a key management framework that provides redundancy and robustness in the establishment of Security Association (SA) between pairs of nodes. Their proposed key management system (KMS) adopts a modified hierarchical Public Key Infrastructure (PKI) model where nodes can dynamically take management roles. The scheme is designed to provide high service availability based on trust-based SA among nodes. However, trust relationships are derived solely from certificate chains. Adams *et al.* [44] also extended their prior work [63] with a node-centric reputation management approach that considers feedback about a node's behavior in generating a reputation index to determine the trustworthiness of its peers before establishing

IPSec security associations. They considered the decay of trust over time using a three-window weighted average. They also derived reputation values from past experiences and current observations and introduced a rehabilitation mechanism to give a second chance to bad nodes. However, no details were given on the type of information that should be directly observed to derive reputation.

Li *et al.* [100] demonstrated an on-demand, fully localized, and hop-by-hop public key management protocol for MANETs. In this protocol each node generates its own public/private key pairs, issues its certificate to neighboring nodes, keeps received certificates in its certificate repository, and provides authentication service by adapting to the dynamic network topology, without reliance on any centralized server. However, only certificate chains are used to derive trust.

Chang and Kou [101] proposed a Markov chain trust model to obtain the trust values (TVs) for 1-hop neighbors. They designed a trust-based hierarchical key management scheme by selecting a certificate authority server (CA) and a backup CA with the highest TVs. This work gives a rigorous analysis of TVs and considers a variety of attacks. However, it computes TVs only based on direct observations and does not consider trust decay due to using recommendations from remote nodes.

A survey of key management techniques for network-layer security may be found in the work by Hegland *et al.* [102].

In contrast to secure routing that produces an operational MANET, authentication, intrusion detection, access control, and key management are general trust contexts that also exist outside the area of MANETs. In these applications, it is useful to abstract out the properties of MANETs and consider only the influence of MANETs on any information/evidence gathering, aggregation, and other computation, and design a trust management scheme that considers influences such as the cost/likelihood of obtaining a piece of information in computing trust.

F. Trust Evidence Distribution and Evaluation

Several trust management schemes have been proposed in order to provide a general framework for trust evidence distribution or evaluation in MANETs.

Yan *et al.* [64] proposed a trust evaluation based security solution for data protection, secure routing, and other network activities. This trust evaluation model called Personal Trusted Bubble (PTB) considers many factors including experience statistics, data value (the higher the value of the data, the higher is the trust needed from other PTBs to transfer it), intrusion black list, reference (reputation/recommendation), personal preference, and PTB policy (related to the entire network's security requirements and policy). Interestingly, personal preference and PTB reflect the subjective characteristic of trust in deriving trust values. Yan *et al.* [64] do not validate whether their proposed trust management is correct or useful compared to the actual trust levels, say, based on trustworthiness in Josang and Solhaug's terminology. In general, validation of trust models is difficult, given the inherent subjectivity in the trust metric, but it is also critical. Jiang and Baras [103] proposed a trust distribution scheme called ABED (Ant-Based trust Evidence Distribution) based on the swarm intelligence paradigm, which is highly distributed and

adaptive to mobility. The swarm intelligence paradigm is widely used in dynamic optimization problems (e.g., the traveling salesman problem, routing in communication networks). The key principle in swarm interaction is called stigmergy, indirect communication through the environment. In ABED, "pheromones" are deposited at nodes by mobile agents called "ants" and provide the mechanism for information exchange and interactions. These "ants" can identify the optimal path toward their food, resembling trust evidence in this case. The pheromone regulation process is known to be suitable for dynamically changing environments such as MANETs. However, no specific attackers are considered to prove the robustness of the proposed scheme in the presence of attacks.

In the continuing work, Baras and Jiang [104] addressed distributed trust computation and establishment using random graph theory. This work uses the theory of dynamic cooperative games and identifies how a phase transition from a distrusted state to a trusted state can occur in a dynamic MANET. This work is unique in that it describes how phase transitions occur in MANETs and how these are related to node mobility and network topology in the process of initial trust establishment. Trust relationships are ternary (yes, no, don't care) and the emphasis is on understanding steady-state behaviors. Incorporating continuous valued trust variables, dynamics, and transient behaviors in this framework would be useful.

Theodorakopoulos and Baras [50] proposed a trust evidence evaluation scheme for MANETs. The evaluation process is modeled as a path problem in a directed graph where vertices represent entities and edges represent trust relations. The authors employed the theory of Semirings to show how two nodes can establish trust relationships without prior direct interactions. Their case study uses the PGP web of trust to express an example trust model based on *Semirings* and shows that their scheme is robust in the presence of attackers. However, their work assumes that trust is transitive. Further, trust and confidence values are represented as binary rather than continuous values. Even though no centralized trusted third party exists, their work makes use of a source node as a trusted infrastructure, which introduces vulnerability in MANETs.

Recently, Boukerche and Ren [105] proposed a distributed reputation management mechanism called GRE (Generalized Reputation Evaluation), using a comprehensive computational reputation model. GRE seeks to prevent malicious nodes from entering a trusted community. However, no specific attack model was addressed.

Moloney and Weber [106] presented a trust-based security system that generates appropriate trust levels based on the consideration of the main characteristics of MANETs as well as context-awareness. The scheme leverages two existing projects at Trinity College, Dublin, called *SECURE* and *Aithe*. *SECURE* is used for trust management using a trust engine and a risk engine while *Aithe* collects and manages context information forwarded from sensors. It is worthwhile to extend this work to consider attacks that can propagate incorrect information to generate trust levels.

Very recently, Cho *et al.* [107] proposed a trust management scheme for group communication systems in MANETs. This

work proposed a composite trust metric reflecting various aspects of a MANET node such as sociability (i.e., social trust) and task performance capability (i.e., QoS trust), and investigated the effect of the trust chain length used by a node to establish acceptable trust levels through subjective trust evaluation. They also discussed the concept of objective trust evaluation based on global knowledge as the basis of validating subjective trust evaluation. More work remains to be done to ascertain feasibility.

The Appendix summarizes trust management schemes surveyed in this section. In the Appendix, the methodology explains how trust evidence is collected and performance metrics refer to the metrics used to evaluate various trust management schemes.

V. FUTURE RESEARCH DISCUSSION

It is clear that sooner or later intelligence will be embedded in each node with cognitive functionality, adopting recent ideas about cognitive networks in wireless networks [108]. Mahmoud [108] defines a cognitive network as having a *cognitive process* that is capable of perceiving current network conditions and then planning, deciding, and acting on those conditions. Cognitive networks are able to reconfigure the network infrastructure based on past experiences by adapting to continuously changing network behaviors to improve scalability (e.g., reducing complexity), survivability (e.g., increasing reliability), and QoS (e.g., facilitating cooperation among nodes) as proactive mechanisms [48][108]. We suggest using this concept of cognitive networks so that nodes can adapt to changing network behaviors, such as attacker behaviors, degree of hostility, node disconnection due to physical environment such as terrain, energy depletion, or voluntary disconnection for energy saving. Cognition is more than adaptation; it incorporates learning and reasoning.

Another potentially fruitful research direction is to use social relationships in evaluating trust among collaborators in a group setting by employing the concept of *social networks*. Golbeck *et al.* [37][38][39] define a social network as a social structure of individuals who may be related directly or indirectly to each other in order to pursue common interests. Yu *et al.* [109] and Maheswaran *et al.* [110] use social networks to evaluate the trust value of a node. Examples of social networks are strong social relationships including colleagues or relatives, membership in the same platoon, and loose social relationships including school alumni or friends with common interests or membership in coalition activities. Social trust may include friendship, honesty, privacy, and social reputation or recommendation derived from direct or indirect interactions for "sociable" purposes. In MANETs, metrics used to measure these social trust properties can be frequency of communications, malicious or benign behaviors (e.g., false accusation or recommendation, impersonation), private information revealed, and quality of reputation. The notion of social trust is being incorporated into communication networks. Trust propagation models, some based on notions of social networking, have been proposed in multi-agent systems [114] [115] [116].

An important and interesting research direction is to construct a composite trust metric based on social trust and

other trust components representing quality-of-service (QoS) to successfully perform tasks to meet both performance and trust requirements. We have seen some work in the literature moving in this direction. Cho *et al.* considered honesty and intimacy (for social trust), and unselfishness and energy (for QoS trust) for trust evaluation [107]. Kohlas *et al.* [111] used honesty, competency, reliability, and maliciousness and their corresponding negations as trust components to define trust relationships. Yin *et al.* [112] computed composite reputation values of peers based on evidences from various domains such as customers' reputation scores or ranks in commercial sites or the certified roles in certain organizations with different weights indicating the importance and robustness of the reputation computation processes. Boursas and Hommel [113] considered QoS aspects such as the visual quality in multimedia and commitment in interactions to calculate node trust levels in large distributed systems. More work remains to be done to understand the best combination of social trust versus QoS trust components used to construct the composite trust metric, as well as the best weights associated with social trust and QoS trust, especially when given application context information for critical mission executions in MANETs.

Not much work has been done in trust management for mobile vehicular systems. A trust architecture for vehicular networks is proposed in [117] that incorporates a policy control model, a proactive trust model, and a social network based system, and takes into account dynamics. When the environment is volatile, associating trust with data becomes even more challenging; a solution is provided in [117] and a case study is discussed in the context of vehicular networks.

The overall qualities of trust in decision making depends on complex interactions between the information, social/cognitive, and communications networks. Trust metrics might be separately defined in each of the networks, but the key issue is to elucidate the mapping of qualitative and quantitative metrics across the networks, to define an end-to-end notion of composite trust, to determine the attributes (presumably many others than trust) in the different networks that affect this composite metric, and identify those that can be controlled and those that cannot [118], especially for trust management in a coalition environment [119].

We suggest that the following design concepts be considered for building MANET trust management systems:

- A trust metric must reflect the unique properties of trust in MANETs, including possibly imperfect transitivity, asymmetry, subjectivity, non-binary nature, decay over time and space, dynamicity, and context-dependency.
- A trust metric must incorporate adequate trust components (e.g., social trust and QoS trust) capable of reflecting mission difficulty (e.g., high risk upon task failure), changing network environments (e.g., lack of bandwidth, increasingly hostile environment as attackers' strength increases, high communication load), and conditions of participating nodes (e.g., low energy, compromised status).
- A trust management design must support cognitive functionality for each node to achieve adaptability to changing network conditions and MANET environments including

node density, node mobility patterns, scheduling algorithms, and traffic patterns.

- A trust management system should be situation specific or situation aware [120][121][122]. Situational awareness includes mission contexts and requirements in terms of security, performance and reliability. Depending on the required levels of security, performance and/or reliability, a different level of trust can be adopted reflecting mission contexts and situations.
- A trust metric must adequately reflect tradeoffs in altruism versus selfishness, trust versus reliability, availability, survivability, or security so as to contribute to improved system performance. In addition, since gathering information from spatially remote areas will consume more resources (e.g., time or energy) but improve decision making, one should investigate the tradeoff between resource consumption and decision making accuracy and timeliness. One may utilize aggregation technique to reduce resource consumption in obtaining information from distant nodes.
- A trust management design must allow optimal settings to be identified under various network and environmental conditions so as to maximize the overall trust of the system for successful mission executions. Equally important is an understanding of sensitivity to deviations from the optimal settings.
- There has been no comparison of trust management schemes versus conventional security schemes in terms of metrics of interest in MANETs. One example could be the comparison of trust management schemes to cryptographic schemes in detecting misbehaving nodes.
- Local trust is easy to understand and compute, since it only involves tracking behaviors of neighboring nodes. Local trust is easy to defend from malicious attacks. Global trust is harder to compute and update; Eigentrust [123] is an example of a global trust metric. But a non-local definition of trust is subject to subversion and manipulation by colluding nodes. Zhang *et al.* [124] provide a robust version of the Eigentrust algorithm. A critical question is: is trust inherently local? How can a global trust metric be computed and distributed reliably?
- Recently, social trust derived from social networks has received considerable attention for establishing trust in various applications. MANET designers may also want to take into account social trust.
- The survey has focused on a trust value associated with individual nodes. But often we may be interested in associating trust with data or with a group of nodes or entities. Many of the concepts discussed here will extend naturally.

VI. CONCLUDING REMARKS

Trust is a multidimensional, complex, and context-dependent concept. Although trust-based decision making is in our everyday life, trust establishment and management in MANETs face challenges due to the severe resource constraints, the open nature of the wireless medium, the complex dependence between the communications, social and application networks, and, hence, the complex dependency

of any trust metric on features, parameters, and interactions within and amongst these networks.

In this paper, we surveyed and analyzed existing trust management schemes in MANETs to provide MANET trust network protocol designers with multiple perspectives on the concept of trust, an understanding of trust properties that should be observed in developing trust metrics for evaluating trust, and insights on how a trust metric can be customized to meet the requirements and goals of the targeted system. A composite trust metric that captures aspects of communications and social networks, and corresponding trust measurement, trust distribution, and trust management schemes are interesting research directions. For dynamic networks, such as military MANETs, these schemes should have desirable attributes such as ability to adapt to environmental dynamics, scalability, reliability, and reconfigurability.

ACKNOWLEDGMENT

This project is supported in part by an appointment to the U.S. Army Research Laboratory Postdoctoral Fellowship Program administered by the Oak Ridge Associated Universities through a contract with the U.S. Army Research Laboratory. The authors appreciate the many discussions with and critical insights provided by our internal ARL staff including Elizabeth Bowman, Kevin Chan, Natalie Ivanic, and Brian Rivera. The authors also give special thanks to Dakshi Agrawal and Mudhakar Srivatsa from IBM T. J. Watson Research Center for their valuable comments.

APPENDIX

A SURVEY ON EXISTING TRUST MANAGEMENT SCHEMES IN MANETs

See Tables I-VI.

REFERENCES

- [1] S. Corson and J. Macker, "Mobile Ad Hoc Networking (MANET): Routing Protocol Performance Issues and Evaluation Considerations," RFC 2501, Jan. 1999.
- [2] J. Jubin and J. Tornow, "The DARPA Packet Radio Network Protocols," *Proc. IEEE*, vol. 75, no. 1, Jan. 1987, pp. 21-32.
- [3] A. J. Tardiff and J.W. Gowens, Editors, "ARL Advanced Telecommunication and Information Distribution Research Program (ATIRP)," *Final Report*, 1996-2001, June 2001.
- [4] T. Plesse, J. Lecomte, C. Adjih, M. Badel, P. Jacquet, A. Laouiti, P. Minet, P. Muhlethaler, and A. Plakoo, "OLSR Performance Measurement in a Military Mobile Ad Hoc Network," *Proc. 24th Int'l Conf. on Distributed Computing Systems*, 2004, pp. 704-709.
- [5] K. S. Cook (editor), *Trust in Society*, vol. 2, Feb. 2003, Russell Sage Foundation Series on Trust, New York.
- [6] M. Blaze, J. Feigenbaum, and J. Lacy, "Decentralized Trust Management," *Proc. IEEE Symposium on Security and Privacy*, 6-8 May, 1996, pp. 164 - 173.
- [7] R. B. Bobba, L. Eschenauer, V. Gligor, and W. Arbaugh, "Bootstrapping Security Associations for Routing in Mobile Ad Hoc Networks," *Proc. IEEE GLOBECOM*, San Francisco, CA, Dec. 2003, pp.1511-1515.
- [8] L. Eschenauer, V. D. Gligor, and J. Baras, "On Trust Establishment in Mobile Ad Hoc Networks," *Proc. 10th Int'l Security Protocols Workshop*, Cambridge, U.K., Apr. 2002, vol. 2845, pp. 47-66.
- [9] J. S. Baras and T. Jiang, "Managing Trust in Self-Organized Mobile Ad Hoc Networks," *Proc. 12th Annual Network and Distributed System Security Symposium Workshop*, Feb. 2005, San Diego, CA.
- [10] S. Ruhomaa and L. Kutvonen, "Trust Management Survey," P. Herrmann *et al.* (Eds.), *iTrust 2005, Lecture Notes in Computer Science*, vol. 3477, pp. 77-92.

TABLE I

Authors, Year, Ref. no	Purpose	Methodology	Attacks considered	Performance metrics	Trust property	Trust management model
Marti (2000) [67]	Secure routing	Direct observation Reputation	Black hole False accusation	Throughput Overhead Detection accuracy	Dynamicity	Watchdog and Pathrater Trust revocation introducing redemption Underlying routing protocol: DSR
Buchegger & Boudec (2002) [68]	Secure routing	Direct observation Reputation	Various malicious packet forwarding DoS	N/A	Weighted transitivity Dynamicity	An extension of DSR using a hybrid scheme of selective altruism and utilitarianism
Buchegger & Boudec (2002)[69]	Secure routing	Direct observation Reputation	Forward defection (e.g., route diversion)	Throughput Goodput Dropped packets Overhead Utility ^a	Weighted transitivity Dynamicity	CONFIDANT Bayesian Model Incentive mechanism No punishment against misbehaving nodes An extension of DSR
Paul & Westhoff (2002)[70]	Secure routing	Direct observation Reputation	Masquerading Packet modification	N/A	N/A	Contextaware Inference Mechanism An extension of DSR
Michiardi & Molva (2002) [71]	Secure routing	Direct observation Reputation	Selfish nodes False information propagation DoS attack	N/A	Dynamicity Subjectivity	Extension of [67] Functional trust concept introduced to combine subjective direct observation plus indirect information.
He <i>et al.</i> (2004)[72]	Secure routing	Direct observation Reputation	Packet dropping Selfish nodes Impersonation False information propagation	Throughput Overhead	Weighted transitivity	Secure and Objective Reputation-based Incentive (SORI) based on DSR Incentive mechanism
Nekkanti & Lee (2004)[73]	Secure routing	N/A	General outside attackers	Average endtoend delay Packet delivery ratio	Trust value ranges from 0 to 10 as an integer	Trust-based adaptive AODV
Li <i>et al.</i> (2004) [74]	Secure routing	Direct observation Recommendation	General malicious nodes	N/A	Dynamicity Asymmetry Weighted transitivity ^b	An extension of AODV using subjective logic

^a“Utility” metric refers to the ratio of the number of transmissions originated at the node itself to the number forwarded as an intermediate node on behalf of other nodes [69]. This metric can be represented as $A/(A+B)$ where A is the number of packets transmitted by a node for itself and B is the number of packets transmitted for others.

^b“Weighted transitivity” means that trust is transitive only with a weight reflecting decaying of trust depending on confidence level, credibility, reliability, time, reputation, distance, etc.

- [11] S. Ruhomaa, L. Kutvonen, and E. Koutrouli, “Reputation Management Survey,” *2nd Int’l Conf. on Availability, Reliability, and Security*, 10-13 Apr. 2007, Vienna, Austria, pp. 103-111.
- [12] T. Grandison and M. Sloman, “A Survey of Trust in Internet Applications,” *IEEE Commun. Surveys and Tutorials*, vol. 3, no. 4, pp. 2-16, 2000.
- [13] J. H. Cho and A. Swami, “Towards Trust-based Cognitive Networks: A Survey of Trust Management for Mobile Ad Hoc Networks,” *14th Int’l Command and Control Research and Technology Symposium*, Washington D.C. 15-17 June 2009.
- [14] Merriam Webster’s Dictionary [Online]: <http://www.merriamwebster.com/dictionary/trust%5B1%5D>.
- [15] D. Gambetta, “Can We Trust Trust?” *Trust: Making and Breaking Cooperative Relations*, Basil Blackwell, Oxford, 1990, pp. 213-237.
- [16] N. Luhmann, *Trust and Power*, Wiley, 1979.
- [17] W. J. Adams, N. J. Davis, “Toward a Decentralized Trust-based Access Control System for Dynamic Collaboration,” *Proc. 6th Annual IEEE SMC Information Assurance Workshop*, 15-17 June, 2005, West Point, NY, pp. 317-324.
- [18] T. Harford, “The Economics of Trust,” [Online]: http://www.forbes.com/2006/09/22/trust-economy-markets-tech_cx_th_06trust_0925harford.html
- [19] H. S. James, “The Trust Paradox: A Survey of Economic Inquiries into the Nature of Trust and Trustworthiness,” *Journal of Economic Behavior and Organization*, vol. 47, no. 3, 2002.
- [20] A. B. MacKenzie and S. B. Wicker, “Game Theory and the Design of Self-Configuring, Adaptive Wireless Networks,” *IEEE Commun. Mag.*, vol. 39, no. 11, pp. 126-131, Nov. 2001.
- [21] R. Axelrod, “The Evolution of Cooperation,” *Science*, vol. 211, no. 4489, pp. 1390-1396, March 1981.
- [22] M. Srivatsa, S. Balfé, K. G. Paterson, and P. Rohatgi, “Trust Management for Secure Information Flows,” *Proc. 15th ACM Conf. on Computer and Communications Security*, Alexandria, VA, Oct. 2008, pp. 175-188.
- [23] Stanford Encyclopedia of Philosophy, Feb. 20, 2006 [Online]: <http://plato.stanford.edu/entries/trust/>
- [24] B. Lahno, “Olli Lagerspetz: Trust. The Tacit Demand,” *Ethical Theory and Moral Practice*, vol. 2, no. 4, pp. 433-435, Dec. 1999, Published Springer Netherlands.
- [25] Wikipedia-Trust in Social Science, 16 Sept. 2009 [Online]: [http://en.wikipedia.org/wiki/Trust_\(sociology\)](http://en.wikipedia.org/wiki/Trust_(sociology))
- [26] M. Deutsch, *The Resolution of Conflict: Constructive and Destructive Processes*, Carl Hovland Memorial Lectures Series, New Haven and London: Yale University Press, 1973.
- [27] R. Hardin, “The Street-Level Epistemology of Trust,” *Politics and Society*, vol. 21, no. 4, 1993, pp. 505-529.
- [28] J. B. Rotter, “Interpersonal Trust, Trustworthiness, and Gullibility,” *American Psychologist*, vol. 35, no. 1, Jan. 1980, pp. 1-7.
- [29] D. McKnight and N. Chevany, “The Meanings of Trust,” Carlson School of Management, University of Minnesota, Technical Report TR 94-04, 1996.
- [30] F. D. Schoorman, R. C. Mayer, and J. H. Davis, “An Integrative

TABLE II

Authors, Year, Ref. no	Purpose	Methodology	Attacks considered	Performance metrics	Trust property	Trust management model
Pisinou <i>et al.</i> (2004) [75]	Secure routing	Direct observation	Black hole Route injection Selfish nodes	Route overhead Algorithm running time Number of routes selected Route errors sent	Transitivity Dynamicity	An extension of AODV called Trust-embedded AODV
Buchegger & Boudec (2004) [76]	Secure routing	Direct observation Reputation	False information propagation	Mean detection time for misbehaving nodes False alarm	Dynamicity	Bayesian Model Trust revocation introducing redemption
Ghosh (2005) [77]	Secure routing	Reputation Direct observation	Black hole Gray hole False accusation DoS	Overhead Routes selected Route errors	Weighted transitivity	Trust-embedded AODV (TAODV) Incentive mechanism
Wang <i>et al.</i> (2005) [78]	Secure routing	Direct observation Reputation	False accusation False information	Detection rate False alarm	N/A	Specification-based approach as an extension of AODV
Zouridaki <i>et al.</i> (2005) [79] (2006) [80]	Secure routing	Direct observation [79][80] Reputation by secondhand information [80]	Packet dropping Packet misrouting Packet injection Added in [2006] False accusation propagation Malicious node colluding Replay Duplicate packet forwarding	Confidence level over trust value Trustworthiness Opinion values about other nodes	Weighted transitivity Dynamicity	<i>Hermes</i> Bayesian Model Trust revocation introducing Window scheme to flush out stale trust information
Pirzada <i>et al.</i> (2006) [81]	Secure routing	Direct observation	Packet modification Black hole Gray hole	Packet loss Packet forwarded Throughput Overhead Latency Path optimality Detection probability	Dynamicity	Trust-based reactive routing protocols (DSR, AODV, TORA) Effortreturnbased trust model
Sun <i>et al.</i> (2006) [46]	Secure routing	Direct observation on packet dropping rate Recommendation	False recommendation Newcomer attack Sybil attack	Trust level Packet dropping ratio	Trust is a continuous value Subjectivity Asymmetry Weighted transitivity	Information theory-based modeling: Entropy-based trust model and Probability-based trust model

Model of Organizational Trust: Past, Present, and Future," *Academy of Management Review*, vol. 31, no. 2, 2007, pp. 344-354.

- [31] J. D. Lee and K. A. See, "Trust in Automation: Designing for Appropriate Reliance," *Human Factors*, vol. 46, no. 1, Spring 2004, pp. 50-80.
- [32] R. Parasuraman, "Humans and Automation: Use, Misuse, Disuse, Abuse," *Human Factors*, vol. 39, no. 2, 1997, pp. 230-253.
- [33] S. Staab (Editor), "The Pudding of Trust," *IEEE Intelligent Systems*, vol. 19, no. 5, pp. 74-88, 2004.
- [34] L. Capra, "Toward a Human Trust Model for Mobile Ad-hoc Networks," *Proc. 2nd UK-UbiNet Workshop*, 5-7 May 2004, Cambridge University, Cambridge, UK.
- [35] H. Li and M. Singhal, "Trust Management in Distributed Systems," *Computers*, vol. 40, no.2, Feb. 2007, pp. 45-53.
- [36] E. Aivaloglou, S. Gritxalis, and C. Skianis, "Trust Establishment in Ad Hoc and Sensor Networks," *Proc. 1st Int'l Workshop on Critical Information Infrastructure Security, Lecture Notes in Computer Science*, vol. 4347, pp. 179-192, Samos, Greece, 31 Aug. – 1 Sep. 2006, Springer.
- [37] J. Golbeck, "Computing with Trust: Definition, Properties, and Algorithms," *Securecomm and Workshops-Security and Privacy for Emerging Areas in Communications Networks*, Baltimore, MD, 28 Aug. – 1 Sep. 2006, pp. 1-7.
- [38] J. Golbeck and J. Hendler, "Inferring Trust Relationships in Web-based Social Networks," *ACM Transactions in Internet Technology*, Nov. 2006, vol. 6, no. 4, pp. 497-529.
- [39] J. Golbeck (Ed.), *Computing with Social Trust*, Human-Computer Interaction Series, Springer, 2009.
- [40] H. C. Wong, K. P. Sycara, "Adding Security and Trust to Multiagent

Systems," *Applied Artificial Intelligence*, vol. 14, no. 9, pp. 927-941, Oct. 2000.

- [41] A. Josang and S. LoPresti, "Analyzing the Relationship between Risk and Trust," *Proc. 2nd Int'l Conf. Trust Management*, LNCS, Springer-Verlag, 2004, pp. 135-145.
- [42] B. Solhaug, D. Elgesem, and K. Stolen, "Why Trust is not proportional to Risk?" *Proc. 2nd Int'l Conf. on Availability, Reliability, and Security*, 10-13 Apr. 2007, Vienna, Austria, pp. 11-18.
- [43] W. E. Walker, P. Harremoes, J. Rotmans, J. P. van der Sluijs, M. B. A. van Asselt, P. Janssen, and M.P. Kraye von Krauss, "Defining Uncertainty: A Conceptual Basis for Uncertainty Management in Model-based Decision Support," *Integrated Assessment*, vol. 4, no. 1, March 2003, pp. 5-17.
- [44] W. J. Adams, G. C. Hadjichristofi and N. J. Davis, "Calculating a Node's Reputation in a Mobile Ad Hoc Network," *Proc. 24th IEEE Int'l Performance Computing and Communications Conference*, Phoenix, AZ, 7-9 April 2005, pp. 303-307.
- [45] A. Abdul-Rahman and S. Hailes, "Using Recommendations for Managing Trust in Distributed Systems," *Proc. IEEE Malaysia Int'l Conf. on Communication*, Kuala Lumpur, Malaysia, Aug. 1997.
- [46] Y. L. Sun, W. Yu, Z. Han, and K. J. R. Liu, "Information Theoretic Framework of Trust Modeling and Evaluation for Ad Hoc Networks," *IEEE J. Sel. Areas Commun.*, vol. 24, no. 2, Feb. 2006, pp. 305-317.
- [47] C. R. Davis, "A Localized Trust Management Scheme for Ad Hoc Networks," *Proc. 3rd Int'l Conf. on Networking*, March 2004, pp. 671-675.
- [48] R. W. Thomas, L. A. DaSilva, and A.B. MacKenzie, "Cognitive Networks," *Proc. 1st IEEE Int'l Symposium on New Frontiers in Dynamic Spectrum Access Networks*, 8-11 Nov. 2005, pp. 352-360.

TABLE III

Authors, Year, Ref. no	Purpose	Methodology	Attacks considered	Performance metrics	Trust property	Trust management model
Abusalah <i>et al.</i> (2006) [81]	Secure routing	Direct observation on forwarding packets Recommendation Evidences	Packet dropping	Routing overhead Route discovery time	N/A	TARP (trustaware routing protocol)
Sen <i>et al.</i> (2006) [83]	Secure routing	Direct observation Evidences	False accusation Packet dropping Tampering	Packet dropping rate Reputation level	Dynamicity	Group trust value is used based on reputations for neighboring nodes
Soltanali <i>et al.</i> (2007) [84]	Secure routing	Reputation only based on direct and indirect observation	Selfish nodes	Throughput Detection percentage	Dynamicity Weighted transitivity Subjectivity	An extension of DSR with the components of monitor, reputation manager, opinion manager, routing and forwarding manager
Balakrishnan <i>et al.</i> (2007) [85]	Secure routing	Direct observation Recommendation	Packet dropping DoS (flooding) Routing information modification False accusation False recommendation	Packet delivery ratio Latency	Contextdependency Weighted transitivity Trust is a continuous value	Fellowship model using DSR
Li <i>et al.</i> (2008) [52]	Secure routing	Reputation Direct observation	Selective misbehaving Bad mouthing Onoff attack Conflicting behavior	Ratio of trustworthiness over reputation for both good and bad nodes	Weighted transitivity	Objective Trust Management Framework (OTMF) Modified Bayesian model
Mundinger & Boudec (2008) [86]	Secure routing	Direct observation Recommendation	False accusation /recommendation Freeriding	The incorrect reputation threshold point that does not affect the system performance	N/A	A general framework to evaluate robustness of reputation systems by analyzing them using deviation test.
Moe <i>et al.</i> (2008) [87]	Secure routing	Direct observation Recommendation	Selective packet dropping by selfish nodes DoS	Trustworthiness of a node	Dynamicity	Trustbased Secure Routing (TSR) An extension of DSR Incentive mechanism
Reidt <i>et al.</i> (2009) [88]	Secure routing	N/A (assume that information can be derived through observation or other mechanisms)	N/A	Communication cost Probability to reach Trust Authority (TA) nodes	N/A	A group of TA nodes are selected based on their reliability, energy level, and connectedness with the network.

- [49] Z. Liu, A. W. Joy, and R. A. Thompson, "A Dynamic Trust Model for Mobile Ad Hoc Networks," *Proc. 10th IEEE Int'l Workshop on Future Trends of Distributed Computing Systems*, Sushou, China, 26-28 May 2004, pp. 80-85.
- [50] G. Theodorakopoulos and J. S. Baras, "On Trust Models and Trust Evaluation Metrics for Ad Hoc Networks," *IEEE J. Sel. Areas Commun.*, vol. 24, no. 2, Feb. 2006.
- [51] R. Li, J. Li, P. Liu, H. H. Chen, "An Objective Trust Management Framework for Mobile Ad Hoc Networks," *Proc. IEEE 65th Vehicular Technology Conf.*, 22-25 Apr. 2007, pp. 56-60.
- [52] J. Li, R. Li, and J. Kato, "Future Trust Management Framework for Mobile Ad Hoc Networks: Security in Mobile Ad Hoc Networks," *IEEE Commun. Mag.*, vol. 46, no. 4, Apr. 2008, pp. 108-114.
- [53] F. Yunfang, "Adaptive Trust Management in MANETs," *Proc. 2007 Int'l Conf. on Computational Intelligence and Security*, Harbin, China, 15-19 Dec. 2007, pp. 804-808.
- [54] P. G. Argyroudis and D. O'Mahony, "Secure Routing for Mobile Ad Hoc Networks," *IEEE Commun. Surveys and Tutorials*, vol. 7, no. 3, pp. 2-21, 2005.
- [55] D. Djenouri, L. Khelladi and N. Badache, "A Survey of Security Issues in Mobile Ad Hoc and Sensor Networks," *IEEE Commun. Surveys and Tutorials*, vol. 7, no. 4, pp. 2-28, 2005.
- [56] B. Wu, J. Chen, J. Wu, and M. Cardei, "A Survey of Attacks and Countermeasures in Mobile Ad Hoc Networks," *Wireless Network Security-Signals and Communication Technology*, Part II, 2007, pp. 103-135, Springer U.S.
- [57] P. Kruus, D. Sterne, R. Gopaul, M. Heyman, B. Rivera, P. Budulas, B. Luu, T. Johnson, N. Ivanic, and G. Lawler, "In-Band Wormholes and Countermeasures in OLSR Networks," *Securecomm and Workshops 2006*, Baltimore, MD, 28 Aug. – 1 Sept. 2006, pp. 1-11.
- [58] R. Maheshwari and S. R. Jie Gao Das, "Detecting Wormhole Attacks in Wireless Networks Using Connectivity Information," *Proc. 26th IEEE Int'l Conf. on Computer Communications*, Anchorage, AK, 6-12 May 2007, pp. 107-115.
- [59] D. Sterne, G. Lawler, R. Gopaul, B. Rivera, K. Marcus, and P. Kruus, "Countering False Accusations and Collusion in the Detection of In-Band Wormholes," *Proc. 23rd Annual Computer Security Applications Conf.*, Miami Beach, FL, Dec. 2007, pp. 243-256.
- [60] Y. Hu and A. Perrig, "A Survey of Secure Wireless Ad Hoc Routing," *IEEE Security and Privacy*, vol. 2, no. 3, May 2004, pp. 28-39.
- [61] C. Kardof and D. Wagner, "Secure Routing in Wireless Sensor Networks: Attacks and Countermeasures," *Proc. 1st IEEE Int'l Workshop on Sensor Network Protocols and Applications*, Anchorage, AK, USA, 11 May 2003, pp. 113-117.
- [62] P. L. Campbell, "The Denial-of-Service Dance," *IEEE Security and Privacy*, vol. 3, no. 6, pp. 34-40, Nov./Dec. 2005.
- [63] G. C. Hadjichristofi, W. J. Adams, and N. J. Davis, "A Framework for Key Management in a Mobile Ad Hoc Network," *Proc. Int'l Conf. on*

TABLE IV

Authors, Year, Ref. no	Purpose	Methodology	Attacks considered	Performance metrics	Trust property	Trust management model
Adnane <i>et al.</i> (2009) [90]	Secure routing	Direct & indirect information Evidences (PKI)	Fake identity General malicious nodes	N/A	N/A	Extension of OLSR No specific trust metric shown
Ayachi <i>et al.</i> (2009) [89]	Secure routing	Direct information	Message replication/ forgery/modification	N/A	N/A	Extension of AODV No specific trust metric shown
Weimerskirch <i>et al.</i> (2001) [91]	Authentication	Recommendation References	Packet modification Breach of confidentiality DoS	N/A	Weighted transitivity	Distributed Trust Model
Verma <i>et al.</i> (2001) [92]	Authentication	Direct observation Indirect information	General inside and outside attackers	N/A	Transitivity	An extension of DSR and ZRP
Pirzada & McDonald (2004) [93]	Authentication	Direct observation	Packet modification Packet fabrication Impersonation	N/A	Weighted transitivity Dynamicity	An extension of DSR An extension of Marsh's trust model [125]
Davis (2004) [47]	Authentication	Evidence-based (i.e., certificates)	False accusation	N/A	N/A	Certificate issuance, storage, validation, and revocation are considered
Ngai & Lyu (2004) [94]	Authentication	Direct observation Recommendation	False certificate	Successful, failure, and unreachable rate for detecting false certificates	Trust is a continuous value Asymmetry	Distributed trust-based authentication
Albers <i>et al.</i> (2002) [95]	Intrusion Detection	Direct observation for anomaly detection or misuse detection Policybased	General misbehaving nodes	N/A	Symmetry	Local Intrusion Detection System (LIDS)
Ahmed <i>et al.</i> (2006) [96]	Intrusion Detection	Direct observation	Black hole Packet dropping Malicious flooding Routing loop	Overhead False alarm rate	N/A	Leverage IDS to evaluate trust level of other nodes
Gray <i>et al.</i> (2002) [97]	Access control	Policy-based (local and global policies)	Loss of authorization	Trust level per session	Context-dependency Weighted transitivity Trust is a continuous value	Trustbased admission control
Luo <i>et al.</i> (2004) [98]	Access control	Direct observation	General misbehaving nodes	Overhead Delay and number of retries before ticket is received	Dynamicity	URSA(Ubiquitous and Robust Access control) Localized group trust model based on threshold cryptography

Information Technology: Coding and Computing, Tiejun Huang, China, 4-6 April 2005, vol. 2, pp. 568-573.

- [64] Z. Yan, P. Zhang, and T. Virtanen, "Trust Evaluation Based Security Solutions in Ad Hoc Networks," *Proc. 7th Nordic Workshop on Security IT Systems*, Gjøvik, Norway, 15-17 Oct. 2003.
- [65] P. Resnick, R. Zeckhauser, E. Friedman, and K. Kuwabara, "Reputation Systems," *Communications of the ACM*, vol. 43, no. 12, pp. 45-48, 2000.
- [66] N. Bhalaji and A. Shanmugam, "Reliable Routing against Selective Packet Drop Attack in DSR based MANET," *Journal of Software*, vol. 4, no. 6, Aug. 2009, pp. 536-543.
- [67] S. Marti, T. Giuli, K. Lai, and M. Baker, "Mitigating Routing Misbehavior in Mobile Ad Hoc Networks," *Proc. 6th Annual ACM/IEEE Mobile Computing and Networking*, Boston, MA, Aug. 2000, pp. 255-265.
- [68] S. Buchegger and J. -Y. Le Boudec, "Node Bearing Grudges: Towards Routing Security, Fairness, and Robustness in Mobile Ad Hoc Networks," *Proc. IEEE 10th Euromicro Workshop on Parallel, Distributed, and Network-based Processing*, pp. 403-410, Canary Islands, Spain, Jan. 2002.
- [69] S. Buchegger and J. -Y. Le Boudec, "Performance Analysis of the CONFIDANT Protocol: Cooperation Of Nodes- Fairness In Dynamic

Ad-hoc NeTworks," *Proc. 3rd IEEE/ACM Symposium on Mobile Ad Hoc Networking and Computing*, Lausanne, CH, 9-11 June 2002, pp. 226-236.

- [70] K. Paul and D. Westhoff, "Context-Aware Detection of Selfish Nodes in DSR based Ad Hoc Networks," *Proc. IEEE Globecom Conf.*, Taipei, Taiwan, 2002.
- [71] P. Michiardi and R. Molva, "CORE: A Collaborative Reputation Mechanism to Enforce Node Cooperation in Mobile Ad Hoc Networks," *The 6th IFIP Conf. on Security Communications, and Multimedia*, Porotoz, Slovenia, 2002.
- [72] Q. He, D. Wu, and P. Khosla, "SORI: A Secure and Objective Reputation-based Incentive Scheme for Ad-Hoc Networks," *Proc. IEEE Wireless Communications and Networking Conf.*, vol. 2, pp. 825-830, March 2004.
- [73] R. K. Nekkanti and C. Lee, "Trust-based Adaptive On Demand Ad Hoc Routing Protocol," *Proc. 42th Annual ACM Southeast Regional Conf.*, Huntsville, Alabama, 2004, pp. 88-93.
- [74] X. Li, M. R. Lyu and J. Liu, "A Trust Model Based Routing Protocol for Secure Ad Hoc Networks," *Proc. 2004 IEEE Aerospace Conf.*, Bug Sky, Montana, 6-13 Mar. 2004, vol. 2, pp. 1286-1295.
- [75] N. Pisinou, T. Ghosh and K. Makki, "Collaborative Trust-based Routing in Multi-hop Ad Hoc Networks," *Proc. 3rd Int'l IFIP-TC06*

TABLE V

Authors, Year, Ref. no	Purpose	Methodology	Attacks considered	Performance metrics	Trust property	Trust management model
Adams & Davis (2005) [17]	Access control	Direct observation Reputation	General misbehaving nodes	N/A	Conditional transitivity ¹ Trust is a continuous value	Bayesian Model for risk assessment
Yunfang (2007) [53]	Access control	Direct observation Reputation Policybased	General misbehaving nodes	N/A	Weighted transitivity	Integrated (policy-based plus reputation-based) adaptive trust management
Virendra <i>et al.</i> (2005) [99]	Key Management	Direct/indirect observation	False key generation Compromise of other nodes' keys	N/A	Weighted transitivity Subjectivity Dynamicity Trust is a continuous value	Physical-Logical Trust Domains (PLTDs)
Hadjichristofi <i>et al.</i> (2005) [63]	Key Management	Direct observation Reputation	Stacking attack General malicious nodes	% of available nodes with capability of service provision Average shortest path % of isolated nodes Success ratio to obtain system service	Trust ranges from 1 to 100 Dynamicity	A modified hierarchical trust PKI model
Adams <i>et al.</i> (2005) [17]	Key Management Nonrepudiation	Direct observation Reputation	Selfish nodes Blackmailing Stacking attack	Trust value	Contextdependency Trust is a continuous number Subjectivity Dynamicity	Interpersonal trust model Redemption Simple weighted model
Li <i>et al.</i> (2006) [100]	Key Management	Direct observation	Fake certificate Tampering	Average overhead of the repository in each node	Transitivity	Localized Public-Key Management (LPM) Combining certificate chain and communication path based on PGP
Chang & Kuo (2009) [101]	Key Management	Direct observation	On-Off attack Conflicting behavior attack Newcomer attack Fake ID attack Cheating attack Collusion attack	Trust value Packet delivery ratio	Trust value is a discrete value	Markov chain trust model
Yan <i>et al.</i> (2003) [64]	Trust evaluation	Direct observation Reputation Recommendation	Black hole DoS	Planned metric: security level	Subjectivity Weighted transitivity	Personal Trusted Bubble (PTB)

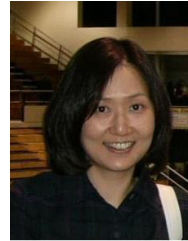
- Networking Conf., Lecture Notes in Computer Science*, Athens, Greece, 9-14 May 2004, vol. 3042, pp. 1446-1451.
- [76] S. Buchegger and J.Y.L. Boudec, "A Robust Reputation System for P2P and Mobile Ad-hoc Networks," *Proc. 2nd Workshop on the Economics of Peer-to-Peer Systems*, 15 Nov. 2004.
- [77] T. Ghosh, N. Pissinou, and K. Makki, "Towards Designing a Trust Routing Solution in Mobile Ad Hoc Networks," *Mobile Networks and Applications*, vol. 10, pp. 985-995, 2005.
- [78] B. Wang, S. Soltani, J. Shapiro, and P. Tab, "Local Detection of Selfish Routing Behavior in Ad Hoc Networks," *Proc. 8th Int'l Symposium on Parallel Architectures, Algorithms and Networks*, 7-9 Dec. 2005, pp. 392-399.
- [79] C. Zouridaki, B. L. Mark, M. Hejmo and R. K. Thomas, "Quantitative Trust Establishment Framework for Reliable Data Packet Delivery in MANETs," *Proc. 3rd ACM Workshop on Security for Ad Hoc and Sensor Networks*, Alexandria, VA, Nov. 7, 2005.
- [80] C. Zouridaki, B. L. Mark, M. Hejmo, and R. K. Thomas, "Robust Cooperative Trust Establishment for MANETs," *Proc. 4th ACM Workshop on Security of Ad Hoc and Sensor Networks*, Alexandria, VA, 30 Oct. 2006, pp. 23-34.
- [81] A. A. Pirzada and C. McDonald, "Establishing Trust in Pure Ad Hoc Networks," *Proc. 27th Australasian Computer Science Conf.*, vol. 26, pp. 47-54, 2004.
- [82] L. Abusalah, A. Khokhar, and M. Guizani, "A Survey of Secure Mobile Ad Hoc Routing Protocols," *IEEE Commun. Surveys and Tutorials*, vol. 19, no. 4, pp. 78-93, 2008.
- [83] J. Sen, P. Chowdhury, and I. Sengupta, "A Distributed Trust Mechanism for Mobile Ad Hoc Networks," *Int'l Symposium on Ad Hoc and Ubiquitous Computing*, 20-23 Dec. 2006. Surathkal, India, pp. 62-67.
- [84] S. Soltanali, S. Pirahesh, S. Niksefat, and M. Sabaei, "An Efficient Scheme to Motivate Cooperation in Mobile Ad Hoc Networks," *Int'l Conf. on Networking and Services*, Athens, Greece, 19-25 June 2007, pp. 98-103.
- [85] V. Balakrishnan, V. Varadarajan, U. K. Tupakula, and P. Lucs, "Trust and Recommendations in Mobile Ad Hoc Networks," *Int'l Conf. on Networking and Services*, Athens, Greece, 19-25 June 2007, pp. 64-69.
- [86] J. Munding and J. Le Boudec, "Analysis of a Reputation System for Mobile Ad Hoc Networks with Liars," *Performance Evaluation*, vol. 65, no. 3-4, pp. 212-226, Mar. 2008.
- [87] M. E. G. Moe, B. E. Helvik, and S. J. Knapkog, "TSR: Trust-based Secure MANET Routing using HMMs," *Proc. 4th ACM Symposium on QoS and Security for Wireless and Mobile Networks*, Vancouver, British Columbia, Canada, 27-28 Oct. 2008, pp. 83-90.
- [88] S. Reidt, S. D. Wolthusen, and S. Balf, "Robust and Efficient Communication Overlays for Trust Authority Computations," *Proc. 2009 IEEE Sarnoff Symposium*, March 2009.

TABLE VI

Authors, Year, Ref. no	Purpose	Methodology	Attacks considered	Performance metrics	Trust property	Trust management model
Jiang & Baras (2004) [103]	Trust evidence distribution	Evidence-based (certificates) Direct observation	General misbehaving nodes	Number of hops and delay to obtain the certificate Success rate obtaining the certificate		Ant-Based adaptive trust Evidence Distribution (ABED) based on a <i>swarm intelligence paradigm</i>
Baras & Jiang (2004) [104]	Trust computation	Local direct observation Evidencebased (certificates) Recommendation (i.e., voting)	General misbehaving nodes	Probability of having at least one secure path between trusted pairs percentage of trusted nodes in the network Time taken to converge to a steady state in trustworthiness of all nodes	Dynamicity	Distributed trust computation model using graph theory and random theory
Theodorakopoulos & Baras (2006) [50]	Trust evaluation	Direct observation Recommendation	False accusation Impersonation	Confidence level Opinions about other nodes	Transitivity Trust and confidence value is binary	Trust evaluation model based on <i>Semirings</i> theory
Boukerche & Ren (2008) [105]	Reputation evaluation	Direct observation Reputation	General misbehaving nodes	Query overhead Security overhead Percentage of packets Number of nodes Percentage of malicious nodes	Weighted transitivity	Generalized Reputation Evaluation (GRE) Prototype Groupbased trust model
Moloney & Weber (2005) [106]	General security level identification	Direct/indirect observation Recommendation	General misbehaving nodes	N/A	Context-dependency	Context-aware security system for MANETs
Cho <i>et al.</i> (2009) [107]	Battlefield trust establishment under no prior interactions	Direct/indirect observation Recommendation	General misbehaving nodes	Trust level	Dynamicity Weighted transitivity Context-dependency Asymmetry Subjectivity	Quantitative modeling technique used called hierarchical Stochastic petri nets

- [89] M. A. Ayachi, C. Bidan, T. Abbes, and A. Bouhoula, "Misbehavior Detection Using Implicit Trust Relations in the AODV Routing Protocol," *2009 Int'l Conf. on Computational Science and Engineering*, Vancouver, Canada, vol. 2, 29-31 Aug. 2009, pp. 802-808.
- [90] A. Adnane, C. Bidan, R. T. de Sousa, "Trust-based Countermeasures for Securing OLSR Protocol," *2009 Int'l Conf. on Computational Science and Engineering*, Vancouver, Canada, vol. 2, 28-31 Aug. 2009, pp. 745-752.
- [91] A. Weimerskirch and G. Thonet, "A Distributed Light-Weight Authentication Model for Ad-hoc Networks," *Proc. of 4th Int'l Conf. on Information Security and Cryptology*, 6-7 Dec. 2001.
- [92] R. R. S. Verma, D. O'Mahony and H. Tewari, "NTM – Progressive Trust Negotiation in Ad Hoc Networks," *Proc. 1st Joint IEI/IEEE Symposium on Telecommunications Systems Research*, Dublin, Ireland, 27 Nov. 2001.
- [93] A. A. Pirzada, C. McDonald, and A. Datta, "Performance Comparison of Trust-based Reactive Routing Protocols," *IEEE Trans. Mobile Comput.*, vol. 5, no. 6, June 2006, pp. 695-710.
- [94] E. C. H. Ngai and M. R. Lyu, "Trust and Clustering-based Authentication Services in Mobile Ad Hoc Networks," *Proc. 24th Int'l Conf. on Distributed Computing Systems Workshops*, 23-24 March 2004, pp. 582-587.
- [95] P. Albers, O. Camp, J.-M. Percher, B. Jouga, L. Me, R. Puttini, "Security in Ad Hoc Networks: a General Intrusion Detection Architecture Enhancing Trust Based Approaches", *Proc. 1st Int'l Workshop on Wireless Information Systems*, Apr. 2002, pp. 1-12.
- [96] E. Ahmed, K. Samad and W. Mahmood, "Cluster-based Intrusion Detection (CBID) Architecture for Mobile Ad Hoc Networks." *AusCERT Asia Pacific Information Technology Security Conf.*, Gold Coast, Australia, 21-26 May 2006.
- [97] E. Gray, P. O'Connell, C. Jensen, a. Weber, J.-M. Seigneur, and C. Yong, "Towards a Framework for Assessing Trust-based Admission Control in Collaborative Ad Hoc Applications," *Technical Report*, TCD-CS-2002-66, Trinity College Dublin, 2002.
- [98] H. Luo, J. Kong, P. Zerfos, S. Lu, and L. Zhang, "URSA: Ubiquitous and Robust Access Control for Mobile Ad Hoc Networks," *IEEE/ACM Trans. Netw.*, vol. 12, no. 6, Dec. 2004, pp. 1049-1063.
- [99] M. Virendra, M. Jadliwala, M. Chandrasekaran, and S. Upadhyaya, "Quantifying Trust in Mobile Ad-Hoc Networks," *Proc. Int'l Conf. Integration of Knowledge Intensive Multi-Agent Systems*, 18-21 April 2005, pp. 65-70.
- [100] R. Li, J. Li, P. Liu, and H. H. Chen, "On Demand Public Key Management for Mobile Ad Hoc Networks," *Wiley's Wireless Communications and Mobile Computing*, May 2006, vol. 6, no. 3, pp. 295-306.
- [101] B. J. Chang and S. L. Kuo, "Markov Chain Trust Model for Trust Value Analysis and Key Management in Distributed Multicast MANETs," *IEEE Trans. Veh. Technol.*, vol. 58, no. 4, May 2009, pp. 1846-1863.
- [102] A. Hegland, E. Winjum, S. F. Mjolsnes, C. Rong, O. Kure and P. Spilling, "A Survey of Key Management in Ad Hoc Networks," *IEEE Commun. Surveys and Tutorials*, vol. 8, no. 3, pp. 48-66, 2006.
- [103] T. Jiang and J. S. Baras, "Ant-based Adaptive Trust Evidence Distribution in MANET," *Proc. 2nd Int'l Conf. on Mobile Distributed Computing Systems Workshops*, Tokyo, Japan, 23-24 March 2004, pp.588-593.

- [104] J. S. Baras and T. Jiang, "Cooperative Games, Phase Transition on Graphs and Distributed Trust in MANETs," *Proc. 43th IEEE Conf. on Decision and Control*, Atlantis, Bahamas, 14-17 Dec. 2004, vol. 1, pp. 93-98.
- [105] A. Boukerche and Y. Ren, "A Security Management Scheme using a Novel Computational Reputation Model for Wireless and Mobile Ad Hoc Networks," *Proc. Int'l Workshop on Modeling Analysis and Simulation of Wireless and Mobile Systems*, Vancouver, British Columbia, Canada, pp. 88-95, 2008.
- [106] M. Moloney and S. Weber, "A Context-aware Trust-based Security System for Ad Hoc Networks," *Proc. 1st Int'l Conf. on Security and Privacy for Emerging Areas in Communication Networks-Workshop*, 5-9 Sept. 2005, pp. 153-160.
- [107] J. H. Cho, A. Swami and I.R. Chen, "Modeling and Analysis of Trust Management for Cognitive Mission-driven Group Communication Systems in Mobile Ad Hoc Networks," *2009 Int'l Conf. on Computational Science and Engineering*, vol. 2, Vancouver, Canada, 29-31 Aug. 2009, pp. 641-650.
- [108] Q. Mahmoud (Editor), "Cognitive Networks: Towards Self-Aware Networks," Wiley, Sept. 2007.
- [109] H. Yu, M. Kaminsky, P. B. Gibbons, and A. D. Flaxman, "SybilGuard: Defending Against Sybil Attacks via Social Networks," *IEEE/ACM Trans. Netw.*, vol. 16, no. 3, June 2008, pp. 576-589.
- [110] M. Maheswaran, H. C. Tang, and A. Ghunaim, "Toward a Gravity-based Trust Model for Social Networking Systems," *Proc. 27th Int'l Conf. on Distributed Computing Systems Workshops*, 22-29 June 2007, pp. 24-31.
- [111] R. Kohlas, J. Jonczyk, and R. Haenni, "A Trust Evaluation Method Based on Logic and Probability Theory," *Trust Management II: IFIP Int'l Federation for Information Processing*, vol. 263, 2008, Springer Boston.
- [112] G. Yin, D. Shi, H. Wang, and M. Guo, "RepCom: Towards Reputation Composition over Peer-to-Peer Communities," *2009 Int'l Conf. on Computational Science and Engineering*, vol. 2, Vancouver, Canada, 29-31 Aug. 2009, pp. 765-771.
- [113] L. Boursas and W. Hommel, "Multidimensional Dynamic Trust Management for Federated Services," *2009 Int'l Conf. on Computational Science and Engineering*, vol. 2, Vancouver, Canada, 29-31 Aug. 2009, pp. 684-689.
- [114] R. Guha, R. Kumar, P. Raghavan, and A. Tomkins, "Propagation of Trust and Distrust," *Proc. 13th Int'l Conf. on World Wide Web*, New York, NY, 19-21 May 2004, pp. 403-412.
- [115] Y. Wang and M. P. Singh, "Trust Representation and Aggregation in a Distributed Agent System," *Proc. 21st National Conf. on Artificial Intelligence (AAAI)*, 2006, Boston, MA, pp. 1425-1430.
- [116] Y. Wang and M. P. Singh, "Formal Trust Model for Multiagent Systems," *Proc. 20th Int'l Joint Conf. on Artificial Intelligence*, Jan. 2007, pp. 1551-1556.
- [117] X. Hong, D. Huang, M. Gerla, and Z. Cao, "SAT: Building New Trust Architecture for Vehicular Networks," *ACM SIGCOMM 3rd Int'l Workshop on Mobility in the Evolving Internet Architecture*, Seattle, WA, 22 Aug. 2008.
- [118] U. S. Army Research Laboratory, Program Announcement for Network Science CTA, [Online]: <http://www.arl.army.mil/www/DownloadedInternetPages/CurrentPages/CTA/Documents/NSCTAFINAL23JAN09.pdf>, 23 Jan. 2009.
- [119] D. Agrawal, H. Chivers, J. Clark, C. Jutla, and J. McDermid, "A Proposal for Trust Management in Coalition Environments," *26th Army Science Conf.*, 14 Dec. 2008.
- [120] M. Blaze, S. Kannan, I. Lee, O. Sokolsky, J.M. Smith, A.D. Keromytis, and W. Lee, "Dynamic Trust Management," *Computer*, vol. 42, no. 2, Feb. 2009, pp. 44-52.
- [121] M. Tavakolifard, "Situation-aware Trust Management," *Proc. 2009 ACM Conf. on Recommender Systems*, New York, USA, Oct. 2009, pp. 413-416.
- [122] M. Tavakolifard, P. Herrmann, and S. J. Knapkog, "Inferring Trust based on Similarity with TILLIT," *Proc. 3rd IFIP WG 11.11 International Conference on Trust Management (IFIPTM 2009)*, *IFIP Advances in Information and Communication Technology: Trust Management III*, vol. 300, Springer Boston, West Lafayette, USA, June 2009, pp. 138-148.
- [123] S. D. Kamvar, M. T. Schlosser, and H. Garcia-Molina, "The Eigentrust Algorithm for Reputation Management in P2P Networks," *Proc. 12th Int'l Conf. on World Wide Web*, New York, NY, 20-23 May 2003, pp. 640-651.
- [124] H. Zhang, A. Goel, R. Govindan, K. Mason, and B. Van Roy, "Making Eigenvector-based Reputation Systems Robust to Collusion," *Proc. 3rd Int'l Workshop on Algorithms and Models for the Web-Graph*, LNCS, vol. 3243, Oct. 2004, pp. 92-104.
- [125] S. Marsh, "Formalizing Trust as a Computational Concept," Ph. D. Dissertation, *Department of Mathematics and Computer Science*: University of Stirling, 1994.



Jin-Hee Cho received her BA from Ewha Womans University, and MA from Washington University in St. Louis, MO in 1997, and 1999 respectively. She also received her MS, and PhD in Computer Science from Virginia Tech in 2004, and 2008 respectively. She received an IREAN fellowship through the NSF IGERT program during her Ph.D. study and a postdoctoral research fellowship through the Army Research Laboratory/Oak Ridge Associated Universities postdoctoral fellowship program from January 2009 to June 2010. After then, she joined ARL,

Adelphi, MD as a computer scientist in the Network Science Division, Computational and Information Sciences Directorate. Her research interests include wireless mobile networks, mobile ad hoc networks, sensor networks, secure group communications, group key management, network security, intrusion detection, performance analysis, trust management, social/cognitive networks, and network economic modeling. She is a member of the IEEE and ACM.



Ananthram Swami received the B.Tech. degree from the Indian Institute of Technology (IIT), Bombay; the M.S. degree from Rice University, Houston, TX, and the Ph.D. degree from the University of Southern California (USC), Los Angeles, all in electrical engineering.

He has held positions with Unocal Corporation, USC, CS-3 and Malgudi Systems. He was a Statistical Consultant to the California Lottery, developed HOSAT, a MATLAB-based toolbox for non-Gaussian signal processing, and has held visiting faculty positions at INP, Toulouse, France. He is the ST for Network Science at the U.S. Army Research Laboratory. His work is in the broad areas of signal processing, wireless communications, sensor and mobile ad hoc networks. He is co-editor of the book *Wireless Sensor Networks: Signal Processing and Communications Perspectives* (New York: Wiley, 2007).

Dr. Swami is a member of the IEEE Signal Processing Society's (SPS) Technical Committee on Sensor Array and Multichannel systems and serves on the Senior Editorial Board of the IEEE Journal on Selected Topics in Signal Processing. He was a tutorial speaker on Networking Cognitive Radios for Dynamic Spectrum Access at IEEE ICC 2010, co-chair of IEEE SPAWC'10, and has served on the IEEE SPS BoG.



Ing-Ray Chen received the BS degree from the National Taiwan University, Taipei, Taiwan, and the MS and PhD degrees in computer science from the University of Houston. He is a professor in the Department of Computer Science at Virginia Tech. His research interests include mobile computing, wireless networks, security, fault tolerance, multimedia, trust management, real-time intelligent systems, and performance analysis. Dr. Chen currently serves as an editor for *The Computer Journal*, *Wireless Personal Communications*, *Wireless Communica-*

tions and Mobile Computing, *Security and Communication Networks*, and *International Journal on Artificial Intelligence Tools*. He is a member of the IEEE and ACM.

Temporal Complexity of the Order Parameter at the Phase Transition

Malgorzata Turalska, Bruce J. West, and Paolo Grigolini

Physical Review E, 83, 061142 (2011)

Temporal complexity of the order parameter at the phase transition

Malgorzata Turalska,¹ Bruce J. West,² and Paolo Grigolini¹

¹*Center for Nonlinear Science, University of North Texas, P.O. Box 311427, Denton, Texas 76203-1427, USA*

²*Information Science Directorate, US Army Research Office, Durham, North Carolina 27709, USA*

(Received 9 February 2011; revised manuscript received 25 April 2011; published 24 June 2011)

We study a decision making model in a condition where it is equivalent to the two-dimensional Ising model, and we show that at the onset of phase transition it generates temporal complexity, namely, nonstationary and nonergodic fluctuations. We argue that this is a general property of criticality, thereby opening the door to the application of the recently discovered phenomenon of complexity matching: For an efficient transfer of information to occur, a perturbing complex network must share the same temporal complexity as the perturbed complex network.

DOI: [10.1103/PhysRevE.83.061142](https://doi.org/10.1103/PhysRevE.83.061142)

PACS number(s): 05.40.-a, 05.10.-a, 05.50.+q, 05.70.Jk

I. INTRODUCTION

Phase transitions and critical phenomena occur frequently in nature and have been widely studied by physicists, see for instance [1]. The Ising model [2] originally introduced to explain ferromagnetic phase transition is well known, and the exact solution found by Onsager [3] for the occurrence of phase transition in the two-dimensional case is widely recognized as an example of outstanding theoretical achievement. In the last few years some scientists have used the Ising model to shed light on biological and neurophysiological processes [4–7]. More precisely, the authors of [4] used the Ising model to explain the collective behavior of biological networks and the authors of [5–7] adopted the Ising model for the purpose of supporting their hypothesis that the brain works at criticality without establishing a clear distinction between phase transition and self-organized criticality [8]. Finally, we have to mention that the Ising model is frequently used, see for instance [9,10], to model neurophysiological data with the constraint of maximal entropy. Although relevant to explore the cognition properties of the brain, this is a perspective different from the one adopted in this paper.

Couzin [11] made the conjecture that the cooperative interaction between the birds of a flock may mimic the brain cognition properties, and the experimental observation of Cavagna *et al.* [12] confirmed the criticality condition of a coordinated flock of birds. It is important to emphasize that the connection between phase transition processes and cooperative behavior of biological systems was already stressed in the pioneering paper of Vicsek *et al.* [13]. It is thought [4] that biological systems in general operate at criticality.

The phase transition condition is not confined to biological systems. The recent work on econophysics [14,15] suggests that the same arguments can be applied to sociological systems. As a matter of fact, Sornette [15] proposes a model of cooperative economical interaction, of the same type as the Ising model, which generates at criticality a transition from subcritical to supercritical patterns very similar to those produced by the Ising model. As stressed by the authors of [5], the Ising patterns at criticality correspond to the emergence of correlation links yielding a scale-free network statistically indistinguishable from that experimentally observed within the brain, using functional magnetic resonance imaging.

These studies emphasize the spatial and network complexity emerging from the cooperative interaction of the network's units, but overlook the temporal complexity of these networks. Herein we are attempting to fill this gap and prove that the temporal complexity emerges at criticality. Temporal complexity is defined as follows. The time dynamics of complex networks is characterized by the occurrence of significant events, which may be financial crashes [15], brain quakes [5,6], or the changes of direction of a flock of birds [12,13]. The time interval between two consecutive events is given by a distribution density $\psi(t)$, which, drastically departing from the conventional Poisson statistics, has the inverse-power-law form

$$\psi(\tau) \propto \frac{1}{\tau^\mu}, \quad (1)$$

with $\mu < 2$. The occurrence of an event does not have any memory of the occurrence of earlier events. This property is usually denoted as renewal, but it must not be confused with the ordinary Poisson and Markov condition: The signal generated by these events is characterized by long-range correlation in time, and, most importantly, it is essentially nonstationary, thereby breaking the ergodicity that is a fundamental property of statistical physics [16]. We refer to it as the non-Poisson renewal condition. A significant event is interpreted as a failure whose occurrence brings the network back to a brand new condition. We refer to these as *crucial events*.

Events of this kind may be very difficult to detect. The theoretical discussion [16], for instance, applies to the case of dichotomous signals, where crucial events correspond to the abrupt transition from one to the other value of the signal. In the case of the decision making model (DMM) under study, the single units in isolation produce perfect dichotomous signals. They can be easily detected, but they are of a Poisson kind, thereby strikingly departing from the condition of temporal complexity. When the control parameter is extremely large, the global signal undergoes abrupt transitions that however depart again from the condition of temporal complexity, because they are predominantly of a Poisson kind. At criticality the global signal loses these abrupt transitions that are replaced by smoother fluctuations around the mean value. Herein we consider a model generating a signal whose time mean value vanishes. We assume the crossing of the origin to be the proxy of a significant event. Thus, we interpret the signal as a

dichotomous fluctuation making abrupt changes from 1 to -1 and back again. We evaluate the correlation function of this ideal dichotomous signal, denoted by the symbol $\Psi(t, t')$, and we prove that its dependence on the times t and t' exactly fits the prediction of the non-Poisson renewal condition.

The connection between phase transition, and its spatial and network complexity, with temporal complexity is not well known. In the literature there are only a few papers where this connection is discussed. One is [17], which converts the 3D Ising model into a critical map generating type I intermittent dynamics and consequently the same temporal complexity as the one under discussion herein. The emergence of non-Poisson renewal properties was also discussed in [18,19], which is devoted to illustrating the cooperative properties of a DMM. The foundation of these papers is sociological and similar to that of the economical model illustrated in the work of Sornette [15]. Thus, the authors [18,19] did not discuss the connection of the DMM with the Ising model and adopted the nonrealistic but often made assumption of all-to-all coupling among the network's units, thereby confining the emergence of an inverse power law, namely, of temporal complexity, to the same time scale as that of the units in isolation.

The motivation for the present research work is given by the transfer of information from a complex network to another complex network [20]. Rather than using entropic arguments, as is usually done with the transfer of information, we open the door to the concept of complexity management recently advocated in [21]. This latter work established that a complex network driven by crucial events is sensitive to stimuli with the same complexity. In other words, the transfer of information rests on temporal complexity and this explains the motivation to prove that criticality also generates temporal complexity.

In Sec. II we discuss under which conditions the DMM [18, 19] is equivalent to the Ising model. In Sec. III we prove that at criticality the function $\psi(t)$ becomes an inverse power law for over four decades. We shall also argue that with increasing the network's size $\psi(t)$ may become an infinitely extended inverse power law. Section IV shows that this is a renewal process. Finally we devote Sec. V to concluding remarks.

II. DETAILED DESCRIPTION OF THE MODEL

We consider a system of L discrete variables located at the nodes of a two-dimensional square lattice. Each unit s_i is a stochastic oscillator and can be found in either of two states, $+1$ or -1 . The dynamic is introduced by choosing a single unit on site i and updating it in an elementary time step with a transition rate g :

$$g(s_i^{+1} \rightarrow s_i^{-1}) = g_0 \exp \left[\frac{K}{M} (M_{+1} - M_{-1}) \right], \quad (2)$$

$$g(s_i^{-1} \rightarrow s_i^{+1}) = g_0 \exp \left[-\frac{K}{M} (M_{+1} - M_{-1}) \right]. \quad (3)$$

Here M denotes the total number of nearest neighbors, and M_{+1} and M_{-1} the number of nearest neighbors being in the state $+1$ and -1 , respectively. Single units change its states, thereby making M_{+1} and M_{-1} fluctuate in time, while, of course, the total number of nearest neighbors is conserved, $M_{+1} + M_{-1} = M$.

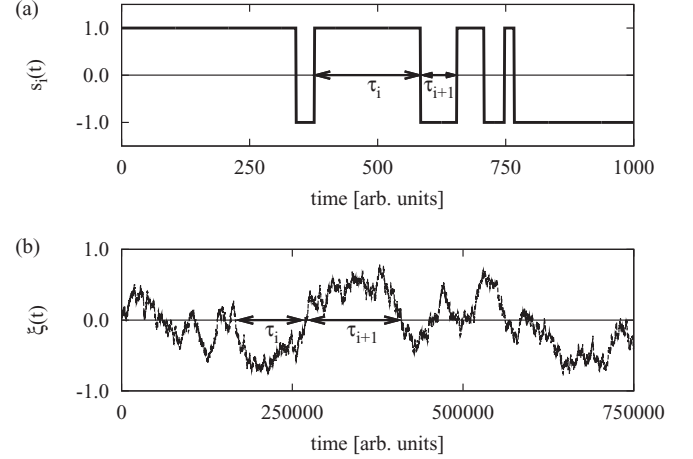


FIG. 1. (a) Temporal evolution of a single unit $s_i(t)$ and (b) of the global order parameter $\xi(t)$ for the decision making model realized on a square lattice of $L = 50 \times 50$ nodes, with $g_0 = 0.01$ and $K = 1.70$. To illustrate the concept of crucial events we mark the time intervals τ between two consecutive events, according to their definitions assumed in this paper. Notice different time scales on both plots.

All numerical calculation are performed on a square lattice of either $L = 50 \times 50$ or $L = 100 \times 100$ nodes with periodic boundary conditions. In a single time step a run over the whole lattice is performed and for every unit s_i the transition rate of Eqs. (2) or (3) is calculated according to which a node is given the possibility to change its state. The single unit in isolation, $K = 0$, fluctuates between states $+1$ and -1 with the transition rate $g = g_0$. When coupling constant $K > 0$, a unit in the state $+1$ (-1) makes a transition to the state -1 ($+1$) faster or slower according to whether $M_{-1} > M_{+1}$ ($M_{+1} > M_{-1}$) or $M_{-1} < M_{+1}$ ($M_{+1} < M_{-1}$), respectively.

Next, we define the global order parameter $\xi(t) = \frac{1}{L} \sum_{i=1}^L s_i(t)$, which is characterized by the variability that does not possess the dichotomous character of single units. In Fig. 1 we show exemplary temporal evolution for the single unit $s_i(t)$ and for the global order parameter $\xi(t)$. Note that the amplitude of variable $\xi(t)$ depends on the value of the coupling constant K . When $K = 0$, all units in the system are independent Poisson processes; thereby an average taken at any moment of time over all of them is zero. Once the value of the coupling increases, $K > 0$, single units are less and less independent, resulting in a nonzero average. The quantity K_C is the critical value of the control parameter K , at which point a phase transition to a global majority state occurs. In numerical calculations we use the time average $\xi_{eq} = \langle |\xi(t)| \rangle$ as a measure of this global majority. More precisely, after initial 10^6 time steps, the average is taken over the same number of the consecutive time steps of the model.

Note that in the special case when M is the same for all the nodes and $g_0 \ll 1$, we find that our model generates the same phase transition as the two-dimensional Ising model discussed in the seminal paper of Onsager [3]. This is an expected result insofar as the Ising model rests on the Hamiltonian

$$H = -J \sum_i^L \sigma_i \sigma_j, \quad (4)$$

where σ_i and σ_j denote the Pauli operators with eigenvalues ± 1 . According to Boltzmann statistics equilibrium is described by the density matrix

$$\rho = \frac{\exp(-\beta H)}{Z}, \quad (5)$$

with $\beta = \frac{1}{k_B T}$, k_B being the Boltzmann constant and T the absolute temperature. Thus, the off-diagonal elements of the transfer matrix [22] become equivalent to the transition rates of Eqs. (2) and (3), under the condition

$$k_B T = \frac{J}{K} = \frac{M}{K}. \quad (6)$$

As examples of conditions yielding this equivalence, we consider two cases. The former is the case of all-to-all coupling, where $M = L$. The latter is considered here, and it is the two-dimensional lattice where each node is coupled to its 4 nearest neighbors, thereby setting $M = 4$.

The thermodynamical condition $M = L = \infty$ was discussed extensively by authors of [18,19], who showed that under those conditions the ratios $\frac{M_{\pm 1}}{M}$ are equivalent to the probabilities $p_{\pm 1}$ for a node s_i to be in one of two allowed states. The dynamic evolution of a single unit state is then described by a two-state master equation

$$\frac{d}{dt} p_{+1} = -g(s_i^{+1} \rightarrow s_i^{-1})p_{+1} + g(s_i^{-1} \rightarrow s_i^{+1})p_{-1}, \quad (7)$$

$$\frac{d}{dt} p_{-1} = -g(s_i^{-1} \rightarrow s_i^{+1})p_{-1} + g(s_i^{+1} \rightarrow s_i^{-1})p_{+1}. \quad (8)$$

Solving the above for the difference in probabilities $\Pi(t) = p_{+1}(t) - p_{-1}(t)$, which corresponds to the earlier defined global order parameter $\xi(t)$, one obtains

$$\frac{d}{dt} \Pi = 2g_0[\sinh(K\Pi) - \Pi \cosh(K\Pi)]. \quad (9)$$

This equation yields two solutions, corresponding to global majority states, for the values of coupling constant $K > K_C$, where $K_C = 1$.

The solution to the latter condition of $M = 4$, $L = \infty$ can be found in [23] and yields the condition for the global variable to be $\xi_{eq} = (1 - [\sinh(K/2)]^{-4})^{1/8}$. In this case the critical value of the coupling constant is $K_C = 2 \ln(1 + \sqrt{2}) = 1.7627$. In Fig. 2, we show the phase diagram in the latter condition and we find that, as expected, the numerical evaluation of $\xi_{eq}(K)$ is very close to the theoretical prediction of Onsager [3], thereby confirming that the DMM is equivalent to the Ising model in the limiting case $g_0 \rightarrow 0$.

This equivalence between the DMM and the Ising model is merely formal, because the DMM does not have a Hamiltonian origin and does not require the action of a thermal bath at temperature T to work as does the Boltzmann picture. This explains why the equivalence with the Ising model requires that g_0 vanish, so as to freeze the dynamics of the single units, in the absence of cooperation.

When we release the condition $g_0 \rightarrow 0$, the equivalence of the DMM with the Ising model is lost. In Fig. 3, we see that, if the condition of $g_0 \ll 1$ is abolished, the phase transition emerges at values of K lower than K_C of the theoretical prediction. Simultaneously, further increase of g_0 ($g_0 \approx 0.40$) leads to a new regime, in which every unit is surrounded by

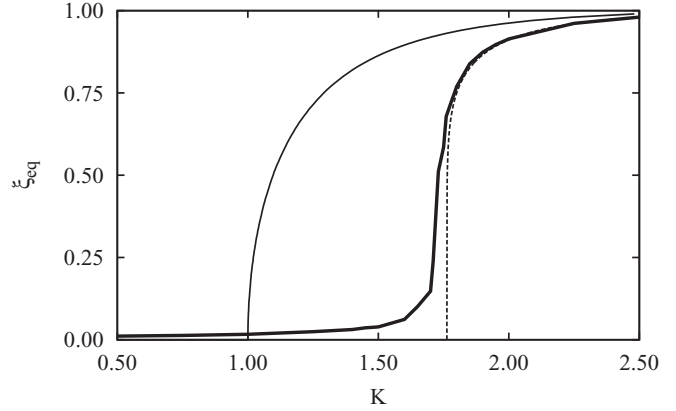


FIG. 2. The phase diagram for global variable ξ_{eq} . Thin solid line and dashed line are the theoretical predictions for the fully connected and two-dimensional regular network, respectively. In both cases $L = \infty$ and the latter case is the Onsager theoretical prediction [3] for 2D regular lattice. The thick solid line corresponds to the global states observed for two-dimensional regular lattice ($L = 100 \times 100$ nodes) and $g_0 = 0.01$. Periodic boundary conditions were applied.

nearest neighbors in the opposite state, yielding an update of its state at every time step and generating the condition in which the order parameter $\xi(t)$ is exactly zero at all times. It is worth pointing out that when a network characterized by a large transition rate g (transition rate $g \approx 1$) is studied, it shows sensitivity to the initial random configuration of the lattice. We observed that in a limited number of cases the order parameter evolves to a global majority state, in which all the nodes are in the same state rather than in condition $\xi(t) = \xi_{eq} = 0$. Therefore one may consider a bifurcation in the phase space of the model parameters in this regime.

III. ORDER PARAMETER REVERSAL TIMES

Let us now study the temporal complexity of the order parameter $\xi(t)$. As pointed out in Sec. I, to prove temporal complexity of $\xi(t)$ we have to observe significant events and prove that they are crucial. At criticality the signal is not dichotomous and, as we shall see hereby, there are good reasons why it *must depart from the dichotomous condition*.

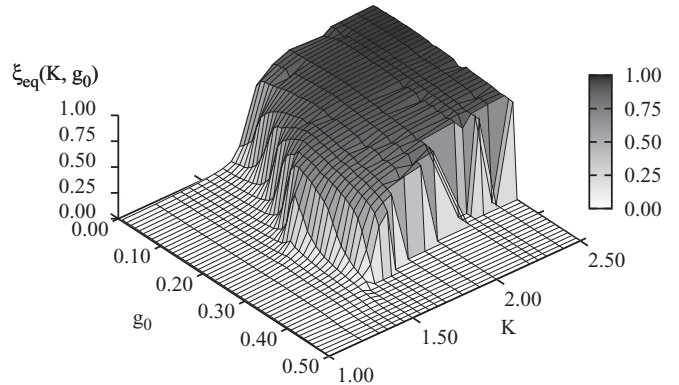


FIG. 3. The two-dimensional phase diagram of global variable ξ_{eq} evaluated for a range of model parameters, g_0 and K , on a two-dimensional regular lattice of size $L = 100 \times 100$ nodes.

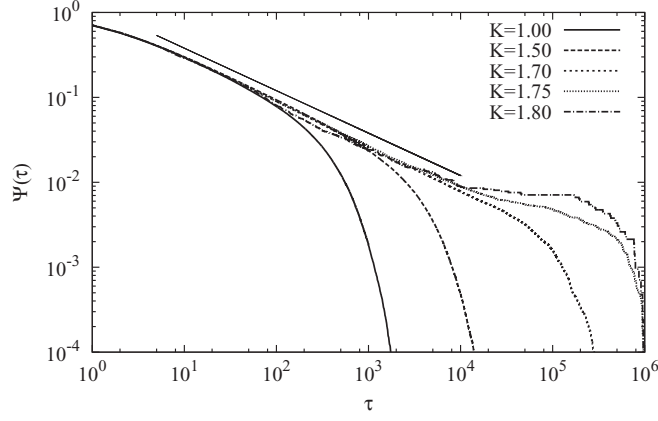


FIG. 4. Survival probability function $\Psi(\tau)$ for the order parameter $\xi(t)$ evaluated on a two-dimensional lattice of size $L = 50 \times 50$ for $g_0 = 0.01$ and increasing values of coupling constant K . The straight line corresponds to the slope of -0.50 , namely to $\mu = 1.50$, since $\Psi(\tau) \sim \frac{1}{\tau^{\mu-1}}$.

We make the conjecture that the crossing of the origin, namely the times at which $\xi(t)$ changes sign, are the significant events to observe. As illustrated on Fig. 1, we interpret the time interval τ between two consecutive crossings as the time duration of a given decision, even if this decision may rest on a slight and fluctuating majority.

We evaluate the distribution density of decision-time durations τ , $\psi(\tau)$, and the corresponding survival probability $\Psi(\tau)$, where $\Psi(t) = \int_t^\infty d\tau \psi(\tau)$. Although emerging from a simple regular lattice, that is, one with no structural complexity, the survival probability presented in Fig. 4 shows a scale-free property that extends over more than four decades in time for $K \approx K_C$. A further increase of K does not affect the power-law region and has the effect of producing a more and more extended exponential shoulder. The exponential shoulder is expected to become predominant for $K \rightarrow \infty$.

As mentioned earlier, a single unit in isolation fluctuates between two states with the transition rate $g = g_0$. The corresponding survival probability function is an exponential function $\Psi(\tau) = \exp(-g_0\tau)$. At the same time, as illustrated on Fig. 5, a coupled unit tends to update its state with a transition rate smaller than g_0 . This is a property of criticality that is lost completely for very large values of the control parameter K . Although it is a computational challenge to explore the dynamics corresponding to extremely large values of K , our numerical results suggest that when K is very close to the critical value, and a decision is reached by a slight majority, the single units have a dynamics almost indistinguishable from the Poisson dynamic that they would have in isolation. As we increase the control parameter K and the majority becomes larger the single units keep their Poisson dynamics with a smaller rate. Although it is not possible because of computer-time limitations to study the network's dynamics for values of K much larger than $K = 1.80$, it is plausible to make the conjecture that the single units maintain their Poisson dynamics and that these dynamics become closer and closer to that of the global variable that will lose its power-law structure and will become predominantly exponential. In other words, unanimous and permanent consensus must be perceived as the

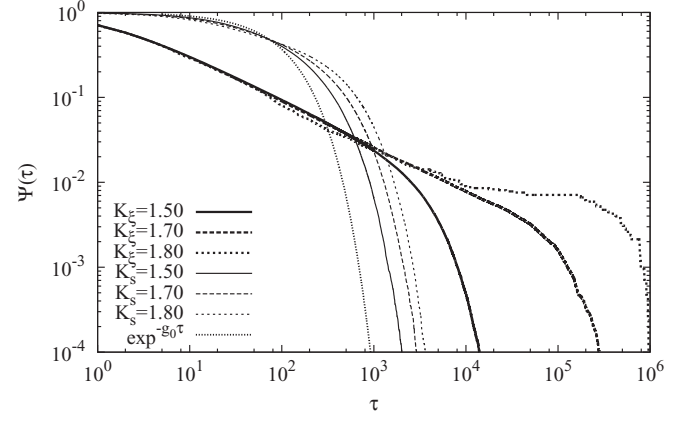


FIG. 5. The survival probability function $\Psi(\tau)$ of the global order parameter $\xi(t)$ is compared with the transitions between two states for a single unit s_i . Simulations were performed on a lattice of size $L = 50 \times 50$ for $g_0 = 0.01$ and increasing values of coupling constant K .

manifestation of a limiting condition of Poisson but infinitely slow dynamics, where the behavior of the single units becomes identical to that of the global signal.

To make this argument more compelling let us discuss the properties of the observed exponential shoulder. Since one observes the network in an organized phase ($K > K_C$) it is not surprising that one perceives the exponential signature of an equilibrium regime. Therefore we assume that under those conditions the global variable $\xi(t)$ follows the dynamics of a particle diffusing in a double potential well. In the equilibrium condition one would expect the survival time of staying in one well to be $\Psi(\tau) = \exp(-a\tau)$, where $a = A \exp(-Q/D)$. The parameter Q denotes the height of the potential barrier separating the wells, and D stands for the diffusion coefficient. Following [19] we expect the barrier to be a function of the coupling constant K and the diffusion to depend on the number of nodes L . By fitting the shoulder, once for a case where L is kept constant and K varies, and secondly for an opposite condition, we assess the above hypothesis. The fitting procedure revealed that the barrier height Q is a linear function of K ($Q \sim K$) and that the diffusion coefficient D is inversely proportional to the system size L ($D \sim 1/L$). For $L \rightarrow \infty$ the transition rate becomes infinitely small and the exponential shoulder becomes predominant and virtually coincident with the Poisson dynamics of the single units.

While in the organized phase the effect of increasing L is that of making the process exponential, although with a virtually infinite transition time. At criticality the increase of L has a dramatically different effect. The authors of [19], based on this DMM in the all-to-all condition, found that at criticality an inverse-power-law behavior emerges, which is confined, however, to a time region with the same size as the Poisson time $\tau_P \approx 1/g_0$. However, this is not the case when the units are the nodes of a regular two-dimensional lattice, interacting only with the four nearest-neighbor nodes. We have evaluated the time size of the inverse-power-law region appearing before the exponential shoulder and we found that its size tends to increase with increasing L as $\tau_P \sim L^{-1.25}$. Unfortunately, this observation is limited to values of L

smaller than $L = 10\,000$, since going beyond would exceed the limits of our computer facilities. However, on the basis of this observation we reach the conclusion that for $L \rightarrow \infty$ the size of the temporal complexity must become infinitely large. Thus, criticality is a kind of complex singularity embedded in a Poisson sea.

These intuitive arguments also explain why the signal $\xi(t)$ at criticality must depart from the dichotomous condition. This is a consequence of the fact that the single units are not rigidly bound to follow the opinion of the majority. There is, consequently, a subtle connection between criticality, free will, and correlation between different units. Although the single units may change opinion, they cannot do that in a way totally uncorrelated from the behavior of the other units, insofar as this would be incompatible with the emergence of a majority, as slight as it might be.

IV. TESTING RENEWAL PROPERTIES

As pointed out earlier, the signal $\xi(t)$ at criticality is not dichotomous. However, replacing it with a dichotomous signal corresponding to 1 (yes) when $\xi(t) > 0$ and to -1 (no) when $\xi(t) < 0$, thereby turning it into an ideal dichotomous signal, is the most convenient way to reveal the emergence of crucial events at criticality. The theory [24] (see also the earlier work [25]) allows us to evaluate the nonstationary correlation function $\Psi(t, t')$ in the specific case when the renewal process rests on the waiting time distribution density $\psi(t)$ assumed to be an ideal inverse power law. In general, regardless of whether this ideal condition of infinitely extended inverse power law is realized or not, it is possible to establish whether the process is renewal by noticing that

$$\Psi(t, t') = \Psi(\tau, t_a), \quad (10)$$

where $\tau = t - t'$ and $t_a = t'$. As explained [26], the function $\Psi(\tau, t_a)$ can be evaluated by using the time series $\{t_i\}$, where t_i are the times at which the fluctuation $\xi(t)$ crosses the origin. We use a mobile window of length t_a to evaluate the waiting time distribution $\psi(\tau, t_a)$ and the corresponding survival probability $\Psi(\tau, t_a)$, by locating the origin of the window on the time of occurrence of an event and measuring the time distance between the end of the window and the time of occurrence of the first event after the window end. To establish whether the process is renewal or not we shuffle the sequence of reversal times, thereby generating a new time series $\{t_i^s\}$. We use the same procedure based on a mobile window to determine $\Psi(t_{a,s}, \tau)$, which corresponds to the nonstationary correlation function in the renewal case. If the two survival probabilities coincide, we conclude that the process is renewal. If the renewal process is exponential, the correlation function is stationary, and there is no aging.

In the ideal case of an infinitely extended inverse power law, with power index $\mu < 2$, as discussed in earlier work [16,24], aging is perennial. In the case studied in this paper, we have to take into account that this ideal condition would be realized by assigning an infinitely large value to L , with the ensuing consequence that temporal complexity would become virtually invisible, due to the joint effect of an extremely slight majority and of a very extended sojourn in a given decision state. To make temporal complexity visible, we need a compromise,

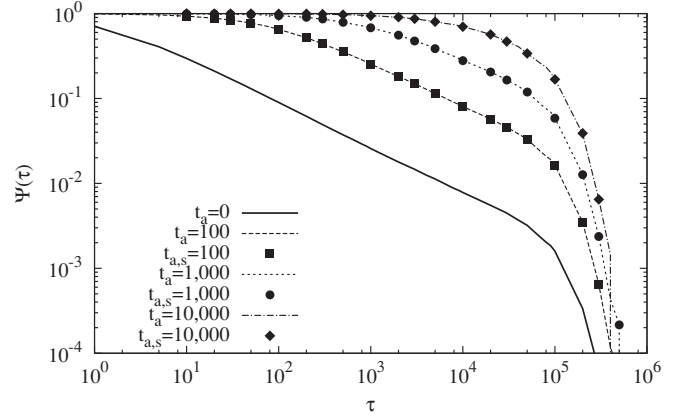


FIG. 6. Testing for renewal property. Survival probability function $\Psi(\tau)$ of the order parameter $\xi(t)$ evaluated on lattice of size $L = 50 \times 50$ and $g_0 = 0.01$, $K = 1.70$ was aged respectively by time $t_a = 100$, $t_a = 1000$, and $t_a = 10\,000$. Those aged survival probabilities $\Psi(t_{a,s}, \tau)$ are compared with the aged renewal prediction $\Psi(t_a, \tau)$.

and we have to set a limit on the time extension of the inverse power law. As a consequence, we obtain the very interesting result depicted in Fig. 6, where aging, namely the slowing down of the survival probability, becomes very large in the inverse-power-law region, with the survival probability remaining virtually constant, and in the correspondence of the exponential shoulder it is virtually suppressed, in accordance with the principle that Poisson statistics annihilates aging.

V. CONCLUSIONS

This paper establishes that at the onset of phase transition, in addition to the spatial and network complexity shown by a number of earlier investigations [4–7,9,12,14,15], we also have temporal complexity. This significant result reveals a path for the transport of information from one complex network to another. As pointed out in Sec. I, there is a general agreement that complex systems are a set of many units interacting at the onset of phase transition. The present analysis proves that these complex networks are characterized also by temporal complexity, and consequently a perturbing complex network is expected to exert its influence on another complex network via the recently discovered complexity management process [21,31]. Although the present theoretical predictions are based on the assumption that $\psi(\tau)$ is an ideal inverse power law and the real complex networks, as shown herein, reach this ideal condition only when their size is infinitely large, the result in Fig. 5 indicates that the time region generating ergodicity breakdown may become so extended as to make a complex network virtually insensitive to stimuli that do not share the same extended nonergodic condition.

In the last few years the attention of investigators has been moving from chaos synchronization of two nonlinear oscillators [27] to the synchronization dynamics of many units in large-scale networks [28], called *inner synchronization* [29] for convenience. The cooperation induced phase transition discussed herein can to some extent be thought of as a form of

inner synchronization. As pointed out [29] the challenge that the researchers in the field of complexity have now to address is the phenomenon of *outer synchronization* [30].

In this light, we conclude that the results presented here provide a way of addressing outer synchronization, redirecting the attention of researchers from the details of the topology of the complex networks to the analysis of the temporal complexity that inner synchronization may generate. In fact the

principle of complex management [21,31] rests on temporal complexity, regardless of the way it is generated.

ACKNOWLEDGMENTS

M.G. and P.G. acknowledge financial support from ARO and Welch through Grants No. W911NF-05-1-0205 and No. B-1577, respectively.

-
- [1] H. E. Stanley, *Introduction to Phase Transition and Critical Phenomena* (Oxford University Press, New York, 1987).
 - [2] E. Ising, *Z. Phys.* **31**, 253 (1925).
 - [3] L. Onsager, *Phys. Rev.* **65**, 117 (1944).
 - [4] T. Mora and W. Bialek, e-print arXiv:1012.2242v1.
 - [5] D. Fraiman, P. Balenzuela, J. Foss, and D. Chialvo, *Phys. Rev. E* **79**, 061922 (2009).
 - [6] D. R. Chialvo, *Nature Phys.* **6**, 744 (2010).
 - [7] M. G. Kitzbichler, M. L. Smith, S. R. Christensen, and E. Bullmore, *PLoS Comput. Biol.* **5**, 1 (2009).
 - [8] P. Bak and M. Paczuski, *Proc. Natl. Acad. Sci. USA* **92**, 6689 (1995).
 - [9] W. Truccolo, L. R. Hochberg, and J. P. Donoghue, *Nature Neurosci.* **13**, 105 (2010).
 - [10] E. Schneidman, M. J. Berry II, R. Segev, and W. Bialek, *Nature (London)* **440**, 1007 (2006).
 - [11] I. Couzin, *Nature (London)* **445**, 715 (2007).
 - [12] A. Cavagna, A. Cimarelli, I. Giardina, G. Parisi, R. Santagati, F. Stefanini, and M. Viale, *Proc. Natl. Acad. Sci. USA* **107**, 11865 (2010).
 - [13] T. Vicsek, A. Czirók, E. Ben-Jacob, I. Cohen, and O. Shochet, *Phys. Rev. Lett.* **75**, 1226 (1995).
 - [14] H. E. Stanley and V. Plerou, *Quant. Finance* **1**, 563 (2001).
 - [15] D. Sornette, *Phys. Rep.* **378**, 1 (2003).
 - [16] A. Rebenshtok and E. Barkai, *J. Stat. Phys.* **133**, 565 (2008).
 - [17] Y. F. Contoyiannis and F. K. Diakonos, *Phys. Lett. A* **268**, 286 (2000); Y. F. Contoyiannis, F. K. Diakonos, and A. Malakis, *Phys. Rev. Lett.* **89**, 035701 (2002).
 - [18] S. Bianco, E. Geneston, P. Grigolini, and M. Ignaccolo, *Physica A* **387**, 1387 (2008).
 - [19] M. Turala, M. Lukovic, B. J. West, and P. Grigolini, *Phys. Rev. E* **80**, 021110 (2009).
 - [20] G. Tkačik, A. M. Walczak, and W. Bialek, *Phys. Rev. E* **80**, 031920 (2009).
 - [21] G. Aquino, M. Bologna, P. Grigolini, and B. J. West, *Phys. Rev. Lett.* **105**, 040601 (2010).
 - [22] M. Plischke and B. Bergersen, *Equilibrium Statistical Physics* (World Scientific Publishing Company, 2006).
 - [23] B. M. McCoy and T. T. Wu, *The Two-Dimensional Ising Model* (Harvard University Press, Cambridge, 1973).
 - [24] P. Allegrini, G. Aquino, P. Grigolini, L. Palatella, A. Rosa, and B. J. West, *Phys. Rev. E* **71**, 066109 (2005).
 - [25] C. Godrèche and J. M. Luck, *J. Stat. Phys.* **104**, 489 (2001).
 - [26] S. Bianco, P. Grigolini, and P. Paradisi, *J. Chem. Phys.* **123**, 174704 (2005).
 - [27] L. M. Pecora and T. L. Carroll, *Phys. Rev. Lett.* **64**, 821 (1990).
 - [28] S. Boccaletti, V. Latora, Y. Morento, M. Chavez, and D. U. Hwang, *Phys. Rep.* **424**, 175 (2006); J. Zhou, L. Xiang, and Z. Liu, *Phys. A* **385**, 729 (2007); A. Arenas, A. Diaz-Guilera, J. Kurths, Y. Moreno, and C. Zhou, *Phys. Rep.* **469**, 93 (2008); W. Yu, G. Chen, and J. Lü, *Automatica* **45**, 429 (2009); M. Chen, Y. Shang, C. Zhou, Y. Wu, and J. Kurths, *Chaos* **19**, 013105 (2009).
 - [29] X.-J. Wu and H.-T. Lu, *Chinese Phys. B* **19**, 070511 (2010).
 - [30] E. Montbrío, J. Kurths, and B. Blasius, *Phys. Rev. E* **70**, 056125 (2004); C. P. Li, W. G. Sun, and J. Kurths, *ibid.* **76**, 046204 (2007).
 - [31] G. Aquino, M. Bologna, B. J. West, and P. Grigolini (unpublished).

Noncoherent Physical-Layer Network Coding with FSK Modulation: Relay Receiver Design Issues

Matthew C. Valenti, Don Torrieri, and Terry Ferrett

IEEE Transactions on Communications, 59(9), 2595-2604 (2011)

Noncoherent Physical-Layer Network Coding with FSK Modulation: Relay Receiver Design Issues

Matthew C. Valenti, *Senior Member, IEEE*, Don Torrieri, *Senior Member, IEEE*,
and Terry Ferrett, *Student Member, IEEE*

Abstract—A channel-coded physical-layer network coding strategy is refined for practical operation. The system uses frequency-shift keying (FSK) modulation and operates noncoherently, providing advantages over coherent operation: there are no requirements for perfect power control, phase synchronism, or estimates of carrier-phase offset. In contrast with *analog* network coding, which relays received analog signals plus noise, the system relays *digital* network codewords, obtained by digital demodulation and channel decoding at the relay. The emphasis of this paper is on the relay receiver formulation. Closed-form expressions are derived that provide bitwise log-likelihood ratios, which may be passed through a standard error-correction decoder. The role of fading-amplitude estimates is investigated, and an effective fading-amplitude estimator is developed. Simulation results are presented for a Rayleigh block-fading channel, and the influence of block length is explored. An example realization of the proposed system demonstrates a 32.4% throughput improvement compared to a similar system that performs network coding at the link layer. By properly selecting the rates of the channel codes, this benefit may be achieved without requiring an increase in transmit power.

Index Terms—Network coding, two-way relay channel, frequency-shift keying, noncoherent reception, channel estimation.

I. INTRODUCTION

IN the two-way relay channel (TWRC), a pair of source terminals exchange information through an intermediate relay without a direct link between the sources [1]. The exchange can occur in two, three, or four orthogonal time slots, depending on how the information is encoded [2]. With a *traditional transmission scheduling scheme*, the exchange requires four slots. In each of the first two slots, one of the terminals transmits a packet to the relay, while in each of the last two slots, the relay transmits a packet to each of the terminals. By using *network coding* [3], the number of slots can be reduced. With *link-layer network coding* (LNC), the third and fourth slots are combined into one slot by having the relay add (modulo-2) the packets that it receives from the

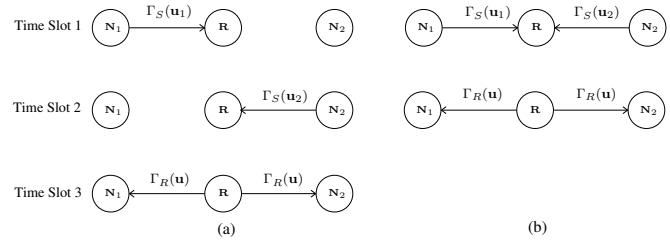


Fig. 1. (a) Link-layer network coding, and (b) Physical-layer network coding.

two terminals. During the third step, the relay sends the sum of the two packets, and each terminal is able to recover the information from the other terminal by subtracting (or adding, modulo-2) its own packet from the received signal. With *physical-layer network coding* (PNC), the first two slots are combined by having the two terminals transmit their packets at the same time [2]. The relay receives a combination of both modulated packets during the first slot, which it broadcasts (after appropriate processing) to the two terminals during the second slot. PNC-based strategies capable of supporting more than just two source terminals over the TWRC may be found in [4].

The transmission schedules for LNC and PNC are illustrated in Fig. 1. The source terminals N_1 and N_2 transmit messages u_1 and u_2 , respectively, where each message is a packet containing many information bits. The messages are (channel) encoded and modulated by the function $\Gamma_S(\cdot)$. In the case of LNC, the two messages are sent in orthogonal time slots, while in the case of PNC, they are sent to the relay at the same time over a multiple-access channel (MAC). For both LNC and PNC, the relay broadcasts the encoded and modulated signal $\Gamma_R(u)$ in the final time slot, where u is the *network codeword* and $\Gamma_R(\cdot)$ is the function used by the relay to encode and modulate the network codeword. Using the received version of $\Gamma_R(u)$ and knowledge of its own message, each terminal is able to estimate the message sent by the other terminal.

There are several options for implementing PNC. The relay may simply amplify and forward the signal received from the end nodes, without performing demodulation and decoding. This PNC scheme is referred to as *analog network coding* (ANC) in [5] and *PNC over an infinite field* (PNCI) in [6]. Another option is for the relay to perform demodulation and decoding in an effort to estimate the network codeword, which is remodulated and broadcast to the terminals. This scheme is simply called PNC in [2] and *PNC over a finite field* (PNCf) in [6], but in this paper we refer to it as *digital network coding* (DNC) to distinguish it from ANC. Under

Paper approved by G. Bauch, the Editor for MIMO, Coding and Relaying of the IEEE Communications Society. Manuscript received January 12, 2011; revised March 25, 2011.

Portions of this paper were presented at the IEEE Military Communication Conference (MILCOM), San Jose, CA, Oct. 2010.

M. C. Valenti's contribution was sponsored by the National Science Foundation under Award No. CNS-0750821, and by the United States Army Research Laboratory under Contract W911NF-10-0109.

M. C. Valenti and T. Ferrett are with West Virginia University, Morgantown, WV (e-mail: {valenti, terry.ferrett}@ieee.org).

D. Torrieri is with the US Army Research Laboratory, Adelphi, MD (e-mail: dtorr@arl.army.mil).

Digital Object Identifier 10.1109/TCOMM.2011.063011.110030

many channel conditions, DNC offers enhanced performance over ANC. This is because the decoding operation at the relay helps DNC to remove noise from the MAC phase, while the noise is amplified by the relay when ANC is used. However, ANC avoids the computational complexity of demodulation and decoding at the relay.

Symbol timing is a critical consideration in systems employing PNC. Synchronization of the clocks and packet transmissions at the two source nodes can be achieved by network timing updates. These updates are routine in networks with scheduling mechanisms, such as cellular networks. When the propagation times of the signals from the sources differ, the symbols arrive at the relay misaligned. The timing offset is $\tau = \Delta_d/c$, where c is the speed of light, and Δ_d is the difference in link distances from the sources to the relay. For insignificant delay, we need $\tau \ll T_s/2$, where T_s denotes the symbol period. This constraint limits the symbol rate. As an example, assume $\Delta_d = 300$ meters. Then, $T_s \gg 2 \mu s$ is required, and the symbol rate is limited to 250 kilosymbols/s. An alternative is to delay the transmission of the node closer to the relay by τ . However, this requires tracking the distances between the sources and the relay.

A common assumption made in the PNC literature is that the signals are coherently demodulated and that perfect channel-state information (CSI) is available at the receivers. For instance, decode-and-forward relaying has been considered for binary phase-shift keying [7] and minimum-shift keying [8] modulations, but in both cases the relay must perform coherent reception. An amplify-and-forward protocol is considered in [9], which allows the decision to be deferred by the relay to the end-node, though detection is still coherent. When two signals arrive concurrently at a common receiver, neither coherent detection nor the cophasing of the two signals (so that they arrive with a constant phase offset) is practical. The latter would require preambles that detract from the overall throughput, stable phases, and small frequency mismatches. To solve this problem, frequency-shift keying (FSK) was proposed for DNC systems in [10] and [11]. A key benefit of using FSK modulation is that it permits noncoherent reception, which eliminates the need for phase synchronization. An alternative to noncoherent FSK is to use differential modulation, which has been explored in [12].

In PNC systems, it is desirable to protect the data with a channel code. The combination of channel coding and physical-layer network coding is considered in [13]. In [11], we investigate the use of a binary turbo code in a noncoherent DNC system. When using a binary turbo code in a DNC system, the relay demodulator must be able to produce bitwise log-likelihood ratios (LLRs) that are introduced to the input of the channel decoder.

Channel estimation is an important issue, especially when a channel code is used. A training-based channel estimation scheme for PNC at the relay assuming amplify-and-forward operation is considered in [14]. The relay estimates channel parameters from training symbols and adapts its broadcast power in order to maximize the signal-to-noise ratio at the end nodes. Estimation of both channel gains in the two-way relay channel at the end nodes, rather than the relay, is considered in [15]. Novel channel estimators are presented which provide

better performance than common techniques such as least-square and linear-minimum-mean-squared error estimation. In [16], we propose a blind channel estimator for the relay of the noncoherent DNC system.

In this paper, we investigate receiver-design issues related to the use of noncoherent FSK in DNC systems. While noncoherent FSK has been previously proposed for DNC systems in [10], we make the following specific contributions:

- 1) We provide *closed-form* expressions for the relay receiver decision rule with different types of CSI. This is in contrast with [10], which resorted to numerical methods to solve the decision rule (see the comment below equation (8) in [10]).
- 2) We consider the use of a turbo code for additional data protection. This requires that the relay receiver be formulated so that it produces bitwise LLRs, which may be passed through a standard turbo decoder.
- 3) We provide results for Rayleigh block-fading channels. The results in [10] were only for a phase-fading channel.
- 4) We propose a channel estimator that is capable of determining the fading amplitudes of the channels from the two terminals to the relay. The estimator does not require pilot symbols.

The remainder of this paper is organized as follows. Section II presents the system model used throughout the paper. Section III derives the relay receiver, while Section IV discusses channel-estimation issues. Section V provides simulation results, and Section VI concludes the paper.

II. SYSTEM MODEL

The discrete-time system model shown in Fig. 2 gives an overview of the processing at all three nodes. Terminal $\mathcal{N}_i, i \in \{1, 2\}$, generates a length- K information sequence, $\mathbf{u}_i = [u_{i,1}, \dots, u_{i,K}]$. The two terminals channel-encode and modulate their information sequences using the function $\Gamma_S(\cdot)$, which is common to both nodes. A rate- r_1 turbo code is used, and the resulting length $L_S = K/r_1$ turbo codeword generated by \mathcal{N}_i is denoted by $\mathbf{b}_i = [b_{i,1}, \dots, b_{i,L_S}]$ (not shown in the diagram). The signal transmitted by node \mathcal{N}_i during signaling interval $kT_s \leq t \leq (k+1)T_s$ is

$$s_i(t) = \sqrt{\frac{2\mathcal{E}_i}{T_s}} \cos \left[2\pi \left(f_{c_i} + \frac{b_{i,k}}{T_s} \right) (t - kT_s) \right] \quad (1)$$

where \mathcal{E}_i is the transmit energy, f_{c_i} is the carrier frequency of node \mathcal{N}_i (in practice, the carrier frequencies of the two nodes are not necessarily the same), and T_s is the symbol period. Note that (1) is continuous-phase frequency-shift keying (CPFSK) with a unity modulation index, which is orthogonal under noncoherent demodulation and has a continuous phase transition from one symbol to the next [17]. The orthogonally-modulated signal $s_i(t)$ may be represented in discrete time by the $2 \times L_S$ matrix $\mathbf{X}_i = [\mathbf{x}_{i,1}, \dots, \mathbf{x}_{i,L_S}]$ with k^{th} column

$$\mathbf{x}_{i,k} = \begin{cases} \begin{bmatrix} 1 & 0 \end{bmatrix}^T & \text{if } b_{i,k} = 0 \\ \begin{bmatrix} 0 & 1 \end{bmatrix}^T & \text{if } b_{i,k} = 1. \end{cases} \quad (2)$$

For the DNC system, the signals are transmitted simultaneously by the two source nodes over a MAC channel. The relay receives the noisy electromagnetic sum of interfered and

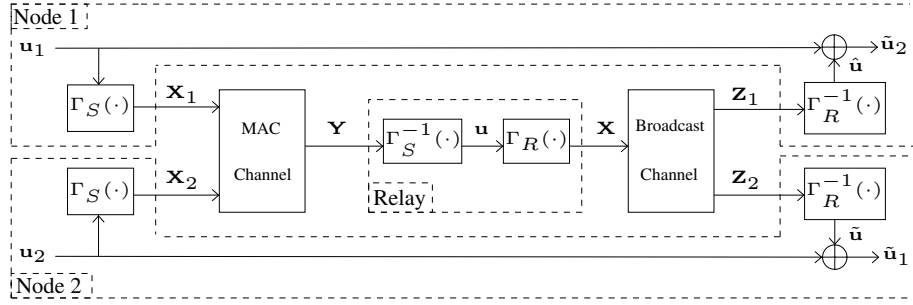


Fig. 2. Discrete-time system model.

faded signals, \mathbf{Y} , and applies the demodulation and channel-decoding function $\Gamma_S^{-1}(\cdot)$. The demodulation operation yields a soft estimate of the network-and-channel-coded message $\mathbf{b} = \mathbf{b}_1 \oplus \mathbf{b}_2$ (not shown), while the channel-decoding operation yields a hard-decision on the network-coded message $\mathbf{u} = \mathbf{u}_1 \oplus \mathbf{u}_2$. With the LNC system, the two sources transmit during orthogonal time slots. The received versions of \mathbf{X}_1 and \mathbf{X}_2 are demodulated independently to provide soft estimates of \mathbf{b}_1 and \mathbf{b}_2 . These soft estimates are combined and turbo decoded to yield a hard estimate of \mathbf{u} . The key distinction between DNC and LNC is that with the DNC system, the estimate of \mathbf{b} is obtained directly from \mathbf{Y} , while with LNC it is found by independently demodulating the two source signals and then combining them.

During the broadcast phase, the relay encodes and modulates \mathbf{u} using the function $\Gamma_R(\cdot)$, which may be different than the function $\Gamma_S(\cdot)$ used by the sources. The channel code applied by the relay is a rate- r_2 turbo code, yielding a length $L_R = K/r_2$ turbo codeword. The code rates r_1 and r_2 used by the sources and relays, respectively, do not need to be the same. In the simulation results, we contemplate using a stronger code for the MAC phase than the broadcast phase, i.e. $r_1 < r_2$. The relay broadcasts its encoded and modulated signal, which may be represented in discrete-time by the $2 \times L_R$ matrix \mathbf{X} . The signal traverses two independent fading channels, and the end nodes receive independently faded versions of \mathbf{X} : \mathbf{Z}_1 at \mathcal{N}_1 and \mathbf{Z}_2 at \mathcal{N}_2 . The end nodes demodulate and decode their received signals using the function $\Gamma_R^{-1}(\cdot)$, and form estimates of \mathbf{u} . Let $\hat{\mathbf{u}}$ denote the estimate at \mathcal{N}_1 and $\tilde{\mathbf{u}}$ denote the estimate at \mathcal{N}_2 . Next, estimates of the transmitted information messages are formed, $\tilde{\mathbf{u}}_2 = \hat{\mathbf{u}} \oplus \mathbf{u}_1$ at \mathcal{N}_1 and $\tilde{\mathbf{u}}_1 = \tilde{\mathbf{u}} \oplus \mathbf{u}_2$ at \mathcal{N}_2 . Since the links in the broadcast phase are conventional point-to-point links, specific details of the receiver formulation will not be presented here. A detailed exposition of receiver design for turbo-coded CPFSK systems in block fading channels can be found in [18].

All of the channels in the system are modeled as *block-fading* channels. A block is defined as a set of N symbols that all experience the same fading amplitude. The duration of each block corresponds roughly to the channel coherence time. Ideally both sources transmit with the same carrier frequency $f_{c1} = f_{c2}$. However, due to instabilities in each source node's oscillator and different Doppler shifts due to independent motion, it is not feasible to assume that these two frequencies are the same at the relay receiver. At best, the relay receiver could lock onto one of the two frequencies, in which case the received phase of the other signal would

drift from one symbol to the next. To model this behavior, we let the phase shift within a block vary independently from symbol to symbol.

The signal matrix \mathbf{X}_i transmitted by node \mathcal{N}_i may be partitioned into $N_b = L_S/N$ blocks according to

$$\mathbf{X}_i = \begin{bmatrix} \mathbf{X}_i^{(1)} & \dots & \mathbf{X}_i^{(N_b)} \end{bmatrix} \quad (3)$$

where each block $\mathbf{X}_i^{(\ell)}$, $1 \leq \ell \leq N_b$, is a $2 \times N$ matrix, and N_b is assumed to be an integer. The channel associated with block $\mathbf{X}_i^{(\ell)}$ is represented by the $N \times N$ diagonal matrix

$$\mathbf{H}_i^{(\ell)} = \alpha_i^{(\ell)} \times \text{diag}(\exp\{j\theta_{i,1}^{(\ell)}\}, \dots, \exp\{j\theta_{i,N}^{(\ell)}\}) \quad (4)$$

where $\alpha_i^{(\ell)}$ is a real-valued fading amplitude and $\theta_{i,k}^{(\ell)}$ is the phase shift of the k^{th} symbol. The $\{\theta_{i,k}^{(\ell)}\}$ are independent and identically distributed over the interval $[0, 2\pi)$. The $\{\alpha_i^{(\ell)}\}$ are normalized so that \mathcal{E}_i represents the average energy of terminal \mathcal{N}_i received by the relay. The ℓ^{th} block at the sampled output of the relay receiver's matched-filters is then

$$\mathbf{Y}^{(\ell)} = \mathbf{X}_1^{(\ell)} \mathbf{H}_1^{(\ell)} + \mathbf{X}_2^{(\ell)} \mathbf{H}_2^{(\ell)} + \mathbf{N}^{(\ell)} \quad (5)$$

where $\mathbf{N}^{(\ell)}$ is a $2 \times N$ noise matrix whose elements are i.i.d. circularly-symmetric complex Gaussian random variables with zero mean and variance N_0 .

III. RELAY RECEIVER

At the relay, each block $\mathbf{Y}^{(\ell)}$ of the channel observation matrix \mathbf{Y} is passed to a channel estimator, which computes estimates of the $\alpha_1^{(\ell)}$ and $\alpha_2^{(\ell)}$. A full description of the estimator is given in Section IV. The fading-amplitude estimates and channel observations are used to obtain soft estimates of the network-and-channel-coded sequence \mathbf{b} . The demodulator operates on a symbol-by-symbol basis, and therefore we may focus on a single signaling interval by dropping the dependence on the symbol interval k and the block index ℓ . Let b_1 and b_2 be the turbo-coded bits transmitted by terminals \mathcal{N}_1 and \mathcal{N}_2 , and let $b = b_1 \oplus b_2$ be the corresponding network-coded bit. The relay demodulator computes the LLR

$$\Lambda(b) = \log \frac{P(b=1|\mathbf{y})}{P(b=0|\mathbf{y})} = \log \frac{P(b_1 \oplus b_2 = 1|\mathbf{y})}{P(b_1 \oplus b_2 = 0|\mathbf{y})} \quad (6)$$

where \mathbf{y} is the corresponding column of \mathbf{Y} . The event $\{b_1 \oplus b_2 = 1\}$ is equivalent to the union of the events $\{b_1 = 0, b_2 = 1\}$ and $\{b_1 = 1, b_2 = 0\}$. Similarly, the event $\{b_1 \oplus b_2 = 0\}$

is equivalent to the union of the events $\{b_1 = 0, b_2 = 0\}$ and $\{b_1 = 1, b_2 = 1\}$. It follows that

$$\begin{aligned}\Lambda(b) &= \log \frac{P(\{b_1 = 0, b_2 = 1\} \cup \{b_1 = 1, b_2 = 0\} | \mathbf{y})}{P(\{b_1 = 0, b_2 = 0\} \cup \{b_1 = 1, b_2 = 1\} | \mathbf{y})} \\ &= \log \frac{P(\{b_1 = 0, b_2 = 1\} | \mathbf{y}) + P(\{b_1 = 1, b_2 = 0\} | \mathbf{y})}{P(\{b_1 = 0, b_2 = 0\} | \mathbf{y}) + P(\{b_1 = 1, b_2 = 1\} | \mathbf{y})}\end{aligned}\quad (7)$$

where the second line follows from the first because the events are mutually exclusive.

A. LNC Receiver

In the LNC system, the LLR's of b_1 and b_2 are first computed independently during the orthogonal time slots and are then combined according to the rules of LLR arithmetic. The LLR of the signal sent from node \mathcal{N}_i to the relay is

$$\Lambda(b_i) = \log \frac{P(b_i = 1 | \mathbf{y})}{P(b_i = 0 | \mathbf{y})} \quad (8)$$

where \mathbf{y} is the signal received during the time slot that node \mathcal{N}_i transmits. When the fading amplitudes $\alpha_i, i = 1, 2$, are known, but the phases $\theta_i, i = 1, 2$, are not known, then (8) is found using [19]

$$\Lambda(b_i) = \log I_0 \left(\frac{2\alpha_i |y_2|}{N_0} \right) - \log I_0 \left(\frac{2\alpha_i |y_1|}{N_0} \right) \quad (9)$$

where $I_0(\cdot)$ is the zeroth-order Bessel function of the first kind and y_1 and y_2 are the components of \mathbf{y} . If the fading amplitudes are not known, but have Rayleigh distributions, then (8) is found using [19]

$$\Lambda(b_i) = \frac{(\mathcal{E}_i/N_0)^2}{1 + \mathcal{E}_i/N_0} \{|y_2|^2 - |y_1|^2\}. \quad (10)$$

Once the individual LLR's from each end node are found using (9) or (10), the LLR of the LNC system's network codeword can then be found from (7) and the independence of b_1 and b_2 when \mathbf{y} is given:

$$\begin{aligned}\Lambda(b) &= \log \frac{e^{\Lambda(b_1)} + e^{\Lambda(b_2)}}{1 + e^{\Lambda(b_1) + \Lambda(b_2)}} \\ &= \max^* [\Lambda(b_1), \Lambda(b_2)] - \max^* [0, \Lambda(b_1) + \Lambda(b_2)]\end{aligned}\quad (11)$$

where $\max^*[x, y] = \log(e^x + e^y)$.

B. PNC Receiver

In the PNC system, it is not sensible to compute $\Lambda(b_1)$ and $\Lambda(b_2)$ separately. Instead, use (7) and assume that the four events are equally likely along with Bayes' rule to obtain

$$\begin{aligned}\Lambda(b) &= \log [p(\mathbf{y} | \{b_1 = 0, b_2 = 1\}) + p(\mathbf{y} | \{b_1 = 1, b_2 = 0\})] \\ &\quad - \log [p(\mathbf{y} | \{b_1 = 0, b_2 = 0\}) + p(\mathbf{y} | \{b_1 = 1, b_2 = 1\})].\end{aligned}\quad (12)$$

The computation of each $p(\mathbf{y} | \{b_1, b_2\})$ by the PNC relay receiver given various levels of channel state information is the subject of the remainder of this section.

1) *Coherent PNC Receiver:* When the fading amplitudes and phases are known, $p(\mathbf{y} | \{b_1, b_2\})$ is conditionally Gaussian. The mean is a two-dimensional complex vector whose value depends on the values of $\{b_1, b_2\}$ and the complex fading coefficients $\{h_1, h_2\}$, which are the corresponding entries of the \mathbf{H} matrix. Let $\mathbf{m}[b_1, b_2]$ be the mean of \mathbf{y} for the given values of b_1 and b_2 . When $b_1 \neq b_2$, the two terminals transmit different frequencies and

$$\begin{aligned}\mathbf{m}[0, 1] &= \begin{bmatrix} h_1 & h_2 \end{bmatrix}^T \\ \mathbf{m}[1, 0] &= \begin{bmatrix} h_2 & h_1 \end{bmatrix}^T.\end{aligned}\quad (13)$$

When $b_1 = b_2$, the two terminals transmit the same frequency and

$$\begin{aligned}\mathbf{m}[0, 0] &= \begin{bmatrix} (h_1 + h_2) & 0 \end{bmatrix}^T \\ \mathbf{m}[1, 1] &= \begin{bmatrix} 0 & (h_1 + h_2) \end{bmatrix}^T.\end{aligned}\quad (14)$$

Since there is a one-to-one correspondence between the event $\{b_1, b_2\}$ and the mean vector $\mathbf{m}[b_1, b_2]$, it is equivalent to write $p(\mathbf{y} | \{b_1, b_2\})$ as $p(\mathbf{y} | \mathbf{m}[b_1, b_2])$, where

$$p(\mathbf{y} | \mathbf{m}[b_1, b_2]) = \left(\frac{1}{\pi N_0} \right)^2 \exp \left\{ -\frac{1}{N_0} \|\mathbf{y} - \mathbf{m}[b_1, b_2]\|^2 \right\}. \quad (15)$$

The coherent receiver computes each of the $p(\mathbf{y} | \{b_1, b_2\})$ required by (12) by substituting the corresponding $\mathbf{m}[b_1, b_2]$ defined by (13) and (14) into (15).

2) *Noncoherent PNC Receiver with CSI:* Suppose that the receiver does not know the *phases* of the elements of the complex-valued $\mathbf{m}[b_1, b_2]$ vectors, but does know the *magnitudes* of the elements. The knowledge of the magnitudes constitutes a type of *channel-state information* (CSI). Define $\boldsymbol{\mu}[b_1, b_2]$ to be the two-dimensional real vector whose elements are the magnitudes of the elements of the complex vector $\mathbf{m}[b_1, b_2]$. When $b_1 \neq b_2$, both frequencies are used, and

$$\begin{aligned}\boldsymbol{\mu}[0, 1] &= \begin{bmatrix} |h_1| & |h_2| \end{bmatrix}^T = \begin{bmatrix} \alpha_1 & \alpha_2 \end{bmatrix}^T \\ \boldsymbol{\mu}[1, 0] &= \begin{bmatrix} |h_2| & |h_1| \end{bmatrix}^T = \begin{bmatrix} \alpha_2 & \alpha_1 \end{bmatrix}^T.\end{aligned}\quad (16)$$

When $b_1 = b_2$, only one frequency is used, and

$$\begin{aligned}\boldsymbol{\mu}[0, 0] &= \begin{bmatrix} |h_1 + h_2| & 0 \end{bmatrix}^T = \begin{bmatrix} \alpha & 0 \end{bmatrix}^T \\ \boldsymbol{\mu}[1, 1] &= \begin{bmatrix} 0 & |h_1 + h_2| \end{bmatrix}^T = \begin{bmatrix} 0 & \alpha \end{bmatrix}^T\end{aligned}\quad (17)$$

where $\alpha = |h_1 + h_2| = \sqrt{\alpha_1^2 + \alpha_2^2 + 2\alpha_1\alpha_2 \cos(\theta_2 - \theta_1)}$.

The pdf of \mathbf{y} conditioned on $\boldsymbol{\mu}[b_1, b_2]$ may be found by marginalizing over the unknown phases

$$p(\mathbf{y} | \boldsymbol{\mu}[b_1, b_2]) = \int_0^{2\pi} \int_0^{2\pi} p(\phi_1, \phi_2) p(\mathbf{y} | \mathbf{m}[b_1, b_2]) d\phi_1 d\phi_2. \quad (18)$$

where ϕ_1 and ϕ_2 are the phases of the first and second elements of $\mathbf{m}[b_1, b_2]$, respectively.

Assume that the α_i are Rayleigh distributed so that the h_i are circularly-symmetric zero-mean complex Gaussian*.

*The receiver derived in this subsection is valid even for non-Rayleigh fading, provided that the received phases over the two channels are independent and uniform over $(0, 2\pi)$.

When $b_1 \neq b_2$ each element of $\mathbf{m}[b_1, b_2]$ is a circularly-symmetric zero-mean complex Gaussian and therefore has uniform phase. On the other hand, when $b_1 = b_2$, one element is $h_1 + h_2$, which is the sum of two circularly-symmetric zero-mean complex Gaussians, while the other element is zero. Since the sum of two circularly-symmetric complex Gaussians is also a circularly-symmetric complex Gaussian, it follows that $h_1 + h_2$ is a zero mean circularly-symmetric complex Gaussian and therefore its phase is uniform. Since the other element is zero, its phase is irrelevant and may be set to any arbitrary distribution, which is most conveniently chosen to be uniform. Thus, it follows that ϕ_1 and ϕ_2 are i.i.d. uniform. Therefore, the pdf conditioned on the magnitudes is

$$p(\mathbf{y}|\boldsymbol{\mu}[b_1, b_2]) = \frac{1}{\pi N_0} \int_0^{2\pi} \exp\left\{-\frac{|y_1 - \mu_1[b_1, b_2]e^{j\phi_1}|^2}{N_0}\right\} d\phi_1 \\ \times \frac{1}{\pi N_0} \int_0^{2\pi} \exp\left\{-\frac{|y_2 - \mu_2[b_1, b_2]e^{j\phi_2}|^2}{N_0}\right\} d\phi_2 \quad (19)$$

where $\mu_k[b_1, b_2]$ is the k^{th} element of $\boldsymbol{\mu}[b_1, b_2]$ and

$$\frac{1}{2\pi} \int_0^{2\pi} \exp\left\{-\frac{|y_k - \mu_k[b_1, b_2]e^{j\phi_k}|^2}{N_0}\right\} d\phi_k \\ = \exp\left\{-\frac{|y_k|^2 + (\mu_k[b_1, b_2])^2}{N_0}\right\} I_0\left(\frac{2|y_k|\mu_k[b_1, b_2]}{N_0}\right). \quad (20)$$

Substituting (20) into (19),

$$p(\mathbf{y}|\boldsymbol{\mu}[b_1, b_2]) = \beta \prod_{k=1}^2 \exp\left\{-\frac{(\mu_k[b_1, b_2])^2}{N_0}\right\} \\ \times I_0\left(\frac{2|y_k|\mu_k[b_1, b_2]}{N_0}\right) \quad (21)$$

where

$$\beta = \left(\frac{2}{N_0}\right)^2 \exp\left\{-\left(\frac{|y_1|^2 + |y_2|^2}{N_0}\right)\right\} \quad (22)$$

which is common to all four $\{b_1, b_2\}$ and will therefore cancel in the LLR (12).

For each event $\{b_1, b_2\}$, substitute the $p(\mathbf{y}|\boldsymbol{\mu}[b_1, b_2])$ given in (21) with the $\boldsymbol{\mu}[b_1, b_2]$ given by (16) and (17) as the corresponding $p(\mathbf{y}|\{b_1, b_2\})$ in (12). This results in

$$\Lambda(b) = \log \left[e^{-\alpha_1^2/N_0} I_0\left(\frac{2\alpha_1|y_1|}{N_0}\right) e^{-\alpha_2^2/N_0} I_0\left(\frac{2\alpha_2|y_2|}{N_0}\right) \right. \\ \left. + e^{-\alpha_2^2/N_0} I_0\left(\frac{2\alpha_2|y_1|}{N_0}\right) e^{-\alpha_1^2/N_0} I_0\left(\frac{2\alpha_1|y_2|}{N_0}\right) \right] \\ - \log \left[e^{-\alpha^2/N_0} I_0\left(\frac{2\alpha|y_1|}{N_0}\right) + e^{-\alpha^2/N_0} I_0\left(\frac{2\alpha|y_2|}{N_0}\right) \right]. \quad (23)$$

As discussed in Section IV, it is possible to accurately estimate α_1 and α_2 in the considered block fading environment, provided the blocks are sufficiently long. However, it is not generally feasible to precisely estimate α because the phases θ_1 and θ_2 are varying on a symbol-by-symbol basis. Since $E[\cos(\theta_2 - \theta_1)] = 0$, a reasonable approximation when an estimate of α is not available is to use

$$\alpha \approx \sqrt{\alpha_1^2 + \alpha_2^2}. \quad (24)$$

3) *Noncoherent PNC Receiver without CSI*: Suppose that besides not knowing the phases θ_1, θ_2 , the relay receiver does not know the magnitude vector $\boldsymbol{\mu}[b_1, b_2]$. Then, the relay must operate without any channel state information except for the average energies $\mathcal{E}_1, \mathcal{E}_2$ and the noise variance N_0 . When the magnitudes $\boldsymbol{\mu}[b_1, b_2]$ are not known, then the conditional pdf is found by marginalizing (21) over the unknown magnitudes

$$p(\mathbf{y}|\{b_1, b_2\}) = \int_0^\infty \int_0^\infty p(\mu_1, \mu_2) p(\mathbf{y}|\boldsymbol{\mu}[b_1, b_2]) d\mu_1 d\mu_2. \quad (25)$$

where μ_1 and μ_2 are the magnitudes of the first and second elements of $\boldsymbol{\mu}[b_1, b_2]$, respectively.

According to (16), when $b_1 \neq b_2$, one of the $\mu_k = \alpha_1$ while the other $\mu_k = \alpha_2$. Since α_1 and α_2 are independent and each α_i is Rayleigh with energy \mathcal{E}_i , it follows that the joint pdf of μ_1 and μ_2 when $(b_1, b_2) = (0, 1)$ is

$$p(\mu_1, \mu_2) = \left(\frac{2\mu_1}{\mathcal{E}_1} \exp\left\{-\frac{\mu_1}{\mathcal{E}_1}\right\}\right) \left(\frac{2\mu_2}{\mathcal{E}_2} \exp\left\{-\frac{\mu_2}{\mathcal{E}_2}\right\}\right) \quad (26)$$

for $\mu_1, \mu_2 \geq 0$, and when $(b_1, b_2) = (1, 0)$ it is

$$p(\mu_1, \mu_2) = \left(\frac{2\mu_1}{\mathcal{E}_2} \exp\left\{-\frac{\mu_1}{\mathcal{E}_2}\right\}\right) \left(\frac{2\mu_2}{\mathcal{E}_1} \exp\left\{-\frac{\mu_2}{\mathcal{E}_1}\right\}\right) \quad (27)$$

for $\mu_1, \mu_2 \geq 0$. Substituting (26) and (21) into (25) yields

$$p(\mathbf{y}|\{b_1 = 0, b_2 = 1\}) = \frac{|y_1|^2}{\frac{N_0^2}{\mathcal{E}_1} + N_0} + \frac{|y_2|^2}{\frac{N_0^2}{\mathcal{E}_2} + N_0} \\ + \log \left[\left(\frac{1}{\mathcal{E}_1 \mathcal{E}_2}\right) \left(\frac{1}{\mathcal{E}_1} + \frac{1}{N_0}\right) \left(\frac{1}{\mathcal{E}_2} + \frac{1}{N_0}\right) \right]^{-1} \quad (28)$$

Similarly, substituting (27) and (21) into (25) yields

$$p(\mathbf{y}|\{b_1 = 1, b_2 = 0\}) = \frac{|y_1|^2}{\frac{N_0^2}{\mathcal{E}_2} + N_0} + \frac{|y_2|^2}{\frac{N_0^2}{\mathcal{E}_1} + N_0} \\ + \log \left[\left(\frac{1}{\mathcal{E}_1 \mathcal{E}_2}\right) \left(\frac{1}{\mathcal{E}_1} + \frac{1}{N_0}\right) \left(\frac{1}{\mathcal{E}_2} + \frac{1}{N_0}\right) \right]^{-1} \quad (29)$$

As indicated by (17), when $b_1 = b_2$, one of the $\mu_k = \alpha$ while the other $\mu_k = 0$. As discussed below (18), in a Rayleigh-fading environment, h_1 and h_2 are independent, complex-valued, circularly-symmetric Gaussian variables, and therefore $h = h_1 + h_2$ is also a complex-valued, circularly-symmetric Gaussian variable. It follows that $\alpha = |h|$ is Rayleigh with energy $\mathcal{E}_1 + \mathcal{E}_2$, and the pdf of the nonzero μ_k is

$$p(\mu_k) = \frac{2\mu_k}{\mathcal{E}_1 + \mathcal{E}_2} \exp\left\{-\frac{\mu_k}{\mathcal{E}_1 + \mathcal{E}_2}\right\}, \quad \mu_k \geq 0. \quad (30)$$

For the $\mu_k = 0$, its pdf may be represented by an impulse at the origin, i.e. $p(\mu_k) = \delta(\mu_k)$. Substituting these pdfs with the appropriate $\boldsymbol{\mu}[b_1, b_2]$ into (25) yields

$$p(\mathbf{y}|\{b_1, b_2\}) = \log \left[\left(\frac{1}{\mathcal{E}_1 + \mathcal{E}_2}\right) \left(\frac{1}{\mathcal{E}_1 + \mathcal{E}_2} + \frac{1}{N_0}\right) \right]^{-1} \\ + \frac{|y_i|^2}{\frac{N_0^2}{\mathcal{E}_1 + \mathcal{E}_2} + N_0} \quad (31)$$

where $i = 1$ when $(b_1, b_2) = (0, 0)$ and $i = 2$ when $(b_1, b_2) = (1, 1)$.

Substituting (28) and (29) for the two $b_1 \neq b_2$ and (31) for the two $b_1 = b_2$ into (12) yields

$$\begin{aligned} \Lambda(b) &= \log \left[\frac{\xi_1 \xi_2}{\xi N_0} \right] \\ &+ \log \left[\exp \left\{ -\frac{|y_1|^2}{\xi} - \frac{|y_2|^2}{N_0} \right\} + \exp \left\{ -\frac{|y_1|^2}{N_0} - \frac{|y_2|^2}{\xi} \right\} \right] \\ &- \log \left[\exp \left\{ -\frac{|y_1|^2}{\xi_1} - \frac{|y_2|^2}{\xi_2} \right\} + \exp \left\{ -\frac{|y_1|^2}{\xi_2} - \frac{|y_2|^2}{\xi_1} \right\} \right] \end{aligned} \quad (32)$$

where $\xi_1 = \mathcal{E}_1 + N_0$, $\xi_2 = \mathcal{E}_2 + N_0$, and $\xi = \mathcal{E}_1 + \mathcal{E}_2 + N_0$.

IV. CHANNEL ESTIMATOR

The goal of the channel estimator is to estimate the values of the fading amplitudes α_1 and α_2 for a particular fading block. Let the fading amplitudes of a block be represented by the pair $\{A, B\}$, where $A \geq B$. Thus, $A = \max\{\alpha_1, \alpha_2\}$ and $B = \min\{\alpha_1, \alpha_2\}$. Note that in (23), exchanging α_1 and α_2 does not change the final expression. Therefore (23) is *commutative* in α_1 and α_2 , and may be written as

$$\begin{aligned} \Lambda(b) &= \max * \left[F \left(\frac{2A|y_1|}{N_0} \right) + F \left(\frac{2B|y_2|}{N_0} \right), \right. \\ &\quad \left. F \left(\frac{2B|y_1|}{N_0} \right) + F \left(\frac{2A|y_2|}{N_0} \right) \right] \\ &- \max * \left[F \left(\frac{2\sqrt{A^2 + B^2}|y_1|}{N_0} \right), F \left(\frac{2\sqrt{A^2 + B^2}|y_2|}{N_0} \right) \right] \end{aligned} \quad (33)$$

where the approximation $\alpha \approx \sqrt{\alpha_1^2 + \alpha_2^2}$ has been used and $F(x) = \log[I_0(x)]$, which may be efficiently and accurately computed through the following piecewise polynomial fit:

$$F(x) = \log[I_0(x)] \approx \begin{cases} 0.22594x^2 + 0.012495x - 0.0011272 & 0 < x \leq 1 \\ 0.12454x^2 + 0.21758x - 0.10782 & 1 < x \leq 2 \\ 0.028787x^2 + 0.63126x - 0.56413 & 2 < x \leq 5 \\ 0.003012x^2 + 0.88523x - 1.2115 & 5 < x \leq 15 \\ 0.00053203x^2 + 0.95304x - 1.6829 & 15 < x \leq 30 \\ 0.00013134x^2 + 0.97674x - 2.0388 & 30 < x \leq 60 \\ 0.9943x - 2.6446 & 60 < x \leq 120 \\ 0.99722x - 3.0039 & 120 < x \leq 500 \\ 0.99916x - 3.6114 & x > 500. \end{cases} \quad (34)$$

A. Fading Amplitude Estimator

To estimate A and B , first add the two elements of each \mathbf{y}_i to obtain

$$r_i = y_{i,1} + y_{i,2} = h_{i,1} + h_{i,2} + \underbrace{n_{i,1} + n_{i,2}}_{\nu_i} \quad (35)$$

where ν_i is circularly-symmetric complex Gaussian noise with variance $2N_0$, and $h_{i,k}$ is the channel coefficient between terminal \mathcal{N}_k , $k = \{1, 2\}$, and the relay during the i^{th} signaling interval. The signal r_i is the noisy sum of two complex fading

coefficients, and therefore the fading-amplitude estimation algorithm proposed by Hamkins in [20] may be used. To determine the values of A and B , a system of two equations with two unknowns is required. The first equation, found by taking the expected value of $|r_i|^2$ under the assumption that the fading amplitudes are fixed for the block in question, is

$$\begin{aligned} E[|r_i|^2] &= E[\alpha_1^2 + \alpha_2^2 + 2\alpha_1\alpha_2 \cos(\theta_{i,2} - \theta_{i,1})] \\ &= E[\alpha_1^2 + \alpha_2^2] = \alpha_1^2 + \alpha_2^2 = A^2 + B^2. \end{aligned} \quad (36)$$

The second equation is found by conditioning on the event $\{|r|^2 > A^2 + B^2\}$, which is equivalent to $\{\cos(\theta_{i,2} - \theta_{i,1}) > 0\}$ and has expected value [20]

$$E[|r|^2 | |r|^2 > A^2 + B^2] = A^2 + B^2 + \frac{4AB}{\pi}. \quad (37)$$

Solving (36) and (37) for A and B yields

$$\begin{aligned} A &= \frac{1}{2} \left(\sqrt{X + \frac{\pi}{2}(Y - X)} + \sqrt{X + \frac{\pi}{2}(X - Y)} \right) \\ B &= \frac{1}{2} \left(\sqrt{X + \frac{\pi}{2}(Y - X)} - \sqrt{X + \frac{\pi}{2}(X - Y)} \right) \end{aligned} \quad (38)$$

where $X = E[|r|^2]$ and $Y = E[|r|^2 | |r|^2 > A^2 + B^2]$.

Since the expected values required for (38) are not known, they may be estimated by using the corresponding statistical averages,

$$\begin{aligned} \hat{X} &= \frac{1}{N} \sum_{i=1}^N |r_i|^2 \\ \hat{Y} &= \frac{2}{N} \sum_{i: |r_i|^2 > \hat{X}} |r_i|^2 \end{aligned} \quad (39)$$

where N is the size of the fading block and the factor $2/N$ used to compute \hat{Y} assumes that $|r_i|^2 > \hat{X}$ for approximately $N/2$ symbols. If this assumption is not true, then the multiplication by $2/N$ can be replaced with a division by the number of samples that satisfy $|r_i|^2 > \hat{X}$. As an alternative to summing over the $|r_i|^2 > \hat{X}$, Hamkins proposes summing over those $|r_i|^2$ greater than the median value of $\{|r_1|^2, \dots, |r_N|^2\}$ [20].

The estimator works by computing estimates \hat{X} and \hat{Y} using (39) and the $\{r_1, \dots, r_N\}$ for the block. These estimates are used in place of X and Y in (38), which yields estimates \hat{A} and \hat{B} of A and B . These estimates are then used in place of A and B in (33).

B. Transmission-Case Detection

According to (35), the two elements of \mathbf{y}_i are always added together. When $b_1 = b_2$, only one tone is used, and the noise can be reduced if the receiver processes only the tone used and ignores the other tone. This requires that the receiver be able to detect whether the first tone, the second tone, or both tones were used, which may be implemented using a variation of the “no-CSI” receiver described in subsection III-B3. In [16], we contemplate an estimator that uses such a *transmission-case detector*. However, we found that the performances with and without the transmission-case detector were virtually identical and do not consider it further in this paper. At best, proper use of the transmission-case detector reduces the noise variance

from $2N_0$ to N_0 during the symbol intervals that both nodes transmit the same tone. As will be seen in the numerical results, the estimator is resilient enough against noise that this reduction in noise variance is not meaningful and does not justify the additional complexity.

C. Amplitude Estimation for Single-Transmitter Links

During the broadcast phase, there is only a single transmission, and the dual-amplitude estimator described in subsection IV-A is not necessary. Similarly, the estimator is not needed by the LNC system during the MAC phase since the two transmissions are over orthogonal channels. To estimate the fading amplitudes for the links involving only a single transmitter and receiver, the simple averaging technique given by (29) in [21] is used, which is described as follows. Consider the i^{th} signaling interval during the ℓ^{th} fading block. Given transmission of tone k , in the absence of noise, the k^{th} matched-filter output at the receiver is $y_{k,i} = \alpha e^{j\theta_i}$, and has magnitude $|y_{k,i}| = \alpha$. All other matched-filter outputs in the i^{th} signaling interval are 0. An estimate could be formed by taking the maximum $|y_{k,i}|$ over any column of \mathbf{Y}_ℓ . In the presence of noise, an estimate of α can be formed by averaging across all columns of the fading block

$$\hat{\alpha} = \frac{1}{N} \sum_{i=1}^N \max_k |y_{k,i}|. \quad (40)$$

V. SIMULATION STUDY

This section presents simulated performance results for the relay receiver described in Section III. The simulated link model is as described in Section II, with specific simulation parameters given in the following subsections. The goal of the simulations is to compare the performance of comparable DNC and LNC systems and to assess the robustness of the channel estimator proposed in IV. Because the relay-broadcast phase of the DNC and LNC systems operate in exactly the same manner and have the same performance, we only focus on the performance of the MAC phase.

A. Uncoded Performance with Perfect Channel Estimates

We initially consider a system that does not use an outer error-correcting code, and thus $\mathbf{b}_i = \mathbf{u}_i$, $i = 1, 2$. We compare the performance of the LNC and DNC systems. With the LNC system, the two nodes transmit their messages in orthogonal time slots and the relay receiver first generates the individual LLR's during each time slot using either (9) or (10), and then the two LLR's are combined using (11). When there is no outer error-correcting code, performance using (9) is approximately the same as that using (10). A bit error is declared at the relay whenever a hard decision using (11) results in an erroneous decision on the corresponding bit of the network codeword \mathbf{b} . Such an error will usually occur if one of the two bits b_1, b_2 is received incorrectly, and therefore the error rate of the LNC system is approximately $P_b \approx 2p(1-p)$ where p is the bit error rate of noncoherent binary FSK modulation [17].

With the DNC system, the two nodes transmit simultaneously, and the relay receiver computes the LLR using (23)

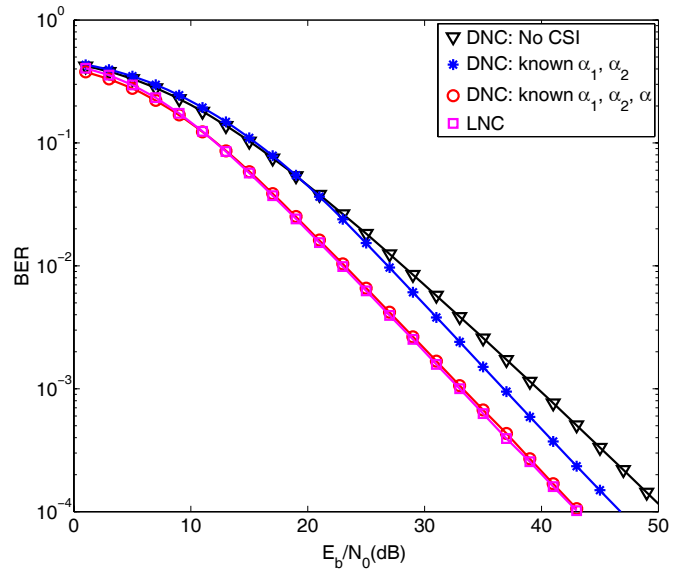


Fig. 3. Bit error rate at the relay in Rayleigh fading when DNC and LNC is used and $\mathcal{E}_2 = \mathcal{E}_1$. Depending on the amount of channel state information that is available, the PNC system will use one of three different relay receivers.

when the magnitudes $\mu[b_1, b_2]$ are known or (32) when they are not. A hard decision is made on the LLR and a bit error is declared if the estimate of the corresponding network codeword bit b is incorrect. We assume that the channel estimates are perfect, and since there is no error-correction coding, the size of the fading block is irrelevant provided that the channel coherence time is not exceeded.

Initially, we set the average received energy to be the same over both channels, i.e. $\mathcal{E}_2 = \mathcal{E}_1 = \mathcal{E}_s = \mathcal{E}_b$. Fig. 3 shows the performance of the LNC and DNC systems in Rayleigh fading with equal energy signals. As anticipated, the LNC system offers the best performance, which is approximately 3 dB worse than a standard binary CPFSK system with noncoherent detection (the loss relative to conventional CPFSK is due to the fact that both bits must usually be received correctly). Three curves for the DNC system are shown in Fig. 3, corresponding to receivers that exploit different amounts of available channel state information. The best performance is achieved using a receiver implemented with (23), which requires knowledge of α_1, α_2 , and α . The performance of the DNC system implemented with (23) is only about 0.25 dB worse than that of the LNC system. The worst performance is achieved using a receiver implemented using (32), which does not require knowledge of the fading amplitudes. The loss due to using (32) instead of (23) is about 10 dB, indicating that estimating the fading amplitudes at the relay is necessary.

While it may be feasible to estimate α_1 and α_2 , estimating α may prove to be more difficult because it will depend on not only the individual fading amplitudes, but also on the phase difference between the two channels. Since the phase difference might change more quickly than the individual amplitudes, it might not be practical to estimate α . If that is the case, then the approximation given by (24) can be used in place of the actual value of α . The performance using this technique is also shown in Fig. 3 and shows a loss of about 3 dB with respect to the known- $\mu[b_1, b_2]$ system, which requires knowledge of α .

The performance of DNC is sensitive to the balance of

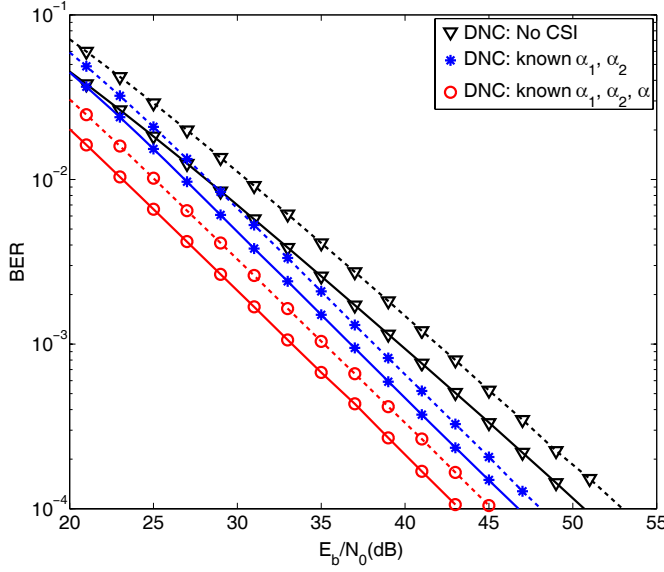


Fig. 4. Bit error rate at the relay in Rayleigh fading of DNC with three different receivers and either $\mathcal{E}_2 = \mathcal{E}_1$ (solid line) or $\mathcal{E}_2 = 4\mathcal{E}_1$ (dashed line).

power received over the two channels. Performance is best when $\mathcal{E}_1 = \mathcal{E}_2$. In order to evaluate how robust the DNC relay receivers are to an imbalance of power, the simulations were repeated with $\mathcal{E}_2 = 4\mathcal{E}_1$, while keeping $\mathcal{E}_b = \mathcal{E}_s = (\mathcal{E}_1 + \mathcal{E}_2)/2$. These results are shown in Fig. 4 for the three receiver formulations that were considered in the previous figure. When the power is imbalanced in this way, there is a loss of about 2 dB. However, the loss is the same for all three receiver implementations, suggesting that they are robust to an imbalance of power.

B. Uncoded Performance with Channel Estimation

We now consider the influence of channel estimation, but still assume that the system does not use error-correction coding. In the simulations, the information frames generated at the end nodes contain $K = 2048$ bits per frame. The fading blocks are length $N = \{8, 32, 128\}$ symbols per block. The DNC relay implements (32) and then makes a hard decision on each information bit.

The bit error-rate performance of the uncoded system is shown in Fig. 5. The performance is shown with the estimator using the three block sizes $N = \{8, 32, 128\}$ as well as for the case of perfect estimates of α_1 and α_2 . A narrow range of error rates is shown to better highlight the differences in performance. In general, smaller fading blocks lead to a less accurate estimation of the fading amplitudes, as the number of samples available for estimation decreases. Moving from block size $N = 128$ to 32 worsens performance by roughly 0.25 dB, and from $N = 32$ to 8 by 0.75 dB.

C. Performance with an Outer Turbo Code

Now consider a system that uses an outer turbo code. The terminals each encode length $K = 1229$ information sequences into length $L = 2048$ codewords, using a rate $r_1 \approx 0.6$ UMTS turbo code [22]. The relay performs turbo decoding using the codeword LLR's computed by (32). The

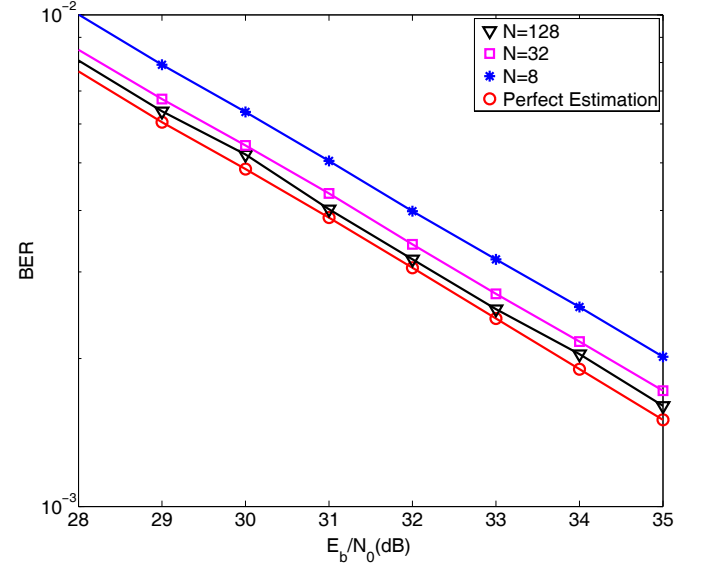


Fig. 5. Influence of fading-block length N on uncoded DNC error-rate performance at the relay. In addition to curves for three values of N , a curve is shown indicating the performance with perfect fading-amplitude knowledge.

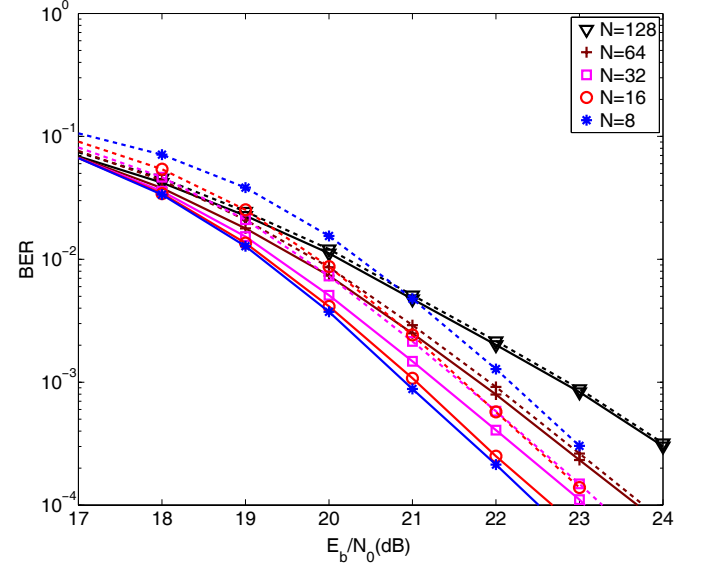


Fig. 6. Influence of fading-block length N on turbo-coded DNC error-rate performance at the relay. Two curves are shown for each value of $N = \{8, 16, 32, 64, 128\}$. Solid curves denote perfect fading-amplitude knowledge. Dashed curves denote estimated fading amplitudes.

fading-block lengths simulated are $N = \{8, 16, 32, 64, 128\}$ symbols per block.

The error performance of the coded system is shown in Fig. 6, both with perfect channel estimates and with estimated fading amplitudes. A good tradeoff between diversity and estimation accuracy is achieved for block sizes $N = 16$ and $N = 32$, which exhibit the best performance of all systems that must estimate the fading amplitudes. For $N < 16$ performance degrades due to the lack of enough observations per block for accurate channel estimates, while for $N > 32$ performance degrades due to the reduction in time diversity.

Fig. 7 shows the SNR required to reach an error rate of 10^{-4} at the relay as a function of the block length N . In each case, information is coded with the same (2048, 1229) turbo code used for Fig. 6. Curves for three systems are shown: The noncoherent receiver with known $\{\alpha_1, \alpha_2\}$, the noncoherent

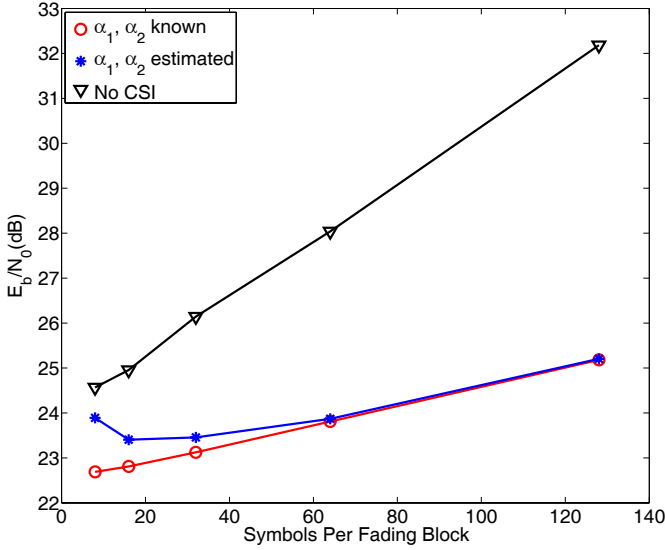


Fig. 7. Signal-to-noise ratio required to reach a bit error rate of 10^{-4} at the relay as a function of fading-block length. The performance of three systems is shown: The noncoherent receiver with known $\{\alpha_1, \alpha_2\}$, the noncoherent receiver with estimated $\{\alpha_1, \alpha_2\}$, and the noncoherent receiver that does not use CSI. All systems use a Turbo code with rate 1229/2048.

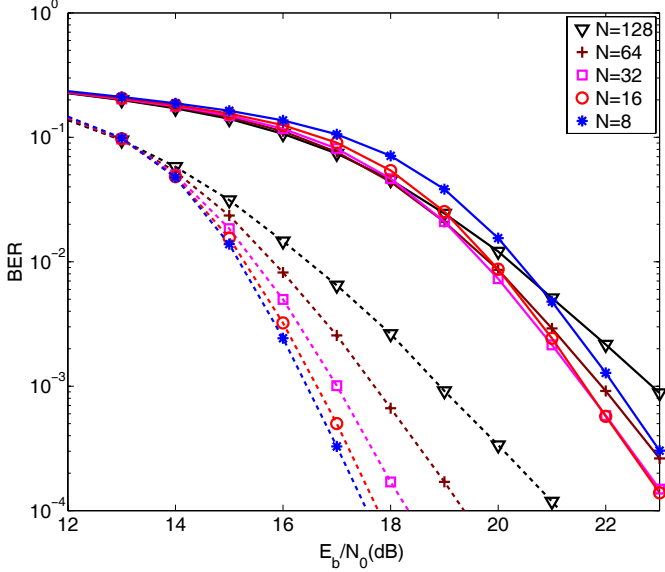


Fig. 8. Comparison of error-rate performance between the turbo-coded DNC and LNC systems at the relay. The solid lines denote DNC, while the dashed lines denote LNC.

receiver with estimated $\{\alpha_1, \alpha_2\}$, and the noncoherent receiver that does not use CSI. When $\{\alpha_1, \alpha_2\}$ are not estimated, performance improves with decreasing N because of the increased number of blocks per codeword, which increases the time diversity. However, when $\{\alpha_1, \alpha_2\}$ are estimated, the performance gets worse when the block size is smaller than $N = 16$. The loss of time diversity as the block size increases is a common problem for any system operating over a slow-fading channel, and the system proposed in this paper is no exception. The performance gap between the known-CSI and no-CSI receiver formulations widens with increasing block length.

An error-rate performance comparison between DNC and LNC is shown in Fig. 8. Both systems use the same (2048, 1229) turbo code. The LNC system outperforms the

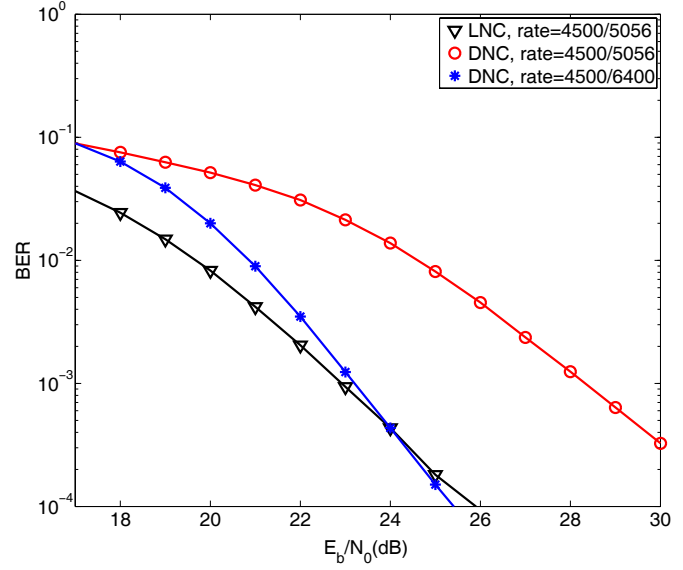


Fig. 9. Comparison of the performance of turbo-coded DNC and LNC at the relay with block size $N = 32$. For the DNC system, two code rates are shown, with the lower rate code offering comparable performance to the LNC system.

DNC system by margins ranging between 4 and 6 dB.

While the LNC system is more energy efficient than the DNC system when the same-rate turbo code is used, the throughput of the LNC system is worse than that of the DNC system because the two terminals must transmit in orthogonal time slots. The loss in energy efficiency from using DNC versus LNC can be recovered by having the source terminals use a lower-rate turbo code. Consider the performance comparison shown in Fig. 9 for block size $N = 32$. At $E_b/N_0 \approx 24$ dB, DNC using a rate $r_1 = 4500/6400$ code matches the error-rate performance of LNC using a rate $r_1 = 4500/5056$ code. Because the two terminals transmit at the same time, the end-to-end throughput of DNC is higher than that of LNC, even though the DNC terminals transmit to the relay with a lower-rate channel code.

To illustrate the throughput improvement of DNC over LNC, consider the following transmission schedule for the two systems. Assume the source terminals use rate $r_1 = 4500/6400$ in DNC, and $r_1 = 4500/5056$ in LNC. Assume operation at $E_b/N_0 = 24$ dB, yielding approximately equal relay error-rate performance. Further, assume that both systems use code rate $r_2 = 4500/5056$ for relay broadcast, yielding approximately equal end-to-end performance. DNC requires 6400 channel uses for transmission to the relay versus $2 \times 5056 = 10112$ for LNC. Both systems require 5056 channel uses for relay broadcast. The throughput for DNC is thus $T^{(DNC)} = 9000/(6400 + 5056) = 9000/11,456$ bits per channel use, and for LNC $T^{(LNC)} = 9000/(3 \times 5056) = 9000/15,168$ bits per channel use. The percentage throughput increase of DNC over LNC is thus $(T^{(DNC)}/T^{(LNC)} - 1) \times 100 \approx 32.4\%$.

VI. CONCLUSION

A throughput-improving technique for relaying in the two-way relay network, *digital network coding*, is refined for practical operation. The system operates noncoherently, providing advantages over coherent operation: there are no requirements

for perfect power control, phase synchronism, or estimates of carrier-phase offset.

A computationally simple technique for estimating fading amplitudes at the relay is implemented. Error-rate performance in the noncoherent Rayleigh block-fading channel at several block sizes is presented. The system is simulated with and without an outer error-correcting code. The coded error-rate performance of the system using estimation differs from that with ideal estimates by margins between 0.7 – 1.5 dB.

When the same-rate turbo code is used, digital network coding has a higher throughput but lower energy-efficiency than link-layer network coding. The energy loss of DNC can be recovered by using a lower-rate turbo code during the MAC phase. Even when the loss of spectral efficiency due to the lower-rate turbo code is taken into account, the DNC system is able to achieve a higher throughput than LNC at the same energy-efficiency. In the particular example presented in this paper, the DNC system is capable of achieving throughputs that are 32.4% larger than that of the equivalent LNC system, while operating at the same energy efficiency.

REFERENCES

- [1] B. Rankov and A. Wittneben, "Achievable rate regions for the two-way relay channel," in *Proc. Int. Symp. Inf. Theory*, pp. 1668-1672, July 2006.
- [2] S. Zhang, S. C. Liew, and P. P. Lam, "Hot topic: physical-layer network coding," in *Proc. ACM Annual Int. Conf. Mobile Comput. Netw.*, pp. 358-365, Sep. 2006.
- [3] R. Ahlswede, N. Cai, S. Li, and R. Yeung, "Network information flow," *IEEE Trans. Inf. Theory*, vol. 46, pp. 1204-1216, July 2000.
- [4] M. Chen and A. Yener, "Multiuser two-way relaying: detection and interference management strategies," *IEEE Trans. Wireless Commun.*, vol. 8, no. 8, pp. 4296-4305, Aug. 2009.
- [5] S. Katti, S. Gollakota, and D. Katabi, "Embracing wireless interference: analog network coding," in *Proc. ACM SIGCOMM*, pp. 397-408, Aug. 2007.
- [6] S. Zhang, S. C. Liew, and L. Lu, "Physical layer network coding schemes over finite and infinite fields," in *Proc. IEEE Global Telecommun. Conf.*, pp. 1-6, Dec. 2008.
- [7] E. Peh, Y. Liang, and Y. L. Guan, "Power control for physical-layer network coding in fading environments," in *Proc. IEEE Personal Indoor Mobile Radio Commun. Conf.*, pp. 1-5, 2008.
- [8] S. Katti, H. Rahul, W. Hu, D. Katabi, M. Medard, and J. Crowcroft, "XORs in the air: practical wireless network coding," *IEEE/ACM Trans. Netw.*, pp. 497-510, June 2008.
- [9] P. Popovski and H. Yomo, "Wireless network coding by amplify-and-forward for bi-directional traffic flows," *IEEE Commun. Lett.*, vol. 11, pp. 16-18, Jan. 2007.
- [10] J. Sørensen, R. Krigslund, P. Popovski, T. Akino, and T. Larsen, "Physical layer network coding for FSK systems," *IEEE Commun. Lett.*, vol. 13, no. 8, pp. 597-599, Aug. 2009.
- [11] M. C. Valenti, D. Torrieri, and T. Ferrett, "Noncoherent physical-layer network coding using binary CPFSK modulation," in *Proc. IEEE Military Commun. Conf.*, pp. 1-7, Oct. 2009.
- [12] T. Cui, F. Gao, and C. Tellambura, "Physical layer differential network coding for two-way relay channels," in *Proc. IEEE Global Telecommun. Conf.*, Dec. 2008.
- [13] S. Zhang and S. C. Liew, "Channel coding and decoding in a relay system operated with physical-layer network coding," *IEEE J. Sel. Areas Commun.*, vol. 27, pp. 788-789, June 2009.
- [14] B. Jiang, F. Gao, X. Gao, and A. Nallanathan, "Channel estimation and training design for two-way relay networks with power allocation," *IEEE Trans. Wireless Commun.*, vol. 9, no. 6, pp. 2022-2032, June 2010.
- [15] F. Gao, R. Zhang, and Y. C. Liang, "On channel estimation for amplify-and-forward two-way relay networks," in *Proc. IEEE Global Telecommun. Conf.*, Dec. 2008.
- [16] T. Ferrett, M. C. Valenti, and D. Torrieri, "Receiver design for noncoherent digital network coding," in *Proc. IEEE Military Commun. Conf.*, Nov. 2010.
- [17] J. G. Proakis and M. Salehi, *Digital Communications*, 5th edition. McGraw-Hill, Inc., 2008.
- [18] S. Cheng, M. C. Valenti, and D. Torrieri, "Robust iterative noncoherent reception of coded FSK over block fading channels," *IEEE Trans. Wireless Commun.*, vol. 6, pp. 3142-3147, Sep. 2007.
- [19] M. C. Valenti and S. Cheng, "Iterative demodulation and decoding of turbo coded M -ary noncoherent orthogonal modulation," *IEEE J. Sel. Areas Commun.*, vol. 23, pp. 1738-1747, Sep. 2005.
- [20] J. Hamkins, "An analytic technique to separate cochannel FM signals," *IEEE Trans. Commun.*, vol. 48, pp. 543-546, Apr. 2000.
- [21] D. Torrieri, S. Cheng, and M. C. Valenti, "Robust frequency hopping for interference and fading channels," *IEEE Trans. Wireless Commun.*, vol. 56, pp. 1343-1351, Aug. 2008.
- [22] European Telecommunications Standards Institute, "Universal mobile telecommunications system (UMTS): multiplexing and channel coding (FDD)," 3GPP TS 25.212 version 7.4.0, June 2006.

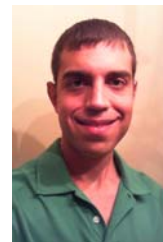


Matthew C. Valenti is a Professor in Lane Department of Computer Science and Electrical Engineering at West Virginia University. He holds B.S. and Ph.D. degrees in Electrical Engineering from Virginia Tech and a M.S. in Electrical Engineering from the Johns Hopkins University. From 1992 to 1995 he was an electronics engineer at the U.S. Naval Research Laboratory. He serves as an associate editor for IEEE TRANSACTIONS ON WIRELESS COMMUNICATIONS and as co-chair of the Technical Program Committee for Globecom-

2013, and has served as an editor for IEEE TRANSACTIONS ON VEHICULAR TECHNOLOGY and as track or symposium co-chair for the Fall 2007 VTC, ICC-2009, Milcom-2010, and ICC-2011. His research interests are in the areas of communication theory, error correction coding, applied information theory, wireless networks, simulation, and grid computing. His research is funded by the NSF and DoD.



Don Torrieri is a research engineer and Fellow of the US Army Research Laboratory. His primary research interests are communication systems, adaptive arrays, and signal processing. He received the Ph.D. degree from the University of Maryland. He is the author of many articles and several books including *Principles of Spread-Spectrum Communication Systems*, 2nd ed. (Springer, 2011). He teaches graduate courses at Johns Hopkins University and has taught many short courses. In 2004, he received the Military Communications Conference achievement award for sustained contributions to the field.



Terry Ferrett is a research assistant at West Virginia University, Morgantown, WV completing his Ph.D. degree in electrical engineering. He received the B.S. degrees in electrical engineering and computer engineering in 2005 and the M.S. degree in electrical engineering in 2008 from West Virginia University. He is the architect of a cluster computing resource utilized by electrical engineering students at West Virginia University to conduct communication theory research. His research interests are network coding, digital receiver design, the information theory of relay channels, cluster and grid computing, and software project management.

Transmission of Information Between Complex Systems: $1/f$ Resonance

Gerardo Aquino, Mauro Bologna, Bruce J. West, and Paolo Grigolini

Physical Review E, 83, 051130 (2011)

Transmission of information between complex systems: $1/f$ resonance

Gerardo Aquino,^{1,*} Mauro Bologna,² Bruce J. West,³ and Paolo Grigolini⁴

¹*Faculty of Natural Sciences, Imperial College London, SW7 2AZ London, United Kingdom*

²*Instituto de Alta Investigación, Universidad de Tarapacá-Casilla 7-D Arica, Chile*

³*Physics Department, Duke University, North Carolina, USA*

⁴*Center for Nonlinear Science, University of North Texas, P.O. Box 311427, Denton, Texas 76203-1427, USA*

(Received 21 February 2011; published 31 May 2011)

We study the transport of information between two complex systems with similar properties. Both systems generate non-Poisson renewal fluctuations with a power-law spectrum $1/f^{3-\mu}$, the case $\mu = 2$ corresponding to ideal $1/f$ noise. We denote by μ_S and μ_P the power-law indexes of the system of interest S and the perturbing system P , respectively. By adopting a generalized fluctuation-dissipation theorem (FDT) we show that the ideal condition of $1/f$ noise for both systems corresponds to maximal information transport. We prove that to make the system S respond when $\mu_S < 2$ we have to set the condition $\mu_P < 2$. In the latter case, if $\mu_P < \mu_S$, the system S inherits the relaxation properties of the perturbing system. In the case where $\mu_P > 2$, no response and no information transmission occurs in the long-time limit. We consider two possible generalizations of the fluctuation dissipation theorem and show that both lead to maximal information transport in the condition of $1/f$ noise.

DOI: 10.1103/PhysRevE.83.051130

PACS number(s): 05.40.-a, 87.18.Tt, 87.19.lm, 89.70.Hj

I. INTRODUCTION

Linear response theory (LRT) [1] is one of the basic ways of obtaining information from fluctuations in nonequilibrium statistical physics [2,3] that is currently adopted to address new phenomena such as glassy systems [2] and granular matter [3]. An even more challenging issue is the application of LRT to complex processes such as physiological processes and especially the understanding of brain dynamics.

It is becoming more widely accepted that the brain operates at criticality [4,5] and that the critical condition of a phase transition has manifestations that extend beyond the conventional condition of temperature driven systems [6]. Frantsuzov *et al.* [7] adopted a model of cooperatively interacting units to propose a solution to the long-standing mystery of the origin of the power-law distribution of the blinking times in colloidal quantum dot fluorescence. On the other hand, this form of intermittence is characterized by the condition of renewal aging [8] and by the consequent ergodicity breakdown [9] that makes it impossible to use conventional LRT. We refer to these systems as *complex systems*. It is now very well understood [10] that the breakdown of the ergodic condition is caused by the occurrence of *crucial events*. It is interesting to remark that the same perspective applies to complex networks, when the cooperation-induced phase transition produces temporal complexity and crucial events as illustrated in the work of Ref. [11]. These events are renewal, namely, the time interval between two consecutive events does not have any relation whatsoever with the earlier or later time intervals between two consecutive events. Yet, if a Gibbs ensemble is suitably *prepared* initially, namely, in all the systems of the ensemble an event occurs at the time origin, then the rate of event production turns out to be time dependent rather than constant as in the ordinary Poisson case. The authors of Refs. [12,13] applied this theoretical perspective to the liquid crystal dynamics and

experimentally realized a true cascade of renewal events. The time interval between two consecutive crucial events is given by a waiting times probability density function (PDF) $\psi(\tau)$ with the following asymptotic form

$$\psi(\tau) = (\mu - 1) \frac{T^{\mu-1}}{(\tau + T)^{\mu-1}}, \quad (1)$$

and the power-law index μ fulfilling the inequality

$$1 < \mu < 3. \quad (2)$$

It is important to explain the origin of the special form of Eq. (1). First of all we want to stress that according to a point of view in the field of complexity, only the asymptotic time behavior matters, namely, $\psi(\tau) \propto 1/\tau^\mu$. The adoption of this widely shared point of view, as we shall see hereby, would prevent us from establishing a correct accordance with the experiments on the response of complex systems to external perturbations. Thus, the choice of Eq. (1) is dictated by the need for defining a border between the asymptotic time regime ($\tau \gg T$) and the microscopic time regime ($\tau \leq T$). Given the neurophysiology interest of this paper and especially the focus on brain dynamics, we refer the interested reader to the work of Ref. [14], where the waiting times PDF of Eq. (1) is obtained by means of a Fechner transformation [14] from the conventional Poisson distribution.

The rate of cascade of renewal events tends to a vanishing value as $1/t^{2-\mu}$ when $\mu < 2$ and to a constant value as $1/t^{\mu-2}$ when $\mu > 2$. It is evident that in both cases the time duration of the out-of-equilibrium condition is infinite, thereby raising the challenging task of going beyond conventional LRT to describe the dynamics.

Conventional LRT is given by the following expression:

$$\sigma(t) = \langle \xi_S(t) \rangle = \epsilon \int_0^t ds \chi(t,s) \xi_P(s), \quad (3)$$

where $\xi_S(t)$ is the fluctuation produced by the system of interest S . The symbol $\langle \xi_S(t) \rangle$ denotes the Gibbs average

*g.aquino@imperial.ac.uk

over the fluctuations. In the absence of perturbation this average is assumed to vanish. The variable $\xi_P(t)$ denotes the time-dependent perturbation and ϵ its intensity. LRT predicts the response of S on the basis of the unperturbed correlation function of ξ_S . In fact, the function $\chi(t, s)$, called the linear response function, is related to the correlation function of the fluctuation ξ_S , whose quadratic mean value is assumed for simplicity to be normalized to unity

$$\Psi_S(t, s) \equiv \langle \xi_S(t) \xi_S(s) \rangle, \quad (4)$$

by the following expression

$$\chi(t, s) = \frac{d}{ds} \Psi_S(t, s). \quad (5)$$

Note that the traditional LRT refers to the stationary case

$$\Psi_S(t, s) = \Psi_S(t - s), \quad (6)$$

and as a consequence

$$\frac{d}{ds} \Psi_S(t, s) = -\frac{d}{dt} \Psi_S(t, s). \quad (7)$$

This condition is not fulfilled by complex systems. For these latter systems the choices of linear response functions

$$\chi(t, s) = \frac{d}{ds} \Psi_S(t, s), \quad (8)$$

and

$$\chi(t, s) = -\frac{d}{dt} \Psi_S(t, s), \quad (9)$$

are not equivalent.

The authors of Refs. [15–18] have discussed the foundation of both choices and have established that the new form of LRT is determined by the physical way through which perturbation determines a bias. For the sake of simplicity these authors have made the assumption that $\xi_S(t)$ is a dichotomous signal. Using the jargon of turbulence theory they called the time intervals between two consecutive crucial events *laminar regions*. At the moment of a crucial event occurrence, unperturbed dynamics are realized by the random selection of either the positive, $\xi_S = 1$, or the negative value, $\xi_S = -1$. In other words, they assume that the occurrence of a crucial event generates the tossing of a fair coin which determines the sign of the next laminar region. Consequently, the external perturbation can generate a bias in two different ways. The first way rests on affecting the fairness of the coin tossing process. If $\xi_P(t) > 0$ ($\xi_P(t) < 0$) the choice of the positive (negative) sign is more probable than the choice of the negative (positive) sign. This prescription leads to the choice of Eq. (8) and is denoted as *phenomenological* LRT.

The experiments done by the authors of Refs. [12,13] show that nature prefers Eq. (9), the dynamic LRT. What is the theoretical argument in favor of the dynamical theory? To afford a convincing answer to this important question, let us go back to the special form of Eq. (1). We note that we do not know the Hamiltonian of our complex system, and we do not even know if a satisfactory discussion of the complex dynamics can be made using a Hamiltonian formalism. Let us assume that Eq. (1) is a reliable representation for the distribution length of the laminar region. In this case, a

reasonable conjecture is that the external perturbation affects either μ or T , or both parameters defining the form of Eq. (1). We know that μ defines the system's complexity and emerges from the cooperative interaction among interacting units. A weak external perturbation is not expected to change the system's complexity. It is therefore reasonable to assume that the external perturbation affects T , by enlarging (reducing) its value if ξ_P and ξ_S have the same (opposite) sign. This assumption leads to the choice of Eq. (9), as shown earlier [15–18].

It is important to notice that the response of a complex system of the same nature as the one discussed in this paper has been studied by many authors [19–28]. These authors did not establish a connection between their results and the LRT of Refs. [15–18] and in some cases they made the misleading conjecture that their results establish the “death of LRT.” Actually, these theoretical treatments are asymptotic in time and the only possible connection with LRT is through the adoption of the phenomenological theory of Eq. (8), as the readers can establish by a careful reading of Ref. [28].

We are now in a position to define the main purpose of this paper. We draw the attention of the readers to the recent results of the authors Ref. [29]. This paper addresses the important issue of studying the response of a complex system to a complex external perturbation with the surprising result that a complex system does not respond to stimuli that are not complex (i.e., that have a stationary Fourier spectrum). It is important to stress that the authors of Ref. [29] focused on the correlation between $\xi_S(t)$ and $\xi_P(t)$ in the long-time limit. This is an ideal condition that has the effect of restraining the definition of complexity to the systems with $\mu \leq 2$. In fact, in the long-time limit a system with $\mu > 2$ reaches the normal condition of a constant rate of event production, thereby recovering the ordinary Poisson condition. The condition $\mu = 2$ is of fundamental importance for brain function. In fact, recent work [30,31] established that the brain works with $\mu = 2$, which, in turn, is known [32] to correspond to making the brain action become the source of ideal $1/f$ noise. The results of the authors of Ref. [29] may therefore have important applications to design the most convenient stimuli to drive complex networks, and especially brain dynamics, via what was defined as “complexity management” [29]. However, an apparent weakness found in Ref. [29] is that these results are derived from the adoption of the phenomenological LRT, thereby raising doubt that those complex systems, which have been proven to obey the dynamical LRT [12,13], may not obey the principle of *complexity management* (CM) established in Ref. [29]. Herein we prove that the more realistic dynamical LRT generates CM. In addition to this main purpose, the present paper affords technical details on the theory developed in Ref. [29] that, due to space limitations, were not conveniently illustrated.

II. FDT FOR THE NONERGODIC RENEWAL REGIME: PHENOMENOLOGICAL AND DYNAMICAL APPROACH

The authors of Refs. [15,16] discovered a form of FDT that applies to systems or networks whose dynamics are dominated by non-Poisson renewal events. In the stationary case this

FDT becomes indistinguishable from the ordinary theoretical prediction [1].

Herein we investigate the consequences of the adoption of either the “phenomenological” choice Eq. (8) or the “dynamical” choice (9), in the special case where both $\xi_P(t)$ and $\xi_S(t)$ are event-dominated processes and show that the transmission of information from P to S is determined by the dialogue between the critical events of $\xi_S(t)$ and the critical events of $\xi_P(t)$. Specifically, this discussion is devoted to studying the transport of information from P to S , using both forms of generalized FDT (gFDT). Note that there is no limitation on the form of ξ_P provided that the coupling is weak enough as to be compatible with the emergence of the linear response form of Eq. (3).

To discuss the problem of the transmission of information from P to S , it is convenient to imagine the ideal case of a Gibbs ensemble of composite systems $S + P$. Thus, in this paper we imagine that P generates a fluctuating signal $\xi_P(t)$ and that for any signal $\xi_P(t)$ there exists a response $\xi_S(t)$. For each perturbing signal we have to make infinitely many experiments and average over all possible responses. For simplicity we take both signals $\xi_S(t)$ and $\xi_P(t)$ to be dichotomous and fluctuating between values ± 1 . It is important to remark that Eq. (3), for the response of the system S to the perturbation P , is valid when the system is prepared at time $t = 0$ and placed at the beginning of a laminar phase, and the interaction with the perturbation P is turned on at the same time.

In the general case of a dichotomous renewal process $\xi(t)$, generated with a waiting-times PDF $\psi(t)$, the probability density that fixed a time t' , the first next event is observed at time $t > t'$ is given [33] by

$$\psi(t, t') = \psi(t) + \sum_{n=1}^{\infty} \int_0^{t'} R(t'') \psi(t - t'') dt'', \quad (10)$$

with

$$R(t) = \sum_{n=1}^{\infty} \psi_n(t), \quad (11)$$

where $\psi_n(t)$ denotes the n -times convolution of $\psi(t)$. $R(t)$ is therefore the probability density of having an event occurring exactly at time t .

It can be shown as well, see Ref. [33], that the autocorrelation function of the process is related to $\psi(t, t')$ by

$$\langle \xi(t) \xi(t') \rangle = \int_t^{\infty} dx \psi(x, t') = \Psi(t, t'), \quad (12)$$

and therefore coincides with the survival probability $\Psi(t, t')$ for the first event (i.e., the probability that, for fixed t' , no event is observed until time $t > t'$). We assume that the fluctuation $\xi_S(t)$ generated by S is a dichotomous renewal process defined by the probability density

$$\psi_S(t) = (\mu_S - 1) \frac{T_S^{\mu_S - 1}}{(t + T_S)^{\mu_S}}. \quad (13)$$

We therefore name, respectively, $\psi_S(t, t')$, $R_S(t)$, and $\Psi_S(t, t')$ the functions obtained by replacing in Eqs. (10), (11), and (12) $\psi(t)$ with $\psi_S(t)$.

Let us consider now the Gibbs ensemble of composite systems $S + P$, and evaluate the average $\langle \xi_S(t) \rangle_{SP}$. Note that

the average is over the separate statistics of the two systems S and P

$$\langle \xi_S(t) \rangle_{SP} = \langle \langle \xi_S(t) \rangle_S \rangle_P. \quad (14)$$

We select all the responses to the same perturbation, characterized by a given $\xi_P(t)$, we evaluate their average, denoted by $\langle \xi_S(t) \rangle_S$, and finally we construct the average over all possible perturbations denoted by $\langle \dots \rangle_P$ so as to obtain the final result denoted by $\langle \dots \rangle_{SP}$. In conclusion with this procedure we obtain

$$\langle \sigma(t) \rangle = \langle \langle \xi_S(t) \rangle \rangle = \epsilon \int_0^t dt' \chi(t, t') \langle \xi_P(t') \rangle, \quad (15)$$

where, for notational convenience, we drop the subscripts, but we understand the averages in the sense described above.

If necessary, the signal $\xi_P(t)$ must share the same properties as $\xi_S(t)$ and for simplicity they are both assumed to be dichotomous signals with random renewal fluctuations between the values $+1$ and -1 . $\xi_P(t)$ is therefore a non-Poissonian dichotomic fluctuation with the following waiting-time PDF:

$$\psi_P(t) = (\mu_P - 1) \frac{T_P^{\mu_P - 1}}{(t + T_P)^{\mu_P}}. \quad (16)$$

It is therefore convenient to define the additional functions $\psi_P(t, t')$, $R_P(t)$, and $\Psi_P(t, t')$ obtained, analogously as for S , from Eqs. (10), (11), and (12) after replacing $\psi(t)$ with the waiting-time distribution $\psi_P(t)$.

The spectrum of this type of fluctuating signal, in the absence of perturbation, as calculated in Refs. [32,34], is

$$S(f) \propto L^{\mu - 2} f^{\mu - 3}, \quad (17)$$

valid for $\mu < 2$, remarkably, even though a stationary autocorrelation function cannot be defined in this case. In the case $\mu > 2$, $S(f) = A/f^{3-\mu}$, with A independent of L , the length of the sequence under study.

At this point it should be clear to the reader that to get the important results of this paper on the transmission of the statistical properties of P to S we must use Eq. (15). This leads us to give a prescription to define $\langle \xi_P(t) \rangle$. We assume that the perturbation P is prepared at $t = 0$ at the beginning of a laminar phase (i.e., with the analogous prescription adopted for the system S). This assumption allows us to replace $\langle \xi_P(t') \rangle$ with $\Psi_P(t')$ in Eq. (15).

III. PHENOMENOLOGICAL APPROACH

In this section we study the response of a complex system producing non-Poissonian renewal fluctuations to a perturbing signal with similar properties within the phenomenological approach. We analyze both the average response and the input-output correlation [i.e., the correlation between the perturbing fluctuating signal (input) and the signal produced by the system of interest S (output)]. In the phenomenological approach, the waiting times between the events generating the dichotomic fluctuations remain unchanged by the perturbation. The external perturbation introduces a bias so that when an event occurs the probability that the dichotomic variable changes or keeps its value is slightly different. The function $\chi(t, s)$ in this approach is given by [15,16]

$$\chi(t, t') = \frac{d\Psi_S(t, t')}{dt'} = R_S(t') \Psi_S(t - t'). \quad (18)$$

The function $\Psi_S(t, t')$ is the autocorrelation function of $\xi_S(t)$, namely, the survival probability of age t' , and $R_S(t)$ for the case of the discrete signals considered here, is the rate at which events are produced by S prepared at $t = 0$ [i.e., the bits per second encoded in $\xi_S(t)$]. This rate is time independent only in the Poisson case. In the non-Poisson case it depends on time, thereby making $\Psi_S(t, t')$ nonstationary. The brand new survival probability $\Psi_S(t) = \Psi_S(t, t'=0)$ is given by [15, 16, 18]

$$\Psi_S(t) = (1 + t/T_S)^{1-\mu_S}, \quad (19)$$

from which the corresponding waiting-times PDF $\psi_S(t) = -d\Psi_S(t)/dt$ is derived. In the range of parameters $1 < \mu_S < 3$ considered here, it is known [10] that

$$R_S(t) \approx -\frac{\sin \pi \mu_S}{T_S} (T_S/t)^{2-\mu_S}, \quad \text{for } 1 < \mu_S < 2, \quad (20)$$

$$R_S(t) \approx \frac{1}{\tau_S} [1 + (T_S/t)^{\mu_S-2}], \quad \text{for } 2 < \mu_S < 3, \quad (21)$$

with $\tau_S = T_S/(\mu_S - 2)$ the mean value of $\psi_S(t)$.

When $\mu_S < 2$ the experimental preparation of S induces a sequence of events whose rate R_S tends to vanish for $t \rightarrow \infty$, yielding a perennial out-of-equilibrium condition, and an explanation of the death of linear response [18–24, 28] as well. In fact, the response to a harmonic perturbation of frequency f is proportional to $1/(ft)^{2-\mu_S}$ [18]. In the case $2 < \mu_S < 3$, on the contrary, the preparation-induced cascade of events, in the limit $t \rightarrow \infty$, becomes stationary and virtually identical to that of a Poisson process. The theoretical analysis of this paper is done in the asymptotic time regime. Thus, we refer to the case $2 < \mu < 3$ as *stationary*, in contrast to the *nonstationary* case $\mu \leq 2$ of perennial transition. Similarly to the rate of events $R_S(t)$ the spectral intensity per unit time tends to vanish for $\mu < 2$ as an effect of increasing L [see Eq. (17)]. The ideal $1/f$ -noise condition, corresponding to $\mu = 2$, generates instead a logarithmic decrease of the spectral intensity with time, and consequently a spectrum virtually independent of L .

A. Average response to perturbation

As previously mentioned, the nonstationary LRT (NSLRT) of Eq. (3) rests on the preparation of S at time $t = 0$. We apply the same preparation condition to P , thereby generating the cascades $R_S(t)$ and $R_P(t)$ described by Eqs. (20) and (21), with the appropriate indexing. Under this condition the relaxation of $\langle \xi_P(t) \rangle$ becomes identical to the survival probability $\Psi_P(t)$. Assuming the condition of Eq. (18) we have the following expression for the average response

$$\langle \sigma(t) \rangle = \varepsilon \int_0^t R_S(t') \Psi_S(t - t') \Psi_P(t') dt'. \quad (22)$$

The preparation of both S and P makes the average over many realizations of the response $\sigma(t)$ to a given stimulus P vanish for $t \rightarrow \infty$.

Stationary case: $2 < \mu_S < 3$.

In this regime a finite time scale for the fluctuation ξ_S exists and $R_S(t)$ reaches the constant value $1/\tau_S$. The inverse power-

law relaxation of $\Psi_S(t)$ allows us to approximate Eq. (22) by replacing $R_S(t')$ with its value for $t' \simeq t$, that is,

$$\langle \sigma(t) \rangle \simeq \varepsilon \int_0^t dt' \Psi_S(t - t') \Psi_P(t') / \tau_S, \quad (23)$$

which becomes exact for $t \rightarrow \infty$. The asymptotic behavior of Eq. (23) is easily obtained in the Laplace domain

$$\langle \hat{\sigma}(s) \rangle \simeq \varepsilon \frac{1}{\tau_S} \frac{1 - \hat{\Psi}_S(s)}{s} \frac{1 - \hat{\Psi}_P(s)}{s}, \quad (24)$$

which can be studied in the limit of small s . In fact, since [35]

$$\hat{\Psi}(s) \simeq 1 - \tau s + \Gamma(\mu - 2)s^{\mu-1}, \quad \mu > 2, \quad (25)$$

and

$$\hat{\Psi}(s) \simeq 1 + \Gamma(\mu - 2)s^{\mu-1}, \quad \mu < 2, \quad (26)$$

it follows that for $1 < \mu_P < 2$ and $2 < \mu_P < \mu_S$, the time-asymptotic behavior is $\langle \sigma(t) \rangle \sim t^{1-\mu_P}$, which is proportional to $\langle \xi_P(t) \rangle$ for large t , meaning that the system S “inherits” the relaxation properties of the perturbation P .

For $2 < \mu_S < \mu_P$, instead, the asymptotic dominant term is $\langle \sigma(t) \rangle \sim t^{1-\mu_S}$, which is proportional to the ordinary unperturbed relaxation to equilibrium $\langle \xi_S(t) \rangle$, when an initial bias for $\xi_S(t)$ is introduced. We see therefore that for $\mu_P < \mu_S$, when $\xi_P(t)$ is slower than $\xi_S(t)$, the perturbation P imposes on the system S its own relaxation properties thereby allowing one to “manage” the complexity of a system or network by using an appropriate stimulus.

Nonstationary case: $1 < \mu_S \leq 2$.

In this regime, the system S violates the finite-time scale condition necessary for stationary dynamics and, in fact, $R_S(t) \propto t^{\mu_S-2}$, see Eq. (20). With such replacement in Eq. (22), a convolution form appears which can easily be studied via a Laplace transformation. In the Laplace domain (see Appendix A for details on coefficients)

$$\langle \hat{\sigma}(s \simeq 0) \rangle \simeq a_S s^{\mu_S-2} + a_P s^{\mu_P-2}, \quad (27)$$

which implies that if $\mu_P > 2$ or if $1 < \mu_S < \mu_P$ then $\langle \sigma(t) \rangle \sim t^{1-\mu_S}$. When $1 < \mu_P < \mu_S$, we have $\langle \sigma(t) \rangle \sim t^{1-\mu_P}$. Also in this case the perturbation P forces onto S its own relaxation properties to equilibrium.

B. Input-output correlation function

We study the cross-correlation (or input-output correlation) function between the system S and the stimulus P : $C(t) \equiv \langle \langle \xi_S(t) \xi_P(t) \rangle \rangle$, which is also used as an indicator of aperiodic stochastic resonance [36]. Multiplying both sides of Eq. (3) by $\xi_P(t)$ and averaging over the fluctuations of the perturbation P we obtain

$$\Phi(t) \equiv C(t)/\varepsilon = \int_0^t dt' R_S(t') \Psi_S(t - t') \Psi_P(t, t'). \quad (28)$$

Note that both Eqs. (22) and (28) depend on the survival probability of P , but in the former such survival probability depends on the single time t' whereas in the latter it depends on both t' and t . We limit ourselves to report the results for the asymptotic value Φ_∞ of $\Phi(t)$. When $\xi_S(t)$ and $\xi_P(t)$ are

not stationary, that is, when $1 < \mu_S \leq 2$ and $1 < \mu_P \leq 2$, Eq. (28), in the limit $t \rightarrow \infty$, gives

$$\Phi_\infty = \zeta(\mu_S, \mu_P) \equiv \frac{\Gamma(\mu_S + \mu_P - 2)}{\Gamma(2 - \mu_P)\Gamma(\mu_P)^2\Gamma(\mu_S - 1)} \times \frac{{}_3F_2[\{\mu_P - 1, \mu_P - 1, \mu_P + \mu_S - 2\}, \{\mu_P, \mu_P\}, 1]}{\Gamma(2 - \mu_P)\Gamma(\mu_P)^2\Gamma(\mu_S - 1)}, \quad (29)$$

where ${}_3F_2$ is the generalized hypergeometric function. For more details see Appendix A. In the case $2 < \mu_P < 3$, Φ_∞ is simply zero.

In the case $2 < \mu_S < 3$, inserting into Eq. (28) expression (21) for $R_S(t)$, leads to

$$\Phi(t) = \int_0^t dt' \frac{\Psi_S(t-t')}{\tau_S} \Psi_P(t, t') = \tilde{\Psi}_S(0) \Psi_P(t, t) - \tilde{\Psi}_S(t) \Psi_P(t, 0) - \int_0^t dt' \tilde{\Psi}_S(t-t') \frac{d\Psi_P(t, t')}{dt'}, \quad (30)$$

where $\tilde{\Psi}_S(t)$ is given by Eq. (19) after replacing μ_S with $\mu_S - 1$. Equation (30) is exact for $t \gg \tau_S$ and for $1 < \mu_P \leq 2$ it leads to $\Phi_\infty = 1$ since both the second and third terms disappear for $t \rightarrow \infty$ and the first is trivially 1 in the same limit. For Eq. (30) $2 < \mu_P < 3$ it yields

$$\Phi_\infty = 1 - (\mu_P - 2) T_P^{\mu_P - 2} T_S^{\mu_S - 2} \Delta T^{4 - \mu_S - \mu_P} \times B \left[\frac{\Delta T / T_P}{\Delta T / T_S}, \mu_S + \mu_P - 4, \frac{2 - \mu_P}{3 - \mu_S} \right] \stackrel{\Delta T \rightarrow 0}{=} \times \frac{\mu_S - 2}{\mu_P + \mu_S - 4}, \quad (31)$$

where $\Delta T = |T_S - T_P|$, $B[x, a, b]$ is the incomplete Beta function and the upper (lower) choice of the parameters refers to the case $T_S > (<) T_P$. The final expression in Eq. (31) corresponds to the case $T_S = T_P$. The results are summarized in Table I. For illustrative purposes, we supplement Table I with Fig. 1, showing the three-dimensional (3D) plot of the cross-correlation function Φ_∞ in the same parameter range: Square II and square III correspond to the condition of minimal and maximal correlation, respectively. Intuitively it is so because of the difference of time scales between S and P in such regions. In III fluctuations $\xi_S(t)$ and $\xi_P(t)$ have a finite and an infinite time scale, respectively, thereby allowing $\xi_S(t)$ to adapt to the stimulus-induced bias so as to yield maximal correlation. In II the role of the time scales is inverted, the bias induced by P on the longer (diverging) time scale of the process $\xi_S(t)$ is asymptotically averaged out due to the many intervening switching events of $\xi_P(t)$, producing no correlation. The vertex $\mu_S = \mu_P = 2$, representing a $1/f$ -noise generating system under the stimulus of a $1/f$ -noise perturbation, marks

TABLE I. Summary of the asymptotic values of the cross-correlation function $\Phi(t)$ in the phenomenological case.

$\mu_S \downarrow \mu_P \rightarrow$	$1 < \mu_P \leq 2$	$2 < \mu_P < 3$
$1 < \mu_S \leq 2$	$\Phi_\infty = \zeta(\mu_S, \mu_P)^*$ I	$\Phi_\infty = 0$ II
$2 < \mu_S < 3$	$\Phi_\infty = 1$ III	$\Phi_\infty = \frac{\mu_S - 2}{\mu_S + \mu_P - 4}$ IV

*See Eq. (29).

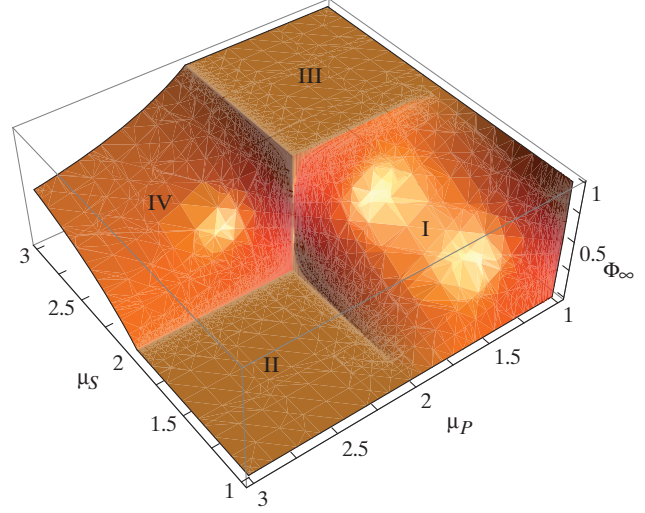


FIG. 1. (Color online) The asymptotic limit of $\Phi(t)$ is displayed for $\mu_S, \mu_P \in [1, 3]$. The vertex $\mu_S = \mu_P = 2$ marks the transition to a condition of maximal input-output cross correlation.

the abrupt transition from vanishing (square II) to maximal correlation (III).

IV. DYNAMICAL APPROACH

In this section we extend the analysis of the previous section to the dynamical approach. Within such approach we derive both the average response and the input-output correlation function.

A. Average response to perturbation

Starting from the property

$$\langle \sigma(t) \rangle = \langle \langle \xi_S(t) \rangle \rangle, \quad (32)$$

obtained by averaging over the fluctuations of both S and P and using the dynamical condition of Eq. (9), one obtains

$$\chi(t, t') = -\frac{d}{dt} \Psi_S(t, t') = \psi_S(t, t'). \quad (33)$$

Equation (3) then becomes

$$\langle \sigma(t) \rangle = \epsilon \int_0^t dt' \psi_S(t, t') \langle \xi_P(t') \rangle. \quad (34)$$

For simplicity we prepare the perturbation $\xi_P(t)$ at $t = 0$. To observe the influence of P on S we select all the systems of the Gibbs ensemble so that $\xi_P(0) = 1$. In this case $\langle \xi_P(t') \rangle$ is given by the survival probability $\Psi_P(t)$ [33]. Thus, Eq. (34) yields

$$\langle \sigma(t) \rangle = \epsilon \int_0^t dt' \psi_S(t, t') \Psi_P(t'), \quad (35)$$

where $\Psi_P(t')$ is the survival probability for the process $\xi_P(t)$

$$\Psi_P(t) = \int_t^\infty dx \psi_P(x) = \left(\frac{T_P}{t + T_P} \right)^{\mu_P - 1}. \quad (36)$$

This slow decay corresponds to the probability that no perturbation event occurs up to time t . The system S evolves in time so as to reach a steady value that corresponds to

a constant perturbation abruptly applied at $t = 0$. However, during this process a perturbation event occurs that has the effect of suddenly changing the external field. Thus, $\sigma(t)$ does not reach a steady value, but after reaching a maximum value will decay. Under the specific conditions discussed in this section, the time asymptotic decay of $\langle\sigma(t)\rangle$ in Eq. (35) has the same power-law index as that of survival probability $\Psi_P(t)$. We interpret this phenomenon as the transmission into S of the statistics of P .

We explore again the whole range of parameters $1 < \mu_S < 3$ and $1 < \mu_P < 3$, respectively, for the system S and the perturbation P , depending on the values of the power-law indexes μ_S, μ_P characterizing their waiting-times PDFs. The value $\mu = 2$ marks the transition from a finite to an infinite mean time (i.e., the transition to a nonergodic, nonstationary condition. In fact, while for $\mu > 2$ a mean time exists, a finite time scale can be defined and a stationary condition is reached, for $\mu < 2$ such condition is never achieved, not even in the infinite mean time.

Stationary case: $2 < \mu_S < 3$.

In this regime the waiting-times PDF $\psi_S(t)$ has a finite mean value τ_S . Therefore a finite time scale t_C exists such that for $t > t' > t_C$ the following approximation corresponding to reaching a stationary condition, is valid [33]

$$\psi_S(t, t') \simeq \frac{1}{\tau_S} \int_t^\infty dx \psi_S(x - t') = \frac{\Psi_S(t - t')}{\tau_S}, \quad (37)$$

where $\tau_S = T_S/(\mu_S - 2)$ is the mean value of $\psi_S(t)$. Equation (37) is exact for $t_C \rightarrow \infty$. We can also use Eq. (3) for the response in the case when the interaction is turned on at a later time t_C that we assume to be so large as to satisfy the approximation Eq. (37) using the following procedure. We introduce into Eq. (3) an effective perturbation which is turned on at time $t = 0$ but is zero until t_C [i.e., $\xi_P^{\text{eff}}(t) = \theta(t - t_C)\xi_P(t - t_C)$]. In this scheme we can assume that the “real” process $\xi_P(t)$ is prepared at time $t = t_C$ in a brand new condition. Time t_C therefore corresponds to the age of the system S . The average response $\langle\sigma(t)\rangle$ of S in this case reads

$$\begin{aligned} \langle\sigma(t)\rangle &= \varepsilon \int_0^t dt' \psi_S(t, t') \langle\theta(t' - t_C)\xi_P(t' - t_C)\rangle \\ &= \varepsilon \int_{t_C}^t dt' \psi_S(t, t') \Psi_P(t' - t_C), \end{aligned} \quad (38)$$

and the approximation (37) can be used to replace $\psi_S(t, t')$. With the substitution $\tau = t' - t_C$ and after renaming $t - t_C$ as t back again, the average response of the system S of age t_C reads

$$\begin{aligned} \frac{\langle\sigma(t)\rangle}{\varepsilon} \Big|_{t_C} &= \int_0^t d\tau \frac{\Psi_S(t - \tau)}{\tau_S} \Psi_P(\tau) = \tilde{\Psi}_S(0) \Psi_P(t) \\ &\quad - \tilde{\Psi}_S(t) \Psi_P(0) - \int_0^t dt' \tilde{\Psi}_S(t - t') \frac{d}{dt'} \Psi_P(t'), \end{aligned} \quad (39)$$

where $\tilde{\Psi}_S(t)$ is defined as

$$\tilde{\Psi}_S(t) = (1 + t/T_S)^{\mu_S - 2}. \quad (40)$$

Equation (39) is exact for $t_C \rightarrow \infty$ and coincides with the expression (23) obtained in the phenomenological case in the same regime. Therefore, in the limit $t \gg T_S, T_P$, the same considerations apply, that is, if $1 < \mu_P < 2$ and $2 < \mu_S < \mu_P$, the time-asymptotic behavior is $\langle\sigma(t)\rangle \sim t^{1-\mu_P}$, which is proportional to $\langle\xi_P(t)\rangle$ for large t , therefore the system S always “inherits” the relaxation properties of the perturbation. If $2 < \mu_S < \mu_P$, the asymptotic dominant term is $\langle\sigma(t)\rangle \sim t^{1-\mu_S}$, which is proportional to the ordinary unperturbed relaxation to equilibrium $\langle\xi_S(t)\rangle$.

Nonstationary case: $1 < \mu_S < 2$.

Let us make the assumption that, although at time $t = 0$ half of the S elements of the Gibbs ensemble are in the state $\xi_S = +1$ and half in the state $\xi_S = -1$, all of them are at the beginning of their sojourn in the corresponding states. This is an out-of-equilibrium condition, corresponding to preparing the system at $t = 0$. The calculations are detailed in Appendix B. Using the dynamic theory we obtain

$$\frac{\langle\sigma(t)\rangle}{\varepsilon} \approx \frac{k_1(\mu_S, \mu_P)}{t^{\mu_P - 1}} + \frac{k_2(\mu_S, \mu_P)}{t^{\mu_P + 1 - \mu_S}}, \quad (41)$$

where the first coefficient is given by

$$k_1(\mu_S, \mu_P) = \frac{T_P^{\mu_P - 1} \sin(\pi \mu_S) \Gamma(2 - \mu_S) \Gamma(1 - \mu_P + \mu_S)}{\pi \Gamma(3 - \mu_P)}, \quad (42)$$

and the second coefficient is determined to be

$$k_2(\mu_S, \mu_P) = \frac{[\sin(\pi \mu_S) \Gamma(3 - \mu_S) \Gamma(1 - \mu_P + \mu_S) \Gamma(2\mu_S - 3) - (2 - \mu_S) \Gamma(2\mu_S - \mu_P - 1)]}{T_P^{1 - \mu_P} T_S^{\mu_S - 2} \pi (\mu_P - 2) (2 - \mu_S) \Gamma(3 - \mu_S) \Gamma(\mu_S - \mu_P) \Gamma(2\mu_S - 3)}. \quad (43)$$

In this range of parameters the dominant term is always the first term in Eq. (41) which, if $\mu_P < \mu_S$, is also slower than the unperturbed relaxation to equilibrium of ξ_S . In the latter range, therefore, the system S relaxes to equilibrium inheriting the same properties of the perturbation P .

The result in Eq. (41) is of special interest since it discriminates between the two approaches in the nonstationary regime. It is this difference that allowed to determine that liquid crystals [13] follow the prediction of the dynamical approach. In fact,

the phenomenological approach disregards the influence of the perturbation on the occurrence time of the S events [19,28], while the dynamical theory does not, thereby affording a criterion for information transport that we judge to be a more appropriate representation of the communication among complex systems with $\mu < 2$. However, the equivalence between the phenomenological and the dynamic theories in the case when the system S is infinitely aged (i.e., for $\mu_S > 2$) indicates that the generalization of FDT given by Eq. (9), namely, the

dynamical theory, becomes active only when the system S is in a far from equilibrium condition and begins drifting toward equilibrium. Although equilibrium is never reached when $\mu < 2$, the correlation function $\Psi_S(t, t')$ tends to recover the property $\Psi_S(t, t') = \tilde{\Psi}_S(t - t')$ that makes the phenomenological theory formally equivalent to the dynamical theory.

B. Input-output correlation function

Herein we study the asymptotic limit of the input-output correlation function

$$\Phi_\infty \equiv \lim_{t \rightarrow \infty} C(t)/\epsilon, \quad (44)$$

within the dynamical approach. The input-output correlation function is again defined by the average over the fluctuations in both the system S and perturbation P

$$C(t) \equiv \langle \xi_S(t) \xi_P(t) \rangle. \quad (45)$$

The asymptotic limit of $C(t)$ is independent of the way the system and the perturbation are prepared, so we can use the prescription leading to Eq. (3) obtained assuming that both S and P are prepared at time $t = 0$. We therefore use the same arguments as those yielding Eq. (28) and, adapting them to the dynamic theory, we obtain

$$\Phi(t) = C(t)/\epsilon = \int_0^t dt' \psi_S(t, t') \Psi_P(t, t'). \quad (46)$$

Nonstationary case I: $\mu_S < 2$, $\mu_P < 2$.

We use Eq. (46) with the general expressions for $\psi_S(t, t')$ and $\Psi_P(t, t')$ as obtained through Eqs. (10) and (12), respectively. In this case, taking the limit $t \rightarrow \infty$ yields (see Appendix B for details)

$$\begin{aligned} \zeta_D = \lim_{t \rightarrow \infty} \Phi(t) = & -\frac{\sin \pi \mu_P}{\pi} \frac{\Gamma(\mu_P + \mu_S - 1)}{(\mu_P - 1)\Gamma(\mu_P + 1)\Gamma(\mu_S - 1)} \\ & \times F[\{\mu_P - 1, \mu_P - 1, \mu_P + \mu_S - 1\}, \{\mu_P, \mu_P + 1\}, 1]. \end{aligned} \quad (47)$$

Nonstationary case II: $\mu_S < 2$, $\mu_P > 2$.

In this case we can assume that, when the interaction is turned on, the perturbation P has already reached a stationary condition, so that in Eq. (46) $\psi_S(t, t')$ is given again by Eq. (10) but $\Psi_P(t, t') = \tilde{\Psi}_P(t - t')$, with

$$\tilde{\Psi}_P(t) = (1 + t/T_P)^{\mu_P - 2}, \quad (48)$$

and this expression has to be directly inserted into Eq. (46).

The power-law index $\mu_P - 2$ reflect the stationary condition realized with the preparation of the perturbation P at a time $t_P = -\infty$. In this case, we obtain

$$\lim_{t \rightarrow \infty} \Phi(t) = 0. \quad (49)$$

In the time asymptotic limit, the system S turns out to be independent of P in spite of the fact that at $t = 0$ we switch on the S - P interaction.

Stationary case I: $\mu_S > 2$, $\mu_P > 2$.

We again use Eq. (46) and assume that, when the interaction is turned on, the perturbation P has already reached a stationary condition so that in Eq. (46) $\Psi_P(t, t') = \tilde{\Psi}_P(t - t')$

with $\tilde{\Psi}_P(t)$ given by Eq. (48). For $\mu_S > 2$ a finite mean time τ_S of $\psi(t)$ exists, therefore a finite time scale $t_C \propto \tau_S$ exists such that for $t > t_C$ Eq. (37) can be used again to approximate $\psi_S(t, t')$. With such substitutions, the expression for the correlation function becomes asymptotically equal to the correlation obtained in the phenomenological approach in the same regime [i.e., Eq. (30), leading to the final result Eq. (31)].

Stationary case II: $\mu_S > 2$, $\mu_P < 2$.

In this case again a finite time scale t_C can be found such that the approximation in Eq. (37) is valid. Thus, again Eq. (46) can be rewritten

$$\begin{aligned} \Phi(t) \simeq & \int_0^{t_C} dt' \psi_S(t, t') \Psi_P(t, t') \\ & + \int_{t_C}^t dt' \left[\frac{d}{dt'} \tilde{\Psi}_S(t - t') \right] \Psi_P(t, t'). \end{aligned} \quad (50)$$

This case is therefore equivalent to what is obtained for the phenomenological case in the same range of parameters. Again, in the asymptotic limit $t \rightarrow \infty$, the first term in Eq. (50) vanishes and after integrating the second term by parts, one obtains

$$\begin{aligned} \Phi(t) \simeq & \tilde{\Psi}_S(0) \Psi_P(t, t) - \tilde{\Psi}_S(t - t_C) \Psi_P(t, t_C) \\ & - \int_{t_C}^t dt' \tilde{\Psi}_S(t - t') \frac{d\Psi_P(t, t')}{dt'}. \end{aligned} \quad (51)$$

In the asymptotic limit the second term on the right-hand side trivially vanishes and also the third term side can be shown to vanish (see Appendix B). The only remaining contribution in Eq. (51) is given by the first term, which is exactly one. It follows

$$\Phi_\infty = \lim_{t \rightarrow \infty} C(t)/\epsilon = 1. \quad (52)$$

Let us make here a few remarks on these results. Of course in the absence of coupling, $\epsilon = 0$, which means that $C(t)$ always vanishes. We switch the interaction on at $t = 0$. Thus, we always have the zero cross-correlation initial condition $C(0) = 0$.

As an effect of switching on the interaction at $t = 0$ we realize the condition $C(t) \neq 0$, for $t > 0$. However, we find that there exist special conditions (region II in Fig. 2) for which the cross correlation again goes to zero, asymptotically

$$\Phi_\infty = \lim_{t \rightarrow \infty} C(t)/\epsilon = 0. \quad (53)$$

This indicates that only in such conditions, the system S , after a transient, recovers the condition of statistical independence of the perturbation $\xi_P(t)$. The fluctuations ξ_S with $\mu_S < 2$ turn out to be statistically independent of $\xi_P(t)$ only when $\mu_P > 2$. The environmental perturbation with $\mu_P < 2$, on the other hand, is characterized by the remarkable property of forcing the system S to respond, regardless of the value of μ_S .

Table II and the plot in Fig. 2 summarize such results and show the same qualitative properties observed for the correlation function in the phenomenological case, with the correlation functions for the two approaches being identical in squares I, II, and IV. The condition of ideal $1/f$ noise (i.e., $\mu_S = \mu_P = 2$) marks the transition from a condition of zero to maximal correlation.

TABLE II. Summary of the asymptotic values of the cross-correlation function $\Phi(t)$ in the dynamical case.

$\mu_S \downarrow \mu_P \rightarrow$	$1 < \mu_P \leq 2$	$2 < \mu_P < 3$
$1 < \mu_S \leq 2$	$\Phi_\infty = \zeta_D(\mu_S, \mu_P)^*$ I	$\Phi_\infty = 0$ II
$2 < \mu_S < 3$	$\Phi_\infty = 1$ III	$\Phi_\infty = \frac{\mu_S - 2}{\mu_S + \mu_P - 4}$ IV

*See Eq. (47).

V. FINITE RESPONSE AND $1/f$ RESONANCE

Herein we proceed to demonstrate that the intensity of the response $\sigma(t)$ to a single realization of the stimulus does not decay if $\Phi_\infty \neq 0$. This demonstration, therefore, is valid for both the dynamical and the phenomenological approach, leading to a general result. Let us define with $p_t(\xi_S^i)$ the probability that at time t the variable ξ_S takes the value $i = \pm 1$ and with $p_t(\xi_S^i | \xi_P^j)$ the conditional probability for the occurrence, at time t , of a value $\xi_S = i = \pm 1$, given the occurrence of a value $\xi_P = j = \pm 1$. By definition, the nonvanishing Φ_∞ yields

$$C(t) \equiv \sum_{i,j=\pm 1} ij p_t(\xi_S^i | \xi_P^j) p_t(\xi_P^j) \rightarrow \varepsilon \Phi_\infty. \quad (54)$$

We note that for $t \rightarrow \infty$, on a time scale such that $\langle \xi_P(t) \rangle$, which decays as $\langle \xi_P(0) \rangle t^{1-\mu_P}$, is a second-order quantity $O(\varepsilon^2)$ we have that

$$p_t(\xi_P^j) = 1/2 + O(\varepsilon^2), \quad (55)$$

and

$$\Phi(t) = \Phi_\infty + O(\varepsilon^2). \quad (56)$$

Thus is due to Eq. (54) and to the symmetry of the considered dichotomous processes

$$p_t(\xi_S^i | \xi_P^j) \rightarrow \frac{1}{2} + i j \varepsilon \frac{\Phi_\infty}{2}. \quad (57)$$

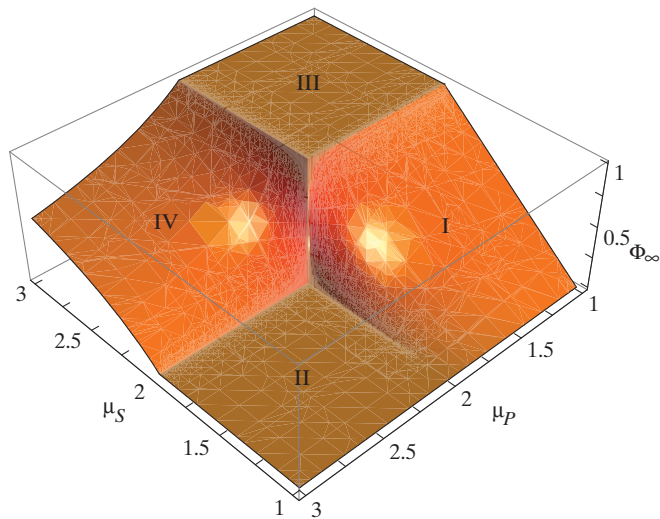


FIG. 2. (Color online) The asymptotic limit of $\Phi(t)$ is displayed for the different regimes of parameters for $1 < \mu_S < 3$ and $1 < \mu_P < 3$, in the dynamical approach.

In the same long-time scale, Eq. (57) yields

$$\langle \sigma(t) \rangle_\pm \equiv \sum_i p_t(\xi_S^i | \xi_P^{\pm 1}) i \simeq \pm \varepsilon \Phi_\infty, \quad (58)$$

where the subscript \pm indicates the value of ξ_P at time t . Summing Eq. (58) over the two values of ξ_P gives a total average null response, as expected. But if the magnitude $|\sigma(t)|$ of the response to a single instance of the input $\xi_P(t)$ is considered instead, its total average is

$$\langle |\sigma(t)| \rangle = \frac{1}{2} \sum_\pm \langle |\sigma(t)| \rangle_\pm \gtrsim \frac{1}{2} \sum_\pm |\langle \sigma(t) \rangle_\pm| \simeq \varepsilon \Phi_\infty, \quad (59)$$

where an equality holds if terms of order $O(\varepsilon^2)$ are neglected. Thus when $\Phi_\infty > 0$, the response $\sigma(t)$ to a single instance of the input $\xi_P(t)$ *does not die out and remains proportional to the stimulus intensity*, no matter how large t becomes. Square III in both Figs. 1 and 2 is the plateau region of maximal cross correlation and response. Claims regarding the *death of linear response*, as in Refs. [19–28], are therefore appropriate only in relation to the vanishing correlation of square II. The total average response $\langle \sigma(t) \rangle$ always tends to vanish for $t \rightarrow \infty$ for reasons that do not imply a lack of response except in the case of square II.

The reason for the striking difference between the response to a harmonic perturbation and the response to a nonergodic stimulus is intimately related to the emergence of $1/f$ noise and to its spectrum described by Eq. (17), which assigns the weight $S(f)/L = 1/(fL)^{3-\mu_P}$ to the spectral component of frequency f of a nonergodic stimulus. As a consequence, the stimulus generates, in time, lower and lower frequencies f so as to keep $1/(fL)^{2-\mu_S}$ (i.e., the response intensity to frequency f [18]) finite, thereby yielding Eq. (59). The death of linear response [19–28] is caused by the fact that stimuli with fixed frequencies cannot cope with the decreasing frequency of the cascade of events of Eq. (20).

We have afforded a compelling proof that the intensity of the single realizations of $\sigma(t)$, with $\mu_S < 2$, does not decay if the perturbation $\xi_P(t)$ falls in the same complexity basin ($\mu_P < 2$). This is the phenomenon of *complexity management* which allows to define the right stimulus to obtain a response from a system or network producing nonergodic fluctuations. Now we argue that $1/f$ stimuli generate the maximum information transport by looking at the mutual information

$$I(t) = \sum_{i,j} p_t(\xi_P^j) p_t(\xi_S^i | \xi_P^j) \log[p_t(\xi_S^i | \xi_P^j) / p_t(\xi_S^i)]. \quad (60)$$

Using Eqs. (55), (56), and (57) it follows that

$$I(t \rightarrow \infty) \simeq \varepsilon^2 \Phi_\infty^2, \quad (61)$$

and the information transmission rate is obtained by multiplying $I(t)$ by the input rate [37], given by $R_P(t)$. If $\mu_P > 2$, Fig. 1 shows that $\Phi_\infty < 1$. Although square III in Figs. 1 and 2, indicates that all stimuli with $\mu_P \leq 2$ induce maximal correlation, $\mu_P < 2$ corresponds to a stimulus with decaying events rate (input bits/s) $R_P(t)$. So even if a response is produced in this regime, the rate of information vanishes in time.

Only at the crucial condition $\mu_P = 2$, of ideal $1/f$ noise, does this algebraic decay become logarithmic, and, consequently, a steady and maximal information transmission rate is

achieved. This is the phenomenon that we call $1/f$ resonance. The above considerations are valid for both the dynamical and phenomenological approaches, therefore we consider the condition of maximal information transmission achieved in the ideal $1/f$ -noise condition, a fundamental property of $1/f$ -noise renewal processes.

VI. CONCLUDING REMARKS

The growing interest for the dynamics of complex networks is shifting the attention of the researchers from the synchronization of two stochastic units [38] to the synchronization of a large number of units [39], an interesting phenomenon that is closely related to the very popular model of Kuramoto [40]. The single units of the processes of chaos synchronization are chaotic and do surprisingly synchronize while maintaining the erratic dynamics that they have in isolation. Although the single units of the Kuramoto model are regular, it is becoming increasingly evident that the emergence of a global synchronization is a condition independent of whether the single units are regular or stochastic. The single units of the work of Refs. [11,41] are Poisson processes and if one of them drove the other, they would obey the principle of aperiodic stochastic resonance [42]. If the two units are bidirectionally coupled they are expected to undergo a condition of perfect synchronization if the coupling is sufficiently intense. When the number of interacting units is very large a phase transition occurs from the noncooperative to the cooperative behavior [11,41]. It is important to stress that at criticality no permanent consensus is reached, and the mean value of the global field vanishes. Yet, this condition is strikingly different from the noncooperative condition. The whole network remains in the “yes” (“no”) state for an extended time before making a transition to the “no” (“yes”) state.

It is surprising that the phase-transition literature seems to have overlooked, with only a few exceptions [11,41,43], that the transitions from the “yes” (“no”) to the “no” (“yes”) state occurring at criticality are the “crucial” events defined in Sec. I. In other words, the time interval between two consecutive transitions is derived from a PDF that has the asymptotic time structure of Eq. (1) with a power index μ fitting the inequality condition of Eq. (2). Some authors [11,41] argued that $\mu = 1.5$ and others, [7], releasing the condition that all the units share the same Poisson rate, generate a global condition with crucial events characterized by $\mu < 2$, but significantly departing from the value $\mu = 1.5$. Note that the theoretical arguments of Ref. [44], yield the misleading impression that the crucial value of μ is a consequence of ordinary statistical physics.

According to some authors [45,46] the Kuramoto phenomenon can be defined as *inner synchronization*. A network of cooperating units located on the nodes of a complex network may reach inner synchronization with different values of the control parameter, depending on the network topology [47]. This is a subject of increasing interest with attractive applications to the dynamics of the human brain [45]. If we adopt this perspective, we can address the problem of information transmission from one to another complex network as a process of *outer synchronization*. This is an interesting issue, but the conditions to fulfill to realize outer synchronization are not yet clear [45].

An important result of this article is the discovery of a promising road to settle the problem of information transmission from one to another complex network. In fact, if the inner synchronization corresponds to a criticality condition and criticality generates crucial events with a power-law index μ fulfilling the inequality of Eq. (2), then a complex network at criticality is a generator of $1/f$ noise, with $S(f) \propto 1/f^{3-\mu}$. Thus the problem of information transmission from one to another complex network, in this regime, becomes equivalent to the phenomenon of $1/f$ resonance illustrated in this article. This is essentially the main result of earlier work [29]. The main conclusions of Ref. [29] are illustrated by Fig. 1, which is obtained using the phenomenological LRT.

What are the limits of this earlier result? The experiments [12,13] yield support to the dynamical rather than the phenomenological LRT, thereby generating doubt that the results of Ref. [27], although very attractive, may not completely reflect reality. It is important to stress that phenomenological LRT is a natural consequence of adopting the asymptotic time perspective replacing the waiting-times PDF $\psi(\tau)$ of Eq. (1) with $\psi(\tau) \propto 1/\tau^\mu$. This way of proceeding, although generating the elegant mathematics of fractional derivatives, has as an ultimate effect the misleading discovery of the death of linear response [19–24,28]. We do not adopt the asymptotic time perspective but the special form of Eq. (1). This is not a unique way of connecting the long-time to the short-time regime. However, whatever form we adopt we are convinced that there will be a parameter playing the same microscope role of the parameter T of Eq. (1). It is reasonable to assume that an external perturbation may perturb either T or μ , or both of them. However, the perturbation of μ is incompatible with the assumption of a weak stimulus. In fact, μ is a consequence of the cooperation among the units of the network, and a perturbation may affect μ only if its strength is large enough to influence the interaction among the units of the network. Thus, an external weak perturbation can only have an effect on T , thereby making the dynamical LRT become the proper way to study the response of a complex network to a weak external stimulus, in accordance with the experimental results [12,13].

For these reasons, we can conclude that Fig. 2 is the original, and important, result of this paper. We hope that it may open the road to the dynamical solution of the problem of information transmission [48] from one to another complex network, a research topic that is still in its infancy.

ACKNOWLEDGMENTS

PG acknowledges financial support from ARO and Welch through Grants No. W911NF-05-1-0205 and No. B-1577, respectively. MB acknowledges financial support from FONDECYT project No. 1110231.

APPENDIX A

In this Appendix we record more details about the derivation of both the average response $\langle \sigma(t) \rangle$ and the input-output correlation function $\Phi(t)$ in the case of the phenomenological approach.

When we adopt the phenomenological theory, we obtain for the average response to external perturbation, in the nonstationary case [cf. Eq. (27)] the following asymptotic

expression:

$$\frac{\langle \sigma(t) \rangle}{\epsilon} = \frac{k_1(\mu_S, \mu_P)}{t^{\mu_P-1}} + \frac{k_2(\mu_S, \mu_P)}{t^{\mu_S-1}}, \quad (\text{A1})$$

where the coefficient of the first term is

$$k_1(\mu_S, \mu_P) = \frac{\Gamma(\mu_P - \mu_S)}{\Gamma(1 - \mu_P)\Gamma(\mu_S)} - \frac{\Gamma(1 - \mu_P + \mu_S)}{\Gamma(2 - \mu_P)\Gamma(\mu_S)}, \quad (\text{A2})$$

and the coefficient of the second term

$$k_2(\mu_S, \mu_P) = \frac{\Gamma(\mu_P - \mu_S)}{\Gamma(1 - \mu_S)\Gamma(\mu_P)}. \quad (\text{A3})$$

Note the logarithmic corrections corresponding to $\mu_S = \mu_P$, with

$$\frac{\langle \sigma(t) \rangle}{\epsilon} \approx \frac{\sin(\pi\mu_S)}{\pi} \frac{\log t}{t^{\mu_S-1}} + \frac{A(\mu_S)}{t^{\mu_S-1}}, \quad (\text{A4})$$

and

$$A(\mu_S) = \frac{\sin(\pi\mu_S)}{\pi} \left[\frac{1}{\mu_S - 1} - 2\gamma - 2\psi_L(\mu_S) \right] - \cos(\pi\mu_S), \quad (\text{A5})$$

where γ is the Euler's constant and $\psi_L(z)$ the logarithm derivative of the Γ function. These predictions are qualitatively equivalent to the dynamical theory predictions with the assumption that the system S has been prepared in the very distant past.

The general expression of the correlation function in the phenomenological approach is given by Eq. (28).

Nonstationary case I: $\mu_S < 2, \mu_P < 2$.

In this range the asymptotic approximation for the function $R(t)$ defined in Eq. (11) for both S and P is

$$R(t) \simeq \frac{\sin \pi \mu}{\pi} t^{\mu-2}. \quad (\text{A6})$$

The power-law properties of $\Psi_S(t)$, in the long-time limit, shift the dominant contribution to the integral of Eq. (28) to the range $t' \sim t$, this allows to adopt the approximation (A6) inside the integral. It follows

$$\begin{aligned} \Phi(t) &\simeq \frac{\sin \pi \mu_S}{\pi} \frac{\sin \pi \mu_P}{\pi} \\ &\times \int_0^t \tau^{\mu_S-2} \Psi_S(t-\tau) d\tau \int_0^\tau x^{\mu_P-2} \Psi_P(t-x) dx. \end{aligned} \quad (\text{A7})$$

Using a generalized Newton binomial expansion of the power-law form of the functions $\Psi_P(t)$ we obtain the following expression:

$$\begin{aligned} \Phi(t) &\simeq \frac{\sin \pi \mu_S}{\pi} \frac{\sin \pi \mu_P}{\pi} \sum_{n=0}^{\infty} \binom{1-\mu_P}{n} \frac{(-1)^n}{(t+T_P)^{n+\mu_P-1}} \\ &\int_0^t t'^{n+\mu_P+\mu_S-3} \Psi_S(t-t') dt', \end{aligned} \quad (\text{A8})$$

while the convolution with $\Psi_S(t)$ in the integral, leads to

$$\begin{aligned} \Phi(t) &\simeq \frac{\sin \pi \mu_S}{\pi} \frac{\sin \pi \mu_P}{\pi} \sum_{n=0}^{\infty} \binom{1-\mu_P}{n} \frac{(-1)^n}{(t+T_P)^{n+\mu_P-1}} \\ &\times \frac{t^{n+\mu_P-1}}{n+\mu_P-1} \frac{\Gamma(n+\mu_P+\mu_S-2)\Gamma(2-\mu_S)}{\Gamma(n+\mu_P)}, \end{aligned} \quad (\text{A9})$$

where we have used the fact that for t large the main contribution to the integral comes from the range of values $x \lesssim \tau \lesssim t$ and therefore the asymptotic approximations for $R_S(t)$ and $R_P(t)$ are justified. The limit for $t \rightarrow \infty$ cancels the time dependence and leaves a sum which leads to the expression of Eq. (47) in the text.

Nonstationary case II: $\mu_S < 2, \mu_P > 2$.

In this case the function $R_P(t)$ tends asymptotically to a constant value and therefore it is easy to see, following analogous procedure to the previous case, that the correlation tends to zero.

Stationary case I: $\mu_S > 2, \mu_P < 2$.

As mentioned in the text, from Eq. (30) it is enough to show that the third term on the right-hand side is zero. Such terms read as

$$\frac{\sin \pi \mu_P}{\pi} \int_0^t \tilde{\Psi}_S(t-t') dt' t'^{\mu_P-2} \Psi_P(t-t'). \quad (\text{A10})$$

Using a generalized binomial expansion for both $\tilde{\Psi}_S(t)$ and $\Psi_P(t)$ we get

$$\begin{aligned} \Phi(t) &\simeq \frac{\sin \pi \mu_P}{\pi} \sum_{n,m} \binom{1-\mu_P}{n} \binom{1-\mu_S}{m} \frac{(-1)^n}{(t+T_P)^{n+\mu_P-1}} \\ &\times \frac{(-1)^m}{(t+T_S)^{m+\mu_S-2}} \int_0^t t'^{m+m+\mu_P-2} dt'. \end{aligned} \quad (\text{A11})$$

Carrying out the integration shows that the leading term in t vanishes for $t \rightarrow \infty$. Such a demonstration is valid also for the dynamical case in the same range of parameters [see Eqs. (51) and (52)].

APPENDIX B

This Appendix is devoted to detailed calculations involved in the evaluation of the asymptotic limits of the function $\Phi(t)$ and $\langle \sigma(t) \rangle$ in the dynamic approach.

Herein only the parameter range $\mu_S < 2, \mu_P < 2$ is considered, the other ranges being analyzed in detail in the main text and in Appendix A.

$\Phi(t)$ is given by the following integral:

$$\Phi(t) = \int_0^t \psi_S(t, t') \Psi_P(t, t') dt', \quad (\text{B1})$$

where $\psi_S(t, t')$ is defined in Eq. (10) and $\Psi_P(t, t')$ in Eq. (12), each with the appropriate labeling. $\Phi(t)$ can be decomposed as sum of four contributions

$$\Phi(t) = \sum_{i=1}^4 \Phi_i(t), \quad (\text{B2})$$

where

$$\Phi_1(t) = t \psi_S(t) \Psi_P(t), \quad (\text{B3})$$

$$\begin{aligned} \Phi_2(t) &= \psi_S(t) \int_0^t \int_0^{t'} R_P(t'') \Psi_P(t-t'') dt'' dt' \\ &= \psi_S(t) \int_0^t (t-t'') R_P(t'') \Psi_P(t-t'') dt'', \end{aligned} \quad (\text{B4})$$

$$\begin{aligned}\Phi_3(t) &= \Psi_P(t) \int_0^t \int_0^{t'} R_S(t'') \psi_S(t - t'') dt'' dt' \\ &= \Psi_P(t) \int_0^t (t - t'') R_S(t'') \psi_S(t - t'') dt'', \quad (\text{B5})\end{aligned}$$

$$\Phi_4(t) = \int_0^t \int_0^{t'} \int_0^{t'} R_S(t'') \psi_S(t - t'') R_P(\tau) \Psi_P(t - \tau) dt' dt'' d\tau. \quad (\text{B6})$$

Here $\psi_S(t)$ and $\Psi_P(t)$ are defined in Eqs. (13) and (36). Using the methods of Ref. [49], Eqs. (B4), (B5) can be evaluated in the asymptotic limit to yield

$$\Phi_1(t) \approx \frac{c_1}{t^{\mu_S + \mu_P - 2}}, \quad \Phi_2(t) \approx \frac{c_2}{t^{\mu_S - 1}}, \quad \Phi_3(t) \approx \frac{c_3}{t^{\mu_P - 1}}.$$

Since in the limit $t \rightarrow \infty$ the three contribute vanish, it is not important the evaluation of the constants c_1, c_2, c_3 . To evaluate $\Phi_4(t)$ we first need an analytical expression for $R_S(t)$ and $R_P(t)$. It can be shown that [49]

$$R_S(t) \approx -\frac{\sin(\pi\mu_S)}{\pi T_S^{\mu_S - 1}} \frac{1}{t^{2 - \mu_S}}, \quad (\text{B7})$$

with the same expression, with the respective parameters being valid for $R_P(t)$. Then we have

$$\int_0^{t'} R_S(\tau) \psi_S(t - \tau) d\tau \approx -\frac{(t + T_S - t')^{1 - \mu_S} t'^{\mu_S - 1} \sin(\pi\mu_S)}{\pi(t + T_S)}.$$

On the other hand

$$\begin{aligned}\int_0^{t'} R_P(\tau) \Psi_P(t - \tau) d\tau &= \frac{T_P^{\mu_P - 1}}{(t + T_P)^{\mu_P - 1}} \sum_{n=0}^{\infty} \binom{1 - \mu_P}{n} \frac{(-)^n}{(t + T_P)^n} \\ &\times \int_0^{t'} R_P(\tau) \tau^n d\tau. \quad (\text{B8})\end{aligned}$$

Using for $R_P(t)$ the same approximation of $R_S(t)$ Eq. (B2), we have

$$\begin{aligned}\int_0^{t'} R_P(\tau) \Psi_P(t - \tau) d\tau &\approx -\frac{\sin \pi \mu_P}{\pi(t + T_P)^{\mu_P - 1}} \sum_{n=0}^{\infty} \binom{1 - \mu_P}{n} \frac{(-)^n}{(t + T_P)^n} \frac{t'^{n + \mu_P - 1}}{n + \mu_P - 1}. \quad (\text{B9})\end{aligned}$$

The function $\Phi_4(t)$ is

$$\begin{aligned}\Phi_4(t) &\approx \frac{\sin \pi \mu_P \sin \pi \mu_S}{\pi^2 (t + T_P)^{\mu_P - 1}} \frac{t^{\mu_S + \mu_P - 1}}{(t + T_S)^{\mu_S}} \sum_{n=0}^{\infty} \left(-\frac{t}{t + T_P} \right)^n \\ &\times \binom{1 - \mu_P}{n} \frac{F\left(n + \mu_P + \mu_S - 1, \mu_S - 1, n + \mu_P + \mu_S, \frac{t}{t + T_S}\right)}{(n + \mu_P - 1)(n + \mu_P + \mu_S - 1)},\end{aligned}$$

where $F(a, b, c, z)$ is the hypergeometric function. Finally

$$\begin{aligned}\Phi_4(t) &\approx \frac{\sin \pi \mu_P \Gamma(\mu_P + \mu_S - 1)(t + T_P)^{1 - \mu_P} t^{\mu_S}}{(1 - \mu_P) \Gamma(\mu_P + 1) \Gamma(\mu_S - 1)(t + T_S)^{\mu_S} t^{1 - \mu_P}} \\ &\times F\left[\{\mu_P - 1, \mu_P - 1, \mu_P + \mu_S - 1\}, \{\mu_P, \mu_P + 1\}, \frac{t}{t + T_S}\right],\end{aligned}$$

where ${}_pF_q(\{a\}, \{b\}, z)$ is the generalized hypergeometric function. In the limit for $t \rightarrow \infty$

$$\begin{aligned}\Phi_\infty &= -\frac{\sin \pi \mu_P \Gamma(\mu_P + \mu_S - 1)}{\pi(\mu_P - 1) \Gamma(\mu_P + 1) \Gamma(\mu_S - 1)} \\ &\times F[\{\mu_P - 1, \mu_P - 1, \mu_P + \mu_S - 1\}, \{\mu_P, \mu_P + 1\}, 1]. \quad (\text{B10})\end{aligned}$$

As far as the evaluation of the function $\langle \sigma(t) \rangle$ is concerned, in the dynamic approach it is given by Eq. (35)

$$\langle \sigma(t) \rangle = \epsilon \int_0^t \psi_S(t, t') \Psi_P(t') dt', \quad (\text{B11})$$

which is to be evaluated in the parameter range $\mu_S < 2, \mu_P < 2$. Let $P_S(t) = R_S(t) + \delta(t)$, Eq. (B11) reads

$$\langle \sigma(t) \rangle = \epsilon \int_0^t dt' \Psi_P(t') \int_0^{t'} dx P_S(x) \psi_S(t - x), \quad (\text{B12})$$

which, after a transformation on the integration domain, turns into

$$\langle \sigma(t) \rangle = \epsilon \int_0^t dx \psi_S(t - x) P_S(x) \int_x^t dt' \Psi_P(t'). \quad (\text{B13})$$

The long-time limit shifts the main weight in the integral on the terms such that $x \lesssim t$. Therefore the approximation Eq. (B7), valid also for $P_S(t)$ in the long-time limit, can be adopted. Inserting such approximation in Eq. (B13) leads to

$$\langle \sigma(t) \rangle \simeq -\epsilon \frac{\sin \pi \mu_S}{\pi T_S^{\mu_S - 1}} \int_0^t dx \psi_S(t - x) x^{\mu_S - 2} \int_x^t dt' \Psi_P(t'). \quad (\text{B14})$$

After getting rid of the integral in t' by direct integration of $\Psi_P(t')$, one is left with a simple convolution which is easy to analyze in Laplace transform. After some straightforward algebra, extracting the two asymptotic leading terms,

leads to

$$\langle \sigma(t) \rangle \simeq k_1 t^{1-\mu_P} + k_2 t^{\mu_S-\mu_P-1}, \quad (\text{B15})$$

that is, the asymptotic expression of Eq. (41), with the coefficients given by Eqs. (42) and (43).

-
- [1] R. Kubo, M. Toda, and N. Hashitsume, *Statistical Physics II: Nonequilibrium Statistical Mechanics* (Springer-Verlag, Berlin, 1985), p. 37.
 - [2] A. Crisanti and F. Ritort, *J. Phys. A Math. Gen.* **36**, R181 (2003).
 - [3] U. Marini Bettolo Marconi, A. Puglisi, L. Rondoni, and A. Vulpiani, *Phys. Rep.* **461**, 111 (2008).
 - [4] D. R. Chialvo, *Nature Physics* **6**, 744 (2010).
 - [5] G. Werner, *Physics of Life Reviews* **7**, 256 (2010).
 - [6] J. P. Garrahan and I. Lesanovsky, *Phys. Rev. Lett.* **104**, 160601 (2010).
 - [7] P. A. Frantsuzov, S. Volkán-Kacsó, and B. Jankó, *Phys. Rev. Lett.* **103**, 207402 (2009).
 - [8] X. Brokmann, J. -P. Hermier, G. Messin, P. Desbiolles, J.-P. Bouchaud, and M. Dahan, *Phys. Rev. Lett.* **90**, 120601 (2003).
 - [9] A. Rebenshtok and E. Barkai, *J. Stat. Phys.* **133**, 565 (2008).
 - [10] B. J. West *et al.*, *Phys. Rep.* **468**, 1 (2008).
 - [11] M. Turala, B. J. West, and P. Grigolini, (unpublished).
 - [12] P. Allegrini, M. Bologna, L. Fronzoni, P. Grigolini, and L. Silvestri, *Phys. Rev. Lett.* **103**, 030602 (2009).
 - [13] L. Silvestri, L. Fronzoni, P. Grigolini, and P. Allegrini, *Phys. Rev. Lett.* **102**, 014502 (2009).
 - [14] P. Grigolini, G. Aquino, M. Bologna, M. Lukovic, and B. J. West, *Physica A* **388**, 4192 (2009).
 - [15] P. Allegrini, M. Bologna, P. Grigolini, and B. J. West, *Phys. Rev. Lett.* **99**, 010603 (2007).
 - [16] G. Aquino, P. Grigolini, and B. J. West, *Europhys. Lett.* **80**, 10001 (2008).
 - [17] A. A. Budini and P. Grigolini, *Phys. Rev. A* **80**, 022103 (2009).
 - [18] F. Barbi, M. Bologna, and P. Grigolini, *Phys. Rev. Lett.* **95**, 220601 (2005).
 - [19] I. M. Sokolov and J. Klafter, *Phys. Rev. Lett.* **97**, 140602 (2006).
 - [20] E. Heinsalu, M. Patriarca, I. Goychuk, and P. Hänggi, *Phys. Rev. Lett.* **99**, 120602 (2007).
 - [21] E. Heinsalu, M. Patriarca, I. Goychuk, and P. Hänggi, *Phys. Rev. E* **79**, 041137 (2009).
 - [22] A. Weron, M. Magdziarz, and K. Weron, *Phys. Rev. E* **77**, 036704 (2008).
 - [23] I. M. Sokolov *et al.*, *Physica A* **302**, 568 (2001); M. Magdziarz, A. Weron, and J. Klafter, *Phys. Rev. Lett.* **101**, 210601 (2008).
 - [24] A. I. Shushin, *Phys. Rev. E* **78**, 051121 (2008).
 - [25] Y.-M. Kang and Y.-L. Jiang, *J. Math. Phys. (NY)* **51**, 023301 (2010).
 - [26] M. Magdziarz, A. Weron, and J. Klafter, *Phys. Rev. Lett.* **101**, 210601 (2008).
 - [27] B. I. Henry, T. A. M. Langlands, and P. Straka, *Phys. Rev. Lett.* **105**, 170602 (2010).
 - [28] I. M. Sokolov, *Phys. Rev. E* **73**, 067102 (2006).
 - [29] G. Aquino, M. Bologna, P. Grigolini, and B. J. West, *Phys. Rev. Lett.* **105**, 040601 (2010).
 - [30] P. Allegrini, D. Menicucci, R. Bedini, L. Fronzoni, A. Gemignani, P. Grigolini, B. J. West, and P. Paradisi, *Phys. Rev. E* **80**, 061914 (2009).
 - [31] P. Allegrini, D. Menicucci, R. Bedini, A. Gemignani, and P. Paradisi, *Phys. Rev. E* **82**, 015103 (2010).
 - [32] M. Lukovic and P. Grigolini, *J. Chem. Phys.* **129**, 184102 (2008).
 - [33] P. Allegrini, G. Aquino, P. Grigolini, L. Palatella, A. Rosa, and B. J. West, *Phys. Rev. E* **71**, 066109 (2005).
 - [34] G. Margolin and E. Barkai, *J. Stat. Phys.* **122**, 137 (2006).
 - [35] G. Zumofen and J. Klafter, *Phys. Rev. E* **47**, 851 (1993).
 - [36] J. J. Collins *et al.*, *Nature (London)* **376**, 236 (1995).
 - [37] C. E. Shannon, *Bell Syst. Tech. J.* **27**, 379, 623 (1948).
 - [38] L. M. Pecora and T. L. Carroll, *Phys. Rev. Lett.* **64**, 821 (1990).
 - [39] X. F. Wang, *International Journal of Bifurcation and Chaos* **12**, 885 (2002).
 - [40] Y. Kuramoto, *Chemical Oscillations, Waves and Turbulence* (Springer, Berlin, 1984).
 - [41] S. Bianco, E. Geneston, P. Grigolini, and M. Ignaccolo, *Physica A (Amsterdam)* **387**, 1387 (2008).
 - [42] M. Luković, M. Ignaccolo, L. Fronzoni, and P. Grigolini, *Phys. Lett. A* **372**, 2608 (2008).
 - [43] Y. F. Contoyiannis and F. K. Diakonou, *Phys. Lett. A* **268**, 286 (2000).
 - [44] M. Turala, M. Lukovic, B. G. West, and P. Grigolini, *Phys. Rev. E* **80**, 021110 (2009).
 - [45] W. Sun, R. Wang, and J. Cao, *Cogn. Neurodyn* **4**, 225 (2010).
 - [46] X.-J. Wu and H.-T. Lu, *Chinese Physics B* **19**, 070511 (2010).
 - [47] Q. Wang, M. Perc, Z. Duan, and G. Chen, *Phys. Rev. E* **80**, 026206 (2009).
 - [48] G. Tkacik, A. M. Walczak, and W. Bialek, *Phys. Rev. E* **80**, 031920 (2009).
 - [49] B. J. West, M. Bologna, and P. Grigolini, *Physics of Fractal Operators* (Springer, New York, 2003).

Robust Control for Mobility and Wireless Communication in Cyber-Physical Systems with Application to Robot Teams

Jonathan Fink, Alejandro Ribeiro, and Vijay Kumar

Proceedings of the IEEE, 100(1), 164-178 (2012)

Robust Control for Mobility and Wireless Communication in Cyber–Physical Systems With Application to Robot Teams

Control of an autonomous robot team with the aim of optimizing network performance is discussed in this paper; the authors design a controller to ensure availability of communication resources.

By JONATHAN FINK, *Student Member IEEE*, ALEJANDRO RIBEIRO, *Member IEEE*, AND VIJAY KUMAR, *Fellow IEEE*

ABSTRACT | In this paper, a system architecture to provide end-to-end network connectivity for autonomous teams of robots is discussed. The core of the proposed system is a cyber–physical controller whose goal is to ensure network connectivity as robots move to accomplish their assigned tasks. Due to channel quality uncertainties inherent to wireless propagation, we adopt a stochastic model where achievable rates are modeled as random variables. The cyber component of the controller determines routing variables that maximize the probability of having a connected network for given positions. The physical component determines feasible robot trajectories that are restricted to safe configurations which ensure these probabilities stay above a minimum reliability level. Local trajectory planning algorithms are proposed for simple environments and leveraged to obtain global planning algorithms to handle complex surroundings. The resulting integrated controllers are robust in that end-to-end communication survives with high probability even if individual point-to-point links are

likely to fail with significant probability. Experiments demonstrate that the global planning algorithm succeeds in navigating a complex environment while ensuring that end-to-end communication rates meet or exceed prescribed values within a target failure tolerance.

KEYWORDS | Mobile ad hoc networks; motion planning; multi-robot systems

I. INTRODUCTION

The confluence of advances in wireless communication, sensing, computing, and control has led to the emergence of cyber–physical systems. Cyber–physical systems go beyond the mere addition of cyber functionalities to physical systems being typified by a tight blending of cyber and physical components and functions. A canonical example of this class of systems is the autonomous robot team where a group of mobile robots cooperate to accomplish tasks assigned by human operators. Consider, for example, a search and rescue mission in a hazardous environment where a team of robots is deployed to scout points of interest. Designated lead members of the team move to specified locations while the remaining robots provide mission support by configuring a multihop wireless network that permits relaying of information back to the operators. Availability of wireless communications is critical for task accomplishment because communications are required to exchange information between robots as well as to relay information to and from the human

Manuscript received March 30, 2011; revised June 22, 2011; accepted June 24, 2011. Date of publication September 6, 2011; date of current version December 21, 2011. This work was supported by the U.S. Army Research Laboratory under Grant W911NF-08-2-0004, and the U.S. Office of Naval Research (ONR) under Grants N00014-08-1-0696 and N00014-07-1-0829.

J. Fink was with the GRASP Laboratory, University of Pennsylvania, Philadelphia, PA 19104 USA. He is now with the U.S. Army Research Laboratory, Adelphi, MD 20783-1197 USA (e-mail: jonfink@grasp.upenn.edu).

A. Ribeiro is with the Electrical and Systems Engineering Department, University of Pennsylvania, Philadelphia, PA 19104 USA (e-mail: aribeiro@seas.upenn.edu).

V. Kumar is with the GRASP Laboratory, University of Pennsylvania, Philadelphia, PA 19104 USA (e-mail: kumar@grasp.upenn.edu).

Digital Object Identifier: 10.1109/JPROC.2011.2161427

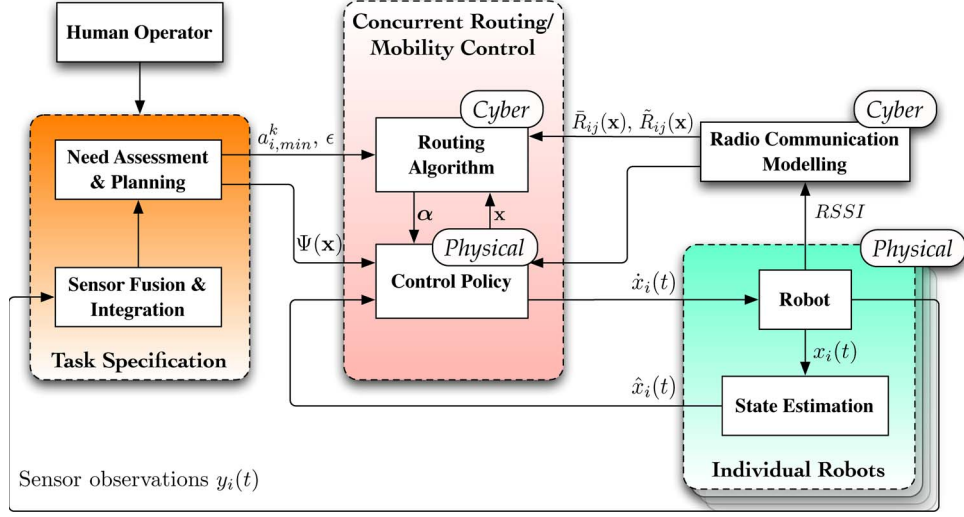


Fig. 1. System architecture. Task specification here represents a generic spatial application defined by a convex task potential function $\Psi(\mathbf{x})$ while providing a stream of data to the human operator. Individual robot components consist of the low-level robot control, estimation, and communication. We additionally assume that a subsystem is available to build an online model of radio communication in the environment. The focus of this work is on developing concurrent methods for routing and mobility control.

operators. It then follows that deployment of the team requires integration of (cyber) wireless communications with (physical) mobility control. The cyber-physical perspective posits that this integration is not just a matter of adding wireless transceivers to the robots but requires a tight conjoining of communications and mobility control.

Tight integration of communications and mobility arises in autonomous robot teams because availability of wireless infrastructure is unlikely in the harsh environments in which they are to be deployed. In the absence of infrastructure, robots have to self-organize into a wireless network capable of supporting the necessary information exchanges. In this context, the spatial placement of the robots affects the feasibility of successful communication because some physical configurations cannot support required transmission rates between, say, human operators and some lead members. We can therefore think of communications as determining a set of virtual obstacles that restrict the movement of the robots. However, this is not a hard limit as it is possible to reconfigure communication variables to alter the set of physical configurations for which communications are feasible. This yields a control loop that begins with communication variables limiting mobility and finishes with mobility determining communication variables. In the end, successful deployment of an autonomous team of robots requires joint cyber-physical controllers that determine (physical) trajectories for the robots while ensuring (cyber) availability of communication resources [1].

An architecture diagram for the cyber-physical control of autonomous teams of robots is shown in Fig. 1. As with any mobility control system, there is a block performing

task specification, a second block executing the control law, and a third block conducting actuation and state estimation. The task specification block interfaces with the human operators and integrates robot observations and requirements to determine specifications that it passes on to the control block. These specifications come in the form of a potential function $\Psi(\mathbf{x})$ and basal end-to-end communication rate requirements $a_{i,min}^k$ —the subindex i here denotes a source and the superindex k a destination; see Section II. The goal of the autonomous team is to minimize the potential $\Psi(\mathbf{x})$ while ensuring that end-to-end communication rates exceed the minimum required level $a_{i,min}^k$.

The control block is the core of the cyber-physical system and the main focus of the work described in this paper. The purpose of this block is to determine physical control inputs $\dot{\mathbf{x}}(t)$ that dictate the movement of the robots and network variables $\alpha(t)$ that determine the communication of information through members of the team. The control inputs $\dot{\mathbf{x}}(t)$ are conducive to task completion, i.e., minimization of the task potential, while ensuring reliable network operation, i.e., communication at or exceeding rates $a_{i,min}^k$ when combined with network variables $\alpha(t)$. Information about achievable rates between different locations is necessary to determine mobility and communication variables. This information is provided by a radio communication modeling block. Due to the difficulty of predicting these rates accurately, the output of this block is in the form of a statistical model of achievable rates. As we discuss in Section III, models that provide the mean and variance of achievable rates are reasonable in practice.

The execution block consists of individual robots implementing the control law $\dot{\mathbf{x}}(t)$ and routing packets

according to variables $\alpha(t)$. Robots also take observations $y_i(t)$, e.g., a video feed, that they relay to task planning and perform position estimation $\hat{x}_i(t)$ that they feedback to the control block. Using available technologies for mapping, control, and state estimation, each robot can estimate its position $\hat{x}_i(t)$ and control its velocity $\dot{x}_i(t)$ with respect to a common known map of the environment. Since we do not provide details about mapping or state estimation in this paper, we refer the interested reader to, e.g., [2].

A. Communication-Aware Mobility Control

In the design of concurrent communications and mobility control algorithms for autonomous robot teams there are three issues that arise naturally: 1) how to translate robot positions into information about the point-to-point rates at which pairs of robots can communicate with each other; 2) how will the cyber-physical control loop in Fig. 1 utilize point-to-point connectivity information in order to ensure end-to-end network integrity; and 3) how to deal with uncertainty in the information about point-to-point channels between individual pairs of robots.

Issues 1) and 2) are related to each other. A simple answer to issue 1) is to identify the ability to communicate with spatial proximity, possibly mixed with line-of-sight information to account for physical obstacles to radio propagation. Using this model, point-to-point links between robots are feasible if they are sufficiently close and within sight of each other and infeasible otherwise. Matched to this simple model of point-to-point connectivity, the ability to establish end-to-end connections is identified with the connectedness of the resulting graph. The problem of ensuring end-to-end network integrity then becomes one of letting robots move to accomplish their task while guaranteeing that the graph of point-to-point connections consists of a single connected component [3]–[10].

The advantage of this approach is that network-wide indicators of connectedness such as the second largest eigenvalue of the graph Laplacian or the k -connectivity of the network's graph are computationally tractable. It is therefore not difficult to insert connectivity constraints into the task planner and, if there is leeway in the selection of different spatial configurations, to find configurations that optimize connectivity in terms of the metric under consideration. Do notice that path planning is computationally challenging even in the absence of communication constraints. The tractability of graph connectedness indicators simply means that the computational complexity of the cyber-physical control loop is comparable to that of a communication-unaware controller.

Aside from the value of simplicity, associating small distance and line-of-sight with connectivity is not entirely justified. Early solutions to wireless networking for systems of dynamic nodes were indeed based on the concept that reliable point-to-point links could be detected and established [11], [12]. However, it was quickly noticed that binary channel models were not accurate representations

of wireless links [13]. As a consequence, attention was devoted to methods that explicitly consider the reliability of point-to-point links and choose routes to optimize end-to-end reliability metrics such as probability of delivery [14]–[16]. These more nuanced models of wireless connectivity can be incorporated without much difficulty into mobility control algorithms that use indicators of graph connectedness [17], [18]. If links are characterized by reliability indicators, the binary connectivity graph can be replaced by a weighted graph. Information about the number of connected components can be similarly extracted from, for example, the second largest eigenvalue of the weighted graph's Laplacian.

Either based on binary or weighted graphs, connectedness is an indirect indicator of the ability to establish end-to-end communications. Having a single connected component just implies that multihop paths from sources to destinations exist but does not determine whether the network formed by the robots is able to support desired communication rates. It is possible that some links in the connectivity graph can support rates that are too low, or that the resulting configuration contains bottlenecks that limit information flow. In the cyber-physical control loop depicted in Fig. 1, graph connectedness does not solve for the network variables $\alpha(t)$. Instead, it restricts movement so that a necessary but not sufficient condition for the existence of feasible network variables $\alpha(t)$ is not violated. In fact, one could argue that these controllers are not cyber-physical because the integration of wireless communications with physical mobility is minimal. A true cyber-physical design should consider end-to-end rates and conjoin the design of mobility and network control as done in the systems described in the following section.

B. Robust Cyber-Physical Control

An honest metric of network integrity has to rely on the achievability of target end-to-end communication rates. Communication rates, however, do not depend solely on the spatial configuration but also on the manner in which packets are routed through the network. This leads to the problem of joint cyber-physical control of trajectories and routing variables [1], [19]. For given spatial configuration \mathbf{x} , pairs of achievable point-to-point communication rates $R_{ij}(\mathbf{x})$ are assumed available at the radio modeling block. The cyber part of the controller queries the modeling block and attempts to determine routing variables $\alpha(\mathbf{x})$ that support desired communication rates $a_{i,\min}^k$. If this attempt is unsuccessful, spatial configuration \mathbf{x} is marked as unallowable. If the attempt succeeds, joint configuration $(\mathbf{x}, \alpha(\mathbf{x}))$ is deemed feasible and, in particular, spatial configuration \mathbf{x} is deemed allowable. The physical part of the controller utilizes the information on allowable configurations \mathbf{x} to plan physical routes that achieve minimization of the task potential $\Psi(\mathbf{x})$ while ensuring that end-to-end rates exceed basal requirements at all points in time. See Section II.

Ensuring continuous reliable communication is challenging, however, because significant uncertainty in achievable rates is inherent to the deployment of an autonomous robot team. Due to shadowing and small scale fading, even small variations in robots' positions lead to significant changes in channel strength [13], [20], [21] which translate into commensurable changes in achievable communication rates between pairs of robots. Precise channel state information can be acquired through measurements over time, but mobility planning algorithms necessitate access to channel quality indicators at future positions to which the robots are yet to be deployed. Thus, from the perspective of the system in Fig. 1, rates $R_{ij}(\mathbf{x})$ are random. The outputs of the radio modeling block are rate estimates $\bar{R}_{ij}(\mathbf{x})$ whose variances $\tilde{R}_{ij}(\mathbf{x})$ are typically large. See Section III.

Since achievability of end-to-end rates cannot be guaranteed because of rate uncertainties, it is natural to redefine network survivability in terms of the probability of end-to-end rates exceeding their basal rates $a_{i,\min}^k$. Packet routing variables $\alpha(\mathbf{x})$ are then determined in order to maximize this probability [1]. The resulting routes are robust because they are chosen to minimize the probability of failure. At this point it has to be noted that the goal of the self-organized network is to maintain reliable end-to-end communication, not point-to-point communication. Consequently, we can think of robust routes as exploiting spatial redundancy to minimize the effect of point-to-point uncertainty in end-to-end communication rates. Indeed, by splitting traffic flows between various neighboring robots, we can ensure that while failure of a particular link may reduce end-to-end communication rates, it does not interrupt them completely. See Section IV.

The integration of robust routing with the physical control loop is discussed in Section V. We develop local planning algorithms for simple environments (Section V-A) that we test in simulations for teams composed of three and four robots (Section V-B). These simulations demonstrate that the performance of local controllers is hindered by local minima. To overcome this problem as well as to handle complex environments, we leverage the local controllers to design global planning algorithms (Section V-C). Global planners are tested with experimental results in an indoor office space at the University of Pennsylvania (Section V-D). The experiments demonstrate that the global planning algorithm succeeds in navigating a complex environment while ensuring that end-to-end communication rates meet or exceed prescribed values within a target failure tolerance. We close the paper with concluding remarks (Section VI).

II. COMMUNICATIONS AND MOBILITY

Consider a team of N robots and denote their positions as x_i , for $i = 1, \dots, N$. The robots are kinematic and fully controllable which allows us to consider simple mobility models of the form $\dot{x}_i(t) = u_i(t)$, where $u_i(t)$ is the control

input to robot i . A human operator is located at the fixed operation center that we index as $i = 0$ at position x_0 . Further define vectors $\mathbf{x} := (x_0, \dots, x_N) \in \mathbb{R}^{2(N+1)}$ and $\dot{\mathbf{x}} := (\dot{x}_0, \dots, \dot{x}_N) \in \mathbb{R}^{2(N+1)}$ to group all positions and velocities, respectively. The task assigned to the team is specified through a generic scalar convex task potential function $\Psi : \mathbb{R}^{2(N+1)} \rightarrow \mathbb{R}$. If the potential minimum Ψ_{\min} is attained at \mathbf{x}^* , i.e., if $\Psi(\mathbf{x}^*) = \Psi_{\min}$, the configuration \mathbf{x}^* satisfies task completion. For example, if a designated leader agent ℓ must visit a target location $x_{\ell,\text{goal}} \in \mathbb{R}^2$, we can define $\Psi(\mathbf{x}) = \|x_\ell - x_{\ell,\text{goal}}\|^2$. The minimum $\Psi_{\min} = 0$ is attained by any configuration $\mathbf{x}^* = (x_0, \dots, x_\ell, \dots, x_N)$ for which $x_\ell = x_{\ell,\text{goal}}$, or equivalently by any member of the set $\mathbf{x}^* \in \{\mathbf{x} = (x_0, \dots, x_\ell, \dots, x_N) : x_\ell = x_{\ell,\text{goal}}\}$. Irrespective of the particular form of $\Psi(\mathbf{x})$, the control problem is to find velocities $\dot{\mathbf{x}}(t)$ such that at some time t_f the team configuration $\mathbf{x}(t_f) = \mathbf{x}(0) + \int_0^{t_f} \dot{\mathbf{x}}(t) dt$ satisfies task completion in that we have $\Psi(\mathbf{x}(t_f)) = \Psi_{\min}$. Mathematically, we can write this mobility control formulation as

$$\begin{aligned} \min_{\dot{\mathbf{x}}(t), t \in [0, t_f]} \quad & \Psi(\mathbf{x}(t_f)) \\ \text{subject to} \quad & \mathbf{x}(t) = \mathbf{x}(0) + \int_0^t \dot{\mathbf{x}}(u) du. \end{aligned} \quad (1)$$

As robots move to accomplish their task, they maintain *end-to-end* data communication flows between members of the team and/or members of the team and the operation center. Information flows are indexed as $k = 1, \dots, K$. Flows may have multiple sources and multiple destinations. The set of destinations of the k th information flow is denoted as $\text{dest}(k)$. For agent i and flow k , the variable $a_{i,\min}^k$ represents the required communication rate between agent i and any of the agents in the set of destinations $\text{dest}(k)$. For example, if the only communications of interest are from the lead robot ℓ to the operation center, there are only $K = 1$ flows. Since the flow $k = 1$ is intended to the operating center, $\text{dest}(1) = 0$ and $a_{\ell,\min}^1$ denotes the minimum level of service for the communication from the leader to the operating center. All other variables $a_{i,\min}^k = 0$ are null.

We model *point-to-point* connectivity through a rate function $R_{ij}(\mathbf{x}) = R_{ij}(x_i, x_j)$ that determines the amount of information that agent i at position x_i can send to agent j at position x_j . Since direct communication between the source and the destination of an information flow is not always possible, terminals self-organize into a multihop network to relay packets for each other. Packet relaying is determined by routing variables α_{ij}^k which describe the fraction of time node i spends transmitting data for flow k to node j ; see Fig. 2. Thus, the product $\alpha_{ij}^k R_{ij}(\mathbf{x})$ determines the rate of point-to-point information transmission from

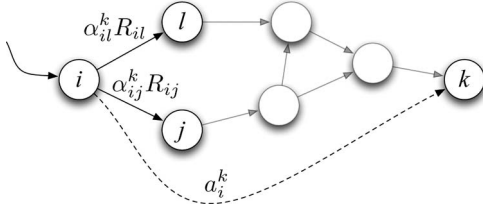


Fig. 2. Communication network. The nodes are deployed to support end-to-end rates from node i to destination (or flow) k . Routing variables α_{ij}^k determine the fraction of time node i sends packets to node j for flow k . R_{ij} is defined as the supported rate of the wireless channel from node i to node j .

i to j . If we consider the transmission to all neighboring terminals for which $R_{ij}(\mathbf{x}) > 0$, the total rate at which packets leave agent i is $\sum_{j=0}^N \alpha_{ij}^k R_{ij}(\mathbf{x})$. Likewise, the total rate at which i receives packets from other terminals is $\sum_{j=0, j \neq \text{dest}(k)}^N \alpha_{ji}^k R_{ji}(\mathbf{x})$. The information rate $a_i^k(\alpha, \mathbf{x})$ available for flow k at source i is the difference between outgoing and incoming rates

$$a_i^k(\alpha, \mathbf{x}) = \underbrace{\sum_{j=0}^N \alpha_{ij}^k R_{ij}(\mathbf{x})}_{\text{Outgoing packets}} - \underbrace{\sum_{j=0, j \neq \text{dest}(k)}^N \alpha_{ji}^k R_{ji}(\mathbf{x})}_{\text{Incoming packets}} \quad (2)$$

where we define the vector α grouping all routing variables α_{ij}^k . Notice that the variables α_{ij}^k represent time slot shares and must therefore satisfy $0 \leq \alpha_{ij}^k \leq 1$ for all i, j , and k . It must also be that $\sum_{j,k} \alpha_{ij}^k \leq 1$ for all i to ensure that the sum of all time shares at terminal i does not exceed 1. It is possible to, alternatively, require $\sum_{i,j,k} \alpha_{ij}^k \leq 1$ if we wish for only one link to be active at any time across the entire network.

Routing variables α and configuration-dependent rates $R_{ij}(\mathbf{x})$ determine the set $a_i^k(\alpha, \mathbf{x})$ of end-to-end communication rates from each node i and flow k as per (2). The task specification requires that end-to-end rates exceed the minimum threshold $a_{i,\min}^k$. Therefore, integrity of the communication network necessitates that

$$a_i^k(\alpha, \mathbf{x}) \geq a_{i,\min}^k, \quad \text{for all } i, k. \quad (3)$$

Notice that $a_i^k(\alpha, \mathbf{x})$ is a function of positions \mathbf{x} and routing variables α . To control end-to-end connectivity, i.e., to satisfy (3), we can resort to control of positions \mathbf{x} , to control of routes α , or both.

Since communication is necessary for task completion, the mobility control problem as summarized in (1) is redefined. The new goal is to find algorithms and control policies that govern robot motions in order to satisfy the

task specifications in (1) and (3). Reducing $\Psi(\mathbf{x})$ as per (1) and ensuring network integrity as per (3) may be conflicting requirements. We therefore replace (1) by a concurrent search of trajectories $\mathbf{x}(t)$ and routes $\alpha(t)$ so that the task potential is minimized without ever breaking communication connectivity. Mathematically, we write this objective as the optimization problem

$$\begin{aligned} \min_{\alpha(t), \dot{\mathbf{x}}(t), t \in [0, t_f]} \quad & \Psi(\mathbf{x}(t_f)) \\ \text{subject to} \quad & a_i^k(\alpha(t), \mathbf{x}(t)) \geq a_{i,\min}^k \\ & \mathbf{x}(t) = \mathbf{x}(0) + \int_0^t \dot{\mathbf{x}}(u) du \end{aligned} \quad (4)$$

where rates $a_i^k(\alpha(t), \mathbf{x}(t))$ are given by the expression in (2) with $\alpha = \alpha(t)$ and $\mathbf{x} = \mathbf{x}(t)$.

A drawback of the formulation in (4) is the difficulty of ensuring that the constraints in (3) are satisfied. As seen in (2), rates $a_i^k(\alpha, \mathbf{x})$ depend on the link reliabilities $R_{ij}(\mathbf{x})$, which are difficult to estimate. Propagation knowledge is used by the radio communication modeling block in Fig. 1 to provide rough rate estimates $\bar{R}_{ij}(\mathbf{x})$. Agents can further measure received signal strength indicators (RSSIs) to refine the rate estimates for the current configuration $\mathbf{x}(t)$; see, e.g., [22]. The challenge here is that $\bar{R}_{ij}(\mathbf{x})$ estimates are needed not only for configuration $\mathbf{x}(t)$, but for nearby configurations to which the robots may move. The high variability of wireless channels makes $\bar{R}_{ij}(\mathbf{x}(t))$ a poor predictor of $R_{ij}(\mathbf{x})$ even if \mathbf{x} is close to $\mathbf{x}(t)$. In general, channel estimates $\bar{R}_{ij}(\mathbf{x})$ at future positions \mathbf{x} follow from radio propagation modeling and corrections from RSSI observations.

In formal terms, uncertainty of channel estimates means that the variances $\tilde{R}_{ij}(\mathbf{x})$ of channel estimates $\bar{R}_{ij}(\mathbf{x})$ are typically large for possible future positions \mathbf{x} . Variances $\tilde{R}_{ij}(\mathbf{x})$ can be provided by the radio modeling block and are therefore assumed to be available at the controller along with the mean estimates $\bar{R}_{ij}(\mathbf{x})$. We seek to redefine (4) in a manner that takes into account this probabilistic formulation of channel rates. The important observation here is that if point-to-point link rates become random, so do the rates $a_i^k(\alpha, \mathbf{x})$ of end-to-end communication flows [cf. (2)]. Consequently, it is not possible to guarantee satisfaction of the constraints in (3). Rather, we introduce a reliability tolerance ϵ and require that for all i and k

$$\mathbb{P}[a_i^k(\alpha, \mathbf{x}) \geq a_{i,\min}^k] \geq \epsilon. \quad (5)$$

That is, we require that the end-to-end link between all sources i and the destinations of all corresponding flows k

exceed their minimum required level of service with probability larger than ϵ . As in the case of the rate requirement in (3), we can satisfy (5) by controlling α and \mathbf{x} separately or jointly.

In order to robustly satisfy the networking constraints in (5), the concurrent routing and mobility problem (4) is replaced by

$$\begin{aligned} & \min_{\alpha(t), \dot{\mathbf{x}}(t), t \in [0, t_f]} \Psi(\mathbf{x}(t_f)) \\ & \text{subject to} \quad \mathbf{P} \left[a_i^k(\alpha, \mathbf{x}) \geq a_{i, \min}^k \right] \geq \epsilon \\ & \quad \mathbf{x}(t) = \mathbf{x}(0) + \int_0^t \dot{\mathbf{x}}(u) du. \end{aligned} \quad (6)$$

The focus of this paper is the solution of (6).

The problem formulation in (6) inherits some standard complications from the control formulation in (1). The problem is infinite dimensional and due to, e.g., the presence of obstacles, not convex. The concurrent search in (6) is further complicated by the entanglement of the routing and mobility problems. We deal with this entanglement by fixing \mathbf{x} and selecting α in a manner that optimizes the reliability $\mathbf{P}[a_i^k(\alpha, \mathbf{x}) \geq a_{i, \min}^k]$ (Section IV). We finish with local and global searches on positions \mathbf{x} to minimize $\Psi(\mathbf{x})$ while keeping reliabilities above the ϵ threshold (Section V).

III. POINT-TO-POINT RATE MODELING

With robots i and j located at positions x_i and x_j , we seek to develop a probabilistic model for the supported communication rate $R_{ij}(\mathbf{x}) = R_{ij}(x_i, x_j)$ between them. More specifically, we wish to model its expected value $\bar{R}_{ij}(\mathbf{x}) = \bar{R}_{ij}(x_i, x_j)$ and variance $\tilde{R}_{ij}(\mathbf{x}) = \tilde{R}_{ij}(x_i, x_j)$. Our intent is to use simple radios that do not perform rate or power adaptation—we use 2.4-GHz Zigbee radios in our experiments; see Section V-D. In that case, the communication rate $R_{ij}(x_i, x_j)$ is a function of the packet error rate of the channel, which in turn is a function of the signal-to-noise ratio [23]. We therefore focus on models of the received

signal strength $P_R(x_i, x_j)$ that we cascade into models of the packet error rate and the supported communication rate $R_{ij}(x_i, x_j)$.

Received signal power $P_R(x_i, x_j)$ is determined by three phenomena: path loss due to the distance from the source, shadowing due to obstacles in the propagation path, and multipath fading that arises as a result of reflections and refractions. Of these three phenomena, path loss and shadowing can be incorporated into a predictive model with relative ease. Fading, however, is difficult to predetermine. Multipath fading arises due to a spatial wave interference pattern generated by reflections and refractions of the electromagnetic wave which, as a consequence, inherits a space constant in the order of the wave's wavelength. Thus, in order to use ray tracing models to predict the interference pattern we need to locate all potential reflectors and refractors with precision smaller than this wavelength. While plausible in principle, this is intractable in practice because wavelengths at common operating frequencies are too small—for example, with radios operating at 2.4 GHz, the wavelength is about 12 cm. Given this difficulty we adopt the following model for the received power $P_{R, \text{dBm}}(x_i, x_j) = 10 \log(P_R(x_i, x_j))$ measured in dBm:

$$\begin{aligned} P_{R, \text{dBm}}(x_i, x_j) &= \underbrace{L_0 - 10n \cdot \log(\|x_i - x_j\|)}_{\text{Path loss}} - \underbrace{W(x_i, x_j)}_{\text{Shadowing}} - \underbrace{\mathcal{F}}_{\text{Fading}} \end{aligned} \quad (7)$$

where the term \mathcal{F} is a zero-mean Gaussian random variable with variance $\sigma_{\mathcal{F}}^2$ modeling fading effects. The term L_0 is the measured power at a reference distance d_0 from the source, n is a path loss exponent, and $W(x_i, x_j)$ is a non-smooth function to model shadowing as a function of the number of obstacles between source and destination. Experimental data collected in an indoor office environment at the University of Pennsylvania along with the function in (7) having parameters fit to the experimental data are depicted in Fig. 3. The parameters in Fig. 3 are $L_0 = -51$ dBm for $d_0 = 1$ m, $n = 2.1$, $W(x_i, x_j) = 0$ for line-of-sight links and $W(x_i, x_j) = 7.6$ dB for non-line-of-sight links, and $\sigma_{\mathcal{F}}^2 = 32$ dB². Notice that fading can cause

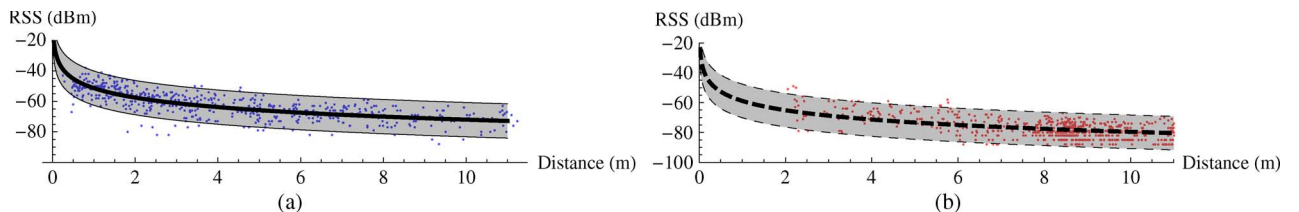


Fig. 3. Experimental characterization of received power model (7) based on 1000 samples when we classify wireless channels based on line-of-sight. (a) Line-of-sight. (b) Non-line-of-sight.

variations in received power in the order of ± 10 dB. This is verified by the standard deviation of \mathcal{F} , which is $\sigma_{\mathcal{F}} \approx 5.7$ dB. Recall that a 10-dB difference corresponds to a change of an order of magnitude for the power measured in linear units.

Translation of received signal strength $P_R(x_i, x_j)$ into packet error rate $p_e(P_R(x_i, x_j))$ depends on the type of modulation and the choice of error correcting codes. Regardless of specifics, a generally good approximation to the packet error rate is

$$p_e(P_R(x_i, x_j)) = \text{erfc}\left(\sqrt{k \frac{P(x_i, x_j)}{P_{N_0}}}\right) \quad (8)$$

where P_{N_0} is the noise power, $\text{erfc}(x)$ is the complementary error function, and k is a constant that depends on modulation and coding [23]. The translation into communication rates $R_{ij}(x_i, x_j)$ is now straightforward as it simply requires multiplying the information rate of transmitted packets R_0 by the probability of successful decoding, i.e., $R_{ij}(x_i, x_j) = R_0[1 - p_e(P_R(x_i, x_j))]$.

The randomness of the fading term \mathcal{F} in (7) propagates into randomness in the error probabilities $p_e(P_R(x_i, x_j))$ and subsequently into randomness in the rates $R_{ij}(x_i, x_j)$. To compute the mean and variance of $R_{ij}(x_i, x_j)$ we need to recall that \mathcal{F} is a Gaussian random variable. We can then invoke the delta method [24] to approximate the mean and variance of $R_{ij}(x_i, x_j)$ in terms of the mean and variance of $P_R(x_i, x_j)$ and the derivatives of the function $p_e(P_R(x_i, x_j))$ in (8). The complete mapping from distance to link rates is depicted in Fig. 4. Observe that except for very short distances smaller than 3 m there is significant variability in achieved link rates. See [1, ch. 4] for details.

While the model we present in this section describes the statistics of the supported rate $R_{ij}(x_i, x_j)$ in terms of distances $\|x_i - x_j\|$, we emphasize that this is not a limitation of the proposed cyber-physical controller. In fact,

the controller is agnostic to the particulars of the radio propagation model and relies only on the ability to query for means and variances. It is reasonable to expect that techniques for spatial mapping of point-to-point communication rates will outperform distance-based models when considering unknown or highly dynamic environments. However, as demonstrated by the experiments in Section V-D, the robust satisfaction of communication constraints affords the possibility to rely on coarse models of point-to-point communication rates while still ensuring maintenance of quality-of-service requirements.

IV. ROBUST ROUTING

The control loop in Fig. 1 embeds a cyber optimization component and a physical reconfiguration module. The cyber optimization component optimizes communication routes for given positions, while the physical component explores spatial reconfigurations that maintain network integrity and are conducive to task achievement. The physical module relies on the cyber module for the determination of configurations that are feasible from the perspective of maintaining target communication rates with some desired reliability.

The major difficulty in designing the cyber component of this control loop is the uncertainty in achievable transmission rates between nearby agents. As we discussed in Section III, simple experiments suffice to demonstrate that achievable rates in wireless links are difficult to predict. Therefore, assuming that the actual channel rates $R_{ij}(\mathbf{x})$ coincide with their estimates $\bar{R}_{ij}(\mathbf{x})$ may result in a drastic difference between predicted and actual end-to-end rates. This mismatch subsequently leads to situations in which the communication optimization module asserts network integrity when actual rates do not suffice to support the task assigned by operators.

A simple way to account for the uncertainty in $R_{ij}(\mathbf{x})$ is to discount $\bar{R}_{ij}(\mathbf{x})$ in order to reduce the likelihood of having actual rates smaller than the assumed value. This is definitely possible but would result in underutilization of communication resources. A better way to account for the uncertainty in channel rates is to recall that end-to-end rather than point-to-point failures are relevant. With reference to Fig. 2, say that robot i decides to convey information to k by forwarding it through l . If the rate $R_{il}(\mathbf{x})$ happens to be substantially smaller than estimated, communication is interrupted. If, on the contrary, robot i decides to send part of the information through l and some other part through j , the communication between i and k survives as long as the rate $R_{ij}(\mathbf{x})$ is larger than estimated. This example illustrates that it is possible to exploit spatial redundancy through traffic splitting in order to devise robust routes that guarantee small changes in end-to-end rates despite large variability in point-to-point rates $R_{ij}(\mathbf{x})$ [25].

To develop robust routing algorithms, start by noticing that computing the probability in (5), which is part of the

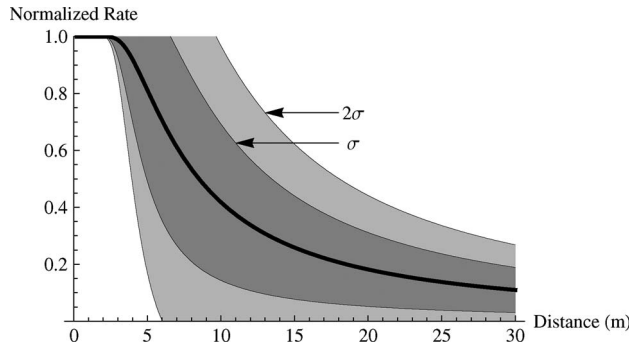


Fig. 4. Mapping from distances $\|x_i - x_j\|$ between a transmitter at location x_i and a receiver at position x_j to normalized link rates $R_{ij}(x_i, x_j)/R_0$.

problem formulation in (6), necessitates modeling the probability distribution of $a_i^k(\alpha, \mathbf{x})$. This is difficult in general. However, if we explicitly consider the stochastic model of point-to-point links via their means and variances, we can compute the mean and variance of end-to-end rates $a_i^k(\alpha, \mathbf{x})$ as

$$\begin{aligned} \bar{a}_i^k(\alpha, \mathbf{x}) &:= \mathbb{E}[a_i^k(\alpha, \mathbf{x})] \\ &= \sum_j \alpha_{ij}^k \bar{R}_{ij}(\mathbf{x}) - \sum_{j \notin \text{dest}(k)} \alpha_{ji}^k \bar{R}_{ij}(\mathbf{x}) \end{aligned} \quad (9)$$

$$\begin{aligned} \tilde{a}_i^k(\alpha, \mathbf{x}) &:= \text{var}[a_i^k(\alpha, \mathbf{x})] \\ &= \sum_j \left(\alpha_{ij}^k \right)^2 \tilde{R}_{ij}(\mathbf{x}) + \sum_{j \notin \text{dest}(k)} \left(\alpha_{ji}^k \right)^2 \tilde{R}_{ij}(\mathbf{x}). \end{aligned} \quad (10)$$

A proxy for the probability in (5) is the difference between $a_i^k(\alpha, \mathbf{x})$ and its mean $\bar{a}_i^k(\alpha, \mathbf{x})$ normalized by its standard deviation $\sqrt{\tilde{a}_i^k(\alpha, \mathbf{x})}$. Indeed, a typical approximation for the probability constraint in (5) is the condition

$$P_i^k(\alpha, \mathbf{x}) := \frac{\bar{a}_i^k(\alpha, \mathbf{x}) - a_{i,\min}^k}{\sqrt{\tilde{a}_i^k(\alpha, \mathbf{x})}} \geq \Phi^{-1}(\epsilon) \quad (11)$$

for some function $\Phi^{-1}(\epsilon)$. If the probability distribution of rates $R_{ij}(\mathbf{x})$ is Gaussian, (11) is equivalent to (5) if $\Phi^{-1}(\epsilon)$ is the inverse of the normal distribution's cumulative distribution function. For other probability distributions, we can apply Chebyshev's inequality with $\Phi^{-1}(\epsilon) = \sqrt{1/\epsilon}$ to demonstrate that (11) is a sufficient condition for satisfying (5) though this will usually be a conservative approximation.

For given positions \mathbf{x} , the goal of the cyber optimization component is to find routing variables α that satisfy (11) which is equivalent to, approximate to, or a sufficient condition to satisfy (5). In either case, there is some indeterminacy because there is a nonunique set of variables α that satisfy the corresponding inequality. This indeterminacy provides a degree of freedom that can be used to increase the reliability beyond the required level. For a given configuration \mathbf{x} , we would like to find routes $\alpha = \alpha(\mathbf{x})$ that provide the maximum possible reliability. Doing so is not conceptually difficult—it requires determination of routes $\alpha(\mathbf{x})$ that maximize the probability proxies $P_i^k(\alpha, \mathbf{x})$ in (11) in some sense. Considering that there is a rate variable a_i^k for each source–destination pair, there are several possible choices to define this maximization. One possibility is to maximize the sum of these probability proxies. Another possibility is to select routes $\alpha(\mathbf{x})$ that make the smallest of these terms as large as possible. Maximizing this minimum implies that the constraints in (11) are satisfied with significant slack and that there is

significant liberty to change the physical configuration without violating communication constraints. This freedom of movement facilitates implementation of the physical mobility control block as we discuss in Section V.

An important observation here is that the probability proxy constraints in (11) can be written in a manner that defines a cone in the joint space of routing variables and end-to-end rates [1, ch. 5]. A consequence of this property is that the optimization problems that need to be solved to maximize them are second-order cone program (SOCPs). SOCPs are a particular class of convex optimization problem that can be solved by efficient polynomial-time algorithms. For the problems considered here, the computational complexity of these algorithms is represented as a polynomial function of the number of agents N and the number of flows (destinations) K , as $O((K \cdot N^2)^{3.5})$. In practical implementations, the N^2 term can be reduced by eliminating links for which rate estimates $\bar{R}_{ij}(\mathbf{x})$ are below a certain threshold.

Recall that the motivation for robust routing algorithms is to reduce uncertainty in end-to-end communication rates. We do so by taking advantage of spatial redundancy, for which it is necessary to split traffic among various different routes. It is fitting that we do expect to obtain this type of solution from the maximization of the probability proxies $P_i^k(\alpha, \mathbf{x})$ in (11). Indeed, increases in these terms can be brought about by either increasing the mean $\bar{a}_i^k(\alpha, \mathbf{x})$ or decreasing the variance $\tilde{a}_i^k(\alpha, \mathbf{x})$. Since the mean is a linear function of α , traffic splitting has a minor effect on $\bar{a}_i^k(\alpha, \mathbf{x})$. However, traffic splitting reduces $\tilde{a}_i^k(\alpha, \mathbf{x})$ by a factor proportional to the splitting because the variance is a quadratic function of α —recall that $\alpha_{ij} \leq 1$. Thus, traffic splitting tends to increase the probability proxies because it keeps $\bar{a}_i^k(\alpha, \mathbf{x})$ more or less constant and reduces $\tilde{a}_i^k(\alpha, \mathbf{x})$ significantly.

V. CONTROL

As per (6), the objective of mobility control is to decrease $\Psi(\mathbf{x})$ while satisfying the probability proxy constraints in (11)—which are equivalent or approximations to $\mathbf{P}[a_i^k(\alpha, \mathbf{x}) \geq a_{i,\min}^k] \geq \epsilon$. To check for the feasibility of a cyber–physical configuration (α, \mathbf{x}) , we define the probability margin as the minimum slack in probability proxy constraints across all flows and sources

$$\nu(\alpha, \mathbf{x}) := \min_{i,k} \left[\frac{\bar{a}_i^k(\alpha, \mathbf{x}) - a_{i,\min}^k}{\sqrt{\tilde{a}_i^k(\alpha, \mathbf{x})}} - \Phi^{-1}(\epsilon) \right]. \quad (12)$$

Notice that a necessary and sufficient condition for feasibility of the physical configuration \mathbf{x} is to have $\nu(\alpha(\mathbf{x}), \mathbf{x}) \geq 0$, with routing variables $\alpha(\mathbf{x})$ as given by the solution of the SOCP described in Section IV. A

sufficient condition for feasibility of physical configuration \mathbf{x}' is the existence of a cyber configuration α for which $\nu(\alpha, \mathbf{x}') \geq 0$. In particular, for \mathbf{x}' close to \mathbf{x} , we expect to have $\nu(\alpha(\mathbf{x}), \mathbf{x}') \geq 0$ since the channel statistics at \mathbf{x} and \mathbf{x}' are close.

A. Gradient Controller

In general, gradient controllers define velocities $\dot{\mathbf{x}}(t)$ proportional to the negative gradients $-\nabla\Psi(\mathbf{x}(t))$ of the task potential. Since the problem in (6) is subject to communication constraints, a local controller will be based on potential gradients projected onto the feasible set $\nu(\alpha, \mathbf{x}) \geq 0$. The complex description of the feasible set, however, precludes computation of projected gradients. Instead, we consider the probability margin $\nu(\alpha(\mathbf{x}), \mathbf{x})$ and modify the potential $\Psi(\mathbf{x})$ by adding the probability margin constraint into the objective through a barrier function

$$\Omega(\mathbf{x}) := \Psi(\mathbf{x}) - \log(\nu(\alpha(\mathbf{x}), \mathbf{x})). \quad (13)$$

Since nonnegativity is necessary and sufficient for feasibility of physical configuration \mathbf{x} , the potential $\Omega(\mathbf{x})$ in (13) is defined if and only if physical configuration \mathbf{x} is feasible.

The local control law is defined to implement gradient descent on the modified potential $\Omega(\mathbf{x})$ introduced in (13), which, in explicit terms, is given by

$$\mathbf{u}(t) = -\nabla\Psi(\mathbf{x}(t)) + \frac{\nabla_{\mathbf{x}}\nu[\alpha(\mathbf{x}(t)), \mathbf{x}(t)]}{\nu[\alpha(\mathbf{x}(t)), \mathbf{x}(t)]}. \quad (14)$$

The term $\nabla\Psi(\mathbf{x}(t))$ in (14) drives the system to satisfy the task potential. The term $\nabla_{\mathbf{x}}\nu[\alpha(\mathbf{x}(t)), \mathbf{x}(t)]/\nu[\alpha(\mathbf{x}(t)), \mathbf{x}(t)]$ serves as a barrier that drives robots away from configurations for which there is a low probability of exceeding the desired reliability in end-to-end rates.

B. Simulation Results

We implement the local controller with mobility control inputs given by (14) and communication variables obtained from Section IV. Computing controls based on local optimization of the network-level end-to-end rates allows for a method of realizing team deployment while maintaining the necessary level of network connectivity. Fig. 5 depicts an example deployment with three robots for a time-varying task potential

$$\Psi(\mathbf{x}(t)) = \begin{cases} x_{2,\text{goal}} = (4, 0), & t < 40 \\ x_{2,\text{goal}} = (8, 0), & t < 60 \\ x_{2,\text{goal}} = (6, 5), & t \geq 60. \end{cases} \quad (15)$$

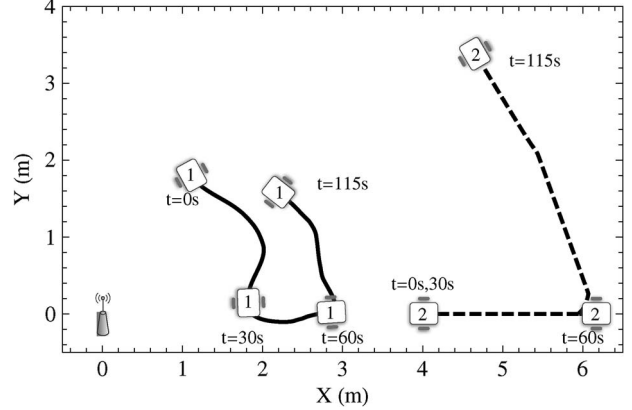


Fig. 5. Deployment via local control law (14) for a system with a fixed access point, relay node x_1 and lead node x_2 , which is controlled by a time-varying task potential $\Psi(\mathbf{x}(t))$.

Most importantly, this example demonstrates convergence of the task potential $\Psi(\mathbf{x})$ while maintaining $\mathbf{P}[a_i \geq a_{i,\min}] > \epsilon$ as depicted in Fig. 6(a) and (c). However, it is also interesting to observe that when the task potential is minimized, e.g., $t \leq 30$ s, the local control law (14) maximizes the probability of each end-to-end rate exceeding its minimum threshold. When the task potential switches so that $\Psi(\mathbf{x})$ is no longer minimized, the probability margin is reduced so that the primary objective, minimization of $\Psi(\mathbf{x})$, is prioritized. Finally, Fig. 6(b) depicts the end-to-end rate of the node x_2 that must remain above $a_{2,\min} = 0.1$. Remember that $R_{ij}(\mathbf{x})$ is a stochastic rate that affects the end-to-end rate. The envelope around \bar{a}_2 in Fig. 6(b) depicts the effect that different realizations of communication channels $R_{ij}(\mathbf{x})$ will have on the end-to-end rate. Since the pursuit of minimization on $\Psi(\mathbf{x})$ is constrained to have a probability margin $\nu(\alpha(\mathbf{x}), \mathbf{x}) > 0$, the end-to-end rate exceeds its threshold in the presence of deviations to $R_{ij}(\mathbf{x})$.

We perform a four robot simulation, depicted in Fig. 7, to demonstrate how the complexity of the objective function (13) increases with more nodes. Similar to the three robot simulation above, the task potential function is time varying so that $\Psi(\mathbf{x}) = 0$ for $t < 50$ s and $\Psi(\mathbf{x}) = \|x_3 - (9, 0)\|$ for $t \geq 50$ s. When $t < 40$ and the task potential is already minimized, control of x_1 and x_2 is based solely on the maximization of $\log \nu(\alpha(\mathbf{x}), \mathbf{x})$. From the symmetric initial configuration, the maximization drives x_1 and x_2 towards a local maxima where they would be positioned at the same point. In fact, if we consider all configurations where $x_1 < x_2$ and both agents are on the line connecting the access point, we find that there are two local maxima as depicted in Fig. 8.

To further illustrate the virtual terrain of the objective function (13) that drives local control, we observe the convergence of $\Psi(\mathbf{x}(t))$ as depicted in Fig. 9(a). For times $70 \text{ s} < t < 90 \text{ s}$, convergence of $\Psi(\mathbf{x}(t))$ slows,

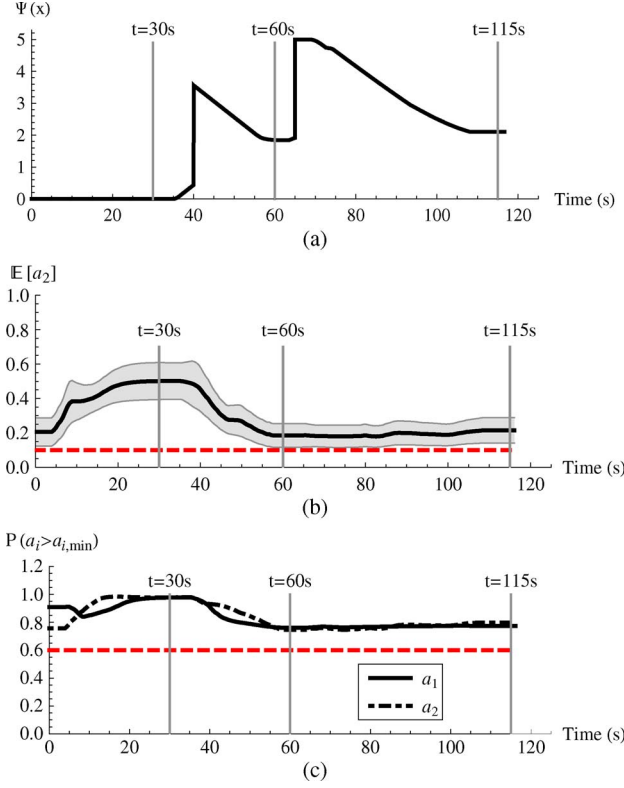


Fig. 6. Performance of the local control law (14) demonstrating convergence of $\Psi(\mathbf{x}(t))$ in (a), the maintenance of expected end-to-end rate greater than the threshold of $a_{2,\min} = 0.1$ in (b), and the $P[a_i \geq \alpha_{i,\min}] > 0.6$. The envelope surrounding $E[a_2]$ in (b) depicts the 60% confidence interval for realizations of the end-to-end rate with stochastic $R_{ij}(\mathbf{x})$.

$\nu(\alpha(\mathbf{x}), \mathbf{x})$ as depicted in Fig. 9(c) shows little change, and x_1 and x_2 cease progress. Fortunately, perturbations in the simulation are enough to pull the system out of the local minima so that it can achieve a global minimum at $t = 140$ s. As the number of agents increases, the frequency of local minima in $-\nu(\alpha(\mathbf{x}), \mathbf{x})$ becomes more and more of an issue for local control. The addition of obstacles into the environment adds further difficulties as it not only

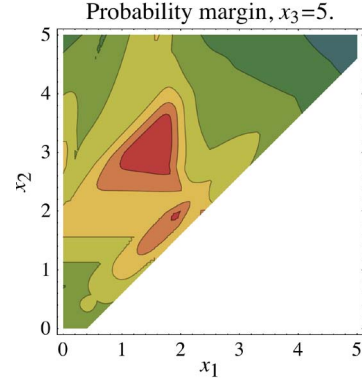


Fig. 8. Evaluation of $\nu(\alpha(\mathbf{x}), \mathbf{x})$, $\forall \mathbf{x} \in \{\mathbf{x} = (x_1, x_2, x_3) : x_1 < x_2 < x_3, x_3 = (5, 0), x_1, \text{ and } x_2 \text{ online connecting access point and } x_3\}$. Local maxima occur at $x_1 = x_2 = 1.9$ m and $x_1 = 1.5$ m, $x_2 = 3$ m.

affects feasible configurations \mathbf{x} due to collision constraints, but also introduces nonsmooth components in the underlying point-to-point communication links $R_{ij}(\mathbf{x})$.

C. Global Planning

Gradient-based control will drive the system towards local minima of (13). However, as we consider larger teams with more complicated network topologies and complex environments with obstacles, local minima become more of an issue. We propose that a global search of (6) is necessary in order to accomplish the high-level situational-awareness tasks we are interested in.

To consider global search of (6), we redefine the problem to be more amenable to motion planning approaches from the robotics literature. Let X be a bounded connected open subset of \mathbb{R}^{2N} that represents the full joint state space for the team of robots where \mathbf{x}_0 is the initial configuration of the team. In general, the goal region will be defined as $X_g = \{\mathbf{x} : \Psi(\mathbf{x}) < \Psi_{\min} + \delta\}$. In the telepresence application where a lead agent must visit the location $x_{\ell,g}$, $\Psi(\mathbf{x}) = \|x_\ell - x_{\ell,g}\|^2$ and $X_g = \{\mathbf{x} : \|x_\ell - x_{\ell,g}\| < \delta\}$. The obstacle region X_{obs} contains any configuration that places an individual robot on a physical obstacle and the infeasible

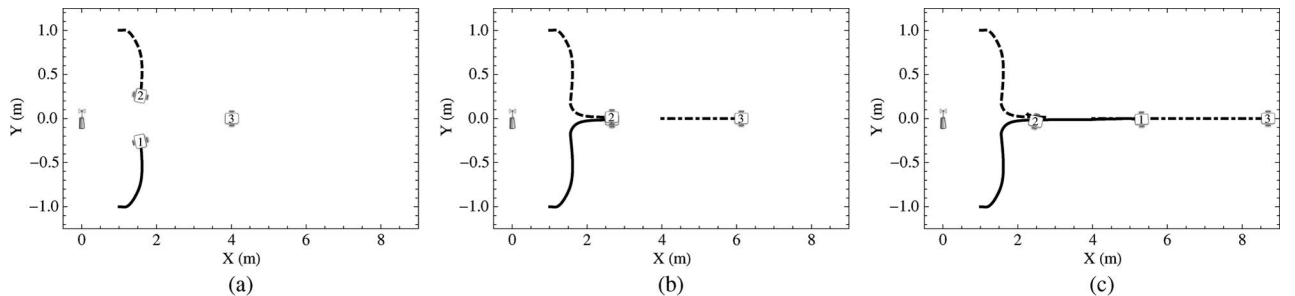


Fig. 7. Snapshots from a four robot trial. The end-to-end rates and probability of meeting the problem specifications are depicted in Fig. 9. $\Psi(\mathbf{x}(t)) = \|x_3 - (9, 0)\|$ for $t > 50$ s and $\Psi(\mathbf{x}(t)) = 0$ for $t \leq 50$ s; (a) $t = 40$ s; (b) $t = 75$ s; (c) $t = 140$ s.

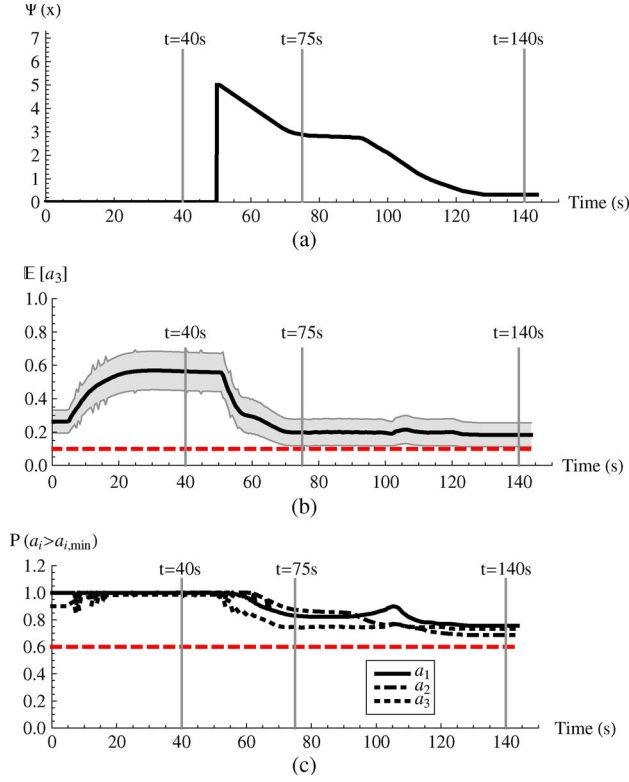


Fig. 9. (a) Convergence of $\Psi(\mathbf{x})$, (b) end-to-end rates, and (c) probability of success for the four robot trial depicted in Fig. 7.

region represents configurations where it is infeasible to satisfy the network constraint (11)

$$X_{\text{inf}} = \left\{ \mathbf{x} : \frac{\bar{a}_i^k(\boldsymbol{\alpha}, \mathbf{x}) - a_{i,\min}^k}{\sqrt{\hat{a}_i^k(\boldsymbol{\alpha}, \mathbf{x})}} < \Phi^{-1}(\epsilon) \right. \\ \left. \forall \boldsymbol{\alpha} \in \left\{ \alpha_{ij}^k : 0 \leq \alpha_{ij}^k \leq 1, \sum_{j,k} \alpha_{ij}^k \leq 1 \right\} \right\}. \quad (16)$$

The free space X_{free} is then $X \setminus (X_{\text{obs}} \cup X_{\text{inf}})$. Finally, a path in X is parameterized by a scalar $s \geq 0$ and given by $\boldsymbol{\sigma} : [0, s] \rightarrow X$. A feasible path, and solution to our global-planning problem, is then $\boldsymbol{\sigma} : [0, s] \rightarrow X_{\text{free}}$ such that $\boldsymbol{\sigma}(0) = \mathbf{x}_{\text{init}}$ and $\boldsymbol{\sigma}(s) \in X_g$.

The dimensionality of our problem and the high computational cost of verifying a state as in X_{free} makes deterministic search algorithms impractical. Instead we turn to probabilistic search methods that offer good space filling properties and efficient exploration of an unknown space like the rapidly exploring random tree (RRT) algorithms [26]. The basic structure of an RRT, as depicted in Fig. 10, is to start with an initial point \mathbf{x}_0 and expand to fully

explore the workspace, adding states in a tree structure \mathcal{T} until a point $\mathbf{x} \in X_g$ is added to the tree \mathcal{T} . At each step of the RRT algorithm, we pick a random state $\hat{\mathbf{x}} = \text{RANDOMSTATE}(X, \mathcal{T})$ and select the point $\mathbf{x}_{\min} = \text{NEAREST}(\mathcal{T}, \hat{\mathbf{x}})$ that is closest to $\hat{\mathbf{x}}$ among those that have already been added to \mathcal{T} . We then attempt a virtual drive from \mathbf{x}_{\min} to $\hat{\mathbf{x}}$ using the subroutine $\mathbf{x} = \text{EXTEND}(\mathbf{x}_{\min}, \hat{\mathbf{x}})$. The point \mathbf{x} is the first intersection of this virtual path with the border of the free space region X_{free} , or, if the border is not reached, the random point $\hat{\mathbf{x}}$. The point \mathbf{x} is then added to the tree \mathcal{T} as a branch connected to the point \mathbf{x}_{\min} that was closest to $\hat{\mathbf{x}}$ among the preexisting elements of the tree. The algorithm terminates when a point $\mathbf{x} \in X_g$ in the goal configuration is added to the tree.

A common problem encountered when applying RRT algorithms to high-dimensional state spaces is that computation of NEAREST is inefficient for increasing tree sizes. We adopt the strategy of storing the tree \mathcal{T} in a KD-tree data structure which stores states in \mathbb{R}^d by recursively subdividing based on alternating axis-aligned hyperplanes [27]. This enables approximate nearest neighbor calculations that maintain performance even as the dimension increases. However, there are two additional difficulties that arise when applying standard RRT algorithms to solve the specific high-dimensional network connectivity problem in (6): 1) the verification of feasible states as EXTEND is used to expand the tree towards $\hat{\mathbf{x}}$; and 2) the prohibitive cost of uniformly exploring X_{free} for our high-dimensional problem with slow-to-compute constraints. We discuss this two issues in the following two sections.

1) *Efficient Verification of Feasible States:* The EXTEND($\mathbf{x}_1, \mathbf{x}_2$) algorithm attempts to virtually drive the system from \mathbf{x}_1 towards \mathbf{x}_2 by successively verifying that points along the line connecting \mathbf{x}_1 and \mathbf{x}_2 are in X_{free} . It returns the state \mathbf{x} as the closest state to \mathbf{x}_2 such that all states sampled with precision $\Delta \mathbf{x}$ between \mathbf{x}_1 and \mathbf{x}_2 are in X_{free} . In traditional motion planning applications,

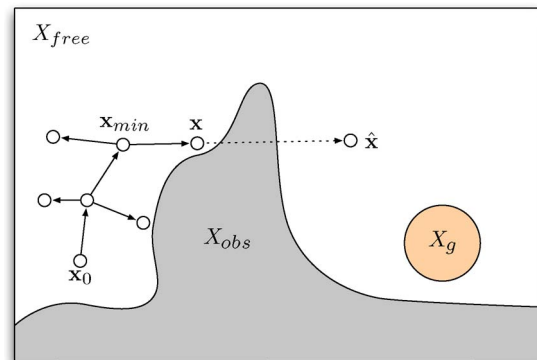


Fig. 10. Graphical depiction of the RRT search process visualized in \mathbb{R}^2 .

verification that $\mathbf{x} \in X_{\text{free}}$ is based on an algebraic constraint or collision query with a multitude of efficient methods for doing so [28]–[30]. While the necessary computation to determine $\mathbf{x} \notin X_{\text{obs}}$ is typically small, computation of $\mathbf{x} \notin X_{\text{inf}}$ requires a solution of the SOCP in Section IV and can be costly for high-dimensional systems.

Consequently, we store $\alpha(\mathbf{x})$ for every node in \mathcal{T} and recompute $\alpha(\mathbf{x})$ only when necessary to extend new states. By relying on the fact that an optimal robust routing solution $\alpha(\mathbf{x})$ will be feasible for neighboring states, it is often possible to extend \mathbf{x} towards $\hat{\mathbf{x}}$ without the costly overhead of numerical optimization.

2) *Biased Space Sampling*: Random states $\hat{\mathbf{x}}$ are chosen to sample the space $X \subset \mathbb{R}^{2N}$ according to a probability distribution $p_{\mathbf{x}}(\mathbf{x})$ representing the belief about configuration \mathbf{x} being part of a feasible path $\sigma(s)$. If nothing is known about $\sigma(s)$, we choose $p_{\mathbf{x}}(\mathbf{x})$ uniform in the space X . In general, at least the final configuration is known in that $\sigma(s) \in X_g$. We can then bias the distribution by designing $p_{\mathbf{x}}(\mathbf{x})$ to choose configurations in X_g with higher probability. Goal biasing improves efficiency of RRT algorithms by reducing the number of samples necessary to find a feasible path $\sigma(s)$ in the high-dimensional space $X \subset \mathbb{R}^{2N}$.

In many cases of interest, however, the volume of X_g is comparable to the volume of X and goal biasing offers little improvement over uniform sampling. In, for example, the telepresence application, the goal position of the leader $x_{\ell,g}$ is known, but the positions of the remaining robots are free. Thus, goal biasing would reduce the exploration cost along the components associated with x_{ℓ} but keep the cost of exploring the remaining $2(N-1)$ dimensions fixed. To further reduce exploration cost in this case we construct a prediction $\tilde{X}_g \subset X_g$ of the final configuration and bias sampling towards this prediction.

Constructing a final configuration prediction \tilde{X}_g is task specific. We describe here a method applicable to the telepresence application. To determine the configuration prediction \tilde{X}_g we determine configuration predictions $\tilde{X}_{i,g}$ for each robot and compute \tilde{X}_g as the Cartesian product of these individual sets, i.e., $\tilde{X}_g = \prod_{i=1}^N \tilde{X}_{i,g}$. Notice that for the lead robot we can make $\tilde{X}_{\ell,g} = \{x_{\ell} \in \mathbb{R}^2 : \|x_{\ell} - x_{\ell,g}\| < \delta\}$.

Observe now that $X \subset \mathbb{R}^{2N}$ is the Cartesian product $X = \prod_{i=1}^N X_i$ of the N decoupled spaces $X_i \in \mathbb{R}^2$ corresponding to each individual robot. If we further assume a homogeneous team of robots, then all robots operate in the same space $X_i = Y$, with a common set of physical obstacles Y_{obs} , and consequently a common free space $Y_{\text{free}} = Y \setminus Y_{\text{obs}}$. It follows that the joint free space X_{free} is also a Cartesian product of N identical sets Y_{free} minus those configurations for which a network cannot be established with sufficient reliability

$$X_{\text{free}} = (Y_{\text{free}})^N \setminus X_{\text{inf}}. \quad (17)$$

While infeasible network configurations are captured by X_{inf} as given in (16), X_{free} can otherwise be described by the free space of individual robots.

To exploit this observation, we first determine an obstacle-free path $\gamma : [0, s] \rightarrow \mathbb{R}^2$ such that $\gamma(0) = x_0$ is the position of the operating center and $\gamma(s) \in X_{\ell,g}$. The obstacle-free path $\gamma : [0, s] \rightarrow Y_{\text{free}}$ is split into $N-1$ equal length segments γ_k . The i th robot is then assigned to a segment by the function $k(i)$ based on Euclidian distance to its midpoint. Segments are enlarged to define the region $\tilde{X}_{i,g}$ for $i \neq 0, \ell$. Since this is a heuristic for the goal configuration, the only requirement on $\tilde{X}_{i,g}$ is that $\gamma_{k(i)} : [0, s] \rightarrow \tilde{X}_{i,g}$. A typical choice is

$$\tilde{X}_{i,g} = \left\{ x_i : \min_s \|x_i - \gamma_{k(i)}(s)\| < \tilde{d}_g \right\}$$

where \tilde{d}_g is a parameter controlling the enlarged size of $\tilde{X}_{i,g}$. The predicted final configuration is then computed as the Cartesian product $\tilde{X}_g = \prod_{i=1}^N \tilde{X}_{i,g}$. The construction of \tilde{X}_g described above is based on the heuristic that a feasible goal configuration in an environment with obstacles will resemble a line-of-sight communication chain. Increasing the size of \tilde{X}_g with large values of \tilde{d}_g limits the implication of this assumption.

D. Experimental Results

The randomized motion planner is able to find feasible configurations that allow target servicing at

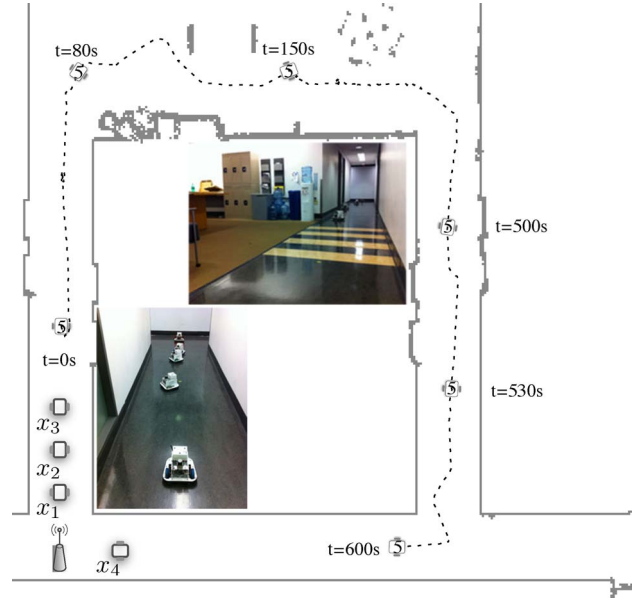


Fig. 11. The global planning task for five robots in a complex environment. We depict the series of waypoints that x_5 must visit and the initial conditions for x_1, x_2, x_3, x_4 . The inset images depict our experimental system deployed in the environment.

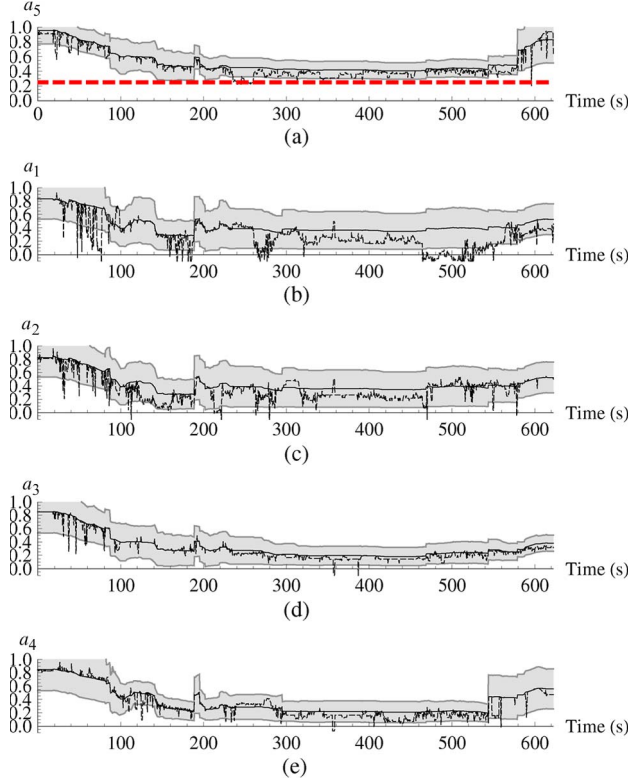


Fig. 12. The end-to-end rates of the nodes during the global planning experiment depicted in Fig. 11. In each plot, the shaded envelope depicts \hat{a}_i and the variations that occur with probability $\epsilon = 0.75$ based on \hat{a}_i while the dashed black line depicts the instantaneous rate \hat{a}_i . Note that $a_{5,\min} = 0.25$ while all other $a_{i,\min} = 0$.

positions not attainable with the local control approach from Section V-A. It can additionally provide a feasible sequence of configurations to get to the target configuration. To test the global planner on a system with one fixed access point and five robots, we introduce a sequence of task potential functions $\Psi_1(\mathbf{x}), \Psi_2(\mathbf{x}), \dots, \Psi_M(\mathbf{x})$ that

require the *lead* node x_5 to visit a sequence of positions while the remaining four robots act as relays to support end-to-end communication with the access point of $a_{5,\min} = 0.25$. We require that this end-to-end rate be satisfied with probability $\epsilon = 0.75$. The problem is made more complicated by the introduction of obstacles that not only block robot motions but also degrade received signal strength in (7) by 7.6 dBm when line-of-sight is lost.

The global planning algorithm described in Section V-C is queried to find a feasible path $\sigma_i : [0, s] \rightarrow \mathbb{R}^{10}$ for each task $\Psi_i(\mathbf{x})$ in order such that $\sigma_i(0) = \sigma_{i-1}(s)$ and $\sigma_1(0) = \mathbf{x}_{\text{init}}$. The trajectory of the lead node x_5 for the concatenation of paths $\sigma = \sigma_1 | \dots | \sigma_M$ is depicted in Fig. 11. After solving for a feasible path, $\dot{\mathbf{x}}^{\text{des}}(t)$ is computed so that $\mathbf{x}(t)$ follows σ .

We conduct an experimental deployment of five robots controlling the feasible trajectory σ for the problem depicted in Fig. 11. In this experiment, each robot is equipped with a 2.4-GHz Zigbee radio that is used to broadcast and receive packets in order to measure instantaneous received signal strength that can be used to estimate the supported communication rate $\hat{R}_{ij}(t)$ between node i and j at time t . Using these measurements, in conjunction with the network routing solution $\alpha(t)$, we can estimate the actual supported end-to-end rate at time t for each node i , $\hat{a}_i(\alpha(t), \mathbf{x}(t))$. The metric for the performance of our approach is then that each $\hat{a}_i(\alpha(t), \mathbf{x}(t)) > a_{i,\min}$ with probability ϵ across the duration of the trial.

Fig. 12 depicts the predicted $\hat{a}_i(\alpha(t), \mathbf{x}(t))$ and measured $\hat{a}_i(\alpha(t), \mathbf{x}(t))$ end-to-end rate of each node for the duration of the experiment. First, note that over the entire trajectory produced with our global planning methods, the prediction of end-to-end rates always satisfies the problem specification that $\mathbf{P}[a_i(\alpha, \mathbf{x}) \geq a_{i,\min}] \geq \epsilon$. Second, when we examine the actual end-to-end rates based on real measurements of point-to-point wireless channels we see that it is generally true that $\hat{a}_i(\alpha(t), \mathbf{x}(t)) \geq a_{i,\min}$. In fact, if we analyze this constraint across the duration of the experiment, we find that the fraction of time spent below

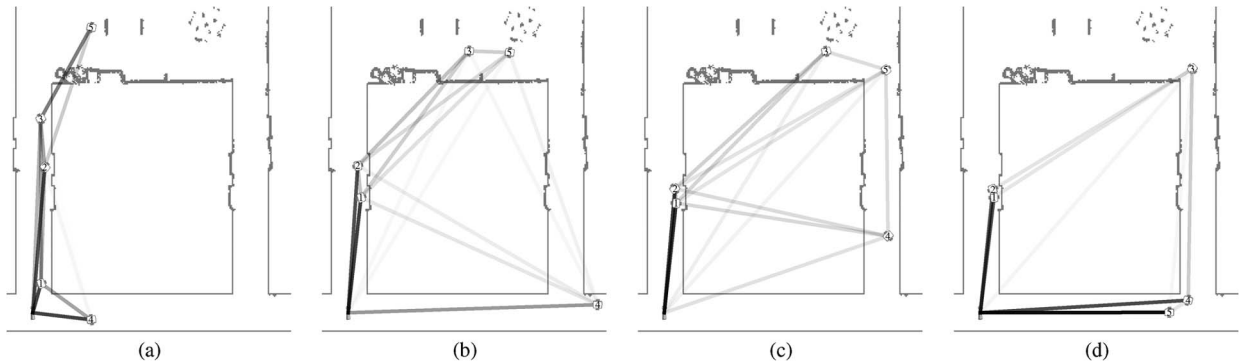


Fig. 13. Snapshots of the network configuration during the experimental deployment based on global planning to satisfy the task in Fig. 11. The end-to-end rate performance is depicted in Fig. 12. (a) $t = 100$ s; (b) $t = 278$ s; (c) $t = 482$ s; (d) $t = 622$ s.

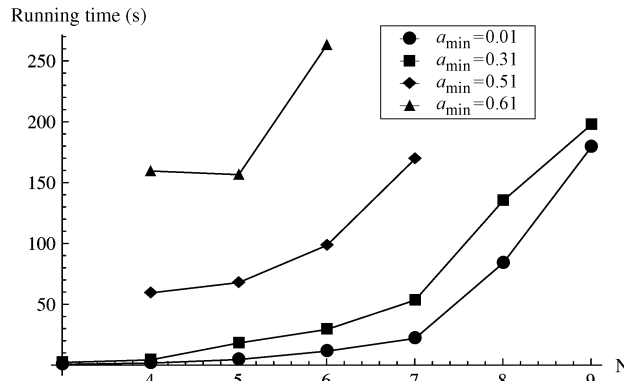


Fig. 14. Running time for a benchmark planning task computed with an increasing number of robots N and different end-to-end rate thresholds a_{\min} . Since the global planning algorithm is randomized, each point is the average running time over ten trials.

the minimum threshold for each of the instantaneous rates $\hat{a}_1, \hat{a}_2, \hat{a}_3, \hat{a}_4$, and \hat{a}_5 is 9.2%, 0.8%, 0.3%, 0.6%, and 2.9%, respectively.

Representative configurations from the experiment are depicted in Fig. 13. In Fig. 13, at $t = 100$ s, the predicted goal state \tilde{X}_g assumes the shortest line-of-sight path which is the left hallway, i.e., a similar result to the reactive methods in our local control algorithm. As the system transitions to Fig. 13(b), where the lead node x_5 has been tasked to a waypoint in the right hallway, the prediction for \tilde{X}_g shifts to a chain of relays going through the right hallway. This shift in the basic topology of \tilde{X}_g focuses on exploration of the joint state space so that x_4 moves towards a configuration that will lower the performance of the network over the short term. As node x_5 completes the desired loop, it utilizes x_4 as a relay channel and is able to maintain the desired end-to-end rate. It is this dramatic shift in network topology that highlights the advantage of our global planning approach as we are able to accomplish continuous end-to-end rate maintenance that would not be possible with a purely reactive method.

With regards to the running time of the randomized global planning algorithm, we note that it is difficult to characterize the performance of randomized search algorithms. One factor is the complexity of X_{free} which is de-

termined both by physical obstacles in the environment as well as the constraints placed on feasible network configurations, i.e., the solution to $\alpha(\mathbf{x})$. Fig. 14 depicts the running time for a benchmark environment as we increase the dimension of the problem N by adding robots to the system. We also vary the end-to-end rate threshold a_{\min} that must be maintained for the lead node to demonstrate how more strict network requirements also increase complexity of the search space.

VI. CONCLUSION

We propose a system architecture that provides end-to-end connectivity for autonomous teams of robots as they pursue operator-assigned tasks. This architecture is composed of a cyber component that determines the configuration of the wireless network and a physical component that handles mobility. Because the performance of point-to-point wireless links is difficult to predict, we adopt a stochastic model for supported rates and develop optimal robust solutions to the wireless routing problem. The strengths of the proposed approach are that: 1) network availability takes into account specific thresholds on the end-to-end rates of individual nodes; 2) considering the stochastic nature of communication channels network availability is further defined in probabilistic terms; 3) by specifically searching for robust solutions, we obtain configurations with spatial diversity and increased probability of success in the face of difficult to predict communication channels.

Robust routing solutions are integrated with a physical component that handles mobility either through local control or global planning. Local controllers converge to solutions that are local minima of the concurrent mobility and network routing problem. The global planner performs a randomized biased search in the space of spatial configurations in an attempt to jointly solve the mobility and optimal network routing problems. We perform experiments to demonstrate that the global planning algorithm succeeds in navigating a complex environment while ensuring that end-to-end communication rates meet or exceed prescribed values within a target failure tolerance. Global planners are able to discover dramatic shifts in communication topology that allow for continuous communication that is not possible with purely local methods. ■

REFERENCES

- [1] J. Fink, "Communication for teams of networked robots," Ph.D. dissertation, Elect. Syst. Eng., Univ. Pennsylvania, Philadelphia, PA, 2011.
- [2] S. Thrun, W. Burgard, and D. Fox, Probabilistic Robotics. Cambridge, MA: MIT Press, 2005.
- [3] M. C. DeGennaro and A. Jadbabaie, "Decentralized control of connectivity for multi-agent systems," in Proc. 45th IEEE Conf. Decision Control, San Diego, CA, Dec. 2006, pp. 3628–3633.
- [4] M. Ji and M. Egerstedt, "Distributed coordination control of multiagent systems while preserving connectedness," IEEE Trans. Robot., vol. 23, no. 4, pp. 693–703, Aug. 2007.
- [5] M. Zavlanos and G. Pappas, "Potential fields for maintaining connectivity of mobile networks," IEEE Trans. Robot., vol. 23, no. 4, pp. 812–816, Aug. 2007.
- [6] E. Stump, A. Jadbabaie, and V. Kumar, "Connectivity management in mobile robot teams," in Proc. IEEE Int. Conf. Robot. Autom., Pasadena, CA, May 2008, pp. 1525–1530.
- [7] M. Schuresko and J. Cortes, "Distributed motion constraints for algebraic connectivity of robotic networks," J. Intell. Robot. Syst., vol. 56, no. 1–2, pp. 99–126, Sep. 2009.
- [8] D. P. Spanos and R. M. Murray, "Motion planning with wireless network constraints," in Proc. Amer. Control Conf., Portland, OR, Jun. 2005, pp. 87–92.
- [9] G. Notarstefano, K. Savla, F. Bullo, and A. Jadbabaie, "Maintaining limited-range connectivity among second-order agents," in Proc. Amer. Control Conf., Minneapolis, MN, Jun. 2006, pp. 2124–2129.
- [10] E. Stump, "Control for localization and visibility maintenance of an independent agent using robotic teams," Ph.D. dissertation, Mech. Eng. Appl. Mech., Univ. Pennsylvania, Philadelphia, PA, 2009.

- [11] C. Perkins, E. Belding-Royer, and S. Das, "Rfc3561: Ad hoc on-demand distance vector (aodv) routing," Internet RFCs, 2003.
- [12] D. Johnson and D. Maltz, "Dynamic source routing in ad hoc wireless networks," *Mobile Comput.*, no. 353, pp. 153–181, 1996.
- [13] H. Lundgren, E. Nordstrom, and C. Tschudin, "The gray zone problem in IEEE 802.11b based ad hoc networks," *ACM SIGMOBILE Mobile Comput. Commun. Rev.*, vol. 6, no. 3, pp. 104–105, Jul. 2002.
- [14] A. Ribeiro, Z.-Q. Luo, N. D. Sidiropoulos, and G. B. Giannakis, "Modelling and optimization of stochastic routing for wireless multihop networks," in *Proc. 26th Annu. Joint Conf. IEEE Comput. Commun. Soc.*, Anchorage, AK, May 2007, pp. 1748–1756.
- [15] D. DeCouto, D. Aguayo, J. Bicket, and R. Morris, "A high-throughput path metric for multihop wireless routing," in *Proc. Int. ACM Conf. Mobile Comput. Netw.*, San Diego, CA, Sep. 2006, pp. 134–146.
- [16] I. Stojmenovic, A. Nayak, and J. Kuruva, "Design guidelines for routing protocols in ad hoc and sensor networks with a realistic physical layer," *IEEE Commun. Mag.*, vol. 43, no. 3, pp. 101–106, Mar. 2005.
- [17] A. Hsieh, A. Cowley, V. Kumar, and C. J. Taylor, "Towards the deployment of a mobile robot network with end-to-end performance guarantees," in *Proc. IEEE Int. Conf. Robot. Autom.*, Orlando, FL, May 16–18, 2006, pp. 2085–2090.
- [18] Y. Mostofi, "Communication-aware motion planning in fading environments," in *Proc. IEEE Int. Conf. Robot. Autom.*, 2008, pp. 3169–3174.
- [19] M. Zavlanos, A. Ribeiro, and G. Pappas, "Mobility and routing control in networks of robots," in *Proc. Conf. Decision Control*, Atlanta, GA, Dec. 15–17, 2010, pp. 7545–7550.
- [20] Y. Mostofi, A. Gonzalez-Ruiz, A. Gaffarkhah, and L. Ding, "Characterization and modeling of wireless channels for networked robotic and control systems—A comprehensive overview," in *Proc. IEEE/RSJ Int. Conf. Intell. Robot. Syst.*, 2009, pp. 4849–4854.
- [21] J. Fink, N. Michael, A. Kushleyev, and V. Kumar, "Experimental characterization of radio signal propagation in indoor environments with application to estimation and control," in *Proc. Int. Conf. Intell. Robot. Syst.*, St. Louis, MO, Oct. 2009, pp. 2834–2839.
- [22] J. Fink and V. Kumar, "Online methods for radio signal mapping with mobile robots," in *Proc. IEEE Int. Conf. Robot. Autom.*, Anchorage, AK, May 2010, pp. 1940–1945.
- [23] R. Shorey, A. Ananda, M. C. Chan, and W. T. Ooi, *Mobile, Wireless and Sensor Networks: Technology, Applications and Future Directions*. New York: Wiley, 2006.
- [24] L. R. Klein, *A Textbook of Econometrics*. Evanston, IL: Row, Peterson, 1953.
- [25] Y. Wu, A. Ribeiro, and G. B. Giannakis, "Robust routing in wireless multi-hop networks," in *Proc. Conf. Inf. Sci. Syst.*, Mar. 14–16, 2007, pp. 637–642.
- [26] J. Kuffner, Jr. and S. LaValle, "RRT-connect: An efficient approach to single-query path planning," in *Proc. IEEE Int. Conf. Robot. Autom.*, 2000, vol. 2, pp. 995–1001.
- [27] A. Atramentov and S. M. LaValle, "Efficient nearest neighbor searching for motion planning," in *Proc. IEEE Int. Conf. Robot. Autom.*, 2002, pp. 632–637.
- [28] M. C. Lin, D. Manocha, J. Cohen, and S. Gottschalk, "Collision detection: Algorithms and applications," in *Algorithms for Robotic Motion and Manipulation*, J.-P. Laumond and M. H. Overmars, Eds. Wellesley, MA: A.K. Peters, 1997, pp. 129–142.
- [29] B. Mirtich, "V-Clip: Fast and robust polyhedral collision detection," Mitsubishi Electron. Res. Lab., Tech. Rep. TR97-05, 1997.
- [30] M. C. Lin and J. F. Canny, "Efficient algorithms for incremental distance computation," in *Proc. IEEE Int. Conf. Robot. Autom.*, 1991, pp. 1008–1014.

ABOUT THE AUTHORS

Jonathan Fink (Student Member, IEEE) received the B.S. degree in electrical and computer systems engineering from Rensselaer Polytechnic Institute, Troy, NY, 2004 and the Ph.D. degree in electrical and systems engineering from the University of Pennsylvania, Philadelphia, in 2011.

He is a Research Scientist with the U.S. Army Research Laboratory, Adelphi, MD. His research interests include collaboration and planning for multirobot systems with emphasis on communication modeling and planning for network connectivity.

Dr. Fink has received the best student paper award at the 2009 Robotics: Science and Systems Conference (RSS 2009).



Alejandro Ribeiro (Member, IEEE) received the B.Sc. degree in electrical engineering from the Universidad de la Republica Oriental del Uruguay, Montevideo, Uruguay, in 1998 and the M.Sc. and Ph.D. degrees in electrical engineering from the Department of Electrical and Computer Engineering, the University of Minnesota, Minneapolis, in 2005 and 2007, respectively.

Since 2008, he has been an Assistant Professor at the Department of Electrical and Systems Engineering, University of Pennsylvania, Philadelphia. From 1998 to 2003, he was a member of the technical staff at Bellsouth Montevideo. His research interests lie in the areas of communication, signal processing, and networking. His current research focuses on wireless communications and networking, distributed signal processing, and wireless sensor networks.

Dr. Ribeiro is a Fulbright scholar and the recipient of a National Science Foundation CAREER award in 2010 and best student paper awards at the 2005 and 2006 International Conference on Acoustics, Speech, and Signal Processing (ICASSP).



Vijay Kumar (Fellow, IEEE) received the Ph.D. degree in mechanical engineering from The Ohio State University, Columbus, in 1987.

He is the UPS Foundation Professor and the Deputy Dean for Education in the School of Engineering and Applied Science, University of Pennsylvania, Philadelphia. He has been on the Faculty in the Department of Mechanical Engineering and Applied Mechanics with a secondary appointment in the Department of Computer and Information Science at the University of Pennsylvania since 1987.

Dr. Kumar is a Fellow of the American Society of Mechanical Engineers (ASME). He has served on the editorial boards of the IEEE TRANSACTIONS ON ROBOTICS AND AUTOMATION, *Journal of Franklin Institute*, the IEEE TRANSACTIONS ON AUTOMATION SCIENCE AND ENGINEERING, *ASME Journal of Mechanical Design*, the *ASME Journal of Mechanisms and Robotics*, and the *Springer Tracts in Advanced Robotics (STAR)*. He is the recipient of the 1991 National Science Foundation Presidential Young Investigator award, the Lindback Award for Distinguished Teaching, and the 1997 Freudenstein Award for significant accomplishments in mechanisms and robotics. He has won best paper awards at the Distributed Autonomous Robotic Systems 2002, the International Conference on Robotics and Automation 2004, the International Conference on Robotics and Automation 2008, the Robotics: Science and Systems 2009, and the Distributed Autonomous Robotic Systems 2010. He is a Distinguished Lecturer in the IEEE Robotics and Automation Society and an elected member of the Robotics and Automation Society Administrative Committee.



Biographies of ARL Authors

Jin-Hee Cho joined ARL in 2009 as a computer scientist with a research focus in developing network protocols for trustworthy tactical cyber space using multi-disciplinary approaches and analyzing their performance and security. Dr. Cho actively collaborates on trust research with ARL's partners on the Network Science Collaborative Technology Alliance (NS CTA) and International Technology Alliance (ITA), in addition to scientists in ARL's Computational and Information Sciences Directorate (CISD) and Sensors and Electron Devices Directorate (SEDD). Wider research interests include wireless mobile networks, sensor networks, delay tolerant networks, secure group communications, key management, intrusion detection, trust management, social/cognitive networks, market-based economic modeling, game theory, and resource allocation. Dr. Cho earned a B.A. from Ewha Womans University, Seoul, Korea and a Masters degree in social work from Washington University in St. Louis, Missouri, before earning a M.S. and Ph.D. in Computer Science from Virginia Polytechnic Institute and State University. She has published over 40 technical articles in the areas of networking and telecommunications, and received a best paper award in 2009 at the Institute of Electrical and Electronics Engineers (IEEE)/International Federation for Information Processing (IFIP) International Symposium on Trusted Computing and Communications (TrustCom09), Vancouver, Canada. She is a member of the IEEE and the Association for Computing Machinery.

Amy M. Dagro is a mechanical engineer in the Soldier Protection Sciences Branch of the Weapons and Materials Research Directorate. Ms. Dagro earned her B.S. in biomedical engineering from Johns Hopkins University and her M.S. in mechanical engineering from Columbia University. She began her research in computational biomechanics with Dr. Reuben Kraft in 2010, and became an ARL civilian employee in 2011. Ms. Dagro leads ARL's research in blast and ballistic effects to the brain.

Jonathan Fink is a researcher in the Asset Control and Behavior Branch, Information Sciences Division of the Computational and Information Sciences Directorate (CISD). He received his Ph.D. from the University of Pennsylvania in 2011, where he worked in the General Robotics, Automation, Sensing and Perception (GRASP) Laboratory on communication-constrained planning for teams of networked robots. Since joining ARL, he has contributed to the development and experimental testing of fundamental capabilities for autonomous ground robots including techniques for mapping and navigation in militarily relevant environments. Dr. Fink has also continued his graduate research into multi-agent planning that takes place at the intersection of networking and robotics through collaborations with the Network Sciences Division of CISD. He is a member of the Institute of Electrical and Electronics Engineers and has published over 20 technical articles in the field of robotics and autonomous systems.

Piotr Franaszczuk joined ARL in July 2011 as a Senior Research Scientist in Neuroscience, with interests focusing on computational methods of signal analysis, neural modeling, and development of large-scale biologically realistic computational models of brain structures. He received his M.S. and Ph.D. in physics from the University of Warsaw in 1978 and 1988, respectively; his doctoral thesis received an award from the Polish Ministry of Science and Education. Dr. Franaszczuk was a Bennett Fellow in neurophysiology and a faculty member at the University of Maryland School of Medicine. He also taught in the Department of Biomedical Physics, University of Warsaw. Since 1999, Dr. Franaszczuk has been a faculty member in the Department of Neurology at the Johns Hopkins University School of Medicine; until June 2011, he co-directed their Epilepsy Research Laboratory. Dr. Franaszczuk has authored or co-authored over 100 journal and conference papers and 12 book chapters. He has been a reviewer for over 10 scientific journals and, since 2005, has served as grants reviewer on several National Institutes of Health scientific review panels.

Russell Harmon is Director of the International Research Office of the U.S. Army Engineer Research and Development Center (ERDC-IRO), where he conducts international science and technology engagement. Prior to joining ERDC-IRO in September 2011, Dr. Harmon was a Program Manager at the Research Development and Engineering Command-ARL Army Research Office, where he managed the extramural basic research program in terrestrial sciences. A geochemist who has worked at the NASA Manned Spacecraft Center, the Scottish Universities Research and Reactor Center, and UK Natural Environment Research Council Isotope Geosciences Laboratory, Dr. Harmon has held faculty positions at Michigan State University; Southern Methodist University; and North Carolina State University, where he is currently an adjunct faculty member in the Marine, Earth, and Atmospheric Sciences Department. He is a Fellow of the Geological Society of America, National Speleological Society, and ARL. Dr. Harmon has authored or coauthored more than 200 peer-reviewed publications and remains actively engaged in geochemical and geospatial research. He holds a B.A. from the University of Texas, a M.S. from the Pennsylvania State University, and a Ph.D. from McMaster University.

Kimberly A. Pollard is a research biologist with the Perceptual Sciences Branch of the Human Research and Engineering Directorate. She earned a B.A. in biology from Rice University and a Ph.D. in biology from UCLA; her dissertation focused on acoustic communication and social complexity in animal behavior. After an Oak Ridge Associated Universities postdoctoral fellowship at ARL from 2009-2012, Dr. Pollard joined ARL as a civilian employee. She currently studies nontraditional forms of communication and perception, including bone-conducted hearing, bone conduction and vibrotactile communication devices, and the role of olfaction in warfare.

Ananthram Swami is the Army's Senior Research Scientist (ST) for Network Science, with interests in the study of interactions and co-evolution; prediction; and control of inter-dependent networks including mobile ad hoc wireless networks, sensor networks, and social networks. Dr. Swami earned a B.Tech. from IIT-Bombay, a M.S. from Rice University, and a Ph.D. from the University of Southern California, all in electrical engineering. Dr. Swami has published more than 300 journal and conference papers in the areas of signal processing, communication networks, and network science; holds three patents; developed a Matlab toolbox on non-Gaussian signal processing; and has co-led multiple tutorials on cognitive networking. He is a Fellow of the Institute of Electrical and Electronics Engineers and an ARL Fellow. His research is currently supported by the Defense Threat Reduction Agency and the Office of the Secretary of Defense.

Don Torrieri is an ARL engineer with primary interests in wireless communication systems, spread spectrum, adaptive arrays, and signal processing. He received M.S. and Ph.D. degrees in physics and electrical engineering, respectively, from the University of Maryland; a M.S. in electrophysics from the Polytechnic University; and a B.S. in electrical engineering from the Massachusetts Institute of Technology. Dr. Torrieri analyzed electronic systems at the Naval Research Laboratory, where he received three Group Achievement awards and three Research Publication awards. Since 1977, he has worked for the Department of the Army, where he spent sixteen years doing classified work for the Survivability Management Office and its predecessors. He wrote many blue-ribbon committee and red-team reports on Army communication systems, and is the author of many books, journal articles, conference papers, and technical and classified reports. He taught graduate courses at both Johns Hopkins University and George Washington University. His awards include the Military Communications Technical Achievement Award and the Best Paper Award of the Institute of Electrical and Electronics Engineers Military Communications Conference. In 1989, he was selected as one of the original Fellows of the Army Laboratory Command, predecessor to the Army Research Laboratory.

Bruce J. West is Chief Scientist Mathematics (ST) of the U.S. Army Research Office, Information Science Directorate. His research focuses on the development of mathematical tools necessary to understand complex phenomena as they apply to the nascent discipline of Network Science. Since 2006, he has led the development of the ARL External Nonlinear Science program. Dr. West graduated with a Ph.D. in nuclear physics from the University of Rochester, was a founding member of the La Jolla Institute, and served as Chair and Professor of Physics at the University of North Texas. He earned the Department of the Army's Research and Development Achievement Award for Technical Excellence, ARL Publication Award, Commander's Award for Civilian Service, and the prestigious Wilks Award in statistics. He has been recognized by Cambridge Who's Who as one of the top 101 Industry Experts and has twice received their Professional of the Year Award in Applied Physical Science and Mathematics. In 2012, Dr. West received the President's Meritorious Rank Award. He has produced more than 350 publications, including 13 books, and his published research has received more than 12,000 citations with an h-factor of 53. Dr. West is a Fellow of the American Physical Society, the American Association for the Advancement of Science, and ARL.

